25 May 2007 | $10

Science

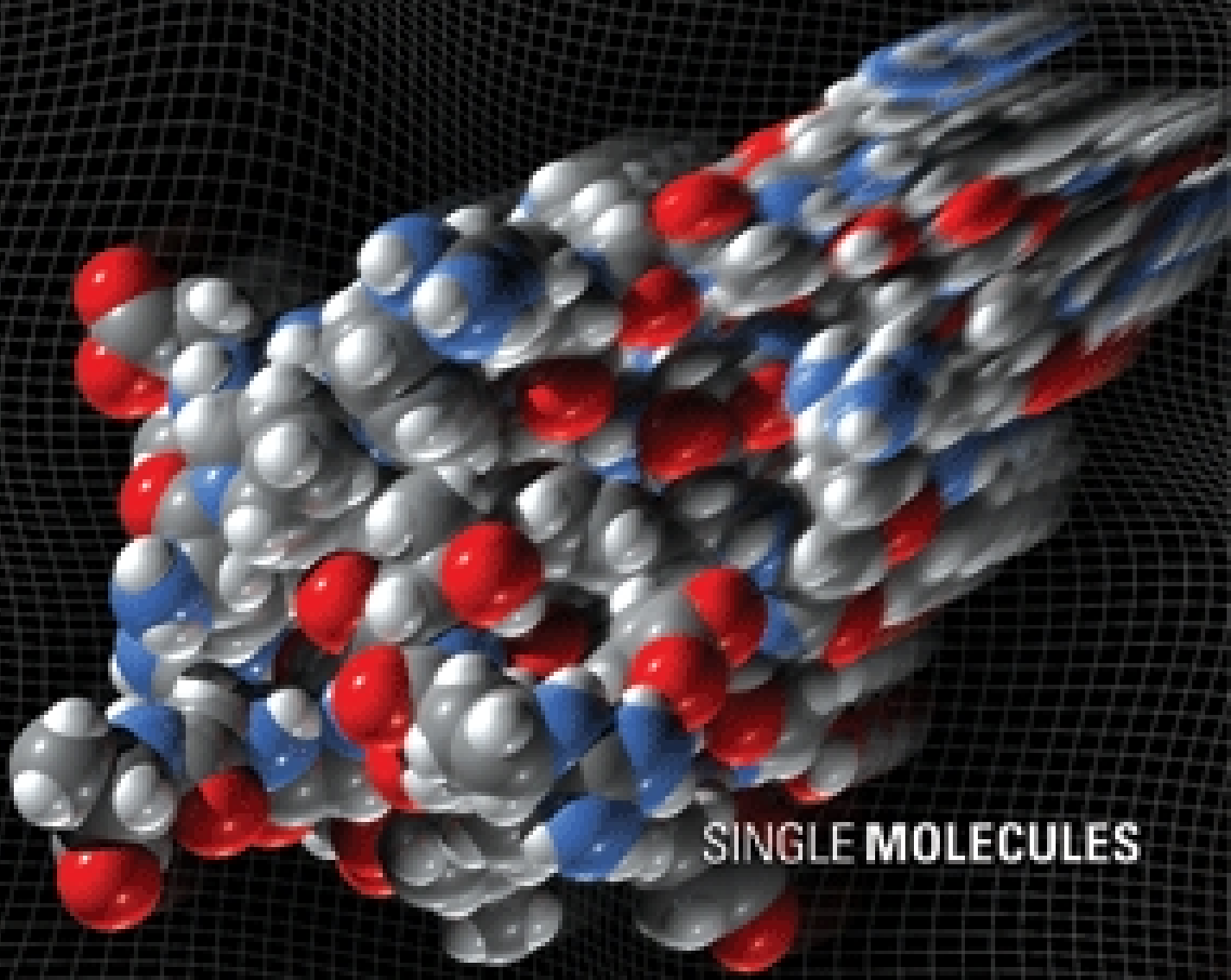

SINGLE **MOLECULES**

AAAS

EDITED BY STELLA HURTLEY AND PHIL SZUROMI

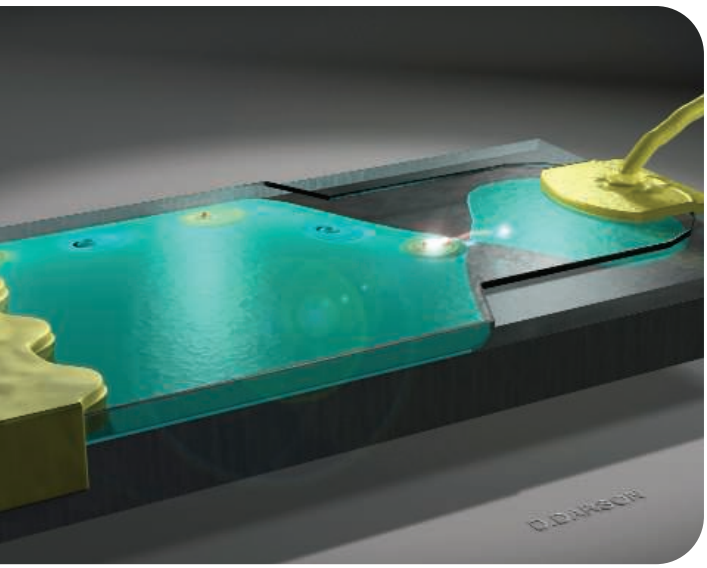

<< Coherent Single-Electron Source

Just as the availability of single photons has enabled the development of secure communications via quantum cryptography, it is expected that an electronic analog would allow similar quantum coherent manipulations in an electronic circuit. **Fève *et al.*** (p. 1169; see the Perspective by **Giblin**) have developed a coherent single-electron source in which the electrons are emitted from a quantum dot into a quantum-coherent two-dimensional conductor. The trigger is the application of a potential step to the quantum dot. The source can also be used as an alternating-current standard for possible applications in metrology.

Dark Heavy Dwarfs

When a massive galaxy collides with another, it can jettison gas that subsequently clumps up to form a crowd of surrounding dwarf galaxies. Theoretical models predict that such tidally produced dwarfs should not contain dark matter, so their gravity should tally with the stars and gas within them. **Bournaud *et al.*** (p. 1166, published online 10 May; see the Perspective by **Elmegreen**) have used gas motions to measure the masses of a series of dwarf galaxies lying in a ring around a massive galaxy that has recently experienced a collision. They find evidence for dark matter within the dwarfs—double that expected from the stars alone. If this extra material is in the form of unseen cold molecular gas originating in the massive galaxy, then it must be more common than now thought and could account for a part of the missing baryons in the universe.

Drying the American Southwest

The large human population and widespread industrial and agricultural economies of the southwestern United States and northern Mexico depend on the cheap and ready availability of water that may be affected by changes in precipitation, evaporation, groundwater storage, and river flow as climate warms. **Seager *et al.*** (p. 1181, published online 5 April) show that a broad array of climate models agree that this region will dry substantially during the next century and that conditions as dry as those of the Dust Bowl will become the normal ones in the region. These changes would be caused by atmospheric circulation patterns that create a poleward expansion of the subtropical dry zones. This aridification should be unlike any climate state that exists in the instrumental record.

Direct Aromatic Coupling

Linking two aromatic rings is a key reaction in organic synthesis that generally requires one coupling partner to be modified with a halide and the other appended with an electropositive group, such as boron or tin. **Stuart and Fagnou** (p. 1172; see the Perspective by **Ellman**) describe a palladium catalyst that promotes the direct coupling of benzene to indoles without the need for any additional activating groups. The reaction proceeds by C–H bond activation and proves remarkably selective for the cross-coupled product; no benzene or indole dimers are observed. High regioselectivity for bonding to the 3-carbon position of a wide range of substituted indoles was seen.

Early Iron Deficit

The timing and processes of the formation of the solar system can be mapped out by measuring long-lived isotopes in meteorites. One such system is ^{60}Fe-^{60}Ni, with a half-life of 1.5 million years; ^{60}Fe only forms in stars. **Bizzarro *et al.*** (p. 1178; see the news story by **Kerr**) find that differentiated meteorites show a very minor deficit of ^{60}Fe compared to Earth, Mars, and chondrites. The authors suggest that the oldest solar system material formed in the absence of ^{60}Fe and that ^{60}Fe was injected into the protoplanetary disk about 1 million years after the solar system formed. This material may have come from a neighboring star, such as a particularly iron-rich supernova.

Engineering Herbicide Resistance

Engineering of crop plants to be resistant to herbicides can allow agricultural strategies that are kinder to the land, with reduced need to till the earth. However, herbicides that are currently in widespread use are starting to lose effectiveness because of increases in resistant weed populations. **Behrens *et al.*** (p. 1185; see the news story by **Service**) describe how crop plants can be engineered to be resistant to dicamba, a well-known environmentally friendly herbicide. By transferring a bacterial gene to the crop plants, the authors engineered plants resistant to the herbicide. However, for the time being at least, weeds are not resistant and die back.

DNA Damage-Response Teams

DNA damage is often a key event in triggering malignancy (see the Perspective by **Petrini**). Much of the cellular response to DNA damage is mediated by two protein kinases, ATM (ataxia telangiectasia mutated) and ATR (ATM and Rad3-related). **Matsuoka *et al.*** (p. 1160) report a proteomic screen that implicates more than 700 proteins in the cellular response to DNA damage caused by ionizing radiation. Antibodies that recognized the phosphorylated forms of peptides containing consensus phosphorylation sites recognized by ATM or ATR were used to search for

Continued on page 1095

CREDITS (TOP TO BOTTOM): D. DARSON/LABORATOIRE PIERRE AIGRAIN, ECOLE NORMALE SUPÉRIEURE, PARIS; BEHRENS *ET AL.*

Published by AAAS

Continued from page 1093

previously unrecognized substrates. These results provide a resource for identification of previously unrecognized proteins that function in control of DNA damage in mammalian cells. Three reports, **Wang *et al*.** (p. 1194), **Sobhian *et al*.** (p. 1198), and **Kim *et al*.** (p. 1202), describe a complex of proteins that interact with the breast cancer–associated tumor suppressor gene product BRCA1 and implicate covalent modification of proteins by ubiquitination in regulating the functions of BRCA1 and its partners in the cellular response to DNA damage. A complex of BRCA1 with the protein Bard1 is known to have ubiquitin ligase activity. In the present work, BRCA1 formed a complex at sites of DNA damage with RAP80, a protein with a ubiquitin-interacting motif domain, and RAP80 contributed to localization of BRCA1 to sites of DNA damage. A third protein, Abraxas, appears to mediate interaction of BRCA1 with RAP80. BRCA1 complexes also contained BRCC36, a deubiquitinating enzyme. The DNA damage checkpoint that halts division of cells with damaged DNA was defective in cells lacking RAP80. Thus, the BRCA1-Abraxas-RAP80 complex appears to target BRCA1 to sites of DNA damage.

Marijuana and Developmental Damage

The effects of marijuana are mediated by cannabinoid receptors on neurons in the brain, and a causal relationship between marijuana use during pregnancy and permanent cognitive deficits in the offspring has been identified. **Berghuis *et al*.** (p. 1212) now define the molecular hierarchy that controls marijuana actions within single neurons and show that activation of cannabinoid receptors by their natural ligands controls the establishment of functional connections between neurons in the brain. These findings define the cellular context through which prenatal marijuana use perturbs brain development.

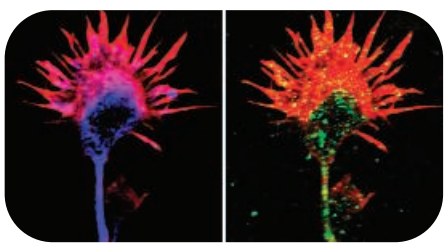

CREDIT: BERGHUIS *ET AL.*

Real-Life Transcription Factor Dynamics

Transcription factors bind to specific sites on chromosomal DNA to regulate gene expression. How transcription factors find their target DNA is generally thought to occur through a combination of diffusion through the cytoplasm as well as diffusion along DNA segments. **Elf *et al.*** (p. 1191) use single-molecule techniques to study the specific and nonspecific binding of a model transcription factor, the *lac* repressor, in living *Escherichia coli*. *Lac* repressor searching for an operator spends 90% of its time diffusing along DNA. If the repressor does not find an operator within 5 milliseconds, it falls off the DNA and diffuses through the cytoplasm to bind to another DNA segment. Such single-molecule approaches will move us toward a quantitative understanding of biochemical processes as they occur in living cells.

From Membrane Curvature to Fusion

Soluble NSF attachment protein receptor (SNARE)–dependent tethering and zippering of vesicles to target membranes promotes vesicle fusion with target membranes. In the synapse, the relevant SNAREs are synaptobrevin2, syntaxin1, and SNAP25, but synaptic vesicle fusion also requires other proteins. **Martens *et al.*** (p. 1205, published online 3 May) show that SNARE-dependent tethering and zippering is only part of the bilayer fusion mechanism—synaptotagmin is also needed. In cell-free experiments, synaptotagmin-1 induced positive membrane curvature in a calcium-dependent manner, which made the membrane more fusogenic and helped bring membranes into contact with each other.

Motor Motion Captured

Myosin V is a two-headed molecular motor that alternates the positions of its leading and trailing heads to move unidirectionally along actin filaments in a "hand-over-hand" mechanism. **Shiroguchi and Kinosita** (p. 1208) have now directly visualized this walking motion. Each head is attached to a long and stiff neck. The adenosine triphosphate–dependent power stroke causes the neck of the leading head, which is bound to the actin track, to lean forward. The trailing head is lifted from the actin track, and a free swivel connection at the neck-neck junction allows the lifted neck to undergo extensive Brownian rotation in a diffusive search for the next binding site. The forward movement of the leading neck moves the pivot point forward so that the unbound head lands at a forward site.

Stephen D. Hopper is director of the Royal Botanic Gardens, Kew, UK.

New Life for Systematics

EARLIER THIS MONTH, THE LAUNCH OF THE ENCYCLOPEDIA OF LIFE, AN ELECTRONIC database for the currently known 1.8 million species of the world, was announced. This coincides with the tercentenary of the birth of Linnaeus, the Swedish scientist who laid the foundation for modern systematics that predictively names and classifies organisms. At last, a complete inventory of Earth's biota is considered achievable. This goal has injected new life into the notion of systematic science as the very underpinning of biodiversity conservation. But do we need such systematics, and is a biodiversity inventory—probably at a cost comparable to that of the human genome project—really essential for human and planetary well-being?

If contributions by thousands of taxonomists dating to Linnaeus are considered a collective enterprise, then systematics is surely a "big science" that has forged a fundamental knowledge base for all of biology. This discipline has provided not only scientific names that enable meaningful organization and dissemination of vast information, but also a robust foundation for comparative studies, with names ordered in a predictive classification based on phylogenetic patterns inferred from fossil, DNA, and other evidence. As Linnaeus said,"each object ought to be clearly grasped and clearly named, for if one neglects this, the great amount of things will necessarily overwhelm us and, lacking a common language, all exchange of knowledge will be in vain."

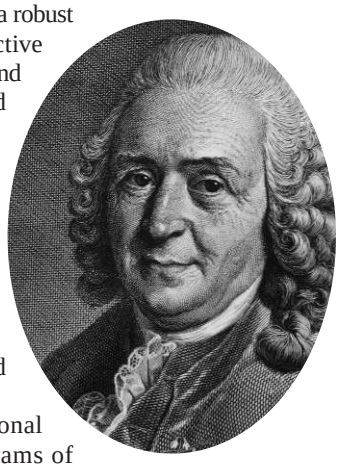

Currently, the Earth's life inventory reflects a nearly global list for birds and mammals, but not of plant species. And many regions on Earth, especially in the Southern Hemisphere, remain poorly surveyed. The deep sea, soil, forest canopy, and inaccessible terrain remain the least explored habitats. Perhaps only 10% of fungi are named. Estimates for most invertebrates and microorganisms, including bacteria and archaebacteria, are even lower.

The good news is that with powerful molecular and computational approaches, strategic training, field work, and accelerated programs of documentation and data access in herbaria, museums, and DNA laboratories, a complete inventory may be only a few decades away. This global effort will rely on new cadres of young systematists circumscribing and classifying species at an unprecedented rate.

We need to complete this work, sooner rather than later, with priority on the most threatened organisms and on those most relevant to human livelihoods. An obvious reason is to help avert a looming extinction crisis by ensuring that species are named and conserved. Other pressing issues such as climate change (for which we need to address a rapidly changing carbon cycle) require assessing and encouraging plant diversity. It is time for a moratorium on further destruction of the world's wild vegetation and for much more science-based repair and restoration of what remains. We also need new approaches to agricultural, urban, and suburban living that will ensure a sustainable future with biodiversity. Such efforts should emphasize locally appropriate, multipurpose plantings. In fact, much of the information needed to support such new approaches already exists in botanic gardens, museums, and the scientific literature. The Encyclopedia of Life will make such information readily accessible to a broad range of users and hopefully promote integration of conservation efforts and other collaborations. However, the Encylopedia will defeat its fundamental purpose if it conveys a sense of an inventory job completed. It is just the beginning for much of Earth's poorly documented biota, and generating the supporting systematic data remains essential.

There are many young scientists wanting to contribute to understanding the Earth's biodiversity, but there are insufficient employment opportunities and teaching and research resources in place to support their enthusiasm. This has to change if we are to encourage future generations to explore the power of biodiversity to help us live sustainably.

We all would be immeasurably diminished if we sat idly by, witness to ongoing biological extinction, in a changing world where rare species may be tomorrow's salvation. Unless we curtail devastation of our biosphere, support systematic science, and harness available data along the way in global inventories and predictive classifications, life's great tapestry will indeed unravel, to our collective peril.

–Stephen D. Hopper

10.1126/science.1144898

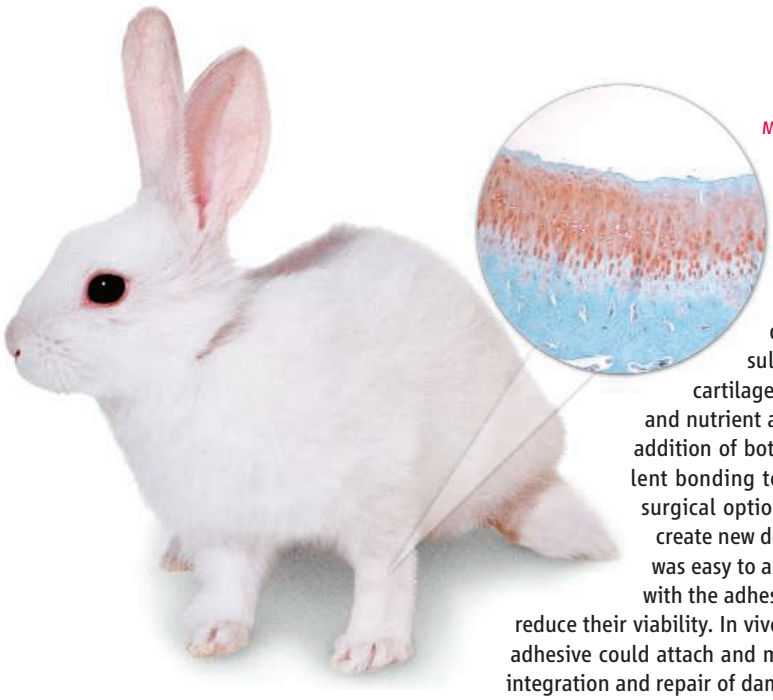

MATERIALS SCIENCE

Superglues for Tissues

A long-standing issue in the development of regenerative tissues is their attachment and integration into the body. Adhesives for this purpose have often shown poor biocompatibility or insufficient bonding strength. Wang *et al.* have devised an adhesive based on the biopolymer chondroitin sulfate (CS), a major component of the extracellular matrix of cartilage. CS has shown anti-inflammatory activity, and aids in water and nutrient absorption as well as wound healing. The CS was modified by addition of both a methacrylate and an aldehyde group, allowing for covalent bonding to both a biomaterial scaffold and a tissue surface. Current surgical options for grafting onto cartilage use sutures or tacks and thus create new defects in the tissue. In vitro tests showed that the CS adhesive was easy to apply and did not damage the cartilage tissue. Contact of cells with the adhesive in either the native tissue or a biomaterial matrix did not reduce their viability. In vivo experiments in mice, rabbits, and goats showed that the CS adhesive could attach and mechanically reinforce a cell-seeded hydrogel, and aid in the integration and repair of damaged tissue (shown above left for a rabbit). — MSL

Nat. Mater. **6**, 385 (2007).

BIOTECHNOLOGY

Straining Pathogen Sequences

Several methods have been explored as platforms for the rapid detection of infectious pathogens, including mass spectrometric analysis of amplified nucleic acid sequences and several microarray schemes. Most of these assays have been tested against a small subset of pathogens, and often do not resolve pathogen subtypes or have the ability to identify emerging strains.

Lin *et al*. tested a microarray, the respiratory pathogen microarray version 1 (RPM v.1), against 424 nasal wash samples collected from military personnel in the Washington, DC, area from December 2004 to February 2005 (influenza season). Human DNA and RNA were removed from these samples before carrying out a single amplification step for viral and bacterial pathogen sequences and subsequent hybridization against 20 pathogens (some of which are represented by more than one strain). Software-based reassembly of incomplete or disconnected sequences improved the identification of pathogens, with an accuracy >98% compared to independent reference assays. In the 58 specimens that contained multiple pathogens, an increase was seen in bacterial colonizers when viral infection was present. In 250 of the samples positive for influenza A, nucleotide variations in the hemagglutinin gene were identified that allowed a phylogenetic tree of strain evolution to be assembled. In 14% of the samples, pathogens were not identified, even though the patients had flu-like symptoms; this finding likely reflects the underrepresentation of rhinovirus and enterovirus sequences in the microarray tiles. — PDS

PLoS ONE **2**, e419 (2007).

APPLIED PHYSICS

Reversible Atomic Memories

A key requirement for quantum information processing applications such as quantum communication or computation is the ability to reliably store, manipulate, and retrieve a piece of information, encoded, for example, in the polarization state of a single photon. Among the many routes presently being explored to achieve these goals is cavity quantum electrodynamics (c-QED), which entails trapping a single atom in a cavity and inducing it to interact with a single photon. In this vein, Boozer *et al.* show that they are able to imprint the state of a single photon onto a single trapped Cs atom, store it for an appreciable fraction of the lifetime of the atom in the trap, and then retrieve that information again sometime later in the form of another photon and send it on its way. They verify that the whole process is coherent, providing further support for c-QED–based systems as promising candidates for nodes in a quantum information processing network. — ISO

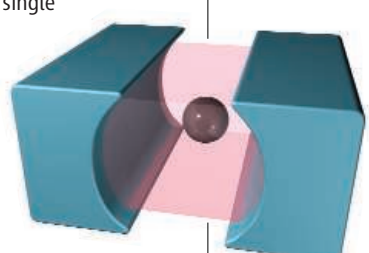

A cavity trap.

Phys. Rev. Lett. **98**, 193601 (2007).

CHEMISTRY

Boron Swap

In boron neutron capture therapy, the radioactive decay induced by neutron collisions with ^{10}B nuclei is channeled toward tumor destruction. Implementation of the technique remains challenging because of the need to devise boron compounds that selectively concentrate in tumors while remaining relatively nontoxic overall. Moreover, ^{10}B is one-fourth as abundant as the heavier ^{11}B isotope, which is inert to neutron bombardment. Thus, synthetic routes to various candidate molecules are hampered by the need for isotopic enrichment.

In a step toward improved efficiency, Yinghuai *et al.* have found that ruthenium nanoparticles can catalyze the isotopic exchange of boron atoms from excess $^{10}B_2H_6$ to the larger $B_{10}H_{14}$ cluster. They prepared the catalyst by reduction of a metallocene precursor in a biphasic mixture of ethylene glycol and a trialkylphosphonium ionic liquid (chosen because imidazolium systems can poison the catalysis). After six successive treatments of the decaborane with the catalyst and diborane, combined Raman and mass spectral analysis were consistent with ~90% ^{10}B enrichment of the larger cluster. The mechanism is as yet unresolved. — JSY

J. Am. Chem. Soc. **129**, 6507 (2007).

Continued on page 1101

Continued from page 1099

BIOCHEMISTRY

Pulling on a Trailor Hitch

Building transmembrane gradients of small molecules, such as protons and alkali metal ions, is the job of ion-transporting enzymes, which convert adenosine triphosphate into an electrochemical potential; this stored energy is then used by coupled transporters for the import of nutrients and the export of waste materials. Gram-negative bacteria feature inner and outer membranes. Members of the porin family of membrane proteins reside in the outer membrane and allow small molecules to pass across freely, but this makes it impossible to establish electrochemical gradients. How then do these bacteria transmit power to the outer-membrane transporters (which collect essential substances such as vitamin B_{12} and chelated iron)?

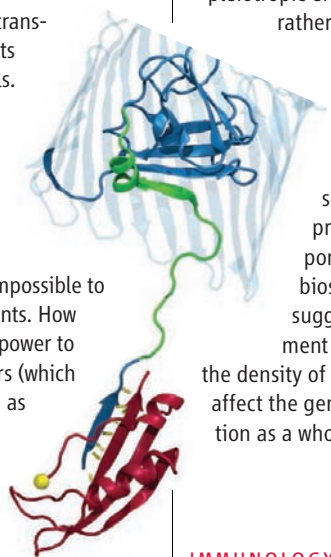

Pulling (at the yellow ball) on TonB (red) begins to unravel the BtuB plug (green/blue).

Using steered molecular dynamics (for more, see Sotomayor and Schulten, Reviews, this issue, p. 1144), Gumbart *et al.* have looked at the interaction between the barrel-like outer-membrane protein BtuB (the vitamin B_{12} transporter) and the inner-membrane protein TonB, which is known to provide the energy that drives the inward transport of many substrates across the outer membrane. They start from a configuration that is based on the crystal structure of a TonB fragment in complex with the TonB-binding region of BtuB, and find that pulling (computationally) on the TonB portion does not distort it. Furthermore, through a network of hydrogen bonds oriented perpendicularly to the direction of applied force, TonB holds tightly to one end of the BtuB lumenal domain, which plugs the barrel. Pulling harder begins to unfold the plug and loosens it enough to allow vitamin B_{12} to squeeze by, but the simulated forces are somewhat higher than experimental measurements of what it takes to unravel a protein. — GJC

Biophys. J. **92**, 10.1529/biophysj.107.104158 (2007).

CREDIT: GUMBART ET AL., *BIOPHYS. J.* **92**, 10.1529/BIOPHYS. J. 107.104158 (2007).

GENETICS

Love Thy Neighbor

Genes not only direct the expression of traits (phenotype) in an individual, but can also influence the phenotypes of neighbors. Mutic and Wolf have examined quantitative trait loci (QTL) governing size, growth, and fitness in *Arabidopsis* and whether they affect an individual directly as well as its neighbors indirectly. Of 15 QTL in the former category, they found that 13 showed indirect effects on the expression of traits in nearby plants. Unexpectedly, most of the pleiotropic effects were positively correlated rather than opposite in sign, as might have been expected on the basis of competition for resources. Facilitative or mutualistic relationships could involve interplant signaling, and several of the loci did map in the proximity of genes encoding components in the ethylene and auxin biosynthetic pathways. These results suggest that for plants, the environment in which they grow, especially the density of conspecific individuals, may affect the genetic composition of the population as a whole. — LMZ

Mol. Ecol. **16**, 10.1111/j.1365-294X.2007.03259x (2007).

IMMUNOLOGY

Selecting the Thymic Rank and File

During their passage through the thymus, developing T cells are selected on the basis of their capacity to recognize foreign antigens while remaining tolerant of the body's own constituents. This is achieved in part through interacting (in the thymic medulla) with specialized epithelial cells that offer up small samples of self proteins whose expression is largely restricted to other tissues. This supplemental expression of the self proteins is regulated by the transcription factor Aire and contributes to preventing autoimmunity.

Rossi *et al.* used organ cultures derived from fetal mouse thymus to ascertain that hematopoietic cells already known to induce peripheral lymphoid tissue, and aptly named lymphoid tissue inducing (LTi) cells, also regulate the development of a subset of medullary epithelial cells and their expression of Aire. This depended on the receptor activator nuclear factor–κB ligand (RANKL), and autoimmunity-like symptoms ensued after the transplantation of RANK-deficient thymus into athymic mice. Previous studies have reported that another tumor necrosis factor family member (lymphotoxin-α) is expressed in LTi cells and has similar effects, so resolving the contributions of each in regulating immunological tolerance will be of interest. — SJS

J. Exp. Med. **204**, 10.1084/jem.20062497 (2007).

Country Cooking

A wood-burning stove that uses sound to generate electricity and refrigeration could one day make waves in developing countries. That's the hope of an international team headed by engineer Paul Riley of the University of Nottingham in the United Kingdom. This month, the U.K. government and the U.S.'s Los Alamos National Laboratory in New Mexico awarded the team almost $4 million to develop a Stove for Cooking, Refrigeration, and Electricity (SCORE). The appliance would rely on external combustion, such as a wood fire, to heat one end of a tube of compressed gas, inducing sound waves that can be harnessed to generate enough electricity to power a light bulb and a small refrigeration unit.

The principle isn't new, but the technology has been too expensive for general use, says thermoacoustician Steven Garrett of Pennsylvania State University in State College.

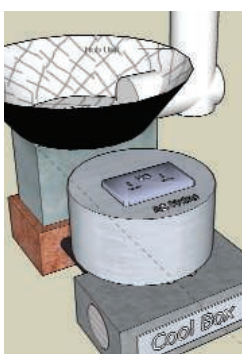

The SCORE team hopes to make it cost-effective with cheaper materials: Compressed air could replace high-pressure helium, for example. "If anybody can pull this off, it's got to be these guys," says Garrett. The device may not cut down on wood consumption, but tests suggest that it will make use of up to 30% of a wood fire's energy, much more than a typical stove's 7% efficiency.

Bring Out Your Dead … Elsewhere

Kenny Johns respects the dead. He just doesn't want them lying about near his airport.

Last month, Provost Perry Moore of Texas State University in San Marcos was finishing plans to build a 7-hectare forensic anthropology research field lab—a "body farm" that would use decomposing human remains to aid in the investigation of outdoor crime scenes—less than a mile from the San Marcos Municipal Airport. But now the university is scouting a new location in response to concerns that circling buzzards would threaten aircraft there. Airport manager Johns notes that one buzzard alone can easily destroy a small plane's engine or shatter a larger one's windshield.

The body farm is to be the cornerstone for a new doctoral program in forensic anthropology, with up to a dozen corpses in various states of decomposition, says university spokesperson Mark Hendricks. Texas State hopes it will open by fall semester. If so, it will be the third in the nation, joining sites in Tennessee (*Science*, 11 August 2000, p. 855) and North Carolina. Forensic anthropologist Jerry Melbye foresees no difficulty in obtaining research material. "Many people are interested" in the university's new donation program, he says.

A New Destination For Dinomaniacs

Those plucky penguins—already passé. Whales and polar bears—just fads. But dinosaurs have kept their scaly grip on our imaginations. The new DinoBase from the University of Bristol in the U.K. offers plenty of information for everyone from dino dabblers to devotees who want to check whether there's such an animal as "Elvisaurus." (There isn't.)

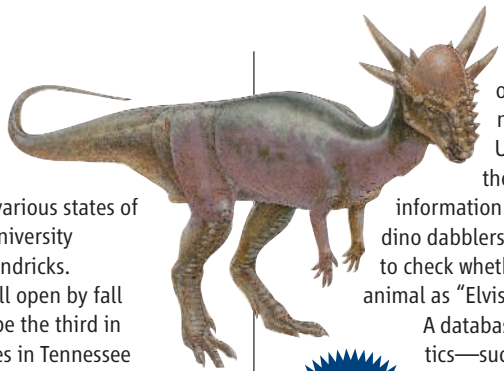

NET WATCH

A database holds vital statistics—such as length, weight, and time span—for several hundred dinosaur species, including *Stygimoloch spinifer* (above), a 3-meter-long herbivore from what is now Montana. Its elaborate headgear might have served as a weapon or as a lure for mates. Visitors can tour a gallery of dino art or dig into the site's forum for announcements of fresh finds and the latest on current debates, such as whether commercial fossil hunters hurt or help paleontology. >> dinobase.gly.bris.ac.uk

Better to Give Than to Receive

Many primates spend up to a fifth of their time going through one another's fur. This grooming behavior helps keep them healthy both physically and mentally—relaxing the animals and helping cement social relationships. Now a study of the so-called Barbary apes finds that the stress reduction benefits the groomers even more than the groomed.

A team led by primatologists Ann MacLarnon and Stuart Semple of Roehampton University in London followed 11 female macaques on the Rock of Gibraltar over 2 months, recording grooming behavior and collecting feces to analyze the stress hormone cortisol. The animals who tended others the most—both in terms of time spent and number of animals groomed—had the lowest cortisol levels, they report in the 7 June issue of *Biology Letters*. The busiest groomer, who averaged almost 16 minutes per hour, had half the cortisol levels of one that only spent a few minutes at it.

For those on the receiving end, there was no correlation between cortisol levels and grooming. The team suggests that more active groomers are less stressed because they have stronger social support networks. Psychologist Robin Dunbar of the University of Liverpool in the U.K. says, "This is a very timely study because we really don't understand what makes grooming so worthwhile for groomers."

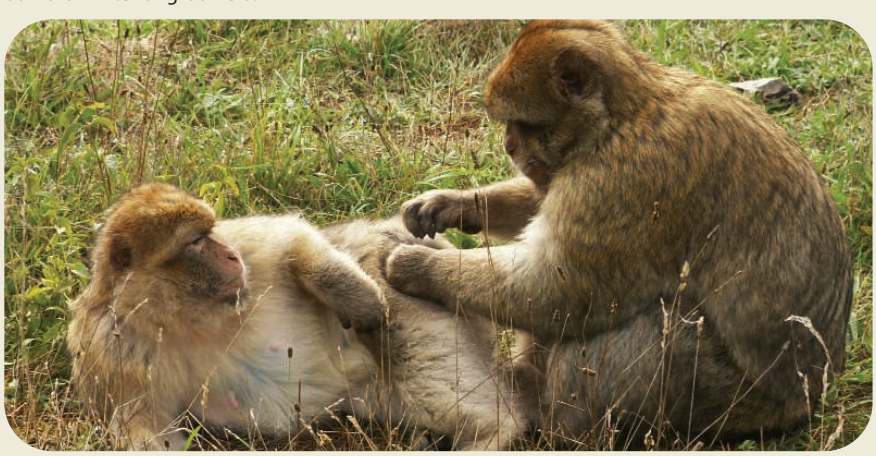

CREDITS (TOP TO BOTTOM): JAMES ROBINS/JR-ILLUSTRATION.CO.UK; PAUL RILEY; DANA PFEFFERLE

EDITED BY YUDHIJIT BHATTACHARJEE

Pioneers

DR. LINNAEUS, I PRESUME? Swedish botanist Carl Linnaeus guaranteed himself a place in scientific history when he founded the field of taxonomy. This week, on the 300th anniversary of his birth, Linnaeus is alive and well in public memory, thanks at least in part to Hans Odöö.

A 54-year-old Swedish writer, Odöö has built a successful second career impersonating Linnaeus. Since 1994, he has given 2600 performances before audiences including the Swedish royal family, scientists, and schoolchildren. Last week, he donned his Linnaeus costume for the opening of an exhibition of erotic art at Leufsta Bruk, a manor outside of Uppsala built in the 1740s by Charles De Geer, an entomologist and friend of Linnaeus. "It's a great honor for you to meet me," he announced, invoking the scholar's comically egoistic personality. "I wrote five autobiographies and 72 books, many of which I reviewed anonymously." In a typical performance, Odöö narrates anecdotes from Linnaeus's life.

Odöö says stepping into Linnaeus's character has become second nature. For example, Odöö reacts in mock anger when somebody in the audience accuses him of mistreating his wife: "Who told you that? That's false." And he beams with pleasure when somebody praises Linnaeus's poetry. "I feel like I'm trapped in Linnaeus," says Odöö, who began playing the botanist while conducting tours at the Linnaeus Garden. "Sometimes I'll get in a cab to go to the airport, in my normal clothes, and the driver will say, 'Ah, Linnaeus is traveling today.' "

CREDITS (TOP TO BOTTOM): LINNÉA BERGMAN; LES TODD/DUKE UNIVERSITY PHOTOGRAPHY; HENRY REGES/COCORAHS

Got a tip for this page? E-mail people@aaas.org

ON CAMPUS

GLIB. When 23-year-old Chen Jia-Zhong graduated from Northwest Normal University in Lanzhou, China, with a bachelor's degree last summer, he found himself without a job. Undeterred, he hit the Chinese academic lecture circuit.

Presenting himself as a "Harvard Ph.D.," a "Loeb Scholar," or a "Harvard professor" working on brane cosmology—the idea that the universe is confined to a hypersurface (brane) within a higher-dimensional space—Chen got himself invited to give seminars at a half-dozen top Chinese institutions, including the Yunnan Astronomical Observatory; Shanghai Jiaotong, Fudan, and Donghua universities, all in Shanghai; and Zhejiang University, whose Center of Mathematical Sciences (CMS) made Chen a short-term visiting scholar, paying him a modest stipend. Last month, after Chen's credentials were questioned by an anonymous posting on a Chinese-language electronic bulletin board, CMS issued a statement saying it had asked Chen to leave after verifying that his Harvard Ph.D. was "fabricated." Faculty members at Harvard University's Laboratory for Particle Physics and Cosmology, to which Chen claimed affiliation, told *Science* they have no knowledge of him.

However, Zhejiang University officials say it was not Chen's claimed Harvard connection that got their attention but rather the papers he wrote. CMS Director Liu Kefeng says Chen has admitted his mistakes but deserves a chance at pursuing actual graduate studies because he "is very devoted to understanding cosmology."

MOVERS

MSRI HEAD. Duke University mathematician Robert Bryant has been named director of the Mathematical Sciences Research Institute (MSRI) in Berkeley, California.

A differential geometer, Bryant served as chair of MSRI's board from 2001 to 2004. He has also been a visiting professor at the institute, founded in 1982 and funded primarily by the National Science Foundation. "MSRI had an enormous influence on my own career, so I think it can be a positive influence on the developing careers of mathematicians around the world," says Bryant. He says he will push to expand MSRI's outreach in fields outside of mathematics, such as biology and medicine, so as to improve the exchange between the math and science communities.

Bryant starts his 5-year term on 1 August, succeeding David Eisenbud.

Milestones >>

MOVED TO ACT. A climatologist haunted by a killer flash flood in his hometown of Fort Collins, Colorado, has been named an "Environmental Hero" for his role in building the Community Collaborative Rain, Hail and Snow Network (CoCoRaHS).

Nolan Doesken, Colorado's state climatologist and a researcher at Colorado State University, was at home the night of 28 July 1997 when it rained more than 35 centimeters in 5 hours. He assumed that the National Weather Service would alert people, but no one called NWS to report the extreme rainfall, which wasn't picked up by radar. "I could have done something, and I didn't," Doesken says about the flood, in which five people died. "It was life-changing."

Within a year, Doesken had organized local citizens to report precipitation in their backyards via the Web—useful data not only when floods are looming but also for climatologists studying drought and water supply. Thanks to federal and state funding, the network now includes 4000 volunteers in 18 states. In December, the National Oceanic and Atmospheric Administration gave him a $200,000 grant to keep CoCoRaHS growing, and last month it honored him. "People are thrilled to help scientists when you make it easy for them to do that," he says.

Published by AAAS

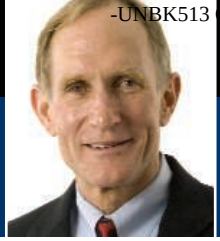

Nobelist considers Senate run
1112

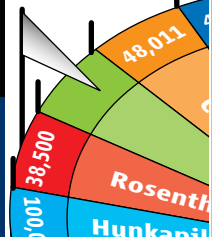

A final gene count?
1113

AVIAN INFLUENZA

Indonesia Earns Flu Accord At World Health Assembly

Indonesia's battle to ensure access to flu vaccines that could save the lives of millions of its citizens during a pandemic reached a fevered climax earlier this week at the World Health Assembly (WHA), the annual meeting of member states of the World Health Organization (WHO) in Geneva, Switzerland. Supported by other developing countries, Indonesia demanded action and once again employed its valuable bargaining chip: cooperation in a 55-year-old global network of virus sample sharing that acts as the cornerstone of the world's defenses against flu.

As *Science* went to press, a WHA committee had approved a draft resolution, hammered out in 5 days of long and often tense meetings, that called on WHO to do more to help developing nations obtain access to vaccines and proposed establishing an international working group to change the rules of the virus-sharing system. (The draft was widely expected to be approved by the entire WHA on Wednesday.) "It was very, very, very difficult to reach an agreement," Indonesian Health Minister Siti Fadilah Supari, who participated in the negotiations, told *Science*.

Under the Global Influenza Surveillance Network, countries send virus samples from the field to one of four WHO centers in London, Australia, Tokyo, and Melbourne. At these sites, analyses of the viruses help track viral evolution and resistance to drugs, judge the risk of a pandemic, and, most critically, guide the development of vaccines.

Indonesia, a continuing H5N1 hot spot, has rebelled against the system, which Supari describes as "very unfair" because Indonesia receives no guarantees about access to pandemic vaccines in return for participating in the surveillance network. Nine Western countries currently have influenza vaccine factories, but experts say they won't be able to produce nearly enough vaccine for the entire world. Indonesia is also angered that researchers in other countries were taking out patents based in part on Indonesian viruses.

In January, Indonesia pulled out of the flu-sharing system, denying WHO new influenza strains. That led to intensive talks between the country and WHO officials—and failed promises from Indonesia to resume sharing. WHO, which shares Indonesia's concerns but says the country's actions are a "threat to global health security," has put forth several proposals to improve access to vaccines. For instance, it has developed a technology-transfer plan that could eventually give some developing nations their own flu vaccine manufacturing capacity; in April, it awarded six countries—Brazil, India, Indonesia, Mexico, Thailand, and Vietnam—a total of $18 million in seed money to develop the necessary plans. WHO has also proposed to form a stockpile of H5N1 vaccine that could be used in developing countries as needed, but its size is uncertain.

Standing her ground. Indonesian Health Minister Siti Fadilah Supari says the current virus-sharing system is "very unfair."

CREDIT: DENIS BALIBOUSE/REUTERS

At the start of the WHA, Supari announced that Indonesia had resumed sharing influenza viruses, and WHO confirms that the network has recently received three samples. But Indonesia also jumped on the opportunity of the WHA to press its case. It pointed to the 1992 Convention on Biological Diversity, which stipulates that a country has to share in the benefits if others make use of its genetic resources. Carlos Correa, an intellectual-property expert at the University of Buenos Aires, agrees that the convention applies to all genetic resources, including viruses. "Indonesia has a fair claim," he concludes. WHO is still consulting legal experts about the issue, says Assistant Director-General David Heymann.

The arguments about exactly what developing nations should get in return for their participation in the flu surveillance network took place behind closed doors in a "drafting group" composed of several dozen countries. Supari says the United States in particular opposed Indonesia's demands. (David Hohman, the health attaché at the U.S. mission in Geneva, was not available for comment.)

The draft resolution that finally emerged late Tuesday afternoon calls on WHO member states to keep sharing their viruses, but it also asks WHO to take a range of measures to ensure that developing countries can produce their own vaccine and to guarantee "fair and equitable distribution" if a pandemic occurs. The resolution also calls for representatives from 24 countries around the world to propose changes to the rules of the global surveillance system that would benefit the developing world. To address another sore point, the group would have to ensure increased participation of scientists from developing countries in flu research and wider recognition of their role.

Supari says Indonesia got most of what it wanted. But David Fedson, a retired pharma executive and a longtime advocate for pandemic preparedness, says the resolution doesn't do enough to address the fundamental problem: the scarcity of vaccine production capacity. "If I were the minister of health of Indonesia, I would not be satisfied," Fedson says. **–MARTIN ENSERINK**

With reporting by Dennis Normile.

Crucial weed killer losing its punch
1114

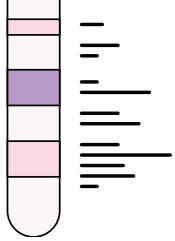

New views of gene regulation
1120

INFECTIOUS DISEASE

Resurgence of Yellow Fever in Africa Prompts a Counterattack

Experts tracking the resurgence of yellow fever across Africa worry about one scenario in particular: simultaneous outbreaks in several of the continent's teeming megacities. In Lagos, Nigeria, with its population of 15 million, an estimated 4.5 million could be infected, says Sylvie Briand of the World Health Organization (WHO), and international stockpiles of vaccine would be rapidly exhausted fighting the outbreak. And that's just for one city.

An urban outbreak in Africa would be "a catastrophe," says David Heymann, WHO's assistant director-general for communicable diseases.

That's why WHO and partner agencies are launching a major initiative to protect the populations at highest risk for yellow fever epidemics. Announced at the World Health Assembly last week and kick-started with $58 million from the Global Alliance for Vaccines and Immunization (GAVI)—a public-private partnership established in 1999 to strengthen immunization and boost the use of new and underused vaccines—the goal is to immunize more than 48 million people in 12 West African countries over the next 5 years. That should be enough, they hope, to reestablish an immune barrier against this often-fatal hemorrhagic fever.

To yellow fever expert Thomas Monath, it's a no-brainer. "This is a very small expenditure that could save a great number of lives," says Monath, a partner with the Kleiner Perkins Caufield & Byers venture-capital group.

Transmitted by the bite of an infected mosquito, yellow fever decimated New Orleans and other cities in the early 1900s. But thanks largely to vector control and the introduction of a remarkably safe and effective vaccine, known as 17D, yellow fever has disappeared from the developed world. But within the tropical belt in Africa and South America, it remains "a very dangerous disease, with a high lethality," says Monath.

At first, the fever and chills can be relatively mild and easily confused with other tropical diseases. But about 15% to 20% of patients progress to the so-called toxic phase, when jaundice rapidly sets in, the kidneys fail, and massive hemorrhaging from the mouth, nose, and eyes begins. Roughly 20% to 50% of those with severe disease die. It is a "horrible thing" to witness, says Monath.

An ounce of prevention. A man receives a vaccination against yellow fever during a mass campaign in Agoto, 150 km northwest of Togo's capital, on 23 February 2007.

In the French-speaking West African countries now considered at highest risk, widespread vaccination campaigns between 1940 and 1960 virtually wiped out yellow fever. But it came back with a vengeance in the 1990s, after the campaigns had halted and a generation had grown up without immunity, says Briand, project manager of the yellow fever initiative at WHO. At the same time, rapid urbanization and population movements have brought susceptible people into closer proximity with infected mosquitoes such as *Aedes aegypti*, an urban mosquito that breeds in water jugs, discarded tires, and other urban detritus.

Since 2000, 18 countries in Africa have reported cases of yellow fever. West Africa is the hardest hit region, with worrisome outbreaks occurring in four major cities. A 2001 outbreak in Abidjan, Côte d'Ivoire, required immunizing 2.6 million people in 12 days, a huge logistical challenge, says Briand. Yellow fever's exact toll is hard to measure, but WHO estimates there are now up to 200,000 cases a year, with 30,000 deaths.

With the increasing threat, many at-risk countries added yellow fever vaccine to their package of routine childhood immunizations. But as outbreaks continued, it quickly became clear that a strategy relying on routine immunization alone would take too long to build up sufficient population immunity, says Michel Zaffran, deputy executive secretary of the GAVI Alliance. What's more, adds Zaffran, limited supplies of vaccine have been diverted from routine immunization programs to deal with emergencies.

As part of the new initiative, the GAVI Alliance will increase the emergency stockpile from 6 million to about 11 million doses a year. UNICEF will negotiate with vaccine manufacturers to ensure production of the 50 million or so doses for the 12-country prevention campaign. The GAVI Alliance will foot the bill for the vaccine, syringes, and half of the operational costs; the 12 countries have committed to raising the rest of the money for the vaccination campaigns, says Zaffran.

It will take commitment, as these countries face other health problems including cholera and meningitis, not to mention malaria, tuberculosis, and AIDS, says Briand. But yellow fever vaccine is one of the best buys out there, she adds, as a single dose of vaccine can confer immunity for decades, perhaps a lifetime. "It is the most effective vaccine we have," agrees Monath.

Already, the 12 countries, with technical assistance from WHO, have begun conducting risk assessments to help determine which districts in each country are at greatest risk and should receive priority vaccination. At the World Health Assembly, other countries were asking whether they could be included in the plan. That may be a possibility later on, says Zaffran, but first, "we need to show it is working." **–LESLIE ROBERTS**

CREDIT: NOEL KOKOU TADEGNON/REUTERS

Published by AAAS

GEOCHEMISTRY

Isotopes Suggest Solar System Formed in a Rough Neighborhood

Astrophysicists have long assumed that a supernova played midwife to the solar system. An exploding star could have collapsed wispy interstellar gas and dust into a dense swirling disk to get things started and loaded it with the intensely radioactive aluminum that cooked up chunks of the nascent solar system. But on page 1178, a group of cosmochemists presents evidence that the sun was born into an even more brutal environment.

What's rougher than a supernova next door? A supernova that, before detonating, blasts its neighborhood with eons' worth of energy in an astrophysical instant. Astrophysicists think such behavior is typical of stars dozens of times as massive as the sun. And if one of those massive stars was so close, our home system must have formed in a dense, swirling cluster of stars. The newborn solar system's neighborhood would have been "a much more violent and turbulent" place than had been assumed, says theoretical astrophysicist Alan Boss of the Carnegie Institution of Washington's Department of Terrestrial Magnetism.

The evidence for our violent beginnings comes from some of the most precise isotopic measurements yet of nickel in samples of Earth, Mars, and meteorites. Martin Bizzarro of the University of Copenhagen in Denmark and colleagues had gone looking for signs of radioactive iron-60 in the oldest meteorite from an asteroid that had melted in the earliest solar system. The iron-60 itself wouldn't be there. It was forged in the heart of a star and spewed into the material that would become the solar system after the star went supernova. Then the iron-60 promptly decayed away into nickel-60. So the researchers looked for the nickel "ash" using a type of mass spectrometer that can ionize all the nickel in a sample. That allows sensitive detection of the isotopes following magnetic separation. They also analyzed each sample many times to drive down the analytical error.

To their surprise, Bizzarro and colleagues did not find the expected extra dose of the iron-60 marker. Instead, the samples contained less nickel-60 than found in younger meteorites. Apparently, the solar system's shot of iron-60 had not arrived when this old meteorite solidified about a million years after the solar system's start. Yet radioactive aluminum-26—also made in stars—had been there all along.

"Iron-60 and aluminum-26 don't seem to be coming into the solar system at the same time," says Bizzarro. "There's only one stellar environment that can do that: very, very massive stars." The bigger the star, the faster it burns its hydrogen fuel. If it has more than 30 times the mass of the sun, a star will blow away much of its outer layers—including its aluminum-26—in the last million years of its brief life of 4 million years or so. That stellar wind could have driven the collapse of interstellar gas and dust to form our sun and the protoplanetary disk that once surrounded it. Later, the massive star exploded, spewing iron-60 from its deep interior.

Just like home? As massive stars (off top of image) blast the Eagle nebula's gas and dust, they may be triggering formation of planetary systems.

The Bizzarro paper "has a great story to tell … based on some truly spectacular nickel-isotope data," says cosmochemist Meenakshi Wadhwa of Arizona State University in Tempe. There is a caveat, however. Three other labs, including her own, have analyzed similar samples with similar levels of precision—albeit using a different data-analysis approach—without finding a deficit of nickel-60 in the oldest samples. Wadhwa still believes the authors make "a pretty good case for the accuracy and precision of their data." But you can bet that "pretty good" won't stop competing labs from gearing up for more analytical runs.

–RICHARD A. KERR

CREDITS (TOP TO BOTTOM): NASA, ESA, AND THE HUBBLE HERITAGE TEAM STSCI/AURA; BENOIT TESSIER/REUTERS

Big Money for Little Stuff

With nanomaterials already a part of 500 commercial products, the U.S. Environmental Protection Agency (EPA) must make sure the particles are safe. That's the conclusion of a report released this week by former EPA assistant administrator J. Clarence Davies, now advising the Woodrow Wilson International Center for Scholars in Washington, D.C. Davies urges Congress to allocate $50 million more a year for research on the health and environmental impacts of nanotech and revise the Toxic Substances Control Act. He also suggests a joint government-industry nanoscience research institute and that EPA launch its proposed voluntary program to collect nanomaterials information from companies.

"EPA needs to seriously consider the constructive and thoughtful changes that Davies puts forward in his report," says former EPA Administrator William Ruckelshaus.

–ROBERT F. SERVICE

Steep Learning Curve

The new French cabinet will feature a full minister for research and higher education, a boost from the previous junior minister status. That indicates the growing political importance of French science, researchers say, but the woman to head the new position is a career politician who's virtually unknown among scientists.

Valérie Pécresse (below), 39, is a National Assembly member for Yvelines, a suburban department near Paris. She was an adviser to former president Jacques Chirac and a spokesperson for the Union for a Popular Movement, the party of newly elected president Nicolas Sarkozy; in January, she published a book entitled *Being a Woman in Politics … It's Not That Easy!* Those may be prophetic words, some say, as Pécresse will be charged with a reform of the university system that is expected to trigger protests (*Science*, 11 May, p. 819).

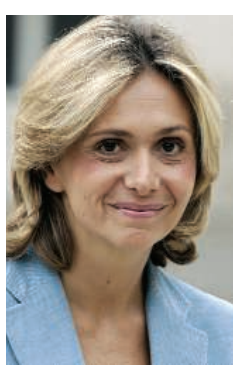

Immunologist Alain Trautmann, former spokesperson of the movement Sauvons la Recherche, says the scientific community had hoped for someone with more experience in science or science policy but adds that Pécresse will get the benefit of the doubt.

–MARTIN ENSERINK

Published by AAAS

U.S POLITICS

Nobelist Eyes Minnesota Senate Seat

Peter Agre wants to do something no Nobelist has done before: get elected to the U.S. Senate. After a colleague disclosed it in a newspaper op-ed column last week, the 2003 chemistry laureate confirmed that he is considering a run for the Senate seat now held by Minnesota Republican Norm Coleman.

Agre, 58, plans to take leave this summer from Duke University in Durham, North Carolina, where he is a professor of cell biology and vice chancellor for science and technology. He aims to test his welcome among Democrats in Minnesota, his childhood home, which he left 3 decades ago to pursue a career on the U.S. East Coast. With no campaign kitty, little public visibility, and no political experience, he concedes that the odds of winning a Democratic primary, much less the general election in November 2008, are long. But he says that Minnesota has promoted "some very unusual candidates over the years," including another student at his high school, Jesse Ventura, the professional wrestler who was elected governor.

The news that Agre is weighing a run for the Senate came as a surprise to science policy leaders, some of whom were pleased. "That he would even consider this is an extraordinary public service, for which he should be applauded," said Neal Lane, former director of the National Science Foundation and science adviser to President Bill Clinton. "It's pretty clear … that we're in dire need of serious leadership by people who think that facts are important, that evidence should be considered." Lewis Branscomb, professor emeritus of the John F. Kennedy School of Government at Harvard University, thinks that Agre's Nobel credentials would enable him to "fight for rational, fact-based policy decisions so essential to the survival of democracy." Former Republican House Science Committee chair Robert Walker says, "It's always positive to have scientists involved," adding that many are uncomfortable with the compromises required in public life.

New experiment. Chemist Peter Agre may test his popularity in one of the hottest U.S. races.

Agre drew some media attention several years ago when he helped his friend Thomas Butler, a microbiologist at Texas Tech University in Lubbock, Texas, fight charges that he had violated biohazard and accounting regulations (*Science*, 19 March 2004, p. 1743). Butler was convicted and sent to prison—a "disgrace," says Agre, who figures that he spent a large part of his Nobel Prize money on Butler's legal defense. Agre also endorsed a 2004 report by the Union of Concerned Scientists accusing the Bush Administration of manipulating U.S. science for political aims. His political views are left of center, although within the mainstream for Minnesota; for example, he favors universal health insurance, strong action to control carbon emissions, and more public aid for poor women seeking abortions.

Political strategists say that the Minnesota Senate race could cost candidates more than $30 million. And two well-heeled candidates are already seeking the Democratic nomination: political comic Al Franken and a popular Minneapolis attorney, Michael Ciresi. Agre says he will spend the summer with Minnesota voters to see whether his own candidacy "has traction or not."

–ELIOT MARSHALL

NONPROLIFERATION

Gloomier Prospects for Indo–U.S. Nuclear Pact

NEW DELHI—A landmark civilian nuclear deal between India and the United States has hit "a possibly fatal impasse," says a U.S. official. Sources in both capitals say that negotiations to implement the agreement are deadlocked over long-standing sticking points, including India's desire to retain the right to reprocess spent nuclear fuel and to conduct future nuclear weapons tests.

"We're far apart, and the gap is far from closing," says a U.S. State Department official. On 1 May, after the most recent round of negotiations, State announced that its top negotiator, Under Secretary R. Nicholas Burns, would fly to India "in the second half of May to reach a final agreement." The U.S. Embassy in New Delhi now says that Burns has no imminent travel plans.

The pact seeks to end India's nuclear pariah status. Under the deal's terms, India has designated civilian nuclear facilities to be placed under international safeguards by 2014, in exchange for clearance to import technology and fuel for its civilian nuclear program. In March 2006, Indian Prime Minister Manmohan Singh and U.S. President George W. Bush hailed the accord as the anchor of a new "strategic partnership."

The mood on both sides has soured since then. Indian scientists have assailed plans to segregate the nuclear establishment into civilian and military facilities. Critics also contend that U.S. legislation would penalize India over further nuclear tests (*Science*, 22 December 2006, p. 1863). Subsequent negotiations on the "123 Agreement," a bilateral treaty that would spell out how to implement the pact, have hit several snags. The biggest bone of contention, sources say, is India's demand for an explicit acknowledgment of its right to reprocess spent nuclear fuel.

A coup de grâce for the pact may come this summer, when India's Supreme Court hears a case from a metallurgist challenging the legal basis of the 123 Agreement. The petitioner is seeking full disclosure of all agreement drafts on the grounds that "the security, sovereignty, dignity and honour of the country [are] likely to be jeopardized and compromised" by the agreement. No matter how the court decides, a happy ending looks more elusive than ever. "There is no place for change in the Indian position," says a top official at India's atomic agency. "If the twain does not meet, so be it."

–RICHARD STONE AND PALLAVA BAGLA

CREDIT: DUKE UNIVERSITY MEDICAL CENTER

GENETICS

Working the (Gene Count) Numbers: Finally, a Firm Answer?

COLD SPRING HARBOR, NEW YORK—How many genes are in the human genome? Seven years ago, researchers were predicting that our genetic code was anywhere from 28,000 to 150,000 genes strong. Those were the outliers in a betting pool organized by Ewan Birney of the European Bioinformatics Institute in Hinxton, U.K. Birney predicted the answer would be in by 2003, when the human genome was due to be finished (*Science*, 19 May 2000, p. 1146).

He was wrong—and so was everybody who bet.

Today, the gene number is still "a mess," according to Michele Clamp, a computational biologist at the Broad Institute of the Massachusetts Institute of Technology and Harvard in Cambridge, Massachusetts, who spoke at the Biology of Genomes meeting here earlier this month. The three databases that track protein-coding genes can't seem to agree, giving totals of 23,000, 19,000, and 18,000 genes. The real answer is 20,488—well below the lowest guess—with perhaps 100 more yet to be discovered, Clamp reported.

This count may hold up. "I've looked at her data very carefully," says Francis Collins, director of the U.S. National Human Genome Research Institute in Bethesda, Maryland. "It's a pretty good number."

In the classical sense, a gene is a sequence of DNA that codes for a particular protein. For proteins to be produced, a gene must first be transcribed, a process in which the cell makes a matching RNA molecule that carries the gene's instructions to the centers of protein production. Gene-prediction programs rely heavily on identifying the so-called open reading frames between the three-base codes that start and stop transcription. But there's been an explosion of discoveries of confusing RNA "genes": transcribed sequences that have a biological function but don't produce a protein. And at the meeting, Birney and his colleagues reported finding several thousand other genes that also don't code for proteins, but researchers have no clues as to what they do.

Thus an open reading frame "is not enough" to identify a gene that codes for a protein, said Clamp: "It's time to produce an integrated catalog of protein-coding genes based on the comparative evidence."

Clamp compared all the human genes in a database called Ensembl with those cataloged for dog and mouse. In all, 19,209 were the real, protein-coding McCoy, 3009 had been erroneously put on the gene list, and 1177 remained ambiguous, she reported.

She rated the "geneness" of these leftovers by comparing them to random stretches of DNA. Almost all made the grade with respect to a genelike proportion of the bases G and C, but not for features such as the distribution of short insertions and deletions in their sequences. Overall, 1167 were "bogus" and lacked any independent evidence that they coded for proteins, she reported. She did a similar analysis with the other gene databases, then summed the unique genes of all of them to get her final count.

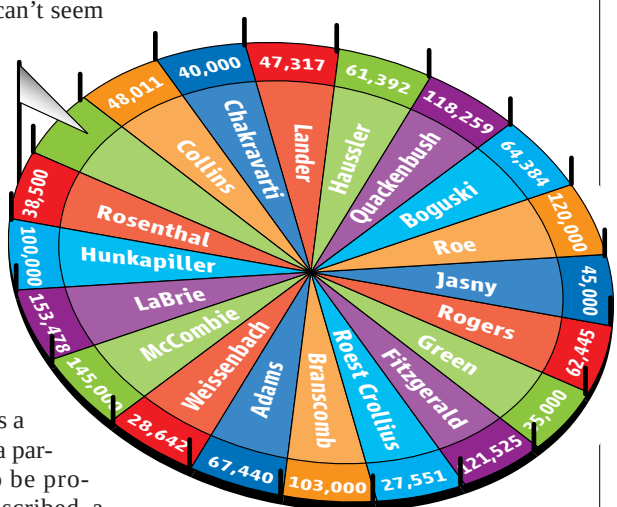

Not even close. For a betting pool set up in 2000, genome experts estimated the number of human genes. Even the winning—and lowest—number, 26,000, was 6000 genes too high.

For Clamp to take a firm stand and call for a reconciliation of differences among the official gene-counters "was kind of brave and a lot of hard work," says Jim Kent of the University of California, Santa Cruz. Now, says Stephen Richards, a genomicist at Baylor College of Medicine in Houston, Texas, anyone who disagrees with this number "will have to prove her wrong."

–ELIZABETH PENNISI

CREDITS (TOP TO BOTTOM): IMAGE COURTESY OF AMY BACO-TAYLOR/HURL/NOAA; ILLUSTRATION BY C. FABER SMITH/*SCIENCE*

Red Coral in the Red

The United States has proposed international controls on the little-known trade of red coral, a deep-water species found in the Pacific and the Mediterranean.

The U.S. wants it listed as threatened at next month's meeting of the Convention on International Trade in Endangered Species (CITES) in The Hague, The Netherlands. This would force importers and exporters of 27 species of *Corallium* to seek CITES approval for each transaction, "allowing us to learn more about the trade," says Lance Morgan of the Marine Conservation Biology Institute in Glen Ellen, California. The listing would also bring more focus on destructive bottom-trawling methods historically used to gather this coral prized by jewelers, he adds. Stephen Cairns, a coral taxonomist at the Smithsonian Institution in Washington, D.C., says red coral is "more valuable and depleted than any others," such as the already listed black coral and hard coral.

–CHRISTOPHER PALA

A Northern Vision

Although short on specifics, Canada's latest S&T strategy suggests where the new Conservative government is headed. Unveiled by Prime Minister Stephen Harper last week, the 110-page road map vows to focus government-funded research in four broad areas: environment, natural resources and energy, health, and information technologies. It emphasizes a move to policies "more conducive to private-sector investment in R&D and commercialization," although it rules out new tax credits, already among the most generous in the world.

The corporate emphasis disturbs Canadian Association of University Teachers Executive Director James Turk. "That's not how good research gets done, and that's not how research which has commercial benefits gets done," he says. But Michael Julius of the University of Toronto Sunnybrook Health Sciences Center says the report "provides a policy framework, and we've not had one." Julius, a research administrator, will chair a committee established by the advocacy group Research Canada to study the strategy, although the government has not formally asked for input on how to implement the plan.

–WAYNE KONDRO

A Growing Threat Down on the Farm

Farmers have become dependent on a herbicide called glyphosate and on crops engineered to resist it. Now, weeds are becoming resistant, and researchers are scrambling for alternatives

CONVENTIONAL WISDOM HAS IT THAT biotech drugs have flourished while genetically modified (GM) crops have foundered because of protests in Europe and elsewhere. Not so. Biotech drugs are doing just fine and, it turns out, so are GM crops. Last year, 10 million farmers in 22 countries planted more than 100 million hectares with GM crops. Over the past 11 years, biotech crop area has increased more than 60-fold, making GM crops one of the most quickly adopted farming technologies in modern history (see figure, p. 1115). Even the European Union is beginning to embrace them, with six E.U. countries now planting GM crops.

What's behind this blossoming of transgenics? Oddly enough, a herbicide called glyphosate. The compound is the world's best-selling herbicide by far, prized by farmers for its safety and effectiveness at wiping out hundreds of different kinds of weeds. That effectiveness has not only convinced farmers to make the switch but also prompted seed companies to engineer crops to be impervious to glyphosate's effects. That has allowed farmers to spray their growing crops to wipe out encroaching weeds without fear of wiping out their livelihood. The model has proven so successful that of the transgenic crops planted worldwide last year, approximately 80% were engineered to be glyphosate-resistant (GR). "The rate at which this technology has been adopted floors me," says Donald Weeks, a plant biochemist at the University of Nebraska, Lincoln.

But this success has sown the seeds of its own potential demise. Much of modern agriculture is now dependent on a single chemical. "Glyphosate is as important to world agriculture as penicillin is to human health," says Stephen Powles, who directs the Western Australian Herbicide Resistance Initiative in Perth. It's an apt comparison, because just as pathogens have grown resistant to penicillin and other antibiotics, weeds resistant to glyphosate have recently begun sprouting and spreading around the globe. For now, the scale of the outbreak remains small. But agricultural experts worry that herbicide-resistant weeds are

Superweed. Glyphosate-resistant Johnsongrass in a soybean field in northern Argentina.

CREDIT: M. VILA-AIUB/UNIVERSITY OF BUENOS AIRES

Published by AAAS

poised for their own takeover. "There is going to be an epidemic of glyphosate-resistant weeds," Powles says. "In 3 to 4 years, it will be a major problem." If farmers and seed companies lose their ability to rely on glyphosate, it could cost them billions of dollars in lost productivity. But the damage will likely be more than monetary, as it could also have a major environmental consequence as well (see sidebar, p. 1116).

In the face of this threat, agricultural researchers are mounting a multipronged campaign to safeguard glyphosate and come up with other options in case its effectiveness withers. On page 1185, for example, Weeks and his colleagues at Nebraska report that they have developed the first transgenic crops resistant to an alternative herbicide called dicamba. Down the road, growers may soon switch transgenic crops much as doctors select antibiotics to stay one step ahead of pathogens. But for now, the fight is on to save glyphosate.

Fantasy league

The love affair between farmers and glyphosate was kindled long before biotech crops hit the fields. In 1970, John Franz, a chemist at Monsanto, discovered that the compound acted as a broad-spectrum herbicide, capable of killing an enormous variety of plants when deposited on the leaves of young seedlings. Later, researchers found that glyphosate wreaks its havoc by inhibiting an essential plant enzyme known as 5-enolpyruvylshikimate-3 phosphate synthase (EPSPS). The enzyme catalyzes an intermediate step in the construction of a trio of aromatic amino acids, which in turn are vital for the production of key plant metabolites. Without EPSPS, the plants are starved of these metabolites and quickly wither and die.

Just as enticing was what glyphosate does not do. Although concerns have been raised about the surfactants that are used alongside glyphosate in most formulations, glyphosate itself does not appear to affect animals and insects, which don't have EPSPS and rely on their diet for the amino acids the enzyme helps produce. And when sprayed on fields, glyphosate doesn't readily leach into water systems. Instead, it latches tightly to soil particles and degrades within weeks into harmless byproducts. By contrast, herbicides such as atrazine have been widely implicated in contaminating groundwater.

Monsanto began selling glyphosate in 1974 under the trade name Roundup. Sales remained modest for years—until researchers engineered GR crops to use in combination with the herbicide. By 1983, researchers had isolated a gene known as *CP4* in bacteria that synthesized aromatic amino acids through a different route from that of the EPSPS in plants. By 1986, they had spliced *CP4* into plants and shown that the plants could withstand the effects of glyphosate with no apparent damage.

It was another 10 years before Roundup Ready soybeans hit the market, but their impact was dramatic. In 1995, U.S. farmers used 4.5 million kilograms of glyphosate; they now use 10 times that amount. "If I were playing in an herbicide fantasy league, my first pick would be Roundup Ready cropping systems with glyphosate, and I would let you have the next three selections," says John Wilcut, a crop scientist at North Carolina State University (NCSU) in Raleigh.

Since 1996, Monsanto and other seed companies have introduced GR canola, cotton, corn, sugar beets, and alfalfa. The popularity of the herbicide was further fueled when the compound went off patent in 2000, which has triggered a 40% price drop in the years since. That combination produced a massive shift from traditional crop varieties to GR versions. In just a 5-year span, GR soybeans commanded 50% of the land cultivated for soy in the United States, and GR corn a 40% share. Today, GR soybeans make up more than 90% of soybeans planted in the United States, and corn more than 60%. By comparison, organic agriculture accounts for about 1% of cultivated land. "Farmers are normally very conservative," says Weeks. "Clearly, this was a real winner."

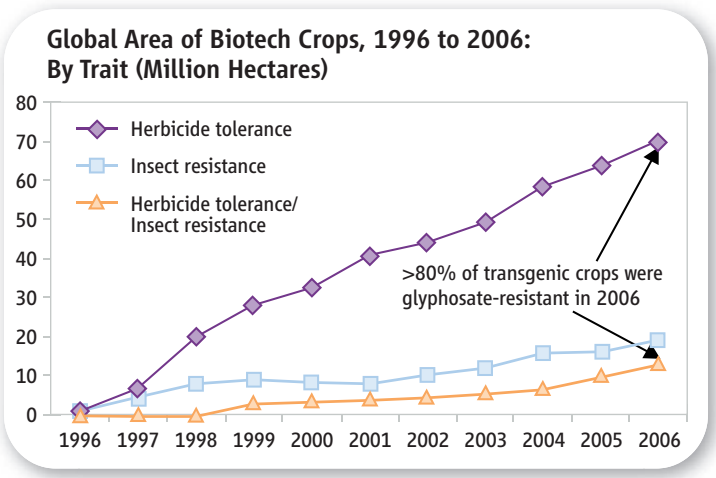

Success story. Over the past decade, herbicide-resistant varieties have come to dominate the world market for genetically engineered crops.

CREDIT: C. JAMES/ISAAA

Awaiting the inevitable

One effect of that winning combination has been to slash the market for competing herbicides. According to data from the U.S. Department of Agriculture (USDA), the prices of two popular herbicides—chlorimuron and trifluralin—have dropped 20% to 40% since 1998. Over the same period, U.S. sales of all herbicides, including glyphosate, have declined by about $1 billion, nearly 20% of the industry total. Faced with this shrinking market and the glyphosate juggernaut, herbicide companies have been backing out of the market. Nearly 20 herbicides with different mechanisms of killing plants were sprayed on soybeans a decade ago; now, farmers are increasingly relying on glyphosate for most or all of their herbicide needs. In a survey of 400 farmers in the U.S. Midwest, for example, researchers at Syngenta found that 56% of soybean growers in northern states and 42% in southern states use glyphosate as their sole herbicide. As a result, "the selective pressure for weeds to develop resistance has been huge," says Stephen Duke, a plant physiologist at USDA's Agricultural Research Service in Oxford, Mississippi. "From a biological perspective, this is inevitable," adds Jerry Green, a weed scientist with DuPont Crop Protection in Newark, Delaware.

For years, many researchers doubted that plants would be able to overcome their vulnerability to glyphosate, because EPSPS plays such a vital role in plant metabolism. One 1997 paper in the journal *Weed Technology* even stated that "the complex mutations required for the development of glyphosate-resistant crops are unlikely to be duplicated in nature to evolve glyphosate-resistant weeds." Unfortunately, that was written just after the first GR weeds were discovered in 1996. Today, about a dozen different varieties of weeds are known to have developed resistance. And the spread of resistance to new weed species is increasing. Resistant weeds have now been spotted in countries around the globe, including the United States, Argentina, South Africa, Israel, and Australia. According to WeedScience.com, an international herbicide-resistance tracking service, GR "horseweed" was first identified in a Delaware field of GR soybeans in 2000, and since then it has turned up in 14 states as well as in Brazil and China.

Again, like many microbes that evolve to outwit antibiotics, it now appears that

Stop loss. Plowed fields (*left*) suffer much more soil erosion than their no-till counterparts.

GLYPHOSATE—THE CONSERVATIONIST'S FRIEND?

Weeds resistant to the powerhouse herbicide glyphosate not only threaten the livelihoods of farmers worldwide, but they could have environmental downsides as well. Among the worst, glyphosate's disappearance could increase the loss of topsoil, require farmers to switch to more harmful herbicides, and force them to use more fuel to rid their fields of weeds.

The current combination of herbicide-resistant crops and herbicide use is hardly an environmental panacea. A 2003 farm-scale evaluation in the United Kingdom, for example, found that the combination contributed to a loss of biodiversity both by reducing the numbers of weeds and by indirectly affecting insects that rely on those weeds for food. Many governments have also been cautious about allowing the use of herbicide-resistant crops for fear that genes that confer herbicide resistance could spread far beyond agricultural fields.

Despite such concerns, many agricultural researchers now say glyphosate-resistant (GR) crops have had widespread environmental benefits, at least compared with the previously used alternatives. "Glyphosate-resistant crop weed management systems are generally safer to the environment than what they replace, and in many cases much safer," says Stephen Duke, a plant physiologist at the U.S. Department of Agriculture's Agricultural Research Service in Oxford, Mississippi.

One of the biggest benefits of GR crops is their indirect impact on topsoil. Modern farming encourages heavy topsoil losses because farmers traditionally plow fields before planting seeds. Turning over the topsoil buries many weed seeds that were present under 4 to 6 inches of dirt. Although that reduces the likelihood that weeds will compete with emerging crop plants, it also dramatically increases the amount of topsoil that washes away with rain and irrigation.

By contrast, many farmers don't plow their fields before planting GR crops. Instead, they simply plant seeds and spray glyphosate on their fields shortly after their crops have emerged, wiping out their weedy competitors. The upshot is that herbicide-resistant crops often require minimal

GR weeds don't make a frontal attack on glyphosate. According to Christopher Preston, a weed-management scientist at the University of Adelaide in Australia, one common resistance mechanism centers on the way glyphosate moves within plants. In a presentation at a symposium on glyphosate resistance held as part of the American Chemical Society (ACS) meeting in March in Chicago, Illinois, Preston noted that when glyphosate is sprayed on the leaves of a susceptible plant, it is normally absorbed quickly and moves readily throughout its tissues. Once inside, it accumulates at the growth point in roots and stems and kills the plants. However, when Preston and his colleagues looked at a resistant form of rigid ryegrass, they found that the glyphosate accumulated in the leaf tips. The plant was essentially steering the compound away from areas where it could inflict lethal damage. Preston's team found a similar mechanism of resistance in two populations of horseweed as well, suggesting that glyphosate sequestering could be a mode of resistance common to many weeds.

For now, however, resistant weeds are still the minority. According to the Syngenta survey, 24% of farmers in the northern portion of the Midwestern United States and 29% in the south say they have GR weeds. But only 8% say it's a problem across all of their acreage. Still, Syngenta's Chuck Foresman, who presented the data at the ACS meeting, says, "the resistance issue is across the Midwest, South, and Southeast. Nobody is exempt." Crop scientists from Argentina, Brazil, and Australia echoed growing concerns about the problem in their countries as well.

Backlash. Weeds that tolerate glyphosate are starting to appear throughout the world.

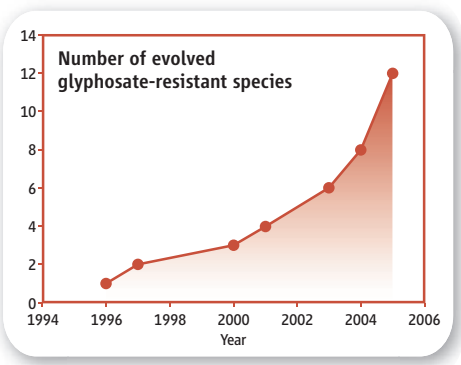

What to do?

Fighting resistance is something of an uphill battle, says Duke. At the moment, not all farmers see resistance as a major issue, but by the time they do, resistance may be so widespread that it will be hard to combat. In recent decades, when resistance to one herbicide has spread, farmers have simply switched to another. But glyphosate's recent dominance of the herbicide market has reduced work on alternatives just when they are needed most. "Weed control is shifting to herbicide-resistant crops, and so are the research budgets," Green says. That's bad news, NCSU's Wilcut says: "We need to have more of a diversity of herbicides out there." But there are no new silver-bullet herbicides that are safe and broadly effective waiting in the wings. "We are not likely to get additional herbicide modes of action," Wilcut says.

With a multibillion-dollar market for herbicides and transgenic seeds at risk, agricultural researchers underscore the need to educate farmers to use long-standard methods of combating weeds, to preserve glyphosate's effectiveness as long as possible. Among these, says Weeks, are traditional resistance-management strategies of rotating crops and using a variety of different herbicides to combat weeds, practices that hinder resistant organisms from gaining a foothold in their fields. In many cases, that's likely to mean rotating in crops that don't rely on using glyphosate.

Aside from proper stewardship practices, most researchers feel that the best hope for combating herbicide-resistant weeds is the continued development of transgenic crops. Nicholas Duck and colleagues at Athenix, a crop sciences start-up in Durham, North Carolina, for example, are developing crop varieties that are resistant to even higher levels of glyphosate. Planting them may allow farmers to buy some time by applying heavier doses of the herbicide to their crops, but it could add to the selective pressure on weeds to develop resistance.

Other companies, meanwhile, are pushing crops resistant to herbicides other than glyphosate. Bayer Crop Sciences, for example, has already commercialized soybean and corn seeds resistant to glufosinate, a herbicide that kills plants by a different mechanism from glyphosate's. These crops, sold under the trade

tilling or no tilling at all. In March, at a symposium on glyphosate at the American Chemical Society meeting in Chicago, Illinois, Pedro Christoffoleti of the University of São Paolo in Brazil reported a recent study in South America that found that growing soybeans with conventional tillage produced topsoil losses of 1.2 tons per hectare. With GR crops planted with no-till practices, those losses shrank to 0.2 tons per hectare, a reduction of more than 80%.

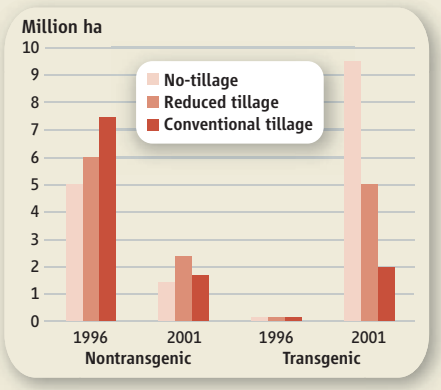

No-till agriculture saves farmers time and money, and for that reason the practice has grown dramatically with the rise of GR crops. In one recent study, the American Soybean Association in Washington, D.C., found that in just 5 years from 1996 to 2001 when herbicide-resistant soybeans first came on the market, the area of soybean land farmed by no-till agriculture in the United States increased from about 5 million hectares to more than 11 million hectares, whereas conventional tillage dropped from close to 8 million hectares to under 4 million hectares. By 2001, almost all no-tillage soybeans were GR varieties. What is more, because no-till agriculture requires less tractor use, the practice reduces soil compaction and cuts fuel use on farms. All those benefits could take big hits should the emergence of GR weeds prompt farmers to abandon glyphosate, Duke says.

Additional impacts could come as farmers switch to herbicides that are more toxic to mammals. Gerald Nelson, an agricultural economist at the University of Illinois, Urbana-Champaign, and his colleagues have recently begun looking at the likely impact of that shift. To do so, they used a common yardstick, known as the LD_{50} dose, to compare the toxicity of various herbicides. The LD_{50} dose is a widely available measurement of the amount of a particular compound required to kill half of a population of rats in lab studies. When the researchers looked at the effect of switching from GR crops to conventional seeds with other herbicides, they found that the switch would require farmers to increase the LD_{50} doses applied to the average U.S. farm by about 10% per hectare in soybeans and 25% per hectare in cotton. Nelson says it's not yet clear how such changes will translate into impacts on organisms other than mammals, such as insects and birds. However, Nelson adds, "there will be some more effects on anything else susceptible to these [alternative] herbicides." **–R.F.S.**

name Liberty Link, have not done as well in the market as glyphosate has because the herbicide is more expensive yet less effective at killing a broad range of weeds. But if GR crops continue to falter, Bayer could find itself a beneficiary.

Dicamba, another cheap herbicide that has been on the market for 4 decades, could also emerge as a successor. Researchers in Texas created dicamba-resistant plants in 2003 by adding the gene for an enzyme that deactivates the herbicide. Seed companies have never managed to develop varieties that expressed enough of the enzyme to fully protect the crops. But in their report in this issue, Weeks and his colleagues managed to do just that, developing soybeans that in 3 years of field trials proved highly resistant to dicamba.

As with previous herbicide-resistant crops, Weeks's team engineered their soybeans to express a bacterial gene that confers resistance, in this case by breaking down the herbicide. But in an ingenious twist, the Nebraska researchers targeted the engineered gene to be expressed in the plants' photosynthetic chloroplasts. The move offers two benefits, Weeks explains. First, the resistance-conferring enzyme works better because it can swipe the electrons it needs from the steady stream generated during photosynthesis. Also, like mitochondrial DNA, chloroplast DNA is inherited through the maternal side. That means a GM crop can't spread resistance through wind- or insect-carried pollen, which comes from the male side.

Weeks says Monsanto has licensed the technology and that it could be commercially available within 3 to 4 years. If so, he says, it could allow growers to rotate their crops between varieties resistant to two different herbicides. "It gives farmers an alternative to the continual use of glyphosate-resistant crops," Weeks says. And the development of herbicide-resistant crops won't stop with dicamba. "We have the technology today to develop herbicide resistance to about anything we want to," Green says.

New front. Soybeans resistant to the herbicide dicamba may help farmers diversify their antiweed arsenal.

SOURCE: S. DUKE, NPURU/USDA/ARS; CREDIT (BOTTOM): D. WEEKS/UNIVERSITY OF NEBRASKA

Another approach being pursued at Monsanto and elsewhere is to combine, or "stack," genes for resistance to multiple herbicides in the same plants. Researchers at Pioneer HiBred, a division of DuPont, for example, are working to create crops that are resistant to both glyphosate and herbicides that target a plant enzyme called acetolactate synthase. ALS inhibitors have also been on the market for years and face resistant weeds of their own. And scientists elsewhere announced last year that they plan to create crops resistant to herbicides that inhibit ACCase, an initial enzymatic step in lipid synthesis that is critical to grasses.

In addition to stacking traits for resistance to multiple herbicides, researchers at Pioneer and elsewhere are looking to add other traits to crops, such as heat and drought resistance, increased yield, and insect resistance. In some cases, they hope to add genes for novel nutrsients and even pharmaceutical compounds. "There is a tremendous opportunity to do this for the next generation of traits," Duck says. Although such efforts are still in the early stages, he adds, "in the future, everything is going toward product stacks." The question is whether crops resistant to multiple herbicides will prolong the life of one of the farming community's favorite herbicides.

–ROBERT F. SERVICE

Special delivery. Antonio Giordano (*left*) shows off a lab to one of his backers, pizza magnate Mario Sbarro.

PROFILE: ANTONIO GIORDANO

'Dr. Hustle' Sells His Dream For Italian Medical Research

After making his mark in the United States, an Italian cancer researcher with a knack for raising private money seeks to inject new life into biomedical science back home

It may not look like much now, but a dilapidated mansion in the green and hilly region of Umbria, far from any major research university or institution, is being touted as the future birthplace of an Italian renaissance in biomedical science. That's the dream of Antonio Giordano, who 20 years ago left Naples to make his scientific name in the United States. Giordano now runs his own cancer research institute in Philadelphia, thanks in part to a relentless pursuit of support from corporate and private donors. The magazine *Philadelphia* even dubbed Giordano "Dr. Hustle" in a profile that detailed how he obtained a large donation for his institute after wooing a pizza magnate during weekly strolls.

By supplementing grants from the National Institutes of Health (NIH) with privately raised money, the 44-year-old Giordano has gained some freedom in the United States to pursue his own research agenda; he even established a private foundation that funds graduate students and postdocs at his institute. Now, after securing commitments for more than €60 million from Italian financial services institutions, Giordano would like to help a generation of young Italians back home pursue biomedical research. And by offering an alternative to the charity and governmental funding systems that he believes are narrow-minded and stifle Italy's science, Giordano hopes to persuade many of his protégés to stay there. "In Italy, there are not many possibilities for research, and many Italians … look at me not only as an example but [also] as a person that can help them," he says.

Giordano's reputation in Italy is such that when politicians in the Umbrian town of Terni, 108 kilometers north of Rome, heard of his plans to set up a biomedical research institute, they called to offer a city-owned mansion. The building, currently being refurbished, should open its doors in 2009.

> "[Giordano's] personality makes it possible to **integrate the picture of research into something that is sellable."**
>
> —Paul Fisher, Columbia University

That wasn't fast enough for the impatient Giordano and his sponsors, however. So an interim laboratory is being built not far from the mansion. This fall, 20 to 30 students and postdocs should be working there. When the mansion is ready, the new institute will ultimately provide lab space for another 50 young researchers to work, primarily on cancer, but on cardiovascular disease and diabetes too. It will also include a facility to treat cancer patients, run trials of therapies, and develop research in cancer prevention.

Paul Fisher, a cancer researcher at Columbia University in New York, notes that what really set Giordano apart from other good scientists are his entrepreneurial spirit and capacity to exploit nontraditional avenues of funding. "His personality makes it possible to integrate the picture of research into something that is sellable," says Fisher.

Breaking the mold

Giordano initially set his heart on a career in medicine. But while training at the University of Naples back in the 1980s, he had second thoughts. "I realized that medicine can be very routine [and] that there were too many devastating illnesses that needed more … research work," Giordano says. After earning his medical degree in 1986, Giordano decided to swap medicine for genetics and cancer research.

In 1987, he came to America to be a postdoc, at New York Medical College in Valhalla, and then under Nobel Prize winner James Watson at Cold Spring Harbor Laboratory. There he won recognition for isolating the cyclin A protein, a cell growth regulator. That discovery, says Giordano, provided "the first physical evidence of a link between cell division and cancer."

Since then, Giordano has had other successes, including cloning the *Rb2/p130* tumor-suppressor gene, which was subsequently found to be involved in many cancers. He's had "an outstanding career with some very exciting findings … that really helped launch a number of fields within cell cycle research," says Fisher.

Giordano moved in 1992 to Temple University in Philadelphia, Pennsylvania, and set up a 10-person lab conducting cell cycle and cancer research with an initial 3-year NIH grant. It quickly became clear to him, however, that private sources of support were also needed. "I saw colleagues, also very good, who disappeared because they didn't realize how it was important to be independent and search for your own funding," he says.

As Giordano began to envision a research institute of his own, he got lucky. His wife-to-be, whom he met during his time at Cold Spring Harbor, lived in the same New York neighborhood as the owners of Sbarro, a U.S.-based chain of fast-food restaurants

CREDIT: SBARRO HEALTH RESEARCH ORGANIZATION

that sells pizza and Italian dishes. Giordano soon encountered fellow Neapolitan Mario Sbarro and after almost a year of Sunday-morning walks on Long Island won from him an initial donation of about $1 million to create the Sbarro Institute for Cancer Research and Molecular Medicine. Sbarro says he was impressed by Giordano, particularly his vision of "creating an environment where talented [young] people … could work together … free of bureaucracy."

To retain control of his private money, Giordano felt he needed to break free from the university's authority. But he also wanted the university's administrative support and infrastructure to keep nonresearch costs minimal. Convincing Temple to go along was not easy. In fact, in 1994, Giordano moved his lab to Thomas Jefferson University, also in Philadelphia, where he was offered an agreement that included the university matching Sbarro's donation. "After 2 years, my lab had tripled in number of people and space," Giordano says. But nearly a decade later, in 2002, Giordano returned to Temple after securing, in his words, "complete independence" in administering the funds, staff, research programs, and patent rights.

Giordano's return also marked the launch of a nonprofit organization—the Sbarro Health Research Organization (SHRO)—to collect additional private funds for the institute. Sbarro, who had continued to support Giordano's work, kicked in another $200,000 a year for 3 years as seed money. To date, Giordano has raised $3 million in private funding, supplementing about $27 million that he and other investigators at his institute have obtained through NIH grants and earmarks from the state of Pennsylvania and the Department of Defense, which has also just awarded SHRO $2 million a year for 2 years for breast cancer research.

The private money raised by SHRO comes with fewer entanglements than those attached to NIH grants, contends Giordano. As a result, he's free to dedicate a great part of these private research dollars to risky projects, such as the development of a novel gene-therapy approach for the treatment of lung, liver, and ovarian cancers. SHRO mainly funds young scientists, through research grants and 1- to 3-year fellowships of $25,000 a year for students and between $35,000 and $40,000 for postdocs. Although SHRO has an external scientific advisory board, Giordano has largely decided which areas are investigated and who gets funded. But then, he says, "we want these people to … pursue their own independent ideas and careers."

Going home

With the project in Terni, Giordano is extending his reach into Italy, hoping eventually to use it as a springboard to fund scientists across Europe. He had in 2000 started to use his privately raised money to fund graduate students and postdocs in a few labs at places such as the University of Siena, University of Rome "La Sapienza," and the University of Naples. As in Philadelphia, the universities offer the researchers access to equipment and other infrastructure.

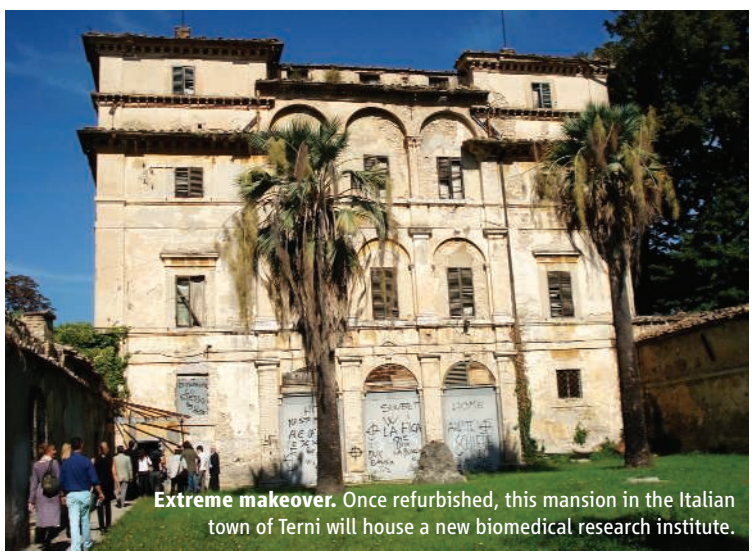

Extreme makeover. Once refurbished, this mansion in the Italian town of Terni will house a new biomedical research institute.

CREDIT: HUMAN HEALTH FOUNDATION

Once SHRO was established, it became Giordano's avenue for distributing funds abroad. SHRO's money is welcome because it is more difficult to find funding for cancer research in Europe than in the United States. In 2002–03, the whole of Europe spent €1.43 billion on public cancer research with the 25 E.U. Member States disbursing only one-seventh the per capita amount spent by the United States, according to the European Cancer Research Managers Forum. "European minds are excellent," says Giordano, but they often do not flourish until they get to America, where there is better support.

By creating the Terni institute, as well as a new nonprofit, the Human Health Foundation (HHF), Giordano says he's throwing a lifeline to researchers in Italy, where only a few institutions—"oases," he calls them—typically receive money from the country's major research funding bodies. Already, HHF has collected €60 million from two Italian financial institutions, the Banca Popolare di Spoleto and Spoleto Credito e Servizi. Giovanni Antonini, the president of the Spoleto bank, has even agreed to head HHF; Giordano will head its scientific committee. By funding HHF, says Antonini, his bank hopes to encourage "the return of the Italian minds who were constrained to leave Italy to improve their professional careers."

Fifteen million euros will be used to refurbish the Terni mansion. The remainder of the HHF money will go directly into research projects and the creation of additional labs. And Giordano stresses that the foundation's funds will be awarded through a transparent process involving peer review. By this summer, between 10 and 15 early-career scientists will start working on HHF-funded projects in Siena and Philadelphia while the interim lab in Terni, which will cost €500,000, gets up and running.

At the moment, Giordano supports about 100 young researchers across Italy and the United States together. About 70% of the students and postdocs Giordano has trained or funded so far, a network that today counts more than 250, are Italian. He has been able to aid that many in part thanks to complementary national and European funding programs.

Giordano "acts as a role model and mentor," says Alessandro Bovicelli, 39, who came to the Sbarro Institute in 2000 for a postdoc in gynecological oncology and still collaborates with Giordano. "He is … very focused on the objectives that the young doctor would like to pursue." Now a faculty member at the Department of Obstetrics and Gynecology at the University of Bologna, Bovicelli says that Giordano's continuous encouragement was vital.

Normally confident, Giordano admits uncertainty about whether he will be as successful in his new project as he's been in the United States. "In Italy, there is not the infrastructure there is in the U.S.," he says, and building an institute from scratch is a major undertaking. Giordano notes that his mother asks why he can't be satisfied with what he has already done on the U.S. side of the Atlantic. His answer is simple: "I owe this to Italy. This is where I grew up and was trained."

–ELISABETH PAIN

Elisabeth Pain is a contributing editor for ScienceCareers.org and a freelance science writer based in Barcelona, Spain.

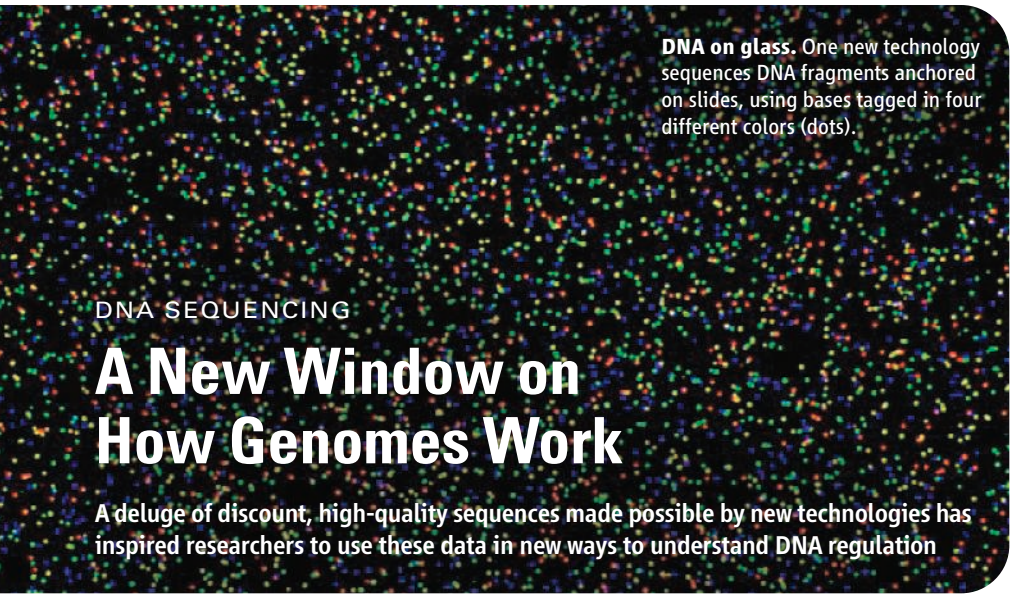

DNA on glass. One new technology sequences DNA fragments anchored on slides, using bases tagged in four different colors (dots).

DNA SEQUENCING

A New Window on How Genomes Work

A deluge of discount, high-quality sequences made possible by new technologies has inspired researchers to use these data in new ways to understand DNA regulation

COLD SPRING HARBOR, NEW YORK—Starting with the Human Genome Project, researchers and companies have been racing to make DNA sequencing faster and cheaper. The dream is to decipher a person's genome for $1000, a price that would open up a wealth of medical applications. Nobody is close yet, but recent successes in driving costs down have opened up a different application: New high-throughput sequencing machines are giving researchers unprecedented views of where and how proteins interact with DNA.

Like viewing the planet through Google Earth, researchers are using these machines to swoop down on genomic neighborhoods to reveal details of the complex landscape of gene regulation: the places where proteins turn genes on or prevent them from being expressed. "It's showing us things we've never seen before," says computational biologist Michele Clamp of the Broad Institute of the Massachusetts Institute of Technology and Harvard in Cambridge, Massachusetts.

DNA is nothing without its proteins. At any one time, tens of thousands of proteins are latching onto or backing away from the genome, creating the dynamic biochemistry that fuels life. Transcription factors turn the appropriate genes on and off. Some proteins, in particular histones, shape chromosomes, grabbing onto and holding DNA in its characteristic spiral, closing genes down, or unwinding it to allow genes to function. Others cut DNA at specific locations. It's this control of gene expression that differentiates brain from liver, T cell from pancreatic islet cell. Researchers want to pin down the sites where all this action takes place, and the latest sequencing technologies—including the star of the moment, Illumina Inc. (Solexa)—are proving adept at doing just that. The new technologies, which began making their debut last year (*Science*, 17 March 2006, p. 1544), promise greater accuracy while reducing the costs of sequencing several-fold below those of the Human Genome Project. But they all share one potential drawback for sequencing whole genomes: They can only sequence short DNA fragments—so-called reads. Short reads are difficult to reassemble accurately into a completed genome. But for researchers studying genome function, short, inexpensive reads are just what they need to characterize—rapidly and cheaply—the sites where a particular protein binds to the genome.

The process, dubbed tag sequencing, had a coming-out party at the Biology of Genomes meeting here last month. It drew rave reviews. "[These] sequencing technologies are really transforming the way we do things and what we are able to do," says Bradley Bernstein, a pathologist at Massachusetts General Hospital in Boston. Tag sequencing has been limited because of its cost, but now "if you are not thinking about your experiments on a whole-genome level, you are going to be a dinosaur," says molecular biologist John Stamatoyannopoulos of the University of Washington, Seattle.

One protein's reach

Richard Myers and Ali Mortazavi of Stanford University in Palo Alto, California, are using tag sequencing to nail down where a transcription factor called neuron restrictive silencer factor (NRSF/REST) shuts down nerve-cell genes in non-nerve cells. Like many other researchers, the Stanford duo, along with Barbara Wold and David Johnson of the California Institute of Technology in Pasadena, start with a technique called chromatin immunoprecipitation to isolate the sites where the transcription factor binds to DNA. In this procedure, they break up the genome from an immortalized T cell and add antibodies to NRSF/REST to pick out the pieces of DNA with NRSF/REST attached.

Until recently, they used microarrays—expensive chips studded with thousands of snippets of DNA from known locations on a reference genome—to identify the segments of DNA bound to NRSF/REST. But now they simply sequence all the DNA to which NRSF/REST is attached and map those sequences directly to the reference genome. "This represents an order of magnitude increase in resolution compared to [microarrays]," says Martin Hirst, a molecular biologist at the British Columbia Cancer Agency Genome Sciences Centre in Vancouver, Canada. "And this is achieved at a fraction of [the] cost."

Myers, Wold, and their colleagues found more than 1950 NRSF/REST binding sites—30% more than they were able to identify by microarrays—and pinned them down to within 50 bases. They also discovered that NRSF/REST has three types of DNA landing sites. One is a 21-base stretch already known to bind NRSF/REST. Another consists of those 21 bases split in half, with 17 other bases stuck in the middle. A third consists of just half the bases, the researchers reported at the meeting. By looking at more types of cells, they expect to learn about how these various landing sites evolved.

Defining genes

Bernstein had a different protein-DNA interaction in mind when he turned to tag sequencing. In the nucleus, DNA is wrapped around proteins called histones, which help control the DNA's state of readiness. Depending on where a methyl group sits on the histone, the protein can activate or silence a gene, in part by making the gene's regulatory DNA more or less accessible to transcription factors. Bernstein and his colleagues have used methylated histones—which are attached to their nearby DNA—to find active and inactive parts of chromosomes in mouse embryonic stem cells and cells that have differentiated into specific types.

Bernstein used one set of antibodies against a histone with a methylation profile known to silence DNA and repeated the process with antibodies against histones whose methylation activates DNA. Tarjei Mikkelsen of the Broad Institute and his colleagues then sequenced and analyzed the DNA fragments attached to each type of histone.

CREDIT: OMEAD OSTADAN/SOLEXA

When they mapped the sequences back onto the mouse genome, a striking contrast emerged. In differentiated cells, the map of silencing histones was different from the map of activating ones—as one might expect. But in the stem cells, the maps overlapped in some places. Genes important, say, in turning that cell into a nerve cell tended to bear both a silencing and an activating histone, Bernstein reported. The former kept the gene quiet to enable the stem cell to keep its options open, but by having the activating histone on board as well, those genes "are poised for activation," he suggested.

Bernstein is also finding that gene boundaries can be defined by their histone companions, something that genomicists have had a lot of trouble doing. One type of histone is present at the beginning of a gene; another is attached all along the gene. The histone map "basically tells you not only where the exons are but where the gene starts and stops," says Francis Collins, director of the U.S. National Human Genome Research Institute in Bethesda, Maryland. "It looks awfully good."

Hirst too has used histones to tag sequences, but in cancer cells. "We have been able to find functional classes of genes, which are enriched for specific combinations of [histone] modifications," he reported. If he and others are able to pinpoint tagging patterns that are characteristic of cancer, "diagnostics could be designed to probe for these regions," he pointed out.

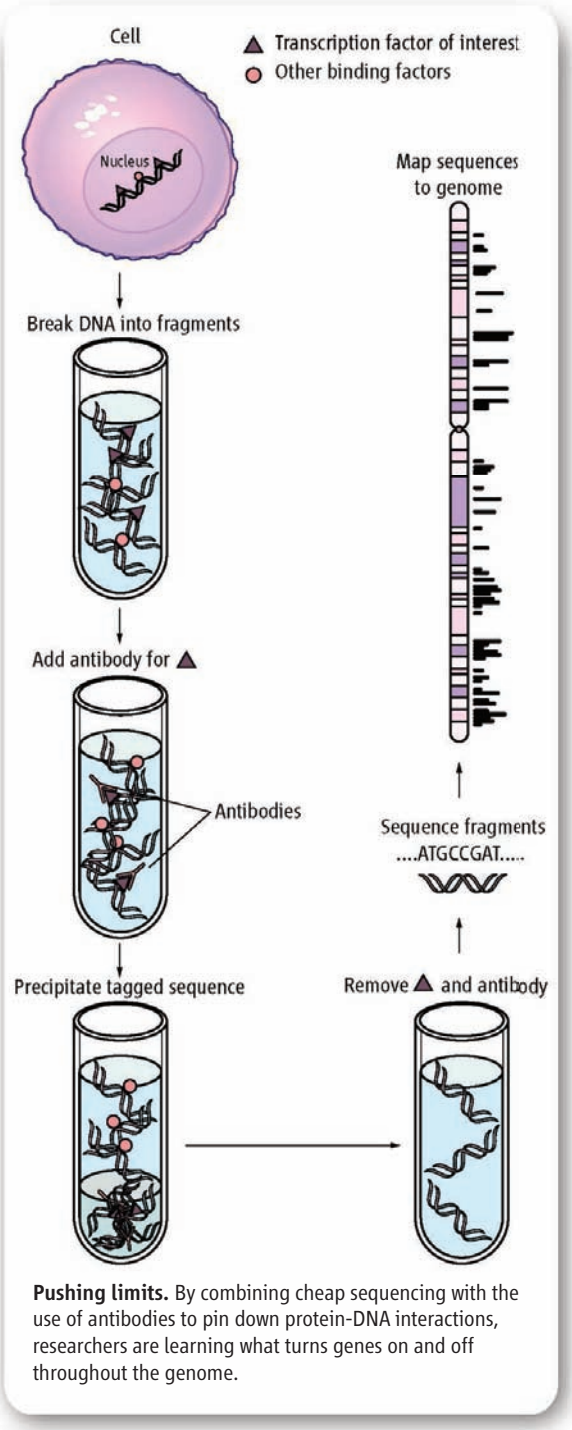

Pushing limits. By combining cheap sequencing with the use of antibodies to pin down protein-DNA interactions, researchers are learning what turns genes on and off throughout the genome.

CREDIT: C. BICKEL/*SCIENCE*, ADAPTED FROM J. D. WATSON, A. A. CAUDY, R. M. MYERS, AND J. A. WITKOWSKI, *RECOMBINANT DNA: GENES AND GENOMES*, 3RD EDITION (2007)

Broad overview

Greg Crawford, a molecular biologist at Duke University in Durham, North Carolina, and, independently, Stamatoyannopoulos have even bigger plans for using sequencing as a tool to understand genome regulation. Instead of using chromatin immunoprecipitation, they depend on a biochemical trick—an enzyme called DNase I—to track down docking sites for the full gamut of regulatory proteins. "Those regions are hidden in the genome and historically have been very difficult to find," says Crawford.

Where regulatory proteins dock onto DNA, the chromosome begins to unwind and expose the DNA. Those are also sites where the DNA is hypersensitive to DNase I, which is now able to get to the DNA itself to cut it. For decades, molecular biologists have used this enzyme to track down docking sites a few at a time. More recently, microarrays have made it possible to search for them more broadly. However, the DNA probes on microarrays are not always reliable because they can't detect docking points buried in repetitive DNA and at times incorrectly flag other spots.

At the meeting, Crawford described how, instead of using microarrays, he simply sequences all the spots that DNase I targets across the entire genome. Stamatoyannopoulos, too, is moving ahead with tag sequencing. Both are finding hundreds of thousands of docking sites, many in unexpected locations. Only about 40% are at the starts of genes, Crawford reported. Others are in the introns, the sequence in between a gene's protein-coding regions, and some are 200,000 bases from the nearest gene. "Some are mapping to gene deserts where people didn't think there was much going on," he said.

At the same time that Crawford, Stamatoyannopoulos, Bernstein, and Myers are mapping regulatory sites along DNA, Yijun Ruan and Chia-Lin Wei of the Genome Institute of Singapore are probing how DNA from different parts of a chromosome, or even different chromosomes, affect gene activity from afar. Some of the regulatory DNA associated with a particular gene can reside a long way from the gene itself. Sometimes a protein attached to DNA in one part of the genome contacts a protein attached at another location, causing DNA to form loops, and both play a role in the gene's activity.

To "see" these long-distance interactions, Ruan and Wei have combined chromatin precipitation, sequencing, and a technique for freezing these DNA loops in place. In this way, they are able to track down exactly where these interacting proteins operate throughout the whole genome. "It's a high-throughput way of looking at these molecular interactions in three-dimensional space," says Ross Hardison of Pennsylvania State University in State College. With this technique, the Singapore team has studied the effects of estrogen on gene regulation in breast cancer cells. Estrogen activates the estrogen receptor, which in turn activates genes. They found that more often than researchers have realized, the estrogen receptor binds to DNA quite far away from its target gene.

Just as Google Earth can take you from the whole planet to a neighborhood, these new approaches are providing glimpses of gene regulation at different levels of resolution. DNase I provides a global view, and transcription factor studies a very focused view, with histones helping to tag a variety of regulatory landmarks. And Ruan's technique may reveal connections between remote regulatory regions of the genome. It's a complex network, but Collins is confident of rapid progress. By combining these levels, he predicts, "you can really start to figure out what's happening."

–ELIZABETH PENNISI

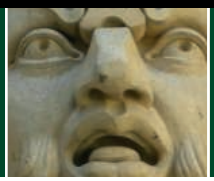

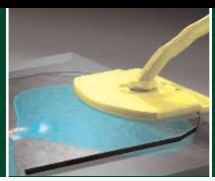

LETTERS

edited by Etta Kavanagh

Lessons from Science Communication Training

ALAN I. LESHNER'S EDITORIAL "OUTREACH TRAINING NEEDED" (12 JAN., p. 161) calls for increased communication training for science graduate students. In March, a bill was introduced to the U.S. House of Representatives (HR1453), requesting funding from the National Science Foundation (NSF) to provide graduate students in the sciences with science communication training. Currently, most communication training for scientists begins after a prominent scientific discovery, and the training often occurs in a trial-by-fire style. However, a cultural shift is under way, reflecting the higher stakes of research, and an increased recognition by scientists, stakeholders, and policymakers that (i) scientists need to get their message out, (ii) scientists need training to learn how to do so, and (iii) training should begin at the graduate level.

Over the past year, we developed and recently completed a science communication course for graduate students in the Biogeochemistry and Environmental Biocomplexity program at Cornell University (funded by a NSF Integrative Graduate Education and Research Traineeship grant). The goal of this course was to improve our ability to discuss our research with both the general public and the professionals writing and reporting on science in the media. This was achieved through a combination of guest lectures, field trips, and development of individual projects.

From this experience, we strongly encourage other graduate programs to implement science communication training. We have three key pieces of advice based on our effort that we hope will help others in their course development:

First, involve people from multiple fields across your college or university. In particular, we highly recommend involving staff from the press relations office. These specialists have a unique perspective on what topics are newsworthy and on the challenges scientists face in communicating effectively. Include scientists who have personal experience communicating their research to the public and journalists from your campus or local newspaper.

Second, visit a news room (radio, print, or television) and talk to reporters—not just science reporters, but reporters in all fields. Ask to sit in on a meeting where reporters and editors pitch stories to each other. This process reveals what stories interest reporters and how those stories are developed. Understanding this process will help scientists identify and explain the newsworthy attributes of their own research.

Third, get hands-on experience communicating science as part of the class. Do not just set up a series of lectures and field trips: write press releases, write articles, conduct interviews, get interviewed, create a Web page, and set up a science blog. Ask your collaborating journalists and PR specialists to facilitate and critique student projects. Hands-on experience with feedback from media professionals and other students provided some of the most useful learning experiences in our course.

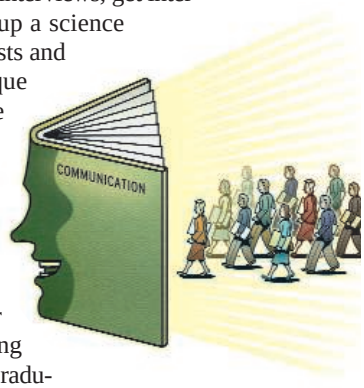

We learned that this course is just the beginning of a career-long process of practicing and refining our science communication skills. Starting public communication training at the graduate level will increase the frequency and confidence with which scientists communicate, with positive feedback for both science and public understanding.

DANA R. WARREN,[1] MARISSA S. WEISS,[2] DAVID W. WOLFE,[3] BLAINE FRIEDLANDER,[4] BRUCE LEWENSTEIN[5]

[1]Department of Natural Resources, [2]Department of Ecology and Evolutionary Biology, [3]Department of Horticulture, [4]Press Relations Office, [5]Department of Communications, Cornell University, Ithaca, NY 14853, USA.

Establishing Rights over the Arctic Ocean

KEVIN KRAJICK PROVIDES A COMPREHENSIVE description of issues related to the development of extended continental shelves by the five coastal states that surround the Arctic Ocean in his article "Race to plumb the frigid depths" (Special Section on Polar Science: News, 16 Mar., p. 1525). However, he addresses certain topics in a way that could foster wrong or misleading impressions, and it is important to set the record straight.

Krajick suggests that the Russian Federation is seeking to extend sovereign rights beyond 200 nautical miles over an unjustifiably large sector of the central Arctic Ocean. Three points need to be noted here:

1) In the process of defining maritime boundaries, a well-established principle is that the extent of a coastal state's offshore jurisdiction is largely determined by the length and the configuration of its coastline (*1*). Since nearly half of the Arctic Ocean's coastline fringes Russia's northern territory, it does not seem unwarranted for that country, in accordance with the provisions of the UN Convention on the Law of the Sea (UNCLOS) Article 76, to pursue an extended continental shelf that encompasses a significant portion of the sea floor beyond 200 nautical miles.

2) Many observers and commentators appear to have missed the proviso (perhaps because it appears in Russian and in fine print at the bottom of a key document) that the

CREDIT: PETER HOEY

Published by AAAS

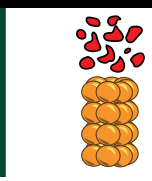

Clock precision

1135

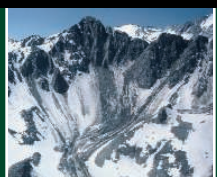

Landslide prediction

1136

proposed Russian outer limits are "subject to more precise determination through negotiations [with neighbouring States]," according to a translation posted on the Division of Ocean Affairs and the Law of the Sea Web site (*2*). This indicates a readiness to seek accommodations with other coastal states in the region.

3) Independent studies have considered the continental shelf implications for all coastal states that border the Arctic Ocean (*3*, *4*). Derived from data sets that differed from those used by Russian investigators, the outcomes of these studies have tended to mirror the outer limits that were proposed by Russia in its 2001 submission to UNCLOS.

On a more personal level, the article contains statements attributed to me that appear to disparage the Russian continental shelf submission. I did not suggest that the Russian initiative lacked merit; in fact, recent studies have further substantiated the Russian case (*5*). I did not claim to speak for the Canadian Polar Commission, as implied by Krajick; the views expressed during the course of our exchanges were mine alone.

RON MACNAB

Geological Survey of Canada (retired), 11 Lyngby Avenue, Dartmouth, NS B3A 3T6, Canada. E-mail: ron.macnab@ns.sympatico.ca

References

1. United Nations, Handbook on the Delimitation of Maritime Boundaries (United Nations, New York, 2000).
2. United Nations, Website of the Division of Ocean Affairs and the Law of the Sea (DOALOS), Legends to the attached maps, www.un.org/Depts/los/clcs_new/submissions_files/rus01/RUS_page5_Legend.pdf (2001).
3. R. Macnab, P. Neto, R van de Poll, Cooperative preparations for determining the outer limit of the juridical continental shelf in the Arctic Ocean: a model for regional collaboration in other parts of the world ocean?, Proceedings of a Continental Shelf Workshop hosted by the Argentine Council for International Relations (CARI), Buenos Aires, 13 to 15 November 2000 (reprinted with permission in *Boundary and Security Bulletin*, vol. 9, no. 1, pp. 86–96, International Boundaries Research Unit, Durham University, NC, Spring 2001).
4. P. Neto, R. van de Poll, *Int. Hydrogr. Rev.* **2** (no. 1), 37 (2001).
5. V. D. Kaminsky, V. A. Poselov, V. Y. Glebovsky, A. V. Zayonchek, V. V. Butsenko, *Eos Trans. AGU* **86** (no. 52), Fall Meet. Suppl., Abstr. T12C-06 (2005).

IN THE ARTICLE "RACE TO PLUMB THE FRIGID depths" (Special Section on Polar Science: News, 16 Mar., p. 1525), Kevin Krajick gives a rather negative view on the work our Russian colleagues are doing on the topic of territorial claims to underwater rights in the Arctic Ocean. To understand the kind of work being done to fulfil the requirements of the United Nations Convention on the Law of the Sea, readers should be aware that the way data are being interpreted inevitably will be in the national interest of the country doing the interpretation, which will then be countered by the UN's Commission on the Limits of the Continental Shelf (CLCS). It is a legal process. There is no given line on the sea floor marking the "end of the natural prolongation of the land mass." The problem about the process lies elsewhere: in the secrecy in dealings between a submitting nation and CLCS.

In the article, I am quoted as agreeing with the statement (made by Arthur Grantz): "They're [the Russians] under great pressure. Their government gave them a lot of money, and it expects them to come up with a certain result." However, I did not express agreement with this point of view when talking to Kevin Krajick.

TRINE DAHL-JENSEN AND KAI SØRENSEN

GEUS, Geological Survey of Denmark and Greenland, Oester Voldgade 10, DK 1350 Copenhagen K, Denmark.

The March of HIV Vaccines

A QUARTER CENTURY HAS PASSED SINCE THE first clinical descriptions of AIDS, and no HIV vaccine is in sight. The global community has recognized that alternative approaches must be pursued if discovery and development of preventive vaccines are to be accomplished, hence, the call for the HIV Vaccine Enterprise in 2003 (*1*). Since then, a scientific plan was proposed (*2*), and new funding has been distributed (*3*, *4*). But in the absence of a conceptual framework, focus, and effective leadership, the Enterprise has neither challenged nor changed current HIV vaccine approaches. Although experience with national or global programs for vaccine discovery and development is not extensive, a comparison with the March of Dimes approach to developing a polio vaccine may be illustrative (*5*). In 1946, polio vaccine research was diffuse and free floating. Polio research had been progressing slowly in too many different directions, with a lack of knowledge among scientists about what other scientists were achieving. With very little accountability, there was no way to assess progress. The ultimate production of two effective polio vaccines was due to the leadership of the National Foundation for Infantile Paralysis (March of Dimes Foundation) and its razor-sharp focus on product development and involvement of industry.

The call for a global HIV vaccine research enterprise comes at a time when several new vaccines for major global infectious diseases such as rotavirus and human papillomavirus (HPV) infections have recently been produced (*6*–*8*). The example of the HPV vaccine is illustrative of new scientific capabilities that were unimaginable a few years ago (*9*). HPV cannot currently be cultured in vitro; its life cycle in host cells is unknown; there are no animal models for evaluation of vaccine efficacy; and there are no surrogates of adaptive immunity. Nevertheless, the HPV genome was sequenced, its proteins characterized, and their functions defined. The crucial step for vaccine discovery came in two laboratories attempting in vitro expression of the most conserved viral gene, L1. The resulting protein folded into viruslike particles that turned out to be strongly immunogenic and induced protection in humans. Within a few years, vaccines were developed by two manufacturers, and one was recently launched in the United States, Europe, and several other countries.

Ideally, the Global Enterprise should become the enabling mechanism to attract the best scientific minds worldwide. This community has to be tapped for innovative scientific concepts, but not the usual "me too" approaches. The Enterprise scientific plan is faced with two challenges: (i) how to seek innovative new science, and (ii) how to shift to product discovery and development. The effort needs the best of the private and public sectors and commitment of adequate resources. A well-articulated business plan with specific objectives, performance targets, evaluation criteria, and a timetable are essential. The Enterprise also must avoid parallel structures and duplicative processes that undermine its credibility and independence. Lessons from recent global experiences should inform the development of the Enterprise structure. For example, the Global Alliance for Vaccines and Immunization (GAVI) and its fundraising and independent arm, the Vaccine Fund, have resulted in an impaired global vaccine effort. The recent appointment of one person to lead both organizations did not resolve the existence of two separate entities (*10*).

The challenge in this third decade of the HIV/AIDS pandemic is not only our scientific limitation, but also fundamental limitations in our organizational capabilities and our ability to conceptualize the full diversity of the

problem. HIV vaccine development is the major public health challenge of our time; there is no alternative but to engage into and continue an aggressive and tenacious global effort.

ADEL MAHMOUD

Woodrow Wilson School and Department of Molecular Biology, Princeton University, 228 Lewis Thomas Laboratory, Princeton, NJ 08544, USA. E-mail: amahmoud@princeton.edu

References

1. R. D. Klausner *et al.*, *Science* **300**, 2036 (2003).
2. Coordinating Committee of the Global HIV/AIDS Vaccine Enterprise, *PLoS Med.* **2**, e25 (2005).
3. Center for HIV-AIDS Vaccine Immunology, www.chavi.org (accessed 13 Oct. 2006).
4. J. Cohen, *Science* **313**, 283 (2006).
5. D. O. Oshinsky, in *Polio: an American Story* (Oxford Univ. Press, New York, 2005), pp. 112–127.
6. Centers for Disease Control and Prevention, *Morbid. Mortal. Weekl. Rep.* **55**, 841 (2006).
7. H. F. Clark *et al.*, *Pediatr. Infect. Dis. J.* **25**, 577 (2006).
8. L. L. Villa *et al.*, *Lancet Oncol.* **6**, 271 (2005).
9. D. R. Lowy, J. T. Schiller, *J. Clin. Invest.* **116**, 1167 (2006).
10. See www.gavialliance.org/EC telecom (29 Dec. 2004; accessed 25 Nov. 2006).

CORRECTIONS AND CLARIFICATIONS

Table of Contents: (6 Apr., p. 9). The one-sentence summary for the Report by Mulugo *et al.*, "A conserved family of enzymes that phosphorylate inositol hexakisphophate," is incorrect. It should read, "A yeast enzyme that synthesizes the inositol pyrophosphate IP_6 is identified."

This Week in *Science*: "Understanding inositol pyrophophates" (6 Apr., p. 15). The second and third sentences are incorrect and should instead read, "Mulugu *et al.* (p. 106) purified an inositol pyrophosphate synthase from yeast called Vip1."

Special Section on Germ Cells: News: "Melting opposition to frozen eggs" by M. Leslie (20 Apr., p. 388). The two scientists pictured cryopreserving humans eggs on page 388 are Pasquale Patrizio of Yale Fertility Center in New Haven, Connecticut (left) and Veronica Bianchi from Tecnobios Procreazione in Bologna, Italy (right).

TECHNICAL COMMENT ABSTRACTS

COMMENT ON "Dispersal Limitations Matter for Microbial Morphospecies"

Jason Pither

Telford *et al*. (Brevia, 19 May 2006, p. 1015) reported that freshwater diatoms exhibit regional-scale richness-pH relationships that depend substantially on regional habitat availability. On this basis, the authors argued that, despite their microscopic size, diatoms are not ubiquitously dispersed. Here, I describe my demonstration that their primary evidence against the ubiquitous dispersal hypothesis is spurious.

Full text at www.sciencemag.org/cgi/content/full/316/5828/1124b

RESPONSE TO COMMENT ON "Dispersal Limitations Matter for Microbial Morphospecies"

Richard J. Telford, Vigdis Vandvik, H. J. B. Birks

Pither argues that the relationship we found between regional species-richness maxima and modal lake pH is expected because both values are constrained by the regional pH range and therefore cannot be interpreted as a signal of regional metacommunity dynamics. However, the null model he uses sets inappropriate parameters, generating unrealistic simulated data. We confirm our previous conclusions using a more appropriate null model.

Full text at www.sciencemag.org/cgi/content/full/316/5828/1124c

Letters to the Editor

Letters (~300 words) discuss material published in *Science* in the previous 3 months or issues of general interest. They can be submitted through the Web (www.submit2science.org) or by regular mail (1200 New York Ave., NW, Washington, DC 20005, USA). Letters are not acknowledged upon receipt, nor are authors generally consulted before publication. Whether published in full or in part, letters are subject to editing for clarity and space.

Published by AAAS

Comment on "Dispersal Limitations Matter for Microbial Morphospecies"

Jason Pither

Telford *et al*. (Brevia, 19 May 2006, p. 1015) reported that freshwater diatoms exhibit regional-scale richness-pH relationships that depend substantially on regional habitat availability. On this basis, the authors argued that, despite their microscopic size, diatoms are not ubiquitously dispersed. Here, I describe my demonstration that their primary evidence against the ubiquitous dispersal hypothesis is spurious.

Telford *et al*. (*1*) argued that if dispersal is ubiquitous among freshwater diatoms, as hypothesized by Finlay and colleagues (*2*, *3*), then all geographic regions should share one underlying richness-environment relationship, governed by the global species pool. If, on the other hand, diatoms experience some dispersal limitation, then they should form regional-scale metacommunities that vary with respect to key properties such as colonization-extinction dynamics. On this premise, Telford *et al*. predicted that "if dispersal is limited, regional richness relationships will depend upon regional habitat availability." In apparent support of this prediction, they found that across 16 regional-scale surveys [see table S1 in (*1*)], the pH at which diatom richness peaked (which they call "richness pH optima") was significantly correlated with the modal pH of the region [see figure 1C in (*1*)]. Unfortunately, this correlation is spurious, because the richness pH optima and the modal pH values were necessarily constrained to lie between the variable, region-specific pH extremes. The following sampling exercise illustrates this point.

First, draw N pairs of values from a uniform distribution U(0,1), where N represents the number of regional samples (e.g., 16) and each pair of values represents the region-specific minimum and maximum pH values. Next, obtain a modal pH value for each of the N regions by drawing a single value from the available range of pH for each region, U(pH_{min},pH_{max}). Then, obtain a richness pH optimum for each region by drawing another single value from the available range of pH for each region, U(pH_{min},pH_{max}). Finally, calculate the correlation between the resulting N modal pH values and N richness pH optima values. I conducted this sampling exercise 100 times (using N = 16) and obtained an average Pearson correlation coefficient of 0.76 (SD = 0.146). This suggests that the correlation reported by Telford *et al*. is inconsequential and therefore cannot be used to test the merits of the ubiquitous dispersal hypothesis.

In contrast, the observation that richness-pH relationships vary in form among regions, even among neighboring regions [see figures 1B and S1 in (*1*)], is informative. Telford *et al*. interpret this pattern as evidence against the ubiquitous dispersal hypothesis, but a more accurate interpretation is that it is inconsistent with the hypothesis that all diatom taxa are ubiquitously dispersed. In other words, the hypothesis that some diatom taxa are ubiquitously dispersed remains unchallenged by the results presented by Telford *et al*. Identifying which taxa are ubiquitously dispersed represents an important task for future research. Preliminary evidence (*3*–*5*) suggests that environmental generalists and/or taxa adapted to the most common environments represent strong candidates, because these achieve large abundances over geographically extensive regions.

Department of Ecology and Evolutionary Biology, University of Arizona, BSW 310, 1041 East Lowell Street, Tucson, AZ 85721, USA. E-mail: pitherj@email.arizona.edu. Address as of 1 July 2007: Biology and Physical Geography Unit, Irving K. Barber School of Arts and Sciences, University of British Columbia–Okanagan, 3333 University Way, Kelowna, BC, Canada V1V 1V7.

References

1. R. J. Telford, V. Vandvik, H. J. B. Birks, *Science* **312**, 1015 (2006).
2. B. J. Finlay, *Science* **296**, 1061 (2002).
3. B. J. Finlay, E. B. Monaghan, S. C. Maberly, *Protist* **153**, 261 (2002).
4. M. G. Potapova, D. F. Charles, *J. Biogeogr.* **29**, 167 (2002).
5. J. Pither, L. W. Aarssen, *Ecol. Lett.* **9**, E6 (2006).

13 November 2006; accepted 30 April 2007
10.1126/science.1137525

Response to Comment on "Dispersal Limitations Matter for Microbial Morphospecies"

Richard J. Telford,[1,2]* Vigdis Vandvik,[1] H. J. B. Birks[1,2,3]

Pither argues that the relationship we found between regional species-richness maxima and modal lake pH is expected because both values are constrained by the regional pH range and therefore cannot be interpreted as a signal of regional metacommunity dynamics. However, the null model he uses sets inappropriate parameters, generating unrealistic simulated data. We confirm our previous conclusions using a more appropriate null model.

The ubiquitous dispersal hypothesis (*1*) of microbial biogeography has been difficult to test because of undersampling and taxonomic uncertainties. We developed a novel test of this hypothesis (*2*), arguing that if dispersal is ubiquitous, microbial metacommunities should be global in scale, but that if dispersal is limited, metacommunity processes will operate at regional scales. We predicted that regional species richness–environment relationships would reflect sampling from the global diatom species pool if there was ubiquitous dispersal [see figure 1A in (*2*)] but would be modified by the regional environmental commonness if dispersal was limited. Figure 1B in (*2*) showed that for three regions with different modal lake pH, the statistically significant richness maxima [referred to as "optima" in (*2*)] are very different and reflect the regional environmental commonness. The majority of the 16 regions presented in figure S1 in (*2*) had statistically significant richness maxima that reflected the regional pH commonness rather than a global species pool: This was our primary evidence against the ubiquitous dispersal hypothesis.

Figure 1C in (*2*) summarized the data shown in figures 1B and S1 and showed a strong positive relationship between the regional pH modes and richness maxima. This is expected if diatom metacommunities are regional in scale; if they are global, no trend is expected. Pither (*3*) demonstrates that, because the regional pH mode and the richness maximum are both constrained to lie within the pH range of each data set, a positive correlation between these two variables is also expected if the maxima are randomly located. Exploring the consequences of this constraint with a null model, Pither (*3*) drew two values from a uniform distribution U(0,1) to represent the range of pH values, and then drew two values from within this range to represent the pH mode and the richness maximum, for each of 16 simulated data sets. The correlation coefficient between the modes and maxima was then calculated.

We were initially surprised by the strength of the relationship reported by Pither's null model: The mean correlation coefficient between the modes and the maxima (0.76) is almost as high as the observed value (0.85), which would suggest that the relationship we showed can be expected by chance. However, Pither's simulation generates data sets that do not reflect reality. Most of the observed data sets span more than half the entire pH gradient found across all the data sets, and all span more than a third of the pH gradient [table S1 in (*2*)]. In contrast, half the simulated ranges generated by Pither's (*3*) null model span less than a third of the gradient, and a sixth span less than 10%. This imposes a much stronger constraint on the relationship between pH modes and richness maxima in the simulation than in the actual data.

A more appropriate null model is to maintain the observed pH range and mode for each data set and randomize only the position of the richness maxima within the pH range. The mean Pearson correlation coefficient between the modes and maxima in 1000 simulations of this null model is 0.44, and the observed correlation is significant ($P = 0.01$). Therefore, although Pither (*3*) identifies a potential confounding factor, it does not affect our original conclusions.

In rejecting the "everything is everywhere" hypothesis, we took the position that "not everything is everywhere" (*2*) rather than the proposition that "nothing is everywhere," which Pither appears to ascribe to us (*3*), but which cannot be tested with our data. Pither's conclusion that common generalist diatom taxa are likely to experience less dispersal limitation is entirely consistent with our position that specialists in rare habitats will be most affected (*2*).

[1]Ecological and Environmental Change Research Group, Department of Biology, University of Bergen, Allégaten 41, N-5007 Bergen, Norway. [2]Bjerknes Centre for Climate Research, Allégaten 55, N-5007 Bergen, Norway. [3]Environmental Change Research Centre, University College London, London, WC1E 6BT, UK.

*To whom correspondence should be addressed. E-mail: Richard.Telford@bjerknes.uib.no

References

1. B. J. Finlay, *Science* **296**, 1061 (2002).
2. R. J. Telford, V. Vandvik, H. J. B. Birks, *Science* **312**, 1015 (2006).
3. J. Pither, *Science* **316**, 1124 (2007); www.sciencemag.org/cgi/content/full/316/5828/1124b.

14 December 2006; accepted 1 May 2007
10.1126/science.1137697

PHILOSOPHY OF MIND

Who Watches the Watcher?

Christoph C. Adami

Douglas Hofstadter has made a career of thinking about thinking, and he is rightfully famous for writing the Pulitzer-winning *Gödel, Escher, Bach: An Eternal Golden Braid* (*1*) at the tender age of 27. That book was a roller-coaster ride that defied classification then as today, but much to the author's chagrin the central message that he tried to convey, concerning the nature of human consciousness, seemed to have been lost among the fireworks. It is this shortcoming that Hofstadter (a professor of cognitive science at Indiana University) seeks to correct in the playful and intensely personal *I Am a Strange Loop*, in which he explains human consciousness while exploring (and coming to grips with) his own.

I Am a Strange Loop
by Douglas Hofstadter
Basic Books, New York, 2007. 436 pp. $26.95, C$32.50. ISBN 9780465030781.

The nature of human consciousness has been debated through the centuries, at least since Descartes posited that a special substance, the *res cogitans*, conferred upon humans (and only humans) the ability to think and feel; have ideas, wishes, and concerns; display empathy, dislikes, or wonder. This dualist view of the world—dual because it presupposes the existence of two radically different substances, one to make the mind, and another to make everything else in the world—still, in one form or another, informs the thinking of a surprising (to me) number of philosophers of the mind. Hofstadter is not one of those. His approach is decidedly materialistic, that is, he seeks an explanation of the phenomenon of consciousness using physical law only. However, he is not interested in a neurobiological explanation (even though he is fully convinced that consciousness must be explainable within neurobiology) because he believes that as our consciousness is perceived at the level of symbols and thoughts, our explanation of it should occur at this level of description also.

Hofstadter's explanation of human consciousness is disarmingly simple. Even though he spends most of the book giving examples and analogies from realms as disparate as particle physics and boxes of envelopes, the main idea is simply that our feeling of a conscious "I" is but an illusion created by our neuronal circuitry: an illusion that is only apparent at the level of symbols and thoughts, in much the same way as the concepts of pressure and temperature are only apparent at the level of 10^{23} molecules but not the level of single molecules. In other words, Hofstadter denies consciousness an element of ontological reality, without denying that our thoughts and feelings, pains and longings have an "inner reality" when we have them. But to show that consciousness is a collective phenomenon of sorts, he needs to delve deep into the theory of computation and, in particular, Austrian mathematician Kurt Gödel's proof of his incompleteness theorem, as these concepts are key to the idea the author wants to convey. And he does this admirably in a mostly playful manner, choosing carefully constructed analogies more often than mathematical descriptions.

Gödel showed in 1931 that any formal system that is complicated enough must contain statements that are patently true but remain unprovable within that formal system. The important point here is that the true statements Gödel explicitly constructed play a dual role: they can be understood at a higher—that is, symbolic—level, while representing purely number-theoretic assertions at the same time. To achieve this, Gödel constructed a mapping between conceptual statements (such as "This statement is not provable within the formal system XYZ") and purely number-theoretic identities that effectively creates a barrier between levels of description that is as impenetrable as the barrier between our thoughts and the patterns of neuronal firings. In the same manner, Hofstadter suggests, our ability to construct symbols and statements that are about these symbols and statements creates the "strange" reflexive loop of the book's title out of which our sensation of "I" emerges.

This ambitious program aimed at a deconstruction of our consciousness is not without peril. For example, if we posit that our consciousness is an illusion created by our thoughts "watching ourselves think" [as the philosopher of mind Daniel Dennett had previously suggested (*2*)], we might ask "Who watches the watcher?" Or, if I am hallucinating an "I," who is hallucinating it? However, an infinite regress is avoided because on the level of the neuronal circuitry, the impression of having a mind is just another pattern of firings—something consciousness researcher and neuroscientist Christof Koch of the California Institute of Technology calls "the neuronal correlate" of consciousness.

In fact, Hofstadter's book and Koch's recent *The Quest for Consciousness* (*3*) make for an interesting juxtaposition. Each addresses the same problem but entirely on different levels. Yet both authors reach some of the same conclusions, sometimes using precisely the same metaphor (as when they compare the activity of "making up one's mind" in terms of a voting process). In the end, both authors could have profited from peeking at each other's arsenal: Hofstadter would probably be delighted to see some of the putative neural underpinnings of consciousness, to peer underneath the strange loop as it were, at the inordinately complex firework and the neuroanatomy that supports it. For his part, Koch would no doubt appreciate the computational trick that Gödel incompleteness plays on us, as well as the developmental aspect of consciousness that Hofstadter advocates.

Bathsheba Grossman's sculpture *MG*. A self-intersecting, figure-eight knot.

CREDIT: COURTESY BATHSHEBA GROSSMAN/WWW.BATHSHEBA.COM

I believe that Hofstadter's views on consciousness will play an important part, on at least two levels, as we go forward in exploring our mind. First, Hofstadter implicitly provides a blueprint for how one should go about constructing a conscious machine, because no less is implied by these ideas. When constructed, we should not expect that such a machine would be conscious from the get-go: after all, Hofstadter's "I" is an outcome, not a starting point. We should give such a machine a good decade or so to form its own personality, as we ourselves are afforded that much. Second, the Gödelian construction suggests a tantalizing hypothesis, namely that a level of consciousness could exist far beyond human consciousness, on a level once removed from our level of symbols and ideas (which themselves are once removed from the level of neuronal firing patterns). Indeed, Gödel's construction guarantees that, while statements on the higher level can be patently

The reviewer is at the Keck Graduate Institute, 535 Watson Drive, Claremont, CA 91711, USA. E-mail: adami@kgi.edu

true but not provable on the lower level, an extension exists that makes the system complete on that higher level. However, new unprovable statements emerge on the next higher level—that is, on a level that maps an improbable jumble of our thoughts and ideas to, well, something utterly incomprehensible to us, who are stuck at our pedestrian echelon. How incomprehensible? At least as inscrutable as the love for Bartok's second violin concerto is to a single neuron firing away.

References

1. D. R. Hofstadter, *Gödel, Escher, Bach: An Eternal Golden Braid* (Basic, New York, 1979).
2. D. C. Dennett, *Consciousness Explained* (Little, Brown, Boston, 1991).
3. C. Koch, *The Quest for Consciousness: A Neurobiological Approach* (Roberts, Englewood, CO, 2004); reviewed by P. Haggard, *Science* **304**, 52 (2004).

10.1126/science.1141809

GENETICS

More Means of Regulating Genes

Armelle Corpet and Geneviève Almouzni

What is "epigenetics"? Surprisingly, searching in a dictionary won't tell you much about the word because there is a good chance that you won't find it. Yet the popularity of its use in recent years illustrates the flourishing rebirth of a research area that originated in the 1930s. It is perhaps not so surprising that in our postgenome era people's interest is drawn to phenomena that cannot be explained by classical genetics. Famous examples include paramutation in maize, position effect variegation in the fruit fly *Drosophila*, X chromosome inactivation in mammals, and genomic imprinting. Today, efforts to understand the mechanisms underlying these fascinating phenomena have coalesced into a field of their own, epigenetics.

The expanding interest in this broad field is reflected in the range of topics covered in the volume *Epigenetics*. The editors—David Allis (Rockefeller University), Thomas Jenuwein (Research Institute of Molecular Pathology, Vienna), and Danny Reinberg (University of Medicine and Dentistry of New Jersey)—recognized that, with the pace of epigenetics research, a compilation of expert reviews would probably soon become outdated. So they instead recruited 44 authors, experts in the field, to produce 24 conceptual chapters that highlight a wide variety of aspects of epigenetic gene regulation. Collectively, the chapters provide a reference foundation for both curious newcomers and researchers in the field as well as an effective tool for teachers. The editors, aided by the efforts of Marie-Laure Caparros, have put together a quite coherent volume, one strengthened by the numerous (and relatively consistently styled) illuminating diagrams and figures.

To start off, Gary Felsenfeld offers a brief historical sketch. He reminds us that the word "epigenetics" has its conceptual roots in the theory of epigenesis, which holds that complexity emerges progressively during development. (That view was opposed by the theory of preformation, which held that individuals develop by the enlargement of minute, fully formed organisms, the homunculus; the distinction can be traced back to Aristotle.) Conrad Waddington, in the early 1940s, coined the term epigenetics to describe "the interactions of genes with their environment, which bring the phenotype into being" (*1*)—a fairly broad definition. In its etymological sense, epigenetics refers to additional methods of biological inheritance (the prefix epi- means above or over in Greek) that do not relate to the inheritance of DNA and its mutations.

Epigenetics

C. David Allis, Thomas Jenuwein, and Danny Reinberg, Eds.

Cold Spring Harbor Laboratory Press, Cold Spring Harbor, NY, 2007. 512 pp. $150, £85. ISBN 9780879697242.

Daniel Gottschling notes that at the 69th Cold Spring Harbor Symposium on Quantitative Biology (2004)—attended by many of the volume's authors—"epigenetics" seemed to have a different meaning for each person. He attributes part of this variation to the dual distinct origins of the word recognized by David Haig (*2*): Waddington's causal interactions and David Nanney's application of the term to the control systems that allowed cells of the same genotype to have different phenotypes (*3*). Gottschling favors a definition [from Robin Holliday (*4*)] that was a major trigger for the explosion in the use of the word during the 1990s: an epigenetic phenomenon is "a change in phenotype that is heritable but does not involve DNA mutation." Gottschling refines this definition by requiring that the change be switchlike (on-off) rather than gradual and that epigenetic inheritance should occur "even if the initial conditions that caused the switch disappear." These concepts encompass most of the important aspects of current views concerning the definition of epigenetics. But the volume's introductory chapters do not adequately recognize the reversible character of epigenetics, which is demonstrated by the capacity to reprogram somatic nuclei. (That topic is, however, addressed in the chapters by Azim Surani and Wolf Reik and by Rudolf Jaenisch and John Gurdon.)

In their own chapter, "Overview and Concepts," the editors offer a modern molecular definition of epigenetics as the "sum of the alterations to the chromatin template that collectively establish and propagate different patterns of gene expression (transcription) and silencing from the same genome." This definition reflects the excitement for chromatin-based mechanisms—a driving force for research on histone modifications and variants, RNA, and nonhistone chromatin proteins. But it leaves aside potential non–chromatin-based epigenetic phenomena such as prions, and it only briefly touches on the aspect of higher-order structures at the level of nuclear organization and gene expression. For these reasons, readers should bear in mind alternative perspectives.

The authors also aim to convey how the study of various model organisms has proven crucial for current epigenetic research. Some of the organisms and their respective phenomena include the budding yeast *Saccharomyces cerevisiae* (mating-type switching), the fruit fly *Drosophila* (position effect variegation, for example), fungi such as *Neurospora crassa* and *Schizosaccharomyces pombe* (e.g., centromeric heterochromatin and the role of small interfering RNAs), ciliates, plants, the nematode *Caenorhabditis elegans*, and mammals (e.g., genomic imprinting). As French readers, we were struck by the fact that frogs did not appear among these models. *Xenopus laevis*, used for the first cloning experiments, is however mentioned in a chapter discussing the mechanisms of nuclear reprogramming of the genome. It is worth remembering that this exotic organism provided useful tools and assays for epigenetics, including pioneering work on chromatin assembly. Of course, still other model systems (such as the callipyge sheep or the planarian *Schmidtea mediterranea*) could have been mentioned had the authors chosen to discuss different intriguing phenomena.

The contributors discuss the substantial progress achieved through studies of covalent and noncovalent modifications of DNA and histone proteins as well as how combinations of these modifications potentially affect chromatin dynamics and epigenetic

The reviewers are at the Laboratory of Nuclear Dynamics and Genome Plasticity, UMR218 CNRS/Institut Curie, 26 rue d'Ulm, 75248 Paris cedex 05, France. E-mail: armelle.corpet@curie.fr; genevieve.almouzni@curie.fr

true but not provable on the lower level, an extension exists that makes the system complete on that higher level. However, new unprovable statements emerge on the next higher level—that is, on a level that maps an improbable jumble of our thoughts and ideas to, well, something utterly incomprehensible to us, who are stuck at our pedestrian echelon. How incomprehensible? At least as inscrutable as the love for Bartok's second violin concerto is to a single neuron firing away.

References

1. D. R. Hofstadter, *Gödel, Escher, Bach: An Eternal Golden Braid* (Basic, New York, 1979).
2. D. C. Dennett, *Consciousness Explained* (Little, Brown, Boston, 1991).
3. C. Koch, *The Quest for Consciousness: A Neurobiological Approach* (Roberts, Englewood, CO, 2004); reviewed by P. Haggard, *Science* **304**, 52 (2004).

10.1126/science.1141809

GENETICS

More Means of Regulating Genes

Armelle Corpet and Geneviève Almouzni

What is "epigenetics"? Surprisingly, searching in a dictionary won't tell you much about the word because there is a good chance that you won't find it. Yet the popularity of its use in recent years illustrates the flourishing rebirth of a research area that originated in the 1930s. It is perhaps not so surprising that in our postgenome era people's interest is drawn to phenomena that cannot be explained by classical genetics. Famous examples include paramutation in maize, position effect variegation in the fruit fly *Drosophila*, X chromosome inactivation in mammals, and genomic imprinting. Today, efforts to understand the mechanisms underlying these fascinating phenomena have coalesced into a field of their own, epigenetics.

The expanding interest in this broad field is reflected in the range of topics covered in the volume *Epigenetics*. The editors—David Allis (Rockefeller University), Thomas Jenuwein (Research Institute of Molecular Pathology, Vienna), and Danny Reinberg (University of Medicine and Dentistry of New Jersey)—recognized that, with the pace of epigenetics research, a compilation of expert reviews would probably soon become outdated. So they instead recruited 44 authors, experts in the field, to produce 24 conceptual chapters that highlight a wide variety of aspects of epigenetic gene regulation. Collectively, the chapters provide a reference foundation for both curious newcomers and researchers in the field as well as an effective tool for teachers. The editors, aided by the efforts of Marie-Laure Caparros, have put together a quite coherent volume, one strengthened by the numerous (and relatively consistently styled) illuminating diagrams and figures.

To start off, Gary Felsenfeld offers a brief historical sketch. He reminds us that the word "epigenetics" has its conceptual roots in the theory of epigenesis, which holds that complexity emerges progressively during development. (That view was opposed by the theory of preformation, which held that individuals develop by the enlargement of minute, fully formed organisms, the homunculus; the distinction can be traced back to Aristotle.) Conrad Waddington, in the early 1940s, coined the term epigenetics to describe "the interactions of genes with their environment, which bring the phenotype into being" (*1*)—a fairly broad definition. In its etymological sense, epigenetics refers to additional methods of biological inheritance (the prefix epi- means above or over in Greek) that do not relate to the inheritance of DNA and its mutations.

Epigenetics

C. David Allis, Thomas Jenuwein, and Danny Reinberg, Eds.

Cold Spring Harbor Laboratory Press, Cold Spring Harbor, NY, 2007. 512 pp. $150, £85. ISBN 9780879697242.

Daniel Gottschling notes that at the 69th Cold Spring Harbor Symposium on Quantitative Biology (2004)—attended by many of the volume's authors—"epigenetics" seemed to have a different meaning for each person. He attributes part of this variation to the dual distinct origins of the word recognized by David Haig (*2*): Waddington's causal interactions and David Nanney's application of the term to the control systems that allowed cells of the same genotype to have different phenotypes (*3*). Gottschling favors a definition [from Robin Holliday (*4*)] that was a major trigger for the explosion in the use of the word during the 1990s: an epigenetic phenomenon is "a change in phenotype that is heritable but does not involve DNA mutation." Gottschling refines this definition by requiring that the change be switchlike (on-off) rather than gradual and that epigenetic inheritance should occur "even if the initial conditions that caused the switch disappear." These concepts encompass most of the important aspects of current views concerning the definition of epigenetics. But the volume's introductory chapters do not adequately recognize the reversible character of epigenetics, which is demonstrated by the capacity to reprogram somatic nuclei. (That topic is, however, addressed in the chapters by Azim Surani and Wolf Reik and by Rudolf Jaenisch and John Gurdon.)

In their own chapter, "Overview and Concepts," the editors offer a modern molecular definition of epigenetics as the "sum of the alterations to the chromatin template that collectively establish and propagate different patterns of gene expression (transcription) and silencing from the same genome." This definition reflects the excitement for chromatin-based mechanisms—a driving force for research on histone modifications and variants, RNA, and nonhistone chromatin proteins. But it leaves aside potential non–chromatin-based epigenetic phenomena such as prions, and it only briefly touches on the aspect of higher-order structures at the level of nuclear organization and gene expression. For these reasons, readers should bear in mind alternative perspectives.

The authors also aim to convey how the study of various model organisms has proven crucial for current epigenetic research. Some of the organisms and their respective phenomena include the budding yeast *Saccharomyces cerevisiae* (mating-type switching), the fruit fly *Drosophila* (position effect variegation, for example), fungi such as *Neurospora crassa* and *Schizosaccharomyces pombe* (e.g., centromeric heterochromatin and the role of small interfering RNAs), ciliates, plants, the nematode *Caenorhabditis elegans*, and mammals (e.g., genomic imprinting). As French readers, we were struck by the fact that frogs did not appear among these models. *Xenopus laevis*, used for the first cloning experiments, is however mentioned in a chapter discussing the mechanisms of nuclear reprogramming of the genome. It is worth remembering that this exotic organism provided useful tools and assays for epigenetics, including pioneering work on chromatin assembly. Of course, still other model systems (such as the callipyge sheep or the planarian *Schmidtea mediterranea*) could have been mentioned had the authors chosen to discuss different intriguing phenomena.

The contributors discuss the substantial progress achieved through studies of covalent and noncovalent modifications of DNA and histone proteins as well as how combinations of these modifications potentially affect chromatin dynamics and epigenetic

The reviewers are at the Laboratory of Nuclear Dynamics and Genome Plasticity, UMR218 CNRS/Institut Curie, 26 rue d'Ulm, 75248 Paris cedex 05, France. E-mail: armelle.corpet@curie.fr; genevieve.almouzni@curie.fr

Epigenetics in stone. Two complex expressions.

CREDIT: COURTESY J. C. PETTINOTTI

states. DNA methylation, one of the best-characterized modifications, is described in depth in the chapter by En Li and Adrian Bird and is also discussed in chapters focusing on transcriptional regulation, heterochromatin formation, and genomic imprinting. Several chapters consider the changes in chromatin states imposed through covalent and noncovalent modifications of histones. The nearly exhaustive table of histone modifications presented in an appendix will undoubtedly be very useful for many researchers. The absence of a table of the corresponding modifying enzymes may reflect the difficulties in creating such a list with all the names from various species and the as-yet-unmet requirement for coherent terminology.

The discussions of the "histone code hypothesis," which describes how histone modifications can convey information (*5*, *6*), raise the issues of the likely complexity of such a marking system and the extent to which it is possible to appreciate whether a given combination is heritable (thus epigenetic) or merely a signal for a short-term response. *Drosophila* genetics provides a beautiful example of how histone modifications and epigenetics can be linked. In the fruit fly, key components in the regulation of homeotic genes during development, the polycomb group and the trithorax group, proved to promote specific histone modification. Two chapters (by Ueli Grossniklaus and Renato Paro and by Robert Kingston and John Tamkun) illustrate the role of these complexes in transcriptional regulation. Steven Henikoff and Mitchell Smith describe another layer of complexity, which arises in the potential of histone variants to regulate gene expression. Other contributors note recent findings showing the involvement of noncoding RNAs in epigenetic phenomena.

In the last chapters, contributors discuss recent molecular insights into the roles of epigenetics during development and human disease—topics that have been of interest since the birth of epigenetics. Clarifying the picture of molecular epigenetic mechanisms that may act during nuclear reprogramming or human cancer, these chapters open the discussion to the implications of epigenetics in medicine.

With its focus on recent conceptual advances concerning chromatin-based epigenetics, this relatively concise book has, of course, neglected some aspects of a rapidly evolving field. Interested readers can find helpful complemental coverage in a recent special issue of *Cell* (*7*). Given the technical challenges to understanding epigenetic events, the book might have included more detailed discussions of the methods used to study DNA methylation or the modification status of chromatin at gene-specific and global levels. We would also have welcomed a chapter dedicated to emerging technologies in epigenomic research. New methodological approaches will clearly be needed to understand epigenetic-based events that regulate cell fate. Lastly, although the conceptual perspectives provided by the contributors may well last longer than a compilation of reviews, research in the field is moving very fast, and even conceptual outlines can evolve.

As a whole, *Epigenetics* is an impressive volume. The contributors provide an accurate survey of the field, from where it began, through where it is today, to where it is heading. Their accounts help set the stage for deepening our understanding of epigenetic phenomena and mechanisms. And the volume will undoubtedly prove to be very useful for students and researchers alike.

References

1. C. H. Waddington, *Endeavor* **1**, 18 (1942).
2. D. Haig, *Cold Spring Harbor Symp. Quant. Biol.* **69**, 67 (2004).
3. D. L. Nanney, *Proc. Natl. Acad. Sci. U.S.A.* **44**, 712 (1958).
4. R. Holliday, *Science* **238**, 163 (1987).
5. T. Jenuwein, C. D. Allis, *Science* **293**, 1074 (2001).
6. B. Turner, *Nature Cell Biol.* **9**, 2 (2007).
7. Epigenetics and Chromatin Organization, *Cell* **128**, 627–802 (2007).

10.1126/science.1142138

BROWSING

Academic Charisma and the Origins of the Research University. William Clark. University of Chicago Press, Chicago, 2006. 668 pp. $45, £28.50. ISBN 9780226109213.
Focusing on changes between the 1770s and the 1830s, Clark offers detailed accounts of lecture and seminar formats, grading systems, the conduct of examinations, the doctoral dissertation, library catalogs, and the appointment of professors. He argues that traditional academic customs and practices were transformed by market forces and competition among the small states of 18th-century Germany. To reap the benefits of having prestigious universities and scholars, bureaucrats established criteria for monitoring classroom diligence and publication productivity. This wide-ranging, thought-provoking book will reward anyone interested in the origins and early evolution of modern *Homo academius* and its environment.

MATHEMATICS

Cognitive Supports for Analogies in the Mathematics Classroom

Variations in the effective use of analogies in math instruction across countries may contribute to performance differences in the TIMSS studies.

Lindsey E. Richland,[1]* Osnat Zur,[2] Keith J. Holyoak[2]

Mathematics education is a critical concern worldwide. Within the United States, the mathematics educational system needs improvement (*1*, *2*). By the time U.S. students reach middle school, they have fallen below their international peers on assessments of mathematics performance (*3*, *4*). Failures in students' mathematics learning reduce high-school retention and become formidable barriers to college admissions and entry into math and science careers. Many factors contribute to mathematics achievement. We investigated how certain mathematics classroom activities differ between the United States and nations in which students score higher on international tests (*3*, *4*). We focused on factors of cognition and memory, which can be distinguished from cultural differences in instruction.

The video portion of the Trends in International Mathematics and Science Study (TIMSS 1999 Video Study), a large-scale international video study of classroom mathematics instruction, indicated that American teachers introduced conceptually connected, rich problems at rates similar to teachers from higher-achieving countries. However, they engaged students in complex connected reasoning and problem-solving substantially less often (*5*). One sophisticated reasoning practice available to children is the use of analogy and similar relational comparisons, which promote flexible conceptual learning and problem-solving (*6*). Analogy allows students to use commonalities between mathematical representations to help understand new problems or concepts, thereby contributing to integral components of mathematical proficiency (*1*, *7*).

Learning by analogy typically involves finding a set of systematic correspondences (a mapping) between a better-known source analog and a more novel target. The source and the target can be within a single domain (e.g., solving inequalities is like solving equations) or across domains (e.g., balancing equations is like balancing a scale) (*8*, *9*). Mathematical reasoning involves understanding abstract relations (such as equality, proportion, and integral) that can appear in different contexts (*7*, *10*). Such abstract relations may be best taught by drawing parallels between similar examples (*9*, *11*–*13*). Even so, children and novices often fail to notice or benefit from such instructional comparisons (*9*, *14*, *15*) when they are presented without supportive cues, such as hints, prompting questions, or elaborations of the analogy (*9*, *12*, *16*, *17*).

Mathematics teachers in the United States commonly introduce analogy-based instruction in their lessons, but not always in ways that encourage active reasoning by the students (*18*, *19*). We analyzed the ways that analogies are used in U.S. classrooms compared with two high-achieving regions in Asia: Hong Kong (Special Administrative Region, China) and Japan. All instances of relational comparisons (analogies) were identified in 10 eighth-grade lessons from different teachers videotaped in each country, randomly sampled from the TIMSS 1999 Video database (*5*). Hong Kong and Japan were selected for comparison to the United States because their students consistently outperform U.S. students on the TIMSS International achievement tests (*3*, *4*). In addition, their classroom instructional practices are very different from each other (*5*). Each relational comparison was then analyzed using qualitative codes to gather quantitative data about these reasoning events. Based on techniques developed in previous video surveys, codes were developed in an iterative strategy by alternating between the research literature and observations of the classrooms (*5*, *20*). Intercoder reliability was calculated between coders and the first two authors.

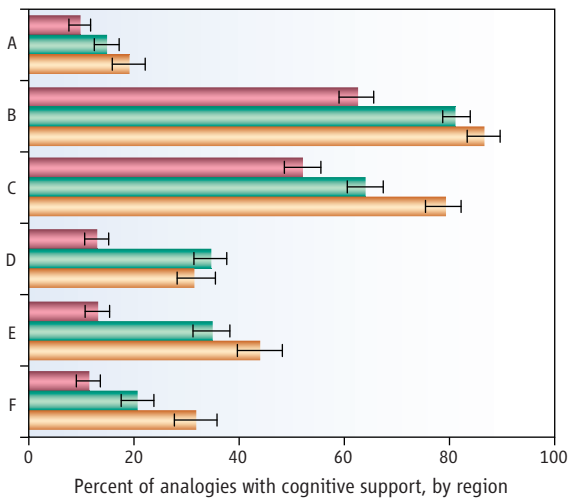

Frequency of cognitive support for analogies. Teachers reinforced a percentage of their analogies (bars) by providing cognitive supports (labeled A through F; defined in the text). Supports were provided less frequently by U.S. teachers (red) than by teachers from Hong Kong (green) or Japan (orange). Error bars represent standard error per country per support code.

Coders were native to the three videotaped countries and were psychologically naïve, although they were not blind to the country identity because video data precluded this possibility (*21*).

Codes identified teaching strategies that did or did not exhibit the use of sound cognitive principles for supporting relational learning, identified in laboratory studies over the past three decades. Part of the novelty of this research was to translate well-established principles of relational learning into codable behaviors relevant to classroom instruction in mathematics and across cultures. Our codes were motivated by the body of basic research on relational learning, imagery, gesture, and working memory (*9*, *11*, *19*, *22*–*27*).

Codes fell into two categories: those measuring characteristics of the source (e.g., using a scale as a familiar source to teach about balancing equations) and those measuring properties that increased the vividness of the alignment and mapping of the analogy as a whole (e.g., using a real scale while practicing balancing equations). These codes captured strategies that reduce processing demands on retrieval and working

[1]Department of Education, University of California, Irvine, CA 92697, USA. [2]Department of Psychology, University of California, Los Angeles, CA 90095, USA.

*Author for correspondence. E-mail: l.e.richland@uci.edu

memory and that draw attention to alignment of relations—all of which are aids to learning in laboratory studies of analogy and transfer. For example, children show greater transfer when the source is relatively familiar, as in the case of a scale and balancing of equations (*26*, *27*). Augmenting the source with visual representations such as a diagram can also increase transfer (*9*, *28*). Relative to auditory presentation, a visual display normally persists over time, reducing demands on working memory (*25*). Providing spatial cues such as position and arrows (*11*, *25*), or comparative gestures (*22*, *23*, *29*) can serve to highlight correspondences.

Adherence to six principles was coded (see figure). Three of the principles concerned the teachers' sources: The teachers (A) used a familiar source analog to compare to the target analog being taught; (B) presented the source analog visually; and (C) kept the source visible to learners during comparison with the target. Other principles served to enhance the vividness of the relational comparison used: Teachers (D) used spatial cues to highlight the alignment between corresponding elements of the source and target (e.g., diagramming a scale below the equal sign of an equation); (E) used hand or arm gestures that signaled an intended comparison (e.g., pointing back and forth between a scale and an equation); and (F) used mental imagery or visualizations (e.g., "picture a scale when you balance an equation"). Principles B to F can be viewed as special cases of the overarching principle that appropriate visual and spatial cues aid comprehension of abstract relations (*11*, *22*, *23*, *25*, *28*, *29*).

Teachers in all three countries produced numerous relational comparisons during the 10 eighth-grade mathematics lessons. Every lesson contained relational comparisons. A total of 195 units were identified in the U.S. lessons (mean of 20, range of 9 to 30 per lesson), 185 were identified in Hong Kong lessons (mean of 18, range of 7 to 27 per lesson), and 139 were identified in Japanese lessons (mean of 14, range of 9 to 25 per lesson).

National differences emerged in adherence to sound cognitive principles for teaching by relational comparisons. For all six principles that we coded, the U.S. sample yielded lower scores, indicating less promotion of relational learning, than did either of the Asian samples (see figure) (*30*). For example, teachers in both Asian regions used spatial supports for comparison more than twice as often as did their U.S. counterparts. These teachers also used far more gestures that emphasized comparison than did U.S. teachers, even though the latter used gestures of some kind almost equally often. Hong Kong teachers were almost twice as likely to prompt mental and visual imagery as were U.S. teachers, and Japanese teachers were even more likely.

This "teaching gap" may reflect different cultural orientations to relational reasoning. Hong Kong and Japanese teachers appear to be more attentive to the processing demands of relational comparisons than are U.S teachers. Their teaching reflects the use of strategies to reduce processing demands on their students. Such differences in adherence to sound cognitive principles may have a real impact on the likelihood that students benefit from analogies as instructional tools. If the source analog is not familiar and not visible, then students may struggle with processing. First, students will need to perform a taxing memory search to understand the source. Then, assuming that memory retrieval is successful, lack of visual availability will place further burdens on working memory during production of the relational comparison. Finally, lack of supporting cues to guide the comparison itself may result in the student learning much less than, or something quite different from, the new relational concept the teacher means to convey. Unsuccessful analogies may produce misunderstandings that can even lead to harmful misconceptions (*12*, *31*).

These cross-national differences in teaching practices suggest ways in which American mathematics education might be improved by building on existing practices. Relative to nations in which students achieve high TIMSS scores, U.S. mathematics educators introduce a similar number of analogies but offer less in terms of cognitive backup to help their students benefit from these analogies. Findings fit an emerging pattern: U.S. teachers provide high-quality learning opportunities to their students but provide less of the support that would enable their students to reap maximal benefits (*32*).

References and Notes

1. J. Kilpatrick, J. Swafford, B. Findell, Eds., *Adding It Up: Helping Children Learn Mathematics* (National Research Council, National Academy Press, Washington, DC, 2001).
2. E. A. Silver, P. A. Kennedy, Eds., *Results from the Seventh Mathematics Assessment of the National Assessment of Educational Progress* (National Council of Teachers of Mathematics, Reston, VA, 2000).
3. P. Gonzales *et al*., *Pursuing Excellence: Comparisons of International Eighth Grade Mathematics and Science Achievement from a U.S. Perspective, 1995 and 1999* (NCES 2001-028, U.S. Department of Education, National Center for Education Statistics, Washington, DC, 2000).
4. M. O. Martin, I. V. S. Mullis, S. J. Chrostowski, Eds., TIMSS 2003 Technical Report (TIMSS and PIRLS International Study Center, Boston College, Chestnut Hill, MA, 2004).
5. J. Hiebert *et al*., *Teaching Mathematics in Seven Countries: Results from the TIMSS 1999 Video Study* (NCES 2003-013, U.S. Department of Education, NCES, Washington, DC, 2003).
6. U. Goswami, *Analogical Reasoning in Children* (Erlbaum, Hillsdale, NJ, 1992).
7. R. Gelman, *J. Appl. Devel. Psych*. **21**, 27 (2000).
8. D. Gentner, *Cognit. Sci*. **7**, 155 (1983).
9. M. L. Gick, K. J. Holyoak, *Cognit. Psych*. **15**, 1 (1983).
10. The Polish mathematician Stefan Banach famously declared, "Good mathematicians see analogies between theorems or theories; the very best ones see analogies between analogies." Quoted by S. M. Ulam, in *Analogies Between Analogies: The Mathematical Reports of S. M. Ulam and His Los Alamos Collaborators* (Univ. of California Press, Berkeley, CA, 1990), p. 513; available online (http:/ark.cdlib.org/ark:/13030/ft9g50091s/).
11. L. R. Novick, M. Bassok, in *Cambridge Handbook of Thinking and Reasoning*, K. J. Holyoak, R. G. Morrison, Eds. (Cambridge Univ. Press, New York, 2005), pp. 321–349.
12. J. Clement, *J. Res. Sci. Teach*. **30**, 1241 (1993).
13. D. Gentner *et al*., *J. Educ. Psych*. **95**, 393 (2003).
14. J. D. Bransford *et al*., *How People Learn: Brain, Mind, Experience, and School* (National Research Council, National Academy Press, Washington, DC, 1999).
15. M. Chi *et al*., *Cognit. Sci*. **5**, 121 (1981).
16. S. M. Glynn, R. Duit, R. B. Thiele, in *Learning Science in the Schools: Research Reforming Practice* (Erlbaum, Mahwah, NJ, 1995), pp. 247–273.
17. L. E. Richland, R. G. Morrison, K. J. Holyoak, *J. Exp. Child Psych*. **94**, 249 (2006).
18. L. E. Richland *et al*., *Cognit. Instruct*. **22**, 37 (2004).
19. L. D. English, G. S. Halford, *Mathematics Education: Models and Processes* (Erlbaum, Hillsdale, NJ, 1995).
20. J. Stigler *et al*., *Educ. Psych*. **35**, 87 (2000).
21 Methods are available on *Science* Online.
22. M. Gattis, *Cognit. Sci*. **28**, 589 (2004).
23. S. Goldin-Meadow, *Hearing Gesture: How Our Hands Help Us Think* (Harvard Univ. Press, Cambridge, MA, 2003).
24. J. E. Hummel, K. J. Holyoak, *Psych. Rev*. **110**, 220 (2003).
25. S. M. Kosslyn, *Graph Design for the Eye and Mind* (Oxford Univ. Press, Oxford, UK, 2006).
26. S. Carey, *Conceptual Change in Childhood* (MIT Press, Cambridge, MA, 1985).
27. K. Inagaki, G. Hatano, *Child Devel*. **58**, 1013 (1987).
28. M. C. Linn *et al*., *Science* **313**, 1049 (2006).
29. M. W. Alibali, M. J. Nathan, in *Video Research in the Learning Sciences*, R. Goldman, R. Pea, B. Barron, S. J. Derry, Eds. (Erlbaum, Mahwah, NJ, 2007).
30. All reported strategy differences were statistically reliable ($P < 0.05$) by chi-square tests.
31. K. B. Zook, J. M. Maier, *J. Educ. Psych*. **86**, 589 (1994).
32. Reference S12 in the supporting online material includes Web addresses with further information.

33. The research reported here was supported by the Institute of Education Sciences, U.S. Department of Education, through grant R305H030141 to the University of California, Los Angeles and Irvine. The opinions expressed here are those of the authors and do not represent views of the Institute or the U.S. Department of Education. J. Stigler provided helpful consultations. Preliminary versions of this work were presented at the meetings of the Cognitive Science Society, the Society for Research in Child Development, and the American Educational Research Association.

Supporting Online Material

www.sciencemag.org/cgi/content/full/316/5828/1128/DC1

10.1126/science.1142103

APPLIED PHYSICS

One Electron Makes Current Flow

A single electron pumped in and out of a quantum dot could be useful as a calibration standard for electronics or as the basic unit of a quantum computer.

Stephen Giblin

Even the smallest components in a modern desktop computer use tens of thousands of electrons at a time to implement classical logic (the conventional 1s and 0s of binary computation). A computer that operated on single electrons, however, could in principle implement quantum logic functions (quantum bits or "qubits" that could perform computational tasks that are beyond the ability of classical computers). One proposed architecture for a single-electron computer could be realized in a two-dimensional electron gas (2DEG), a special kind of reservoir in which electrons can travel without dissipation (*1*). On page 1169 of this issue, Fève *et al.* (*2*) report on an important step toward this vision: a device that can emit single electrons into a 2DEG and absorb them again on nanosecond time scales. With such a controllable electron source, researchers will now be able to set up one or more electrons in well-defined quantum states, which are crucial for any future quantum computer.

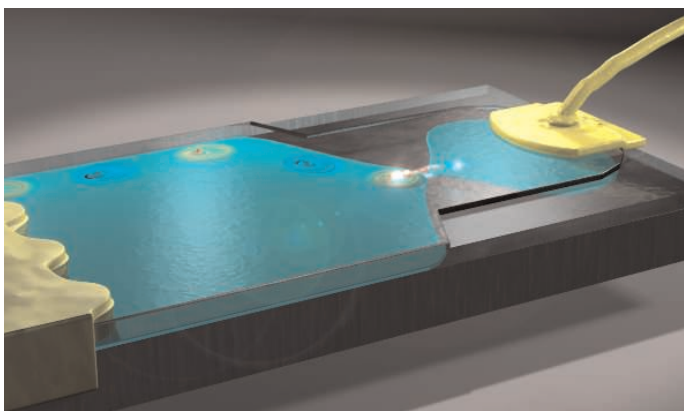

One at a time. A quantum dot (blue region at right) can emit single electrons through a tunnel barrier into a 2DEG (blue region at left) in response to changing the voltage on a nearby control electrode (gold contact at right). If an ac voltage is applied to the control electrode, an ac current will flow through the device. Fève *et al.* have calculated this current by considering the dot and barrier as a quantum *RC* circuit. (The image is greatly exaggerated in size.)

A macroscopic electric current, as measured by an ammeter, is the result of the movement of many discrete charges around a circuit. But this discreteness manifests itself as "shot noise"—one of the sources of random fluctuation in the current that engineers need to understand in order to design working components and circuits. Shot noise was first observed by Schottky in 1914, but it was not until the late 1980s that advances in nanofabrication technology first enabled control over the movement of individual electrons, giving birth to the field of single electronics (*3*).

The key requirement of a single-electron device is that a small (typically <100 nm) conducting island should be isolated from the rest of the electrical circuit by tunnel barriers, thin regions of insulator through which electrons can "tunnel" according to the laws of quantum mechanics. If the island is small enough, the number of electrons it holds can be changed precisely by adjusting external voltages. Suitable islands and tunnel barriers have been made with metals and metal oxides (*4*), and also with the versatile gallium arsenide 2DEG system (*5*), which has the additional advantage that the height of the tunnel barriers can be changed easily with a control voltage, making it more or less likely for electrons to pass through. Islands formed in a 2DEG are usually referred to as "quantum dots" or "artificial atoms," because the electrons trapped inside them occupy quantum energy levels similar to those in a real atom.

By combining tunnel barriers with one or more islands, researchers can make charge detectors with subelectron resolution, called single-electron transistors, as well as devices, known as turnstiles or pumps, that can transfer electrons one at a time from a source to a drain electrode (*6*). Pumps and turnstiles continue to be of great interest to the electrical metrology community because they offer a new way of generating an accurately known dc current—a primary standard—based on only the electronic charge e and frequency f. Pumps based on metal-oxide technology (*7*, *8*) and on gallium arsenide 2DEGs (*9*) are being extensively studied.

The device studied by Fève *et al.*, illustrated schematically in the figure, is much simpler than a pump or turnstile. It consists of just one quantum dot and a tunnel barrier through which electrons can enter and leave the dot. Changing the voltage applied to the control electrode alters the spacing of the dot energy levels, and thus the number of electrons in the dot. Another voltage changes the height of the tunnel barrier. Because of the gap between the control electrode and the dot, no dc current will flow through the device. The authors measure, and calculate, the ac current I_{ac} in response to an ac voltage V_{ac} applied to the electrode.

To calculate I_{ac}, it is necessary to know the impedance of the device (that is, the extent of its opposition to current flow). The tunnel barrier behaves like a variable resistor R, and the dot forms a capacitance C with the electrode. Hence, the device impedance is due to the sum of C and R in series. One would imagine it should be possible to calculate R from the properties of the tunnel barrier, and C from the properties of the quantum dot and the geometry of the electrode, thus determining the impedance. However, in the 2DEG, where electrons can propagate for some distance without interacting with other electrons, R and C cannot be treated as separate entities.

The main achievement of Fève *et al.* is their calculation of the impedance by theoretically treating the device as a quantum *RC* circuit. Starting from an equation describing the microscopic quantum-mechanical motion of electrons through the tunnel barrier and into the capacitor, they are able to work out the macroscopic parameters R and C. The quantum *RC* circuit has some bizarre properties. For example, changing the height of the tunnel barrier changes C but not R, exactly the reverse of what one would expect.

In an earlier paper, they restricted the scope of the experiment and theory to small values of V_{ac} (*10*). In the present work, they expand both theory and experiment to encompass large-amplitude excitations—large enough to cause electrons to tunnel in and out of the dot. In all cases, the quantum *RC* circuit theory successfully predicts I_{ac} as a function of the two control parameters, V_{ac} and the height of the tunnel barrier. Over a particular range of these two parameters,

The author is in the Quantum Detection Group, National Physical Laboratory, Teddington, Middlesex TW11 0LW, UK. E-mail: stephen.giblin@npl.co.uk

something rather special happens: Exactly one electron is ejected from the dot and then reabsorbed during one cycle of V_{ac}. Then, I_{ac} has an exactly quantized value, analogous to the quantized dc currents generated by pumps and turnstiles.

The authors have used the macroscopic quantity I_{ac} as a probe of the circuit dynamics and have shown that electrons can be emitted into, and reabsorbed from, the 2DEG in a controllable manner on nanosecond time scales. This is an important first step toward a 2DEG quantum computer. The next step will be to show that two electrons can be made to interact in a "coherent" manner, that is, without their delicate quantum states being disturbed by external influences. This will require advances in single-electron detectors, which do not currently operate fast enough to probe the dynamics of electrons in the 2DEG. There is much interesting work to be done and, in the future, scientists and engineers might think of single-electron behavior not just as a cause of noise but as a tool to solve problems.

References

1. T. M. Stace, C. H. W. Barnes, G. J. Milburn, *Phys. Rev. Lett.* **93**, 126804 (2004).
2. G. Fève *et al.*, *Science* **316**, 1169 (2007).
3. K. K. Likharev, *Proc. IEEE* **87**, 606 (1999).
4. G. J. Dolan, J. H. Dunsmuir, *Physica B* **152**, 7 (1988).
5. H. van Houten, C. W. J. Beenakker, A. A. M. Staring, in *Single Charge Tunneling* (Plenum, New York, 1992), chap. 5.
6. M. H. Devoret, D. Esteve, C. Urbina, *Nature* **360**, 547 (1992).
7. M. W. Keller, J. M. Martinis, A. H. Steinbach, N. M. Zimmerman, *IEEE Trans. Instr. Meas.* **46**, 307 (1997).
8. S. V. Lotkhov, S. A. Bogoslovsky, A. B. Zorin, J. Niemeyer, *Appl. Phys. Lett.* **78**, 946 (2001).
9. M. D. Blumenthal *et al.*, *Nature Phys.* **3**, 343 (2007).
10. J. Gabelli *et al.*, *Science* **313**, 499 (2006); published online 12 July 2006 (10.1126/science.1126940).

10.1126/science.1143429

CHEMISTRY

The Direct Approach

Aromatic compounds can be coupled without having to preactivate the reactants. The method is more efficient and generates less waste than other approaches.

Jonathan A. Ellman

The formation of carbon-carbon bonds is central to organic synthesis because it provides the carbon skeleton that often defines the structure and function of an organic compound. Coupling one aromatic compound with another is one of the most useful types of carbon-carbon bond formation, allowing chemists to construct the carbon frameworks for a wide range of materials, electronic devices, and pharmaceutical agents (*1*). On page 1172 of this issue (*2*), Stuart and Fagnou report an innovative new approach for accomplishing this type of bond formation by metal-catalyzed oxidative coupling of the simplest of aromatic starting materials.

Most methods for coupling two aromatic compounds require both reaction partners to be converted into an intermediate before the reaction. In one reaction partner, a halogen or related electrophilic group is attached to the site where a bond is to be formed; the other reaction partner is similarly preactivated by placing a metal at the site of bond formation (see the figure, reaction type 1) (*1*, *3*). Several transition metal catalysts have been developed to accomplish general, extremely efficient, high-yield reactions between such preactivated partners. However, although the approach is very powerful and extensively used, it produces metal and halide byproducts. Furthermore, preparation of the preactivated coupling partners often requires additional synthetic operations.

Over the past decade, impressive advances have been made in enhancing the efficiency of coupling aromatic compounds by direct arylation processes. In this approach, one of the preactivated starting materials is replaced with a simpler structure that does not incorporate the activating group (see the figure, reaction type 2) (*4*). This approach is no longer just of academic interest but is also being used increasingly for industrial applications (*5*), because only one preactivated partner needs to be prepared and waste byproducts can be reduced.

Stuart and Fagnou have now gone one step further by coupling two simple aromatic compounds, neither of which requires the attachment of activating groups (see the figure, reaction type 3). The authors have solved a number of potential problems, not the least of which is the selective coupling of the two aromatic compounds to produce the desired product without each compound also coupling with itself to produce undesired side products (*6*). The authors were able to avoid this type of side reaction by coupling two classes of aromatic compounds that have different electronic character and C-H acidity; one of these classes is the indole structure that is prevalent in drugs. The use of palladium trifluoroacetate as the catalyst and of 3-nitropyridine and cesium pivalate as additives were critical to the success of this coupling reaction. Excess copper acetate was also required as the terminal oxidant to enable catalyst turnover.

The approach demonstrated by Stuart and Fagnou could have immense practical importance for the synthesis of materials, electronic devices, and drugs. However, further advances will be required to enhance reaction efficiency, for example, by reducing catalyst and terminal oxidant loading levels. It also remains to be seen how many different combinations of aromatic compounds can effectively be coupled without the occurrence of undesired self-coupling side reactions.

An additional challenge of this aromatic coupling process is to ensure selective coupling at a specific site on each molecule when

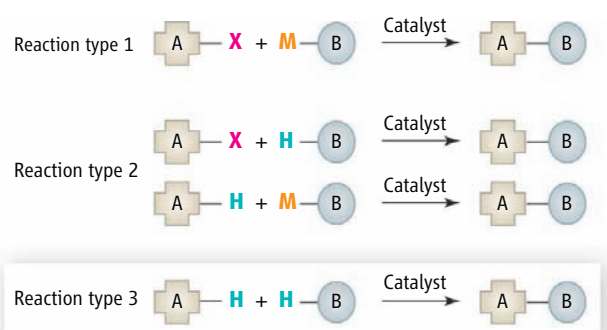

How to couple two different aromatic compounds. In reaction type 1, both aromatic compounds are preactivated (compound A with a halide X and compound B with an electropositive metal M). In reaction type 2, only one of the aromatic compounds is preactivated. In reaction type 3, simple aromatic compounds are coupled, neither of which is preactivated. Stuart and Fagnou now show how reaction type 3 can be realized.

The author is in the Department of Chemistry, University of California, Berkeley, CA 94720, USA. E-mail: jellman@berkeley.edu

aromatic compounds with more than one type of aromatic C-H bond are used. For other types of C-H functionalization processes (*1*, *7*–*10*), selective reaction at specific C-H bonds has been achieved by two means: either the catalyst first interacts with a heteroatom in the molecule and is thereby delivered preferentially to a proximal C-H bond, or the C-H bonds present in the molecule differ in their reactivity and accessibility. Similar tactics could presumably be applied to this new and exciting approach for coupling aromatic compounds without preactivation.

References and Notes

1. J. Hassan, M. Sevignon, C. Gozzi, E. Shulz, M. Lemaire, *Chem. Rev.* **102**, 1359 (2002).
2. D. R. Stuart, K. Fagnou, *Science* **316**, 1172 (2007).
3. A. de Meijere, F. Diederich, Eds., *Metal-Catalyzed Cross-Coupling Reactions* (Wiley-VCH, Weinheim, 2nd ed., 2004).
4. D. Alberico, M. E. Scott, M. Lautens, *Chem. Rev.* **107**, 174 (2007).
5. D. R. Gauthier Jr. *et al.*, *J. Org. Chem.* **70**, 5938 (2005).
6. K. L. Hull, E. L. Lanni, M. S. Sanford *J. Am. Chem. Soc.* **128**, 14047 (2006).
7. F. Kakiuchi, N. Chatani, *Top. Organomet. Chem.* **11**, 45 (2004).
8. M. Miura, M. Nomura, *Top. Organomet. Chem.* **14**, 55 (2005).
9. K. Godula, D. Sames, *Science* **312**, 67 (2006).
10. G. Dyker, Ed., *Handbook of C-H Transformations* (Wiley-VCH, Weinheim, 2005).

11. J.A.E. thanks NIH for support (grant GM69559).

10.1126/science.1143373

ASTRONOMY

Dark Matter in Galactic Collisional Debris

Our ideas about galaxy formation and the nature of dark matter have been changed by the unexpected observation that galaxies that formed from the collisions of other galaxies contain dark matter.

Bruce G. Elmegreen

Galaxies that are born in clusters occasionally get so close to each other that material from their outer regions, which is only weakly bound by gravity, gets flung into space, producing long tidal tails. Other material can fall from one galaxy to the other, making a bridge. When these tails and bridges disperse, they can leave behind clumps that may become independent galaxies. Small galaxies can also collide with and travel through large galaxies, producing giant circular wakes and more clumps. As the colliding galaxies eventually lose their orbital energy and merge, some of the debris falls back in. These are the processes that are thought to have built up most of today's galaxies from the small clumps produced in the early universe. An important question that goes back 50 years (*1*) is whether the smallest of today's galaxies, the dwarfs, are old surviving remnants from early times, or young debris from recent collisions. On page 1166 of this issue, Bournaud *et al*. (*2*) report the presence of dark matter in tidal dwarfs. This is contrary to most theoretical predictions, providing new details about galaxy formation and about the nature of dark matter.

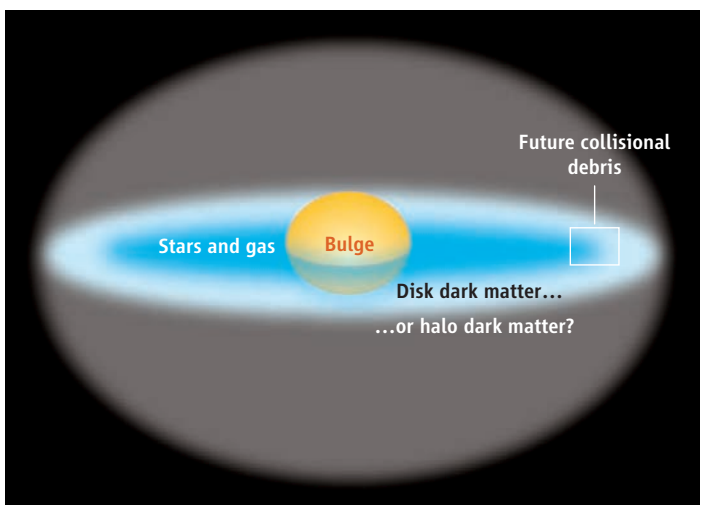

Dark matter and dwarf origins. Collisional debris, from which dwarf galaxies form, has to get all of its mass from the previous spiral galaxy's disk, shown here. Any dark matter in this debris has to be rotating with the disk. Normally, dark matter is assumed to be in the halo of a galaxy. Do spiral disks have such a component of unseen matter? Bournaud *et al.* present the first evidence that they do, and suggest it is in the form of cold molecular hydrogen.

The formation of dwarf galaxies has been difficult to understand because essentially all small galaxies have relatively large amounts of dark matter, usually 10 times the visible matter evident with optical and radio telescopes. However, collisional debris is not supposed to have dark matter. Galaxies should be born with their dark matter in equilibrium, having an orbital energy comparable to the gravitational potential energy. Giant spirals should therefore have dark-matter particles moving at high speeds. This means that small, weakly bound collisional debris cannot hold onto the dark matter from their former galaxies. The dwarfs just get the cold gas and whatever slow-moving stars are in the part of the disk they came from (see the figure).

The discovery of collisional debris with dark matter comes as a welcome surprise: It begins to clarify the origin of some dwarf galaxies, but it also implies a new kind of dark matter, something that cools like baryons (e.g., neutrons and protons) or stays cool from birth and ends up in galaxy disks. Bournaud *et al*. observed neutral hydrogen at high resolution in several dwarf galaxies that formed in the ringlike debris of a collision involving the galaxy NGC 5291. These dwarfs show rotation curves (which plot orbital velocity of stars versus their distance from the galactic center) indicating that the total mass exceeds the visible mass by a factor of 2. This is not the factor of 10 commonly observed in other dwarf galaxies, but it is good evidence for dark matter, anyway.

One can imagine four possibilities for this new dark matter: (i) exotic particles that dissipate energy yet give off no detectable light; (ii) normal dark matter that stays cool even in deep potential wells; (iii) dim stars or stellar remnants that give off too little light to see; or (iv) gas that gives off too little light to see. Bournaud *et al.* favor interpretation (iv). They suggest that because the most abundant gas is hydrogen, and molecular hydrogen (H_2) at ultralow temperature does not radiate well, a likely source of unseen disk mass is H_2.

The suggestion that some or perhaps all dark matter is cold H_2 goes back to Lequeux *et al*. (*3*) and Pfenniger *et al*. (*4*). This idea gained little traction at first because emission

The author is in the IBM Research Division, T. J. Watson Research Center, Yorktown Heights, NY 10598, USA. E-mail: bge@us.ibm.com

CREDIT: ADAPTED BY P. HUEY/*SCIENCE*

from the dust that is supposed to accompany the cold H_2 was not observed in the Milky Way (*5*), and because the extra mass should make disks too unstable and too thin if it is all inside the gas layer (the thin disk in the figure) (*6*). Moreover, Kuijken and Gilmore (*7*) and others previously showed that the vertical motions of stars in the disk do not require the presence of dark matter. Crézé *et al.* (*8*) found the same result more recently using densities and velocities of A-type stars within 125 pc (1 pc = 3.26 light-years) of the Sun. The thickness of any dynamically significant component of dark matter has to exceed ~4 kpc (*9*, *10*), which is thicker than the visible gas disk by a factor of 8. Revaz and Pfenniger (*11*) found bending instabilities for massive thin disks that are in nice agreement with observed galaxy warps, but they did not consider other observational constraints.

The dark matter in the dwarfs studied by Bournaud *et al*. is not excessive—a factor of 2, not 10—and some H_2 can certainly be hidden when only CO emission is used as a proxy. However, the mass of hidden H_2 has to be large, three times that of the atomic hydrogen plus the molecular hydrogen already inferred from CO emission. Observations might be expected to show this much H_2 or its associated dust in emission. So far, only warm H_2 (400 to 460 K) has been seen in these dwarfs and its total mass is low, 5×10^{-4} of the H_2 traced by CO (*12*). The hidden H_2 has to be much colder to be invisible, only a few kelvin. Dust-related polycyclic aromatic hydrocarbon emission has also been observed, but it is warm too (140 K versus the more usual 50 K in starbursts) (*12*). The stars in the Bournaud *et al*. dwarfs are unusual as well: No evolved stellar population has been detected at 1.6 μm, so most of the stars are young (*12*). This is to be expected if the dwarf stars formed because of the interaction, but it is an anomaly for normal dwarf galaxies.

The most famous interacting system is the Antenna, which is composed of two spiral galaxies merging in a dense core and two long tails that extend for 120 kpc. A clump in the larger tail has about the same mass as the dwarfs studied by Bournaud *et al*., and it also needs a factor of ~2 more matter to be gravitationally bound than is visible (*13*). This clump is not a dense galaxy yet and it does not rotate like the objects studied by Bournaud *et al*. Still, it could be a younger version of these objects, and perhaps more clues to disk dark matter can be found there. In any case, the dwarfs in NGC 5291 are unique at the present time, and they appear to be telling us something important about the nature of dark matter in the universe and its existence in galaxies.

References

1. F. Zwicky, *Naturwissenschaften* **29**, 344 (1956).
2. F. Bournaud *et al*., *Science* **316**, 1166 (2007).
3. J. Lequeux, R. J. Allen, S. Guilloteau, *Astron. Astrophys*. **280**, L23 (1993).
4. D. Pfenniger, F. Combes, L. Martinet, *Astron. Astrophys*. **285**, 79 (1994).
5. T. J. Sodroski *et al*., *Astrophys. J*. **480**, 173 (1997).
6. B. G. Elmegreen, in *New Extragalactic Perspectives in the New South Africa: Cold Dust and Galaxy Morphologies*, D. Block, Ed. (Kluwer, Dordrecht, Netherlands, 1996), p. 468.
7. K. Kuijken, G. Gilmore, *Mon. Not. R. Astron. Soc.* **239**, 651 (1989).
8. M. Crézé, E. Chereul, O. Bienaymé, C. Pichon, *Astron. Astrophys*. **329**, 920 (1998).
9. O. Bienaymé, *Astron Astrophys*. **341**, 86 (1999).
10. P. M. W. Kalberla, *Astrophys. J.* **588**, 805 (2003).
11. Y. Revaz, D. Pfenniger, *Astron. Astrophys*. **425**, 67 (2004).
12. S. J. Higdon, J. L. Higdon, J. Marshall, *Astrophys. J*. **640**, 768 (2006).
13. J. E. Hibbard, J. M. van der Hulst, J. E. Barnes, R. M. Rich, *Astrophys. J.* **122**, 2969 (2001).

10.1126/science.1143506

MATERIALS SCIENCE

Hydrogel Cell Cultures

Three-dimensional synthetic gels that mimic the extracellular matrix provide a promising tool for studying cell interactions.

Melinda C. Cushing and Kristi S. Anseth

Cells often behave differently when they are isolated from the complex architecture of their native tissues and constrained to Petri dishes. For example, human breast epithelial cells proliferate abnormally (like tumor cells) when cultured as a two-dimensional monolayer, but display normal cell growth behavior and form structures typical of breast tissue when cultured in three-dimensional membranes that resemble their native environment (*1*). Embryonic stem cells differentiate more efficiently to blood-forming stem cells when cultured in three-dimensional scaffolds compared to cells cultured in two dimensions (*2*).

This difference in cell behavior has constituted a major obstacle for tissue engineers. But in the past 10 years, the field has made progress in creating successful three-dimensional cellular microenvironments with hydrogels—networks of interacting polymer chains that are highly hydrated, with elasticity similar to that of natural tissues. The structure and composition of these gels can be tailored to bear the appropriate chemical, biological, and physical cues that encourage the development of tissuelike structures in vitro. However, it remains uncertain which endogenous factors of a tissue must be recapitulated in a gel, and better strategies must be developed for delivering those factors to the right place, at the right time, and in the right context within the gel.

Regardless of the nature of the hydrogel, challenges must be overcome related to the general approach of three-dimensional cell culture. First, even in two-dimensional culture, heterogeneities exist in the cellular microenvironment, and these will only be further exaggerated in three-dimensional gels. Second, engineering functional tissue equivalents requires careful attention to oxygen availability, because no cell in a metabolically active tissue is further than 100 μm from a high-oxygen source. Oxygen-sensing transcription systems, such as hypoxia-inducible factors, play an important role in regulating the differentiation of stem cells (*3*), as does the distribution of diffusing growth factors. Finally, many standard techniques for analyzing proteins and protein distributions are more difficult to perform, because they require isolation of the cells from the matrix. Thus, new fluorescent probes coupled with noninvasive live-imaging and real-time analyses will be critical to examine the cause and effect of stratification on cellular functions in three dimensions.

Physiological processes are guided by interactions between cells and their extracellular matrix, the proteins and polysaccharides that cells secrete into their environment to support tissue structure and survival. "Naturally based" hydrogels such as Matrigel (made of native extracellular matrix proteins) and collagen (the major extracellular matrix

M. C. Cushing is in the Department of Chemical and Biological Engineering, University of Colorado, Boulder, CO 80309, USA. K. S. Anseth is in the Department of Chemical and Biological Engineering and the Howard Hughes Medical Institute, University of Colorado, Boulder, CO 80309, USA. E-mail: kristi.anseth@colorado.edu

protein) have been explored extensively for applications in three-dimensional tissue culture and regenerative medicine. Natural gels provide a milieu of endogenous signals that promote the cellular interactions that underlie tissue formation. However, the complexity, variability, and ill-defined nature of these interactions make it difficult to understand the proliferation, differentiation, and migration of cells embedded within these natural gels.

Hydrogels can also be created from inert synthetic molecules such as poly(ethylene glycol). The advantages of synthetic gels include their consistent composition and predictable manipulation of properties, but they lack functional sites to interact with soluble or cell-surface proteins. Thus, synthetic gels provide little more than a blank slate to permit undirected cell function (*4*). Researchers are now bridging the gap between natural and synthetic gels by combining well-characterized synthetic materials with biomimetic cues to support physiologically relevant cell-gel interactions (see the figure).

Sophisticated synthetic hydrogels can be created through highly controlled, selective, and orthogonal reaction schemes—such as Click reactions that efficiently link small molecular subunits (*5*). Further, Click reactions allow cross-linking of biologic and synthetic precursors under physiological conditions. For example, light-initiated reactions that result in chemical cross-linking between functionalized poly(ethylene glycols) and biomimetic peptides have been used to encapsulate human mesenchymal stem cells (*6*). This process promotes their survival by facilitating specific cellular interactions with the covalently bound peptides. The peptide concentration, peptide conformation, and degradation behavior of such a system can be controlled through simple manipulation of reactant stoichiometry and functionality. Gels with this type of regulated chemistry and molecular structure will help to decouple the complex effects of structural (or mechanical) signals from biochemical ones on cellular activities in a three-dimensional environment (*7*).

Improved artificial hydrogels can also be generated through physical cross-linking (such as hydrogen bonding). For example, protein folding and protein-protein interactions can be used to create well-ordered and modular networks. This approach has been used to create a synthetic hydrogel from the self-assembly of leucine zipper domains—a protein motif that facilitates protein-protein interactions; the rate of gel degradation and mass loss can be precisely controlled in this gel (*8*).

In addition to controlling the structure and chemistry of synthetic hydrogels, advances in gel materials that respond to some form of stimulation allow manipulation of the temporal and spatial availability of bioactive moieties within the cellular microenvironment. Cell-initiated proteolysis of chemical cross-links in a gel allows cell migration by mimicking proteolytic processes that occur in native tissues and has been shown to facilitate bone tissue regeneration (*9*); it may also be useful as a model for studying cell metastasis in tumors.

Some gel networks undergo abrupt conformational changes in response to a stimulus. These changes allow control of gel swelling, which in turn dictates the release of encapsulated biomacromolecules. For example, gels made from calcium-sensitive protein building blocks (*10*) or single-stranded DNA components (*11*) can expand or contract in response to the addition of calcium or single-stranded DNA, respectively, to sense, gate, and transport biomolecules within hydrogels. Photolabile linkers (*12*) and photosensitive reactions provide a means to spatially pattern gel environments with biological signals. Target molecules might include chemotactic agents to direct cell movement or orientation, tissue morphogens to influence cell fate, and/or physical structures to control cell morphology and interactions over multiple size scales.

These hydrogels may prove useful in controlling the distribution of biological signals in the three-dimensional environment (*13*). For example, photopatterning has been used to create latticelike gels that minimize diffusion distances, thereby facilitating the three-dimensional regeneration of hepatic tissue (*14*). Bending and folding of materials that undergo temperature-dependent shrinkage are enabling gels to assume complex surface topologies and macroscopic structures (*15*). These advances will be important for tissue engineers aiming to recapitulate the shapes of small physiologic structures, such as aortic heart valves.

Tissue-engineering strategies are also focused on generating dynamic gels that allow the presentation of multiple biological factors to cells that vary in space and time. Gels that selectively bind cell-secreted factors are providing glimpses of the cell–extracellular matrix feedback that occurs during wound healing and normal tissue homeostasis. These sophisticated advances in gel design are creating new tools for hypothesis testing in cell biology and advancing cell-based approaches to repair and regenerate tissues.

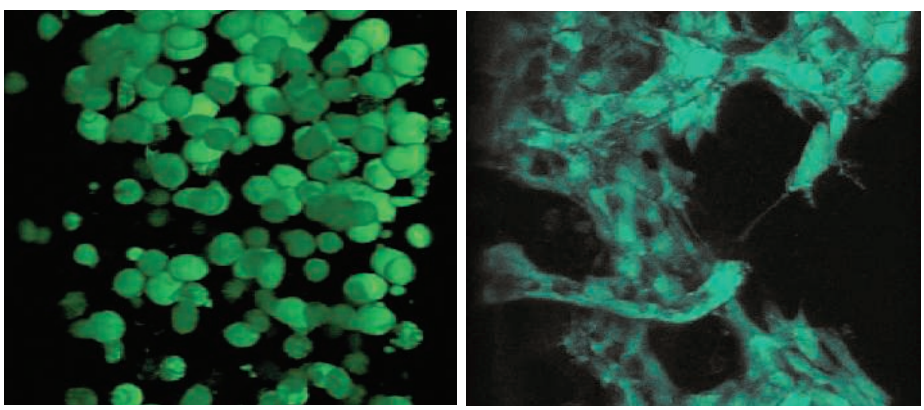

The power of synthetic hydrogels. In this example, degradable poly(ethylene glycol) gels were modified with signals to promote the function of human mesenchymal stem cells and their evolution into a tissuelike structure. Scanning confocal microscopy of fluorescently labeled cells was used to visualize changes in cell morphology in the gel microenvironment. At the start of the experiment, the cell-laden gel contains rounded cells with few interactions (**left**). Over the course of 2 weeks, the gel forms a dynamic system with multiple cell-gel interactions that promote attachment, migration, and ultimately, differentiation of the encapsulated cells to bone-forming osteoblasts (**right**).

References

1. O. W. Petersen, L. Ronnov-Jessen, A. R. Howlett, M. J. Bissell, *Proc. Nat. Acad. Sci. U.S.A.* **89**, 9064 (1992).
2. H. Liu, K. Roy, *Tissue Eng.* **11**, 319 (2005).
3. C.-J. Hu *et al.*, *Mol. Cell. Biol.* **26**, 3514 (2006).
4. M. J. Mahoney, K. S. Anseth, *Biomaterials* **27**, 2665 (2006).
5. M. Malkoch *et al.*, *Chem. Commun.*, 2774 (2006).
6. C. N. Salinas, B. B. Cole, A. M. Kasko, K. S. Anseth, *Tissue Eng.* **15**, 1025 (2007).
7. A. J. Engler, S. Sen, H. L. Sweeney, D. E. Discher, *Cell* **126**, 677 (2006).
8. W. Shen, K. Zhang, J. A. Kornfield, D. A. Tirrell, *Nat. Mater.* **5**, 153 (2006).
9. M. P. Lutolf *et al.*, *Nat. Biotechnol.* **21**, 513 (2003).
10. J. D. Ehrick *et al.*, *Nat. Mater.* **4**, 298 (2005).
11. Y. Murakami, M. Maeda, *Biomacromolecules* **6**, 2927 (2005).
12. Y. Luo, M. S. Shoichet, *Nat. Mater.* **3**, 249 (2004).
13. M. C. Dodla, R. V. Bellamkonda, *J. Biomed. Mater. Res. A* **78**, 213 (2006).
14. V. L. Tsang *et al.*, *FASEB J.* **21**, 790 (2007).
15. Y. Klein, E. Efrati, E. Sharon, *Science* **315**, 1116 (2007).

10.1126/science.1140171

PHYSIOLOGY

Proteasomes Keep the Circadian Clock Ticking

Regulated protein degradation underlies the precision of the mammalian circadian timekeeper.

David Gatfield and Ueli Schibler

The accumulation of a protein within a cell is determined by the rates of its synthesis and decay. Because only a minor fraction of all proteins actually executes rate-limiting functions, organisms are quite resilient to moderate changes in the concentrations of most proteins. However, some proteins must be regulated in a particularly precise manner, and this applies to components of the circadian clock, a biological device that regulates a range of physiological processes in many organisms, over a roughly 24-hour cycle. Two papers in a recent issue of *Science*, by Godinho *et al.* (*1*) and Busino *et al.* (*2*), and a recent study in *Cell* by Siepka *et al.* (*3*), exemplify the necessity of this precision by showing that mistimed degradation of two circadian clock proteins (cryptochromes) in the mouse causes their accumulation throughout the day. Their presence at the wrong time dampens the expression of other clock proteins and as a result, lengthens the period of the circadian cycle.

In mammals, most physiological processes such as sleep-wake cycles, heart rate, blood pressure, and metabolism oscillate in a daily cycle, influenced by the circadian clock (*4*). The rhythm-generating molecular circuitry in hypothalamic neurons and peripheral cells (*5*) relies on a negative-feedback loop involving the Cryptochrome (Cry1 and Cry2) and Period (Per1 and Per2) proteins. Cry and Per proteins are transcriptional repressors, and their expression is activated by a heterodimer containing the transcription factor Bmal1 and either of two other transcription factors, Clock or Npas2 (see the figure) (*6*). Once Per and Cry proteins reach critical concentrations, they form heterotypic complexes that bind to the Bmal1-Clock/Npas2 heterodimers and thereby annul their transcriptional activation potential. Consequently, *Cry* and *Per* transcription is reduced, Cry and Per protein accumulation falls below the concentrations required for autorepression, and a new cycle of *Cry* and *Per* expression can ensue. Although both Per and Cry proteins are indispensable in establishing the negative-feedback loop, the latter are the rate-limiting repressors of the molecular oscillator (*7*). Hence, the cyclic accumulation of Cry proteins must be controlled in a particularly rigorous manner.

Most short-lived proteins are degraded by the proteasome, a multisubunit molecular shredding machine. To be recognized by the proteasome, proteins must be tagged with multiple ubiquitin polypeptides on particular lysine residues. However, mammals express thousands of unstable proteins, and the question arises of how specificity of degradation by the proteasome is accomplished. This has now been solved for Cry proteins through biochemical and genetic experiments.

Busino *et al.* used mass spectrometry to identify Cry1 and Cry2 in a complex with Fbxl3, as revealed by coimmunoprecipitation of the proteins from cell lysates. Fbxl3 (which contains a motif called an F-box that mediates protein interactions) is a subunit of one of the more than 70 mammalian ubiquitin ligase complexes that recognizes targets for degradation by proteasomes. Specificity of the Fbxl3-Cry interaction was confirmed by showing that nine other F-box proteins did not associate with Cry proteins. Of these F-box proteins, only the overexpression of Fbxl3 reduced the stability of Cry2 in cultured cells. Perhaps more importantly, reduction of endogenous *Fbxl3* messenger RNA (mRNA) by RNA interference (and the consequential decrease in Fbxl3 protein) abolished the cyclic expression of *Cry* and *Per* genes, supposedly due to the continually high expression of the repressor proteins Cry1 and Cry2. Fbxl3 appears to influence clock gene expression specifically through its interaction with Cry proteins, because reducing Fbxl3 expression in mouse fibroblasts lacking *Cry1* and *Cry2* genes did not alter the constitutively high accumulation of *Per1* and *Per2* mRNAs in these cells.

By another approach, Godinho *et al.* and Siepka *et al.* used genetic screens in mice to search for mutations that affect circadian behavior. In both studies, mice were treated with a strong mutagen, and their offspring were examined for wheel-running activity in constant darkness (a condition in which the circadian oscillator is free-running). Whereas Godhino *et al.* analyzed animals for mutations that manifest themselves if only one of the two alleles is

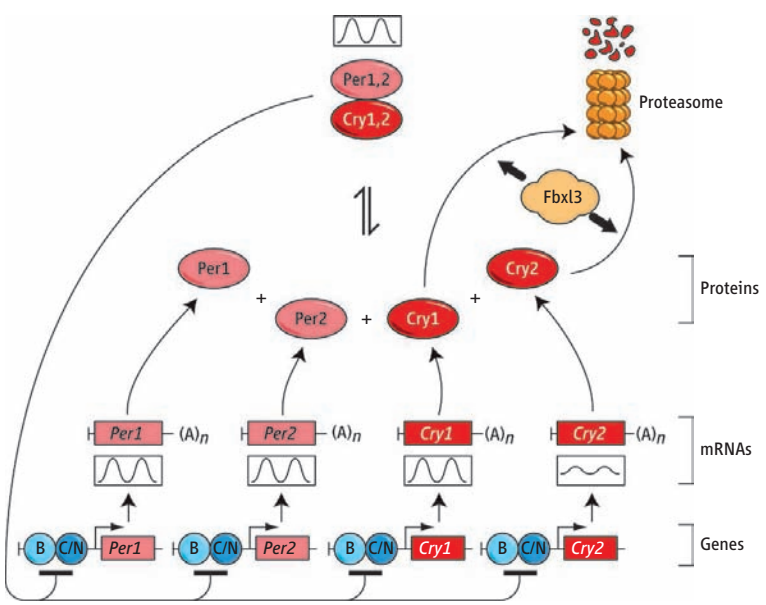

Cry, no more. The mammalian circadian clock proteins Cry1 and Cry2 repress their own expression and that of the clock genes *Per1* and *Per2* in a negative-feedback loop. Once these clock genes reach a critical concentration, they form a complex that attenuates the transcription factors complex comprising Bmal1 (B) and Clock/Npas2 (C/N). The negative-feedback loop drives robust circadian cycles only if *Cry* and *Per* mRNAs and proteins are short-lived. Fbxl3, a component of a specific ubiquitin ligase complex, participates in the proteasome-mediated decay of Cry proteins. Although *Cry2* mRNA oscillates with weak amplitude, Cry2 protein displays robust oscillations.

CREDIT: NICHOLAS ROGGLI

D. Gatfield and U. Schibler are in the Department of Molecular Biology and NCCR Frontiers in Genetics, Sciences III, University of Geneva, CH-1211 Geneva-4, Switzerland. E-mail: david.gatfield@molbio.unige.ch, ueli.schibler@molbio.unige.ch

affected (dominant, semi-dominant, or haploid-insufficient mutations), Siepka *et al*. also included recessive mutations (displaying phenotypes only when both alleles are mutated). Godhino *et al*. identified a mouse with a free-running circadian period length of ~24 hours, about 20 min longer than that of wild-type mice. This phenotype was called *after hours* (*Afh*), and positional cloning revealed *Fbxl3* as the culprit gene for the deranged circadian locomotor activity. Sequencing identified a serine residue, rather than a cysteine residue, at position 358 in the mutated Fbxl3 protein. The peptide segment encompassing this mutated amino acid is involved in substrate recognition by Fbxl3. Indeed, Busino *et al*. found reduced affinity of mutated Fbxl3 for Cry proteins.

The importance of this evolutionarily conserved peptide segment is underscored by the study by Siepka *et al*. Again, the mutant phenotype, called overtime (*Ovtm*), was due to a mutation in *Fbxl3*. Sequencing revealed a mutation of an isoleucine to a threonine at position 364 of Fbxl3, six amino acids downstream of the residue change linked to the *Afh* phenotype. The *Ovtm* founder mouse was likely homozygous for the mutation, because it free-ran with a period of ~26 hours; mice homozygous for the *Afh*-associated mutation free-ran with a period of ~27 hours.

Despite the strong resemblance of the *Afh* and *Ovtm* phenotypes, however, *Ovtm* Fbxl3 bound to Cry only slightly less avidly than did wild-type Fbxl3 in cultured mouse cells. Moreover, the reduced abundance of *Cry1* and *Cry2* mRNA in the livers of *Ovtm* mice was not accompanied by equivalent changes in Cry1 and Cry2 protein accumulation. Nonetheless, the assignment of two independent mutations affecting circadian physiology to the same gene is unlikely to be a pure coincidence. Although it is difficult to reach statistical conclusions with the few circadian clock genes identified by "forward genetics" (using mutagenesis followed by screening to study gene function) (*2*, *3*, *8*, *9*), the identification of *Fbxl3* in two independent mouse mutant screens indicates that viable mutations affecting circadian clock functions are relatively rare in mammals.

Although groundwork for studying the regulation of Cry degradation has now been laid, two interrelated questions will have to be addressed. What signal triggers Fbxl3-Cry interaction? Is it a specific post-translational modification of Cry? The other question concerns the temporal regulation of Cry degradation rates. At least in liver, Cry2 protein accumulates with a markedly higher circadian amplitude than *Cry2* mRNA (*10*). We do not yet know whether daily fluctuations in protein synthesis or decay rates account for this discrepancy. It may be that free Cry proteins are better substrates for Fbxl3-mediated degradation than Cry that is associated with Per proteins (see the figure). Now that we know that regulated protein destruction is essential to clock precision, deciphering its exact molecular mechanism is no longer a far cry away.

References

1. S. I. H. Godinho *et al*., *Science* **316**, 897 (2007); published online 26 April 2007 (10.1126/science.1141138).
2. L. Busino *et al*., *Science* **316**, 900 (2007); published online 26 April 2007 (10.1126/science.1141194).
3. S. M. Siepka *et al.*, *Cell* 10.1016/j.cell.2007.04.030 (25 April 2007).
4. F. Gachon, E. Nagoshi, S. A. Brown, J. Ripperger, U. Schibler, *Chromosoma* **113**, 103 (2004).
5. S. M. Reppert, D. R. Weaver, *Nature* **418**, 935 (2002).
6. J. P. Debruyne, D. R. Weaver, S. M. Reppert, *Nat. Neurosci.* **10**, 543 (2007).
7. K. Kume *et al.*, *Cell* **98**, 193 (1999).
8. D. P. King *et al.*, *Cell* **89**, 641 (1997).
9. P. L. Lowrey *et al.*, *Science* **288**, 483 (2000).
10. N. Preitner *et al.*, *Cell* **110**, 251 (2002).

Published online 10 May 2007;
10.1126/science.1144165
Include this information when citing this paper.

GEOLOGY

Assessing Landslide Hazards

Despite their widespread occurrence and often deadly nature, it remains difficult to predict when and where landslides are likely to occur.

David K. Keefer and Matthew C. Larsen

On 31 May 1970, a large earthquake shook the highest part of the Peruvian Andes. Millions of cubic meters of rock dislodged from a mountainside and initiated a rock avalanche that traveled more than 14 km in 3 min, burying a city and killing more than 25,000 people (*1*, *2*). On 17 February 2006, a landslide of 15 million m^3 that initiated on a slope weakened by long-term tectonic activity buried more than 1100 people on Leyte Island in the Philippines (*3*).

Landslides such as these are a hazard in almost all countries, causing billions of dollars of damage and many casualties (*4*). Landslides also contribute to landscape evolution and erosion in mountainous regions (see the first figure). Here we discuss the latest strategies used to assess and mitigate landslide hazards.

The basic physics governing the initiation of landslides—the interactions among material strength, gravitational stress, external forces, and pore-fluid pressure—has been well understood for decades. The factors that govern whether landslide movements, once begun, will be catastrophic are less well understood. Nonetheless, much recent progress has been made in understanding those factors, as exemplified by basic research on fracture development in brittle materials (*5*) and on the properties of flowing material (*6*, *7*).

Major causes of landslides are also well known, and these include rainfall, seismic shaking, human construction activities, landscape alteration, and natural processes of erosion that undermine slopes. Yet predicting just where and when a landslide will occur continues to be a complex proposition, because the properties of earth materials and slope conditions vary greatly over short distances, and the timing, location, and intensity of triggering events—such as storm precipitation or earthquake shaking—are difficult to forecast.

Two landslides at La Conchita in California illustrate the complexity of landslide occurrence and behavior. In 1995, a landslide consisting of a relatively coherent block of earth at La Conchita caused property damage but no fatalities. Ten years later, another landslide remobilized from the 1995 deposit, transformed rapidly into a highly fluid debris flow, and traveled downslope at a speed of 5 to 10 m/s, causing 10 fatalities (see the second figure) (*8*).

Current landslide hazard analyses and mitigation strategies tend to concentrate at one of two scales: intensive, site-specific analyses of individual slopes or landslide bodies, and regional-scale evaluations that seek to identify hazardous zones that are best avoided when construction is planned.

D. K. Keefer is with the U.S. Geological Survey, Menlo Park, CA 94025, USA. E-mail: dkeefer@usgs.gov M. C. Larsen is with the U.S. Geological Survey, Reston, VA 20192, USA. E-mail: mclarsen@usgs.gov

Landslides in mountain regions. These rock avalanches were triggered by the 1980 Mammoth Lakes earthquake sequence. Several thousand rock falls and slides were associated with this event in central California.

In a site-specific landslide evaluation, instruments may be installed into the slope to determine water pressures, measure subsurface slippage, and monitor surface deformation. Materials may be sampled for laboratory testing of shear strengths and other properties such as mineralogy and density. Because these methods are expensive, extensive and site-specific analyses are commonly restricted to slopes where the costs of construction, potential for damage, or risk to population justify the expense.

A range of analytical techniques is used to evaluate the potential for landslide initiation at the site-specific scale. The decades-old and generalized limit-equilibrium method envisions a landslide as a rigid sliding block, and this has proved useful for many engineering and construction applications. Some newer, more sophisticated methods are specialized for the analysis of such processes as volcano-flank collapses (*9*) and initiation of debris flows (*6*, *7*). In the case of volcano-flank collapses, for example, these new methods incorporate coupled numerical modeling of heat and groundwater flow to analyze the potential for landslide initiation involving steep volcano flanks due to hydrothermal pressurization. Such modeling predicts the occurrence of deep-seated landslides that match the dimensions of many observed landslides, whereas more traditional slope-stability analyses predict that the landslides would be shallow (*9*).

Regional-scale evaluations of landslide hazards also use a range of analytical techniques. For example, modeling that combines analysis of groundwater flow with slope-stability calculations has been used to predict the timing and location of shallow, precipitation-triggered landslides (*10*), and the Newmark analysis (which combines slope-stability calculations with seismic ground-motion records) is widely used to evaluate the potential for landslides that could be triggered by earthquake shaking (*11*, *12*). Regional-scale analyses may also include empirical methods based on mapping landslide occurrences and developing statistical correlations among landslide occurrence, material and slope properties (such as rock type and slope steepness), and the strength of triggering events such as seismic shaking (*13*) or rainfall intensity and duration (*10*, *14*–*17*).

Regional-scale landslide analyses took a leap forward with the advent of high-resolution remote-sensing imagery and the use of geographic information systems (GIS) technology. The first automated event-based mapping of landslides from satellite imagery was carried out after the 1999 Chi-Chi earthquake in Taiwan (*18*). More recently, landslides triggered by the 2004 Niigata Ken Chuetsu earthquake in Japan were mapped using a similar technique (*19*). Further automated landslide mapping of this kind would greatly extend the database on which regional-scale hazard and risk models may be constructed.

Several other techniques also have promise for increasing the accuracy, precision, and effectiveness of landslide hazard evaluation. For example, synthetic aperture radar interferometry can be used for early detection of landslide movements (*20*). Models are being developed to predict landslide motion based on detailed analyses of motion-induced changes in pore-fluid pressures and material properties in landslide shear zones (*21*, *22*). Finally, landslide warning systems can be used to issue public alerts and warnings for a particular region when accumulated and/or forecast amounts of rainfall equal or approach those amounts that have triggered landslides there in the past (*23*, *24*).

Current landslide research efforts around the world are generally small relative to the costs of landslide damage. A recent report by the U.S. National Research Council recommended a 15-fold increase in funding for landslide research and development in the United States (*25*). Although landslide hazard evaluation and mitigation strategies are

Dangerous complexity. This landslide at La Conchita, California, on 10 January 2005 destroyed 13 houses, severely damaged 23 others, and killed 10 people (*8*).

CREDIT: (TOP) DAVID K. KEEFER/U.S. GEOLOGICAL SURVEY; (BOTTOM) MARK E. REID/U.S. GEOLOGICAL SURVEY

advancing in many fundamental areas, the loss of life and destruction of property by landslides around the world will probably continue to rise as the world population increases, urban areas of many large cities impinge more on steep slopes, and deforestation and other human landscape alterations affect ever-larger areas.

References and Notes

1. G. Plafker, G. E. Ericksen, in *Rockslides and Avalanches 1, Natural Phenomena*, B. Voight, Ed. (Elsevier, Amsterdam, 1978), pp. 277–314.
2. Data on casualties are from conversations of D. K. Keefer with survivors.
3. S. D. Evans *et al.*, *Nat. Hazards Earth Syst. Sci.* **7**, 89 (2007).
4. R. L. Schuster, in *Landslides Investigation and Mitigation*, A. K. Turner, R. L. Schuster, Eds. (National Research Council, Washington, DC, 1996), pp. 12–35.
5. D. N. Petley *et al.*, *Geology* **33**, 201 (2005).
6. R. M. Iverson, R. P. Denlinger, *J. Geophys. Res.* **106B**, 537 (2001).
7. R. P. Denlinger, R. M. Iverson, *J. Geophys. Res.* **106B**, 553 (2001).
8. R. W. Jibson, *U.S. Geol. Surv. Open-File Rep. 2005-1067* (2005).
9. M. E. Reid, *Geology* **32**, 373 (2004).
10. M. Casadei *et al.*, *Earth Surf. Process. Landforms* **28**, 925 (2003).
11. R. W. Jibson *et al.*, *Eng. Geol.* **58**, 271 (2000).
12. R. W. Jibson, M. W. Jibson, *U.S. Geol. Surv. Open-File Rep. 03-005* (2003).
13. S. B. Miles, D. K. Keefer, *U.S. Geol. Surv. Open-File Rep. 2007-1072* (2007).
14. N. Caine, *Geogr. Ann.* **62A**, 23 (1980).
15. S. D. Ellen, G. W. Wieczorek, Eds., *U.S. Geol. Surv. Prof. Pap. 1434* (1988).
16. M. C. Larsen, A. Simon, *Geogr. Ann.* **75A**, 13 (1993).
17. F. Fiorillo, R. C. Wilson, *Eng. Geol.* **75**, 263 (2004).
18. W. N. Wang *et al.*, *J. Jpn. Landslide Soc.* **38**, 18 (2002).
19. D. S. Kieffer *et al.*, *Earthquake Spectra* **22** (suppl. 1), S47 (2006).
20. C. Colesanti, J. Wasowski, *Eng. Geol.* **88**, 173 (2006).
21. R. M. Iverson, *J. Geophys. Res.* **110**, F02015 (2005).
22. T. R. Davies *et al.*, *Q. J. Eng. Geol. Hydrogeol.* **39**, 115 (2006).
23. D. K. Keefer *et al.*, *Science* **238**, 921 (1987).
24. R. L. Schuster, L. M. Highland, *Bull. Eng. Geol. Environ.* **66**, 1 (2007).
25. National Research Council, *Partnerships for Reducing Landslide Risk* (National Academies Press, Washington, DC, 2003).

10.1126/science.1143308

CELL SIGNALING

A Touching Response to Damage

An extensive network of proteins, and their combinatorial diversity, account for biological functions that are regulated in response to damaged DNA.

John H. J. Petrini

There are many things in day-to-day life that have the potential to cause mutations. Environmental exposure to chemicals and sunlight, and assaults from within such as free radicals produced when cells use sugar to make energy, all share the property of causing mutagenic damage to DNA. Despite this, the genetic information stored in DNA is remarkably stable. This is largely attributable to the existence of a complex cellular signaling network called the DNA damage response. Its role in maintaining genome integrity requires the integration of three general processes: sensing the damage, regulating the cell division cycle, and repairing DNA. The effectiveness of each, and their integration, relies heavily on the proper spatiotemporal dynamics of the components of this signaling network. Four papers in this issue—by Matsuoka *et al.* (*1*) on page 1160, Wang *et al.* (*2*) on page 1194, Sobhian *et al.* (*3*) on page 1198, and Kim *et al.* (*4*) on page 1202—collectively underscore that these dynamics are influenced by modifications of proteins that are catalyzed, and subsequently recognized, by components of the network itself.

The DNA damage response is loosely analogous to signal transduction networks activated by extracellular stimuli such as hormones and growth factors. Just as such factors (ligands) are bound by receptors on the cell surface to initiate the appropriate signal, damaged DNA engages proteins that sense genetic lesions. In both scenarios, the interaction of ligand with the receptor initiates a signaling cascade that leads to the phosphorylation of proteins functioning in the pathway. And in both cases, this chain of events culminates in the alteration of cellular processes.

Within the context of the DNA damage response, this general scheme also implicitly provides a critical piece of information: the location of the DNA damage. This feature is a consequence of the fact that DNA damage sensors recruit specific protein-phosphorylating enzymes (kinases) to the sites of damage. Among these kinases are ataxia telangiectasia mutated (ATM), ATM and Rad3-related kinase (ATR), and DNA-dependent protein kinase. This recruitment is a requisite first step in activating the DNA damage response.

Matsuoka and colleagues cataloged substrates of ATM and ATR, the major signal-transducing kinases of the DNA damage response, through the large-scale identification of peptides that are phosphorylated in response to ionizing radiation. For this approach, they used a panel of 68 phospho-specific antisera to purify, and ultimately identify the peptides in question from cells treated with ionizing radiation, a DNA damaging agent. Although the antisera were raised against 68 known ATM and ATR substrates, 700 additional targets were found; hence, almost 10 novel peptides were recovered for each phospho-specific reagent used. This suggests that sites phosphorylated by ATM and ATR are structurally similar.

From a biological perspective, this presumptive similarity suggests that phosphorylation "marks" inscribed by the transducing kinases may be recognized by protein domains common to mediators of the DNA damage response to facilitate protein interactions (see the figure). This idea is supported by the fact that the breast cancer C-terminal (BRCT) domain and forkhead-associated (FHA) domain—both phosphopeptide binding motifs–are commonly found in members of the DNA damage response signaling network. On the other hand, from a technical perspective, it's hard to imagine a more eloquent word of caution regarding the interpretation of immunofluorescence data obtained using those cross-reactive antisera to assess the disposition of DNA damage response proteins.

The central issue, and the major advance that Matsuoka *et al.* provide, is that the targets identified represent a comprehensive catalog of ATM and ATR substrates. To assess whether their approach accurately identified bona fide members of the DNA damage response network, Matsuoka *et al.* picked 37 of the new ATM and ATR targets and depleted them from human osteosarcoma cells with small interfering RNA. Although these proteins had not previously been implicated in the DNA damage response, more than 90% of the new targets queried in this manner exhibited defects in one or more indices of DNA damage response functions such as the activation of cell cycle checkpoints and DNA repair. These validations illustrate that this data set provides a solid foundation for

Molecular Biology Program, Memorial Sloan-Kettering Cancer Center, 1275 York Avenue, New York, NY 10021, USA. E-mail: petrinij@mskcc.org

understanding the logic of the DNA damage response network.

The small interfering RNA–based validation solidly implicates these new ATM and ATR substrates in the DNA damage response, but the functional importance of the phosphorylation events themselves remains an open question. The fact that inducible protein interactions are often at the heart of signal transduction makes it an appealing possibility that phosphorylation by these two kinases drives protein, interactions relevant to execution of the DNA damage response. This general mechanism is well established in the budding yeast *Saccharomyces cerevisiae*. In that context, DNA damage or DNA replication stress induces signal transducing kinases (Mec1 and Tel1) to phosphorylate several proteins including the histone variant H2AX, replication protein A, checkpoint proteins such as Rad9 and Mrc1, and their binding partners Rad53 and Dun1. These phosphorylation marks are required for physical associations between these proteins, essential for propagating the damage signal, and for affecting the biological outcomes of the response pathway. Many of these phosphorylation-dependent interactions in yeast require FHA domains (found in Rad53 and Dun1) and BRCT domains (in Rad9). The same theme is exemplified by 14-3-3 proteins. Like FHA and BRCT domains, 14-3-3 proteins preferentially bind to phosphorylated residues. And similarly, this protein family participates in DNA damage signaling in yeast and mammals through phosphorylation-dependent protein interactions with members of the DNA damage response (*5*–*8*). Although the functional importance of the 900 or so phosphorylation events detected by Matsuoka *et al.* certainly goes beyond simply driving proteins to interact, the weight of precedent augurs this outcome as being among the most important.

The three papers accompanying Matsuoka *et al.* introduce a different variation on this mechanistic theme. These papers identify three distinct and mutually exclusive complexes containing the tumor suppressor protein BRCA1 (breast cancer 1, early onset) which is a member of the DNA damage response network. Two of the complexes rely on the protein RAP80 to form ionizing radiation–induced foci of BRCA1. RAP80 is an ubiquitin binding protein, and therefore recognizes proteins that have been modified by the addition of ubiquitin. Hence, as with phosphorylation site recognition, identifying and binding an ubiquitinated target drives functionally important spatiotemporal alterations in the disposition of DNA damage response proteins. The mutual exclusivity of each of the three BRCA1 complexes described—complex A, containing the novel protein Abraxas identified by Wang *et al.*; complex B, containing the DNA repair protein BACH1 (*9*); and complex C, containing the tumor suppressor protein CtIP (*10*)—reflects the exclusive binding of the BRCA1 BRCT domain to Abraxas, BACH1, and CtIP. Although the interactions occur at ATM or ATR phosphorylation sites on the respective BRCA1 binding partners, their association is not induced by DNA damage. This suggests that, rather like the pilot light of a stove, ATM and ATR may phosphorylate certain substrates under nonstressed conditions to keep the DNA damage response primed for quick activation when DNA damage sensors initiate the signal.

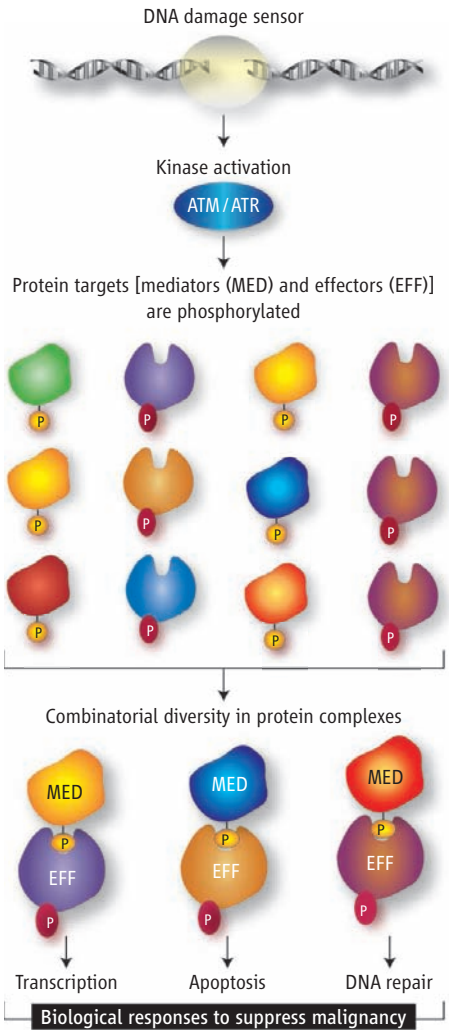

Protein interactions in the DNA damage response. The transducing kinases such as ATM and ATR phosphorylate components of the DNA damage response network, driving the formation of protein complexes vital for DNA damage signaling. Because certain complexes may form in specific tissues or cell cycle phases, this combinatorial scheme provides diversity in the biological functions regulated by the DNA damage response.

The existence of distinct BRCA1 protein complexes has been previously demonstrated (*11*–*13*), as has the link between BRCA1 and protein ubiquitination, in the DNA damage response. However, in contrast to previous data describing protein ubiquitination at sites of DNA damage catalyzed by the E3 ubiquitin ligase activity of BRCA1 (*14*, *15*), the data presented by Wang *et al.*, Sobhian *et al.*, and Kim *et al.* link BRCA1 to the recognition of ubiquitination sites through its association with RAP80. Just as the relevant substrates of the BRCA1 E3 ligase remain at large, the ubiquitinated target to which RAP80 binds and recruits the BRCA1 A and C complexes remain unsolved pieces of the puzzle surrounding the role of BRCA1 in the DNA damage response. A parsimonious, although purely speculative, possibility is that the initial recruitment of the various BRCA1 complexes is unrelated to recognition of an ubiquitinated protein by RAP80. In this scenario, recruitment would occur by a different mechanism, and permit BRCA1-mediated ubiquitination of DNA damage–proximal substrates to stabilize the localization of components of the damage response signaling network or otherwise regulate molecular events in the vicinity of DNA damage via RAP80 tethering. However the matter turns out, the four papers bring fundamental new information to the table, while at the same time reminding us that the more we know, the more complicated things get.

References

1. S. Matsuoka *et al.*, *Science* **316**, 1160 (2007).
2. B. Wang *et al.*, *Science* **316**, 1194 (2007).
3. B. Sobhian *et al.*, *Science* **316**, 1198 (2007).
4. H. Kim *et al.*, *Science* **316**, 1202 (2007).
5. E. Wilker, M. B. Yaffe, *J. Mol. Cell Cardiol.* **37**, 633 (2004).
6. G. Tzivion, Y. H. Shen, J. Zhu, *Oncogene* **20**, 6331 (2001).
7. T. Usui, J. H. Petrini, *Proc. Natl. Acad. Sci. U.S.A.* **104**, 2797 (2007).
8. M. B. Yaffe, A. E. Elia, *Curr. Opin. Cell Biol.* **13**, 131 (2001).
9. S. B. Cantor *et al.*, *Cell* **105**, 149 (2001).
10. X. Yu, L. C. Wu, A. M. Bowcock, A. Aronheim, R. Baer, *J. Biol. Chem.* **273**, 25388 (1998).
11. D. A. Bochar *et al.*, *Cell* **102**, 257 (2000).
12. S. F. Anderson, B. P. Schlegel, T. Nakajima, E. S. Wolpin, J. D. Parvin, *Nat. Genet.* **19**, 254 (1998).
13. J. Chen *et al.*, *Mol. Cell* **2**, 317 (1998).
14. G. Y. Zhao *et al.*, *Mol. Cell* **25**, 663 (2007).
15. L. J. Barber, S. J. Boulton, *DNA Repair (Amst)* **5**, 1499 (2006).

10.1126/science.1143700

SCIENCE POLICY

S&T Forum: States, Industry Play Key Roles in U.S. Innovation Drive

With the U.S. government hobbled by financial constraints and political divisions, state policy-makers are pressing new initiatives—often with partners in business or foundations—to improve the climate for science-related innovation and education, experts said at the AAAS Forum on Science and Technology Policy.

California is well known for its $3 billion ballot measure to fund stem cell research. Pennsylvania is pursuing an ambitious program to promote energy independence, biosciences, nanotech, and 21st-century manufacturing. Georgia has set aside $400 million to build research facilities and recruit top scholars. New Mexico, already home to two national laboratories and a booming high-tech sector, is joining with Virgin Companies Chairman Richard Branson to build a spaceport.

Susan Hackwood

"We read about a few states in the headlines," said Mary Jo Waits, director of the Pew Center on the States, "but people would be amazed at how many states are putting in initiatives to support … research and development."

The 32nd annual Forum, held just a few blocks from the White House on 3 to 4 May, attracted some 450 policy-makers from government, education, industry, and other fields. The event included discussions of surveillance; R&D in the developing world and Europe; and "sequestered science," in which research findings are kept secret. The overarching theme was U.S. innovation policy—and its uncertain future—in a world growing smaller and more competitive.

"The Forum covered a remarkable range of topics," said Al Teich, director of AAAS Science and Policy Programs, "but the willingness of states to invest in research and innovation, largely unhindered by ideology, was a real attention-getter. They are truly becoming 'laboratories of democracy.' "

Many Forum speakers cited the urgent message of *Rising Above the Gathering Storm*, the National Academies' seminal 2005 report on U.S. innovation policy, and their presentations suggested that it has helped galvanize a movement that now reaches into statehouses, universities, foundations, and businesses nationwide.

Federal R&D investment still dwarfs that made by the states, and at the Forum, national science policy leaders representing both major political parties emphasized the importance of federal innovation and education initiatives.

John H. Marburger III, director of the White House Office of Science and Technology Policy, urged support for the American Competitiveness Initiative (ACI) offered by President George W. Bush. ACI would double the budgets for the National Science Foundation, the National Institute of Standards and Technology, and the Department of Energy's Office of Science over 10 years, but Marburger said it is falling behind schedule because Congress has failed to provide full funding.

U.S. Representative Bart Gordon, the Tennessee Democrat who chairs the House Committee on Science and Technology, later noted that the House has approved two major bills drawn from recommendations in *Rising Above the Gathering Storm*, one of which implements many of the study's K-12 education proposals, while the other creates an array of programs to encourage young researchers.

Overall, the funding prospects at the federal level remain "fairly bleak," said Kei Koizumi, director of the AAAS R&D Budget and Policy Program. If President Bush's fiscal year 2008 budget were approved, he said, big gains would go to weapons systems, space exploration, and the three ACI agencies. But cuts in other areas would leave inflation-adjusted federal basic and applied research investment down for the fourth straight year.

Innovation requires more than research and funding, said William A. Wulf, outgoing president of the National Academy of Engineering. But the broader U.S. innovation ecology is geared for a past age, not for the future. The patent system, intellectual property laws, and the tax code all need an overhaul, Wulf added, yet "inertia" is impeding reform.

A number of the state innovation initiatives are geared toward education. In California, 66% of new mathematics teachers and 54% of new science teachers do not hold a preliminary credential, said Susan Hackwood, executive director of the state's Council on Science and Technology. The Council this spring released a report on California's education needs, and its efforts have drawn "phenomenal support" from business leaders, Hackwood said.

Science Foundation Arizona plans grants totaling $3.5 million for K-12 education, said President William C. Harris. "We can no longer sit back and say…'We can throw away some of these kids,' " he said. "We need every brain."

Sherwood Boehlert, the New York Republican who formerly chaired the House Science Committee, urged scientists to be active not only in debates over science funding, but in helping inform the debate about other science-related issues. But scientists need to recognize that science is only one factor in policy decisions, and that policy-makers must weigh an array of conflicting pressures, ideas, and values, Boehlert cautioned in the 2007 William D. Carey Lecture.

Sherwood Boehlert

"If scientists are going to be more effective participants in the policy arena, they have to do their homework and learn more about the policy world," he advised. "It should go without saying that policy-makers have to do their homework about science … Unfortunately, I don't know how to force anyone in either the scientific or political communities to do their homework."

For materials from the AAAS Forum, see www.aaas.org/spp/rd/forum.

SCIENCE AND SOCIETY

New Director Expands Human Rights Program

After Janjaweed militants burned the village of Bir Kedouas in Chad in 2005, satellite photos analyzed by AAAS's Science and Human Rights Program (SHRP) brought the devastation into sharp relief. Now, with a new director at the helm, SHRP is looking at other ways to bring 21st-century science to the service of human rights.

Recruiting "on-call" scientists who consult on human rights crises and exploring the potential of wireless Internet technologies to monitor human rights abuses in real time are a few of the programs that SHRP hopes will make scientists as essential as lawyers in the human rights field, according to the program's new director, Mona Younis.

Younis believes that the greater engagement of scientists "is essential to securing human rights. We can't allow another century to pass without seeing that promise realized."


Mona Younis

Human rights organizations increasingly depend on scientific methods and technology to monitor human rights and collect evidence on violations. At the same time, the international human rights framework also requires governments to address rights related to health, climate change, urban development, and the benefits of scientific discovery itself.

"These are human rights that are very directly related to the work of scientists, as they have substantial scientific components to them," said Younis.

With this in mind, SHRP has four key areas in its new portfolio: engaging scientists in human rights efforts, applying scientific tools to human rights problems, promoting the right to enjoy the benefits of scientific progress, and exploring the human rights implications of new technologies and scientific discoveries. Details about the program's new framework will be posted in June at http://shr.aaas.org/.

Younis wants to enlist scientists and their professional societies in the important human rights work being undertaken in the United States and around the world. In keeping with this plan, SHRP is reviving its Science and Human Rights Coalition, an umbrella group of affiliated scientific societies with human rights interests, with a membership meeting planned for the AAAS Annual Meeting in Boston next February.

In the realm of scientific tools, SHRP has already had great success with its year-old geospatial technologies project, which has documented human rights violations in Zimbabwe, Sudan, and other countries. Now, the program staff is researching ways to use wireless technologies to document human rights violations and to scrutinize government budgets for their effects on health, housing, and education. The program is also looking at the social science tool of structure mapping, which graphically represents webs of human relationships. Structure mapping can help human rights workers understand how multiple groups in a society—from the police to the medical community—may work together to promote the use of torture in some countries, for example.

The impact of new technologies and of scientific research itself on human rights issues is another new area for SHRP, but one that follows naturally from the program's work, according to Younis. "For instance, there are privacy issues related to using geospatial technologies, so how do we proceed without violating privacy rights?" she said.

In the three decades since the program began, SHRP has been a trailblazer in using science to aid human rights work. It brought human rights issues involving scientists to the forefront, beginning with its vigorous defense of Soviet physicist Andrei Sakharov and other scientists similarly persecuted worldwide. More recently, SHRP applied forensic science to the identification of victims of mass atrocities in Argentina and Guatemala, and worked with truth and reconciliation commissions in Guatemala, South Africa, Peru, and Sierra Leone.

Younis worked as the human rights program officer at the Mertz Gilmore Foundation and was coordinator of the International Human Rights Funders Group before coming to AAAS in January. SHRP's experience, she says, has shown that "across disciplines, when scientists are aware of what's needed and what they can do, they contribute inimportant ways."

—Becky Ham

DIPLOMACY

Building Libraries—and Partnerships—in the Middle East

Many Middle Eastern nations are making significant investments in higher education systems, and some have built libraries on par with the best in the world. But most colleges and universities in the region are only at the early stages of building electronic collections, and a few still rely on the card catalogues of earlier times.

Nikolas Coffrin, a senior sales coordinator in the AAAS Office of Publishing and Member Services, was in the Middle East for a month this spring, co-hosting a workshop, visiting libraries, and talking with librarians. In their meetings—and in many casual conversations over coffee or tea—he found them eager to engage with AAAS and *Science* and to build expertise that will aid their libraries and their nations' economies.

The workshop was "the first meeting of its kind we've attended" in the Middle East, said *Science* Publisher Beth Rosner. "We're very excited about working with the universities, schools, and institutes in that part of the world. We think that the scholarly tools we're offering, and the dissemination of scientific information, could be very valuable to them. Eventually, this collaboration really could help bring all of our communities closer."

The workshop emerged from discussions last year between Tom Ryan, director of site license sales for *Science*, and Mohamed Ghali Rashid, a librarian at Arabian Gulf University, during a meeting of the Special Libraries Association-Arabian Gulf Chapter (SLA-AGC).

Convening from 31 March to 2 April, "Electronic Collection Development for Health & Medicine E-Libraries" brought 30 librarians from the region's universities and medical research centers to Manama, Bahrain, for lectures, hands-on training, and networking. It was co-sponsored by SLA-AGC/Mondesic TechKnowledge, a publishing agent based in Dubai, and AAAS/*Science*. The workshop was followed by the 2007 SLA-AGC annual meeting, where Coffrin made informal presentations to many of the 200 librarians who attended.

Meeting with representatives of the publishing world "provided us with the opportunity to explain the difficulties medical libraries of the region face in the rapidly evolving world of electronic information, the vast increases of journal prices, and the shrinking library budgets," said Randa Al-Chidiac, electronic resource librarian at the University of Balamand in Lebanon. "I hope that it will be the launching pad for further cooperation and collaboration in the near future."

Coffrin later met with librarians at 15 colleges and universities in Jordan, Lebanon, Bahrain, Kuwait, and the United Arab Emirates.

CAREERS

Booklet Covers the Basics of Science Job Seeking

Career Basics is a new booklet that compiles the best advice and resources for scientists looking for their first jobs from the thousands of articles on ScienceCareers.org, the Web's most comprehensive site for science career information. The booklet can be downloaded for free at the ScienceCareers.org Web site (www.sciencecareers.org/careerbasicspdf).

The articles were chosen by the site's editorial staff to reflect the essential elements of landing a good job in science. "It's the fundamentals, basic career information that will help every scientist," said John Meyers, AAAS's Director of Marketing, Office of Publishing and Member Services

Although several of the chapters deal with challenges common to all job seekers—making the most of your résumé and curriculum vitae and preparing for interviews, for example—the authors home in on issues specific to research careers. For instance, are interviewers impressed by a tide of technical details in a job talk? Should pregnant researchers ask for a special risk assessment of their lab conditions?

The booklet also offers advice on sprucing up grant proposals, managing a lab, pursuing alternative careers, finding unusual sources of funding, and making the most of networking opportunities.

—Becky Ham

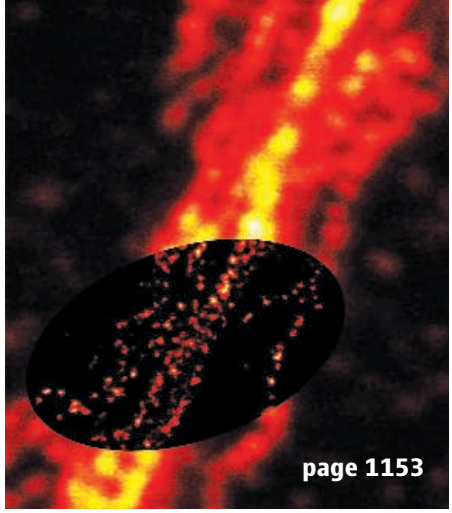

CREDIT: GERALD DONNERT, LARS MEYER, STEFAN W. HELL

INTRODUCTION

Lights, Camera, Action

AT THE END OF A LONG DAY IN THE LAB, WHAT WE'D ALL LIKE IS AN award-winning movie. What makes for a good movie? An engrossing story, deft cinematography, and an extraordinary ensemble of actors. The goal of single-molecule research is to produce a movie of the cell. Biochemistry and biophysics done in the test tube already provide an understanding of the dynamic behavior of molecules; from these studies, what goes on in cells, minute by minute or even second by second, can be inferred. Ultimately, however, the goal is to film single molecules in single cells, focusing in closely enough not only to observe spatial and temporal characteristics but also to decipher molecular mechanisms. We're not there yet, but recent advances in single-molecule techniques bring us tantalizingly close to a molecule-scale movie of cellular life.

Because cells are optically transparent, light microscopy is ideal for noninvasive imaging of cells in three dimensions. However, until recently, the resolution of lens-based optical microscopes was constrained by the diffraction barrier, which gave a resolution cutoff at half the wavelength of light. In his Review, Hell (p. 1153) discusses concepts that show how the diffraction barrier can be broken in fluorescence spectroscopy and how these techniques have been applied to achieve nanoscale resolution. His Review gives hope that real-time three-dimensional imaging of live cells with electron-microscopy resolution may not be too far away.

Many single-molecule techniques remain in vitro, but take on the challenge of transferring the results into the realm of cellular systems. In their Review, Evans and Calderwood (p. 1148) describe how combining molecular cell biology with single-force spectroscopy provides a tool to explore eukaryotic cell adhesion, revealing how forces applied to cell-surface bonds affect intracellular interactions or chemical reactions. Although these techniques are a powerful probe of mechanical function, understanding molecular mechanisms generally requires molecular dynamics simulations of atomic structural molecules. Sotomayor and Schulten (p. 1144) describe in silico single-molecule experiments that use steered molecular dynamics simulations to explore how macromolecules respond to external forces at an atomic level.

Two Reports in this issue also highlight single-molecule techniques. In in vitro experiments, Shiroguchi and Kinosita (p. 1208) provide a clear view of myosin V motion, showing that it walks using a combination of lever action and Brownian motion. Elf *et al.* (p. 1191) use single-molecule imaging of the lac repressor to directly observe the function of this regulatory system in live *Escherichia coli* cells.

In related online resources, *Science*'s Signal Transduction Knowledge Environment (STKE) focuses on how single-molecule analysis is increasing understanding of cellular signaling (www.sciencemag.org/sciext/singlemolecules/). Chazin describes how x-ray crystallography and nuclear magnetic resonance studies have provided insights into the function of Ca^{2+}-sensing proteins. Navratil *et al.* discuss the application of microfluidic technology to the counting of low-abundance proteins in single cells, and Ghosh and Wirth present an algorithm for analyzing the movement of receptors in the plasma membrane.

We'll be watching with interest as single-molecule approaches move us toward a quantitative and mechanistic understanding of cellular processes.

– VALDA VINSON AND GILBERT CHIN

Single Molecules

CONTENTS

Reviews

See also related Reports on pages 1191 and 1208;
Science*'s STKE material on page 1091 or at*
www.sciencemag.org/sciext/singlemolecules/

Science

Published by AAAS

REVIEW

Single-Molecule Experiments in Vitro and in Silico

Marcos Sotomayor and Klaus Schulten*

Single-molecule force experiments in vitro enable the characterization of the mechanical response of biological matter at the nanometer scale. However, they do not reveal the molecular mechanisms underlying mechanical function. These can only be readily studied through molecular dynamics simulations of atomic structural models: "in silico" (by computer analysis) single-molecule experiments. Steered molecular dynamics simulations, in which external forces are used to explore the response and function of macromolecules, have become a powerful tool complementing and guiding in vitro single-molecule experiments. The insights provided by in silico experiments are illustrated here through a review of recent research in three areas of protein mechanics: elasticity of the muscle protein titin and the extracellular matrix protein fibronectin; linker-mediated elasticity of the cytoskeleton protein spectrin; and elasticity of ankyrin repeats, a protein module found ubiquitously in cells but with an as-yet unclear function.

Modelers, carrying out molecular dynamics (MD) simulations (*1*), are not content anymore to merely describe biomolecules in a hands-off manner. Rather, they move from pure description to investigative manipulation, seeking knowledge from poking with Nature's biomolecules in so-called steered molecular dynamics (SMD) (*2*) simulations. Modelers got the idea from single-molecule force spectroscopy, which stretches proteins and DNA in manifold ways in vitro (*3*–*5*), but also from the living cell itself, which makes its molecules endure manifold forces in vivo as a result of countless mechanical processes, from control of the unwieldy genome to motor-driven transport (*6*, *7*). The modelers reenact "in silico" (through computer modeling) what atomic force microscopy (AFM), optical tweezer experiments, or the cell do to biomolecules, but they also devise their own "experiments," ones that are as-yet impossible to do in the laboratory.

In silico single-molecule force spectroscopy grew up fast: Nurtured first with ideas from experiments, modelers quickly became partners in the laboratory, explaining old and suggesting new experiments and now even moving ahead of in vitro work. Yet conventional experimentalists observe the real world, whereas computational experimentalists observe only the virtual world of simulation. Can their message be trusted? Clearly there is no general answer, but successes suggest that computational experiments reveal valuable new information on the molecular mechanisms underlying cellular mechanics. We review discoveries made through in silico experiments on the muscle protein titin (*8*–*10*), the closely related extracellular matrix protein fibronectin (*11*), the cytoskeleton protein spectrin (*12*, *13*), and the repeat protein ankyrin (*14*). Appreciation for the value of in silico experiments may be best evidenced by the fact that single-molecule spectroscopists have started to do simulations (*15*, *16*)

Molecular dynamics simulations that mechanically manipulate proteins (*17*, *18*) were initiated a decade ago in response to one of the first AFM experiments on biomolecules by Gaub *et al*. (*19*). The experiments made use of reagents widely used in the laboratory as gluing biomaterials, avidin and biotin. The tetrameric protein avidin binds biotin in its four pockets; biotinylating substrates A and B and adding avidin can bond A and B together. Biotinylating an AFM tip and a substrate permitted Gaub *et al*. to measure, as a function of distance, the forces experienced in making and breaking the biotin-avidin bond. Distance-force curves obtained by Grubmüller *et al*. (*20*) and by Schulten *et al*. (*21*) in SMD simulations revealed that avidin not only has a strong affinity for biotin when completely bound but also follows an unbinding pathway characterized by a series of interactions between biotin and avidin's amino acid side groups. Evans and Ritchie (*22*) used the data from simulation (*21*) to construct the energetics of biotin binding in good agreement with observations. This was only a beginning but illustrates the process that is still used.

Mechanical Unfolding of Titin and Fibronectin

A key mechanical function of the human body is motion due to its skeletal muscles and the involuntary muscles of its heart and intestines. Well-known molecular components of muscle are the thin and thick filaments made of actin and myosin, proteins involved in muscle contraction; less known is titin, a protein that gives muscle elasticity and mechanical stability (*23*). Titin is made of about 300 domains and a few random coil segments, all of which are arranged like pearls on a string and act like an elastic, accordion-like band.

Titin is encoded by the longest gene in the human genome; one gene serves for all types of muscle by way of posttranscriptional modification. Although titin in regard to its length is an extreme protein, its architecture is typical of cellular proteins with mechanical function: The protein is highly modular, the modules being homologous in sequence and structure and having systematic sequence differences that translate into specific mechanical properties. One seeks to understand the design of each module and how it contributes individually to titin's mechanical properties while at the same time understanding how all modules together contribute to these properties. The multidomain elasticity stems from pairwise angular reorientations of adjacent domains and is referred to as tertiary structure elasticity, whereas the single-domain elasticity stems from an unraveling of secondary structure elements and thus is called secondary structure elasticity. Random coil segments contribute elasticity that is largely entropic, like in rubber.

Titin in muscle, like other mechanical proteins, must endure and elastically respond to a broad range of forces, acting like a spring in response to weak forces and extending several-fold in length without actually rupturing in response to strong forces. The design principles of titin were little understood until recently. Single-molecule force spectroscopy became a key source of information on mechanical functioning, starting with titin's I91 domains (formerly known as I27), one of the first domain to be structurally resolved (*24*) (Fig. 1 A). In a series of elegant experiments, Gaub *et al*., Bustamante *et al*., and Simmons *et al*. (*25*–*27*) stretched titin by using AFM and optical tweezers. In subsequent work, Fernandez *et al*. stretched engineered tandem domains of I91s in series and monitored the extension-force curve between a substrate and an AFM tip (*28*). In the resulting saw-tooth curves (similar to those shown in Fig. 1, C and E), each tooth represents the stretching and sudden unfolding of one of the domains according to its secondary structure elasticity function. Yet, the information the curves convey, breakpoint extensions and breakpoint forces, is rather limited.

The titin I91 AFM measurements called for an interpretation in terms of the domain's structure, a β-sheet sandwich, as shown in Fig. 1A. The key question was what feature of the structure constitutes the force-bearing part that protects the domain from beginning to unravel apparently without further resistance. SMD simulations offered an opportunity to obtain an answer that could then be tested.

The first SMD simulations (*8*) revealed the force-bearing parts of titin's I91 domain, namely

Department of Physics, University of Illinois at Urbana-Champaign, and Beckman Institute for Advanced Science and Technology, 405 North Mathews Avenue, Urbana, IL 61801, USA.

*To whom correspondence should be addressed. E-mail: kschulte@ks.uiuc.edu

a set of nine interstrand hydrogen bonds between strands A′ and G and between strands A and B (Fig. 1A). The terminal strands A and G are subject to tension when the domain termini are being pulled apart. First, strand A detaches from strand B, leading to an intermediate conformation (Fig. 1B). Then, strand G detaches from strand A′, and, once all nine hydrogen bonds are broken, the remaining strands unravel by unzipping hydrogen bonds one by one. The reverse of the unraveling process most likely is not the route for spontaneous refolding, which rather involves a hydrophobic folding nucleus that is also important for temperature- and denaturant-induced unfolding (*29*–*31*). The force-induced unraveling immediately suggests mutants that should affect the extension-force relation observed in AFM experiments. A key mutant was investigated in a collaboration between Fernandez, Schulten, and co-workers. The mutant, designed to take advantage of the fact that the A-B interstrand hydrogen bonds break a bit more easily than the A′-G bonds do, destabilized further the intermediate and abolished an experimental signature ("hump") in the extension-force curve, corroborating the scenario depicted by simulations (*28*) (Fig. 1C).

Like physical experiments, computational experiments can yield puzzling results. In the case of I91, the height of the energy barrier to stretching the large set of interstrand hydrogen bonds was not well understood (*32*). However, modelers had overlooked a key player, water (*9*). Water molecules continuously attack I91's surface-exposed interstrand hydrogen bonds; one is cut every 10 ps but quickly reforms. This random weakening of hydrogen bonding lowers the force needed to stretch I91 apart and is likely controlled by properties of side groups surrounding them, as is the case for fibronectin (see below) (*33*). Other factors, such as packing interactions, may also influence the mechanical stability of this domain (*31*).

Titin's function likely goes beyond being the passive element of muscle elasticity, acting also as a biomechanical sensor. SMD simulations have suggested that tension can induce exposure of a kinase active site in titin (*34*), thereby transforming mechanical force into a biochemical signal. Similarly, buried binding sites may get exposed when molecules are subject to force, as postulated for other modular proteins (*7*).

Multidomain proteins, made of subunits similar to the ones in titin, act in the extracellular matrix of cells in higher organisms. These proteins, fibronectins, form fibrils that anchor themselves to cell surface receptors, such as integrins, and hold tissue cells together. The fibrils can stretch out to several times their contracted length, giving tissues flexibility. The structures of individual domains and of several tandem domains have been resolved, and their mechanical properties have been investigated by AFM experiments and SMD simulations, showing excellent agreement between the measured and the predicted hierarchy of mechanical stability (*33*, *35*–*37*). Moreover, prediction of intermediate unfolding states has been confirmed by experiments (*38*–*40*). An observed saw-tooth pattern is shown in the Fig. 1E inset. A double peak arises at the tooth that is due to fibronectin domain $FnIII_1$ (*35*), posing a puzzle that was resolved by simulations (*11*).

$FnIII_1$ (Fig. 1 E), like titin I91, has a sandwich architecture of two sheets of β strands but, in contrast to other fibronectin domains, features a small and a large sheet, the size being characterized by substantially different numbers of interstrand hydrogen bonds. This suggested that the main force-bearing hydrogen bonds, i.e., the ones sealing the two β sheets shut, are broken first and the small sheet unravels quickly, but then the large sheet resists further unraveling by aligning itself to the external forces such that a second set of multiple interstrand hydrogen bonds needs to be ruptured before the remainder of the sheet unzips. This pathway depends on detailed structural features that were unknown because of the lack of a resolved structure. Homology modeling based on the known structures of other fibronectin domains proved that the proposal could explain the intermediate states observed in AFM experiments (Fig. 1E). Our collaboration with Campbell led to the structure of $FnIII_1$ being solved by nuclear magnetic resonance (NMR) spectroscopy. This structure further corroborated the model, revealing key details that strengthen the large $FnIII_1$ sheet (*11*).

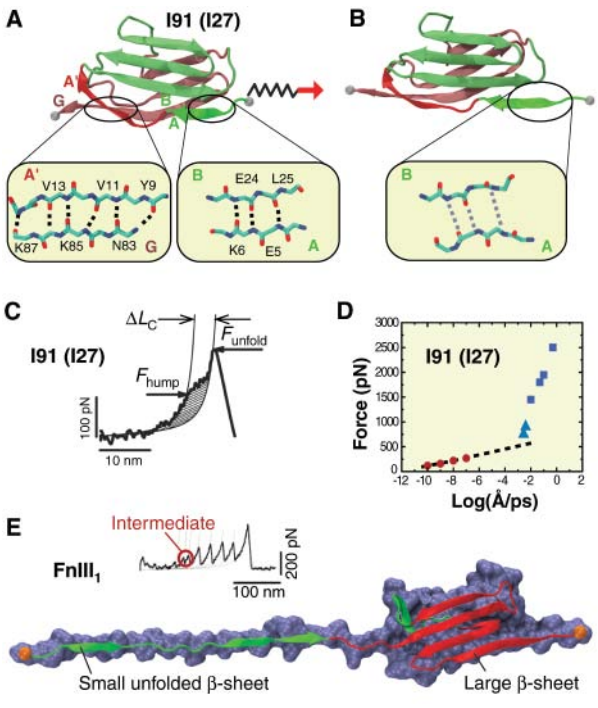

Fig. 1. Titin I91 and $FnIII_1$ elasticity. (**A**) Titin I91 (formerly known as I27) is shown in cartoon representation. The two β sheets forming the domain are shown in green and red. Detail of backbone hydrogen bonds involving β strands A-B and A′-G are shown. E, Glu; K, Lys; L, Leu; N, Asn; V, Val; and Y, Tyr. (**B**) Stretching of titin I91 through SMD simulation reveals an intermediate state in which β strand A is detached from β strand B, yet β strands A′ and G are still connected. (**C**) Force peak corresponding to unfolding of one titin domain obtained through AFM experiments [adapted from (*28*)]. The unusual "hump" observed in the force peak arises due to the unfolding intermediate [(B)] identified by SMD simulations (*70*). A point mutation disrupting backbone hydrogen bonds that link β strands A and B removed the observed hump. (**D**) Dependence on stretching velocity (in units of Å/ps) of the rupture force peak of titin I91. Red circles represent values from AFM experiments; blue squares and triangles represent values from constant velocity and constant force SMD simulations, respectively [adapted from (*10*); see also (*71*)]. The SMD data approaches the extrapolated AFM force peak curve upon reduction of velocity, as expected. (**E**) Intermediate state of $FnIII_1$ obtained through SMD simulations (shown in cartoon and surface representations). The small, unfolded β sheet is shown in green. (Inset) A "saw-tooth" pattern for $FnIII_1$, revealing the existence of intermediate states [adapted from (*35*)]. This intermediate state is thought to be relevant in the formation and strengthening of fibronectin fibrils.

What is the purpose of the peculiar architecture of $FnIII_1$? It was suggested that the large $FnIII_1$ sheet offers interstrand binding opportunities to domains of parallel fibers, leading to cross-linking in a sufficiently stretched extracellular matrix (*11*). Amazingly, the large sheet of $FnIII_1$ is an anticancer drug, anastellin, that apparently prevents metastasis by strengthening the adhesion of cancer cells to primary tissue cells (*11*, *41*).

Linker-Mediated Elasticity of Spectrin

The discoidal shape and mechanical properties of red blood cells assist their rapid adaptation to wide arteries and narrow capillaries. Diseases, such as hereditary spherocytosis and elliptocytosis, causing hemolytic anemia are associated with a lack of an elastic, adaptable shape caused by mutations affecting the red blood cell cytoskeletal network made of spectrin, ankyrin, and associated proteins (*42*–*44*).

The elastic architecture of the protein modules forming titin and fibronectin described above differs from that of spectrin repeats found in the red blood cell cytoskeleton. Crystal structures

of the superfamily of spectrin proteins, including spectrin itself, α-actinin, and dystrophin, reveal building blocks made of three-helix bundles repeated in series (Fig. 2) and forming part of heterotetrameric assemblies arranged in elongated filaments (*42*, *45*). The structures also revealed an α-helical linker. However, the static structures cannot reveal elastic properties, and therefore researchers turned to AFM experiments and SMD simulations to investigate spectrin elasticity.

Initial AFM experiments (*46*) suggested that spectrin repeats mechanically unfold predominantly one by one in an independent, all-or-none fashion. Force peaks were found to be substantially smaller than those observed for other proteins made of β strands instead of α helices. Further AFM experiments confirmed the relative weakness of spectrin and the one-by-one unfolding pathway but also revealed that different sets of spectrin repeats may exhibit intermediates and cooperative unfolding events involving more than one repeat (*47*–*49*) (bottom trace in Fig. 2 inset). Forces and distances obtained from AFM characterized well the elasticity of spectrin, but the molecular mechanism underlying spectrin elasticity could only be identified through simulation.

SMD simulations of two or more spectrin repeats solvated in explicit water (*12*, *13*) confirmed the relative weakness of spectrin when compared with the immunoglobulin-like domains of titin and fibronectin. The simulations also confirmed the existence of different unfolding pathways and suggested that the spectrin elastic response is rate dependent (*12*). Despite the large stretching velocities used in the simulations (*50*), the results matched qualitatively the prior experimental characterization. Moreover, simulations identified the linker regions between spectrin repeats as key elastic elements (*12*, *13*). Analysis of simulated unfolding, which followed the motion of all the atoms of the protein-solvent system during stretching, permitted researchers to identify which regions unfold first (the linker regions), the key amino acids involved in rupture of secondary and tertiary structure elements, and the role of water during unfolding (Fig. 2).

The detailed unfolding pathway gleaned from SMD simulations complement the AFM experiments. However, can the simulations also be predictive? Indeed they can. Recent work identified mutations at the linker regions of spectrin causing disease (*44*), thereby corroborating the relevance of linkers in the mechanical response of this protein as indicated by simulations. The mutations, involving substitution of amino acids by proline, destabilize the α-helical structure of the linker and favor temperature-mediated unfolding of spectrin as probed through in vitro experiments (*44*).

Ankyrin Elasticity

The third protein system reviewed here, ankyrin, is an example of simulation being ahead of experiments. Ankyrin proteins were first identified as essential components of the red blood cell cytoskeleton, providing a link between spectrin and membrane-bound ion channels (*42*). Although the specific role of ankyrins was unknown, their sequence revealed a repetitive motif of 33 amino acids named the ankyrin repeat. This motif is found in sets of 24 throughout the family of ankyrins. Such ankyrin repeats were later found to be part of the sequence of hundreds of other proteins (*51*) and are now widely recognized as ubiquitous molecular components of living cells. Ankyrin repeats are thought to mediate protein-protein interactions (*52*), but otherwise their function remains unclear.

The three-dimensional structure of the ankyrin repeat motif is well conserved (*52*–*54*). Each repeat is made of two antiparallel α helices and a short loop. Repeats stack in parallel, sharing a large hydrophobic interface and featuring another, slightly larger, connecting loop (Fig. 3A). The parallel arrangement of ankyrin repeats contrasts the arrangement of the modular proteins described above. Titin, fibronectin, and spectrin feature modules arranged linearly in series, whereas the ankyrin parallel arrangement results in elongated proteins featuring a superhelical conformation when multiple repeats are put together (Fig. 3B). Moreover, amino acids that are close in sequence are also close in space. An interest in ankyrin repeats came from the finding that transient receptor potential channels, thought to mediate mechanotransduction in higher organisms, contain up to 29 ankyrin repeats that might gate such channels (*55*, *56*). Both experimental and computational groups sought to characterize the elasticity of ankyrin.

SMD simulations performed on multiple crystal structures and models of ankyrin repeats were the first to examine the elastic properties of these repeat proteins (*14*). Simulations performed on structures containing 4, 12, and 24 ankyrin repeats revealed a two-stage elastic response. On application of force, the protein first changes its shape from helical to straight by rearranging tertiary structure elements but keeping the secondary structure intact (Fig. 3B). Then, on increasing force, repeats detach and unfold from the structure. The initial curved-to-straight transition is reversible, and, indeed, large stacks of ankyrin repeats behave like an overdamped spring. The response corresponds to tertiary structure elasticity.

After the initial elongation, simulations revealed a saw-tooth pattern depicting detachment and unfolding of individual repeats, one at a time (Fig. 3C), corresponding to secondary structure elasticity. Constant-force SMD simulations found stepwise unfolding of ankyrin repeats characterized by steps of ~100 Å (*14*).

AFM experiments by Marszalek *et al*. and Fernandez *et al*. confirmed the simulation results (*57*, *58*). Experiments performed on 24 ankyrin repeats of human ankyrin-B showed a Hookean response at low force that closely matched (within a factor of two) the linear elastic response observed in simulations of human ankyrin-R attributed to tertiary structure elasticity (*57*) (Fig. 3D). Experiments also revealed the stepwise unfolding of individual repeats separated by distances of 11 nm (*57*, *58*) (Fig. 3D, inset). Although the forces observed for unfolding of individual ankyrin domains in vitro are substantially lower than those observed in silico [as expected because of the high stretching velocity used in simulations (*50*)], the hierarchy of mechanical stability and the observed peak-to-peak distances determined using both methods are consistent (*59*).

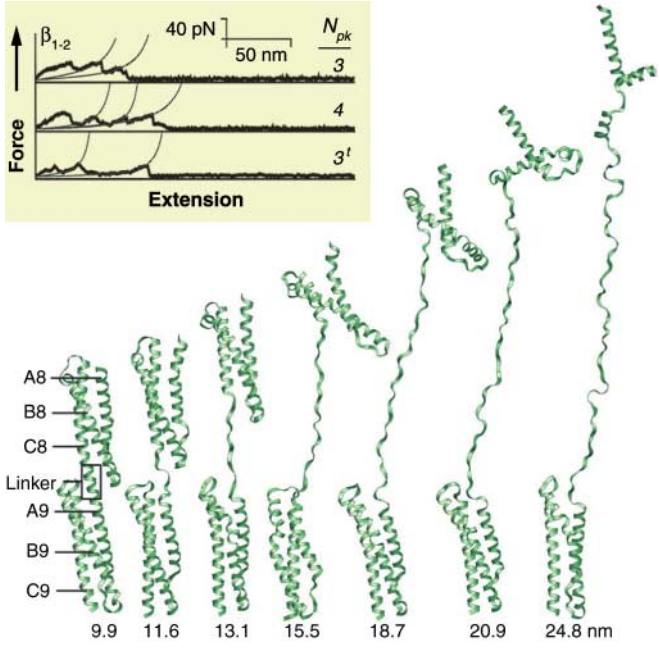

Fig. 2. Elasticity of spectrin. Mechanical unfolding of a double-repeat β-spectrin from human erythrocytes [adapted from (*13*)]. Each spectrin repeat (labeled 8 and 9) is made of three α helices denoted as A, B, and C. The unfolding sequence shows how the linker region unfolds first. (**Inset**) Force-extension curves for a two-β-spectrin repeat construct [adapted from (*48*)]. The bottom trace shows cooperative unfolding. Mutations weakening the linker region of spectrin have been shown to cause hereditary spherocytosis (*44*).

Outlook

The examples described highlight the role of modeling in the quest to

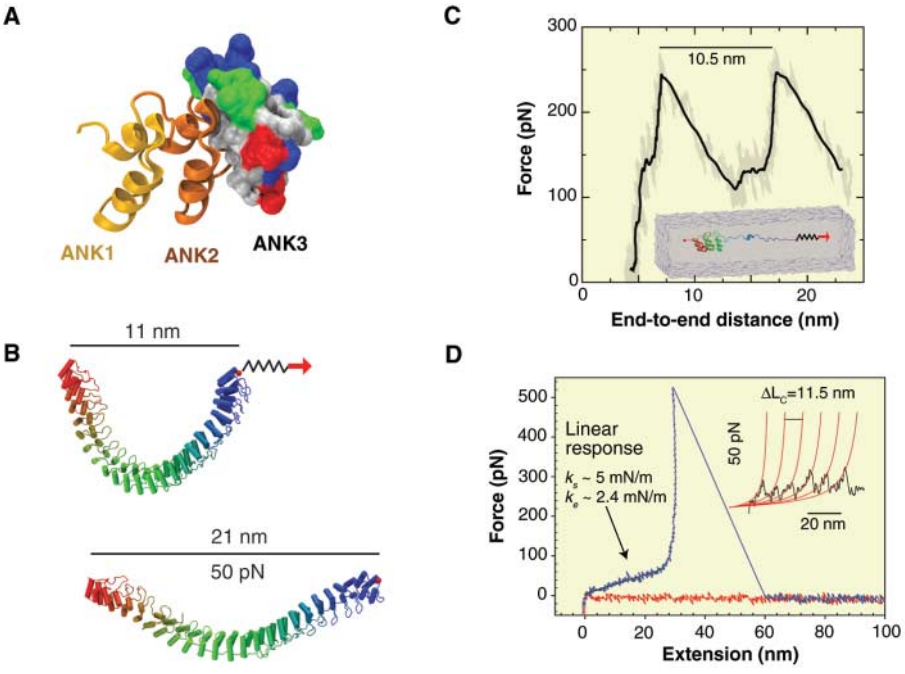

Fig. 3. Elasticity of repeat proteins. (**A**) Architecture of three ankyrin repeats (two shown in yellow and orange cartoon, and one shown in surface representation with colors indicating residue type). (**B**) Equilibrated conformation of human ankyrin-R (24 repeats) and a stretched state obtained after 6 ns of SMD simulation using a constant force of 50 pN (k_s ~ 5 mN/m). Molecules are shown in cartoon representation and colored from red (repeat 1) to blue (repeat 24). (**C**) The simulated force-extension profile of ankyrin unfolding exhibits two force peaks separated by 10.5 nm, corresponding to unraveling and unfolding of individual repeats (secondary structure elasticity). (Inset) The hydrated system simulated. (**D**) The experimental force-extension profile obtained upon stretching of 24 ankyrin repeats of human ankyrin-B is shown in blue [adapted from (*57*)]. The linear response ($\langle k_e \rangle$ ~ 2 mN/m) observed in AFM experiments corresponds well to predicted tertiary structure elasticity (k_s ~ 5 mN/m) observed in SMD simulations of 24 ankyrin repeats (*14*). (Inset) The force-extension profile of six ankyrin repeats obtained through AFM experiments [adapted from (*58*)] features six peaks separated by 11.5 ± 0.7 nm, in close agreement with predicted secondary structure elasticity. The magnitude of the forces are about one order of magnitude smaller than those observed in SMD simulations, as expected from the dependence of force peak values on the stretching velocity (*50*).

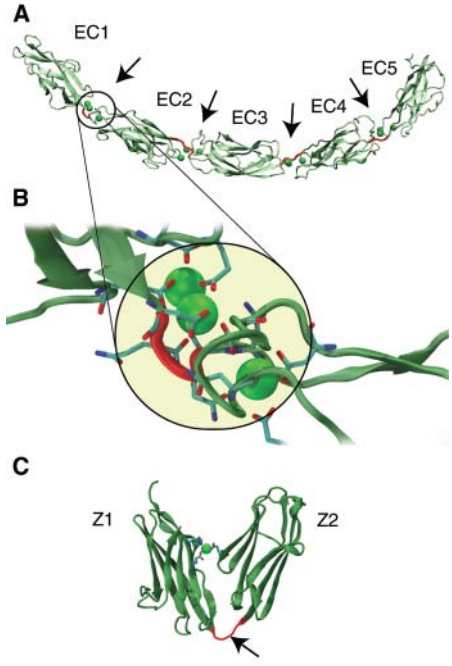

Fig. 4. Linker-mediated elasticity of modular proteins. (**A**) Crystal structure of the complete C-cadherin extracellular domain, featuring five modules labeled EC1 to EC5 (*61*). The protein is shown in cartoon representation. Arrows point at linker regions depicted in red. Calcium ions binding at the linker regions are shown as green spheres. (**B**) Detail of C-cadherin EC1-EC2 linker. Interactions of calcium ions with charged amino acids at the linker region determine the elastic behavior of the protein and its adhesive properties. (**C**) Crystal structure of titin Z1Z2 modules (*65*) shown in cartoon representation. The structure depicts a closed-hinge conformation induced by binding of a metal ion and flexibility of the linker region (arrow) depicted in red.

determine the mechanical properties of proteins that are subject to force in vivo. Although in vitro experiments in which force is applied to biomolecules opened a completely new field of research, in silico experiments, despite their limitations (*50*, *59*), have resolved the molecular mechanisms underlying the elastic response of biomolecules. Identification of the force-bearing regions of titin, the role of hydrogen bonds and water during mechanical unfolding of immunoglobulin-like domains, the intermediate states of fibronectin, the role of linkers in spectrin mechanics, and the tertiary structure elasticity of ankyrin repeats were only possible through simulations combined with experiments.

Simulations are now going beyond single domain proteins as crystal structures of larger protein complexes become available and computing power increases. Such simulations seek to characterize the important role of linkers in the elasticity of proteins containing many globular domains. Cadherins (*5*, *60*, *61*), for instance, mediate calcium-dependent cell-cell adhesion. SMD simulations of a single cadherin domain (*14*) had already shown the relevance of linkers and calcium ions on its elastic response. Equilibrium (*62*) and SMD simulations of proteins containing multiple cadherin domains have now revealed the flexibility and tertiary structure elasticity of these modular proteins (Fig. 4A). SMD simulations have shown how tertiary and secondary structure elasticity of the complete cadherin domain is controlled through calcium ions bound to linker regions (Fig. 4B), a property that is not only relevant for cell-cell adhesion but also important in hearing (*56*, *14*) where cadherin-23 forms part of the mechanotransduction apparatus (*63*, *64*).

A recent structure of Z1-Z2 domains of titin (*65*) (Fig. 4C) indicates that linkers may play a role in titin elasticity as well. Depending on the length and structure of the linker, different titin modules may exhibit a varied repertoire of elastic responses. Even more suggestive is the fact that a divalent ion outside of the linker region induces a "closed-hinge" conformation in the crystal structure; similar binding sites were predicted through modeling for titin I91 (*8*).

Ultimately, understanding the molecular mechanisms involved in the force response of proteins should lead to the design of structures with desired elastic properties, and surely modeling will play an important role in such endeavor.

References and Notes

1. Molecular dynamics (MD) simulations have their bases in theoretical models describing interactions between atoms through so-called force fields (*66*–*68*). In a typical MD simulation, initial coordinates of the atoms in a macromolecule are obtained from crystallographic or NMR structures. The structure is then solvated in water, and the motion of atoms in time is determined through integration of Newton's equations (*68*) assuming the mentioned force field. Current simulation packages, such as NAMD (*68*), use standardized force fields and provide the source code of the simulation engine. The widespread use and availability of the software and force fields ensures constant verification and reproducibility of results.
2. SMD simulations apply, in addition to indigenous forces, external forces to biomolecules (*17*). There are two typical protocols for SMD simulations: constant force and constant velocity. In constant force SMD simulations, a force is directly applied to one or more atoms, and extension or displacement is monitored throughout dynamics. Customized time-dependent forces may be applied as well. In constant velocity

SMD simulations, a moving harmonic potential (spring) is used to induce motion along a reaction coordinate. The free end of the spring is moved at constant velocity, while the protein atoms attached to the other end of the spring are subject to the steering force. The force applied is determined by the extension of the spring and can be monitored throughout the entire simulation.
3. A. D. Mehta, M. Rief, J. A. Spudich, D. A. Smith, R. M. Simmons, *Science* **283**, 1689 (1999).
4. J. Zlatanova, K. van Holde, *Mol. Cell* **24**, 317 (2006).
5. D. Leckband, A. Prakasam, *Annu. Rev. Biomed. Eng.* **8**, 259 (2006).
6. M. Gao, M. Sotomayor, E. Villa, E. Lee, K. Schulten, *Phys. Chem. Chem. Phys.* **8**, 3692 (2006).
7. V. Vogel, *Annu. Rev. Biophys. Biomol. Struct.* **35**, 459 (2006).
8. H. Lu, B. Isralewitz, A. Krammer, V. Vogel, K. Schulten, *Biophys. J.* **75**, 662 (1998).
9. H. Lu, K. Schulten, *Biophys. J.* **79**, 51 (2000).
10. M. Gao, H. Lu, K. Schulten, *J. Muscle Res. Cell Motil.* **23**, 513 (2002).
11. M. Gao *et al.*, *Proc. Natl. Acad. Sci. U.S.A.* **100**, 14784 (2003).
12. V. Ortiz, S. O. Nielsen, M. L. Klein, D. E. Discher, *J. Mol. Biol.* **349**, 638 (2005).
13. S. Paramore, G. A. Voth, *Biophys. J.* **91**, 3436 (2006).
14. M. Sotomayor, D. P. Corey, K. Schulten, *Structure* **13**, 669 (2005).
15. Z. Lu, H. Hu, W. Yang, P. E. Marszalek, *Biophys. J.* **91**, L57 (2006).
16. M. Carrion-Vazquez *et al.*, *Nat. Struct. Biol.* **10**, 738 (2003).
17. B. Isralewitz, M. Gao, K. Schulten, *Curr. Opin. Struct. Biol.* **11**, 224 (2001).
18. H. Grubmüller, *Methods Mol. Biol.* **305**, 493 (2005).
19. E.-L. Florin, V. T. Moy, H. E. Gaub, *Science* **264**, 415 (1994).
20. H. Grubmüller, B. Heymann, P. Tavan, *Science* **271**, 997 (1996).
21. S. Izrailev, S. Stepaniants, M. Balsera, Y. Oono, K. Schulten, *Biophys. J.* **72**, 1568 (1997).
22. E. Evans, K. Ritchie, *Biophys. J.* **72**, 1541 (1997).
23. L. Tskhovrebova, J. Trinick, *Nat. Rev. Mol. Cell Biol.* **4**, 679 (2003).
24. S. Improta, A. Politou, A. Pastore, *Structure* **4**, 323 (1996).
25. M. Rief, M. Gautel, F. Oesterhelt, J. M. Fernandez, H. E. Gaub, *Science* **276**, 1109 (1997).
26. M. S. Z. Kellermayer, S. Smith, H. Granzier, C. Bustamante, *Science* **276**, 1112 (1997).
27. L. Tskhovrebova, J. Trinick, J. Sleep, R. Simmons, *Nature* **387**, 308 (1997).
28. P. E. Marszalek *et al.*, *Nature* **402**, 100 (1999).
29. S. B. Fowler *et al.*, *J. Mol. Biol.* **322**, 841 (2002).
30. P. M. Williams *et al.*, *Nature* **422**, 446 (2003).
31. R. B. Best *et al.*, *J. Mol. Biol.* **330**, 867 (2003).
32. H. Lu, K. Schulten, *Proteins Struct. Funct. Genet.* **35**, 453 (1999).
33. D. Craig, M. Gao, K. Schulten, V. Vogel, *Structure* **12**, 21 (2004).
34. F. Gräter, J. Shen, H. Jiang, M. Gautel, H. Grubmüller, *Biophys. J.* **88**, 790 (2005).
35. A. F. Oberhauser, C. Badilla-Fernandez, M. Carrion-Vazquez, J. Fernandez, *J. Mol. Biol.* **319**, 433 (2002).
36. D. Craig, A. Krammer, K. Schulten, V. Vogel, *Proc. Natl. Acad. Sci. U.S.A.* **98**, 5590 (2001).
37. R. W. S. Rounsevell, J. Clarke, *Structure* **12**, 4 (2004).
38. E. Paci, M. Karplus, *J. Mol. Biol.* **288**, 441 (1999).
39. M. Gao, D. Craig, V. Vogel, K. Schulten, *J. Mol. Biol.* **323**, 939 (2002).
40. L. Li, H. H. Huang, C. L. Badilla, J. M. Fernandez, *J. Mol. Biol.* **345**, 817 (2005).
41. M. Yi, E. Ruoslahti, *Proc. Natl. Acad. Sci. U.S.A.* **98**, 620 (2001).
42. V. Bennett, A. J. Baines, *Physiol. Rev.* **81**, 1353 (2001).
43. D. E. Discher, P. Carl, *Cell. Mol. Biol. Lett.* **6**, 593 (2001).
44. C. P. Johnson *et al.*, *Blood* **109**, 3538 (2007).
45. H. Kusunoki, R. I. MacDonald, A. Mondragón, *Structure* **12**, 645 (2004).
46. M. Rief, J. Pascual, M. Saraste, H. Gaub, *J. Mol. Biol.* **286**, 553 (1999).
47. S. M. Altmann *et al.*, *Structure* **10**, 1085 (2002).
48. R. Law *et al.*, *Biophys. J.* **84**, 533 (2003).
49. L. G. Randles, R. W. S. Rounsevell, J. Clarke, *Biophys. J.* **92**, 571 (2007).
50. The magnitude and fluctuations of the monitored forces in constant-velocity SMD simulations will depend on the stretching velocity and spring constant used (*21*, *22*). The smaller the velocity used, the less drastic the perturbation of the system is, and more details along the reaction coordinate are likely to be captured. Because of limitations in computational resources, even the slowest stretching velocities used in simulations are orders of magnitude faster than those used in equivalent AFM stretching experiments. The force peak values observed will then be larger than those recorded in experiments (Fig. 1D). The dependence of the monitored force on the stretching velocity is more relevant for secondary structure elasticity than for tertiary structure elasticity, because in the latter case solvent effects due to friction and hydrogen bond attack play a less important role.
51. P. J. Mohler, A. O. Gramolini, V. Bennett, *J. Cell Sci.* **115**, 1565 (2002).
52. L. K. Mosavi, T. J. Cammett, D. C. Desrosiers, Z. Peng, *Protein Sci.* **13**, 1435 (2004).
53. L. K. Mosavi, D. L. Minor, Z. Peng, *Proc. Natl. Acad. Sci. U.S.A.* **99**, 16029 (2002).
54. P. Michaely, D. R. Tomchick, M. Machius, R. G. W. Anderson, *EMBO J.* **21**, 6387 (2002).
55. J. Howard, S. Bechstedt, *Curr. Biol.* **14**, R224 (2004).
56. D. P. Corey, M. Sotomayor, *Nature* **428**, 901 (2004).
57. G. Lee *et al.*, *Nature* **440**, 246 (2006).
58. L. Li, S. Wetzel, A. Pluckthun, J. M. Fernandez, *Biophys. J.* **90**, L30 (2006).
59. It is often noticed that SMD simulations yield "wrong" unfolding force values when compared with AFM measurements. Such a statement is obviously illogical, because SMD simulations must yield stronger forces because of the faster pulling velocity. Faster pulling may alter the nature of the protein's elastic response, but AFM extensions can be directly compared with SMD extensions, offering a test of the concern.
60. M. Takeichi, *Annu. Rev. Biochem.* **59**, 237 (1990).
61. T. J. Boggon *et al.*, *Science* **296**, 1308 (2002); published online 18 April 2002 (10.1126/science.1071559).
62. F. Cailliez, R. Lavery, *Biophys. J.* **89**, 3895 (2005).
63. C. Söllner *et al.*, *Nature* **428**, 955 (2004).
64. J. Siemens *et al.*, *Nature* **428**, 950 (2004).
65. M. Marino *et al.*, *Structure* **14**, 1437 (2006).
66. A. MacKerell Jr. *et al.*, *J. Phys. Chem. B* **102**, 3586 (1998).
67. S. A. Adcock, J. A. McCammon, *Chem. Rev.* **106**, 1589 (2006).
68. J. C. Phillips *et al.*, *J. Comput. Chem.* **26**, 1781 (2005).
69. W. Humphrey, A. Dalke, K. Schulten, *J. Mol. Graph.* **14**, 33 (1996).
70. H. Lu, K. Schulten, *Chem. Phys.* **247**, 141 (1999).
71. M. Rief, H. Grubmüller, *ChemPhysChem* **3**, 255 (2002).
72. The work reviewed here involved many researchers from our own and other groups. We apologize to all researchers whose pioneering work could not be reviewed because of space limitation. We thank M. Gao, B. Isralewitz, S. Izrailev, H. Lu, J. C. Gumbart, and members of the Theoretical and Computational Biophysics Group for their contributions and helpful discussions; our long-time collaborator, V. Vogel, for guidance and inspirations; collaborators D. P. Corey, D. Craig, A. Krammer, O. Mayans, and M. Wilmanns; and J. Fernandez and P. Marszalek for a wonderful experimental-theoretical collaboration. The molecular images in this paper were created with the molecular graphics program VMD (*69*) and Tachyon. This work was supported by funds of the NIH (grant no. P41 RR05969 and grant no. 1 R01 GM073655) and the Humboldt Foundation (K.S.). The authors also acknowledge computer time provided by the NSF through the Large Resource Allocations Committee grant MCA93S028.

10.1126/science.1137591

REVIEW

Forces and Bond Dynamics in Cell Adhesion

Evan A. Evans[1,2]* and David A. Calderwood[3]

Adhesion of a biological cell to another cell or the extracellular matrix involves complex couplings between cell biochemistry, structural mechanics, and surface bonding. The interactions are dynamic and act through association and dissociation of bonds between very large molecules at rates that change considerably under stress. Combining molecular cell biology with single-molecule force spectroscopy provides a powerful tool for exploring the complexity of cell adhesion, that is, how cell signaling processes strengthen adhesion bonds and how forces applied to cell-surface bonds act on intracellular sites to catalyze chemical processes or switch molecular interactions on and off. Probing adhesion receptors on strategically engineered cells with force during functional stimulation can reveal key nodes of communication between the mechanical and chemical circuitry of a cell.

The physical role of a cell adhesion bond is to hold a cell to other cells or to tissue substrata while supporting the forces involved in cell function. Complicating this task, a single adhesion bond effectively resists force only for time periods less than that needed for its spontaneous dissociation under thermal activation. Thus, the diversity in the mechanochemistry of adhesion bonds reflects how mechanical force applied to a bond between a pair of interacting molecules alters activation energy barriers along kinetic pathways, or switches pathways, that lead to dissociation. Viewed ideally as illustrated by Fig. 1, applying adhesion stress through the local material structure to a bond is conceptually like pulling on the chemical interaction with a mechanical spring that mimics the compliance properties of structures attached to the binding site. Stretching this equivalent spring produces a force that lowers the chemical activation barrier to increase the frequency of bond dissociation while, at the same time, the spring potential defines an "energy well" that captures the dissociated states and regulates the likelihood of rebinding. Focusing our discussion on adhesive interactions in soft tissues and organs of

eukaryotic cell systems, the important insights derived from the simple view in Fig. 1 are that bond survival effectively decreases exponentially with the level of pulling force and that deformations of soft structures even under small forces suppress rebinding after dissociation.

With a precipitous reduction in lifetime under stress and little likelihood of rebinding, bonds in cell adhesion are therefore being continually created, loaded over some period of time, then failing. Even for cells in tissues seemingly under static stress, forces build up transiently on the individual bonds that connect cells, albeit very slowly (maybe at miniscule rates of only ~1 pN/s) until the bonds break and shift their loads to other bonds. The balance of stress is achieved through recruitment of new bonds driven by cytoskeletal movements, resulting in a "bubbly" dynamic process of bond loading, failure, and formation. By comparison, at the other extreme, the initial attachment of an immune system cell in the vasculature can apply force to bonds at an incredibly fast rate (for instance, ~10^4 pN/s), which is then followed by quick release of the cell or rapid activation of new adhesive components to arrest the cell and enable its emigration into the surrounding tissue. Thus, if we ignore many complex features of the force responses of adhesive and structural bonds, the important mechanical property that characterizes these bonds is not static strength but, rather, dynamic strength. As illustrated in Fig. 2, mechanical strength emerges when the stress rate is sufficient to make the bond fail in less time than needed for its spontaneous dissociation and then rises sluggishly by an increment of force for each order of magnitude increase in the stress rate (that is, proportional to a logarithm of stress rate). Adhesion bonds that form "transient high-strength" connections are those that require fast loading to withstand force, whereas bonds that establish "persistent" connections are those that hold firm under conditions of slow loading as well as fast. Unexpectedly, these differences in stress-rate sensitivity cross structural family lines.

Because of the rough topography of a cell membrane, cell adhesion ligands and their receptors in multicellular eukaryotic systems are generally large (30 to 50 nm) multidomain structures that project out from the lipid bilayer surface to overcome steric interference and enable connections between cells [smaller (~7 to 8 nm) signaling molecules often mediate adhesion as well]. Representing a very large number of specific interactions, cell adhesion receptors and ligands are designed for one or more dynamic functions and often work cooperatively to achieve functional outputs (*1*). For many of these interactions, the receptors can be grouped into major families such as the selectins (members of the C-type lectin domain family), the cadherins [considered an offshoot of the immunoglobulin (Ig) superfamily], and the integrins. Although not all-inclusive, these three families serve to illustrate the broad range in mechanical performance among adhesion bonds.

Selectins, which appear on cell surfaces as homodimers of long chains, provide prominent examples of receptors producing transient high-strength connections (Fig. 3A). Ca^{2+}-dependent binding of their outermost C-type lectin domain to cell-surface sialomucin proteins initiates capture of fast-moving white blood cells at vessel walls (*2*). To perform this important function, selectin adhesion bonds require fast loading to resist pulling, and they become very strong when subjected to the extreme force rates (~10^4 pN/s) often experienced when a circulating cell first adheres to endothelium (*3*). Moreover, selectins exhibit a special "catch bond" quality (*4*) characterized by quick release under slow-loading and low-force conditions (Fig. 3A). By comparison, cadherins appear on cell surfaces as multidomain single chains and interact homophilically when Ca^{2+} is present (*5*). Hence, cadherins bind other cadherins on opposing cells to produce trans-bonded connections and may also bind their adjacent neighbors to produce cis-bonded lateral connections. Appearing to be capable of binding through a progression of overlapping antiparallel arrangements (*6*), the force responses of trans-bonded cadherins suggest a hierarchy of mechanical functionality. On the one hand, cadherins form short-lived con-

[1]Department of Biomedical Engineering, Boston University, Boston, MA 02215, USA. [2]Department of Pathology and Laboratory Medicine, Department of Physics and Astronomy, University of British Columbia, Vancouver, BC, Canada V6T 2A6. [3]Department of Pharmacology and Interdepartmental Program in Vascular Biology and Transplantation, Yale University School of Medicine, New Haven, CT 06520, USA.

*To whom correspondence should be addressed. E-mail: evans@physics.ubc.ca

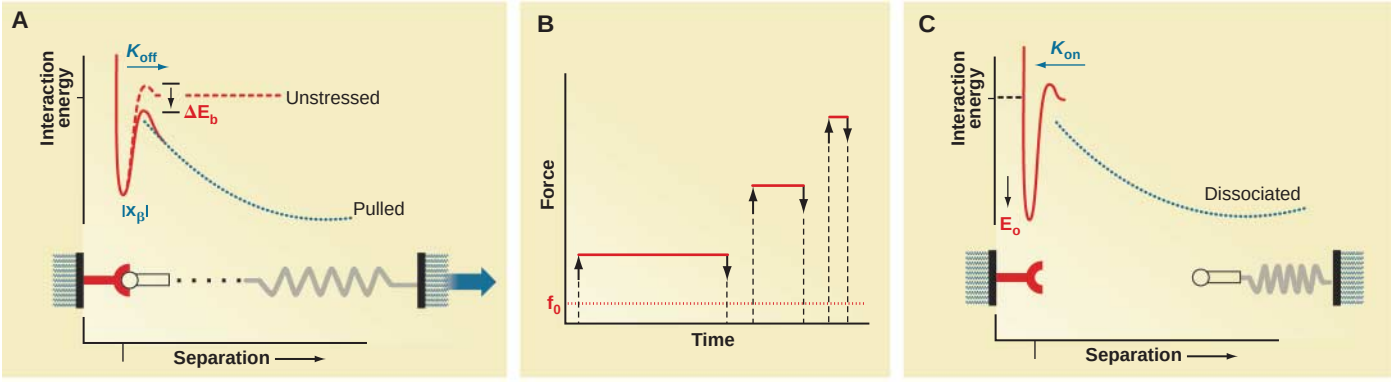

Fig. 1. Conceptual view of force propagation to a bond and its impact on the chemical energy landscape governing bond kinetics. (**A**) Pulling on structural connections to a molecular bond creates a mechanical "springlike" potential (dashed blue curve) that alters the chemical energy of interaction or "landscape" (solid and dashed red curves) along the reaction coordinate defined by the pulling direction (*37*). The slope of the spring potential at the origin of interaction is the pulling force f, the product of the effective spring constant κ_s of the structural linkages with the increase in their separation $x_{separation}$ under pulling. Of greatest impact on bond survival, the spring potential reduces the height of the activation energy barrier governing the off-rate kinetics located at x_β by ~$-fx_\beta$. Brought to our attention years ago by Bell (*38*), the change in Arrhenius factor predicts a large exponential-like reduction in bond survival time, $t_{off}(f) \approx t_{off}^\circ \exp(-f/f_\beta)$, relative to its apparent unstressed lifetime t_{off}° (*39*). The response scale for this accelerated dissociation is the level of force, $f_\beta = k_BT/x_\beta$, that drops the barrier by one unit of thermal energy k_BT (*40*). The reduction in bond lifetime with increase in force is illustrated in (**B**) by the behavior expected in a force-clamp test at different forces. When the anchored molecules unbind, the dissociated states are confined near the displaced minimum of the spring potential, as indicated in (**C**), from which strong thermal excitations can cause them to rebind. However, there is little likelihood of rebinding when the depth of the spring potential in (C) exceeds the binding energy E_o for forces $\geq (2\kappa_s E_o)^{1/2}$. Consequently, molecules anchored by soft structures (small κ_s) rebind very infrequently even under low stress, which suggests why bond recruitment in cell adhesion usually involves bringing the constituents together by large-scale cytoskeletal movements as when forming the immunological synapse in T lymphocyte adhesion (*41*).

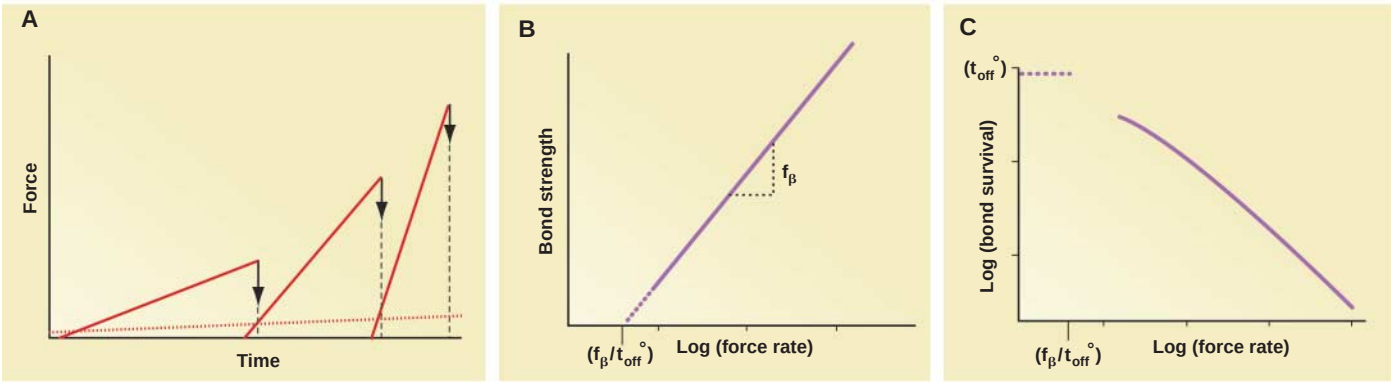

Fig. 2. Dynamic strength of a bond: the "nanorheology" of a molecular interaction. The important dynamical corollary to the Bell exponential model (Fig. 1) for the off rate of bonds under stress is that the strength and lifetime of a bond become interrelated properties governed by the stress rate (*42*), $r_f = \Delta f/\Delta t$, and thereby the speed v_{pull} at which the molecular linking structures are separated, that is, $r_f = \kappa_s v_{pull}$. When loaded by an increasing force, the failure rate of an idealized bond grows exponentially with time, predicting that the bond will break "most often" at a force f^*, increasing by 1 unit of the thermal-activation force f_β for each e-fold exp (1) ~2.72 times increase in the loading rate. The increase in strength and decrease in survival expected for bonds at different force rates (called force ramps) are sketched in (**A**). Derived from tests at several force rates, the most frequent rupture forces for the idealized bond follow a straight line when plotted against logarithms of the force rates as sketched in (**B**), that is, $f^* = f_\beta \log_e(r_f t_{off}^\circ/f_\beta)$. Key to the dynamics, the kinetic scale for force rate, $r_f^\circ = f_\beta/t_{off}^\circ$, defines the loading speed above which the bond is driven "far from equilibrium," dissociating faster than its apparent spontaneous off rate $1/t_{off}^\circ$, and thus resists force. The most frequent "lifetime" t^* of the bond is precisely its strength divided by the loading rate, $t^* = f^*/r_f$. So, while bond strength grows sluggishly with increased loading speed, bond survival falls extremely rapidly, as illustrated in (**C**).

nections and behave as transient connectors when binding just their outer-tip domains, which may be important for the dynamics of recognition and patterning of cells in development. On the other hand, deep-trans bonding of all domains produces strong attachments even under very slow loading, as demonstrated by the force responses of attachments between full-length cadherins (Fig. 3B). With little sensitivity to stress rate, such "persistent" connections may enable formation of durable structures like desmosomes in lateral junctions of epithelial cells, although opposing models based on dense networks of tip interactions have also been proposed (*7*). Last, integrins mediate perhaps the most diverse range of adhesive interactions in eukaryote biology, exhibiting widely different levels of attachment strength and lifetime. Representing one extreme of their dynamical response, many integrin interactions are long-lived and provide the persistent strength needed, for example, to hold together tissues, to transmit force during muscle contraction, and to arrest circulating immune cells on activated endothelium and enable their migration (*8*). A prominent example of persistent strength and the insensitivity to stress rate is demonstrated by the force responses of attachments to the integrin $\alpha_L\beta_2$ (Fig. 3B). Yet, representative of the opposite extreme, other integrin interactions are short-lived and behave as transient connectors that require fast loading for strength, as when integrins at the leading edge of a spreading cell form new attachments to an extracellular matrix (*9*) or when integrins initiate capture of lymphocytes in the systemic circulation (*10*), mimicking the response of a selectin as demonstrated by force responses of attachments to the integrin $\alpha_4\beta_1$ (Fig. 3A). Because of the diversity in integrin mechanical response and the important role of their cytoskeletal connections in adhesion, we will center the remainder of our discussion around integrin bonds.

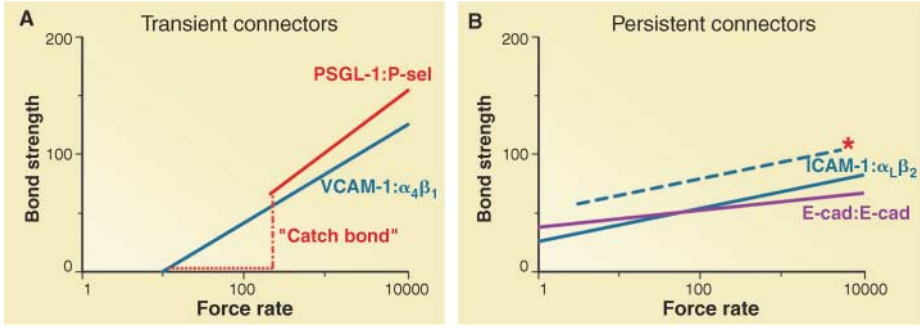

Fig. 3. Transient and persistent cell adhesion bonds. The distinction between these two types of adhesion bonds reflects major differences in their stress rate requirements $r_f^\circ = f_\beta/t_{off}^\circ$ for onset of strength and their scales f_β for amplification of strength under increasing stress rate (Fig. 2). Consistent with the labels, the examples of transient connectors in (**A**) require fast loading for strength, whereas the examples of persistent connectors in (**B**) are strong even under slow loading. Also intriguing is that the transient connectors show much larger amplification of strength at high-loading speeds than persistent connectors, which suggests a fundamental feature of the way in which weak biomolecular bonds are chemically designed to achieve strength (*43*). Taken from in vitro tests of single recombinant receptor and ligand interactions when immobilized on a force probe and microsphere target (*44*), the responses for transient connectors in (A) are demonstrated by the dynamic strengths of P-selectin (PS) bonds to a reactive N-terminal segment of mucin PS glycoprotein ligand–1 (PSGL-1) (*45*) and by the dynamic strengths of integrin $\alpha_4\beta_1$ bonds to a two-domain construct of VCAM-1 (*46*). Although similar to the β_1-integrin interaction at high force rates, the strength of the PS interaction is switched on at a fast loading rate. Called a "catch bond" (*4*), this unusual response represents a mechanochemical switch triggered by force rate to turn off a fast dissociation pathway and lock in a slow dissociation pathway that resists force (*45*). Also taken from in vitro tests, the responses for "persistent connectors" in (B) are demonstrated by the dynamic strengths of homophilic full-length cadherin bonds (*47*, *48*) and by the dynamic strengths of integrin $\alpha_L\beta_2$ bonds to ICAM-1 (*46*). Feedback from chemical pathways inside cells is known to reinforce cell adhesion mediated by integrin bonds. We found a significant parallel upward shift [*, blue-dashed line in (B)] in dynamic strengths of β_2-integrin bonds when testing ICAM-1 bonds to the β_2 integrin (LFA-1) in situ at the surface of cytokine-stimulated white blood cells; this suggests a range of affinity states for the β_2 integrin and demonstrates the "inside-out" feedback at the single-molecule level. The units for force and force rate are pN and pN/s, respectively.

Integrin Bonds: The Archetype of Multifunctional Adhesive Design

Integrins are composed of noncovalently-associated α and β subunits. Each subunit is a type I trans-

membrane glycoprotein with a relatively large multidomain extracellular projection and a single membrane-spanning helix, usually ending with a short (20 to 70 amino acid), largely unstructured cytoplasmic tail (*8*). Humans produce 18 α and 8 β subunits that combine to form at least 24 different heterodimers, each of which binds to a specific overlapping repertoire of extracellular matrix ligands such as fibronectin, collagen, laminin, or fibrinogen and to cell surface counterreceptors like the Ig-superfamily proteins intercellular adhesion molecule–1 (ICAM-1) or vascular cell adhesion molecule–1 (VCAM-1) (*8*). Many of the advances in our understanding of the mechanisms by which integrins bind ligand have come from x-ray crystallography of the extracellular domains of $\alpha_V\beta_3$ and $\alpha_{IIb}\beta_3$, as well as structures of complexes between ligands and isolated α subunit ligand-binding A domains [reviewed in (*11*, *12*)]. These studies have revealed the architecture of integrin extracellular domains, explained the well-established requirement for divalent cations in integrin-ligand binding, and demonstrated that both the α and β subunits participate in binding ligands containing an Arg-Gly-Asp peptide or a related tripeptide motif. Very important in their function, conformational changes in the integrin extracellular domains play a major role in regulating the affinity of integrins for their extracellular ligands through a process termed integrin activation (*8*, *11*, *12*).

Although ligand binding is mediated by the large extracellular domains, the integrin cytoplasmic tails play a key role in cellular control of their adhesive interactions and the subsequent dynamic cellular responses such as cell spreading or migration. Interactions of the short cytoplasmic tails, and of the β tails in particular, with intracellular cytoskeletal and signaling proteins figure prominently in the regulation of integrin activation (*13*). Furthermore, after the binding of an extracellular ligand, complex multiprotein assemblies of cytoskeletal, scaffolding, and signaling proteins are recruited to the integrin cytoplasmic face, where they both link integrins to the actin cytoskeleton and convey signals into the cell (*14*, *15*). Hence, by binding both extracellular and intracellular ligands, integrins provide a transmembrane conduit for the bidirectional transmission of mechanical force and biochemical signals across the plasma membrane to regulate cell adhesion, migration, proliferation, and death.

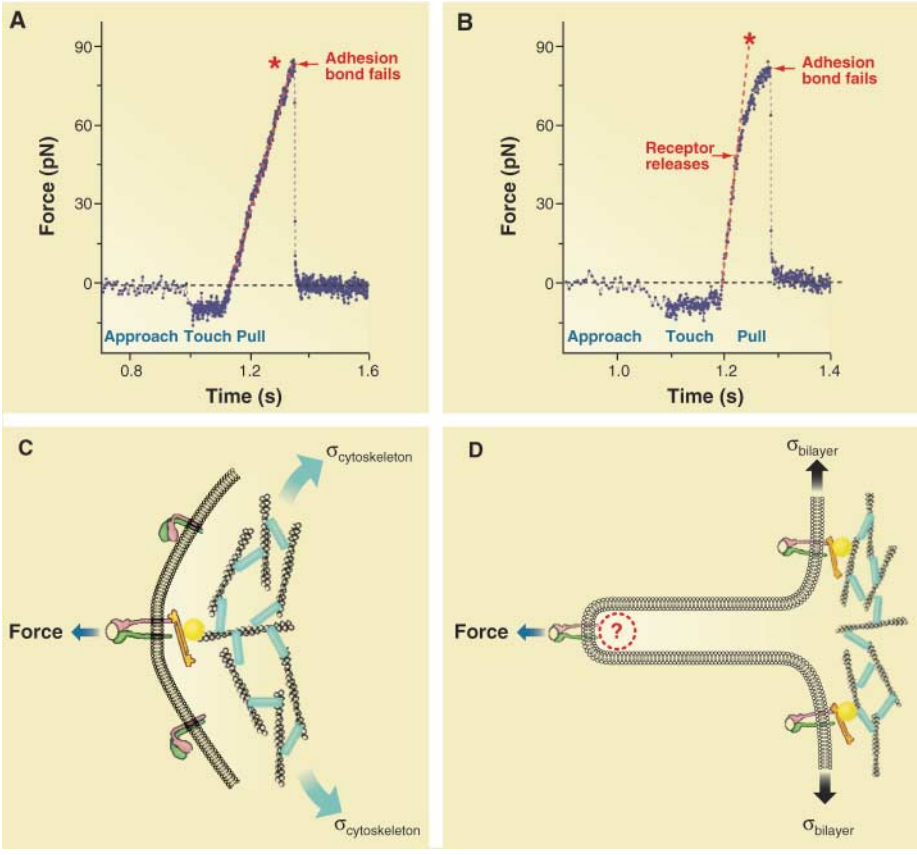

Fig. 4. Receptor unbinding from the cytoskeleton: cohesive failure. When pulling a cell-surface bond with a probe, force usually builds up steadily until either the adhesion bond fails and the probe recoils [as in (**A**) when probing the β_2-integrin LFA-1 on a blood granulocyte (*46*)] or the rise in force slows abruptly for a period of time before failure of the adhesion bond [as in (**B**) when probing the β_1-integrin VLA-4 on a B-lymphocyte (*46*)]. As sketched schematically in (**C**), pulling on the receptor initially deforms the cell surface into a nanoscale "pucker" that increases its extension in proportion to the force, where the elastic-like response reflects the level of tension-like stress in the cortical cytoskeleton (*49*). However, as seen in (B), the elastic-like response can end prematurely with the onset of a fluid-like tether flow enabled by release of the receptor from the cytoskeleton. As sketched in (**D**), continued probe extrusion of this membrane nanotube (tether) quickly distances the receptor from the cell cytostructure (*50*, *51*) and eventually ends when the adhesion bond breaks. The question mark in (D) indicates that the components that stay attached to the receptor tail domain remain to be established.

Integrin Anchoring in Cell Adhesion

The mechanical properties of adhesive attachments to cells are most often attributed to the ligand/receptor interaction. However, formation, strength, and survival of a cell adhesive attachment also depend on how molecular connections below the membrane surface—those anchoring the receptor to the cell cytostructure—respond to force. Integrins generally function in specialized complexes involving assemblies of many adhesion molecules and cytoskeletal and signaling adaptors (*15*). These integrin clusters come in various forms, for example, focal adhesions, focal complexes, fibrillar adhesions, or podosomes, which are defined according to their size, shape, subcellular localization, molecular constituents, and organization (*15*). While some clusters are widespread, others, for example, the immunological synapse or costamers, show strict cell-type specificity. The differences in size and composition of adhesion sites presumably reflect the link to the cytoskeleton and integrin signaling. Nonetheless, despite their various specialized roles in mediating transient or stable adhesion, reorganizing the extracellular matrix, and activating specific signaling pathways, these adhesions share a number of common features. They are sites at which integrins connect intracellular actomyosin-generated cytoskeletal contractility to extracellular ligands and where external forces can be transmitted to the cytoskeleton, for example, sites where they can initiate biochemical signals. Like the exterior ligand/receptor interaction, intracellular molecular bonds are also time-dependent connections whose formation and persistence change considerably with application of force. As illustrated in Fig. 4, the abrupt reduction in interfacial stiffness and the onset of fluid-like tether flow often observed when pulling on an integrin bond suggest that the pulling force can disrupt the molecular-scale complex anchoring the integrin tails to the cytoskeleton.

The many molecules present in adhesion sites imply many, potentially parallel, mechanisms for linking an integrin to the cytoskeleton (*14*, *15*). Nonetheless, several proteins have been identified as prime candidates for direct integrin-actin linkages, including talin, filamin, α-actinin, and tensin [which, along with integrin-associated adaptor and signaling molecules such as vinculin, paxillin, focal adhesion kinase, and Src-family kinases, activate and/or respond to kinase,

phosphatase, and small guanosine triphosphatase signaling cascades (*16*, *17*)]. Each of these large actin-binding proteins also contains a binding site for integrin β subunit cytoplasmic tails (*15*, *16*, *18*, *19*). Of these, talin, an antiparallel homodimer composed of 250-kD subunits, has received the most attention. Acting as a "hub" in the linkage between integrin β tails and the cytoskeleton, talin interacts with a constellation of focal adhesion proteins—including the integrin β-chain tail, vinculin, focal adhesion kinase, phosphatidylinositol phosphate kinase type 1 γ, and F-actin (*20*)—and plays important roles in activation of integrin receptors (*21*), in formation of the initial linkage between ligand-occupied receptors and the cytoskeleton (*9*), and in the subsequent reinforcement of the linkage (*22*). As discussed below, the use of cell lines deficient in these linker proteins (*9*, *19*) or expressing mutations that selectively disrupt an integrin-linker, a linker-linker, or a linker-cytoskeletal interaction (*9*, *19*, *21*, *23*) holds considerable promise for elucidating the roles of specific molecular interactions during cellular response to force.

The Future: Mapping the Communication Between Mechanical and Chemical Circuitry of a Cell

All cells sense and respond to applied forces in a cell-type–specific manner to regulate a broad range of processes from cell migration to stem cell differentiation, tissue formation, and tumorigenesis (*24*, *25*). Although a variety of systems are employed to sense force and convert it into biochemical signals, adhesion molecules (and integrins in particular) are known to play an important role in this mechanosensory process and in how cells respond to the applied stress (*26*, *27*). Although other adhesion receptors, such as the selectins and cadherins, are also regulated through cytoskeletal interactions, a defining feature of integrins is that integrin/ligand and integrin/cytoplasmic connections transmit and receive feedback (through conformational changes) to enhance or reduce their strengths of attachment (*12*, *28*, *29*). Along with the prominent clustering of receptors [increasing what is referred to as "avidity" (*30*)], feedback from inside the cell also acts directly on the integrin adhesion bond, greatly amplifying its mechanical strength as demonstrated by the force responses of attachments to the β_2-integrin LFA-1 on the surface of a cytokine-stimulated white blood cell (Fig. 3B). Because many of the enzymes and signaling molecules involved in this feedback are closely associated with the receptor-cytoskeletal linkage, the effect of pulling on, or even detaching, a receptor from the cytoskeleton as described in Fig. 4 is likely to alter interactions among these proteins, which suggests a physical mechanism for communication between the mechanical (stress-bearing) circuitry and chemical circuitry of a cell. Pulling forces can catalyze cellular processes in many ways (*26*, *29*), including (i) conformational transitions (from limited to full denaturation and unfolding) that expose otherwise cryptic sites to promote new protein-protein interactions or that expose sites with specific posttranslational modification, (ii) reorganization or segregation of specific molecules in an adhesive complex, and (iii) even liberation of a constituent so that it can interact with more distant complexes.

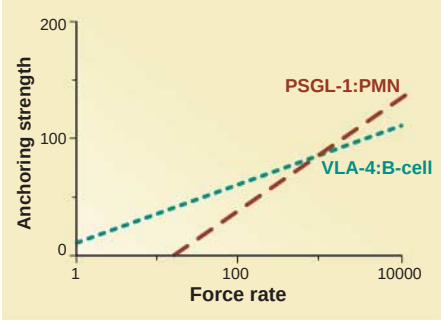

Fig. 5. Receptor-cytoskeletal anchoring strengths. Although only a few cases have been examined in detail (*46*, *52*), the forces for receptor release from the cell cytoskeleton at the onset of tether flow have been found to increase with pulling speed and produce histograms that agree with the idealized bond kinetics described in Figs. 1 and 2. Plotted versus the logarithm of the force rate measured during the elastic-like response before the onset of tether flow, examples are shown of the most frequent forces observed at release of PSGL-1 from the cytostructure of a blood granulocyte [when attached to a PS probe (*52*)] and observed at release of the VLA-4 from the cytostructure of a lymphocyte [when attached to a VCAM-1 probe (*46*)], which provide direct assays of the kinetic stability and rate of failure for the molecular complexes anchoring these receptors beneath the cell surfaces.

Because of the numerous molecules present in adhesion complexes, the experimental challenge is to sort through the many (possibly parallel) intracellular signaling pathways that likely emanate from integrin linkages to the cytoskeleton. Current investigations with engineered knockout or overexpressing cells are making substantial progress in identifying the proteins important for integrin-mediated responses to force (*22*, *31*), which are enhanced by innovative in vitro assays suggesting ways that the integrin-associated proteins can act as force sensors (*32*). Moreover, potentially aiding in this quest, probing individual cell adhesion complexes with ultrasensitive force techniques (Fig. 4) provides an unexpected opportunity to assay the kinetics of molecular connections (Fig. 5) hidden beneath the cell membrane (maybe even deep in the cell, if linked to a long structural filament). Taking advantage of structural and functional assays that identify key mutations selectively targeting integrin-cytoskeletal linkages and signaling pathways, the exciting prospect is to use cell-surface force spectroscopy and engineered cell lines as a material science tool to explore and characterize key nodes in the "mechanical circuitry" that connect receptor tails to the cytostructure and to examine how forces applied to these nodes communicate physical cues from outside the cell to catalyze or trigger specific steps in cell signaling and regulation inside the cell. Even bolder, the next step should be to integrate precision techniques like single-molecule force spectroscopy with high-resolution optical techniques like single-molecule fluorescence (*33*) or novel methods that image the real-time dynamics of coupling between integrins, actin, and other components of adhesion and signaling at the cellular level (*34*, *35*). Together, such integrated approaches can provide access to the molecular machinery by which adhesion molecules transmit force and biochemical signals into and out of the cell during cell migration, tissue remodeling, and differentiation.

References and Notes

1. X. Chen, B. M. Gumbiner, *Curr. Opin. Cell Biol.* **18**, 572 (2006).
2. R. P. McEver, *Curr. Opin. Cell Biol.* **14**, 581 (2002).
3. M. R. King, V. Heinrich, E. Evans, D. A. Hammer, *Biophys. J.* **88**, 1676 (2005).
4. B. T. Marshall *et al.*, *Nature* **423**, 190 (2003).
5. B. M. Gumbiner, *Nat. Rev. Mol. Cell Biol.* **6**, 622 (2005).
6. D. Leckband, A. Prakasam, *Annu. Rev. Biomed. Eng.* **8**, 259 (2006).
7. W. He, P. Cowin, D. L. Stokes, *Science* **302**, 109 (2003).
8. R. O. Hynes, *Cell* **110**, 673 (2002).
9. G. Jiang, G. Giannone, D. R. Critchley, E. Fukumoto, M. P. Sheetz, *Nature* **424**, 334 (2003).
10. M. Sixt, M. Bauer, T. Lämmermann, R. Fässler, *Curr. Opin. Cell Biol.* **18**, 482 (2006).
11. M. A. Arnaout, B. Mahalingam, X. P. Xiong, *Annu. Rev. Cell Dev. Biol.* **21**, 381 (2005).
12. B. H. Luo, T. A. Springer, *Curr. Opin. Cell Biol.* **18**, 579 (2006).
13. D. A. Calderwood, *J. Cell Sci.* **117**, 657 (2004).
14. S. Liu, D. A. Calderwood, M. H. Ginsberg, *J. Cell Sci.* **113**, 3563 (2000).
15. B. Geiger, A. Bershadsky, R. Pankov, K. M. Yamada, *Nat. Rev. Mol. Cell Biol.* **2**, 793 (2001).
16. D. A. Calderwood *et al.*, *Proc. Natl. Acad. Sci. U.S.A.* **100**, 2272 (2003).
17. G. Giannone, M. P. Sheetz, *Trends Cell Biol.* **16**, 213 (2006).
18. B. Garcia-Alvarez *et al.*, *Mol. Cell* **11**, 49 (2003).
19. T. Kiema *et al.*, *Mol. Cell* **21**, 337 (2006).
20. D. A. Calderwood, M. H. Ginsberg, *Nat. Cell Biol.* **5**, 694 (2003).
21. S. Tadokoro *et al.*, *Science* **302**, 103 (2003).
22. G. Giannone, G. Jiang, D. H. Sutton, D. R. Critchley, M. P. Sheetz, *J. Cell Biol.* **163**, 409 (2003).
23. W. H. Ziegler, R. C. Liddington, D. R. Critchley, *Trends Cell Biol.* **16**, 453 (2006).
24. A. J. Engler, S. Sen, H. L. Sweeney, D. E. Discher, *Cell* **126**, 677 (2006).
25. M. J. Paszek *et al.*, *Cancer Cell* **8**, 241 (2005).
26. B. Geiger, A. Bershadsky, *Cell* **110**, 139 (2002).
27. A. W. Orr, B. P. Helmke, B. R. Blackman, M. A. Schwartz, *Dev. Cell* **10**, 11 (2006).
28. R. Alon, M. L. Dustin, *Immunity* **26**, 17 (2007).
29. V. Vogel, M. P. Sheetz, *Nat. Rev. Mol. Cell Biol.* **7**, 265 (2006).
30. C. V. Carman, T. A. Springer, *Curr. Opin. Cell Biol.* **15**, 547 (2003).
31. E. Tzima *et al.*, *Nature* **437**, 426 (2005).
32. Y. Sawada *et al.*, *Cell* **127**, 1015 (2006).
33. B. N. G. Giepmans, S. R. Adams, M. H. Ellisman, R. Y. Tsien, *Science* **312**, 217 (2006).
34. C. M. Brown *et al.*, *J. Cell Sci.* **119**, 5204 (2006).
35. K. Hu, K. T. Applegate, G. Danuser, C. M. Waterman-Storer, *Science* **315**, 111 (2007).

36. M. Sotomayor, K. Schulten, *Science* **316**, 1144 (2007).
37. E. Evans, *Annu. Rev. Biophys. Biomol. Struct.* **30**, 105 (2001).
38. G. I. Bell, *Science* **200**, 618 (1978).
39. For adhesive interactions important in soft tissues and organs of eukaryotic cell systems, the average times t_{off}° reported for spontaneous dissociation of ligand/receptor bonds range from a fraction of a second to 100 s or more.
40. Because of thermal activation, the appropriate unit for "bond strength" is the pN. This scale follows from the ratio of thermal energy k_BT (~4.1×10^{-21} J = 4.1 pN/nm at room temperature) to the nanometer length x_β gained in surpassing an activation-energy barrier (Fig. 1). A force of 10 pN is close to one-billionth of a gram weight (that is, 1 pN ≈ 10^{-10} g wt).
41. C. Wülfing, M. M. Davis, *Science* **282**, 2266 (1998).
42. E. Evans, K. Ritchie, *Biophys. J.* **72**, 1541 (1997).
43. Extending the duration of a ligand-receptor bond by a factor of 100 requires a modest collective increase of 4 to 5 k_BT in the height of the activation-energy barrier that impedes dissociation. Yet, the added persistence appears to be accompanied by a concomitant decrease in sensitivity to stress rate (lower slope f_β), suggesting that the energy landscape changes to increase the length gained in the direction of force when the bond breaks. Advanced computational methods like the "steered molecular dynamics" described in the companion review by Sotomayor and Schulten (*36*) provide valuable tools for investigating how variations in chemical structure affect activation energy barriers and pathways governing bond strength.
44. In typical laboratory tests of single adhesion bonds, constructs of the ligand and receptor molecules are chemically immobilized on solid surfaces at very low surface densities, for example, a ligand to the face of an ultrasensitive force probe and its receptor to a solid target held by a feedback-stabilized piezo translator. The target is then repeatedly moved to/from contact to the probe face, during which time the deflection of the probe is tracked at high precision and multiplied by its "spring" constant κ_f (pN/nm) to report the force history $f(t)$. Bond events are identified by the cycles showing periods of probe stretch ending in precipitous recoil, as sketched in Fig. 2A.
45. E. Evans, A. Leung, V. Heinrich, C. Zhu, *Proc. Natl. Acad. Sci. U.S.A.* **101**, 11281 (2004).
46. E. Evans, K. Kinoshita, in *Methods in Cell Biology: Cell Mechanics, Vol. 83*, Y. L. Wang, D. E. Discher, Eds. (Elsevier, New York, 2007), chap. 16.
47. E. Perret, A. Leung, H. Feracci, E. Evans, *Proc. Natl. Acad. Sci. U.S.A.* **101**, 16472 (2004).
48. M. V. Bayas, A. Leung, E. Evans, D. Leckband, *Biophys. J.* **90**, 1385 (2006).
49. Acting as a soft spring linked in series with the probe spring κ_f, the elastic response of the cell cortex κ_{cell} reduces the force rate r_f relative to the probe rate $\kappa_f v_{pull}$. The ratio $c_{rf} = r_f/(\kappa_f v_{pull})$ provides a direct assay of the cell cortical stiffness, that is, $\kappa_{cell} \approx \kappa_f c_{rf}/(1 - c_{rf})$. It is important to note that different cell types possess very different levels of interfacial stiffness and that these levels often change with cell activation or spreading on a stiffer substrate.
50. As lipid material flows onto a tether, bilayer-spanning proteins (especially those that interact with the cytoskeleton) are expected to remain behind in the cell membrane. However, the acylated proteins bound weakly to the bilayer could build up at the base of the tether, causing some to be expelled from the surface when approaching the tether-cell junction.
51. V. Heinrich, A. Leung, E. Evans, *Biophys. J.* **88**, 2299 (2005).
52. E. Evans, V. Heinrich, A. Leung, K. Kinoshita, *Biophys. J.* **88**, 2288 (2005).

53. Supported by grants from the National Institutes of Health.

10.1126/science.1137592

REVIEW

Far-Field Optical Nanoscopy

Stefan W. Hell

In 1873, Ernst Abbe discovered what was to become a well-known paradigm: the inability of a lens-based optical microscope to discern details that are closer together than half of the wavelength of light. However, for its most popular imaging mode, fluorescence microscopy, the diffraction barrier is crumbling. Here, I discuss the physical concepts that have pushed fluorescence microscopy to the nanoscale, once the prerogative of electron and scanning probe microscopes. Initial applications indicate that emergent far-field optical nanoscopy will have a strong impact in the life sciences and in other areas benefiting from nanoscale visualization.

Despite the enormous advancements brought about by electron and scanning probe microscopy, about 80% of all microscopy investigations in the life sciences are still carried out with conventional lenses and visible light. Taking advantage of the optical transparency of cells, light microscopy uniquely provides noninvasive imaging of the interior of cells in three dimensions (3D). Moreover, it allows the detection of specific cellular constituents, such as proteins, nucleic acids, and lipids, through fluorescence tagging. Lens-based fluorescence microscopy would be almost ideal for investigating life at the subcellular level if it could discern details below a quarter of a micrometer. However, since the work of Abbe, such a resolution seemed entirely out of reach, at least until recently.

When focusing a propagating beam of light, the lens ensures that the light wave interferes constructively at a point in space. The result is an intensity pattern $I(x, y, z)$ featuring a main "diffraction" maximum, referred to as the focal spot (Fig. 1A). The full width at half maximum of the spot is given by $\Delta r \approx \lambda/(2n \sin \alpha)$ in the focal plane and by $\Delta z \approx \lambda/(n \sin^2 \alpha)$ along the optical axis (*1*), with λ, α, and n denoting the wavelength, the aperture angle of the lens, and the refractive index, respectively (Fig. 1A). Because all fluorescence markers within this spot are illuminated simultaneously, they also emit at about the same time, which makes their separation virtually impossible. Moreover, the collection of the photons by a lens and their propagation to a detector are governed by a similar function, $I_{em}(x, y, z)$, blurring the coordinate from where each photon was emitted. Thus, for some time, the only pathway to subdiffraction resolution seemed to be given by near-field optical microscopy, which detects nonpropagating light waves from the sample surface with a nanosized mechanical tip (*2*). However, this method is surface-bound and cannot image the interior of cells. Similar arguments apply to the more recent and intriguing concept of imaging with a material of negative refractive index (*3*). Although such a material can project an image at a distance (*4*, *5*), the need to collect nonpropagating waves requires the sample to be placed on top of the material; a lens of negative refractive index is "near-sighted" (*6*). In many applications, especially in the life sciences, collecting the light far away from the sample is mandatory.

In the 1990s, the first concrete and feasible concepts emerged showing that in fluorescence microscopy the diffraction barrier can be broken even with propagating light and regular lenses—that is, in the far-field (*7*, *8*). A hallmark of these concepts was use of the molecular states of the fluorescent marker not just for signal generation, but also for overcoming the limits set by diffraction (*9*). They radically departed from the far-field superresolution strategies prevalent at the time, such as confocal (*10*, *11*) and multiphoton microscopy, because they implied that a resolution far below λ, in fact diffraction-unlimited resolution, is possible without eliminating diffraction per se. Meanwhile, other powerful approaches (*12*–*14*) have emerged, bolstering far-field fluorescence nanoscopy as an emerging field of science. Here, I will review this field with emphasis on the breaking of the diffraction barrier. I will refrain from overly discussing technical implementations, unless I deem them inherent to the concept; particularly, imaging speed, sensitivity, and cost-efficiency are constantly improving as new technology becomes available. Rather, I will show that all fluorescence nanoscopy concepts realized so far have used a bright and a dark state of the fluorescent marker to record sub-λ features sequentially in time. I will classify these concepts according to the states used and show that they differ on whether the sequential recording of the marker occurs molecule by molecule or in molecular ensembles.

Pushing the Diffraction Barrier

Since the mid-20th century, several concepts aimed at pushing the diffraction limits by reducing the focal spot size. Confocal fluorescence microscopy is one of them. Using pointlike illumination and detection, its effective spot is described by $I(x, y, z)I_{em}(x, y, z) \approx I^2(x, y, z)$. The

Department of NanoBiophotonics, Max Planck Institute for Biophysical Chemistry, 37070 Göttingen, and German Cancer Research Center (DKFZ), High Resolution Optical Microscopy Division, 69120 Heidelberg, Germany. E-mail: shell@gwdg.de

squaring reduces the spot by ~$\sqrt{2}$, but in practice this effect is compromised by the finite detector size (*10*). A genuine quadratic dependence is provided by two-photon excitation, but exciting a fluorophore from its ground state S_0 to its fluorescent state S_1 requires photons of half the excitation energy and hence light of about 2λ in wavelength. The concomitant doubling of the spot is not compensated by the ~$\sqrt{2}$ reduction, but even if it were, the barrier would just be shifted, not broken. These considerations are readily extended to *m* photons (*15*). Another approach shrinks the spot by an elaborate phase pattern in the entrance pupil of the lens (*16*), but giant sidelobes leave it impractical. In my view, the failure of all these concepts to provide useful improvements reinforced the notion that, ultimately, the resolution of any far-field light microscope is still bound to $\Delta r \approx \lambda/2n > 200$ nm and to merely $\Delta z \approx \lambda > 450$ nm along the optical axis.

The poorer axial resolution is particularly unfavorable for the 3D imaging of transparent samples, such as cells. The relation $\Delta z > \Delta r$ stems from the fact that a conventional lens may produce only a spherical cap of a wavefront of light (*1*). If the lens could produce a nearly complete spherical wavefront, the focal spot would be almost spherical too, because of symmetry. As a result, the *z* resolution would be similar to its lateral counterpart (*17*, *18*). The same consideration holds for fluorescence detection: The more complete the collected spherical wavefront is, the better the fluorescent marker can be located. Expanding the illumination or the detection wavefront is equivalent to increasing the aperture angle of the system. It is the key element in spot-scanning 4Pi microscopy (*18*) and wide-field I^5M (*19*), both of which provide a three- to sevenfold improved *z* resolution, augmenting the 3D resolution of far-field fluorescence microscopy substantially.

To this end, 4Pi microscopy coherently adds the wavefronts of two large-angle lenses for excitation or detection, or both (Fig. 1B). The resulting main focal spot features $\Delta z \approx \lambda/3n$, which is even slightly narrower than Δr (*20*). However, because the enlarged wavefront is still not close enough to spherical ($\alpha \approx 68° < 90°$), the focal spot exhibits lobes above and below the focal plane. Consequently, practical 4Pi microscopy has relied mostly on two-photon excitation, which reduces the signal from the lobes due to the squaring effect (*20*). The remaining contributions are removed mathematically. Operating with oil, glycerol, and water-immersion lenses, two-photon 4Pi microscopy has delivered 3D images of fixed and live cells with 80- to 150-nm axial resolution (*21*). A compact beam-scanning 4Pi system recently revealed H2AX chromatin cluster formation in the nucleus (*22*), and a multispot version imaged organelles, such as the Golgi apparatus and mitochondria in live cells (*20*).

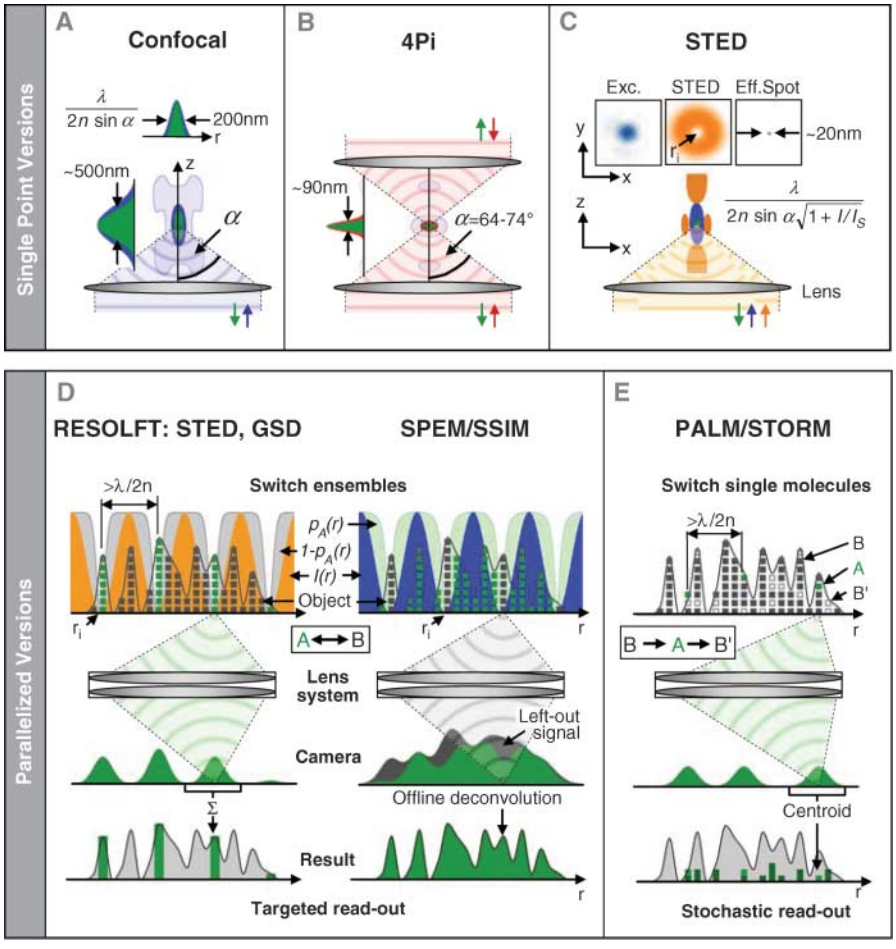

Fig. 1. Fluorescence nanoscopy schemes: single-point scanning (upper row) and parallelized versions (lower row). (**A**) Confocal microscopy. The excitation light wave (blue) formed by the lens to a spherical cap produces a 3D diffraction spot, generating fluorescence in the focal region. A pointlike detector (not shown) registers fluorescence mostly from the main maximum (shown in green), thus providing a slightly improved resolution over regular epifluorescence microscopy. Nevertheless, the confocal microscopy resolution is limited by diffraction to >200 nm in the focal plane (*x*, *y*) and to >450 nm along the optical (*z*) axis. (**B**) By combining the wavefront caps of two opposing lenses, 4Pi microscopy produces a narrower spot along the *z* axis and hence an improved *z* resolution of 80 to 150 nm. (**C**) A typical single-point scanning STED microscope uses a regularly focused excitation beam (blue) that is superimposed by a doughnut-shaped STED beam (orange) that instantly quenches excited molecules at the periphery of the excitation spot, thus confining fluorescence emission to the doughnut zero. Saturated quenching results in a fluorescent spot far below diffraction (green), here 20 nm, whose scanning across the sample yields a subdiffraction-resolution image. The spots represent measured data. (**D**) RESOLFT principle: A focal intensity distribution $I(r)$ featuring zeros that are $>\lambda/2n$ apart confines either the bright state A (left) or the dark state B (right) through a saturable or switching transition, corresponding to a parallelized STED, GSD, or photoswitching approach (on the left) and to the SPEM concept (on the right). In both cases, imaging onto a camera causes the subdiffraction features created by the bright state A (left) or the dark state B (right) at the sample to be blurred on the camera by diffraction. Left: The blur can be dealt with by summing up each diffraction blob individually and allocating the signal to the pertinent coordinate of the zero in the sample space. The image is gained by translating the zeros across the sample and reading out the fluorescence for each coordinate step. (Right) The same holds for SPEM in which the superresolved data are encoded in the narrow regions around the zeros in which the dark state B is deliberately established ("negative data set"). The image is obtained by mathematically converting the negative data set into a positive one. Both strategies rely on a targeted signal readout based on preset positions of the zeros, and both operate with fluorophore ensembles; $p_A(r) \leq 1$ defines the normalized probability of occurrence of A. Small boxes symbolize molecules making up the object (gray-shaded mountains). (**E**) PALM and STORM read out the fluorophore molecules stochastically; the molecules must be switchable. Weak illumination sparsely switches individual fluorophores to the bright state A so that they are further apart than $\lambda/2n$. Detection of $N >> 1$ photons enables the centroid calculation of the diffraction blob of individual fluorophores on the camera, and hence assembling an image with resolution depending on *N*. Concepts (C) to (E) are not diffraction-limited, meaning that they can resolve similar molecules at nanometer distances. The STED, PALM, SPEM, and RESOLFT recording process is sketched in movies S1 to S4.

By providing 6° more angle than their predecessors, the most recent field-corrected oil-immersion lenses ($\alpha = 74°$) have now also enabled bright dual-color 4Pi recordings with standard single-photon excitation (*23*, *24*). Applying two-photon excitation with such a lens pair yields a solitary central spot of $\Delta z \sim \lambda/3n$ and hence an all-physical *z*-resolution improvement (Fig. 4A) (*25*).

In I^5M, the aperture enhancement is implemented just for the detection (*26*) while the whole field of view is illuminated with a set of plane-parallel standing waves. Single-photon excitation provides a bright signal, but the flat standing-wave illumination gives rise to larger lobes requiring a more elaborate computational removal (*20*). The future implementation of 74° lenses and of special illumination schemes should render I^5M an interesting alternative to 4Pi imaging. In any case, the difference made by adding 6° to α underscores that in both concepts, the essential element is the enlargement of the aperture angle of the system (*27*). For the time being, combining the spherical wavefront caps of opposing lenses provides the smallest diffraction spot in the far-field. As a generic development, it may well augment the axial resolution of other light microscopy contrast modes in the future. Nonetheless, it does not break the diffraction barrier but rather pushes diffraction to its limits.

Breaking the Diffraction Barrier

Discerning features that are spectrally disparate is not challenged by diffraction. Likewise, Abbe's barrier does not prevent finding out the coordinate of a molecule with arbitrary precision, e.g., of 1 nm (*28*), if there is no other similar marker molecule within $\lambda/2n$ distance. Breaking Abbe's barrier is about discerning an arbitrary number of densely packed and similarly labeled features within any distance $<\lambda/2n$. This is possible if the features can be recorded sequentially: for example, by successively transferring the markers of each feature to a signal-giving "bright" state A, while keeping the other markers in a state B that is "dark" (*29*, *30*). Reading out the bright ones allows assembly of a subdiffraction image, provided that one knows their coordinate (Fig. 2).

The most direct way to determine the coordinate of the bright molecules is to define their location: r_i. This is possible by applying an optical transition A→B that would send all fluorophores to the dark state B except for those that happen to be at r_i (*29*). Such a transition can be realized by means of a light-intensity distribution $I(r)$ featuring a zero at r_i. Driving A→B, this intensity $I(r)$ must produce a rate $k_{AB}(r) = \sigma I(r)$ that outperforms competing spontaneous rates basically everywhere except at r_i. The competing spontaneous rates are given by the inverse of the lifetimes $\tau_{A,B}$ of the states A and B, respectively, and σ denotes the optical cross-section of the transition. Therefore, applying $I(r) >> (\sigma\tau_{A,B})^{-1} \equiv I_s$ fulfills this condition and confines the possible occurrence of state A to intervals $r_i \pm \Delta r/2$, with $\Delta r << \lambda/2n$. The "saturation intensity" I_s is a measure of the intensity needed to outperform the competing transitions. Translating Δr across the diffraction-blurred zone precludes a signal from any feature except from that lying within $r_i \pm \Delta r/2$, with the result that nearby features are sequentially mapped out with resolution Δr (*29*, *31*). The zeros r_i need not be moved further than $\lambda/2n$, because at $\sim r_i + \lambda/2n$, another zero can resolve the adjacent diffraction zone (*29*); that is, the process can be parallelized (Fig. 1D).

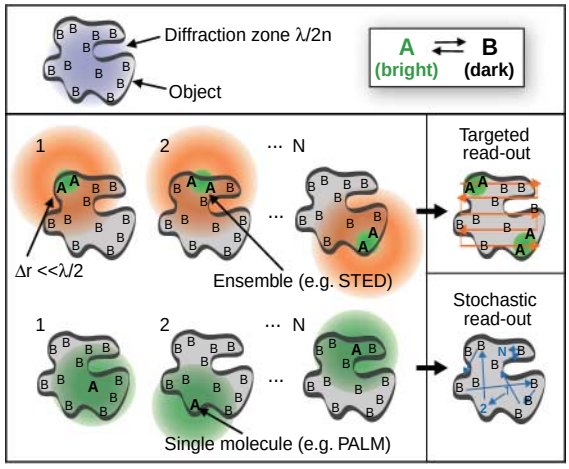

Fig. 2. Targeted versus stochastic time-sequential readout of fluorophore markers of a nanostructured object within the diffraction zone whose lower bound is given by $\lambda/2n$. A and B denote a bright and a dark state, respectively. In the targeted readout mode, one of the two states (here A) is established at a subdiffraction-sized spot at the position of a zero to read out an unknown number of fluorophore molecules. The image is assembled by deliberate translation of the zero. The zero can also be a groove. In the stochastic readout mode, a single switchable fluorophore from a random position within the diffraction zone is switched to a stable state A, while the other molecules remain in B. The coordinate is calculated from the centroid of the diffraction fluorescence spot measured by a pixelated detector. The coordinate pops up stochastically depending on where the interrogated marker molecule is located.

Time-sequential readout from within the diffraction zone at defined coordinates is a hallmark of stimulated emission depletion (STED) (*7*) and ground state depletion (GSD) microscopy (*8*), and of other concepts exploiting reversible saturable or photoswitchable transitions A ↔ B (*29*), such as saturated pattern excitation microscopy (SPEM) (*32*, *33*). These approaches have been generalized under the acronym RESOLFT (*34*), which stands for reversible saturable optically linear fluorescence transitions. With I_{max} denoting the intensity bordering the zero, their practical resolution is well approximated by

$$\Delta r \approx \frac{\lambda}{2n\sin\alpha\sqrt{1 + I_{max}/I_s}}$$

which differs from Abbe's equation in that $I_{max}/I_s \to \infty$ implies "infinite" resolution, i.e., down to a molecule (*7*, *29*, *31*, *35*). The square-root factor stems from the parabolic approximation of ordinary intensity zeros in space. Fluorophores within Δr remain indiscernible because they still are simultaneously recorded. Although it can resolve single molecules (*35*), the RESOLFT concept principally operates with molecular ensembles and with state population probabilities. Δr and the average number of simultaneously recorded fluorophores can be tuned through I_{max}/I_s. The concept has been extended to also exploit the dynamic equilibration of the two states (*36*). Ultimately, the resolution is determined by the actual choice of A and B, which can be basic electronic states, such as the S_0 and the S_1, or "chemical" states such as conformational or binding states of the marker (*29*–*31*).

STED microscopy, which can be regarded as the first concept of the RESOLFT type, uses the most elementary states possible: the S_1 as A and the S_0 as B (Fig. 3). Most implementations of this concept have so far used a focused excitation beam and a red-shifted, doughnut-shaped "STED beam" for quenching excited fluorophores by stimulated emission $S_1 \to S_0$. The few stimulated photons are discarded, as is the stimulating beam. To confine the fluorescence to the zero of the doughnut, the quenching rate outperforms the spontaneous decay of the S_1 given by its inverse lifetime $\tau_{fl} \approx 10^{-9}$ s. With $\sigma \approx 10^{-16}$ cm^2, $I_s = (\sigma\tau_{fl})^{-1}$ typically amounts to 3×10^{25} photons/cm^2 s, i.e., ~10 MW/cm^2. Applying $I_{max} > I_s$ yields subdiffraction fluorescent spots. Translating the zero in any direction sequentially registers the signal from subdiffraction features, thus yielding subdiffraction images (Fig. 4B).

The zero need not be formed by a doughnut, but could also be one or many grooves (Fig. 1D) (*35*) or even planes (*37*). By using a focal zero with a strong quenching peak above and beneath the focal plane (Fig. 1C), STED initially attained $\Delta z = 100$ nm with a single lens (*38*), but in combination with a 4Pi system producing a central zero, $\Delta z = 33$ to 60 nm was possible (*37*). Setting the current benchmark, these STED-4Pi combinations are likely to push the *z* resolution to <10 nm. A similar resolution $\Delta x = 16$ nm was obtained in the focal plane (*35*) with single molecules as test objects, showing that ~λ/45 is possible in the far-field. Realizing such lateral resolution in immunofluorescence imaging has

initially been hampered by photobleaching, but allowing fluorophore dark states to relax enabled $\Delta r = 20$ to 30 nm (Fig. 4C) (*39*).

Meanwhile, the nanoscale resolution provided by STED has tackled cell biology problems. For example, STED resolved synaptotagmin I from individual synaptic vesicles, showing that this protein forms isolated clusters upon vesicle fusion (*40*). STED also revealed the ringlike structure of the protein bruchpilot at synaptic active zones in the *Drosophila* neuromuscular junction (*41*). Further applications included visualizing the SNARE (soluble *N*-ethylmaleimide–sensitive factor attachment protein receptor) protein syntaxin (*42*), the nuclear protein SC35 (*39*), and the nicotinic acetylcholine receptor (*43*). STED has been extended to dual-color recording (*44*), enabling colocalized imaging on the nanoscale. Furthermore, it has revealed the spatial order of self-assembled colloidal particles (*45*) (Fig. 4B). Another application outside biology is to create nanosized spots of excited molecules that serve as the starting point for photochemical reactions (*46*).

Although STED and confocal microscopy are easily combined in the same setup, STED is not an extension of the latter, because it does not rely on a point detector. Sharp discrimination of the fluorescence signal would allow the detector to be placed right at the sample. Specifically, the resolution of a STED microscope is determined solely by the STED beam. For these reasons, parallelized STED microscopy will be possible with arrays of doughnuts or lines (Fig. 1D). Because stimulated emission is a single-photon event with a σ magnitude similar to that of absorption, the light-source requirements for STED are different from those for *m*-photon microscopy (*47*). Subnanosecond, but not femtosecond, pulses render STED effective, leaving laser diodes and photonic crystal fibers as the light sources of the future. Although the use of some fluorophores will be precluded by bleaching, suitable dyes are found in each part of the spectrum.

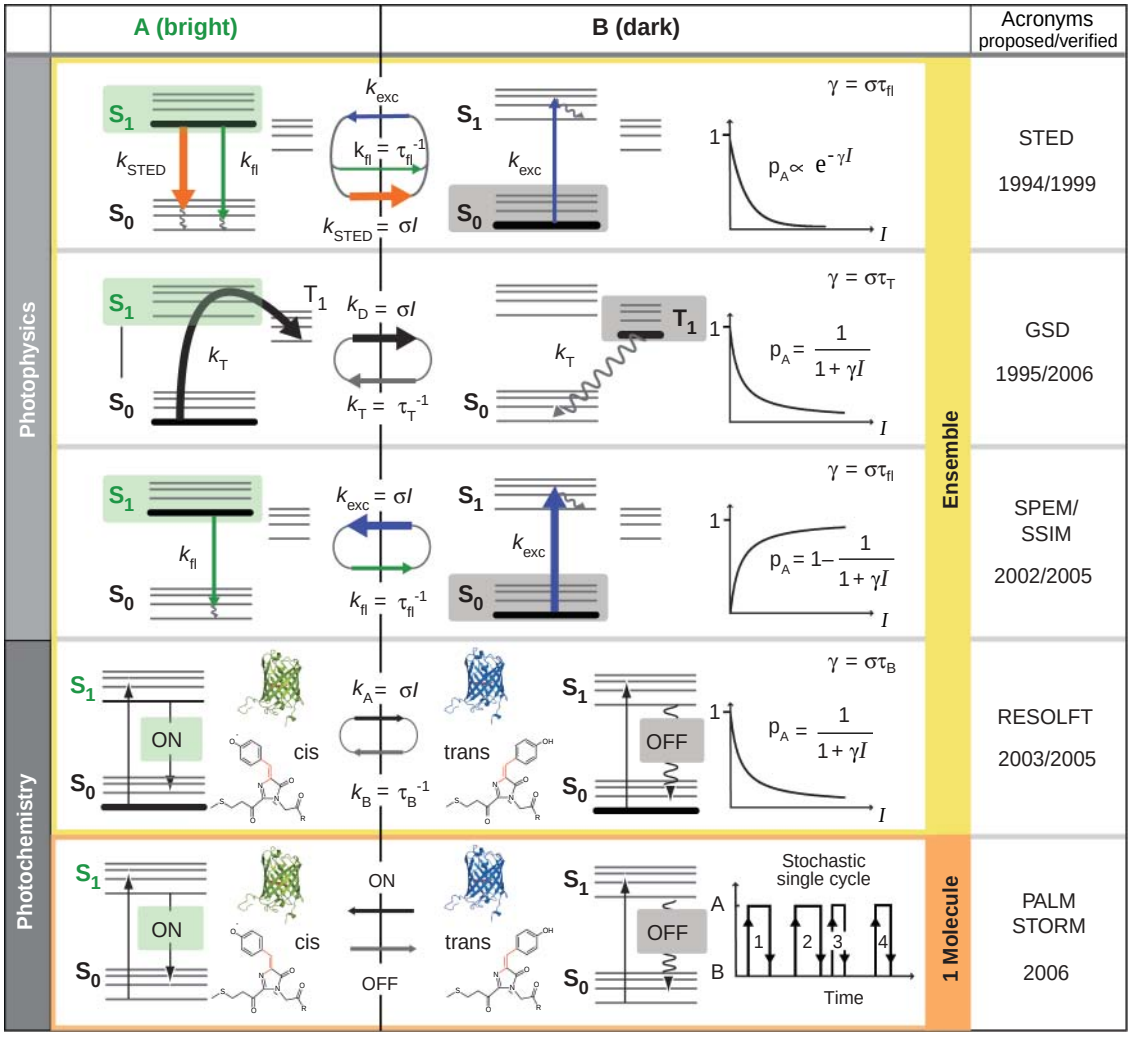

Fig. 3. Bright (**A**) and dark (**B**) molecular states used to break the diffraction barrier. Whereas STED, GSD, and SPEM utilize photophysical transitions, the photoswitching version of the RESOLFT scheme, as well as PALM and STORM, exploit photochemical transitions in which atoms are relocated or bonds formed and broken. PALM and STORM rely on measuring single (or at least identifiable) molecules at a time, whereas the other concepts, although compatible with single-molecule imaging, principally read out ensembles. Ensemble techniques rely on reversible transitions between A and B, as indicated by the rates *k*. The probability p_A of being in state A depends nonlinearly on the light intensity applied, as indicated by the equations, ensuring that either A or B is confined to a subdiffraction area at a targeted coordinate in space. The $e^{-\gamma I}$ and the $(1 + \gamma I)^{-1}$ dependence entail nonlinearities of infinite order $(\gamma I)^m$; $m \to \infty$. By increasing the lifetime of the chosen states, γ strengthens the nonlinear dependence of p_A, thus enabling huge nonlinearities at low *I*. This is radically different from *m*-photon processes that, depending on the concomitant action of *m* photons and hence just on I^m, are firmly limited to order *m* (*15*), which in practice is only $m < 4$. Because it operates with single molecules in a known state, the probability concept breaks down in PALM and STORM, but reminiscent of nonlinearity is the optical switching.

The S_0 and the S_1 states are not the only ones that can be exploited in this way (Fig. 3). GSD microscopy (*8*) breaks the barrier at ~100 times lower I_{max}, because it elects the metastable triplet state T_1 with a lifetime $\tau_T \approx 10^3$ to 10^6 ns as the dark state B and the singlet system (S_0 plus S_1) as A (Fig. 3). Probing A is performed at the same λ as its depletion, i.e., by pumping the dye to B. With a continuous-wave intensity of ~100 kW/cm^2, GSD has recently imaged protein clusters on the plasma membrane of fixed cells with Δr = 50- to 90-nm resolution (*48*). Although challenged by photobleaching, the ubiquity of metastable dark states in fluorophores encourages the exploration of this concept.

Depleting the S_0 state (now B) by populating the S_1 state (now A), SPEM, also known as saturated structured illumination microscopy (SSIM), differs from GSD in that ultrasharp "dark" regions of state B are created with steeply surrounded regions in which the marker, if present, is in A with high probability. Applying $I_{max} > I_s$ confines these regions to $\Delta r << \lambda/2n$ and conceptually yields diffraction-unlimited resolu-

tion like STED and GSD. Applying only $I_{max} < I_s$ gives the diffraction-limited resolution of an ideal confocal system (*49*). I_s is similar in magnitude to that in STED because the same molecular states are used involving the same spontaneous rates. Because it records "negative data," SPEM requires a computational construction of the image and hence an excellent signal-to-noise ratio in the raw data. Recording is performed sequentially in time by translating and rotating line-shaped zeroes that are $>\lambda/2n$ apart from each other and reading out the data with a camera. Initial realizations (*33*) displayed a lateral resolution of 50 nm with beads (after the required computation), thus also demonstrating the potential of line-shaped, quasi-widefield parallelized recording also for other A, B pairs.

The ultimate saturable transition is a photoswitch (*29*–*31*), because the absence of spontaneous interstate transitions implies $I_s \rightarrow 0$ and hence a huge I_{max}/I_s at low I_{max}. Photoswitching between isomerization or binding states, of which only A yields fluorescence, is found in reversibly photoactivatable relatives of the green fluorescent protein, such as asFP595 (*50*) and dronpa (*51*), and in photochromic synthetic compounds. The signal is gained by repeated excitation to a transient fluorescent state A↔A*. Initial experiments with asFP595 evidenced breaking Abbe's barrier by cis-trans photoisomerization with ultralow $I_{max} \approx 10$ W/cm^2 (*34*); similar results were obtained with switchable organic fluorophores (*52*). Selecting long-lived chemical states A and B highlighted that subdiffraction resolution is possible at ultralow intensities and indicated the potential of both protein and dye photoswitching for breaking Abbe's barrier (*29*–*31*). Conversely, these experiments also revealed the Achilles' heel of any concept using reversible saturable transitions, which is the finite number of cycles possible between A and B. However, cycling is required while reading out molecular ensembles from targeted coordinates with diffracted beams (Fig. 2). The reason is that ensuring state A at a chosen coordinate means that nearby molecules must be switched to B.

This problem is avoided in photoactivatable localization microscopy (PALM) (*12*, *14*) and stochastic optical reconstruction microscopy (STORM) (*13*), in which single molecules are read out from random coordinates. To this end, a single molecule is switched on or activated (B→A) such that the next activated one normally is further apart than $>\lambda/2n$; it is then repeatedly excited (A↔ A*) to render N photons forming a magnified diffraction spot on a camera. Switching off adjacent molecules is not needed because they are off (in B) already. Knowing that only a single molecule is in A allows the calculation of its coordinate from the centroid of the spot with precision $\sim\lambda/(2n\sin\alpha\sqrt{N})$. The last step is to switch off the registered molecule, or at least confirm that it is off, so that another one can be switched on and read out. Thus, the image is assembled molecule by molecule by means of a single switching cycle B→A→B′ per molecule.

PALM switches off by bleaching, implying that B may be different from B′, greatly expanding the range of useful compounds (*12*), whereas in STORM B = B′ (*13*). PALM images of thin cryosections of lysosomal transmembrane protein in a mammalian cell displayed a resolution of <25 nm (Fig. 4D). Both approaches require the adaptation of the intensity to the molecular concentration, and in both methods the resolution varies with the brightness of the molecules that are chosen to represent the object in the image. So far PALM involved recording times of hours, but with potentially 10^3 to 10^4 recorded photons per 1 ms, >1000 fluorophores from the diffraction zone could be recorded in a second with 10-nm precision in 2D (*14*). Recording with a camera provides a large field of view while impeding the imperative background rejection. For that reason, PALM was initially demonstrated with <100-nm thin sections and with a total internal reflection (TIRF) 2D recording scheme (*12*). The blur associated with defocusing single molecules should help expand the method to 3D imaging and, once background is dealt with, also to live cells.

Nanolocalization of individual fluorophores was extensively pursued in the past (*28*, *53*). Tracing the bleaching events in fluorophore clusters resolved individual molecules at nanometer distances (*54*). Likewise, individual quantum dots could be separated by disentangling their stochastic excursions to dark states (*55*). Indeed, separating and localizing individual fluorophores differing in their spectra (*56*) has been realized several times since it was proposed (*57*). It has also been known that any process allowing the allocation of N detected photons to the same point in the sample (out of the statistical evaluation of a photon stream) improves the resolution in far-field microscopy and, in fact, gives "infinite" resolution for $N \rightarrow \infty$ (*58*). However, all these precursors did not specify a definite molecular mechanism that would have enabled the sequential readout of an arbitrarily large number of fluorophores, such as the photoswitching between two states.

Most recently, nonswitching fluorophores were also used to form a B→A→B′ cycle by using a specific binding to the target cellular structure B→A and subsequent bleaching A→B′, yielding images (*59*). Complementary to the ensemble concepts, the single-molecule approaches expand the potential of nanoscale imaging. As PALM and STORM obtain their resolution in part computationally, images should be compared with those of the all-physical methods after a deconvolution. The resolution of the latter can be further increased by recording with a pixelated detector, so that both the

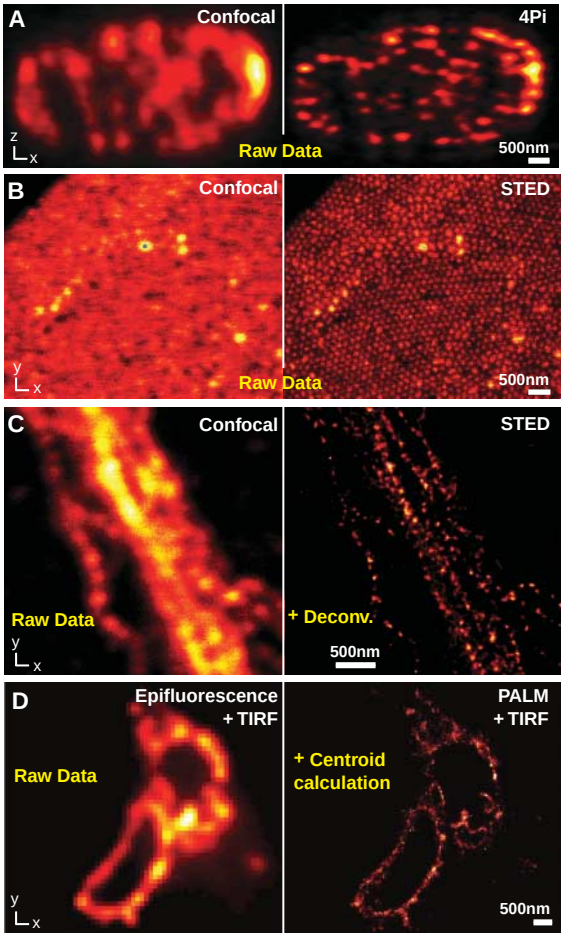

Fig. 4. Side-by-side comparisons. (**A**) Confocal versus 4Pi axial (*xz*) image of microtubules in a neuron: 4Pi image displays 140-nm *z* resolution; lens of $\alpha = 74°$ and with two-photon excitation at 800 nm. The plain 4Pi image is due to a narrow solitary peak without lobes; mathematical lobe-removal is not required. (**B**) Unlike the confocal reference, the STED image reveals the spatial order of self-assembled fused silica nanobeads containing a fluorescence core (*45*). (**C**) Neurofilaments in human neuroblastoma recorded in the confocal mode (left) and with STED after nonlinear deconvolution (right) displaying a focal plane resolution of 20 to 30 nm (*39*). (**D**) Epifluorescence versus PALM recording of a cryoprepared section from a mammalian cell expressing a lysosomal transmembrane protein tagged with a photoswitchable protein; both images were recorded with a TIRF setup. PALM resolution ranges between 20 and 60 nm, whereas individual protein localizations can be 2 nm (*12*).

knowledge of the preset coordinates and those from the detector could be synergistically exploited. Nonetheless, single-molecule bottom-up concepts will develop their strength at small scales and with background-free samples, whereas top-down approaches, such as STED, should be more adequate whenever background dictates registering ensembles. I expect all these methods to complement electron microscopy.

Earlier crude STED imaging of live cells (*38*) should be advanced by emergent fast beam-scanning systems. Furthermore, adjusting the mean number of simultaneously recorded fluorophores via I_{max}/I_s should meet some of the challenges posed by intracellular movements. Moreover, by providing nanosized far-field fluorescent volumes (*38*), STED should facilitate probing the dynamics of tagged biomolecules in live cells through their fluorescence fluctuations (*60*).

Although the recording speed of these concepts may differ in various applications, they must all be slower than epifluorescence microscopy. This stems from the time-sequential readout of the diffraction zone. A potential remedy is to also use other spectroscopic features, such as the emission or absorption wavelength (*57*). Indeed, state B need not be "dark," but just yield a signal different to that of A. Speed can also be gained by simultaneously installing and reading out a large number of states A, B, C, ... within the diffraction zone, either randomly or in a well-chosen order. In my view, many hurdles will be overcome by selecting the right molecular states and transitions (*9*).

In a nutshell, the diffraction barrier is broken by establishing a specific state in a region $<<\lambda/2n$ that characterizes the features from this region (*61*). The region can be as small as, or actually be defined by, a single molecule. This state is established for a period τ within which the established spatial distribution of states is read out with the use of a suitable signal. As a rule, the shorter τ, the harder it is to read out this distribution of states. "Virtual" molecular states are not easy to use because of their transient nature ($\tau < 10^{-15}$ s). This partly explains why no effective thread has yet been described for diffraction-unlimited imaging by pure scattering or reflection. Nonetheless, virtual states could well be involved in the generation of the signal that reads out the longer-lived specific states. In any case, reflection nanoscale imaging would not automatically carry the benefits of molecular labeling and therefore could not easily unravel the biomolecular network in the cell.

A major limitation of fluorescence imaging is the limited flux of emitted photons. It is therefore important to note that none of these concepts ultimately requires fluorescence emission (*31*). Rather, it is sufficient that one of the states, say A, elicits a specific signal that can be detected. For example, if a nonfluorescent marker state A (but not B) absorbs at a particular λ, converting the absorbed photons into heat, the transient change of the refractive index of the surrounding medium could be probed with a beam of light (*62*). The measured change would still perfectly quantify the spatially confined state A. Such a nonfluorescent read-out scheme would benefit from the ultrafast (<3 ps) conversion of photons into heat, providing constant availability for absorption. It would only be limited by the sensitivity of the refractive index measurement; and maintain "multicolor" labeling through λ-specific absorption. Although the probe beam as such would be diffraction-limited, the concept would still give diffraction-unlimited resolution.

Along with improved fluorescence schemes, such nonfluorescent schemes should enable us to take another step in the not-too-distant future: nanoscale 3D imaging at high speed. In any case, the works reviewed herein already broke the barrier of perception of what a lens-based light microscope is able to accomplish. With human perseverance focused on this matter, 3D imaging of live cells with electron microscopy resolution should be possible.

References and Notes

1. M. Born, E. Wolf, *Principles of Optics* (Cambridge Univ. Press, Cambridge, 2002).
2. L. Novotny, B. Hecht, *Principles of Nano-Optics* (Cambridge Univ. Press, Cambridge, 2006).
3. J. B. Pendry, *Phys. Rev. Lett.* **85**, 3966 (2000).
4. Z. Liu, H. Lee, X. Yi, C. Sun, X. Zhang, *Science* **315**, 1686 (2007).
5. I. I. Smolyaninov, Y.-J. Hung, C. C. Davis, *Science* **315**, 1699 (2007).
6. V. A. Podolskiy, E. E. Narimanov, *Opt. Lett.* **30**, 75 (2005).
7. S. W. Hell, J. Wichmann, *Opt. Lett.* **19**, 780 (1994).
8. S. W. Hell, M. Kroug, *Appl. Phys. B* **60**, 495 (1995).
9. S. W. Hell, *Opt. Commun.* **106**, 19 (1994).
10. T. Wilson, C. J. R. Sheppard, *Theory and Practice of Scanning Optical Microscopy* (Academic Press, New York, 1984).
11. J. B. Pawley, Ed., *Handbook of Biological Confocal Microscopy* (Springer, New York, ed. 2, 2006).
12. E. Betzig *et al.*, *Science* **313**, 1642 (2006).
13. M. J. Rust, M. Bates, X. Zhuang, *Nat. Methods* **3**, 793 (2006).
14. S. T. Hess, T. P. K. Girirajan, M. D. Mason, *Biophys. J.* **91**, 4258 (2006).
15. S. W. Hell, A. Schönle, in *Science of Microscopy*, P. W. Hawkes, J. C. Spence, Eds. (Springer, New York, 2006), pp. 790–834.
16. G. Toraldo di Francia, *Nuovo Cimento* **9** (suppl.), 426 (1952).
17. Focusing of a hypothetical spherical wavefront yields a spot of about one-third of the wavelength, but not a far smaller one as was conjectured by Cremer *et al.* (*63*). So, the actual benefit is the *z*-resolution improvement.
18. S. W. Hell, E. H. K. Stelzer, *Opt. Commun.* **93**, 277 (1992).
19. M. G. L. Gustafsson, D. A. Agard, J. W. Sedat, *Proc. SPIE* **2412**, 147 (1995).
20. A. Egner, S. W. Hell, *Trends Cell Biol.* **15**, 207 (2005).
21. H. Gugel *et al.*, *Biophys. J.* **87**, 4146 (2004).
22. J. Bewersdorf, B. T. Bennett, K. L. Knight, *Proc. Natl. Acad. Sci. U.S.A.* **103**, 18137 (2006).
23. M. Lang, T. Müller, J. Engelhardt, S. W. Hell, *Opt. Express* **15**, 2459 (2007).
24. M. Lang, J. Engelhardt, S. W. Hell, *Opt. Lett.* **32**, 259 (2007).
25. M. Lang, J. Engelhardt, S.W. Hell, personal communication.
26. M. G. L. Gustafsson, D. A. Agard, J. W. Sedat, *J. Microsc.* **195**, 10 (1999).
27. By not expanding the microscope's aperture, the interference of unfocused waves from opposing lenses (*64*) produces several peaks of similar height at the focal regions, which strictly cannot superresolve (arbitrary) objects along the *z* axis.
28. C. Kural *et al.*, *Science* **308**, 1469 (2005).
29. S. W. Hell, *Nat. Biotechnol.* **21**, 1347 (2003).
30. S. W. Hell, S. Jakobs, L. Kastrup, *Appl. Phys. A* **77**, 859 (2003).
31. S. W. Hell, *Phys. Lett. A* **326**, 140 (2004).
32. R. Heintzmann, T. M. Jovin, C. Cremer, *J. Opt. Soc. Am. A* **19**, 1599 (2002).
33. M. G. L. Gustafsson, *Proc. Natl. Acad. Sci. U.S.A.* **102**, 13081 (2005).
34. M. Hofmann, C. Eggeling, S. Jakobs, S. W. Hell, *Proc. Natl. Acad. Sci. U.S.A.* **102**, 17565 (2005).
35. V. Westphal, S. W. Hell, *Phys. Rev. Lett.* **94**, 143903 (2005).
36. J. Enderlein, *Appl. Phys. Lett.* **87**, 097105 (2005).
37. M. Dyba, S. W. Hell, *Phys. Rev. Lett.* **88**, 163901 (2002).
38. T. A. Klar, S. Jakobs, M. Dyba, A. Egner, S. W. Hell, *Proc. Natl. Acad. Sci. U.S.A.* **97**, 8206 (2000).
39. G. Donnert *et al.*, *Proc. Natl. Acad. Sci. U.S.A.* **103**, 11440 (2006).
40. K. I. Willig, S. O. Rizzoli, V. Westphal, R. Jahn, S. W. Hell, *Nature* **440**, 935 (2006).
41. R. J. Kittel *et al.*, *Science* **312**, 1051 (2006).
42. J. J. Sieber, K. I. Willig, R. Heintzmann, S. W. Hell, T. Lang, *Biophys. J.* **90**, 2843 (2006).
43. R. Kellner, J. Baier, K. I. Willig, S. W. Hell, F. J. Barrantes, *Neuroscience* **144**, 135 (2007).
44. G. Donnert *et al.*, *Biophys. J.* **92**, L67 (2007).
45. K. Willig, J. Keller, M. Bossi, S. W. Hell, *N. J. Phys.* **8**, 106 (2006).
46. V. S. Letokhov, in *Ultrafast Processes in Chemistry and Photobiology*, M. El-Sayed, Ed. (Blackwell Science, Oxford, 1995), pp. 195–214.
47. W. Denk, J. H. Strickler, W. W. Webb, *Science* **248**, 73 (1990).
48. S. Bretschneider, C. Eggeling, S. W. Hell, personal communication.
49. M. G. L. Gustafsson, *J. Microsc.* **198**, 82 (2000).
50. K. A. Lukyanov *et al.*, *J. Biol. Chem.* **275**, 25879 (2000).
51. R. Ando, H. Mizuno, A. Miyawaki, *Science* **306**, 1370 (2004).
52. M. Bossi, J. Fölling, M. Dyba, V. Westphal, S. W. Hell, *N. J. Phys.* **8**, 275 (2006).
53. W. E. Moerner, *Nat. Methods* **3**, 781 (2006).
54. X. Qu, D. Wu, L. Mets, N. F. Scherer, *Proc. Natl. Acad. Sci. U.S.A.* **101**, 11298 (2004).
55. K. A. Lidke, B. Rieger, T. M. Jovin, R. Heintzmann, *Opt. Express* **13**, 7052 (2005).
56. A. M. van Oijen, J. Köhler, J. Schmidt, M. Müller, G. J. Brakenhoff, *J. Opt. Soc. Am. A* **16**, 909 (1999).
57. E. Betzig, *Opt. Lett.* **20**, 237 (1995).
58. S. W. Hell, J. Soukka, P. E. Hänninen, *Bioimaging* **3**, 64 (1995).
59. A. Sharonov, R. M. Hochstrasser, *Proc. Natl. Acad. Sci. U.S.A.* **103**, 18911 (2006).
60. L. Kastrup, H. Blom, C. Eggeling, S. W. Hell, *Phys. Rev. Lett.* **94**, 178104 (2005).
61. Conceptually, it is enough to establish a steep spatial gradient between the occurrence of at least two states, meaning that the state need not be literally "confined."
62. D. Boyer, P. Tamarat, A. Maali, B. Lounis, M. Orrit, *Science* **297**, 1160 (2002).
63. T. Cremer *et al.*, *Microsc. Acta* **81**, 31 (1978).
64. C. Bailey *et al.*, *Nature* **366**, 44 (1993).

65. I thank M. Lang and J. Engelhardt (DKFZ) for providing Fig. 4A and L. Meyer and G. Donnert for providing Fig. 4C. E. Rittweger and V. Westphal (Max Planck Institute) helped prepare the figures. I also thank G. Donnert, C. Eggeling, A. Egner, S. Jakobs, L. Kastrup, B. Rankin, V. Westphal, K. Willig, and A. Schönle for reading of the manuscript. Funding was from the Max Planck Society, Deutsche Forschungsgemeinschaft, Volkswagen Foundation, Landesstiftung Baden-Württemberg, European Union (New and Emerging Science and Technology, SPOTLITE), and German Ministry of Research and Education. The author consults for Leica Microsystems CMS Gmbh, Mannheim, Germany.

Supporting Online Material

www.sciencemag.org/cgi/content/full/316/5828/1153/DC1
Movies S1 to S4

10.1126/science.1137395

Visual Language Discrimination in Infancy

Whitney M. Weikum,[1]* Athena Vouloumanos,[2] Jordi Navarra,[3,4] Salvador Soto-Faraco,[4,5] Núria Sebastián-Gallés,[4] Janet F. Werker[1]

Talking faces are among the most dynamic and salient stimuli available to infants, and the facial movements accompanying speech influence adult (*1*) and infant (*2*) speech perception. Recently it was reported that facial speech information alone is sufficient for language discrimination in adults (*3*). Although it is well established that young infants can discriminate languages auditorily (*4*, *5*), it is unknown whether infants can discriminate languages visually. We examined whether 4-month-old infants can visually distinguish their native language (English) from an unfamiliar language (French). Because exposure to specific auditory and visual information in infancy is essential for maintaining many early-appearing native language, musical, and face perception sensitivities (*6*–*10*), we compared monolingual English infants to French-English bilingual infants at 6 and 8 months.

Discrimination was tested by using silent video clips of three bilingual French-English speakers reciting sentences in each language. Every trial contained a video clip of a different sentence by one speaker in one language (for example, movies S1 and S2). The infants (n = 36) were presented with video clips from one of the languages until their looking time declined to a 60% habituation criterion. Test trials using the same speakers but different sentences from the other language were shown to examine whether the infants' looking time had increased, indicating that they had noticed the language change. The test trials where the language was switched were compared with a control condition (n = 36) for which the test trials were always different sentences but in the same language as the habituation trials (*11*). A repeated-measures analysis of variance (ANOVA) including age (4, 6, or 8 months), condition (language switch versus control), and trial (habituation versus test) revealed only a significant three-way interaction [$F(2, 66) = 3.71$, $P < 0.05$]. Simple main effects analyses showed that the infants looked significantly longer at the language switch test trials (Fig. 1A), compared with the control trials, at 4 months [$F(1, 22) = 4.70$, $P < 0.05$] and 6 months [$F(1, 22) = 4.19$, $P = 0.05$] but not at 8 months [$F(1, 22) = 1.18$, $P = 0.29$].

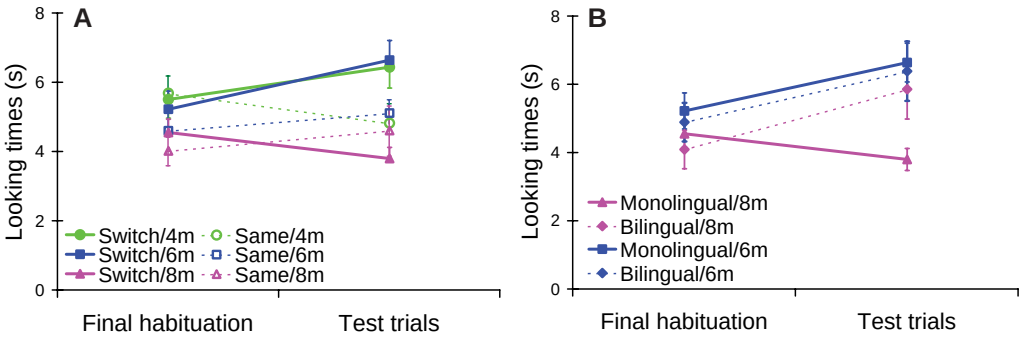

Fig. 1. Mean looking time in seconds to silent talking faces. The *y* axis represents infant looking time; the *x* axis represents the trials that the infant was shown (final habituation trials and test trials). Error bars represent the standard error of the mean. (**A**) Experimental (language switch) and control (language same) conditions for monolingual infants at 4, 6, and 8 months. (**B**) Experimental conditions for monolingual [replotted from (A)] and bilingual infants at 6 and 8 months.

The finding that infants can visually discriminate their native language from an unfamiliar language at 4 and 6 months but not at 8 months parallels declines in performance seen in other perceptual domains. Indeed, across the first year of life, infants' performance declines on the discrimination of nonnative consonant and vowel contrasts (*6*, *7*), nonnative musical rhythms (*8*), cross-species individual faces (*9*), and cross-species face and voice matching (*10*). Thus, it appears that specific experience is necessary for maintaining sensitivity to some initial perceptual discriminations. To determine whether regular exposure to both French and English confers an advantage in visual language discrimination, we compared bilingual French-English infants (n = 24) to their monolingual English counterparts. At an infant age of 6 months, a two-by-two repeated-measures ANOVA analyzing language group (monolingual versus bilingual) and trial (habituation versus test) yielded a significant effect for trial [$F(1, 22) = 6.65$, $P < 0.02$] with no interaction. A similar analysis at the age of 8 months yielded only a significant trial-by-condition interaction [$F(1, 22) = 6.92$, $P < 0.02$]. Simple main effects analyses of this interaction showed that, at 8 months, only the bilingual infants looked significantly longer at the change in language [$F(1, 11) = 7.1$, $P < 0.05$ (Fig. 1B)].

Traditionally, visual speech has been regarded as a redundant signal in verbal communication. The present research shows that visual speech information alone is sufficient for language discrimination in infancy. Moreover, this finding indicates that visual speech may also play a more critical role than previously anticipated in helping infants narrow their perceptual sensitivities to match the distinctions necessary in their language learning environment. Notably, bilingual infants advantageously maintain the discrimination abilities needed for separating and learning multiple languages.

References and Notes

1. W. H. Sumby, I. Pollack, *J. Acoust. Soc. Am.* **26**, 212 (1954).
2. B. Dodd, D. K. Burnham, *Volta Rev.* **90**, 45 (1988).
3. S. Soto-Faraco *et al.*, *Percept. Psychophys.* **69**, 218 (2007).
4. J. Mehler *et al.*, *Cognition* **29**, 143 (1988).
5. L. Bosch, N. Sebastián-Gallés, *Cognition* **65**, 33 (1997).
6. J. F. Werker, R. C. Tees, *Infant Behav. Dev.* **7**, 49 (1984).
7. P. K. Kuhl *et al.*, *Dev. Sci.* **9**, F13 (2006).
8. E. E. Hannon, S. E. Trehub, *Proc. Natl. Acad. Sci. U.S.A.* **102**, 12639 (2005).
9. O. Pascalis *et al.*, *Proc. Natl. Acad. Sci. U.S.A.* **102**, 5297 (2005).
10. D. J. Lewkowicz, A. A. Ghazanfar, *Proc. Natl. Acad. Sci. U.S.A.* **103**, 6771 (2006).
11. Materials and methods are available on *Science* Online.
12. Supported by grant funding through Social Sciences and Humanities Research Council of Canada (SSHRC) and Natural Sciences and Engineering Research Council of Canada (NSERC) to J.F.W., Human Frontier Science Program and James S. McDonnell Foundation to J.F.W. and N.S.-G., and Human Early Learning Partnership to S.S.-F. and by fellowships from Killiam Trusts to S.S.-F. and A.V., NSERC to A.V. and W.M.W., and Michael Smith Foundation for Health Research and SSHRC to W.M.W.

Supporting Online Material

www.sciencemag.org/cgi/content/full/316/5828/1159/DC1
Materials and Methods
Movies S1 and S2

16 November 2006; accepted 12 February 2007
10.1126/science.1137686

[1]University of British Columbia, Vancouver, BC V6T 1Z4, Canada. [2]McGill University, Montreal, QC H3A 1B1, Canada. [3]Oxford University, Oxford OX1 3UD, UK. [4]Parc Científic de Barcelona, Universitat de Barcelona, 08028 Barcelona, Spain. [5]Institut Catatlà de Recerca i Estudis Avançats (ICREA), 08010 Barcelona, Spain.

*To whom correspondence should be addressed. E-mail: whitney@psych.ubc.ca

ATM and ATR Substrate Analysis Reveals Extensive Protein Networks Responsive to DNA Damage

Shuhei Matsuoka,[1] Bryan A. Ballif,[2]* Agata Smogorzewska,[1,3]† E. Robert McDonald III,[1]† Kristen E. Hurov,[1]† Ji Luo,[1]† Corey E. Bakalarski,[2] Zhenming Zhao,[1] Nicole Solimini,[1] Yaniv Lerenthal,[4] Yosef Shiloh,[4] Steven P. Gygi,[2]‡ Stephen J. Elledge[1]‡

Cellular responses to DNA damage are mediated by a number of protein kinases, including ATM (ataxia telangiectasia mutated) and ATR (ATM and Rad3-related). The outlines of the signal transduction portion of this pathway are known, but little is known about the physiological scope of the DNA damage response (DDR). We performed a large-scale proteomic analysis of proteins phosphorylated in response to DNA damage on consensus sites recognized by ATM and ATR and identified more than 900 regulated phosphorylation sites encompassing over 700 proteins. Functional analysis of a subset of this data set indicated that this list is highly enriched for proteins involved in the DDR. This set of proteins is highly interconnected, and we identified a large number of protein modules and networks not previously linked to the DDR. This database paints a much broader landscape for the DDR than was previously appreciated and opens new avenues of investigation into the responses to DNA damage in mammals.

Genotoxic stress is a life-threatening event for organisms as it alters the content and organization of the genetic material. Organisms have developed multiple mechanisms to ameliorate the damage caused by genotoxic stress, including specialized DNA repair processes such as base excision repair, nucleotide excision repair, and nonhomologous end-joining that recognize and repair specific lesions in stereotypical ways. There is also a global signaling network called the DNA damage response (DDR) that senses different types of damage and coordinates a response that includes activation of transcription, cell cycle control, apoptosis, senescence, and DNA repair processes (*1*). This coordination is critical for cell survival, in particular when DNA replication is perturbed.

At the core of the DNA damage signaling apparatus are a pair of related protein kinases, ATM (ataxia telangiectasia mutated) and ATR (ATM and Rad3-related), which are activated by DNA damage. ATM with its regulator the MRN (Mre11-Rad50-NBS1) complex senses double-strand breaks (DSBs) (*2*). ATR with its regulator ATRIP (ATR-interacting protein) senses single-strand DNA (ssDNA) generated by processing of DSBs, as well as ssDNA present at stalled replication forks. Both kinases then phosphorylate proteins to initiate a signaling cascade that includes many common substrates including Chk1 and Chk2 (checkpoint kinases) that initiate a secondary wave of phosphorylation events to extend signaling. About 25 ATM and ATR substrates have been identified (*3*), many as candidates based on known roles in damage signaling.

A key to understanding any kinase network is the identification of the in vivo substrates. However, unbiased identification of kinase substrates is a difficult endeavor. Various technologies have emerged to identify phosphoproteins and kinase substrates (*4*, *5*), but few give in vivo confirmation or the sites of phosphorylation. Protein immunoprecipitation (IP) with antibodies to phosphotyrosine has been used to identify tyrosine kinase substrates (*6*). A newer method uses peptide IP with phosphotyrosine antibodies and mass spectrometry (MS) to identify substrates of tyrosine kinases (*7*). ATM and ATR share substrate specificity, recognizing Ser-Gln (SQ) and Thr-Gln (TQ) motifs (*8*, *9*), and antibodies to phospho-SQ or phospho-TQ sites have enabled identification of a few ATM substrates by protein IP (*10*, *11*). We have combined antibodies to phospho-SQ or phospho-TQ sites, together with peptide IP and SILAC (stable isotope labeling with amino acids in cell culture) (*12*), to identify proteins regulated in response to DNA damage. We discovered a vast network of over 700 human and mouse proteins phosphorylated in response to DNA damage that

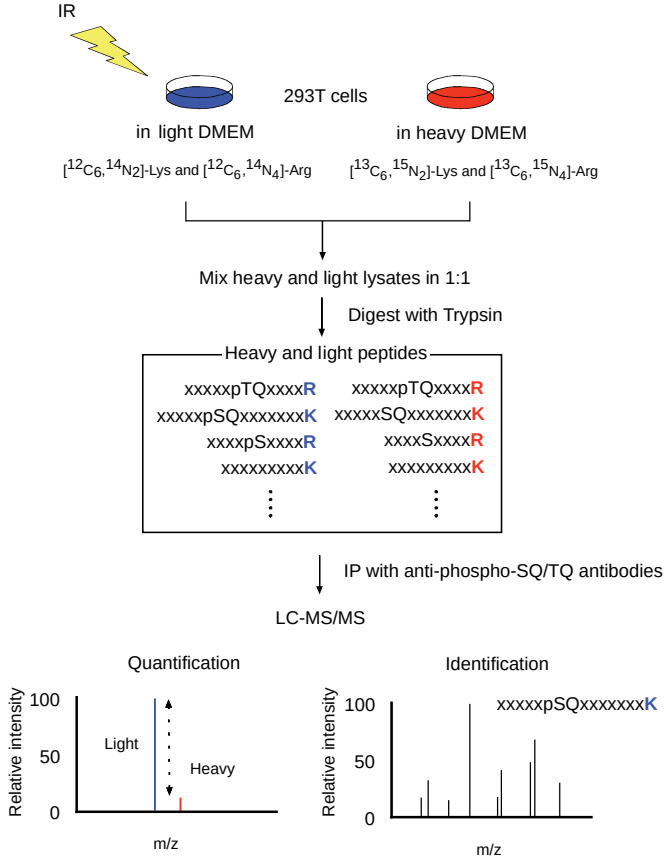

Fig. 1. Schematic for identification of DNA damage–regulated SQ and TQ sites. 293T cells were grown in heavy and light media, and cells in light medium were irradiated with 10 Gy of IR. Heavy and light cell lysates were combined, and peptides were immunoprecipitated with antibodies to phospho-SQ or phospho-TQ and applied to LC-MS/MS. Quantification of phosphorylation on each peptide was achieved by measuring the relative intensity of light and heavy peptides in the MS spectra, which are spaced by 8 daltons for peptides with Lys (K) or by 10 daltons for ones with Arg (R). Each phosphopeptide sequence was obtained from the MS/MS spectra.

[1]Department of Genetics and Center for Genetics and Genomics, Brigham and Women's Hospital, Howard Hughes Medical Institute, Harvard Medical School, Boston, MA 02115, USA. [2]Department of Cell Biology and Taplin Biological Mass Spectrometry Facility, Harvard Medical School, Boston, MA 02115, USA. [3]Department of Pathology, Massachusetts General Hospital, Boston, MA 02214, USA. [4]Department of Human Molecular Genetics and Biochemistry, Sackler School of Medicine, Tel Aviv University, Tel Aviv 69978, Israel.

*Present address: Department of Biology, University of Vermont, Burlington, VT 05405, USA.
†These authors contributed equally to this work.
‡To whom correspondence should be addressed. E-mail: selledge@genetics.med.harvard.edu, steven_gygi@hms.harvard.edu

represents many pathways not previously implicated in the response to DNA damage.

Results

Peptide IP and SILAC. We grew two populations of human embryonic kidney 293T cells in equivalent DMEM (Dulbecco's modified Eagle medium) except that one contained heavy [$^{13}C_6$, $^{15}N_4$]-Arg and [$^{13}C_6$, $^{15}N_2$]-Lys and the other contained light Arg and Lys (Fig. 1). Both cell types grew and responded to ionizing radiation (IR) normally (fig. S1). 293T cells grown in light medium were irradiated with 10 Gy of IR and collected 1 hour after irradiation. Heavy and light lysates were combined (1:1 ratio) and digested with trypsin, then 60 peptide IPs with 68 antibodies to phospho-SQ or phospho-TQ were performed. Bound peptides were applied to liquid chromatography–tandem MS (LC-MS/MS), and the abundance of each phosphopeptide was quantified by measuring the relative intensity of light and heavy peptides in the high-accuracy MS spectra. After quantification of SILAC phosphopeptide pairs, 905 phosphorylation sites on 700 proteins showed an increase in phosphorylation of more than fourfold after DNA damage by IR (table S1). A more limited analysis on mouse NIH3T3 cells identified 95 phosphorylation sites on 86 proteins. Of these, 55 sites were found on 47 mouse proteins whose human homologs were among the 700 human substrates (table S2).

Of the 68 antibodies used, 28 were against phosphorylation sites known to be phosphorylated after DNA damage, and 17 of these were recovered as sites regulated by DNA damage. Several new phosphorylation sites were identified among these targets: three sites each on ATM (T^{86}, S^{367}, and T^{373}), BRCA1 (breast cancer 1, early onset) (S^{1239}, S^{1330}, and T^{1720}), SMC1 (structural maintenance of chromosomes) (S^{358}, S^{360}, and S^{951}), TopBP1 (topoisomerase-binding protein 1) (S^{214}, T^{975}, and S^{1051}), and KAP1 (KRAB domain–associated protein 1) (S^{440}, S^{501}, and S^{824}) and four sites on FANCD2 (Fanconi anemia D2) (S^{178}, T^{596}, S^{717}, and S^{1418}). During the course of this study, some of these were shown to be phosphorylated in vivo after DNA damage (*11*, *13*, *14*). Altogether, we identified 55 regulated phosphorylation sites on the 31 candidate ATM and ATR substrates previously implicated in DNA damage signaling or repair (table S3).

Validation. We confirmed the phosphorylation status for a subset of the candidate substrate proteins by IP and Western blotting. MDC1 (mediator of DNA damage checkpoint 1), 53BP1 (p53-binding protein 1), Orc3 (origin recognition complex subunit 3), and an uncharacterized Zn-finger protein, ZCCHC8, identified with antibodies to phospho-BRCA1 S^{1423} were immunoprecipitated with antibodies to each protein before and after 10 Gy of IR and subjected to Western blotting with antibodies to phospho-BRCA1 S^{1423}. All three were phosphorylated after IR. Although no antibodies to Orc3 for IP were available, we were able to immunoprecipitate Orc3 with antibodies to Orc2 because the two proteins associate (*15*). Thus, Orc3 phosphorylation after IR was confirmed (Fig. 2A).

Sequences around sites identified with antibodies to phospho-BRCA1 S^{1423} are very similar to sequences around BRCA1 S^{1423} (Fig. 2A). We examined the distribution of amino acid residues surrounding the phosphorylation site among the phosphopeptides identified by individual peptide IPs (fig. S2). Most antibodies used recognize one or two amino acids at −1 or +2 position, in addition to the phospho-SQ or phospho-TQ. Normally, linear epitopes are thought to comprise five to seven amino acids. The presence of the phosphate on the epitope may reduce the number of additional contacts needed to form an immunogenic epitope. We also determined the distribution of amino acid residues surrounding the DNA damage–regulated phospho-SQ or -TQ sites on the 700 candidate ATM and ATR substrates. Enrichment of E (Glu) and S around the SQ or TQ sites was observed (Fig. 2B). This is consistent with the notion that E or D (Asp) is often found around SQ or TQ sequence phosphorylated by ATM or ATR in vitro (*8*).

Of the 11 proteins whose phosphorylation after IR was confirmed (Fig. 2A and fig. S3), we

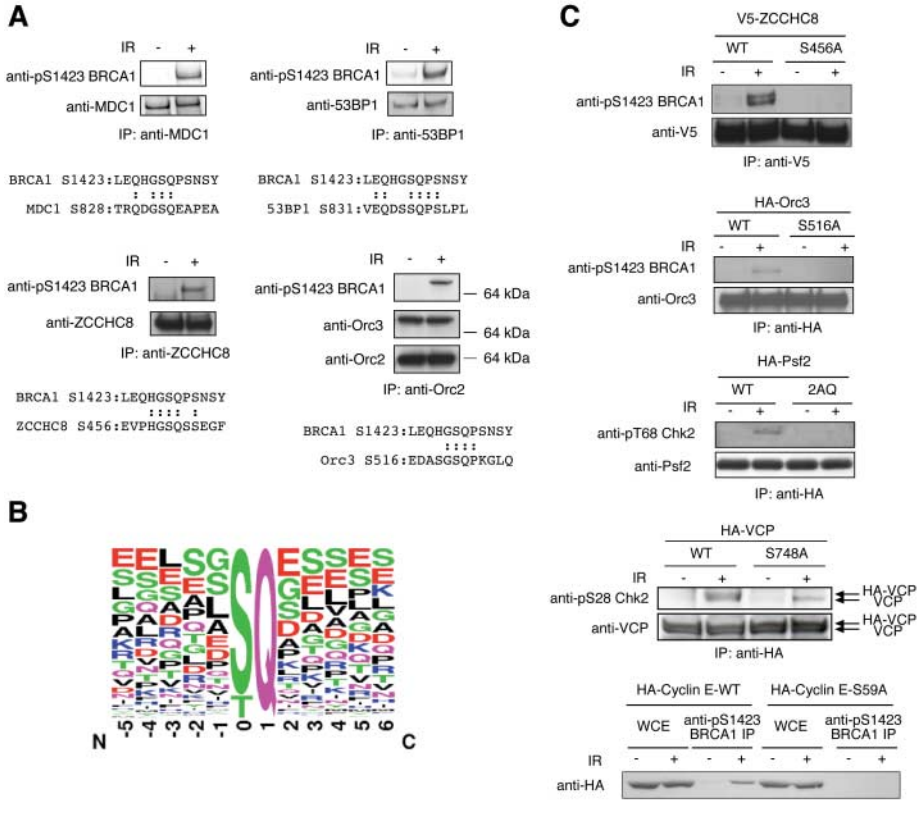

Fig. 2. Validation of protein phosphorylation. (**A**) MDC1, 53BP1, and ZCCHC8 were immunoprecipitated with antibodies against each protein from 293T cells before (-IR) and after (+IR) 10 Gy of IR, and precipitated proteins were subjected to Western blotting with antibodies to phospho-BRCA1 S^{1423}. The same blots were reprobed with antibodies to MDC1, 53BP1, or ZCCHC8. Orc3 was coimmunoprecipitated with antibodies to Orc2, and precipitated proteins were subjected to Western blotting with antibodies to phospho-BRCA1 S^{1423}. The same blot was reprobed with antibodies to Orc3 and Orc2. Sequences around the identified site on each protein were aligned with those around BRCA1 S^{1423}. (**B**) Distribution of amino acid residues (*30*) surrounding the phospho-SQ or -TQ sites on the candidate ATM and ATR substrates that were regulated by DNA damage. Sequence analysis was done with MOTIF-X software (*31*). (**C**) HA-tagged wild-type VCP, Orc3, or Psf2 (WT) or AQ mutant of each protein [VCP S748A, Orc3 S516A, and Psf2 T180A/S182A (2AQ)] was expressed in U2OS cells, and V5-tagged ZCCHC8 wild-type (WT) or AQ mutant (S456A) was expressed in 293T cells. Wild-type and AQ mutant proteins were immunoprecipitated with antibodies to HA or V5 from cells before (-IR) and after 10 Gy of IR (+IR) and probed with the indicated antibodies to phosphorylated sites. The same blots were reprobed with antibodies to each protein or anti-V5. Endogenous VCP (VCP) was coimmunoprecipitated with HA-tagged VCP (HA-VCP) by IP with antibodies to HA because VCP forms a homo hexamer (*32*). HA-tagged wild-type cyclin E (WT) or AQ mutant (S59A) was expressed in U2OS cells, and proteins immunoprecipitated with antibodies to phospho-BRCA1 S^{1423} from cells before (-IR) and after 10 Gy of IR (+IR) and whole-cell extracts (WCE) were subjected to Western blotting with antibodies to HA.

further validated 5 by mutating the identified sites. Substitution of AQ for the identified SQ or TQ site was introduced by site-direct mutagenesis into VCP (valosine-containing protein), Orc3, Psf2 (partner of SLD5), ZCCHC8, and cyclin E. In all five cases, phosphorylation was observed on wild-type proteins but not on AQ mutants (Fig. 2C), indicating that the antibodies were recognizing the identified SQ or TQ site on each protein and supporting the quality of the peptide sequence identifications.

Functional analysis. Kinases may recognize many proteins, only a subset of which are significant to the kinase regulatory network. To examine this, we randomly chose a group of 37 substrates not previously implicated in the DDR to investigate genetically for roles in the DDR. We assayed cells depleted for these proteins with small interfering RNA (siRNA) for six basic phenotypes: the ability to prevent the spontaneous generation of DSBs, the ability to phosphorylate histone H2AX (H2A histone family member X) after IR, the ability to repair DSBs, activation of the G_2-M checkpoint, activation of the intra–S phase checkpoint, and the functionality of homologous recombination (HR).

In osteosarcoma U2OS cells, the γH2AX signal is low in the absence of IR, but rises rapidly and reaches maximal levels within 0.5 to 1 hour after 10 Gy IR. Thereafter, it decays rapidly as damage is being repaired and falls below 30% of peak levels by 6 hours after IR. We examined the effects of siRNA-mediated knockdown of candidate genes on formation of IR-induced γH2AX at these times in U2OS cells by Western blotting (Fig. 3A) to expose the potential roles of a gene in the maintenance of DNA integrity in the absence of damage or in the generation of γH2AX signal in response to damage or in DNA repair. siRNAs against many of the candidate genes altered the γH2AX signal compared with control siRNA (Fig. 3B and fig. S4). Inhibition of multiple genes from the list also showed functional defects in other assays (tables S4 to S6).

In summary, siRNAs against 35 of the 37 genes (94.6%) scored in at least one of the four assays, and more than half of the genes (22 genes) scored in two or more assays. siRNAs against CSTF2 (cleavage stimulation factor 2), DCK (deoxycytidine kinase), KIAA1160, NASP (nuclear autoantigenic sperm protein), RBM10 (RNA binding motif protein 10), SMARCAD1 (SWI/SNF-related, matrix-associated actin-dependent regulator of chromatin, subfamily a, containing DEAD/H-box 1), SRCAP (Snf2-related CBP activator protein), TPR (translocated promoter region), and USP34 (ubiquitin-specific peptidase 34) scored in three categories. LATS1 (large tumor suppressor homolog 1) scored in all four (Fig. 3C), as well as KIAA1794 (not shown), which we have found to encode FANCI, a novel component of the Fanconi anemia (FA) pathway (*16*). During the course of this study, involvement of RENT (regulator of nonsense transcripts) and FOXO1 (forkhead box 1) in the DDR pathway was shown (*17*, *18*), consistent with our observations. Thus, we concluded that our gene list is highly enriched with genes that regulate the DNA damage response or DNA repair.

Bioinformatic analysis of phosphorylation targets. The identified proteins were annotated in the gene ontology format. Of the 700 identified proteins, 421 were annotated with a biological process by the PANTHER program (Fig. 4A). Among these, 202 (48%) were assigned in the nucleic acid metabolism category that includes DNA replication, DNA repair, and other categories that involve nucleic acids. Further subdivision of these 202 revealed that 46 function in DNA replication, repair, or recombination and 101 function in mRNA transcription (Fig. 4B).

Another measure of the significance of certain functional categories among these phosphorylation targets is their enrichment relative to the total numbers in their respective categories. The DNA replication, recombination, and repair category showed a highly significant enrichment. Enrichments were also observed for proteins in the cell cycle, gene expression, and cell signaling categories (Fig. 4C). A surprising category with enrichment was the RNA posttranscriptional modification group that includes splicing factors and other RNA binding proteins potentially im-

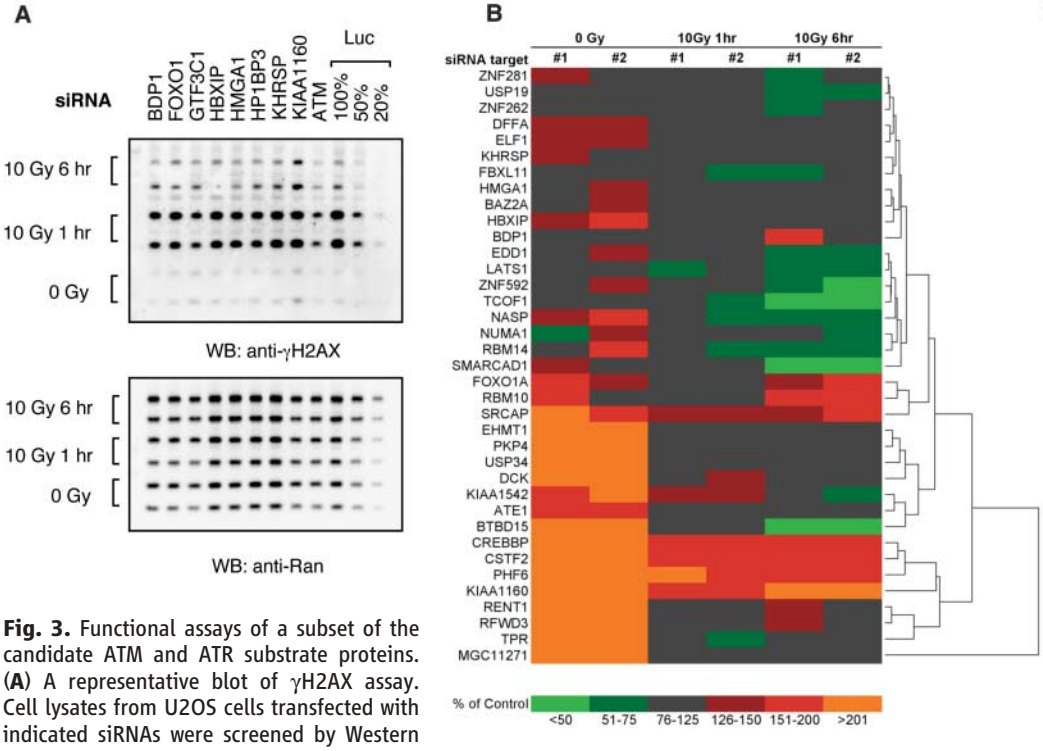

C

HR	G2/M	Intra-S	γH2AX
ATE1	ATE1	ATE1	ATE1
BAZ2A	BAZ2A	BAZ2A	BAZ2A
BDP1	BDP1	BDP1	BDP1
BTBD15	BTBD15	BTBD15	BTBD15
CREBBP	CREBBP	CREBBP	CREBBP
CSTF2	CSTF2	CSTF2	CSTF2
DCK	DCK	DCK	DCK
DFFA	DFFA	DFFA	DFFA
EDD1	EDD1	EDD1	EDD1
EHMT1	EHMT1	EHMT1	EHMT1
ELF	ELF	ELF	ELF
FBXL11	FBXL11	FBXL11	FBXL11
FOXO1A	FOXO1A	FOXO1A	FOXO1A
HBXIP	HBXIP	HBXIP	HBXIP
HMGA1	HMGA1	HMGA1	HMGA1
KHRSP	KHRSP	KHRSP	KHRSP
KIAA1160	KIAA1160	KIAA1160	KIAA1160
KIAA1542	KIAA1542	KIAA1542	KIAA1542
LATS1	LATS1	LATS1	LATS1
MGC11271	MGC11271	MGC11271	MGC11271
NASP	NASP	NASP	NASP
NUMA1	NUMA1	NUMA1	NUMA1
PHF6	PHF6	PHF6	PHF6
PKP4	PKP4	PKP4	PKP4
RBM10	RBM10	RBM10	RBM10
RBM14	RBM14	RBM14	RBM14
RENT	RENT1	RENT	RENT1
RFWD3	RFWD3	RFWD3	RFWD3
SMARCAD1	SMARCAD1	SMARCAD1	SMARCAD1
SRCAP	SRCAP	SRCAP	SRCAP
TCOF1	TCOF1	TCOF1	TCOF1
TPR	TPR	TPR	TPR
USP19	USP19	USP19	USP19
USP34	USP34	USP34	USP34
ZNF262	ZNF262	ZNF262	ZNF262
ZNF281	ZNF281	ZNF281	ZNF281
ZNF592	ZNF592	ZNF592	ZNF592

Fig. 3. Functional assays of a subset of the candidate ATM and ATR substrate proteins. (**A**) A representative blot of γH2AX assay. Cell lysates from U2OS cells transfected with indicated siRNAs were screened by Western blot using antibodies to γH2AX (top) and Ran as the loading control (bottom). (**B**) The normalized γH2AX signal from cells transfected with siRNAs was measured as a percentage of that with siRNA against luciferase and represented by one-dimensional hierarchical clustering. (**C**) Summary of the assay results: homologous recombination assay (HR), G_2-M checkpoint assay (G2/M), intra–S phase checkpoint–radio-resistant DNA synthesis assay (Intra-S), and γH2AX assay (γH2AX). Proteins scored in each assay are marked in red. Abbreviations not mentioned in text are spelled out in table S1. Detailed results of each assay are provided as tables S4 to S6.

plicated in RNA modification or translational control.

Discussion

In this study, we have identified more than 900 phosphorylation sites containing a consensus ATM and ATR phosphorylation motif in 700 proteins that are inducibly phosphorylated in response to IR. The extent of phosphorylation we observed was unanticipated. For example, among the mediator class of proteins, including BRCA1, 53BP1, and TopBP1, a total of 33 regulated sites were identified, 15 in 53BP1 alone. Of these 33, only 6 had been previously identified, and these are considered highly studied substrates. The quality of the identifications is supported by the fact that many sites were found multiple times and in different forms, such as a partial tryptic peptide or a peptide containing an oxidized methionine or in IPs with different antibodies, from cells with different types of DNA damage (table S7), or from different organisms (table S2). Furthermore, we chose a stringent cutoff for identification to reduce the frequency of false calls. Independent analysis of phosphorylation of randomly chosen genes from the list demonstrated that a high percentage could be verified.

Protein kinases are switches that coordinate entire programs dedicated to accomplishing the goals of a given signal transduction pathway. In this study, we discovered that damage-activated kinases do not simply contact key individual proteins in a process, but instead phosphorylate multiple components of particular pathways. Many of the proteins identified cluster into modules of previously known interacting proteins.

Interacting modules involved in DNA replication. Multiple modules involved in DNA replication were identified, such as an Orc module with Orc3 and Orc6 (Fig. 5A); an MCM (minichromosome maintenance protein) module including MCM2, MCM3, MCM6, MCM7, and MCM10; and DBF4, an activating subunit of the Cdc7 kinase needed for initiation of DNA replication (Fig. 5B). In addition, several components of the replication machinery emerged, including an RFC clamp–loader module (Fig. 5C) with RFC1 and RFC3 (replication factors C1 and C3) and a DNA polymerase module that includes the catalytic subunit of DNA polymerase epsilon (POLE), its interacting protein POLE4, and two translesion polymerases PolL and PolQ (Fig. 5D). Furthermore, both components of the Timeless-Tipin complex involved in fork stability were identified along with Claspin, with which they interact (*19*) (fig. S5F). These modules themselves interact in a larger network dedicated to DNA replication (fig. S6). Of these, only MCM2 and MCM3 were previously known ATM substrates (*10*, *20*). These findings indicate that the connections from the DDR to DNA replication are more complex than previously anticipated. As DNA damage signaling is known to control initiation of origins, as well as fork stability, the intra–S phase checkpoint, and restarting of forks after damage, it is likely that these new components take part in executing those processes.

Interacting modules involved in DNA repair. Multiple modules identified in this analysis function in control of DNA repair. A mismatch repair module contained mutS homolog genes MSH2, MSH3, and MSH6, as well as exonuclese 1 (EXO1) (Fig. 5E). This pathway is generally thought to act to repair mismatches during DNA replication.

An excision repair module included XPA and XPC (xeroderma pigmentosum complementation groups A and C); RPA1 (replication protein A1); ERCC6 (excision repair cross-complementing 6, also known as CSB, Cockayne syndrome group B); and components of transcription factor TFIIH (Fig. 5F). Other than RPA1, which participates in many repair pathways, this pathway had not been previously linked to DNA damage signaling.

We also found a module containing the Fanconi anemia (FA) pathway, which includes FANCD2, FANCA, and the newly discovered FANCI gene, which was identified through this screen (Fig. 5G). This module also contains BRCA2 and PALB2 (partner and localizer of BRCA2, FLJ21816), a BRCA2-binding protein involved in the FA pathway (*21*). A total of 12 regulated SQ or TQ phosphorylation sites were present in this module. Related to the FA

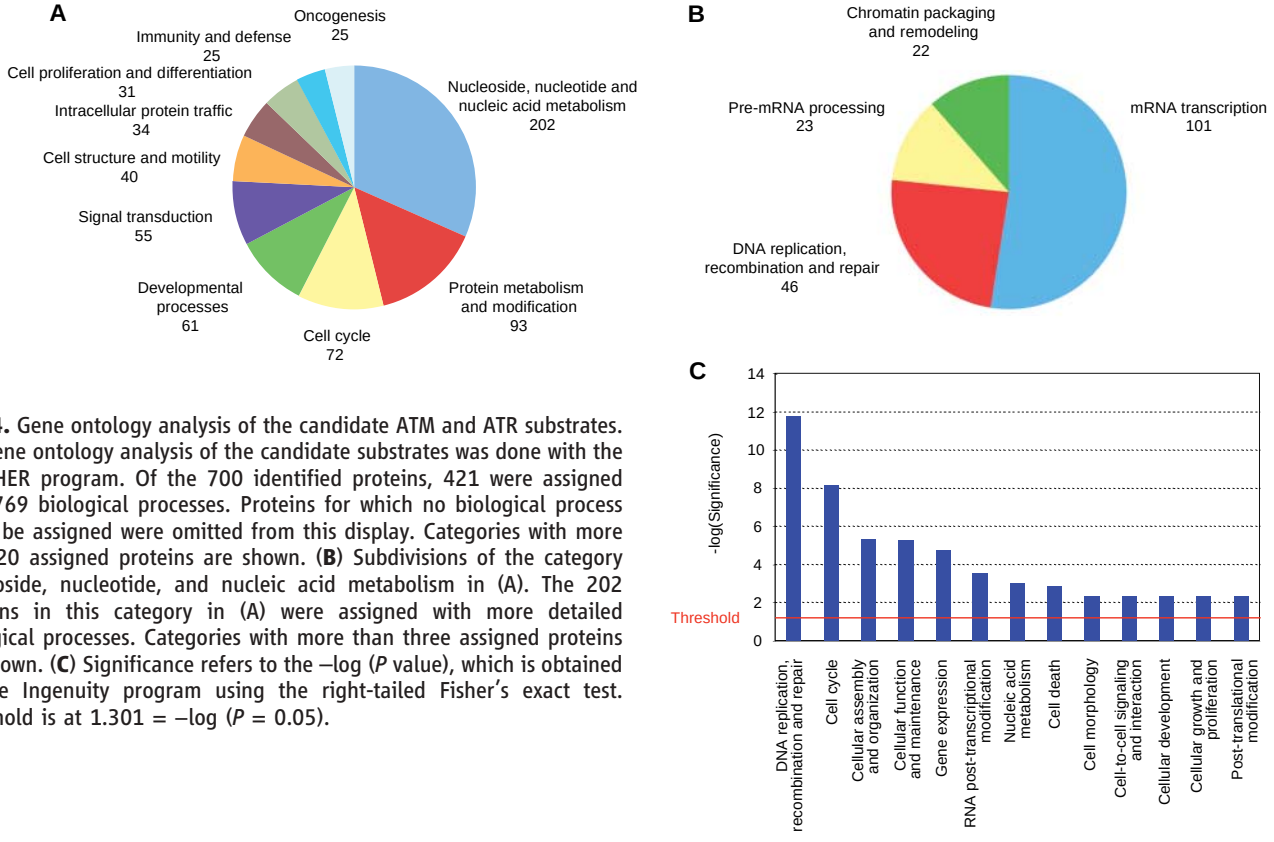

Fig. 4. Gene ontology analysis of the candidate ATM and ATR substrates. (**A**) Gene ontology analysis of the candidate substrates was done with the PANTHER program. Of the 700 identified proteins, 421 were assigned with 769 biological processes. Proteins for which no biological process could be assigned were omitted from this display. Categories with more than 20 assigned proteins are shown. (**B**) Subdivisions of the category nucleoside, nucleotide, and nucleic acid metabolism in (A). The 202 proteins in this category in (A) were assigned with more detailed biological processes. Categories with more than three assigned proteins are shown. (**C**) Significance refers to the –log (*P* value), which is obtained by the Ingenuity program using the right-tailed Fisher's exact test. Threshold is at 1.301 = –log (*P* = 0.05).

pathway is an extensive HR module including RAD50, RAD52, RAD51AP, RAD54, XRCC2, XRCC3, BRCA2, and PALB2, as well as RUVBL2 and TOP3 (not shown), representing essentially every step in the recombination process (Fig. 5H). Of the proteins in these two modules, only FANCD2 was previously known to be phosphorylated in response to DNA damage. These extensive contacts indicate that the processes of cross-link repair and HR are likely to be heavily regulated by the ATM and ATR pathway (Fig. 5, G and H).

An additional module implicated in DNA damage responses was the COP9 signalosome CSN, in which three subunits underwent phosphorylation: CSN1 (GPS1), COP3, and COP7A (Fig. 5I). This complex is involved in the SCF (Skp1–Cullin–F-box protein) pathway, where it participates in a neddylation-deneddylation cycle important in SCF E3 ligase function and alters its association with CSA (Cockayne syndrome type A) and DDB2 (damage-specific DNA binding protein 2), two DCAF (DDB1- and Cul4-associated factors) proteins in Cul4 ligases (*22*). In response to DNA damage, the CSN complex rearranges from DDB2-Cul4 complexes to CSA-Cul4 complexes.

New cell cycle modules. One cell cycle module found comprises cyclin E and two negative regulators of cyclin E: the F-box protein FBW7, which targets cyclin E for ubiquitination and destruction, and the cyclin-dependent kinase (Cdk) inhibitor $p27^{Kip1}$, which binds to cyclin E–Cdk2 complexes and inhibits their activity (Fig. 5J). In addition, the CIZ1 (Cip1 interacting Zn-finger protein), which negatively regulates the Cdk inhibitor $p21^{Cip1}$ and promotes DNA synthesis, is phosphorylated. This suggests that, in addition to causing cell cycle arrest through the Chk2-p53-$p21^{Cip1}$ pathway (*23*), DNA damage might also directly regulate the activity of cyclin E through additional inhibitors and proteolysis to promote cell cycle arrest.

We identified four components of the spindle checkpoint, Bub1, Mad1, Sgo1, and Mad2BP (Mad2 binding protein; also known as $p31^{COMET}$) (Fig. 5K). Bub1, Mad1, and Sgo1 promote mitotic arrest by maintaining Mad2-Cdc20 complex formation in response to unoccupied kinetochores, whereas Mad2BP opposes Mad2 function. In budding yeast, the spindle checkpoint and DNA damage checkpoint regulate a common protein, Pds1, and both checkpoints help to restrain cell cycle arrest in response to DNA damage, but no direct connections had been previously identified in mammals. The spindle checkpoint controls anaphase-promoting

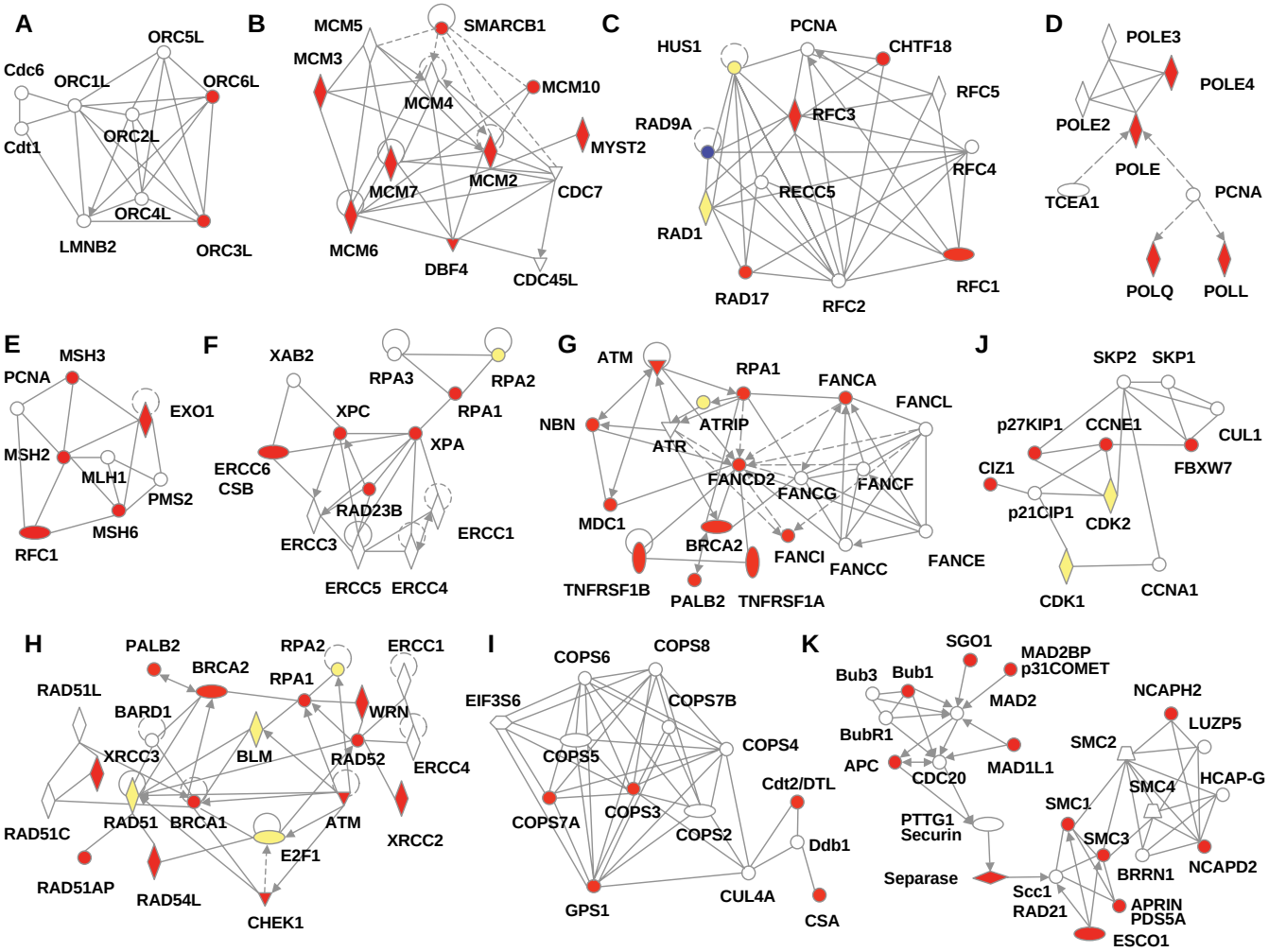

Fig. 5. Network modeling. Modules identified by using the Ingenuity program are (**A**) Orc module, (**B**) MCM module, (**C**) RFC module, (**D**) DNA polymerase module, (**E**) MSH module, (**F**) XP module, (**G**) FANC module, (**H**) BRCA1 module, (**I**) COP9 module, (**J**) cyclin E module, and (**K**) spindle checkpoint module. In each module, a solid line indicates direct interaction; a dashed line indicates indirect interaction; a line without arrowhead indicates binding; an arrow from protein A to protein B indicates A acts on B. Node shapes are indicative: triangle, kinase; diamond, enzyme; hexagon, translation regulator; trapezoid, transporter; oval (horizontal), transcription regulator; oval (vertical), transmembrane receptor. Proteins identified in this screen are marked in red and proteins known to be phosphorylated after IR but not identified in this screen are marked in yellow. Rad9 [marked in blue in (C)] was identified in peptide IP from cells damaged with ultraviolet light (table S7).

complex (APC) activation, which ultimately controls Separase activation, a protease that catalyzes dissolution of sister chromatid cohesion and anaphase entry. Both Cdc26, an APC subunit, and Separase were phosphorylated in response to IR (Fig. 5K). Components of the cohesion regulatory machinery were detected in our screen, including the cohesins SMC1 and SMC3 and the ESCO1 (establishment of cohesion 1 homolog 1) complex required for loading cohesins during S phase. Furthermore, APRIN, the human homolog of the *Saccharomyces cerevisiae* cohesion protein Pds5, was phosphorylated. An additional module that interacts with cohesin involves the Condensin II chromosome-condensation complex, including the substrates NCAPD2 and NCAPH2 (non-SMC condensing I complex subunits D2 and H2), which are both required for proper cohesion between sisters. Of these, only SMC1 was a known ATM substrate (*24*, *25*). These findings suggest that the DDR pathway displays manifold interfaces with other pathways previously implicated in cell cycle control.

Signaling pathways that interface with the DNA damage pathway. Various signaling pathways were also implicated in the DDR through this study. Enrichment was found for proteins in the insulin–IGF-1 (insulin-like growth factor)–PI3K (phosphatidylinositol 3-kinase)–AKT pathway, including the adaptor molecule IRS2 (insulin receptor substrate 2), the kinase AKT3, two regulators of AKT, HSP90 (heat shock protein 90), and PP2A (protein phosphatase 2A), and several downstream effectors of AKT. Examples of these downstream effectors are a transcription factor, FOXO1, and components in the proteins translation control pathway, TSC1 (tuberous sclerosis 1), 4E-BP1 (eIF4E binding protein 1), and p70S6K (ribosomal protein S6 kinase) (Fig. 6). Indeed, S^{111} of 4E-BP1, which we identified as a DNA damage–regulated site, is phosphorylated by ATM in response to insulin (*26*). The enriched set of contacts between the DDR and the insulin signaling pathway suggests that the DDR might induce a survival signal through the activation of AKT. Our study indicates that the DDR is likely to intersect the insulin–IGF-1–PI3K–AKT pathway at many points. In support of this idea, mice lacking the nucleotide excision repair protein ERCC1 show both accelerated aging (due to constitutive DNA damage) and severe growth retardation (due to suppression of the growth hormone–IGF-1 axes) (*27*). Although DNA damage could affect insulin and IGF-1 signaling in vivo through indirect effects such as the depletion of stem cells in the liver and the pancreas, it is also possible that persistent repetitive DNA damage alters cellular insulin–IGF-1 signaling and contributes to diabetes and other age-associated metabolic disorders.

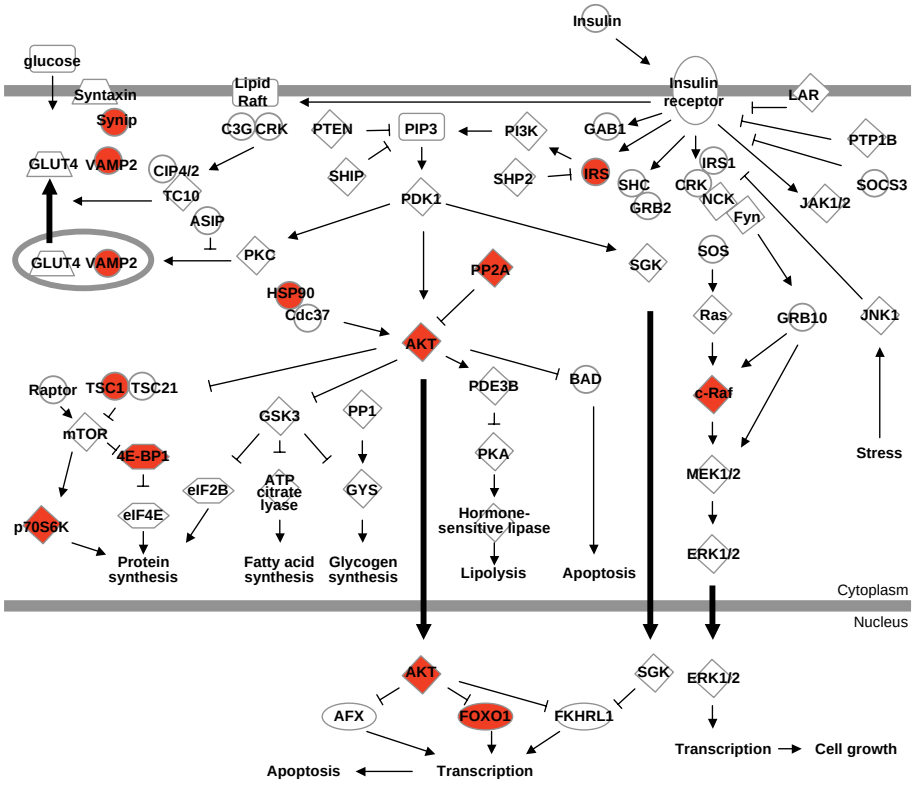

Fig. 6. Possible involvement of the AKT-insulin pathway in the DDR. Node shapes are indicative: rectangle, cytokine; diamond, enzyme; oval (horizontal), transcription regulator; oval (vertical), transmembrane receptor; trapezoid, transporter; hexagon, translation regulator. Proteins identified in this screen were marked in red.

Many other pathways not mentioned here appear to have multiple connections to the DNA damage pathway. At this point it is not clear whether these are all substrates of ATM and ATR or possibly other kinases activated by IR. In addition to DSBs, IR causes oxidative stress and ssDNA breaks. How these events are sensed and whether kinases participate in signaling detection of these events is not known. Any kinase activated by IR could recognize a site that happens to have a Q adjacent to S or T, potentially marking it for identification by our method. In fact, only 70% of our substrates appear to be regulated by ATM (table S8, A and B). Others could be ATR and DNA-PK substrates. Alternatively, it is possible that other phosphatidylinositol 3-kinase–related kinase (PIKK) members respond to secondary stresses generated by this treatment. In this vein, we identified a module around the nonsense-mediated decay pathway containing the PIKK SMG1 and RENT as regulated substrates (fig. S5C). SMG1 can phosphorylate RENT on SQ sites (*28*). This pathway has been previously implicated in the response to IR. It is not clear if it is downstream of ATM, or if SMG1 senses damage to DNA or possibly to RNA.

We also found a large number of proteins involved in chromatin modification and transcription, including subunits of multiple RNA polymerases and many proteins involved in splicing and RNA metabolism (fig. S5, A to C and E). This points to a broad cellular transcriptional, posttranscriptional, and chromatin response that had only been hinted at in previous studies.

It is likely that we have identified the majority of abundant proteins inducibly phosphorylated on SQ or TQ sites after DNA damage. The DNA damage phosphorylation database is a rich resource of information that can be used in multiple ways. In one instance, we identified a novel FA gene by phenotypic analysis (*16*). In another case, we used the BRCT repeats of BRCA1 to pull down tryptic peptides and proteins. By looking for proteins in common between those purifications and this database, we identified two novel BRCA1-binding proteins (*29*). Combining these data and other data sets should allow important damage-response proteins to be identified and new pathways to be explored.

The results of this study illustrate the extraordinarily broad landscape of the DDR, which extends far beyond what was anticipated from previous studies. The large number of functional modules discovered here and the multiple connections to each suggest that the DDR profoundly alters cellular physiology. The elucidation of these newfound connections and the roles played by the many proteins newly implicated in the damage response should provide a solid foundation for a systems biology understanding of the cellular response to DNA damage and replication stress in the future.

References and Notes

1. B. B. Zhou, S. J. Elledge, *Nature* **408**, 433 (2000).
2. M. B. Kastan, J. Bartek, *Nature* **432**, 316 (2004).
3. Y. Shiloh, *Trends Biochem. Sci.* **31**, 402 (2006).
4. J. Ptacek *et al.*, *Nature* **438**, 679 (2005).
5. N. Dephoure, R. W. Howson, J. D. Blethrow, K. M. Shokat, E. K. O'Shea, *Proc. Natl. Acad. Sci. U.S.A.* **102**, 17940 (2005).
6. A. R. Salomon *et al.*, *Proc. Natl. Acad. Sci. U.S.A.* **100**, 443 (2003).
7. J. Rush *et al.*, *Nat. Biotechnol.* **23**, 94 (2005).
8. S. T. Kim, D. S. Lim, C. E. Canman, M. B. Kastan, *J. Biol. Chem.* **274**, 37538 (1999).
9. T. O'Neill *et al.*, *J. Biol. Chem.* **275**, 22719 (2000).
10. D. Cortez, G. Glick, S. J. Elledge, *Proc. Natl. Acad. Sci. U.S.A.* **101**, 10078 (2004).
11. Y. Ziv *et al.*, *Nat. Cell Biol.* **8**, 870 (2006).
12. M. Mann, *Nat. Rev. Mol. Cell Biol.* **7**, 952 (2006).
13. S. V. Kozlov *et al.*, *EMBO J.* **25**, 3504 (2006).
14. G. P. Ho, S. Margossian, T. Taniguchi, A. D. D'Andrea, *Mol. Cell. Biol.* **26**, 7005 (2006).
15. K. C. Thome *et al.*, *J. Biol. Chem.* **275**, 35233 (2000).
16. A. Smogorzewska *et al.*, *Cell* **129**, 289 (2007).
17. C. M. Azzalin, J. Lingner, *Curr. Biol.* **16**, 433 (2006).
18. H. Huang, K. M. Regan, Z. Lou, J. Chen, D. J. Tindall, *Science* **314**, 294 (2006).
19. N. Yoshizawa-Sugata, H. Masai, *J. Biol. Chem.* **282**, 2729 (2006).
20. H. Y. Yoo, A. Shevchenko, W. G. Dunphy, *J. Biol. Chem.* **279**, 53353 (2004).
21. B. Xia *et al.*, *Mol. Cell* **22**, 719 (2006).
22. R. Groisman *et al.*, *Cell* **113**, 357 (2003).
23. A. Hirao *et al.*, *Science* **287**, 1824 (2000).
24. P. T. Yazdi *et al.*, *Genes Dev.* **16**, 571 (2002).
25. S. T. Kim, B. Xu, M. B. Kastan, *Genes Dev.* **16**, 560 (2002).
26. D. Q. Yang, M. B. Kastan, *Nat. Cell Biol.* **2**, 893 (2000).
27. L. J. Niedernhofer *et al.*, *Nature* **444**, 1038 (2006).
28. K. M. Brumbaugh *et al.*, *Mol. Cell* **14**, 585 (2004).
29. B. Wang *et al.*, *Science* **316**, 1194 (2007).
30. Single-letter abbreviations for the amino acid residues are as follows: A, Ala; C, Cys; D, Asp; E, Glu; F, Phe; G, Gly; H, His; I, Ile; K, Lys; L, Leu; M, Met; N, Asn; P, Pro; Q, Gln; R, Arg; S, Ser; T, Thr; V, Val; W, Trp; and Y, Tyr.
31. B. A. Ballif, Z. Cao, D. Schwartz, K. L. Carraway III, S. P. Gygi, *J. Proteome Res.* **5**, 2372 (2006).
32. B. DeLaBarre, A. T. Brunger, *Nat. Struct. Biol.* **10**, 856 (2003).

33. We thank T. de Lange, A. D'Andrea, A. Carr, K. Nakanishi, M. Jasin, H. Takai, F. Graham, D. Zhang, D. Chou, B. Wang, M. Naylor, J.-M. Li, D. Lee, C. Zhou, and C. Cotta-Ramusino for reagents and advice; J. Qin for antibodies and sharing unpublished data; K. Matsuoka for helping with preparation of figures; and P. Park and Q. Xu for help with the bioinformatic analysis. A.S. is supported by T32CA09216 to the Pathology Department at the Massachusetts General Hospital. K.E.H. is a Leukemia and Lymphoma Society Special Fellow. This work was supported by grants from NIH, including National Institute of Allergy and Infectious Diseases 1U19A1067751 (S.J.E.), and Department of Defense (S.J.E. and S.P.G.) and by the A-T (Ataxia-Telangiectasia) Medical Research Foundation, the A-T Children's Project, the Israel Science Foundation, the A-T Medical Research Trust, the Israel-Germany Joint Program on Cancer Research, the German Cancer Center DKFZ (Deutsches Krebsforschungszentrum), and the A-T Ease Foundation (Y.S.). S.J.E. is an investigator with the Howard Hughes Medical Institute.

Supporting Online Material

www.sciencemag.org/cgi/content/full/316/5828/1160/DC1
Materials and Methods
Figs. S1 to S7
Tables S1 to S10
References

24 January 2007; accepted 6 April 2007
10.1126/science.1140321

REPORTS

Missing Mass in Collisional Debris from Galaxies

Frédéric Bournaud,[1]* Pierre-Alain Duc,[1] Elias Brinks,[2] Médéric Boquien,[1] Philippe Amram,[3] Ute Lisenfeld,[4,5] Bärbel S. Koribalski,[6] Fabian Walter,[7] Vassilis Charmandaris[8,9,10]

Recycled dwarf galaxies can form in the collisional debris of massive galaxies. Theoretical models predict that, contrary to classical galaxies, these recycled galaxies should be free of nonbaryonic dark matter. By analyzing the observed gas kinematics of such recycled galaxies with the help of a numerical model, we demonstrate that they do contain a massive dark component amounting to about twice the visible matter. Staying within the standard cosmological framework, this result most likely indicates the presence of large amounts of unseen, presumably cold, molecular gas. This additional mass should be present in the disks of their progenitor spiral galaxies, accounting for a substantial part of the so-called missing baryons.

When galaxies collide, gravitational forces cause the expulsion of material from their disks into the intergalactic medium. In this debris, dense self-gravitating structures form. Because they can reach masses typical of those of dwarf galaxies and they show ordered rotation and active star formation (*1*–*8*), they deserve to be considered galaxies in their own right, albeit "recycled" ones. Whether these recycled dwarf galaxies contain dark matter can put strong constraints on the nature and distribution of this enigmatic constituent of the Universe. Indeed, standard theory (*9*–*11*) predicts that they differ from classical galaxies by being nearly free of nonbaryonic dark matter (*5*, *7*, *12*). According to the widely accepted ΛCDM (cold dark matter with cosmological constant) model (*13*), the matter density of the Universe is dominated by nonbaryonic dark matter. This matter is expected to surround galaxies in the form of large halos supported by random motions (*9*). Recycled galaxies are expected to have little, if any, dark matter of this type, because only material from rotating disks is involved in the galactic recycling process. In addition to nonbaryonic dark matter, part of the baryonic component is "dark" as well [i.e., it is known to have existed in the early Universe (*14*), but it is hard or impossible to detect locally today]. It has been speculated to be cold gas (*15*, *16*) but is most widely thought to reside in a diffuse warm-hot intergalactic medium (WHIM) that surrounds galaxies (*10*, *11*) and that cannot be substantially accumulated in collisional debris. Hence, recycled dwarf galaxies are predicted by conventional views to be mostly free of both baryonic and nonbaryonic dark matter. We put these views to the test, measuring the mass of three galaxies formed in the collisional debris around galaxy NGC5291 (*17*, *18*).

The galaxy NGC5291 is surrounded by a large, gas-rich ring of collisional debris (*17*). In several places, gas has gathered into self-gravitating, rotating dwarf galaxies where new stars form (Fig. 1). We studied the kinematics of atomic hydrogen in the ring through its 21-cm emission line, using the National Radio Astronomy Observatory (*19*) Very Large Array (VLA) interferometer in a high-resolution configuration. We estimated the mass actually present in the dwarf galaxies and compared this to their visible mass (*6*, *18*, *20*, *21*). We used *N*-body simulations that model the gravitational dynamics of stars, gas, and dark matter halos, with 1 million particles for each component. The model also accounts for energy dissipation in the interstellar gas, and the onset of star formation (*22*), reproducing both the global morphology of the NGC5291 system and the formation of recycled dwarf galaxies in it. These simulations enable us to date the formation of the system and to study its three-dimensional morphology. According to our model (*23*), the ring formed during a galaxy collision 360 million years ago and is seen inclined by 45° from the line of sight (Fig. 1 and figs. S1 and S2).

[1]Laboratoire Astrophysique des Interactions Multi-Echelles, Commissariat à l'Energie Atomique (CEA) Direction des Sciences de la Matière–CNRS–Université Paris Diderot, Laboratoire de recherches sur les lois fondamentales de l'Univers (Dapnia)/Service d'Astrophysique, CEA/Saclay, F-91191 Gif-sur-Yvette Cedex, France. [2]Centre for Astrophysics Research, University of Hertfordshire, College Lane, Hatfield, AL10 9AB, UK. [3]Observatoire Astronomique Marseille-Provence, Laboratoire d'Astrophysique de Marseille UMR 6110, 2 place Le Verrier, F-13248 Marseille Cedex 4, France. [4]Departamento Física Teórica y del Cosmos, Universidad de Granada, Spain. [5]Instituto de Astrofísica de Andalucía (CSIC), Post Office Box 3004, 18080 Granada, Spain. [6]Commonwealth Scientific and Industrial Research Organisation (CSIRD), Australia Telescope National Facility (ATNF), Post Office Box 76, Epping NSW 1710, Australia. [7]Max Planck Institut für Astronomie, Königstuhl 17, 69117 Heidelberg, Germany. [8]Department of Physics, University of Crete, GR-71003 Heraklion, Greece. [9]Foundation for Research and Technology (IESL), Hellas, GR-71110, Heraklion, Greece. [10]Observatoire de Paris, F-75014, Paris, France.

*To whom correspondence should be addressed. E-mail: frederic.bournaud@cea.fr

The rotation curve of a galaxy traces the rotational velocity of the disk as a function of radius and provides a direct measure of the total (visible and dark) mass within that radius. We used our VLA observations to derive the rotation curves of three recycled dwarf galaxies around NGC5291 and compared the mass inferred this way with their visible mass. The most luminous recycled galaxy in this system, NGC5291N, contains 5.7×10^8 solar masses ($M_\odot$) of atomic gas, 2×10^8 $M_\odot$ of molecular gas traced by the emission of the CO molecule, and 1.1×10^8 $M_\odot$ of stars. We hence derived a total visible mass of $8.8 \times 10^8 \pm 1 \times 10^8$ $M_\odot$ (where error is SD) inside a radius of 3.7 kpc. The VLA data revealed a velocity gradient tracing the rotation of the object up to radii of ~4.5 kpc (Fig. 2 and fig. S3). The rotational velocity, corrected for inclination as indicated by our model, is 70 km s^{-1} at a radius of 3.2 kpc, implying that the mass actually present in the system—the so-called dynamical mass—is $30 \times 10^8 \pm 8.6 \times 10^8$ $M_\odot$. The error bar accounts for the noise in the data and various uncertainties entering the method for determining the mass (*23*). This system evidently contains an unseen component that accounts for about twice the visible mass. The visible mass is insufficient to explain not only the high rotational velocity but also the flat rotation curve; the rotational velocity remains constant beyond the radius at which the visible material is concentrated (Fig. 2).

In the second-brightest object, NGC5291S, the visible mass is $9.3 \times 10^8 \pm 1 \times 10^8$ $M_\odot$, whereas its dynamical mass is $27 \times 10^8 \pm 8.5 \times 10^8$ $M_\odot$. This object must contain a dark component as well, also with about twice the mass of the visible matter. The data on the third-most-massive object (NGC5291SW) lead to a similar dark-to-visible mass ratio, with a visible mass of $5 \times 10^8 \pm 1.5 \times 10^8$ $M_\odot$ and a dynamical mass of $12 \times 10^8 \pm 4.5 \times 10^8$ $M_\odot$, albeit with larger uncertainties. The other recycled objects in this system are less massive, resulting in error bars that are too large to serve the purpose of constraining the dynamical mass.

It is possible to derive dynamical masses of galaxies from their rotational velocity even when they are barely resolved (*24*), provided that some assumptions are met; in particular, the gas must be in equilibrium and move on quasi-circular orbits. It is therefore important to ascertain that the rotation curves of the recycled dwarfs are not affected by velocity anomalies that result from their young age or the presence of the massive progenitor. The symmetrical rotation pattern already serves as evidence that these objects are rotationally supported and close to equilibrium. To further assess the validity of our results, we applied the same analysis to the dwarf galaxies formed in our numerical simulations. These simulations resolve the internal structure of the dwarf galaxies, including their spiral arms (fig. S7) and indicate that the galaxies have reached a state of rotationally supported equilibrium (fig. S4). The kinematics of the galaxies was analyzed at the same resolution as that of the observations, and we verified that their mass could be retrieved with the required accuracy. Thus, the large observed velocities cannot be caused by any velocity anomalies, and our analysis indicates the presence of a dark component at a confidence level of 98% for both NGC5291N and NGC5291S (*25*) and 95% for NGC5291SW (Fig. 3).

That recycled dwarf galaxies contain a massive unseen component of about twice the visible mass is surprising, even if they do not contain as much dark mass as classical, first-generation, dwarf galaxies (*2*, *6*), for which dark-to-visible mass ratios can be as large as 10 (*26*). Within standard paradigms, recycled galaxies were expected to contain at most a few percent (*12*) of dark matter. This is corroborated by our simulations, which were conducted within the standard framework of all dark matter in spheroidal halos and none in the disks of spiral galaxies; the rotational velocities predicted this way in recycled dwarfs differ from the those that were observed (figs. S6 and S7), which confirms that an additional dark component is required in the observed system. If this dark mass were nonbaryonic, its properties would have to differ from the prevailing CDM model. Only material initially in a rotating disk in the progenitor galaxy can participate in the creation of recycled dwarfs, whereas CDM resides in nonrotating spheroidal halos. Given the success of ΛCDM scenarios in explaining the large-scale structure of the Universe (*27*), we are inclined to consider that the unseen matter in recycled dwarf galaxies is more likely baryonic. This would imply that the "missing baryons" do not all reside in the WHIM; hot gas forms diffuse halos that do not provide material to the recycled galaxies. A substantial fraction of dark baryons would then be located in a (potentially thick) disk. This cannot be in the form of low-luminosity old stars, which are

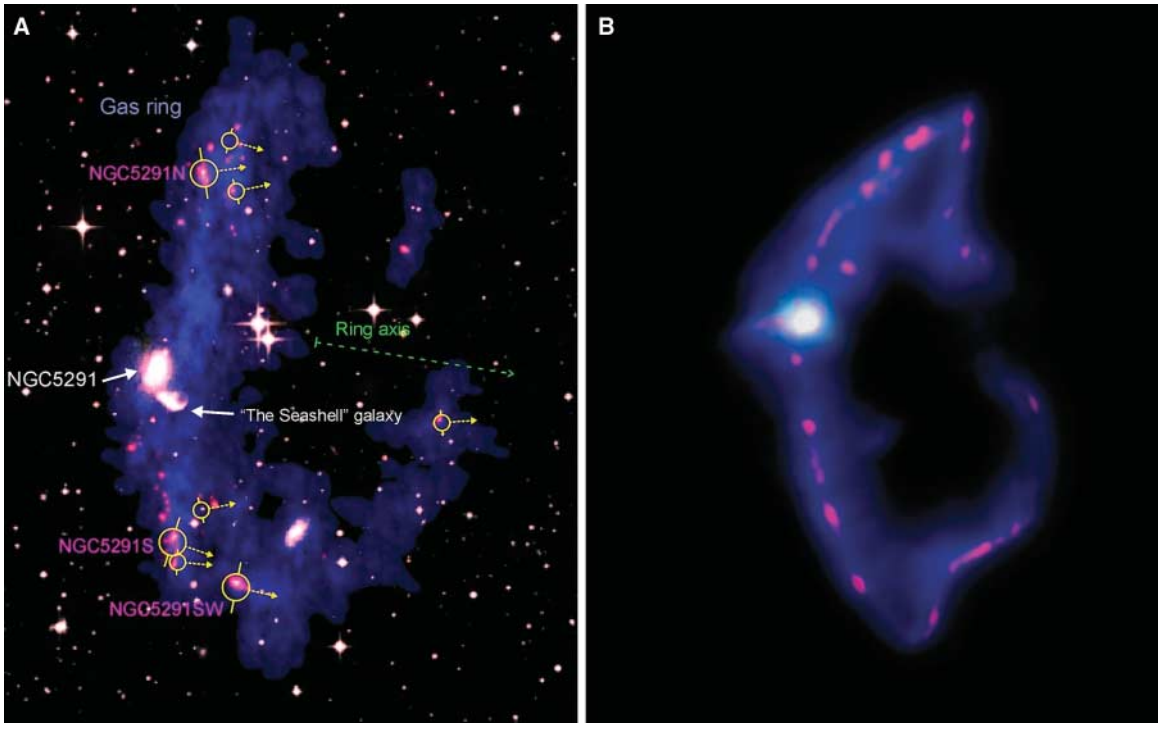

Fig. 1. Gas ring and recycled dwarf galaxies around NGC5291. (**A**) VLA atomic hydrogen 21-cm map (blue) superimposed on an optical image (white). The ultraviolet emission observed by Galaxy Evolution Explorer (pink) traces dense star-forming concentrations. The most massive of these objects are rotating with the projected spin axis as indicated by arrows. In the three most massive companions, we quantify the rotation and estimate their mass content. (**B**) Numerical simulation of a galaxy collision that has led to the formation of a similar system in which the central galaxy is the progenitor of a large, asymmetrical, and partial ring. Self-gravitating clumps have assembled within the ring to become new dwarf galaxies. The ring is seen projected at an angle of 45° from the line of sight. The recycled dwarf galaxies have individual rotation axes closely aligned with that of the large-scale ring axis, which indicates that they are also inclined by 45°.

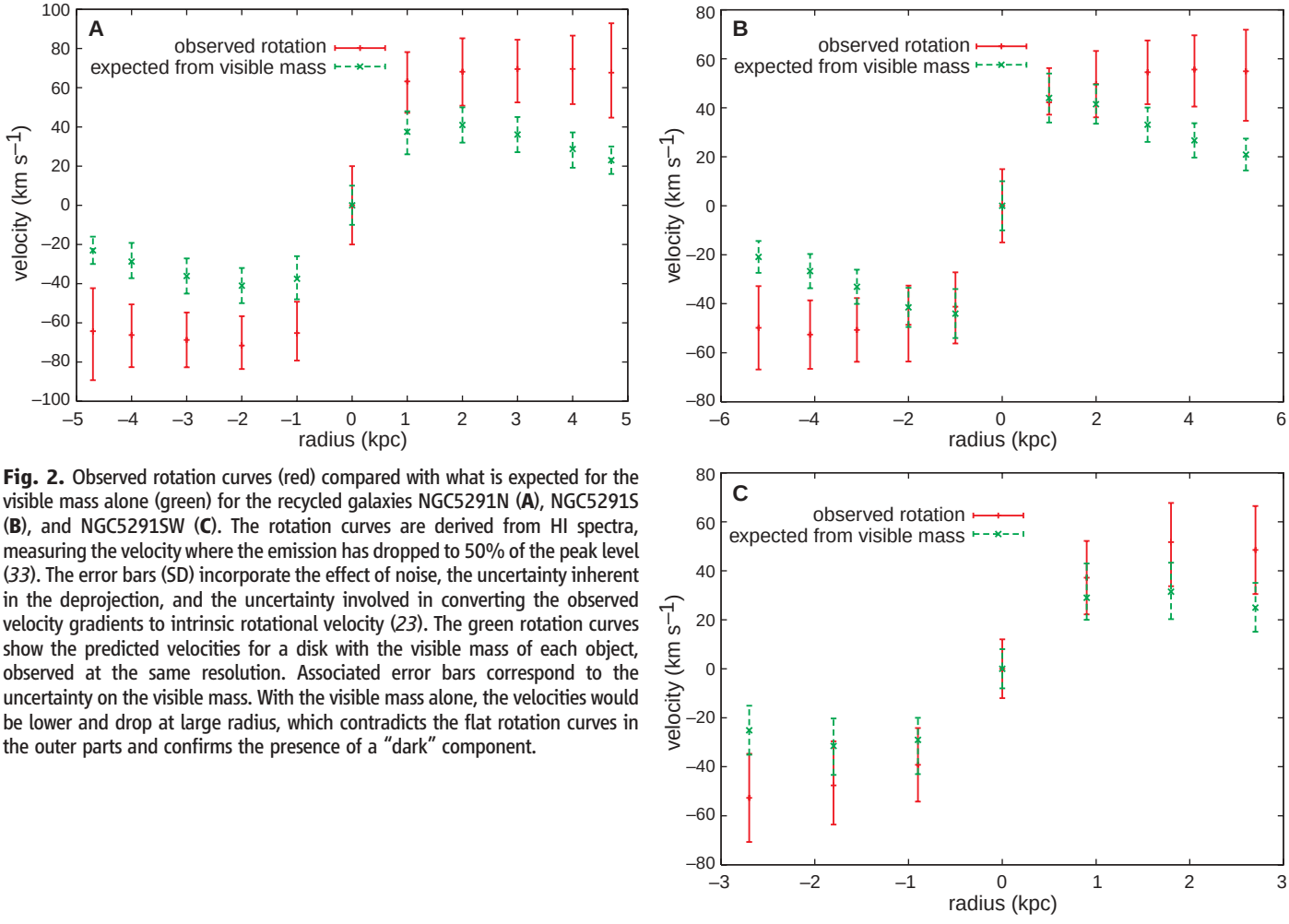

Fig. 2. Observed rotation curves (red) compared with what is expected for the visible mass alone (green) for the recycled galaxies NGC5291N (**A**), NGC5291S (**B**), and NGC5291SW (**C**). The rotation curves are derived from HI spectra, measuring the velocity where the emission has dropped to 50% of the peak level (*33*). The error bars (SD) incorporate the effect of noise, the uncertainty inherent in the deprojection, and the uncertainty involved in converting the observed velocity gradients to intrinsic rotational velocity (*23*). The green rotation curves show the predicted velocities for a disk with the visible mass of each object, observed at the same resolution. Associated error bars correspond to the uncertainty on the visible mass. With the visible mass alone, the velocities would be lower and drop at large radius, which contradicts the flat rotation curves in the outer parts and confirms the presence of a "dark" component.

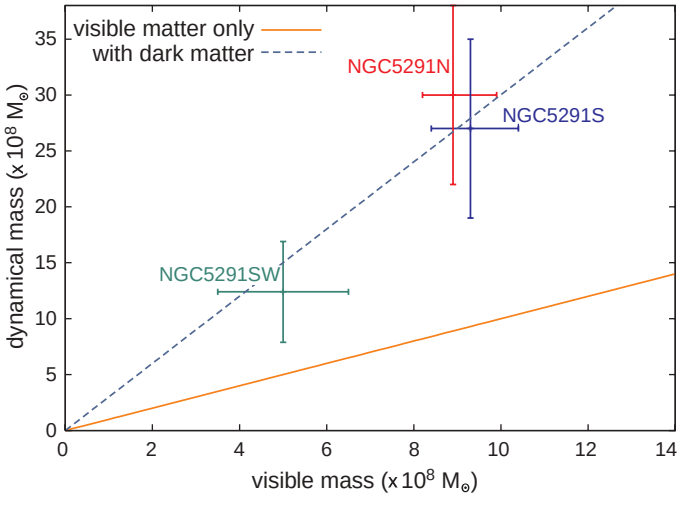

Fig. 3. Visible and dynamical masses of three recycled galaxies. Objects free of dark matter would follow the orange full line. The three systems show a similar trend with a dark mass about twice that of the visible mass inside the same radius. The error bars (SD) for both axes are indicated. The similar result obtained on three objects makes the overall confidence level (*25*) in the detection of dark matter greater than 99%.

known to be absent from the dwarf galaxies around NGC5291 (*28*). The most likely candidate is hydrogen in dense molecular form. The H_2 molecule cannot be directly observed but is usually traced by emission lines of the carbon monoxide (CO) molecule. The emission from CO can be converted to a molecular gas mass (*29*) with the use of a conversion factor that is expected to depend on the heavy element abundance (metallicity) of the gas (*30*). Here, we used the usual conversion factor derived in our Galaxy for gas with solar metallicity. The metallicity of the recycled galaxies in NGC5291 is about half solar (*18*), similar to that encountered in the outer regions of spiral galaxies where the conversion factor could change (*31*, *32*) by factors of typically 2, or at most 3. To account for the missing mass in the recycled galaxies, however, a change of at least a factor of 10 would be needed. This means we would be dealing either with cool H_2, traced by the CO molecule but much less efficiently than generally assumed, or with a sizeable fraction of cold H_2 not traced at all by CO (*15*).

Collisional debris from galaxies hence appears to contain twice as much unseen matter as visible matter. Although this result could be explained by a modification of Newtonian gravity, it more likely indicates that a substantial amount of dark matter resides within the disks of spiral galaxies. The most natural candidate is molecular hydrogen in some hard-to-trace form. Further simulations including this form of dark matter and comparison with higher-resolution observations of recycled galaxies will be required to directly constrain the exact properties of this unseen component.

References and Notes

1. I. F. Mirabel, H. Dottori, D. Lutz, *Astron. Astrophys.* **256**, L19 (1992).
2. J. Braine, U. Lisenfeld, P.-A. Duc, S. Leon, *Nature* **403**, 867 (2000).
3. P.-A. Duc *et al.*, *Astron. J.* **120**, 1238 (2000).
4. B. G. Elmegreen, M. Kaufman, M. Thomasson, *Astrophys. J.* **412**, 90 (1993).
5. J. E. Barnes, L. Hernquist, *Nature* **360**, 715 (1992).

6. F. Bournaud, P.-A. Duc, P. Amram, F. Combes, J.-L. Gach, *Astron. Astrophys.* **425**, 813 (2004).
7. P.-A. Duc, F. Bournaud, F. Masset, *Astron. Astrophys.* **427**, 803 (2004).
8. C. Mendes de Oliveira, H. Plana, P. Amram, C. Balkowski, M. Bolte, *Astron. J.* **121**, 2524 (2001).
9. J. F. Navarro, C. S. Frenk, S. D. M. White, *Astropys. J.* **462**, 563 (1996).
10. F. Nicastro *et al.*, *Nature* **433**, 495 (2005).
11. R. Cen, J. P. Ostriker, *Astrophys. J.* **650**, 560 (2006).
12. F. Bournaud, P.-A. Duc, *Astron. Astrophys.* **456**, 481 (2006).
13. D. N. Spergel *et al.*, *Astrophys. J.* **148** (Supp.), 175 (2003).
14. M. Rauch, *Annu. Rev. Astron. Astrophys.* **36**, 267 (1998).
15. D. Pfenniger, F. Combes, L. Martinet, *Astron. Astrophys.* **285**, 79 (1994).
16. I. A. Grenier, J.-M. Casandjian, R. Terrier, *Science* **307**, 1292 (2005).
17. B. K. Malphrus, C. E. Simpson, S. T. Gottesman, T. G. Hawarden, *Astron. J.* **114**, 1427 (1997).
18. P.-A. Duc, I. F. Mirabel, *Astron. Astrophys.* **333**, 813 (1998).
19. The National Radio Astronomy Observatory is a facility of the NSF operated under cooperative agreement by Associated Universities, Inc.
20. J. Braine *et al.*, *Astron. Astrophys.* **378**, 51 (2001).
21. S. J. Higdon, J. L. Higdon, J. Marshall, *Astrophys. J.* **640**, 768 (2006).
22. F. Bournaud, F. Combes, *Astron. Astrophys.* **401**, 817 (2003).
23. Materials and methods are available as supporting material on *Science* Online.
24. H. Flores, F. Hammer, M. Puech, P. Amram, C. Balkowski, *Astron. Astrophys.* **455**, 107 (2006).
25. The confidence level is evaluated assimilating the uncertainties on all parameters and on the method itself (assuming Gaussian statistics) and combining them as independent variables.
26. M. L. Mateo, *Annu. Rev. Astron. Astrophys.* **36**, 435 (1998).
27. V. Springel, C. S. Frenk, S. D. M. White, *Nature* **440**, 1137 (2006).
28. M. Boquien *et al.*, *Astron. Astrophys.* **467**, 93 (2007).
29. L. J. Sage, S. N. Shore, P. M. Solomon, *Astrophys. J.* **351**, 422 (1990).
30. P. Maloney, J. H. Black, *Astrophys. J.* **325**, 389 (1988).
31. J. Braine, F. Herpin, *Nature* **432**, 369 (2004).
32. F. P. Israël *et al.*, *Astron. Astrophys.* **406**, 817 (2003).
33. J. L. Donley *et al.*, *Mon. Not. R. Astron. Soc.* **369**, 1741 (2006).

34. The numerical simulations were carried out at CEA/Centre de Calcul Recherche et Technologie and CNRS/Institute du Développement et des Ressources en Informatique Scientifique. Numerical models have benefited from input from the collaboration HORIZON, and we thank F. Combes and R. Teyssier. We thank J. Braine, P. Weilbacher, I. Grenier, Y. Revaz, F. Boulanger, and F. Hammer for valuable comments on the dynamical analysis and/or general results. We made use of data from the Digitized Sky Survey, produced at the Space Telescope Science Institute under U.S. Government grant NAG W-2166.

Supporting Online Material

www.sciencemag.org/cgi/content/full/1142114/DC1
Materials and Methods
Figs. S1 to S8
Table S1
References

5 March 2007; accepted 20 April 2007
Published online 10 May 2007;
10.1126/science.1142114
Include this information when citing this paper.

An On-Demand Coherent Single-Electron Source

G. Fève,[1] A. Mahé,[1] J.-M. Berroir,[1] T. Kontos,[1] B. Plaçais,[1] D. C. Glattli,[1,2]* A. Cavanna,[3] B. Etienne,[3] Y. Jin[3]

We report on the electron analog of the single-photon gun. On-demand single-electron injection in a quantum conductor was obtained using a quantum dot connected to the conductor via a tunnel barrier. Electron emission was triggered by the application of a potential step that compensated for the dot-charging energy. Depending on the barrier transparency, the quantum emission time ranged from 0.1 to 10 nanoseconds. The single-electron source should prove useful for the use of quantum bits in ballistic conductors. Additionally, periodic sequences of single-electron emission and absorption generate a quantized alternating current.

In quantum optics, a single-photon source is an essential building block for the manipulation of the smallest amount of information coded by a quantum state: a qubit (*1*, *2*). Combined with beam splitters, polarizers, and projective measurements, several photonic qubits can be manipulated to process quantum information (*3*). The most celebrated case is the secure transmission of information by means of quantum cryptography. Similarly, one expects that electrons propagating ballistically in ultrapure low-dimensional conductors can perform quantum logic tasks in perfect analogy with photons propagating in optical media (*4*–*6*). The analogy has a long history (*7*) and has provided illuminating comparisons between the intensity of light and that of electrical current; between photon noise and electrical shot noise (*8*, *9*); and, more recently, between photon and electron quantum entanglement (*10*–*12*). Because electrons are fermions, entanglement offers new routes not possible with photons (*12*). Practically, electronic analogs of beam splitters and Fabry-Pérot and Mach-Zehnder interferometers (*13*, *14*) have been used in ballistic conductors, providing the necessary quantum gate for an all-linear electron optics quantum computation. Yet missing were a single-electron source and a single-electron detector (*15*) suitable for coherent emission and projective measurements. The former initializes quantum states, whereas the latter reads the final states after electrons have passed through the quantum gates.

Unlike the case of photons, the creation of single-electron sources is expected to be simpler because of Fermi statistics and Coulomb interaction. For example, considering a voltage-biased single-mode conductor, a contact at energy eV above the energy of the other contact is known to inject single electrons into the conductor at a regular rate eV/h, thereby leading to the quantization of dc conductance in quantum point contacts (QPCs) (*16*, *17*). A second example is the electron pump, in which a dc current is produced by sequential time-controlled transfer of single electrons between metallic islands in series (*18*, *19*) or by the manipulation of tunnel barriers of quantum dots (*20*, *21*). The cost in Coulomb charging energy to add or remove an electron ensures a well-defined electron number in each island or dot. These two sources are, however, not useful for quantum information. In the first case, there is no time control of the electron injection. Because only statistical measurements are possible, the biased contact is suitable for demonstrating coherent phenomena such as interferences or electron entanglement (*10*, *11*) but not for manipulating quantum information. In the second example, time-controlled injection can be realized, but the energy of emitted electrons is expected to spread, at random, in an energy range much larger than the tunneling rate (typically a fraction of the charging energy, depending on the pumping conditions). The statistical distribution in energy will smear the coherent effects required for manipulating the quantum information. Finally, a third approach has been theoretically proposed in (*22*–*24*), considering voltage pulses $V(t)$ applied to an ohmic contact. When the Faraday flux $e\int V(t')dt'/h$ is an integer, an integer number of electrons is injected. Here noiseless injection requires that the pulses have a special Lorenzian shape and exact integer Faraday flux, otherwise logarithmic divergence of the charge fluctuations occurs. No experiment is available yet to test these ideas.

We report here on the realization of a time-controlled single-electron source suitable for the coherent manipulation of ballistic electronic qubits, which emits the electrons into a well-defined quantum state. The injection scheme is different from those considered above. The source is made of a quantum dot, realized in a two-dimensional (2D) electron gas in gallium arsenide (GaAs) semiconductors and tunnel-coupled to the conductor through a QPC. By application of a sudden voltage step on a capacitively coupled gate, the charging energy is

[1]Laboratoire Pierre Aigrain, Département de Physique de l'Ecole Normale Supérieure, 24 rue Lhomond, 75231 Paris Cedex 05, France. [2]Service de Physique de l'Etat Condensé, CEA Saclay, F-91191 Gif-sur-Yvette, France. [3]Laboratoire de Photonique et Nanostructures, UPR20 CNRS, Route de Nozay, 91460 Marcoussis Cedex, France.

*To whom correspondence should be addressed. E-mail: glattli@lpa.ens.fr

compensated for and the electron occupying the highest energy level of the dot is emitted. The final state of the electron is a coherent wave packet propagating away in the conductor. Its energy width is given by the inverse tunneling time, as required for an on-demand single-particle source, and is independent of temperature. Its mean energy can be adjusted above the Fermi energy by tuning the voltage step amplitude. The circuit (Fig. 1A), is realized in a 2D electron gas in a GaAsAl/GaAs heterojunction of nominal density $n_s = 1.7 \times 10^{15}$ m^{-2} and mobility $\mu = 260$ V^{-1} m^2 s^{-1}. The dot is electrostatically coupled to a metallic top gate, 100 nm above the 2D electron gas, whose ac voltage, V_{exc}, controls the dot potential at the subnanosecond time scale. For all measurements, the electronic temperature is about 200 mK and a magnetic field $B \approx 1.3$ T is applied to the sample so as to work in the quantum Hall regime with no spin degeneracy. The QPC dc gate voltage V_G is tuned to control the transmission D of a single edge state as well as the dc dot potential. As reported (*25*), this circuit constitutes the paradigm of a quantum-coherent resistor-capacitor (RC) circuit, where coherence is seen to strongly affect the charge relaxation dynamics. From this study, the charging energy $\Delta + e^2/C \approx \Delta \approx 2.5$ K was extracted (*26*). Here the large top-gate capacitance makes the Coulomb energy e^2/C unusually small, and the total charging energy reduces to the energy-level spacing Δ.

In (*25*), the linear response of the current to the ac top-gate voltage was investigated, and the ac charge amplitude was much lower than the elementary charge e. In order to achieve single-charge injection, we had to apply a high-amplitude excitation ($V_{exc} \sim \Delta/e$) and go beyond the linear regime. When an electron is suddenly brought above the Fermi energy of the lead, it is expected to escape the dot at a typical tunnel rate $\tau^{-1} = D\Delta/h$, where Δ/h is the attempt frequency and D is the transmission probability. This gives nanosecond time scales, for which single-charge detection is still out of reach experimentally. To increase the signal-to-noise ratio, a statistical average over many individual events is used by generating repetitive sequences of single-electron emission followed by single-electron absorption (or hole emission) as shown in Fig. 1A. This is done by applying a periodic square wave voltage amplitude $\approx \Delta/e$ to the top gate. Figure 1B shows typical temporal traces of the current averaged over a few seconds for a repetition period of $T = 32$ ns. The single-electron events reconstruct the exponential current decay of an RC circuit. When transmission D is decreased from ≈0.03 to ≈0.002, the relaxation time τ, extracted from the exponential decay, increases from 0.9 to 10 ns. For the two highest transmissions in Fig. 1B, $\tau \ll T/2$, the current decays to zero, and the mean transferred charge per half period is constant. For the smallest transmission, $\tau \sim T/2$, the mean emitted charge decreases because electrons have reduced probability of escaping the dot. These time-domain measurements are limited by the 1-GHz bandwidth of the acquisition card and give access to the few-nanosecond injection times corresponding to small transmissions $D \lesssim 0.03$.

In order to get a better understanding of the above results, we extend the harmonic linear re-

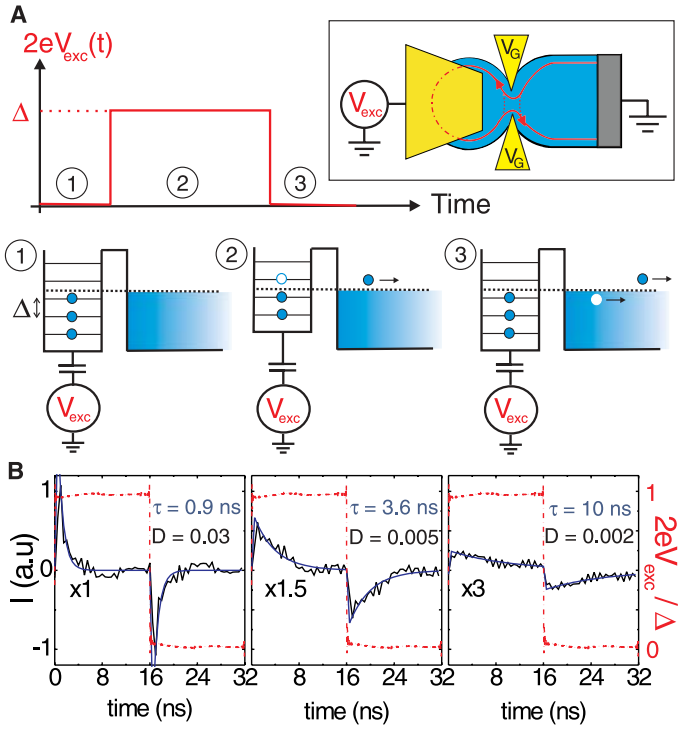

Fig. 1. Single-charge injection. (**A**) Schematic of single-charge injection. Starting from an antiresonant situation where the Fermi energy lies between two energy levels of the dot (step 1), the dot potential is increased by Δ moving one occupied level above the Fermi energy (step 2). One electron then escapes the dot on the mean time $\tau = h/D\Delta$. The dot potential is then brought back to its initial value (step 3), where one electron can enter it, leaving a hole in the Fermi sea. (Inset at right) The quantum RC circuit: one edge channel is transmitted inside the submicrometer dot, with transmission D tuned by the QPC gate voltage V_G. The dot potential is varied by a radio-frequency excitation V_{exc} applied on a macroscopic gate located on top of the dot. The electrostatic potential can also be tuned by V_G because of the electrostatic coupling between the dot and the QPC. (**B**) Time-domain measurement of the average current (black curves) on one period of the excitation signal (red curves) at $2eV_{exc} = \Delta$ for three values of the transmission D. The relaxation time τ is deduced from an exponential fit (blue curve).

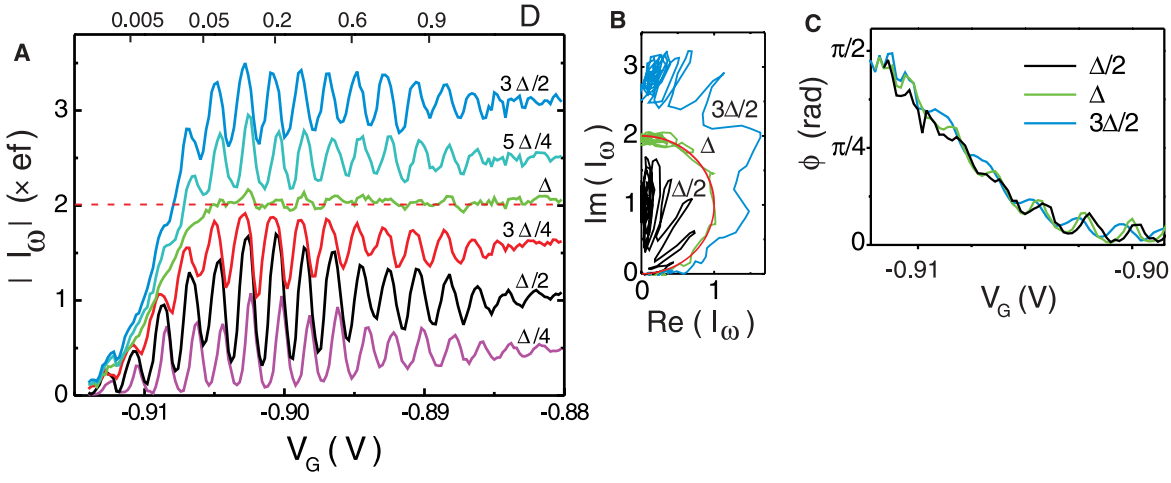

Fig. 2. I_ω as a function of V_G at $f = 180$ MHz for different values of the excitation amplitude $2eV_{exc}$. Transmission D is also indicated. (**A**) Modulus $|I_\omega|$. The horizontal dashed line is the constant value $|I_\omega| = 2ef$. (**B**) Nyquist representation (imaginary part of I_ω versus real part of I_ω). The red curve corresponds to an RC circuit of constant capacitance e^2/Δ and varying resistance. (**C**) Phase ϕ. The phase ϕ is independent of V_{exc}.

sponse theory of a quantum RC circuit (*27*–*29*) to calculate the nonlinear response to a high-amplitude square excitation voltage ($eV_{exc} >> hf$). Calculation shows that the circuit still behaves as an RC circuit with a current given by

$$I(t) = \frac{q}{\tau} e^{-t/\tau} \text{ for } 0 \le \tau \le T/2 \quad (1)$$

$$q = e \int d\varepsilon N(\varepsilon)[f(\varepsilon - 2eV_{exc}) - f(\varepsilon)] \quad (2)$$

$$\tau = \frac{h}{2} \frac{\int d\varepsilon N(\varepsilon)^2 [f(\varepsilon - 2eV_{exc}) - f(\varepsilon)]}{\int d\varepsilon N(\varepsilon)[f(\varepsilon - 2eV_{exc}) - f(\varepsilon)]} \quad (3)$$

where $N(\varepsilon)$ is the dot density of states and $f(\varepsilon)$ denotes the Fermi-Dirac distribution. The nonlinear capacitance and charge relaxation resistance can be defined respectively by $\tilde{C}_q \equiv q/2V_{exc}$ and $\tilde{R}_q \equiv \tau/\tilde{C}_q$. For unit transmission $D = 1$, electrons are fully delocalized, $N(\varepsilon)$ is uniform, and the charge q evolves linearly with V_{exc} as expected. In contrast, for low transmission, $N(\varepsilon)$ is sharply peaked on well-resolved energy levels, and q exhibits a staircase dependence on V_{exc}, with steep steps whenever one electronic level is brought above the Fermi energy. Thus, our calculations establish the process of single-electron injection depicted in Fig. 1. For a dot energy spectrum with constant level spacing Δ, a remarkable situation occurs when $2eV_{exc} = \Delta$, as $q = e$ and $\tilde{C}_q = e^2/\Delta$ irrespective of the transmission D and of the dc dot potential. As a matter of fact, Eq. 2 shows that, in these conditions, q is given by integrating $N(\varepsilon)$ over exactly one level spacing. For $D << 1$, we recover the Landauer formula for the resistance $\tilde{R}_q = h/De^2$, and the escape time is given by $\tau = h/D\Delta$, as expected from a semiclassical approach. The exponential current decay, the constant injection charge for $\tau << T/2$, and the decrease of τ with transmission D account well for our experimental observations in Fig. 1B.

For a more accurate experimental determination of q and τ and to investigate subnanosecond time scales, we consider in the following measurements the current first harmonic I_ω at higher frequencies $f = \omega/2\pi = 1/T$. Following Eq. 1, we have

$$I_\omega = \frac{2qf}{1 - i\omega\tau} \quad (4)$$

so that the modulus $|I_\omega|$ and the phase ϕ [$\tan(\phi) = \omega\tau$] allow for the determination of q and τ.

Figure 2A shows $|I_\omega|$ measured as a function of QPC gate voltage V_G at $f = 180$ MHz for increasing values of the excitation voltage $2eV_{exc}$. The range of V_G maps the full transmission excursion $D = 0$ to 1. The low-excitation $2eV_{exc} = \Delta/4$ data nearly correspond to the linear response reported in (*25*). The current exhibits strong oscillations reflecting the variation with V_G of the dot density of states at the Fermi energy. At larger excitation voltages, the current peaks are broadened as expected from Eq. 2 when $2eV_{exc}$ gets larger than thermal energy (k_BT). For $2eV_{exc} = \Delta$, the oscillations disappear completely and $|I_\omega| = 2ef$, down to a low transmission threshold $D \sim 0.05$. The oscillations reappear for larger excitations. The constant current $|I_\omega| = 2ef$ is the frequency-domain counterpart of the constant charge regime observed in the time domain, for the injection and absorption of a single electron per half period. The cutoff observed for $D \lesssim 0.02$ corresponds to the limit $\omega\tau \gtrsim 1$, where the escape time τ exceeds $T/2$. The constant $\tilde{C}_q$ regime obtained for $2eV_{exc} = \Delta$ can be viewed in the Nyquist representation of Fig. 2B. The corresponding diagram is the half-circle that is characteristic of an RC circuit with a constant capacitance e^2/Δ and transmission-dependent resistance. In contrast, the curves obtained for larger or smaller excitations exhibit strong capacitance oscillations.

Figure 2C represents the phase $\phi = \arctan(\omega\tau)$ of the current as a function of V_G for different excitation voltages. ϕ shows a quasi-monotonic $\pi/2$ sweep in increasing transmission. The absence of residual oscillations proves that τ is nearly insensitive to the dot potential. As seen in Fig. 2C, τ is also independent of V_{exc}. In Fig. 3, we have gathered the values of $\tau(V_G)$ obtained from 1-GHz–bandwidth time-domain measurements at a 31.25-MHz repetition rate and from frequency-domain measurements at 180 and 515 MHz. The measurements probe a very broad transmission range ($D = 0.002$ to 0.2) corresponding to escape times varying from 10 ns to 100 ps. In the overlapping range, the different independent determinations coincide within error bars, agreeing quantitatively with the prediction $\tau = h/D\Delta$ also represented in Fig. 3, where the dependence $D(V_G)$ is deduced from the linear regime (*25*).

We now discuss the conditions for single-electron injection leading to a good quantization of the ac current as a figure of merit of single-charge injection. Figure 4A represents $|I_\omega|$ as function of V_{exc} for typical values of the dc dot potential at fixed transmissions $D \approx 0.2$ and

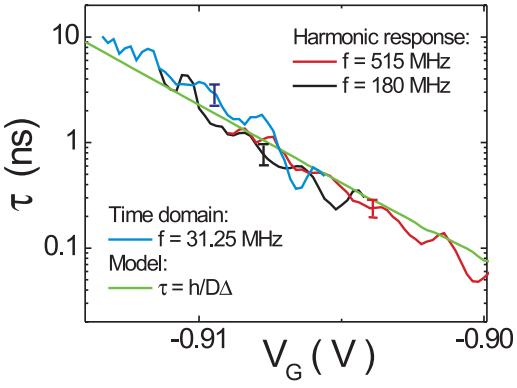

Fig. 3. Escape time τ on a logarithmic scale as a function of QPC gate voltage V_G: experiments (red, blue, and black curves) and model (green curve).

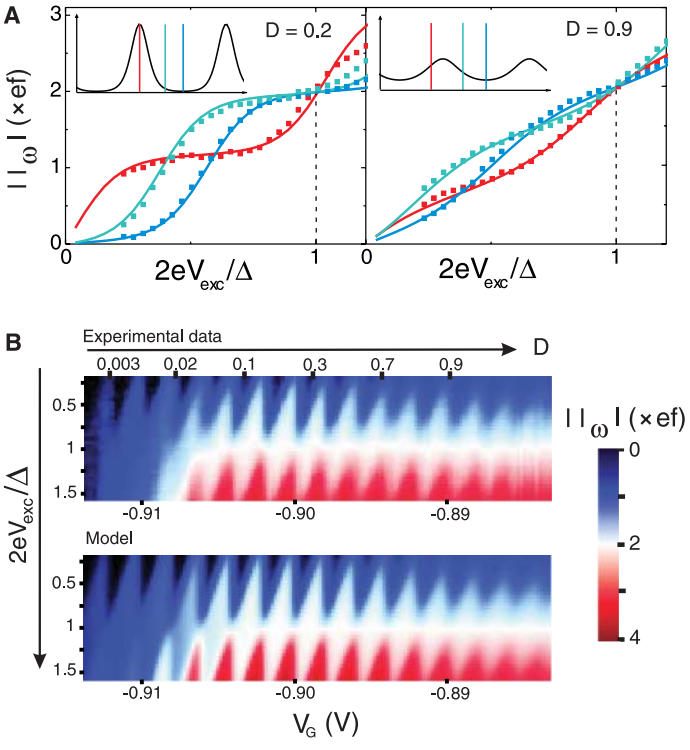

Fig. 4. Quantization of the ac current. (**A**) $|I_\omega|$ as a function of $2eV_{exc}/\Delta$ for different dot potentials at $D \approx 0.2$ (left) and $D \approx 0.9$ (right). Points correspond to experimental values and lines to theoretical predictions. (Insets) Schematic representation of the dot density of states $N(\varepsilon)$. The color bars indicate the dot potential for the corresponding experimental data. (**B**) Color plot of $|I_\omega|$ as a function of $2eV_{exc}/\Delta$ and V_G: experiments (top) and model (bottom).

$D \approx 0.9$. Transmission $D \approx 0.2$ is low enough for the electronic states to be well resolved, as shown in the inset of Fig. 4A (left), but is still large enough for the escape time to be shorter than $T/2$. When the Fermi energy lies exactly in the middle of a density-of-states valley, we observe a well-pronounced $|I_\omega| = 2ef$ current plateau centered on $2eV_{exc} = \Delta$. Whereas the current plateau resolution is noise-limited to better than 1% (for a 10-s acquisition time), the plateau value is determined with an uncertainty of 5% due to systematic calibration error. At this working point, the plateau is robust when the parameters are varied. In contrast, if the Fermi energy lies on a peak, there is still a current plateau, but its value is arbitrary and very sensitive to parameter variations. These two working points illustrate the importance of having a well-defined charge in the dot before injection. In the first case, the charge is well defined and suitable for charge injection. In the second case, the equilibrium dot charge fluctuates. In particular, when the energy level is exactly resonant with the Fermi energy, its mean occupation at equilibrium is 1/2 and the measured value of the plateau is $1/2 \times 2ef = ef$ (Fig. 4A, left). Thus, this working point is not suitable for a single-electron source. When transmission is increased, even for a suitable working point, the dot charge quantization can be lost because of quantum fluctuations. First, the width of the ac current plateaus decreases and finally nearly vanishes for $D \approx 0.9$. For different transmissions, all curves cross at $|I_\omega| = 2ef$ for $2eV_{exc} = \Delta$, reflecting the constant value of $\tilde{C}_q$ discussed above. Finally, domains of good charge quantization are best shown on the 2D color plot of Fig. 4B (top) where the modulus of the current is represented in a color scale. The vertical axis stands for the excitation voltage V_{exc} and the horizontal axis for the gate voltage V_G. The white diamonds correspond to large domains of constant current $|I_\omega| = 2ef$ suitable for single-electron injection. At high transmissions, the diamonds are blurred by dot charge fluctuations as discussed previously. At small transmissions, even when the dot charge quantization is good, current quantization is lost because of the long escape time $\omega\tau >> 1$, and the current goes to zero. At 180 MHz, optimal working conditions are obtained for $D \approx 0.2$. The experimental results in Fig. 4 are compared with our theoretical model (Eqs. 2 and 3) without any adjustable parameter (solid lines in Fig. 4A and lower plot in Fig. 4B) [we use the 1D modeling of our circuit (density of states, transmission, and dot-gates coupling) described in (*25*)]. The agreement between measurements and theoretical predictions is excellent, which shows that our single-electron source lends itself to quantitative modeling.

The availability of a coherent source of single electrons emitted on demand from a single energy level on nanosecond time scales opens the way for a new generation of experiments never possible before. Synchronization of similar sources could be used in the future to probe electron antibunching or electron entanglement in multilead conductors or to generate electronic flying qubits in ballistic conductors.

References and Notes

1. A. Imamoglu, Y. Yamamoto, *Phys. Rev. Lett.* **72**, 210 (1994).
2. N. Gisin, G. Ribordy, W. Tittel, H. Zbinden, *Rev. Mod. Phys.* **74**, 145 (2002).
3. P. Kok *et al.*, *Rev. Mod. Phys.* **79**, 135 (2007).
4. A. Bertoni, P. Bordone, R. Brunetti, C. Jacoboni, S. Reggiani, *Phys. Rev. Lett.* **84**, 5912 (2000).
5. R. Ionicioiu, G. Amaratunga, F. Udrea, *Int. J. Mod. Phys.* **15**, 125 (2001).
6. T. M. Stace, C. H. W. Barnes, G. J. Milburn, *Phys. Rev. Lett.* **93**, 126804 (2004).
7. W. van Haeringen, D. Lenstra, *Analogies in Optics and Micro Electronics* (Kluwer, Dordrecht, Netherlands, 1990).
8. M. Büttiker, *Phys. Rev. B* **46**, 12485 (1992).
9. Ya. M. Blanter, M. Büttiker, *Phys. Rep.* **336**, 2 (2000).
10. C. W. J. Beenakker, C. Emary, M. Kindermann, J. L. van Velsen, *Phys. Rev. Lett.* **91**, 147901 (2003).
11. P. Samuelsson, E. V. Sukhorukov, M. Büttiker, *Phys. Rev. Lett.* **92**, 026805 (2004).
12. C. W. J. Beenakker, in *Quantum Computers, Algorithms and Chaos,* International School of Physics Enrico Fermi, vol. 162, G. Casati, D. L. Shepelyansky, P. Zoller, G. Benenti, Eds. (IOS Press, Amsterdam, 2006), pp. 307–347.
13. C. W. J. Beenakker, H. van Houten, *Solid State Phys.* **44**, 1 (1991).
14. Y. Ji *et al.*, *Nature* **422**, 415 (2003).
15. Single-electrons detectors have been made but are yet too slow as compared with the electron transit time in the measurement leads.
16. B. J. van Wees *et al.*, *Phys. Rev. Lett.* **60**, 848 (1988).
17. D. A. Wharam *et al.*, *J. Phys. C* **21**, L209 (1988).
18. L. J. Geerligs *et al.*, *Phys. Rev. Lett.* **64**, 2691 (1990).
19. H. Pothier, P. Lafarge, C. Urbina, M. H. Devoret, *Europhys. Lett.* **17**, 249 (1992).
20. L. P. Kouwenhoven, A. T. Johnson, N. C. van der Vaart, C. J. P. M. Harmans, *Phys. Rev. Lett.* **67**, 1626 (1991).
21. A. Fujiwara, N. M. Zimmerman, Y. Ono, Y. Takahashi, *Appl. Phys. Lett.* **84**, 1323 (2004).
22. L. S. Levitov, H. Lee, G. B. Lesovik, *J. Math. Phys.* **37**, 4845 (1996).
23. T. Jonckheere, M. Creux, T. Martin, *Phys. Rev. B* **72**, 205321 (2005).
24. J. Keeling, I. Klich, L. S. Levitov, *Phys. Rev. Lett.* **97**, 116403 (2006).
25. J. Gabelli *et al.*, *Science* **313**, 499 (2006).
26. For additional experimental results, see G. Fève, thesis, Université Pierre et Marie Curie, Paris (2006), available at http://tel.archives-ouvertes.fr/tel-00119589.
27. M. Büttiker, H. Thomas, A. Prêtre, *Phys. Lett.* **A180**, 364 (1993).
28. M. Büttiker, A. Prêtre, H. Thomas, *Phys. Rev. Lett.* **70**, 4114 (1993).
29. A. Prêtre, H. Thomas, M. Büttiker, *Phys. Rev. B* **54**, 8130 (1996).
30. The Laboratoire Pierre Aigrain is the CNRS-ENS mixed research unit (UMR8551) associated with universities Paris 6 and Paris 7. The research has been supported by SESAME Ile-de-France and ANR-05-NANO-028 contracts.

Supporting Online Material

www.sciencemag.org/cgi/content/full/316/5828/1169/DC1
SOM Text
Figs. S1 and S2
References

13 February 2007; accepted 17 April 2007
10.1126/science.1141243

The Catalytic Cross-Coupling of Unactivated Arenes

David R. Stuart and Keith Fagnou*

The industrially important coupling of aromatic compounds has generally required differential prefunctionalization of the arene coupling partners with a halide and an electropositive group. Here we report that palladium, in conjunction with a copper oxidant, can catalyze the cross-coupling of *N*-acetylindoles and benzenes in high yield and high regioselectivity across a range of indoles without recourse to activating groups. These reactions are completely selective for arene cross-coupling, with no products arising from indole or benzene homo-coupling detected by spectroscopic analysis. This efficient reactivity should be useful in the design of other oxidative arene cross-couplings as well.

The immense scientific and commercial value of biaryl molecules is illustrated by their ubiquity as building blocks in light-emitting diodes, electron transport devices, liquid crystals, and medicinal compounds (*1*). The structural simplicity of biaryl compounds belies their preparative complexity, and the search for efficient and convergent syntheses has captivated the attention of synthetic chemists for more than a century. Over the past 30 years, biaryl cross-coupling reactions based on carbon fragment preactivation have revolutionized our ability to forge the carbon-carbon biaryl linkage (*1*, *2*). Of these reactions, the most widely accepted and used are the palladium-catalyzed cross-coupling reactions (such as the Suzuki reaction) of aryl halides and aryl organometallics (*3*). As is common today, these reactions are dependent on preactivation of the two aromatic carbon fragments with halides and electropositive groups, such as boronic acids or stannanes (*4*). Incorporation of these functional groups can require several synthetic steps,

Center for Catalysis Research and Innovation, University of Ottawa, Department of Chemistry, 10 Marie Curie, Ottawa, Ontario, Canada K1N 6N5.

*To whom correspondence should be addressed. E-mail: keith.fagnou@uottawa.ca

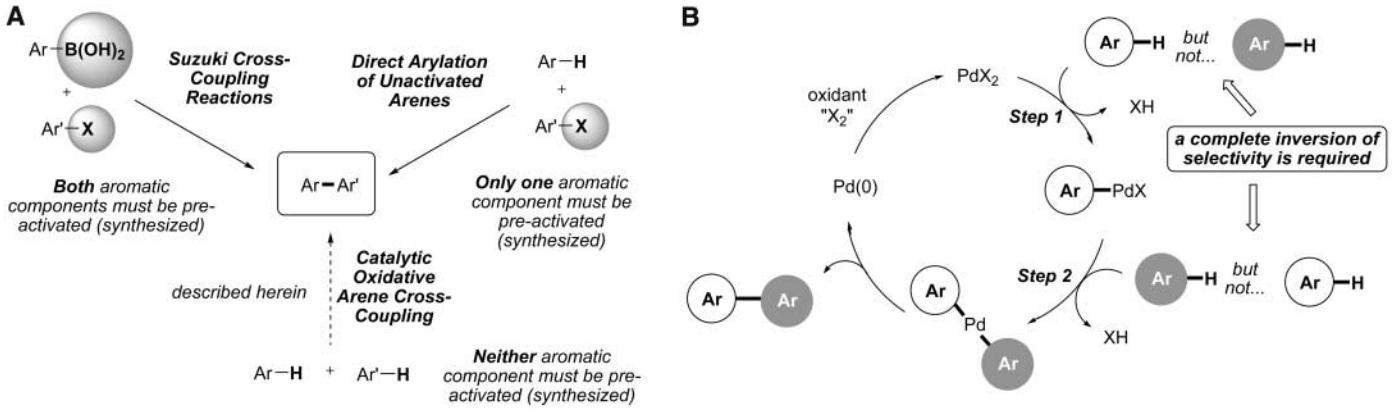

Fig. 1. (**A**) Methods for the preparation of biaryl molecules. X is a halide or sulfonate. (**B**) A prototypical arene catalytic cycle [based on palladium(II) catalysis] illustrating the reactivity-selectivity challenges associated with a catalytic oxidative cross-coupling reaction.

Table 1. Development of a catalytic indole-benzene cross-coupling reaction. The products **1**, **2**, and **3** correspond to those illustrated in Scheme 1, in which R=R′=H. $Pd(TFA)_2$ and (if relevant) $Cu(OAc)_2$, 3-nitropyridine, cesium pivalate (CsOPiv), and/or *N*-acetylindole were added to a Schlenk tube or microwave vessel, which was followed by the addition of benzene (~30 equivalents), pivalic acid, and heating according to the indicated method. Oxidant (equivalent), additive (mol %), and Pd (mol %) values were calculated relative to *N*-acetylindole. Unless otherwise indicated, the values for percent conversion (% conv.), **1**:**2**:**3** ratio, and percent yield **1** were determined by GC-MS. The asterisk denotes isolated yield. nd, not determined.

Entry	Mol % Pd	Oxidant (equiv.)	Additive (mol %)	Heating method	*T* (°C)	Time (h)	% Conv.	1:2:3	% Yield 1
1	100	None	None	Oil bath	110	24	75	4.4:1:2.6	55
2	10	$Cu(OAc)_2$	CsOPiv (40)	Oil bath	110	24	67	27:1:0.3	64
3	0	$Cu(OAc)_2$	3-Nitropyridine (10) CsOPiv (40)	Oil bath	110	24	0	nd	0
4	10	$Cu(OAc)_2$	3-Nitropyridine (10) CsOPiv (40)	Microwave	140	5	100	8.9:1:0.3	87*
5	5	$Cu(OAc)_2$	3-Nitropyridine (5) CsOPiv (40)	Microwave	140	5	92	13.8:1:0.3	84
6	2	$Cu(OAc)_2$	3-Nitropyridine (2) CsOPiv (40)	Microwave	140	5	66	27:1:0	63

Fig. 2. Mechanisms of arene palladation. The electrophilic aromatic metallation pathway (**top**) and concerted proton transfer–metallation pathway (**bottom**) are shown.

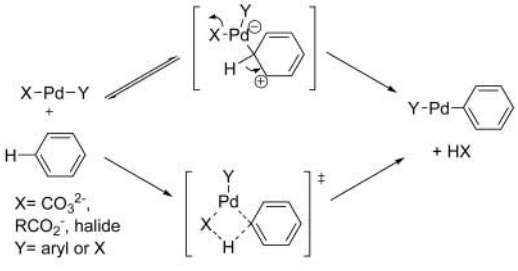

generating waste from reagents, solvents, and purification, and (upon fragment cross-coupling) can produce undesired organometallic by-products. As a means of reducing our dependence on preactivation, increased attention is being focused on direct arylation processes that replace one of the preactivated substrates with the simple arene itself [for a review, see (*5*)]. Important advances have been made, particularly in the past decade, and more can certainly be anticipated. In stark contrast, the investigation of cross-coupling reactions that are devoid of arene preactivation is rarely considered, and a high-yielding process with simple unactivated arenes has yet to be described [for a recent report that shows the challenge in achieving high selectivity, see (*6*); for copper-catalyzed and iron-catalyzed reactions between 2-naphthol and 2-naphthylamine, see (*7*) and (*8*).

Substantial hurdles impede the conception of a catalytic arene cross-coupling process that does not involve substrate preactivation. In addition to issues of reactivity and regioselectivity, the catalyst must avoid the generation of unwanted arene homo-coupling that would consume the starting material and generate unwanted by-products (*9*–*12*). To meet this demand, the catalyst must be able to react with one arene in the first step of the catalytic cycle and then invert its selectivity in the second step to react exclusively with the other arene (Fig. 1). Achieving such an inversion in reactivity and selectivity is simultaneously the most daunting challenge and the most crucial prerequisite.

Here, we describe the discovery, development, and study of reactions that meet these challenges and validate this long-sought synthetic strategy (Scheme 1). Notably, no products of arene homo-coupling are detected in the crude reaction mixture, indicating that a complete inversion in catalyst selectivity occurs at the crucial arene metallation steps of the catalytic cycle. Furthermore, although several regioisomeric products could be formed by reaction at different aromatic C-H bonds, markedly high regioselectivity is obtained. Although the precise sequence of reaction steps cannot presently be described, the demonstrated dichotomous behavior of palladium in the presence of electron-rich heteroaromatics and simple arenes should be applicable to other arene combinations. Given the value of the products and the efficiency with which they can be prepared by the use of this method, our observations should enable the development of this strategy for the synthesis of industrially and medicinally important biaryl molecules.

Our ongoing work in palladium-catalyzed direct arylation led us to believe that the crucial reactivity-selectivity inversion for arene cross-couplings was an achievable goal. It has been shown that palladium(II) complexes can react via an electrophilic aromatic metallation mechanism (S_EAr) with good selectivity for electron-rich arenes (Fig. 2) (*13*–*15*). In 2006, we discovered that a recently described proton transfer–palladation mechanism (*16*) can exhibit complementary reactivity to the S_EAr pathway (*17*, *18*). With simple arenes, this concerted palladation-deprotonation pathway can depend on arene C-H acidity rather than arene nucleophilicity. Important to the current goal, the palladium complexes associated with these two potentially complementary pathways are analogous to the palladium(II) species at step 1 and step 2 of the catalytic cycle in Fig. 1B. We hypothesized that, if the mechanistic duality associated with these two complementary reactivity modes could be accessed within the confines of a single catalytic cycle, the elusive entry point for selective arene cross-coupling could be achieved.

Table 2. Scope of the palladium-catalyzed indole-benzene cross-coupling. $Pd(TFA)_2$ (indicated amount), $Cu(OAc)_2$ (3 equivalents), 3-nitropyridine (1 equivalent to Pd), CsOPiv (40 mol %), and the *N*-acetylindole were added to a microwave vessel. The arene (~30 equivalents) and pivalic acid were then added, which was followed by microwave heating. Percent conversion and the **1**:**2**:**3** ratio values were determined by GC-MS. Values in the percent yield **1** column denote isolated yield. The asterisks denote that samples were heated thermally in a Schlenk tube. nd, not determined.

Entry	Indole	Arene	*T* (°C)	Mol % Pd	% Conv.	1:2:3	% Yield 1
1	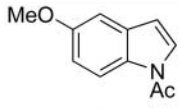		140	10	100	11.2: 1: 0.4	84
2	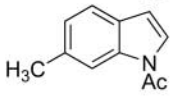		140	10	100	10: 1: 0.6	81
3	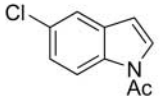		110*	10	83	6.5: 1: 0	63
4	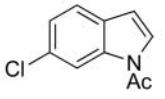		110*	10	81	5.7: 1: 0	61
5	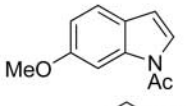		140	10	100	10.5: 1: 0.3	74
6	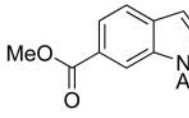		140	20	80	2.8: 1: 0	54
7	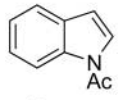	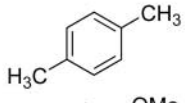	140	20	nd	10.4: 1: 0.4	45
8	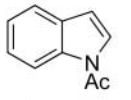	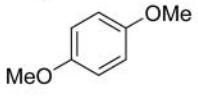	140	20	72	6.7: 1: 0	52
9	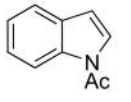	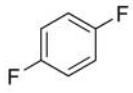	140	20	nd	9.9: 1: 0	42

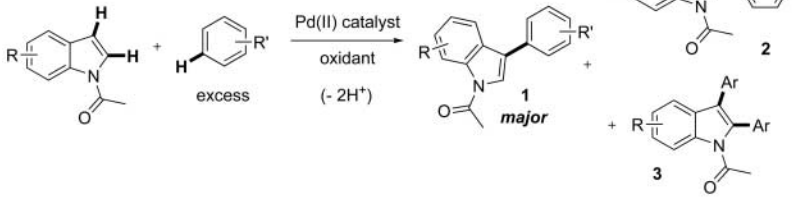

Scheme 1.

An extensive investigation of reaction conditions with a range of substrates, palladium catalysts, and additives led to the establishment of the conditions described in Table 1. A survey of electron-rich arenes, in conjunction with benzene as the second coupling partner, revealed that indoles exhibited promising reactivity. The indole nitrogen substituent also dramatically influences the reaction. In initial screens, the free *N*-H indole did not react, whereas *N*-methylindole produced self-dimerization predominantly. In contrast, the use of *N*-acetylindole gave more promising results, which was selected for further catalyst development studies. Optimal catalytic reactivity was achieved with a palladium trifluoroacetate (TFA) catalyst in combination with catalytic quantities of 3-nitropyridine and cesium pivalate (2,2-dimethylpropionate). Although the addition of these last two additives is not crucial to achieve catalytic turnover, superior turnover numbers and reproducibility are associated with their use. We believe that the pyridine additive may be acting to stabilize the palladium(0) before re-oxidation, preventing or slowing the formation of palladium black, which precipitates from the reaction mixture (*19*). The beneficial impact of the catalytic quantity of cesium pivalate is less clear, but it may interact with the $Pd(TFA)_2$ to generate palladium pivalate early in the reaction. The optimal solvent for the reaction was discovered to be pivalic acid, and a screen of stoichiometric oxidants revealed that copper(II) acetate [$Cu(OAc)_2$] could provide efficient catalytic turnover. The combination of these efforts led to the establishment of optimized conditions involving the treatment of *N*-acetylindole with an excess of benzene (~30 equivalents) with 2 to 10 mole percent $Pd(TFA)_2$, 2 to 10 mol % 3-nitropyridine, 40 mol % cesium pivalate, and 3 equivalents Cu $(OAc)_2$ in pivalic acid (2,2-dimethylpropionic acid) under thermal or microwave heating from 110° to 140°C (*20*).

A drawback of the thermal heating protocol was the prolonged reaction time (typically 48 hours) required to achieve high conversions with 10 mol % palladium. Notably, a change to microwave heating at 140°C provides a 92% conversion with 5 mol % $Pd(TFA)_2$ in less than 5 hours with a 13.8:1:0.3 ratio of the **1**:**2**:**3** isomers and an 84% gas chromatography–mass spectroscopy (GC-MS) yield of the C3 isomer **1** (entry 5 in Table 1). This acceleration is also accompanied by slight drop in C3:C2 selectivity; however, an improvement in C3:C2 regioselectivity occurs with decreased catalyst loadings. For example, with 2 mol % palladium, a 27:1 C3:C2 regioisomeric ratio is obtained with 66% conversion

of *N*-acetylindole (33 turnovers of the palladium catalyst) (entry 6 in Table 1). Under these conditions, the reaction is completely selective for arene cross-coupling, and no compounds arising from indole or benzene homo-coupling are detected by crude proton nuclear magnetic resonance spectroscopy and GC-MS analysis. This finding indicates that the crucial reactivity-selectivity inversion described in Fig. 1 can occur with high precision and fidelity.

Additional examples of reactions with substituted indoles and benzenes are included in Table 2. Thermal heating was used in reactions with chloro-substituted indoles (entries 3 and 4) because small amounts of hydrodechlorination were observed under microwave heating, which hampered product isolation.

Insufficient data exist at present to allow a detailed mechanistic discussion. Although superior reactivity is observed for indoles bearing electron-donating groups, no clear trends have yet emerged with respect to the benzene component. This relative reactivity is also observed in competition studies (see the supporting online material for further details). Nonetheless, these results clearly demonstrate that the dichotomous catalytic behavior required at each of the two metallation steps can be achieved. This knowledge should prompt the investigation and development of a broad range of other palladium-catalyzed oxidative cross-coupling reactions with different substrates.

References and Notes

1. J. Hassan, M. Sévignon, C. Gozzi, E. Shulz, M. Lemaire, *Chem. Rev.* **102**, 1359 (2002).
2. F. Diederich, P. J. Stang, Eds. *Metal-Catalyzed Cross-Coupling Reactions* (Wiley-VCH, New York, 1998).
3. A Chemical Abstracts Service Scifinder keyword search for "Suzuki coupling" gave 5128 hits for the period from 1990 to 2007.
4. Recently, it has been discovered that the carboxylate functionality can act as a substitute for the organometallic moiety (*21*).
5. D. Alberico, M. E. Scott, M. Lautens, *Chem. Rev.* **107**, 174 (2007).
6. R. Li, L. Jiang, W. Lu, *Organometallics* **25**, 5973 (2006).
7. M. Smrčina, M. Lorenc, V. Hanuš, P. Sedmera, P. Kočovsky, *J. Org. Chem.* **57**, 1917 (1992).
8. K. Ding *et al.*, *Chem. Commun.* **1997**, 693 (1997).
9. K. L. Hull, E. L. Lanni, M. S. Sanford, *J. Am. Chem. Soc.* **128**, 14047 (2006).
10. M. Takahashi *et al.*, *J. Am. Chem. Soc.* **128**, 10930 (2006).
11. S. Mukhopadhyay *et al.*, *Adv. Synth. Catal.* **343**, 455 (2001).
12. X. Li, J. B. Hewgley, C. A. Mulrooney, J. Yang, M. C. Kozlowski, *J. Org. Chem.* **68**, 5500 (2003).
13. C. Jia *et al.*, *J. Am. Chem. Soc.* **122**, 7252 (2000).
14. B. S. Lane, M. A. Brown, D. Sames, *J. Am. Chem. Soc.* **127**, 8050 (2005).
15. C. H. Park, V. Ryabova, I. V. Seregin, A. W. Sromek, V. Gevorgyan, *Org. Lett.* **6**, 1159 (2004).
16. D. Garcia-Cuadrado, A. A. C. Braga, F. Maseras, A. M. Echavarren, *J. Am. Chem. Soc.* **128**, 1066 (2006).
17. M. Lafrance, C. N. Rowley, T. K. Woo, K. Fagnou, *J. Am. Chem. Soc.* **128**, 8754 (2006).
18. M. Lafrance, K. Fagnou, *J. Am. Chem. Soc.* **128**, 16496 (2006).
19. E. M. Ferreira, B. M. Stoltz, *J. Am. Chem. Soc.* **125**, 9578 (2003).
20. Materials and methods are available as supporting material on *Science* Online.
21. L. J. Goossen, G. Deng, L. M. Levy, *Science* **313**, 662 (2006).

22. We thank the Natural Sciences and Engineering Research Council [for a Discovery Grant to K.F. and a Postgraduate Scholarship (Doctoral) to D.R.S.], the University of Ottawa, the Ontario government (Premier's Research Excellence Award to K.F.), and the Research Corporation (Cottrell Scholar Award to K.F.) for support of this work. Boehringer Ingelheim (Laval), Merck Frosst Canada, Merck Incorporated, and Astra Zeneca Montreal are thanked for additional unrestricted research support.

Supporting Online Material

www.sciencemag.org/cgi/content/full/316/5828/1172/DC1
Materials and Methods
Table S1
References

1 March 2007; accepted 30 March 2007
10.1126/science.1141956

Chondrite Barium, Neodymium, and Samarium Isotopic Heterogeneity and Early Earth Differentiation

Richard W. Carlson,* Maud Boyet,† Mary Horan

Isotopic variability in barium, neodymium, and samarium in carbonaceous chondrites reflects the distinct stellar nucleosynthetic contributions to the early solar system. We used $^{148}Nd/^{144}Nd$ to correct for the observed s-process deficiency, which produced a chondrite ^{146}Sm-^{142}Nd isochron consistent with previous estimates of the initial solar system abundance of ^{146}Sm and a $^{142}Nd/^{144}Nd$ at average chondrite Sm/Nd ratio that is lower than that measured in terrestrial rocks by 21 ± 3 parts per million. This result strengthens the conclusion that the deficiency in ^{142}Nd in chondrites relative to terrestrial rocks reflects ^{146}Sm decay and early planetary differentiation processes.

Improvements in isotope ratio measurement precision have allowed the exploitation of a number of short-lived radiometric systems for studies of early solar system and planetary history [e.g., (*1*, *2*)]. A critical requirement in this application is the ability to show that the generally small isotopic variations do not simply reflect isotopic heterogeneity in the solar nebula caused by imperfect mixing of various stellar contributions. Analyses of presolar grains and isotopically anomalous refractory inclusions contained in primitive meteorites [e.g., (*3*)] show clearly the distinct contributions of various nucleosynthetic paths, including slow neutron addition (s-process) in asymptotic giant branch (AGB) stars (*4*), rapid neutron addition (r-process) in supernovae (*5*), and the production of proton-rich nuclei (p-process) through photodisintegration reactions in supernovae (*6*). This issue has gained prominence because of the detection of isotope anomalies in Cr (*7*) Mo (*8*, *9*), Os (*10*), Ba (*11*, *12*), and Sm (*13*) in bulk samples of meteorites. Of concern here is the possible implication of these anomalies for the interpretation of the observed difference of ~20 ppm between chondritic and terrestrial $^{142}Nd/^{144}Nd$ (*14*). If caused by the radiogenic decay of ^{146}Sm (half-life = 103 million years), the higher $^{142}Nd/^{144}Nd$ of terrestrial rocks relative to that of chondrites indicates either that Earth has a decidedly nonchondritic bulk composition, or that Earth experienced a global differentiation event within 30 million years of its formation (*14*). If the difference in ^{142}Nd is due to nebular isotopic heterogeneity, then neither of these interpretations need apply. Here, we report Ba, Nd, and Sm isotopic compositions measured on the same sample for carbonaceous, ordinary, and enstatite chondrites (C-, O-, and E-chondrites), as well as lunar and terrestrial samples, to better define the degree and cause of Nd isotope heterogeneity in the early solar nebula and its implications for the use of the ^{146}Sm-^{142}Nd decay scheme for deciphering early planetary history.

Samples for this study included three groups of C-chondrites—CI (Orgueil), CM2 (Cold Bokkveld, Mighei, and Murray), and CV3 (Allende, Grosnaja, and Mokoia)—as well as the E-chondrite Indarch (EH4) and a variety of O-chondrites (Gladstone-H6, Homestead-L5, Peace River–L6, and Ucera-H5). To investigate the consequences of long exposure to galactic cosmic rays on the isotopic composition of these elements, we included data for the low-Ti lunar mare basalt 15555. These data were compared against replicate analyses of various terrestrial laboratory standards and of two kimberlites from the Grizzly Pipe of the Slave Province, Canada (*15*).

All but one C-chondrite analyzed here show elevated $^{135}Ba/^{136}Ba$ ranging from 12 to 58 ppm above the mean of our terrestrial standard (Fig. 1). Given the 2σ external reproducibility of ±7 ppm on $^{135}Ba/^{136}Ba$, among the remaining samples only the E-chondrite Indarch (+18 ± 7 ppm) has $^{135}Ba/^{136}Ba$ marginally outside the

Department of Terrestrial Magnetism, Carnegie Institution of Washington, 5241 Broad Branch Road, NW, Washington, DC 20015, USA.

*To whom correspondence should be addressed. E-mail: carlson@dtm.ciw.edu

†Present address: UMR Magmas et Volcans CNRS 6524/IRD 163, Observatoire de Physique du Globe de Clermont-Ferrand, 23 Rue Dr. Paul Michelon, Université Jean Monnet, 42023 Saint Etienne, France.

external reproducibility of the terrestrial standard (Table 1). Our results contrast with a recent study of whole-rock chondrites (*12*) that found large excesses in $^{138}Ba/^{136}Ba$ (up to 90 ppm in the O-chondrite Grady and up to 60 ppm in Allende), smaller excesses in $^{137}Ba/^{136}Ba$ (48 ppm in Grady, 25 ppm in Allende), yet no resolvable anomalies in $^{135}Ba/^{136}Ba$. Unlike (*12*), we found no anomalies in ^{138}Ba outside our external precision of ±12 ppm. All C-chondrites analyzed here, except for Mokoia, have marginal to resolved excesses in $^{137}Ba/^{136}Ba$, ranging up to 32 ± 6 ppm in Grosnaja. We also determined the abundance of the p-process isotopes ^{130}Ba and ^{132}Ba, and we found only small, if any, anomalies outside of an admittedly large measurement error of 91 to 131 ppm for these low-abundance isotopes.

The Ba isotope anomaly patterns measured here for C-chondrites are similar in shape, although much reduced in magnitude, compared to some C-chondrite leaches and residues (*11*) and to the isotopically anomalous Allende calcium- and aluminum-rich inclusion (CAI) EK1-4-1 (Fig. 1) (*16*). The abundance of CAIs varies among the C-chondrite groups, constituting about 10 volume % of CV, 5% of CM, and much less than 1% of CI chondrites (*17*), yet both the most and least anomalous Ba among the C-chondrites analyzed here were found in the CM samples. The data thus do not obviously correlate with the abundance of CAIs in the samples.

The Ba anomaly pattern is consistent with an excess of isotopes produced by the r-process over those formed by the s-process, because ^{134}Ba and ^{136}Ba are generated only in the s-process, whereas ^{135}Ba, ^{137}Ba, and ^{138}Ba also contain an r-process contribution (*18*). The Ba anomaly pattern is complementary to that measured in s-process–enriched presolar SiC grains from the CM2 chondrite Murchison, where deficits in $^{135}Ba/^{136}Ba$ of up to 67% were found (*19*). The Ba analyses reported here were performed with standard HF-HNO_3 digestion techniques that are known to be incapable of dissolving presolar SiC grains (*20*). Although presolar SiC is of low abundance [<14 ppm by weight (*3*)] in C-chondrites, it would still exert strong influence on the measured Ba isotopic composition were it not included in a "whole-rock" measurement. For example, the largest $^{135}Ba/^{136}Ba$ anomaly measured here, 60 ppm in Cold Bokkveld, could be created by the loss of an amount of presolar SiC [with Ba concentration of 200 ppm (*21*) and an s-process end member $^{135}Ba/^{136}Ba = 0.124$ (*19*, *22*)] equal to only 0.86 ppm by weight of the dissolved whole rock. Loss of this amount of SiC also would create excesses of 36 and 20 ppm in $^{137}Ba/^{136}Ba$ and $^{138}Ba/^{136}Ba$, compared to the values of 31 ± 7 and 9 ± 6 ppm, respectively, measured in Cold Bokkveld. This magnitude of loss of presolar SiC would also lead to excesses in $^{130}Ba/^{136}Ba$ and $^{132}Ba/^{136}Ba$ of ~70 ppm, which is within measurement uncertainty for these two low-abundance isotopes. Thus, the anomaly pattern determined here for Ba in C-chondrites conceivably could be due simply to incomplete dissolution of the presolar SiC grains contained in this group of primitive meteorites. If so, the small to absent anomalies observed in E- and O-chondrites reflect the fact that any presolar SiC originally present is likely to have been destroyed during thermal processing of these meteorites. As discussed below, the fact that the Nd and Sm isotopic anomalies in Allende are not removed by complete dissolution lessens, but does not necessarily eliminate, this explanation for the genesis of the observed Ba isotopic anomalies. Nonetheless, the Ba isotope anomaly pattern observed in C-chondrites appears to be consistent with a deficiency in the s-process isotopes.

Neodymium isotopic compositions of most chondrites show resolvable anomalies only in ^{142}Nd. With the exception of Grosnaja, which has a high Sm/Nd ratio (table S1) and hence a larger contribution from ^{146}Sm decay, the $^{142}Nd/^{144}Nd$ of the C-chondrites is consistently below those measured for E- and O-chondrites, extending to values as low as –46 ppm in Mighei relative to the terrestrial La Jolla Nd standard. Mighei also shows resolved excesses in $^{148}Nd/^{144}Nd$ and $^{150}Nd/^{144}Nd$, a possibility hinted at by data for several other C-chondrites (fig. S1), although the majority of the values are within measurement error of the terrestrial standard. The excess ^{150}Nd in Ucera is believed to represent an analytical artifact (*15*). Absent any nucleosynthetic variations in Nd and Sm, the $^{142}Nd/^{144}Nd$ data for the chondrites would be expected to correlate with $^{144}Sm/^{144}Nd$, with a slope that reflects the age of formation of the solar system and an initial $^{146}Sm/^{144}Sm$ of ~0.008 (*23*). The measured $^{142}Nd/^{144}Nd$ values in the chondrites (Fig. 2) do not correlate with Sm/Nd, which strongly implies that the ^{142}Nd variation is not only caused by ^{146}Sm decay but also includes a nucleosynthetic contribution.

Samarium isotopic compositions in the samples studied here are most clearly marked by the effects of secondary neutron capture on ^{149}Sm to create ^{150}Sm, a result of exposure of the samples to galactic cosmic rays while in space or on the lunar surface. The lunar low-Ti basalt 15555 shows the most extreme effect—a depletion in $^{149}Sm/^{152}Sm$ of 564 ± 6 ppm relative to the terrestrial standard—and provides an opportunity to examine the effect of cosmic ray exposure on other isotopes of Ba, Nd, and Sm. Except for ^{149}Sm, ^{150}Sm, and those isotopes with a radiogenic contribution (^{142}Nd and ^{143}Nd), 15555

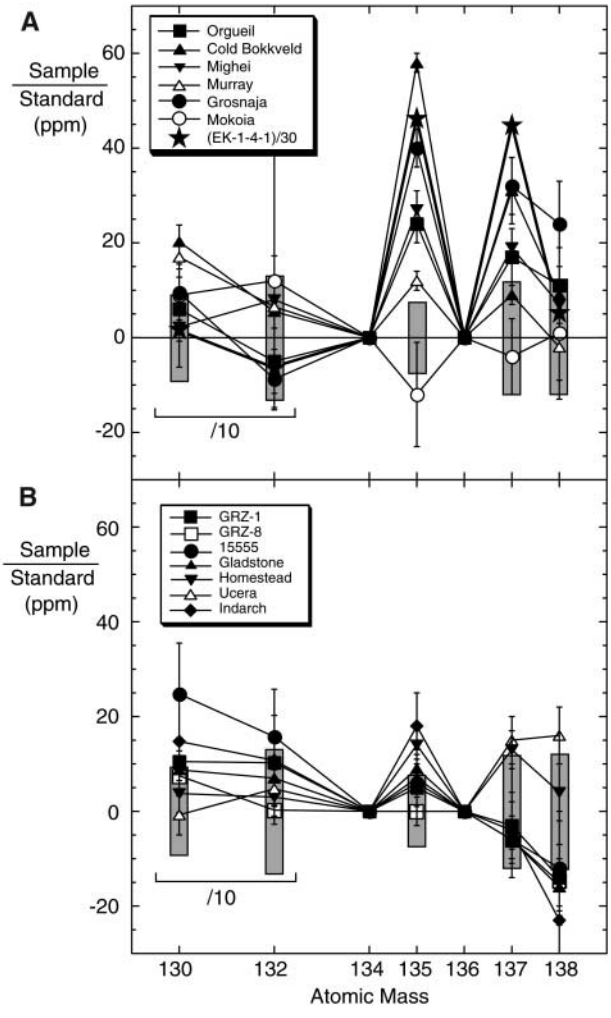

Fig. 1. Ba isotopic variation relative to the average value measured for the terrestrial standard. Gray boxes at each mass show the 2σ external reproducibility obtained on the standard. Both the values and the errors at ^{130}Ba and ^{132}Ba have been divided by 10 to plot on this scale. (**A**) Data for C-chondrites; (**B**) data for O- and E-chondrites and lunar and terrestrial samples. The pattern denoted by the large stars in (A) shows the isotopic composition measured in Allende CAI EK 1-4-1 (*16*) with the anomalies divided by 30 to plot on this scale.

shows only marginally high $^{130}Ba/^{136}Ba$ relative to the terrestrial standard. Thus, we conclude that exposure to cosmic rays does not affect the Ba, Nd, or Sm isotopic composition of the chondrites beyond the obvious creation of ^{150}Sm from ^{149}Sm. In the chondrites, except for ^{149}Sm and ^{150}Sm, the only other resolved anomalies in Sm are large deficits in $^{144}Sm/^{152}Sm$ shown by all analyzed C-chondrites. Low $^{144}Sm/^{152}Sm$ is a signature of a p-process deficiency (*13*). The flux-fused sample of Allende also shows deficits in both ^{142}Nd and ^{144}Sm and possibly a slight excess in ^{148}Nd, and agrees well with Allende Nd (*13*, *14*, *24*) and Sm (*13*) isotope analyses obtained using less aggressive dissolution techniques. These data suggest that neither the s- nor p-process deficiencies in Nd and Sm, at least in this chondrite, result from incomplete dissolution of presolar grains. With the exception of the neutron capture effects on ^{149}Sm and ^{150}Sm, all E- and O-chondrites and lunar samples analyzed here have Sm isotopic compositions indistinguishable from the terrestrial standard.

Given the observed s-process deficiencies in chondritic Ba, examining how or whether these would affect Nd and Sm isotopic compositions is critical to the interpretation of ^{142}Nd anomalies. We modeled the s-process–rich component with the use of the Ba (*19*, *22*) Nd, and Sm (*22*, *25*) isotopic compositions and concentrations (*21*) of presolar SiC. Exclusion of 0.8 ppm by weight of SiC from the whole rock creates the following anomalies (normalized to ^{136}Ba, ^{144}Nd, and ^{152}Sm, respectively, in ppm): $^{135}Ba = +57$, $^{137}Ba = +33$, $^{138}Ba = +18$, $^{142}Nd = -50$, $^{145}Nd = +28$, $^{148}Nd = +47$, $^{148}Sm = -31$, $^{149}Sm = +4$, and $^{150}Sm = -23$. No data are available for the ^{150}Nd, ^{144}Sm, and ^{154}Sm isotopic composition of presolar SiC. If no p-process ^{144}Sm is contributed by the s-process carrier, then an s-process deficiency of the magnitude discussed above would cause $^{144}Sm/^{152}Sm$ to increase by only 7 ppm, which is much smaller than the observed deficits in C-chondrites. Therefore, the carrier of the p-process deficiency in the C-chondrites is not likely to be the same as for the s-process component. The predicted Nd isotopic anomalies are similar to those in Mighei, the most isotopically anomalous of the C-chondrites measured here, although Mighei's deficit in $^{148}Sm/^{152}Sm$ is about half that predicted by this model. Excesses or deficiencies in s-process isotopes would thus be expected to create anomalies in ^{135}Ba, ^{148}Nd, and ^{148}Sm that are similar in magnitude, but opposite in sign, to those expected in ^{142}Nd, depending on the Ba-Nd-Sm concentration ratios in the s-process carrier phase(s).

Correcting ^{142}Nd with the use of measured ^{135}Ba anomalies appears to overestimate the s-process deficiency, thereby worsening the chondrite Sm/Nd versus $^{142}Nd/^{144}Nd$ correlation relative to the uncorrected data (Fig. 2A). The use of ^{135}Ba to correct ^{142}Nd has several weaknesses that may contribute to this outcome (*15*). Our fusion data suggest that conventional HF-HNO_3 digestion dissolves phases having isotopically anomalous rare earth elements, but it is not known whether the phases carrying s-process Ba are completely dissolved. If the Ba and Nd anomalies are contributed by different mineral phases in the primitive chondrites, then they should not both be modeled with data for presolar SiC. Similarly, the corrections to ^{142}Nd based on ^{135}Ba depend on the concentration ratios of Ba and Nd between the chondrites and the s-process carrier phase(s), which are poorly known and may be different for different meteorites. Another possibility is that the isotopic anomalies in Ba may not be nucleosynthetic in origin, but instead may reflect non–mass-dependent fractionation due to the nuclear field influence of the different nuclei during evap-

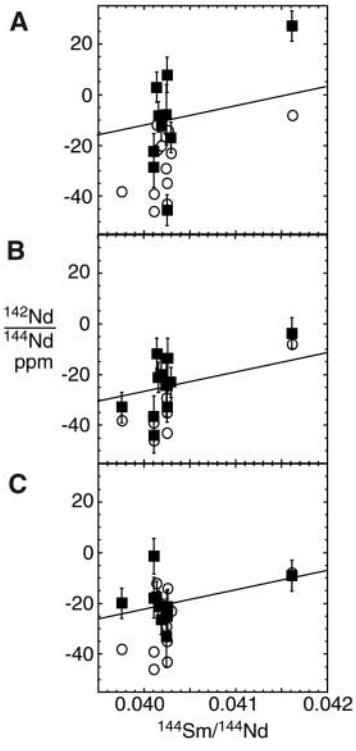

Fig. 2. Sm/Nd versus $^{142}Nd/^{144}Nd$ correlations for measured data (open circles) and data corrected for s- and p-process deficiencies on the basis of measured ^{135}Ba (**A**), ^{144}Sm (**B**), and ^{148}Nd (**C**) variations (*15*). The lines have slopes of 0.008, as expected for rocks with variable Sm/Nd ratios formed 4.567 billion years ago from a reservoir with the initial ^{146}Sm abundance of the solar system (*23*).

Table 1. Barium, neodymium, and samarium isotopic compositions relative to terrestrial standards. Ba data are normalized to ^{136}Ba, fractionation corrected to $^{134}Ba/^{136}Ba = 0.3078$. Nd data are normalized to ^{144}Nd, fractionation corrected to $^{144}Nd/^{146}Nd = 1.385233$. Sm data are normalized to ^{152}Sm, fractionation corrected to $^{147}Sm/^{152}Sm = 0.56081$. Uncertainties shown in parentheses represent the two–standard error internal precisions of individual mass spectrometer runs; the uncertainty in the last row provides the external precision as determined from the 2σ of the population of replicate standard measurements (*15*). Absolute ratios for all samples and standards are given in tables S2 to S4.

Sample	Isotopic composition relative to terrestrial standard (ppm)													
	^{130}Ba	^{132}Ba	^{135}Ba	^{137}Ba	^{138}Ba	^{142}Nd	^{145}Nd	^{148}Nd	^{150}Nd	^{144}Sm	^{148}Sm	^{149}Sm	^{150}Sm	^{154}Sm
GRZ-1	105 (40)	103 (41)	5 (4)	−3 (5)	−15 (7)	−2 (2)	3 (2)	8 (2)	7 (8)	−3 (12)	7 (6)	−1 (4)	−9 (6)	−7 (4)
GRZ-8	76 (31)	3 (30)	0 (3)	−5 (4)	−15 (5)	−6 (7)	9 (5)	12 (11)	−4 (9)					
15555	249 (106)	158 (99)	6 (6)	−6 (8)	−11 (12)	−10 (3)	2 (3)	5 (6)	−5 (8)	−14 (19)	18 (7)	−564 (6)	1034 (8)	−14 (7)
Gladstone	87 (41)	70 (42)	9 (4)	−6 (5)	−16 (6)	−19 (5)	7 (6)	−6 (11)	−21 (14)	2 (22)	3 (8)	−19 (3)	10 (10)	−11 (8)
Homestead	38 (40)	31 (40)	14 (4)	13 (4)	4 (6)	−20 (3)	2 (3)	−1 (6)	−17 (8)	4 (19)	6 (7)	−27 (6)	49 (8)	−19 (6)
Peace River							−17 (8)	26 (9)	−9 (14)	−4 (19)	−9 (30)	6 (13)	17 (10)	−6 (14)
Ucera	−8 (42)	48 (39)	7 (3)	15 (5)	16 (6)	−22 (5)	1 (6)	12 (10)	93 (13)	3 (8)	−3 (8)	−55 (13)	166 (8)	−4 (13)
Indarch	149 (100)	108 (95)	17 (7)	−4 (8)	−23 (11)	−15 (5)	4 (6)	−6 (8)	−20 (11)	−7 (21)	−2 (7)	−41 (6)	65 (8)	−3 (7)
Orgueil	59 (68)	−49 (69)	24 (4)	17 (5)	11 (8)	−28 (12)	−21 (13)	−5 (20)	−29 (28)	−102 (46)	4 (15)	−233 (13)	448 (17)	−24 (13)
Cold Bokkveld	204 (35)	55 (119)	58 (2)	31 (7)	9 (6)	−42 (7)	6 (7)	16 (12)	12 (17)					
Mighei	22 (84)	80 (5)	27 (4)	19 (1)	4 (1)	−45 (7)	12 (7)	41 (13)	59 (18)	−44 (6)	−15 (4)	−73 (1)	81 (6)	−20 (17)
Murray	171 (27)	66 (8)	12 (2)	9 (2)	−2 (7)	−38 (8)	9 (8)	19 (15)	−1 (19)	−56 (1)	−13 (8)	−99 (3)	145 (1)	−16 (10)
Allende						−40 (4)	17 (5)	21 (8)	−4 (11)	−112 (12)	−2 (5)	−34 (4)	100 (6)	−20 (5)
Grosnaja	97 (58)	−86 (61)	40 (4)	32 (6)	24 (9)	−7 (4)	−8 (4)	−1 (6)	−12 (10)	−97 (4)	18 (2)	−37 (2)	42 (1)	−18 (1)
Mokoia	90 (5)	121 (274)	−12 (11)	−4 (8)	1 (13)	−34 (5)	5 (5)	13 (8)	10 (11)	−52 (14)	0 (6)	−138 (5)	220 (6)	−21 (5)
Uncertainty	91	131	7	12	12	5	12	12	13	33	9	10	17	14

oration and condensation processes in the early solar nebula (*26*). This fractionation process has been shown to reproduce the isotopic anomalies observed in Ba in Allende CAI EK1-4-1, and hence the shape of the Ba anomalies measured here, but not the Nd and Sm isotopic pattern (*26*). In this case, the anomalies measured in Ba and Nd would have distinct causes, so that corrections to ^{142}Nd could not be deduced from variations in Ba isotopic composition.

Using the measured ^{144}Sm depletion to correct for possible p-process deficiencies yields a Sm/Nd-^{142}Nd/^{144}Nd correlation slightly better than that obtained by simply using the measured ratios (Fig. 2B). Why the p-process correction does not provide more improvement in the ^{142}Nd/^{144}Nd correlation is not clear. One possibility is that the p-process carrier has relatively more Sm than Nd in comparison to the chondritic Sm/Nd model used by (*13*). Another possibility is that the p-process contribution to ^{142}Nd production is overestimated by (*13*). Current models for s-process nucleosynthesis in AGB stars overproduce ^{142}Nd by about a factor of 6 relative to solar system abundances (*27*). This suggests that the direct p-process production of 4% (relative to s-process) for ^{142}Nd (*28*) used by (*13*) in their correction overestimates the role of the p-process in ^{142}Nd production. Resolving the cause of the p-process deficit measured in ^{144}Sm in C-chondrites and its implications for ^{142}Nd variations remains an important issue, but the minimal improvement in the ^{142}Nd/^{144}Nd versus Sm/Nd correlation created by applying only the p-process correction suggests that p-process nucleosynthetic deficiencies may not be the controlling factor in chondrite ^{146}Sm-^{142}Nd systematics.

A more robust correction, at least for the s-process deficiency, uses ^{148}Nd anomalies measured in the same samples (Fig. 2C). The need for this correction is seen in the observed correlation of ^{148}Nd/^{144}Nd versus ^{142}Nd/^{144}Nd shown by the chondrites but not by standards or terrestrial samples (fig. S1). An obvious advantage of this approach is that it is based on variations within a single element, and thus it does not involve any assumptions about the concentration of Nd in the various materials contributing to the measured isotopic composition. Use of the ^{148}Nd-corrected ^{142}Nd/^{144}Nd ratios (*15*) provides a ^{144}Sm/^{144}Nd versus ^{142}Nd/^{144}Nd correlation for all chondrites that has a slope of 0.0065 ± 0.0048 with a mean square of the weighted deviations (MSWD) from the line of 6.5 (Fig. 2C). The data for Mighei and Orgueil lie above and below this line, respectively. Excluding these two points provides a line fit through the remaining data of slope = 0.0085 ± 0.0046 (MSWD = 1.2). The slope has a large error because of the very limited spread in Sm/Nd ratio of the chondrites, but it is similar to the estimate of 0.008 for the initial ^{146}Sm/^{144}Sm in the solar system (*23*). For an average chondritic ^{147}Sm/^{144}Nd = 0.1966 (*29*), this correlation passes through a ^{142}Nd/^{144}Nd that is –21 ± 3 ppm relative to the terrestrial Nd standard, essentially the same value used by (*14*) to suggest that the sampled part of Earth deviated from chondritic Sm-Nd evolution very early in Earth history.

References and Notes

1. S. S. Russell *et al.*, in *Meteorites and the Early Solar System II*, D. S. Lauretta, H. Y. McSween Jr., Eds. (Univ. of Arizona Press, Tucson, AZ, 2006), pp. 233–251.
2. M. Wadhwa, G. Srinivasan, R. W. Carlson, in *Meteorites and the Early Solar System II*, D. S. Lauretta, H. Y. McSween Jr., Eds. (Univ. of Arizona Press, Tucson, AZ, 2006), pp. 715–731.
3. B. S. Meyer, E. Zinner, in *Meteorites and the Early Solar System II*, D. S. Lauretta, H. Y. McSween Jr., Eds. (Univ. of Arizona Press, Tucson, AZ, 2006), pp. 69–108.
4. R. Gallino, M. Busso, M. Lugaro, in *Astrophysical Implications of the Laboratory Study of Presolar Materials*, T. J. Bernatowicz, E. Zinner, Eds. (American Institute of Physics, New York, 1997), pp. 115–153.
5. Y.-Z. Qian, P. Vogel, G. J. Wasserburg, *Astrophys. J.* **494**, 285 (1998).
6. S. E. Woosley, W. M. Howard, *Astrophys. J.* **36**, (suppl.), 285 (1978).
7. M. Rotaru, J. L. Birck, C. J. Allegre, *Nature* **358**, 465 (1992).
8. Q. Z. Yin, S. B. Jacobsen, K. Yamashita, *Nature* **415**, 881 (2002).
9. N. Dauphas, B. Marty, L. Reisberg, *Astrophys. J.* **569**, L139 (2002).
10. A. Brandon, M. Humayun, I. S. Puchtel, I. Leya, M. Zolensky, *Science* **309**, 1233 (2005).
11. H. Hidaka, Y. Ohta, S. Yoneda, *Earth Planet. Sci. Lett.* **214**, 455 (2003).
12. M. C. Ranen, S. B. Jacobsen, *Science* **314**, 809 (2006); published online 4 October 2006 (10.1126/science.1132595).
13. R. Andreasen, M. Sharma, *Science* **314**, 806 (2006); published online 4 October 2006 (10.1126/science.1131708).
14. M. Boyet, R. W. Carlson, *Science* **309**, 576 (2005); published online 16 June 2005 (10.1126/science.1113634).
15. See supporting material on *Science* Online.
16. M. T. McCulloch, G. J. Wasserburg, *Astrophys. J.* **220**, L15 (1978).
17. A. J. Brearley, R. H. Jones, *Rev. Mineral.* **36**, 3-1 (1998).
18. E. M. Burbidge, G. R. Burbidge, W. A. Fowler, F. Hoyle, *Rev. Mod. Phys.* **29**, 547 (1957).
19. C. A. Prombo, F. A. Podosek, S. Amari, R. S. Lewis, *Astrophys. J.* **410**, 393 (1993).
20. S. Amari, P. Hoppe, E. Zinner, R. S. Lewis, *Astrophys. J.* **394**, L43 (1992).
21. E. Zinner, S. Amari, R. S. Lewis, *Astrophys. J.* **382**, L47 (1991).
22. P. Hoppe, U. Ott, in *Astrophysical Implications of the Laboratory Study of Presolar Materials*, T. J. Bernatowicz, E. K. Zinner, Eds. (American Institute of Physics, New York, 1997), pp. 27–58.
23. G. W. Lugmair, S. J. G. Galer, *Geochim. Cosmochim. Acta* **56**, 1673 (1992).
24. K. Rankenburg, A. D. Brandon, C. R. Neal, *Science* **312**, 1369 (2006).
25. S. Richter, U. Ott, F. Begemann, in *Nuclei in the Cosmos*, F. Kappeler, K. Wisshak, Eds. (Institute of Physics, Bristol, UK, 1993), pp. 127–132.
26. T. Fujii, F. Moynier, F. Albarede, *Earth Planet. Sci. Lett.* **247**, 1 (2006).
27. C. Arlandini *et al.*, *Astrophys. J.* **525**, 886 (1999).
28. K. Wisshak, F. Voss, F. Kappeler, L. Kazakov, G. Reffo, *Phys. Rev. C* **57**, 391 (1998).
29. S. B. Jacobsen, G. J. Wasserburg, *Earth Planet. Sci. Lett.* **67**, 137 (1984).
30. We thank M. Schönbächler for obtaining and dissolving most of the C-chondrites used in this study as part of her study of chondrite Pd-Ag systematics, T. Mock for assistance in keeping the mass spectrometry facility in working order, T. McCoy and L. Welzenbach for meteorite samples, B. Zanda for assistance in obtaining the sample of Orgueil from the Paris Museum of Natural History, C. Smith for the remainder of the C-chondrites, and A. Brandon and two anonymous reviewers for comments. Supported by the Carnegie Institution of Washington. Funds for purchase of the Triton mass spectrometer were provided in part by NSF grant EAR-0320589.

Supporting Online Material

www.sciencemag.org/cgi/content/full/316/5828/1175/DC1
Materials and Methods
Fig. S1
Tables S1 to S5
References

22 January 2007; accepted 27 March 2007
10.1126/science.1140189

Evidence for a Late Supernova Injection of ^{60}Fe into the Protoplanetary Disk

Martin Bizzarro,[1,2]* David Ulfbeck,[1] Anne Trinquier,[1] Kristine Thrane,[1] James N. Connelly,[1,3] Bradley S. Meyer[4]

High-precision ^{60}Fe-^{60}Ni isotope data show that most meteorites originating from differentiated planetesimals that accreted within 1 million years of the solar system's formation have ^{60}Ni/^{58}Ni ratios that are ~25 parts per million lower than samples from Earth, Mars, and chondrite parent bodies. This difference indicates that the oldest solar system planetesimals formed in the absence of ^{60}Fe. Evidence for live ^{60}Fe in younger objects suggests that ^{60}Fe was injected into the protoplanetary disk ~1 million years after solar system formation, when ^{26}Al was already homogeneously distributed. Decoupling the first appearance of ^{26}Al and ^{60}Fe constrains the environment where the Sun's formation could have taken place, indicating that it occurred in a dense stellar cluster in association with numerous massive stars.

Understanding the origin of short-lived isotopes and their daughter products in meteorites can constrain the astrophysical setting of solar system formation and the earliest evolution of the protoplanetary disk and proto-Sun. Whereas early solar system abundances of short-lived isotopes with relatively long half-lives [$t_{1/2} \gtrsim 3.5$ million years (My)], such as ^{53}Mn and ^{182}Hf, broadly reflect input from stellar sources over the history of our

Galaxy, the inferred levels of ^{41}Ca, ^{26}Al, and ^{60}Fe are too high to uniquely derive from galactic production (*1*, *2*). Calcium-41 and ^{26}Al may have formed by particle irradiation near the proto-Sun (*3*) or, alternatively, synthesized in a nearby star and been injected into the nascent solar system (*1*, *2*, *4*, *5*). In contrast, ^{60}Fe is of exclusive stellar origin (*4*, *5*); thus, constraining the timing of its first appearance, initial abundance, and distribution can test models of solar system formation.

Excess ^{60}Ni related to in situ decay of ^{60}Fe ($t_{1/2}$ = 1.5 My, expressed as ϵ^{60}Ni*, the per 10-thousand deviation from the terrestrial ^{60}Ni/^{58}Ni ratio) has been demonstrated in components from least-metamorphosed ordinary chondrites, such as chondrules and sulfides (*5*, *6*), as well as in basalts that formed at the surface of the eucrite parent body (EPB) (*7*). Based on short-lived chronometers, the time of formation of chondrules in ordinary chondrites and eucrites has been constrained to ≳2 My after the start of the solar system (*8*–*10*). Therefore, the timing of the first appearance and initial abundance of ^{60}Fe in the solar system are currently poorly understood. Taking advantage of improved methods for high-precision measurements of Ni isotopes (*11*), we analyzed the Ni isotope composition of various inner solar system objects to constrain the timing of injection and initial abundance of ^{60}Fe in the early solar system and to assess the extent of ^{60}Ni, ^{62}Ni, and ^{60}Fe isotope heterogeneities that may have been present in the protoplanetary disk. Our samples include objects for which radioisotope chronometers indicate formation ages that span 3 My from the start of the solar system [defined by calcium-aluminum–rich inclusions (CAIs) at 4.5672 ± 0.0006 Gy, where error is 2 SD (*12*)].

Eight rock samples from Earth yield average ϵ^{60}Ni* and ϵ^{62}Ni of –0.027 ± 0.034 and 0.034 ± 0.084, respectively, providing an estimate of the reproducibility of the Ni isotope measurements during this study (table S1). The martian dunite NWA2037 has terrestrial Ni isotope compositions. Similarly, ordinary, enstatite, and carbonaceous chondrite meteorites have an average ϵ^{60}Ni* of –0.009 ± 0.066. Therefore, inner solar system bodies that formed after extinction of ^{60}Fe (Earth and Mars) or with solar ^{56}Fe/^{58}Ni ratios (chondrite meteorites) have identical ϵ^{60}Ni* values (Fig. 1), indicating that ^{60}Fe was homogeneously distributed within the accretion regions of Earth, Mars, and chondrite parent bodies. Carbonaceous chondrites show an excess ^{62}Ni of 0.335 ± 0.054 ϵ units compared with samples from Earth, Mars, and the enstatite chondrite Qinghzen, whereas the ordinary chondrite Bjurböle shows a small deficit of –0.201 ± 0.161 ϵ units (Fig. 2).

Although CAIs are the solar system's oldest solids, the likely preservation of nucleosynthetic anomalies in various Ni isotopes renders them inappropriate material to use in an attempt to assess the abundance of ^{60}Fe at the time of their formation [supporting online material (SOM) text 1]. Instead, we turned to samples of differentiated planetesimals such as basaltic crusts (angrites), metallic cores (iron meteorites), core-mantle interfaces (pallasites), and melting residues (ureilites). Radioisotope systems concordantly constrain the accretion of the parent bodies of these materials to have occurred within the first million years of the solar system (*8*, *9*, *13*–*15*). Such samples are ideal for our study; indeed, nucleosynthetic anomalies in differentiated meteorites are of minor importance given that planetary-scale melting has homogenized initial heterogeneities inherited from their precursor materials.

One olivine separate and two bulk rock samples from the SAH99555 angrite yield indistinguishable ϵ^{60}Ni* values of −0.215 ± 0.058, despite elevated ^{56}Fe/^{58}Ni ratios ranging from ~2000 to 5500. Three bulk ureilites with ^{56}Fe/^{58}Ni ratios of ~175 record identical deficits in ϵ^{60}Ni* of −0.301 ± 0.076. Magmatic and nonmagmatic iron meteorites as well as metal fractions from pallasites with ^{56}Fe/^{58}Ni ratios varying from ~6 to 20 record similar deficits to those present in SAH99555 and ureilites (Fig. 1). In agreement with ^{54}Cr anomalies reported for various differentiated meteorite groups (*16*), the SAH99555 angrite, iron meteorites, pallasites, and ureilites are characterized by small deficits in ^{62}Ni (Fig. 2), indicating that nucleosynthetic anomalies in the neutron-rich isotopes of Ni and Cr were coupled and present at the planetary and protoplanetary scale in the accretion disk of the young solar system (Fig. 3).

The presence of similar ^{60}Ni* deficits (Fig. 1) in samples with highly variable superchondritic Fe/Ni ratios from differentiated planetesimals that accreted within 1 My of the solar system (angrites and ureilites) is inconsistent with pervasive distribution of ^{60}Fe in the accretion region of these bodies. For example, assuming an initial ^{60}Fe/^{56}Fe of ~1 × 10^{-6}, crystallization of the SAH99555 angrite within 3 My of solar system formation (*13*, *14*) would result in large excesses in ϵ^{60}Ni* ranging from at least ~13 (olivine separate) to 32 (bulk samples) ϵ units. Although

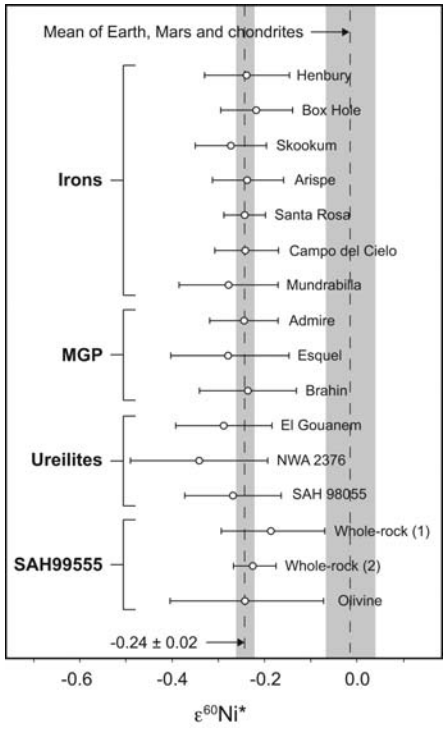

Fig. 1. ϵ^{60}Ni* values for irons, pallasites, ureilites, and the SAH99555 angrite. Error bars are 2 SE. Differentiated meteorites studied here record a uniform deficit of −0.243 ± 0.020 ϵ units [weighted mean, mean square of weighted deviations (MSWD) = 0.48]. MPG, main group pallasites.

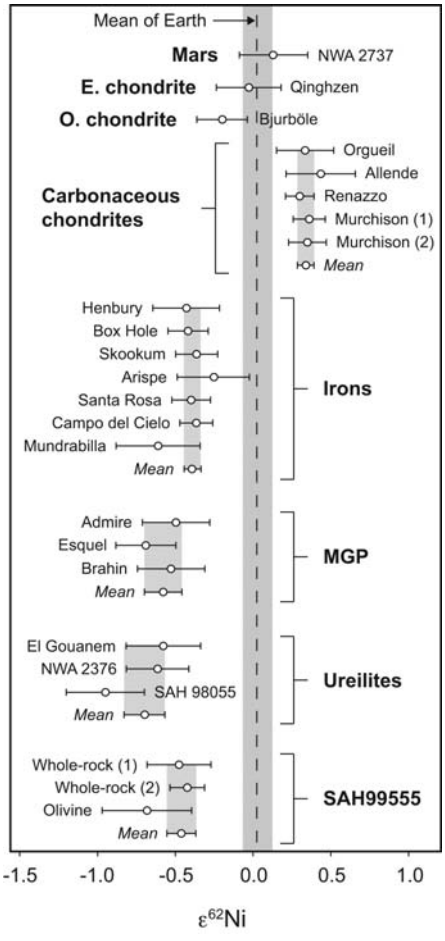

Fig. 2. ϵ^{62}Ni values of inner solar system planets and planetesimals. Error bars are 2 SE. E. chondrite, enstatite chondrite; O. chondrite, ordinary chondrite.

[1]Geological Institute, University of Copenhagen, Øster Voldgade 10, DK-1350, Denmark. [2]Geological Museum, University of Copenhagen, Øster Voldgade 5-7, DK-1350, Denmark. [3]Jackson School of Geosciences, University of Texas at Austin, Austin, TX 78712, USA. [4]Department of Physics and Astronomy, Clemson University, Clemson, SC 29634–0978, USA.

*To whom correspondence should be addressed. E-mail: bizzarro@geol.ku.dk

^{60}Ni deficits in material with subchondritic Fe/Ni ratios such as irons and pallasites could be consistent with formation in the presence of ^{60}Fe, the deficits in ^{60}Ni are not correlated with the measured Fe/Ni ratios (table S1) or inferred Fe/Ni ratios for the parental Fe liquid of magmatic iron meteorites (*17*). Furthermore, ^{60}Fe-^{60}Ni model ages calculated for individual iron and pallasite meteorites analyzed here are inconsistent with time constraints inferred from other short-lived chronometers such as the ^{182}Hf-^{182}W and ^{26}Al-^{26}Mg systems (*9*, *15*). Thus, the uniform deficits in the ϵ^{60}Ni* values for meteorite samples with extremely variable ^{56}Fe/^{58}Ni ratios and different ^{62}Ni anomalies are most easily understood if they reflect formation in the absence of ^{60}Fe (SOM text 2). Conversely, ^{26}Al appears to have been widespread in the accretion regions of most parent bodies from which these meteorites originated.

Our Ni isotope data indicate a decoupling between the presence of ^{26}Al and ^{60}Fe in most differentiated planetesimals, whereas both of these nuclides were extant before or during the accretion of the eucrite (*7*) and chondrite parent bodies (*5*, *6*). Given the homogeneous distribution of ^{26}Al within the early solar system inferred from high-precision Mg isotope measurements of terrestrial planets and bulk chondrite meteorites (*8*, *13*, *18*), the absence of ^{60}Fe in any early accreted planetesimals is not consistent with simultaneous injection of ^{26}Al and ^{60}Fe into the solar system's parental molecular cloud. Therefore, we infer that the absence of ^{60}Fe in irons, pallasites, ureilites, and the SAH99555 angrite reflects a late injection of ^{60}Fe into the protoplanetary disk, at a time when ^{26}Al was already homogeneously distributed in the inner solar system. The injection of ^{60}Fe had to occur before or during the accretion of the EPB, which thermal modeling constrains to within 1 My of solar system formation (*8*). This requires the accretion of the angrite parent body (APB) to have predated that of the EPB, and this conclusion is consistent with the contemporaneous differentiation of these planetesimals (*8*, *9*, *13*, *14*), given the uncertainties associated with the thermal models. Given that chondrules formed over the lifetime of the protoplanetary disk (*10*), we predict that they will provide an ideal record to better constrain the timing of injection of ^{60}Fe.

Decoupling the first appearance of ^{26}Al and ^{60}Fe has far-reaching implications for understanding the formation and early evolution of our solar system. It implies that the stellar process that injected ^{60}Fe to the early solar system was not a thermally pulsating asymptotic giant branch (AGB) star or a type II core collapse supernova (SNII) with initial mass of <30 solar masses ($M_\odot$). This is because copious amounts of ^{26}Al are necessarily co-injected with ^{60}Fe by these stellar processes (*1*, *4*), and this feature is inconsistent with the observation that ^{26}Al was present in the precursor material of Earth, the Moon, Mars, and chondrite meteorites in comparable amounts to that present in CAIs (*8*, *13*, *18*). However, the observed decoupling between ^{26}Al and ^{60}Fe is a predicted feature of rapidly evolving massive stars [$\gtrsim$30 $M_\odot$ (*19*, *20*)], where ^{26}Al is expelled by intense stellar winds during the Wolf-Rayet (WR) stage, and ^{60}Fe is exclusively ejected during the type 1b/c supernova (SNIb/c) event that punctuates the WR stage. Recent calculations (*21*) indicate that WR stars can account for the early solar system abundances of ^{26}Al (as well as ^{41}Ca and ^{107}Pd). Furthermore, ^{60}Fe is predicted to be ejected during the following SNIb/c event, where no ^{26}Al is co-ejected after the removal of the H-rich envelope by stellar winds (*20*). The lifetime of the WR stage, during which most of the original mass of the star is expelled by the winds before the SNIb/c event, is $\lesssim$2 My for rotating WR stars (*22*). This is in excellent agreement with the time difference between the incorporation of ^{26}Al and ^{60}Fe into the early solar system inferred from our study. The presence of ^{53}Mn and ^{182}Hf in planetesimals that formed in the absence of ^{60}Fe, such as the APB (*23*, *24*), implies that the initial abundance of these longer-lived nuclides in the early solar system primarily reflects galactic production.

Our results indicate that the solar system formed in association with a massive star or stars, perhaps similar to star-forming regions such as the Orion and Eagle nebulas (*25*), or even more massive clusters such as the Carina nebula (*26*). In this astrophysical setting, enrichment of ^{26}Al in the interstellar medium by the WR winds begins before enrichment from SNIIs, because WR stars originate from more-massive and shorter-lived progenitors than the majority of SNIIs. Collapse of the solar system's parental molecular cloud in an ^{26}Al-rich environment can be triggered by the cumulative effects of the ionization fronts and/or associated winds from massive stars (*25*). After the collapse and formation of the protoplanetary disk, continued addition of ^{26}Al from the WR winds is difficult because gaseous ejecta are not able to efficiently penetrate the disk (*27*). This readily explains the homogeneous distribution of ^{26}Al within the early solar system as inferred from high-precision Mg isotope measurements of solids, planets, and planetesimals from the inner solar system (*8*, *13*, *18*). As such, late addition of ^{60}Fe into the protoplanetary disk is compatible with injection of supernova condensates such as dust grains associated with the explosion of a dying WR star (SNIb/c). Numerical modeling indicates that homogenization of injected short-lived nuclides such as ^{60}Fe into an active disk occurs over time scales of 1000 years (*28*), in line with the homogeneous ϵ^{60}Ni* recorded by samples from Earth, Mars, and chondrite meteorites.

The anomalous composition in neutron-rich isotopes such as ^{62}Ni and ^{54}Cr (Figs. 2 and 3) recorded by primitive and differentiated bodies may represent residual heterogeneity inherited from the parental molecular cloud, given that neutron-rich iron-group isotopes are commonly synthesized in old supernova sources (*29*) rarely associated with young star-forming regions. Similar to oxygen isotopes, the ^{62}Ni anomalies reported here provide a means to explore potential genetic relationships between diverse meteorite groups and terrestrial planets. Apart from enstatite chondrites, the combined terrestrial ^{60}Ni, ^{62}Ni, and ^{54}Cr isotope composition is unique among the diverse meteorite groups investigated. Because the major element composition of enstatite chondrites is not compatible with that inferred for Earth's primitive upper mantle (*30*), our study supports the idea that Earth accreted from material distinct from that of any known primitive and/or differentiated meteorites.

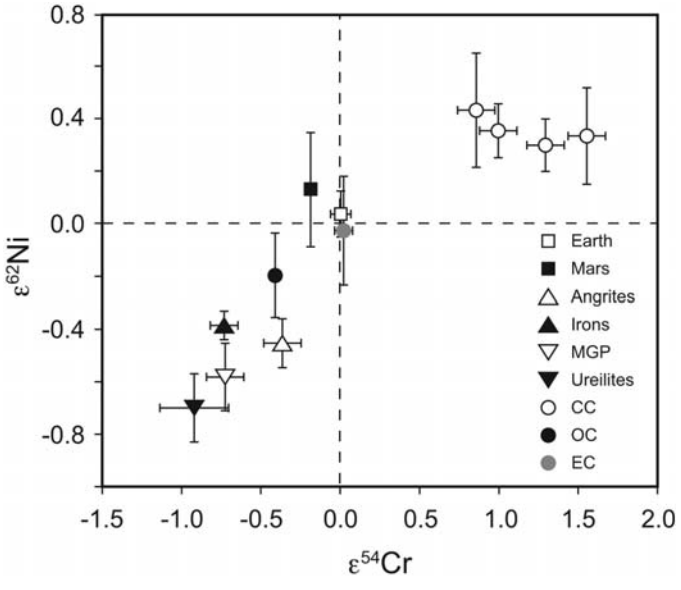

Fig. 3. ϵ^{54}Cr and ϵ^{62}Ni variation diagram for inner solar system planets and planetesimals. Error bars are 2 SD. ^{54}Cr isotope data are from (*16*, *31*). Because neutron-rich iron-group isotopes like ^{54}Cr and ^{62}Ni are produced by the same nucleosynthetic processes (*29*), a positive correlation is expected. The array defined by Earth, Mars, enstatite chondrites (EC), ordinary chondrites (OC) and differentiated meteorites is consistent with mixing of neutron-rich and neutron-poor isotopic components. The trend defined by carbonaceous chondrites (CC) requires additional components and/or processes.

References and Notes

1. G. J. Wasserburg, M. Busso, R. Gallino, K. Nollett, *Nucl. Phys. A.* **777**, 5 (2006).
2. S. B. Jacobsen, in *Chondrites and the Protoplanetary Disk*, A. N. Krot, E. R. D. Scott, B. Reipurth, Eds. (Astrophysical Society of the Pacific, San Francisco, 2005), pp. 548–557.

3. F. H. Shu, H. Shang, A. E. Glassgold, T. Lee, *Science* **277**, 1475 (1997).
4. B. S. Meyer, in *Chondrites and the Protoplanetary Disk*, A. N. Krot, E. R. D. Scott, B. Reipurth, Eds. (Astrophysical Society of the Pacific, San Francisco, CA, 2005), pp. 515–526.
5. S. Tachibana, G. R. Huss, N. T. Kita, G. Shimoda, Y. Morishita, *Astrophys. J.* **639**, L87 (2006).
6. S. Mostefaoui, G. W. Lugmair, P. Hoppe, *Astrophys. J.* **625**, 271 (2005).
7. A. Shukolyukov, G. W. Lugmair, *Earth Planet. Sci. Lett.* **119**, 159 (1993).
8. M. Bizzarro, J. A. Baker, H. Haack, K. L. Lundgaard, *Astrophys. J.* **632**, L41 (2005).
9. A. N. Halliday, T. Kleine, in *Meteorites and the Early Solar System II*, D. S. Lauretta, H. Y. McSween, Eds. (Univ. of Arizona Press, Tucson, AZ, 2006), pp. 775–801.
10. N. Kita *et al.*, in *Chondrites and the Protoplanetary Disk*, A. N. Krot, E. R. D. Scott, B. Reipurth, Eds. (Astrophysical Society of the Pacific, San Francisco, CA, 2005), pp. 558–587.
11. Materials and methods are available as supporting material on *Science* Online.
12. Y. Amelin, A. N. Krot, I. D. Hutcheon, A. A. Ulyanov, *Science* **297**, 1678 (2002).
13. J. Baker, M. Bizzarro, N. Wittig, J. Connelly, H. Haack, *Nature* **436**, 1127 (2005).
14. Y. Amelin, *Lunar Planet. Sci.* **XXXVIII**, 1669 (abstr.) (2007).
15. J. A. Baker, M. Bizzarro, abstract 8612 presented at the *Protostars and Planets V* meeting, Hilton Waikoloa Village, HI, 24 to 28 October 2005.
16. A. Trinquier, J.-L. Birck, C. Allègre, *Astrophys. J.* **655**, 1179 (2007).
17. J. H. Jones, M. J. Drake, *Geochim. Cosmochim. Acta* **47**, 1199 (1983).
18. K. Thrane, M. Bizzarro, J. A. Baker, *Astrophys. J.* **646**, L159 (2006).
19. A. Palacios *et al.*, *Astron. Astrophys.* **429**, 613 (2005).
20. M. Limongi, A. Chieffi, *Astrophys. J.* **647**, 483 (2006).
21. M. Arnould, S. Goriely, G. Meynet, *Astron. Astrophys.* **453**, 653 (2006).
22. G. Meynet, A. Maeder, *Astron. Astrophys.* **429**, 581 (2005).
23. D. P. Glavin, A. Kubny, E. Jagoutz, G. W. Lugmair, *Meteorit. Planet. Sci.* **39**, 693 (2004).
24. A. Markowski *et al.*, *Meteorit. Planet. Sci.* **41**, 5195 (abstr.) (2006).
25. J. J. Hester, S. J. Desch, in *Chondrites and the Protoplanetary Disk*, A. N. Krot, E. R. D. Scott, B. Reipurth, Eds. (Astrophysical Society of the Pacific, San Francisco, CA, 2005), pp. 107–130.
26. J. M. Rathborne *et al.*, *Mon. Not. R. Astron. Soc.* **331**, 85 (2002).
27. N. Ouellette, S. J. Desch, J. J. Hester, L. A. Leshin, in *Chondrites and the Protoplanetary Disk*, A. N. Krot, E. R. D. Scott, B. Reipurth, Eds. (Astrophysical Society of the Pacific, San Francisco, CA, 2005), pp. 527–538.
28. A. P. Boss, *Meteorit. Planet. Sci.* **41**, 1695 (2006).
29. S. E. Woosley, *Astrophys. J.* **476**, 801 (1997).
30. M. J. Drake, K. Righter, *Nature* **416**, 39 (2002).
31. A. Shukolyukov, G. W. Lugmair, *Lunar Planet. Sci.* **XXXVII**, 1478 (abstr.) (2006).
32. Financial support for this project was provided by the Danish National Science Foundation, NASA's Cosmochemistry Program, and the Danish Natural Science Research Council.

Supporting Online Material

www.sciencemag.org/cgi/content/full/316/5828/1178/DC1
Materials and Methods
SOM Text
Tables S1 and S2
References

8 February 2007; accepted 27 March 2007
10.1126/science.1141040

Model Projections of an Imminent Transition to a More Arid Climate in Southwestern North America

Richard Seager,[1]* Mingfang Ting,[1] Isaac Held,[2,3] Yochanan Kushnir,[1] Jian Lu,[4] Gabriel Vecchi,[2] Huei-Ping Huang,[1] Nili Harnik,[5] Ants Leetmaa,[2] Ngar-Cheung Lau,[2,3] Cuihua Li,[1] Jennifer Velez,[1] Naomi Naik[1]

How anthropogenic climate change will affect hydroclimate in the arid regions of southwestern North America has implications for the allocation of water resources and the course of regional development. Here we show that there is a broad consensus among climate models that this region will dry in the 21st century and that the transition to a more arid climate should already be under way. If these models are correct, the levels of aridity of the recent multiyear drought or the Dust Bowl and the 1950s droughts will become the new climatology of the American Southwest within a time frame of years to decades.

The Third Assessment Report of the Intergovernmental Panel on Climate Change (IPCC) reported that the average of all the participating models showed a general decrease in rainfall in the subtropics during the 21st century, although there was also considerable disagreement among the models (*1*). Subtropical drying accompanying rising CO_2 was also found in the models participating in the second Coupled Model Intercomparison Project (*2*). We examined future subtropical drying by analyzing the time history of precipitation in 19 climate models participating in the Fourth Assessment Report (AR4) of the IPCC (*3*). The future climate projections followed the A1B emissions scenario (*4*), in which CO_2 emissions increase until about 2050 and decrease modestly thereafter, leading to a CO_2 concentration of 720 parts per million in 2100. We also analyzed the simulations by these models for the 1860–2000 period, in which the models were forced by the known history of trace gases and estimated changes in solar irradiance, volcanic and anthropogenic aerosols, and land use (with some variation among the models). These simulations provided initial conditions for the 21st-century climate projections. For each model, climatologies were computed for the 1950–2000 period by averaging over all the simulations available for each model. All climate changes shown here are departures from this climatology.

We define an area (shown as a box in Fig. 4A) called "the Southwest" (including all land between 125°W and 95°W and 25°N and 40°N) that incorporates the southwestern United States and parts of northern Mexico. Figure 1 shows the modeled history and future of the annual mean precipitation minus the evaporation ($P - E$), averaged over this region for the period common to all of the models (1900–2098). The median, 25th, and 75th percentiles of the model $P - E$ distribution and the median of P and E are shown. For cases in which there were multiple simulations with a single model, data from these simulations were averaged together before computing the distribution. $P - E$ equals the moisture convergence by the atmospheric flow and (over land) the amount of water that goes into runoff.

In the multimodel ensemble mean, there is a transition to a sustained drier climate that begins in the late 20th and early 21st centuries. In the ensemble mean, both P and E decrease, but the former decreases by a larger amount. $P - E$ is primarily reduced in winter, when P decreases and E is unchanged or modestly increased, whereas in summer, both P and E decrease. The annual mean reduction in P for this region, calculated from rain gauge data within the Global Historical Climatology Network, was 0.09 mm/day between 1932 and 1939 (the Dust Bowl drought) and 0.13 mm/day between 1948 and 1957 (the 1950s Southwest drought). The ensemble median reduction in P that drives the reduction in $P - E$ reaches 0.1 mm/day in midcentury, and one quarter of the models reach this amount in the early part of the current century.

The annual mean $P - E$ difference between 20-year periods in the 21st century and the 1950–2000 climatology for the 19 models are shown in Fig. 2. Almost all models have a drying trend in the American Southwest, and they consistently become drier throughout the century. Only 1 of the 19 models has a trend toward a wetter climate. Of the total of 49 individual projections conducted with the 19 models, even as early as the 2021–2040 period, only 3 projections show a shift to a wetter climate. Examples of modeled history and future precipitation for single simulations of four individual models are shown in Fig. 3 and provide an idea of potential trajectories toward the more arid climate.

[1]Lamont Doherty Earth Observatory (LDEO), Columbia University, Palisades, NY 10964, USA. [2]National Oceanic and Atmospheric Administration (NOAA) Geophysical Fluid Dynamics Laboratory, Princeton, NJ 08540, USA. [3]Program in Atmospheric and Oceanic Sciences, Department of Geosciences, Princeton University, Princeton, NJ 08544, USA. [4]National Center for Atmospheric Research, Boulder, CO 80307, USA. [5]Tel Aviv University, Tel Aviv, Israel.

*To whom correspondence should be addressed. E-mail: seager@ldeo.columbia.edu

The contours in Fig. 4, A to C, show a map of the change in $P - E$ for the decades between 2021 and 2040 minus those in the 1950–2000 period for one of the IPCC models: the Geophysical Fluid Dynamics Laboratory (GFDL) climate model CM2.1 (*5*). In general, large regions of the relatively dry subtropics dry further, whereas wetter, higher-latitude regions become wetter still. In addition to the American Southwest, the southern Europe–Mediterranean–Middle East region also experiences a severe drying. This pattern of subtropical drying and moistening at higher latitudes is a robust feature of current projections with different models of future climate (*6*).

The change (δ) in $P - E$ (in meters per second) is balanced by a change in atmospheric moisture convergence, namely

$$\rho_w g \delta(P-E) = -\delta\left[\int_0^{p_s} \nabla\cdot(\overline{\underline{u}\,\underline{q}})dp + \int_0^{p_s} \nabla\cdot(\overline{\underline{u}\,\underline{q}'})dp\right] \quad (1)$$

Overbars indicate monthly means, primes represent departures from the monthly mean, ρ_w is the density of water, g indicates the acceleration due to gravity, and ∇ indicates the horizontal divergence operator. The change in moisture convergence can be divided into contributions from the mean flow and from eddies. In the former, the atmospheric flow ($\underline{\overline{u}}$) and the moisture ($\overline{q}$) are averaged over a month before computing the moisture transport, whereas the latter is primarily associated with the highly variable wind ($\underline{u}'$) and moisture (q') fields within storm systems. The moisture convergence is integrated over the pressure (p) from the top of the atmosphere ($p = 0$) to the surface (p_s). The mean wind and humidity fields in Eq. 1 can be taken to be their climatological fields. (The rectification of interannual variability in the monthly mean flow and moisture fields is found to be negligible.) Changes in the mean flow contribution can, in turn, be approximated by one part associated with the climatological circulation from 1950 to 2000 ($\underline{\overline{u}}_P$), operating on the increase in climatological atmospheric humidity ($\delta\overline{q}$, a consequence of atmospheric warming), and by another part due to the change in circulation climatology ($\delta\underline{\overline{u}}$), operating on the atmospheric humidity climatology from 1950 to 2000 ($\overline{q}_P$). The nonlinear term involving changes in both the mean flow and the moisture field is found to be relatively small. Hence, Eq. 1 can be approximated by:

$$\rho_w g\delta(P-E) \sim -\int_0^{p_s} \nabla\cdot(\overline{q}_P\delta\,\underline{\overline{u}} + \underline{\overline{u}}_P\delta\overline{q})dp - \delta\int_0^{p_s} \nabla\cdot(\overline{\underline{u}'q'})dp \quad (2)$$

We therefore think in terms of a threefold decomposition of $P - E$, as displayed in Fig. 4 (colors) for the GFDL CM2.1 model: (i) a contribution from the change in mean circulation, (ii) a contribution from the change in mean humidity, and (iii) a contribution from eddies.

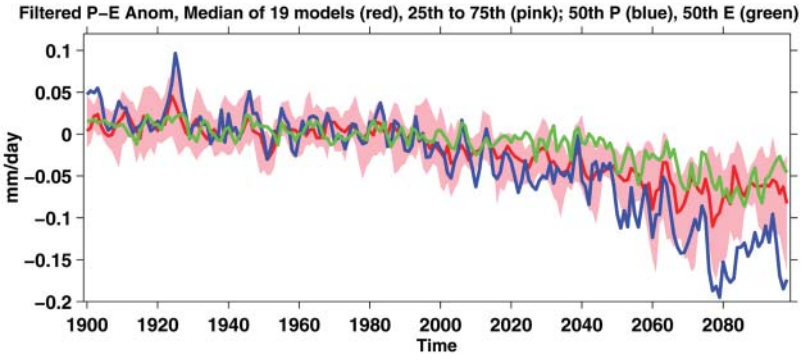

Fig. 1. Modeled changes in annual mean precipitation minus evaporation over the American Southwest (125°W to 95°W and 25°N to 40°N, land areas only), averaged over ensemble members for each of the 19 models. The historical period used known and estimated climate forcings, and the projections used the SResA1B emissions scenario. The median (red line) and 25th and 75th percentiles (pink shading) of the $P - E$ distribution among the 19 models are shown, as are the ensemble medians of P (blue line) and E (green line) for the period common to all models (1900–2098). Anomalies (Anom) for each model are relative to that model's climatology from 1950–2000. Results have been 6-year low-pass Butterworth-filtered to emphasize low-frequency variability that is of most consequence for water resources. The model ensemble mean $P - E$ in this region is around 0.3 mm/day.

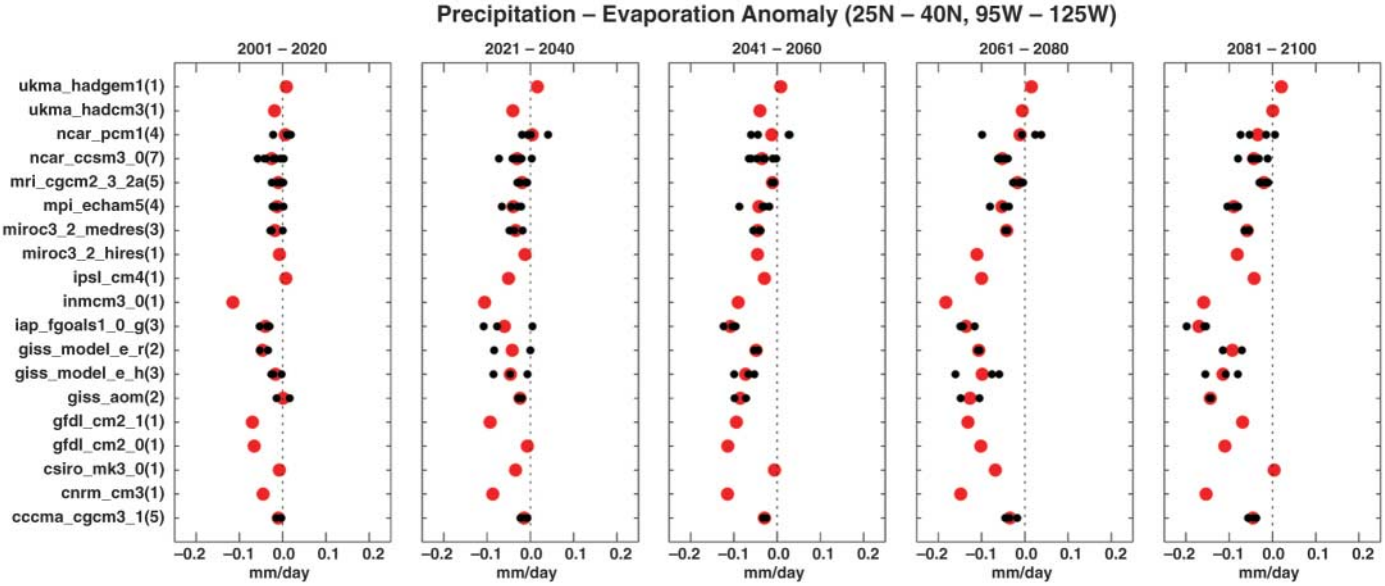

Fig. 2. The change in annual mean $P - E$ over the American Southwest (125°W to 95°W and 25°N to 40°N, land areas only) for 19 models (listed at left), relative to model climatologies from 1950–2000. Results are averaged over 20-year segments of the current century. The number of ensemble members for each projection is listed by the model name at left. Black dots represent ensemble members (where available), and red dots represent the ensemble mean for each model.

The mean flow convergence term involving only changes in humidity (Fig. 4B) causes increasing $P - E$ in regions of low-level mean mass convergence and decreasing $P - E$ in regions of low-level mean mass divergence, generally intensifying the existing pattern of $P - E$ (*6*). This term helps to explain much of the reduction in $P - E$ over the subtropical oceans, where there is strong evaporation, atmospheric moisture divergence, and low precipitation (*6*). Over land areas in general, there is no infinite surface-water source, and $P - E$ has to be positive and sustained by atmospheric moisture convergence. Over the American Southwest, in the current climate, it is the time-varying flow that sustains most of the positive $P - E$, whereas the mean flow diverges moisture away. Here, the "humidity contribution" leads to reduced $P - E$, as the moisture divergence by the mean flow increases with rising humidity. Over the Mediterranean region, there is mean moisture divergence, and rising humidity again leads to increased mean moisture divergence and reduced $P - E$.

Over the ocean, the contribution of humidity changes to changes in $P - E$ can be closely approximated by assuming that the relative humidity remains fixed at its 1950–2000 values (*6*). Over almost all land areas and especially over those that have reduced $P - E$, the relative humidity decreases in the early 21st century. This is because, unlike over the ocean, evaporation cannot keep pace with the rising saturation humidity of the warming atmosphere. Over land, the humidity contribution to the change in $P - E$ is distinct from that associated with fixed relative humidity.

Decreases in $P - E$ can also be sustained by changes in atmospheric circulation that alter the mean moisture convergence, even in the absence of changes in humidity (Fig. 4A). This "mean circulation contribution" leads to reduced $P - E$ at the northern edge of the subtropics (e.g., the Mediterranean region, the Pacific and the Atlantic around 30°N, and parts of southwestern North America). The change in moisture convergence by the transient eddies (Fig. 4C) dries southern Europe and the subtropical Atlantic and moistens the higher-latitude Atlantic, but it does not have a coherent and large impact over North America.

A substantial portion of the mean circulation contribution, especially in winter, can be accounted for by the change in zonal mean flow alone (not shown in the figures), indicating that changes in the Hadley Cell and the extratropical mean meridional circulation are important. Increases in humidity and mean moisture divergence, changes in atmospheric circulation, and the intensification of eddy moisture divergence cause drying in the subtropics, including the area over western North America and the Mediterranean region. For the Southwest region, the annual mean $P - E$ decreases by 0.086 mm/day, which is largely accounted for by an increase in the mean flow moisture divergence. Changes in the circulation alone contribute 0.095 mm/day of drying, and changes in the humidity alone contribute 0.032 mm/day. These changes are modestly offset by an increased transient-eddy moisture convergence of 0.019 mm/day. (*7*).

Within models, the poleward edge of the Hadley Cell and the mid-latitude westerlies move poleward during the 21st century (*8*–*10*). The descending branch of the Hadley Cell causes aridity, and hence the subtropical dry zones expand poleward. In models, a poleward circulation shift can be forced by rising tropical sea surface temperatures (SSTs) in the Indo-Pacific region (*11*) and by uniform surface warming (*12*). The latter results are relevant because the spatial pattern of surface warming in the AR4 models is quite uniform away from the poles. One explanation (*13*, *14*) is that rising tropospheric static stability, an established consequence of moist thermodynamics, stabilizes the subtropical jet streams at the poleward flank of the Hadley Cell against baroclinic instability. Consequently, the Hadley Cell extends poleward (increasing the vertical wind shear at its edge) to a new latitude where the shear successfully compensates for the suppression of baroclinic instability by rising static stability.

Although increasing stability is likely to be a substantial component of the final explanation, a fully satisfying theory for the poleward shift of the zonal mean atmospheric circulation in a warming world must account for the complex interplay between the mean circulation (Hadley Cell and the mid-latitude Ferrell Cell) and the transient eddies (*13*, *14*) that will determine where precipitation will increase and decrease in the future. However, not all of the subtropical drying in the Southwest and Mediterranean regions can be accounted for by zonally symmetric processes, and a full explanation will require attention to moisture transport within localized storm tracks and stationary waves.

The six severe multiyear droughts that have struck western North America in the instrumental record have all been attributed (by the use of climate models) to variations in SSTs in the tropics, particularly persistent La Niña–like SSTs in the tropical Pacific Ocean (*15*–*19*). The projected future climate of intensified aridity in the Southwest is caused by different processes, because the models vary in their tropical SST response to anthropogenic forcing. Instead, it is caused by rising humidity that causes increased moisture divergence and changes in atmospheric circulation cells that include a poleward expansion of the subtropical dry zones. The drying of subtropical land areas that, according to the models, is imminent or already under way is unlike any climate state we have seen in the instrumental record. It is also distinct from the multidecadal megadroughts that afflicted the American Southwest during Medieval times (*20*–*22*), which have also been attributed to changes in tropical SSTs (*18*, *23*). The most severe

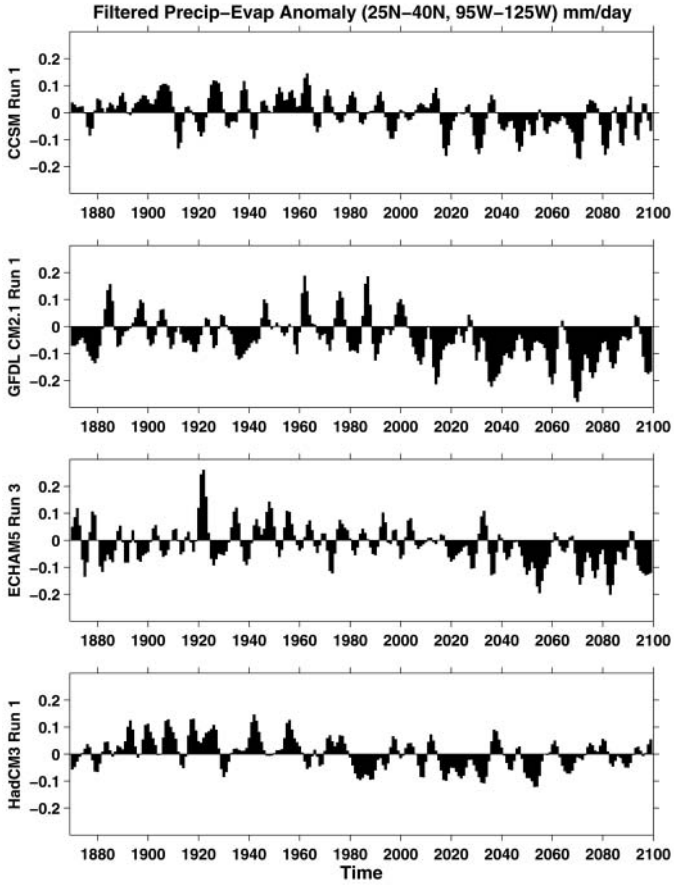

Fig. 3. The change in annual mean $P - E$ over the American Southwest (125°W to 95°W and 25°N to 40°N, land areas only) for four coupled models, relative to model ensemblemean climatologies from 1950–2000. The results are from individual simulations of the 1860–2000 period, forced by known and estimated climate forcings and individual projections of future climate with the SResA1B scenarios of climate forcings. Because the modeled anomalies have not been averaged together here, these time series provide an idea of plausible evolutions of Southwest climate toward a more arid state. The models are the National Center for Atmospheric Research Community Climate System Model (CCSM), GFDL model CM2.1, Max Planck Institut Für Meteorologie model ECHAM5, and Hadley Centre for Climate Change model HadCM3. All time series are for annual mean data, and a 6-year low-pass Butterworth filter has been applied.

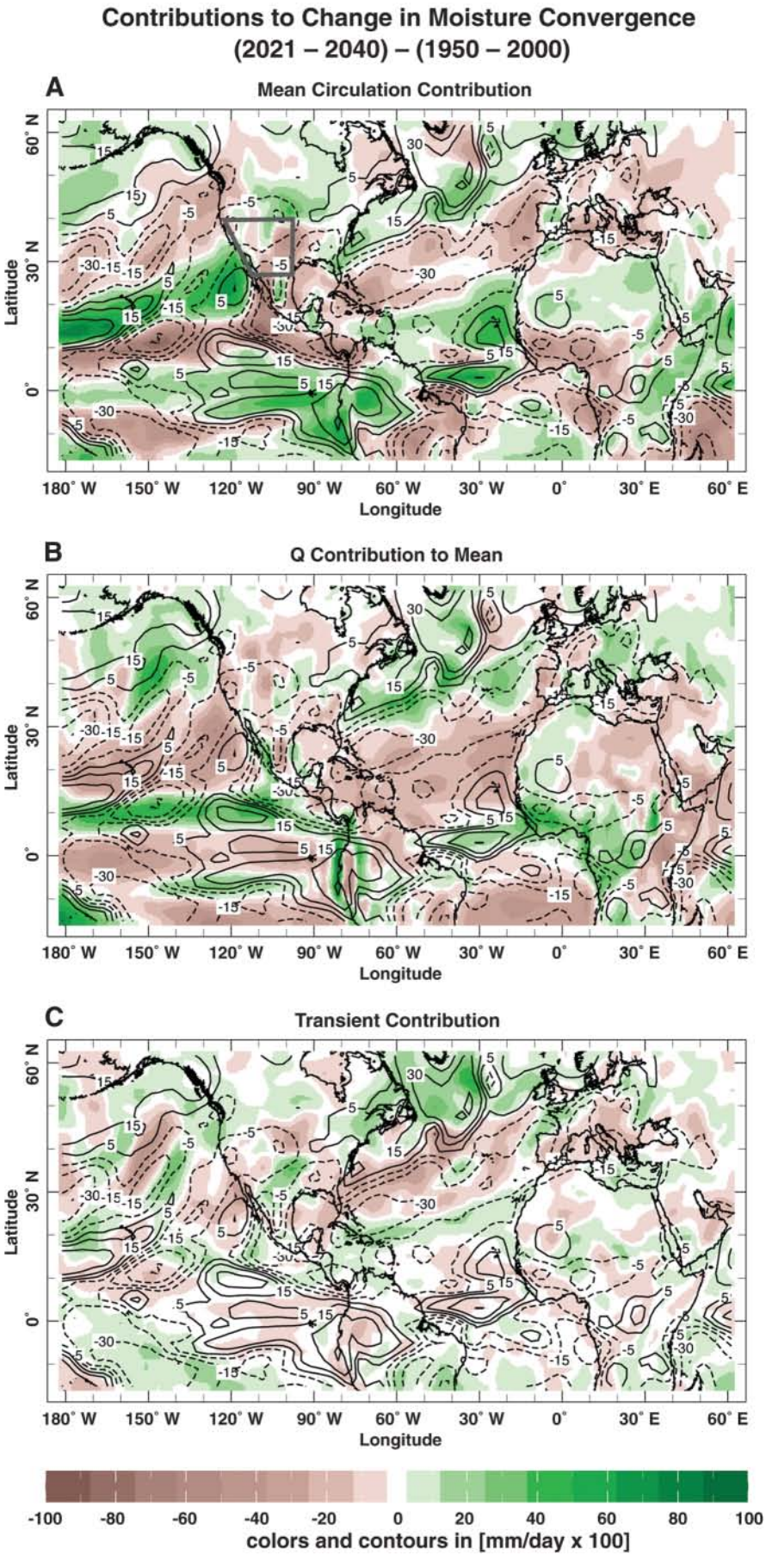

Fig. 4. The change in annual means of $P - E$ for the 2021–2040 period minus the 1950–2000 period [contours in (A) to (C)] and contributions to the change in vertically integrated moisture convergence (colors; negative values imply increased moisture divergence) by the mean flow, due to (**A**) changes in the flow, (**B**) the specific humidity, and (**C**) the transient-eddy moisture convergence, all for the GFDL CM2.1 model. The box in (A) shows the area we defined as "the Southwest."

future droughts will still occur during persistent La Niña events, but they will be worse than any since the Medieval period, because the La Niña conditions will be perturbing a base state that is drier than any state experienced recently.

References and Notes

1. U. Cubasch *et al.*, in *Climate Change 2000–The Scientific Basis: Contribution of Working Group I to the Third Assessment Report of the Intergovernmental Panel on Climate Change*, J. T. Houghton *et al.*, Eds. (Cambridge Univ. Press, Cambridge, 2001), pp. 525–582.
2. M. R. Allen, W. J. Ingram, *Nature* **419**, 224 (2002).
3. Details of the models analyzed can be found at www-pcmdi.llnl.gov/ipcc/model_documentation/ipcc_model_documentation.php, and the data can be found at https://esg.llnl.gov:8443/index.jsp.
4. N. Nakicenovic, R. Swart, Eds., *Special Report on Emissions Scenarios* (Cambridge Univ. Press, New York, 2000).
5. T. L. Delworth *et al.*, *J. Clim.* **19**, 643 (2006).
6. I. M. Held, B. J. Soden, *J. Clim.* **19**, 5686 (2006).
7. The model $P - E$ is not fully accounted for by the computed moisture flow convergence that is calculated by taking the sum of the components of the mean flow and transient eddies (the imbalance is 0.022 mm/day). Calculations were performed with data collected daily on the model grid using closely matching numerics, but errors could be introduced by not using a time resolution of several hours and by neglecting moisture diffusion (potentially large over mountains), which was not archived. The data are available at http:/kage.ldeo.columbia.edu/SOURCES/.LDEO/.ClimateGroup/.GFDL.
8. J. H. Yin, *Geophys. Res. Lett.* **32**, L18701 (2005).
9. P. J. Kushner, I. M. Held, T. L. Delworth, *J. Clim.* **14**, 2238 (2001).
10. L. Bengtsson, K. I. Hodges, E. Roeckner, *J. Clim.* **19**, 3518 (2006).
11. N.-C. Lau, A. Leetmaa, M. J. Nath, *J. Clim.* **19**, 3607 (2006).
12. S. Lee, *J. Atmos. Sci.* **56**, 1353 (1999).
13. T. Schneider, *Annu. Rev. Earth Planet. Sci.* **34**, 655 (2006).
14. C. C. Walker, T. Schneider, *J. Atmos. Sci.* **63**, 3333 (2006).
15. 13. S. D. Schubert, M. J. Suarez, P. J. Pegion, R. D. Koster, J. T. Bacmeister, *Science* **303**, 1855 (2004).
16. S. D. Schubert, M. J. Suarez, P. J. Pegion, R. D. Koster, J. T. Bacmeister, *J. Clim.* **17**, 485 (2004).
17. R. Seager, Y. Kushnir, C. Herweijer, N. Naik, J. Velez, *J. Clim.* **18**, 4065 (2005).
18. C. Herweijer, R. Seager, E. R. Cook, *Holocene* **16**, 159 (2006).
19. H.-P. Huang, R. Seager, Y. Kushnir, *Clim. Dyn.* **24**, 721 (2005).
20. S. Stine, *Nature* **369**, 546 (1994).
21. E. R. Cook, C. A. Woodhouse, C. M. Eakin, D. M. Meko, D. W. Stahle, *Science* **306**, 1015 (2004).
22. C. Herweijer, R. Seager, E. R. Cook, J. Emile-Geay, *J. Clim.* **20**, 1353 (2007).
23. E. R. Cook, R. Seager, M. A. Cane, D. W. Stahle, *Earth Sci. Rev.* **81**, 93 (2007).
24. This work was supported at LDEO by NOAA grants NA03OAR4320179 and NA06OAR4310151 and by NSF grants ATM05-01878, ATM04-34221, and ATM03-47009. We thank R. Dole, W. Robinson, and M. Wallace for useful conversations.

5 January 2007; accepted 26 March 2007
Published online 5 April 2007;
10.1126/science.1139601
Include this information when citing this paper.

Dicamba Resistance: Enlarging and Preserving Biotechnology-Based Weed Management Strategies

Mark R. Behrens,[1]* Nedim Mutlu,[1]* Sarbani Chakraborty,[1] Razvan Dumitru,[1] Wen Zhi Jiang,[1] Bradley J. LaVallee,[2]† Patricia L. Herman,[1]‡ Thomas E. Clemente,[2,3,4] Donald P. Weeks[1,4]§

The advent of biotechnology-derived, herbicide-resistant crops has revolutionized farming practices in many countries. Facile, highly effective, environmentally sound, and profitable weed control methods have been rapidly adopted by crop producers who value the benefits associated with biotechnology-derived weed management traits. But a rapid rise in the populations of several troublesome weeds that are tolerant or resistant to herbicides currently used in conjunction with herbicide-resistant crops may signify that the useful lifetime of these economically important weed management traits will be cut short. We describe the development of soybean and other broadleaf plant species resistant to dicamba, a widely used, inexpensive, and environmentally safe herbicide. The dicamba resistance technology will augment current herbicide resistance technologies and extend their effective lifetime. Attributes of both nuclear- and chloroplast-encoded dicamba resistance genes that affect the potency and expected durability of the herbicide resistance trait are examined.

In the past decade, the availability of biotechnology-derived herbicide-resistant and insect-resistant traits has led to striking advancements in agricultural crop management systems throughout the world. These "input traits" have contributed to greater productivity per hectare, decreased production costs, greater flexibility and efficiencies in production regimes, reduced pesticide use, and improved farmer health (*1*–*3*). In 2006, more than 100 million hectares worldwide were planted with crops having biotechnology-derived traits (*4*). In the United States, for example, Roundup (glyphosate)–resistant crops were planted on almost 90% of the soybean acreage and 60% of the cotton acreage in 2005, along with about 18% of the corn crop (*3*). The recent emergence of weeds resistant to the herbicides used year after year for weed control in fields of herbicide-resistant crops has prompted serious concerns regarding the long-term availability of the facile and economically important weed control provided by current herbicide-resistant crop plants. Also at risk is the greatly expanded use of no-till or reduced-till planting procedures that are made possible by "burndown" of weeds before planting of herbicide-resistant crops. These integrated practices minimize soil loss due to water and wind erosion resulting from traditional methods of soil tillage (*3*).

Among the glyphosate-tolerant weed species currently posing the greatest danger to agricultural productivity are several broadleaf plants such as giant ragweed (*Ambrosia trifida*), horseweed (*Conyza canadenis*), waterhemp (*Amaranthus rudis*), Palmer amaranth (*Amaranthus palmeri*), and common ragweed (*Ambrosia artemisifolia*) (*3*, *5*). To combat these pernicious weeds and to address the potential emergence of other herbicide-resistant broadleaf weeds, we have targeted the development of crop plants resistant to treatment with dicamba. Dicamba is a widely used, low-cost, environmentally friendly herbicide that does not persist in soils and shows little or no toxicity to wildlife and humans (*6*–*10*). Use of the dicamba resistance trait alone or in combination with other herbicide resistance traits will allow rotation of herbicides or use of mixtures of herbicides that will greatly suppress several present or future herbicide-resistant weeds. Here, we describe the use of a genetically engineered bacterial gene, *DMO* (dicamba monooxygenase), that encodes a Rieske nonheme monooxygenase capable of inactivating dicamba when expressed from either the nuclear genome or chloroplast genome of transgenic plants. The DMO enzyme acts to destroy the herbicidal activity of dicamba before the herbicide can build to toxic levels in dicamba-treated transgenic plants, as shown below.

As the first step in the complete mineralization of dicamba, the soil bacterium *Pseudomonas maltophilia* (strain DI-6) converts dicamba to 3,6-dichlorosalicylic acid (DCSA) (*11*, *12*) (Fig. 1A), a compound that lacks appreciable herbicidal activity. The enzyme system responsible for this conversion in the bacterium is the three-component enzyme dicamba *O*-demethylase. This enzyme system serves as an electron transfer chain in which electrons from NADH (the reduced form of nicotinamide adenine dinucleotide) are shuttled through a reductase to a ferredoxin and finally to the terminal component DMO (*13*–*15*). The ferredoxin component of dicamba *O*-demethylase closely resembles the ferredoxin found in plant chloroplasts. Thus, to potentially take advantage of a source of reduced ferredoxin in chloroplasts of transgenic plants to supply electrons for the DMO reaction (and to eliminate the need for the bacterial reductase and ferredoxin genes), we included a chloroplast transit peptide–coding region upstream of the *DMO* gene to allow targeting of DMO to the chloroplast. The DMO expression cassette (Fig. 1B) contained the strong peanut chlorotic streak virus gene promoter FLt36 (*16*) and a terminator region from the pea Rubisco (ribulose-1,5-bisphosphate carboxylase-oxygenase) small subunit gene. The goal then was to determine whether expression of DMO from this expression vector in transgenic broadleaf plants could provide protection against the normally lethal effects of dicamba.

Because of ease of transformation and regeneration, *Arabidopsis thaliana*, tomato, and tobacco were used as model systems to test whether expression of the *DMO* gene alone (i.e., without the ferredoxin and reductase components of dicamba *O*-demethylase) could impart herbicide resistance after application of dicamba. *Agrobacterium*-mediated gene transfer was used to introduce the DMO expression cassette into the nuclear genome of the respective plant species. In regard to tobacco, we used DNA, RNA, and protein blot analyses to test several independently derived T_1-generation plants for the presence and expression of the *DMO* gene (fig.

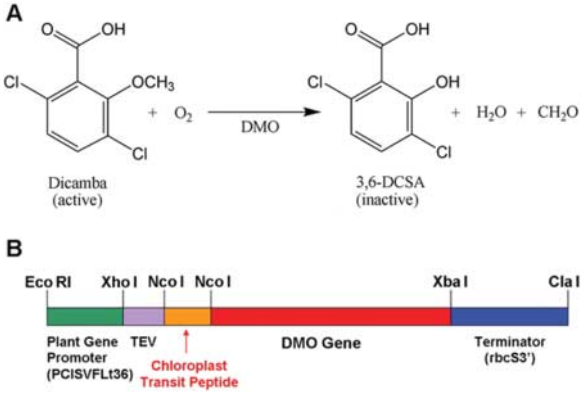

Fig. 1. Dicamba inactivation. (**A**) Conversion of dicamba to DCSA by DMO. (**B**) Genetically engineered version of the *DMO* gene for expression in higher plants, using the FLt36 promoter from peanut chlorotic streak virus, a translational enhancer from the tobacco etch virus (TEV), a chloroplast transit peptide–coding region from the pea Rubisco small subunit gene for chloroplast localization of DMO, and a terminator region from the pea Rubisco small subunit gene (*rbcS3'*).

[1]Department of Biochemistry, University of Nebraska, Lincoln, NE 68588, USA. [2]Center for Biotechnology, University of Nebraska, Lincoln, NE 68588, USA. [3]Department of Agronomy and Horticulture, University of Nebraska, Lincoln, NE 68588, USA. [4]Plant Science Initiative, University of Nebraska, Lincoln, NE 68588, USA.

*These authors contributed equally to this work.
†Present address: Monsanto Company, St. Louis, MO U.S.A.
‡Present address: School of Biological Sciences, University of Nebraska, Lincoln, NE 68588, USA.
§To whom correspondence should be addressed. E-mail: dweeks1@unl.edu

S2). RNA blots demonstrated highly variable levels of *DMO* mRNA in individual transformants that, in general, did not correlate closely with the amount of DMO enzyme produced. We noted (most easily in lanes 2 and 6, fig. S2) that although most of the precursor DMO molecule containing the chloroplast transit peptide was cleaved to the mature form, not all of the precursor was processed.

Most dicotyledonous plants, such as tobacco, are quite sensitive to treatment with dicamba, an auxin-type herbicide. Figure 2A illustrates this point by showing nontransgenic tobacco plants not treated (leftmost plant) and treated with increasing amounts of dicamba. Herbicide damage symptoms are pronounced after spraying dicamba even at the low level of 0.017 kg/ha. Symptoms are quite severe at 0.28 kg/ha and 0.56 kg/ha, the levels normally used for weed control in agricultural applications.

Treatment of transgenic tobacco plants containing the *DMO* gene with 5.6 kg/ha (10 to 20 times the recommended application rate) caused few if any symptoms, whereas a nontransgenic plant suffered severe damage (Fig. 2B). Damage to the lower leaves of the transgenic plants could be duplicated by spraying plants with the surfactant-containing solvent solution used as the vehicle for dicamba application. Leaves produced after treatment of the transgenic plants with dicamba exhibited no visible signs of damage (Fig. 2C). Transgenic tomato plants carrying the genetically engineered *DMO* gene, likewise, showed no damage to newly emerged leaves (fig. S2B) after spraying with dicamba at concentrations as high as 5.6 kg/ha. *Arabidopsis* expressing the *DMO* gene also displayed strong resistance to treatment with dicamba at 1.12 kg/ha, the highest level tested (fig. S3). Over a range of dicamba concentrations tested, an unexpected finding was the observation that tobacco plants transformed with a DMO expression cassette lacking a transit peptide–coding region were resistant to treatments with dicamba at levels on average only slightly below that of plants containing *DMO* genes bearing transit peptide–coding regions (fig. S4; see below).

To determine whether DMO could function exclusively inside chloroplasts, we created the pDMO1 vector bearing the *DMO* gene coding region (fig. S5). This vector allows integration of the *DMO* gene into the chloroplast genome of tobacco by homologous recombination and the isolation of transformants through selection for antibiotic resistance. The *DMO* gene coding region was driven by the strong *psbA* chloroplast gene promoter, containing the complete *psbA* 5′-untranslated region sequence, to obtain high levels of DMO expression. Initial DNA blot analyses of antibiotic-resistant transgenic plants (fig. S6A) demonstrated the presence in chloroplast genomes of both the *DMO* transgene (5.6-kb band) and the native *psbA* gene region (3.3-kb band). Repeated regeneration and selection of transgenic plants on antibiotic-containing medium resulted in apparently homoplastidic chloroplasts bearing the *DMO* gene fragment but not the endogenous native gene region (fig. S6B). Only chloroplast transformants expressing the DMO enzyme were resistant to treatment with dicamba (fig. S7). T_1, T_2, and T_3 generations of progeny from two independently derived chloroplast transformants were tested for resistance to treatment with dicamba at various doses. All exhibited high levels of resistance. Indeed, chloroplast genome transformants displayed no apparent damage (other than "solvent-only damage" to lower leaves) when sprayed with dicamba at a rate of 28 kg/ha (fig. S8). Only transitory damage was observed when plants were treated with extremely high dicamba applications of 112 and 224 kg/ha. At these extremely high levels, initial damage was caused primarily by surfactants and other components of the solvent in which dicamba was delivered. New apex tissues and leaves growing from the damaged plants displayed nearly normal to normal phenotypes, showed no decrease in growth rates, and retained the ability to produce usual numbers and quality of seeds.

The above results were consistent with the hypothesis that reduced ferredoxin in tobacco chloroplasts could be the donor to DMO of electrons needed for oxidation of dicamba to DCSA. As a direct test of this hypothesis, we examined the ability of purified spinach ferredoxin to support the conversion of dicamba to DCSA in the presence and absence of DMO purified from *P. maltophilia* (strain DI-6) or overproduced and purified from *Escherichia coli* (table S1). Results of these experiments demonstrated that reduced ferredoxin from spinach or *Clostridium pasteurianum* was fully capable of donating electrons to DMO in vitro, as measured either by dicamba degradation or by DCSA appearance.

The exceptionally high levels of resistance to dicamba displayed by tobacco plants carrying the *DMO* gene in the chloroplast genome, relative to plants bearing the *DMO* gene as a nuclear gene, suggested the possibility that chloroplast-encoded DMO was produced in greater abundance. Comparison of the amounts of oxygenase as percentage of total soluble protein, fraction of fresh weight, or fraction of dry weight (table S2) showed that chloroplast transformants produced about 20 times as much DMO as did nuclear transformants synthesizing DMO with a chloroplast transit peptide, and about 40 times as much DMO as did nuclear transformants synthesizing DMO without the peptide. The ability to achieve high levels of herbicide resistance and the ability to block gene dissemination through "pollen flow" are attractive features of incorporating the *DMO* gene into the chloroplast genomes of important crop plants as soon as the techniques for such approaches prove practical (*17*, *18*).

Genetic studies of the inheritance of the *DMO* gene in chloroplast transformants revealed that inheritance was maternal, as expected, and was

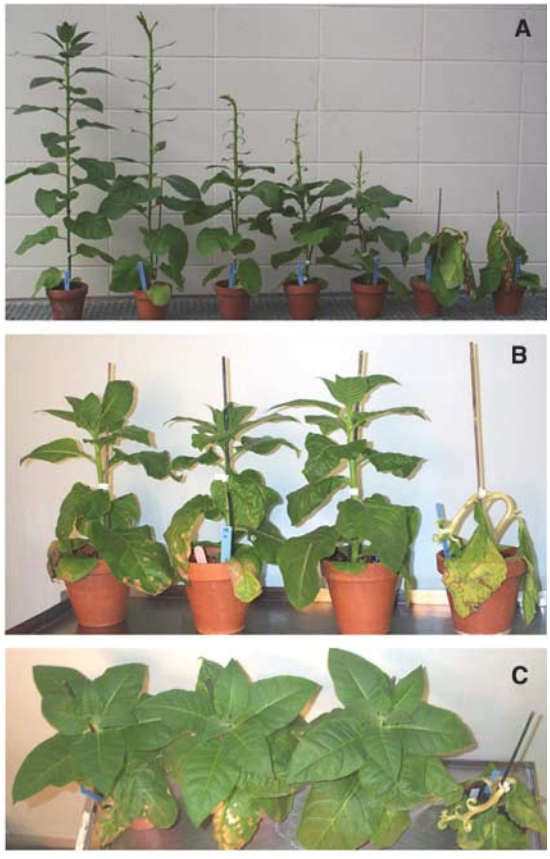

Fig. 2. Effects of dicamba treatment on nontransgenic tobacco plants and plants transformed with a genetically engineered *DMO* gene. (**A**) Demonstration of the sensitivity of nontransgenic tobacco plants to treatment with increasing doses of dicamba (left to right: 0, 0.017, 0.034, 0.07, 0.14, 0.28, and 0.56 kg/ha). (**B**) Three independently derived T_1-generation tobacco plants carrying the dicamba resistance gene (three plants at left) and a nontransgenic plant (right) treated with dicamba at a level of 5.6 kg/ha. (**C**) Top view of plants in (B).

mostly Mendelian in the case of plants carrying DMO as a nuclear gene (table S3). Most plants examined by DNA blot analysis contained a single *DMO* gene insert. Moreover, T_3 and T_4 progeny maintained the original levels of expression in regard to herbicide resistance whether they contained single or multiple copies of the *DMO* gene.

The prime value of the dicamba resistance technology is related to its use in major field crops in which management of broadleaf weeds is essential to maximize production. Because soybean is one such crop, we transformed the soybean varieties Thorne (Ohio State University) and NE3001 (University of Nebraska) with the same DMO expression cassette (Fig. 1B) used to transform tobacco, tomato, and *Arabidopsis*. As a means to derive marker-free soybean transformants, a two–T-DNA binary plasmid was assembled. In this plasmid, the marker-gene T-DNA element carried a bar gene cassette under the control of the *Agrobacterium tumefaciens* nopaline synthase promoter (nos), and the second, separate, T-DNA element carried the DMO expression cassette. More than 50 transgenic soybean events were produced, and seeds from the T_1, T_2, and T_3 generations were collected. Among the population of primary transformants generated, one marker-free event was identified that harbored only the DMO cassette. Most transgenic soybean events showed resistance to treatment with dicamba at 2.8 kg/ha and 5.6 kg/ha under greenhouse conditions (fig. S9) and complete resistance to dicamba at 2.8 kg/ha (the highest level tested in field trials) (Fig. 3). Initial field studies with five independent soybean events on University of Nebraska farms over the past 3 years revealed no compromise in agronomic performance—including yield, date to flowering, height, and lodging—in the transgenic plots treated with dicamba application (1.5 kg/ha) at preplant, V3 stage, or dual preplant spray treatment coupled with post-emergence treatments at the V3 stage of plant development when compared with non–herbicide-treated, weed-free plots of the parental soybean variety Thorne.

Fig. 3. Effects of dicamba treatments on nontransgenic soybean plants and transgenic plants containing the genetically engineered *DMO* gene. Nontransgenic (1) and transgenic soybean plants (2) treated under field conditions with dicamba at a level of 2.8 kg/ha are pictured 8 days after spraying.

Dicamba resistance in all of the plants tested did not require cotransformation with either ferredoxin or reductase genes from *P. maltophilia* (strain DI-6). These results showed that the plants contained one or more molecules that could transfer the requisite electrons to DMO to allow conversion of dicamba to DCSA. The initial targeting of DMO to the chloroplasts by means of a transit peptide sequence was aimed at using reduced ferredoxin abundantly available in the chloroplasts. However, transformation of tobacco plants with a *DMO* gene construct lacking a chloroplast transit peptide–coding sequence unexpectedly resulted in plants that were highly resistant to treatment with dicamba. Results from our limited trials with a small number of T_1-generation plants indicated that the level of resistance obtained with these transgenic plants was only slightly lower on average than that obtained with tobacco plants producing DMO containing a transit peptide.

These observations raise important questions in regard to the molecules in transgenic plants that can productively donate electrons to DMO. The fact that homoplastidic chloroplasts producing DMO internally from a *DMO* gene integrated into the chloroplast genome show resistance to extremely high levels of dicamba (fig. S8) and the fact that purified DMO can function in vitro with reduced spinach chloroplast ferredoxin (table S2) both suggest that chloroplast ferredoxin can productively interact with DMO to allow electron transfer. However, the source of electrons for DMO produced from nuclear genes lacking a chloroplast transit peptide–coding sequence remains unknown. Presuming that ferredoxins do not reside outside of the plant chloroplasts, one must consider the possibility that an unknown cytoplasmic protein can provide DMO with a steady supply of electrons. Alternatively, DMO itself might contain a gratuitous chloroplast transit peptide that allows sufficient DMO to enter the chloroplasts to provide protection from dicamba moving into the cell after dicamba treatment. Further studies, such as microscopic localizations in situ of DMO with and without a chloroplast transit peptide and/or isolation and identification of cytoplasmic proteins that can interact "indiscriminately" with DMO to supply electrons, will be needed to resolve the questions emanating from the present observations.

It is illuminating to consider that dicot plants like tobacco display distinct injury symptoms even at levels of dicamba treatment as low as 0.001 to 0.01 kg/ha (Fig. 2A). Many transgenic tobacco, tomato, *Arabidopsis*, and soybean plants containing a nuclear-encoded *DMO* gene were fully resistant to treatments with dicamba at or above 5.8 kg/ha. This demonstrates that the *DMO* gene, present even in a single copy and expressed at relatively moderate rates (table S2), is capable of decreasing the sensitivity of dicot plants to applications of dicamba by at least a factor of 5000.

Dicamba is an "auxin"-type herbicide that mimics the effects of excess quantities of the natural plant hormone indole-3-acetic acid (IAA) when applied to dicotyledonous plants. It has been used for more than 40 years to efficiently control most broadleaf weeds. Yet despite its widespread use, no new noxious and economically important dicamba-resistant weed species have appeared (*5*). One possible reason for such a situation may be that dicamba may act on some, if not all, of the IAA receptors that are essential in controlling normal growth and development of all plants. If so, the appearance of new dicamba-resistant weeds may not happen rapidly. This is especially true if the dicamba resistance gene is "stacked," for example, with the widely used glyphosate resistance gene to allow farmers to alternate herbicide applications between dicamba and glyphosate or to use mixtures of the two herbicides together. In either case, appearance of weeds resistant to either dicamba or glyphosate will be greatly suppressed. Moreover, the ability to use either or both herbicides before planting or at a variety of points during crop development will allow producers excellent weed control with greater flexibility in their crop management practices. This may be particularly important in the control of existing glyphosate-resistant weeds, such as horseweed, in which application of dicamba before planting can control emerged or emerging glyphosate-resistant weeds. Thus, dicamba-resistant crops can be a valuable asset in strategies to control currently existing herbicide-resistant weeds and to suppress the appearance of additional herbicide-resistant weeds that ultimately could threaten the long-term use and value of current herbicides and herbicide-resistant crops. Likewise, dicamba-resistant crops should further encourage the use of conservation tillage practices that greatly decrease soil erosion and foster more sustainable and environmentally friendly farming.

References and Notes

1. F. Hossain *et al.*, *Int. J. Occup. Environ. Health* **10**, 296 (2004).
2. J. Huang, R. Hu, S. Rozelle, C. Pray, *Science* **308**, 688 (2005).
3. A. L. Cerdeira, S. O. Duke, *J. Environ. Qual.* **35**, 1633 (2006).
4. International Service for the Acquisition of Agri-biotech Applications, *Global Status of Commercialized Biotech/GM Crops: 2006* (see executive summary at www.isaaa.org/resources/publications/briefs/35/executivesummary/default.html).
5. International Survey of Herbicide Resistant Weeds (www.weedscience.org/in.asp).
6. J. T. Stevens, D. D. Sumner, in *Handbook of Pesticide Toxicology*, W. J. Hayes, E. R. Laws Jr., Eds. (Academic Press, New York, 1991), pp. 1317–1408.
7. *Herbicide Handbook* (Weed Science Society of America, Champaign, IL, ed. 7, 1994).
8. *Hazardous Substance Databank* (U.S. National Library of Medicine, Bethesda, MD, 1995).
9. *Health Advisory Summary: Dicamba* (Office of Drinking Water, U.S. Environmental Protection Agency, Washington, DC, 1988).
10. Extoxnet Pesticide Information Profiles: Dicamba (http://extoxnet.orst.edu/pips/dicamba.htm).
11. D. J. Cork, J. Kreuger, *Adv. Appl. Microbiol.* **36**, 1 (1991).

12. J. Yang, X.-Z. Wang, D. Hage, P. Herman, D. Weeks, *Anal. Biochem.* **219**, 37 (1994).
13. P. L. Herman *et al.*, *J. Biol. Chem.* **280**, 24759 (2005).
14. S. Chakraborty *et al.*, *Arch. Biochem. Biophys.* **437**, 20 (2005).
15. X. Wang, B. Li, P. L. Herman, D. Weeks, *Appl. Environ. Microbiol.* **63**, 1623 (1997).
16. I. B. Maiti, R. Shepherd, *Biochem. Biophys. Res. Commun.* **244**, 440 (1998).
17. P. Maliga, *Photochem. Photobiol. Sci.* **4**, 971 (2005).
18. N. Dufourmantel *et al.*, *Plant Mol. Biol.* **55**, 479 (2004).
19. We thank M. Fromm for helpful suggestions regarding the manuscript; L. Allison for the kind gift of the chloroplast transformation vector pFMDV1 and for assistance with chloroplast transformation techniques; G. Graef for seeds of the soybean variety NE3001; and K. Horkey for precise applications of dicamba to greenhouse-grown plants. Dicamba monooxygenase (DMO; oxygenase$_{DIC}$) is GenBank accession number AY786442 (*ddmC*). Supported by the Consortium for Plant Biotechnology Research, United AgriProducts, the Monsanto Company, and the University of Nebraska Agricultural Research Division. D.P. Weeks and P.L. Herman hold a patent entitled "Methods and Materials for Making and Using Transgenic Dicamba-Degrading Organisms." D.P. Weeks, T.E. Clemente, M. Behrens, P.L. Herman, and N. Mutlu will receive royalties from the marketing of dicamba-resistant technology if crop seeds containing the resistance gene are marketed by Monsanto, the licensee of this technology from the University of Nebraska.

Supporting Online Material
www.sciencemag.org/cgi/content/full/316/5828/1185/DC1
Materials and Methods
Figs. S1 to S9
Tables S1 to S3

21 February 2007; accepted 23 April 2007
10.1126/science.1141596

A Manganese(IV)/Iron(III) Cofactor in *Chlamydia trachomatis* Ribonucleotide Reductase

Wei Jiang,[1] Danny Yun,[1]* Lana Saleh,[1]† Eric W. Barr,[1] Gang Xing,[1] Lee M. Hoffart,[1] Monique-Anne Maslak,[1] Carsten Krebs,[1,2]‡ J. Martin Bollinger Jr.[1,2]‡

In a conventional class I ribonucleotide reductase (RNR), a diiron(II/II) cofactor in the R2 subunit reacts with oxygen to produce a diiron(III/IV) intermediate, which generates a stable tyrosyl radical (Y•). The Y• reversibly oxidizes a cysteine residue in the R1 subunit to a cysteinyl radical (C•), which abstracts the 3′-hydrogen of the substrate to initiate its reduction. The RNR from *Chlamydia trachomatis* lacks the Y•, and it had been proposed that the diiron(III/IV) complex in R2 directly generates the C• in R1. By enzyme activity measurements and spectroscopic methods, we show that this RNR actually uses a previously unknown stable manganese(IV)/iron(III) cofactor for radical initiation.

Ribonucleotide reductases (RNRs) provide all organisms with 2' deoxyribonucleotides for DNA synthesis (*1*, *2*). All known RNRs are thought to initiate ribonucleotide reduction by using a cysteine thiyl radical to abstract the hydrogen atom from the 3′-carbon (*3*, *4*). Three distinct strategies to generate the initiating cysteinyl radical (C•) have been described and are, in part, the basis for division of the RNRs into three classes. Class II and III RNRs use strategies involving the 5′-deoxyadenosyl radical, generated either by homolysis of the Co-C bond of 5′-deoxyadenosylcob(III)alamin (class II) or by reductive cleavage of the 5′-C–S bond of *S*-adenosyl-L-methionine by a separate activase protein (class III), as the ultimate oxidant for cysteine activation. The 5′-deoxyadenosyl radical either generates the C• directly (class II) or generates a stable glycyl radical (G•) that reversibly oxidizes the cysteine (class III) (*3*, *5*, *6*). In a conventional class I RNR (e.g., from *Homo sapiens*, *Saccharomyces cerevisiae*, or aerobic *Escherichia coli*), a binuclear iron center in its cofactor subunit, R2, reacts with oxygen to oxidize a tyrosine residue by one electron to a stable tyrosyl radical (Y•). The Y• in R2 generates the C• in the catalytic subunit, R1, where nucleotide reduction occurs (*7*).

An unexpected adaptation of the class I functional architecture was revealed by the recent characterization of the RNR from the bacterium *Chlamydia trachomatis* (*8*), an obligate intracellular parasite and important human pathogen. The presence of a phenylalanine in place of the tyrosine residue in R2 that normally harbors the essential initiating Y• was revealed first by sequence comparisons (*8*) and subsequently by x-ray crystallography (*9*). Consistent with these findings, no evidence for a Y• was found in biochemical studies (*9*–*11*). Sequences of R2 genes from other organisms revealed that the absence of the Y• is not specific to the chlamydial RNRs (*9*). Notably, the presence of genes encoding such R2 proteins in the genomes of other pathogens (e.g., *Mycobacterium tuberculosis*) suggested that the novel RNRs might have arisen as an adaptation to the host's immune response (*9*) and might present specific targets for design of new antibacterial drugs.

To explain how the *C. trachomatis* RNR can function without the essential Y•, Nordlund, Gräslund, and co-workers suggested that an $Fe_2^{III/IV}$ cofactor might be produced in R2 by reaction of the $Fe_2^{II/II}$ cluster with O_2 and directly oxidize the cysteine in R1 (*9*). Biochemical studies by Gräslund and co-workers supported this hypothesis by demonstrating both stabilization of the reactive $Fe_2^{III/IV}$ complex in the presence of the other reaction components (R1, substrate, and allosteric effector) (*10*) and induction of the $Fe_2^{III/IV}$ state from $Fe_2^{III/III}$-R2 under these turnover conditions (*11*).

Although the reported induction and stabilization of the $Fe_2^{III/IV}$-R2 complex were consistent with the earlier Nordlund/Gräslund hypothesis, the fact that this form was never enriched to greater than ~30% of the total protein (*10*) left open the possibility that a different form was responsible for the modest activity observed. After preparing His_6-affinity–tagged forms of *C. trachomatis* R2 and the N-terminally truncated Δ(1 to 248)-R1 (*12*) reported by McClarty and coworkers to be more stable than full-length R1 (*8*), we noted a distinct lack of correlation between the catalytic activities and iron contents of different preparations of R2 (*13*).

By reductive chelation of iron from the purified protein and subsequent dialysis against ethylenedinitrilotetraacetate (EDTA) (*12*), R2 was isolated with less than 0.02 equivalents (equiv) iron (*14*) and very low catalytic activity [velocity (v)/[R2] $\leq 0.01\ s^{-1}$] (*15*). The metal-depleted R2 so obtained was not detectably activated by addition of 2 equiv of Fe^{II}. By contrast, addition of both Fe^{II} and Mn^{II} was found to activate the metal-depleted R2 by a factor of more than 50 (Fig. 1). A Mn^{II}:Fe^{II} ratio of unity gave maximal activation (Fig. 1A), and a total of two divalent metal ions per monomer was sufficient for ~85% of maximal activation (Fig. 1B).

The results in Fig. 1, in particular the 1:1 Mn:Fe ratio giving maximal activity, suggest the use of a Mn/Fe cofactor rather than a Fe_2 cofactor by *C. trachomatis* RNR. Because the raison d'être of the R2 subunit and its metallocofactor is to transiently oxidize the cysteine residue in R1 by one electron (*7*), the fully reduced complex formed upon addition of the divalent metal ions to the protein (Mn^{II}/Fe^{II}-R2) cannot be active but, by analogy with other class I RNRs, might react with O_2 to produce an oxidized state that functions in catalysis. Indeed, we observed no turnover after addition of an O_2-free solution containing R2, Mn^{II}, and Fe^{II} (0.75 equiv of

[1]Department of Biochemistry and Molecular Biology, Pennsylvania State University, University Park, PA 16802, USA.
[2]Department of Chemistry, Pennsylvania State University, University Park, PA 16802, USA.

*Present address: Department of Chemistry, Massachusetts Institute of Technology, Cambridge, MA 02139, USA.
†Present address: New England Biolabs, 240 County Road, Ipswich, MA 01938, USA.
‡To whom correspondence should be addressed. E-mail: ckrebs@psu.edu (C.K.), jmb21@psu.edu (J.M.B.)

each metal) to an O_2-free RNR reaction solution, but we did observe activity when the assay solution to which the Mn^{II}/Fe^{II}-R2 was added contained O_2 and when the Mn^{II}/Fe^{II}-R2 solution was first exposed to O_2 before it was added to the assay solution. In the latter case, activity did not require O_2 in the assay solution, indicating that previous exposure of the Mn^{II}/Fe^{II}-R2 to O_2 activates the subunit.

The active form exhibits no obvious electron paramagnetic resonance (EPR) signal (in X-band, perpendicular mode). A sample prepared with 0.5 equiv Fe and 1.0 equiv Mn (to disfavor formation of $Fe_2^{III/III}$ product) exhibits a Mössbauer quadrupole doublet at 4.2 K and zero field (Fig. 2A). The parameters [isomer shift (δ) = 0.52 mm s^{-1}; quadrupole splitting parameter (ΔE_Q) = 1.32 mm s^{-1}] establish that the iron site is converted to Fe^{III} by the reaction with O_2. The sharp [line width (Γ) = 0.30 mm s^{-1}] doublet in zero magnetic field and marked broadening in a weak (53 mT) field (Fig. 2B) reveal that this complex has a paramagnetic ground state with an integer value of the total electron-spin quantum number, S_{Total}. This characteristic distinguishes the *C. trachomatis* Mn/Fe^{III}-R2 product from the previously characterized product $Fe_2^{III/III}$ clusters in other R2 proteins, which are diamagnetic (S_{Total} = 0) as a result of antiferromagnetic coupling between the two S = 5/2 Fe^{III} ions. The presence of a Mn ion coupled to the Fe^{III} site is demonstrated by the EPR spectra of the one-electron reduced form of the complex produced by a brief (~2 min at 22°C) treatment with 20 mM dithionite. These spectra show hyperfine coupling to both an I (nuclear spin quantum number) = 5/2 ^{55}Mn nucleus (Fig. 3A) and an I = 1/2 ^{57}Fe nucleus (compare Fig. 3, A and B). The EPR spectra establish that the reduced form has a coupled Mn/Fe cluster with S_{Total} = 1/2. The Mössbauer spectrum of the reduced complex acquired at zero field and 190 K (Fig. 2C) is a broad (Γ ~ 0.5 mm s^{-1}) quadrupole doublet (*16*) with parameters (δ = 0.43 mm s^{-1}, ΔE_Q = 0.81 mm s^{-1}) that indicate that the Fe site remains in the +III oxidation state. Thus, the dithionite treatment reduces the Mn site but not the Fe^{III} site of the active state. The reduced Mn site must have an even number of valence electrons for coupling with the odd-electron Fe^{III} site to give S_{Total} = 1/2. Mn^{III} (S = 2) is the only chemically reasonable possibility, establishing that the Mn in the active state is +IV. Most likely, antiferromagnetic coupling between the Mn^{IV} (S_{Mn} = 3/2) and high-spin Fe^{III} (S_{Fe} = 5/2) ions gives S_{Total} = 1, consistent with the observed Mössbauer characteristics (broadening in a 53-mT magnetic field) of the active form.

The EPR spectrum at 4 K of the Mn^{III}/Fe^{III}-R2 is perturbed in the presence of R1, cytidine 5′-diphosphate (CDP), and adenosine 5′-triphosphate (ATP) (compare Fig. 3, A and C). This observation indicates that binding of R1 to Mn^{III}/Fe^{III}-R2 (and possibly binding of the nucleotides to the R1•R2 complex) affects the structure of the buried cofactor, a phenomenon not previously observed in a class I RNR. The spectra at 14 K (Fig. 3, D to G, solid curves) are particularly sharp and featured, and show hyperfine coupling to ^{57}Fe (compare Fig. 3, D and E) as well as ^{55}Mn. By simulation of the spectrum of the ^{56}Fe-containing sample (Fig. 3D, dashed curve), the **g**-tensor of the S = 1/2 ground state (2.030, 2.020, 2.015) and the ^{55}Mn hyperfine coupling tensor, $\mathbf{A}_{Mn}$ [(269, 392, 314) MHz], were determined. The marked anisotropy of $\mathbf{A}_{Mn}$ is consistent with the assigned +III oxidation state (*17*, *18*). Additional evidence for the +III iron valence is provided by the ^{57}Fe hyperfine coupling (Fig. 3E, solid curve), which can be reproduced (Fig. 3E, dashed curve) with an isotropic $\mathbf{A}_{Fe}$ [(-64.5, -64.5, -64.5) MHz] typical of high-spin Fe^{III} (*19*).

The substrate analog, 2′-azido 2′-deoxyadenosine 5′-diphosphate (N_3-ADP), was used to confirm the conclusion that the Mn^{IV}/Fe^{III} cluster is the functional cofactor. It has been shown that treatment of a class I or class III RNR with a 2′-azido–substituted nucleotide results in irreversible loss of the C• generator (*20*, *21*) as a result of aberrant reactions, beginning with loss of the azido moiety (either as N_3^- or $N_3^{\bullet}$) from the initial 3′-centered radical (*22*–*24*). Thus, the Y• or G• is irreversibly reduced (*20*, *21*) instead of being regenerated, as it is at the end of a normal turnover. We predicted from these precedents that treatment of *C. trachomatis* RNR should lead to irreversible conversion of the EPR-silent Mn^{IV}/Fe^{III} cluster to the EPR-active Mn^{III}/Fe^{III} state. Indeed, treatment with N_3-ADP generates the same EPR signal seen upon dithionite reduction of Mn^{IV}/Fe^{III}-R2 in the presence of R1, CDP, and ATP (Fig. 3, F and G). This signal does not develop when the inactivator is replaced by the natural substrate, CDP. The additional features in the 3330 to 3420 G region (marked by arrows; see also fig. S1) that are not part of the spectrum of Mn^{III}/Fe^{III}-R2•R1 (dashed simulations) are attributable to the nitrogen-centered radical previously shown to accumulate during N_3-NDP–mediated inactivation of conventional class I RNRs (*24*–*26*). The formation of the Mn^{III}/Fe^{III} cluster and free radical upon reaction with N_3-ADP confirms the activity of the Mn^{IV}/Fe^{III} cluster.

Scheme 1 summarizes our working hypothesis for how the *C. trachomatis* RNR functions without a Y• initiator. By using manganese in place of one of the irons of the conventional R2 metal center, *C. trachomatis* R2 is able to generate an oxidized cluster that possesses both kinetic stability and sufficient oxidative potency to generate the C• in R1 when triggered to do so by the protein(s). The marked perturbation to the EPR signal of the Mn^{III}/Fe^{III} cluster caused by binding of R1 (and perhaps nucleotides) provides a tool not present in conventional class I RNR systems for investigating the triggering process.

We attempted to reconcile our conclusion that Mn^{IV}/Fe^{III}-R2 is the active form with previous observations suggesting that $Fe_2^{III/IV}$-R2 is active (*9*–*11*). We were unable to reproduce the reported induction of the $Fe_2^{III/IV}$ complex from $Fe_2^{III/III}$-R2 under turnover conditions (*11*), even though we did verify that turnover was occurring (at 4 to 5% of the rate of the Mn/Fe-activated R2). Addition of a solution containing R2 and 1.5 equiv Fe^{II} to a solution containing O_2, R1 (2 equiv relative to R2), CDP, and ATP at 22°C did, as previously reported by the Gräslund group (*10*), result in generation and stabilization

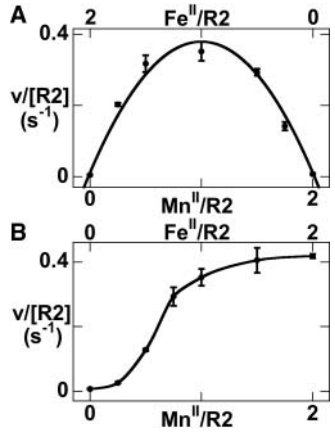

Fig. 1. Dependence of the catalytic activity of *C. trachomatis* R2 on the equivalencies of Mn^{II} and Fe^{II} (**A**) at a constant total metal equivalency of 2 per protein monomer and (**B**) at a constant mole fraction of 0.5 for each metal. Each data point is the mean of three trials, and the error bars are the standard deviations.

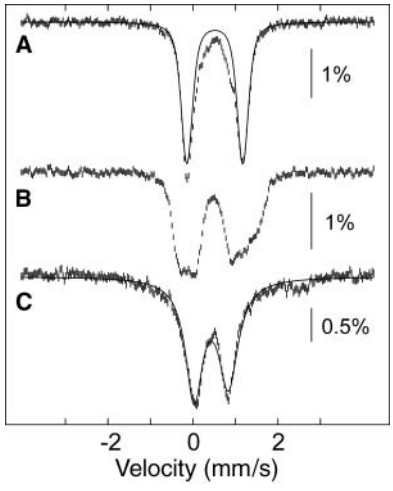

Fig. 2. Mössbauer spectra of active Mn^{IV}/Fe^{III}-R2 and the product of its dithionite reduction, Mn^{III}/Fe^{III}-R2. (**A** and **B**) Spectra of a sample enriched in Mn^{IV}/Fe^{III}-R2 (*12*) acquired at 4.2 K in zero magnetic field (A) and with a 53-mT field applied parallel to the γ beam (B). (**C**) Spectrum at 190 K and zero field of a sample enriched in Mn^{III}/Fe^{III}-R2 by dithionite reduction of Mn^{IV}/Fe^{III}-R2 (*12*). The solid lines in (A) and (C) are theoretical quadrupole doublets for Mn^{IV}/Fe^{III}-R2 and Mn^{III}/Fe^{III}-R2, respectively, with parameters as in the text.

of the $Fe_2^{III/IV}$ cluster (0.15 equiv that decayed by less than 10% over 10 min) (see fig. S2). However, quantification of the 2'-deoxy-CDP (dCDP) product from these samples showed that turnover was occurring at the same rate in the samples that contained the $Fe_2^{III/IV}$ complex as in the identical samples (prepared with $Fe_2^{III/III}$-R2) that lacked detectable levels of this complex. In other words, we find that the activity does not correlate with the $Fe_2^{III/IV}$ content of the R2. Moreover, replacement of CDP with N_3-ADP in the experiment giving the stabilized $Fe_2^{III/IV}$ complex did not accelerate decay of this complex. This observation confirms the incompetence of the $Fe_2^{III/IV}$ cluster for radical initiation.

Suspecting that the modest activity that we and others (*8*–*11*) observe without adding Mn^{II} to R2 might result from a Mn "contaminant" (in R2 or another assay component), we tested for development of the very distinctive EPR signal of the Mn^{III}/Fe^{III}-R2•R1 complex after treatment of our putatively iron-only protein with either dithionite or N_3-ADP in the presence of R1 and ATP. Indeed, in both cases, the spectrum was readily detected (fig. S3A). Its intensity relative to that exhibited by the purposefully generated Mn^{III}/Fe^{III}-R2 sample (~4 to 5%) (compare to fig. S3B) correlated with the ratio of enzymatic activity of the two R2 forms.

We suggest that the activity previously attributed to the $Fe_2^{III/IV}$-R2 complex (*9*–*11*) resulted from a Mn^{IV}/Fe^{III}-R2 contaminant that escaped detection. First, Fig. 1A shows that only ~0.2 equiv contaminating Mn would have been required to give the maximum R2 activity previously reported (230 nmol min^{-1} mg^{-1}, $v/[R2] = 0.155\ s^{-1}$) (*10*). Whereas this quantity is five times the ~0.04 equiv detected in our preparations, the different methods of subunit preparation, and perhaps different enzyme concentrations employed in the activity determinations [not reported in (*10*) but expected to have been lower than in our assays because of their use of the more sensitive radiometric assay], could have resulted in a greater Mn:R2 equivalency in the previous study. Second, much lower activities of <75 nmol min^{-1} mg^{-1} ($v/[R2] < 0.05\ s^{-1}$), similar to the activities of some of our preparations of R2 before activation with Mn^{II} and Fe^{II}, were reported in the subsequent study by the same group (*11*). This large variation in specific activity seems inconsistent with the authors' belief that addition of only Fe^{II} should have fully activated R2 but could be explained by a variable Mn contaminant in their preparations. If Mn^{II} had been present, R2 would [as reported in (*10*)] have been activated by addition of only Fe^{II} in the presence of O_2, but the extent of activation would have depended on the quantity of the contaminating Mn. Third, by contrast to all other (conventional) class I RNRs, the active R2 state has no obvious EPR signal. Thus, if Mn^{II} had been present, addition of Fe^{II} in the presence of O_2 would have trapped the Mn in an EPR-silent state, allowing it to escape detection by the reported EPR experiments (*10*, *11*). We suggest that these considerations can reconcile all previous observations with our proposal that Mn^{IV}/Fe^{III}-R2 is the sole active form.

The demonstrated in vitro activity of the Mn^{IV}/Fe^{III} form of *C. trachomatis* R2 (produced in *E. coli*) strongly suggests that this previously unknown cofactor functions in vivo in the pathogen's RNR. It is possible that other metals might substitute for Mn (or Fe) in vivo, but the subtlety of the cofactor's function (gated electron transfer by a stable high-valent complex) makes this possibility remote. The results raise the questions of why and in what other species this distinctive radical-initiation strategy evolved. Given that the RNR subunits from *C. trachomatis* and other chlamydiae are more similar in sequence to their counterparts from mammalian species such as *H. sapiens* and *Mus musculus* than to the subunits from other bacterial RNRs (with the exception of those from the opportunistic human pathogen, *Pseudomonas aeruginosa*) (*8*), it seems likely that the parasitic bacteria co-opted their host's RNR genes and then evolved them for selective advantage. Without knowledge of the manganese requirement, Nordlund, Gräslund, and co-workers suggested that this selective advantage might have been increased resistance to oxidants (e.g., superoxide and nitric oxide) produced as part of the host's immune response (*9*). This hypothesis, plausible in view of previous evidence that the Y•s of conventional class I RNRs are targets for these chemical defenses (*27*–*29*), seems even more attractive in light of our results: The demonstrated substitution of one iron ion by manganese is strikingly reminiscent of the induction

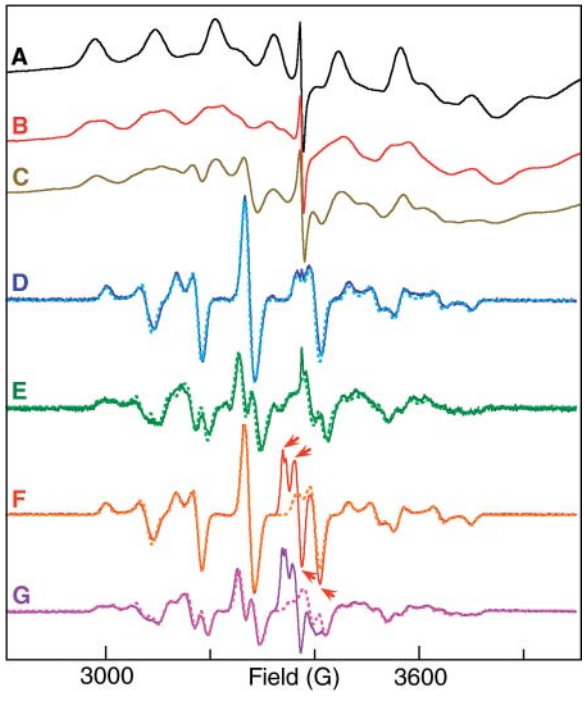

Fig. 3. X-band EPR spectra illustrating formation of the Mn^{III}/Fe^{III} cluster by dithionite reduction of active Mn^{IV}/Fe^{III}-R2 (**A** to **E**) or by treatment of the holoenzyme (Mn^{IV}/Fe^{III}-R2•R1•ATP) with N_3-ADP (**F** and **G**). The dithionite reduction was carried out either in the absence [(A) and (B)] or in the presence [(C) to (E)] of R1, CDP, and ATP. For (A), (C), (D), and (F), the R2 samples were prepared with natural-abundance iron (91.7% ^{56}Fe with $I = 0$); for (B), (E), and (G), ^{57}Fe-enriched iron (95%, $I = 1/2$) was used. All spectra had a microwave frequency of 9.45 GHz and a modulation frequency of 100 kHz. Other spectrometer conditions were [(A) to (C)] temperature, 4 K (nominal temperature indicated on Oxford cryostat); microwave power, 20 mW; modulation amplitude, 10 G; scan time, 167 s; time constant, 167 ms; resolution of field axis, 1024 points; scans per spectrum, 1; [(D) to (G)] temperature, 14.0 ± 0.2 K, microwave power, 0.20 mW; modulation amplitude, 4 G; scan time, 334 s; time constant, 167 ms; resolution of field axis, 2048 points; scans per spectrum, 10. The sharp signal at 3380 G is from the spectrometer cryostat and is prominent in (A) to (C) because of the low temperature and high power used for these spectra. In (D) to (G), a minor contribution from free Mn^{II} has been removed by subtraction of the spectra of control samples either not treated with dithionite [for (D) and (E)] or treated with CDP instead of N_3-ADP [for (F) and (G)]. The dashed, lighter-colored traces in (D) to (G) are simulations of the spectra of Mn^{III}/Fe^{III}-R2•R1 (*12*) with the **g** and **A** tensors as in the text.

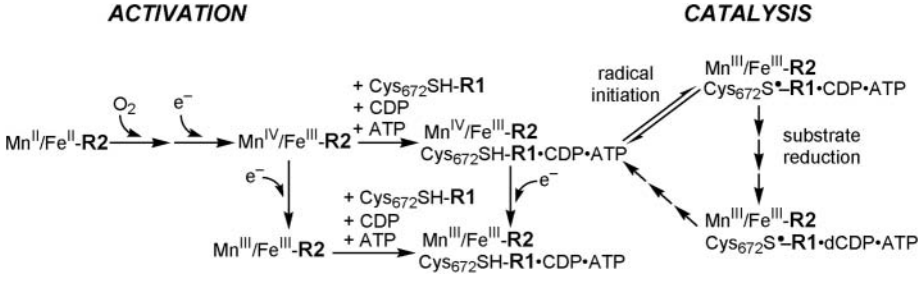

Scheme 1

by *E. coli* in response to oxidative stress of a Mn-dependent paralog to the constitutively expressed, Fe-dependent superoxide dismutase (*30*). Examination of the reactivity of the distinctive Mn/Fe cofactor toward these oxidants may thus provide a biochemical rationale for its evolution.

References and Notes

1. P. Nordlund, P. Reichard, *Annu. Rev. Biochem.* **75**, 681 (2006).
2. J. Stubbe, D. G. Nocera, C. S. Yee, M. C. Y. Chang, *Chem. Rev.* **103**, 2167 (2003).
3. S. Licht, G. J. Gerfen, J. Stubbe, *Science* **271**, 477 (1996).
4. J. Stubbe, *Curr. Opin. Struct. Biol.* **10**, 731 (2000).
5. C. C. Lawrence, J. Stubbe, *Curr. Opin. Chem. Biol.* **2**, 650 (1998).
6. M. Fontecave, E. Mulliez, D. T. Logan, *Prog. Nucleic Acid Res. Mol. Biol.* **72**, 95 (2002).
7. J. Stubbe, *Curr. Opin. Chem. Biol.* **7**, 183 (2003).
8. C. Roshick, E. R. Iliffe-Lee, G. McClarty, *J. Biol. Chem.* **275**, 38111 (2000).
9. M. Högbom *et al.*, *Science* **305**, 245 (2004).
10. N. Voevodskaya, F. Lendzian, A. Gräslund, *Biochem. Biophys. Res. Commun.* **330**, 1213 (2005).
11. N. Voevodskaya *et al.*, *Proc. Natl. Acad. Sci. U.S.A.* **103**, 9850 (2006).
12. Materials and methods are available as supporting material on *Science* Online.
13. For example, preparations from *E. coli* cultures grown in rich medium had the same iron content as preparations from iron-supplemented minimal medium (~0.75 equiv; all metal equivalencies and activities are on a per monomer basis) but ~10 times the activity [velocity (v)/[R2] = 0.035 ± 0.01 s^{-1}, compared with 0.003 ± 0.001 s^{-1}]. Conversely, R2 from rich medium to which the cell-permeative Fe^{II} chelator, 1,10-phenanthroline, was added immediately before induction of overexpression emerged with much less iron (<0.05 equiv) but ~70% of the activity (v/[R2] = 0.025 ± 0.01 s^{-1}) of the R2 from equivalent cultures lacking the chelator.
14. All metal equivalencies and activities for the homodimeric R2 protein are reported on a per monomer basis.
15. To reduce the residual R2 activity to this low level, it was necessary also to dialyze the R1 used in the activity assay against EDTA.
16. The $S = 1/2$ complex exhibits a magnetically split Mössbauer spectrum at low temperature, but the use of this higher temperature makes electronic relaxation fast compared with the ^{57}Fe nuclear precession frequency and collapses the spectrum into a quadrupole doublet.
17. M. Zheng, S. V. Khangulov, G. C. Dismukes, V. V. Barynin, *Inorg. Chem.* **33**, 382 (1994).
18. S. Sinnecker, F. Neese, W. Lubitz, *J. Biol. Inorg. Chem.* **10**, 231 (2005).
19. E. Münck, in *Physical Methods in Bioinorganic Chemistry*, L. Que Jr., Ed. (University Science Books, Sausalito, CA, 2000), pp. 287–319.
20. L. Thelander, B. Larsson, J. Hobbs, F. Eckstein, *J. Biol. Chem.* **251**, 1398 (1976).
21. R. Eliasson, E. Pontis, F. Eckstein, P. Reichard, *J. Biol. Chem.* **269**, 26116 (1994).
22. S. Salowe *et al.*, *Biochemistry* **32**, 12749 (1993).
23. G. Behravan *et al.*, *Biochim. Biophys. Acta* **1264**, 323 (1995).
24. J. Fritscher *et al.*, *J. Am. Chem. Soc.* **127**, 7729 (2005).
25. B. M. Sjöberg, A. Gräslund, F. Eckstein, *J. Biol. Chem.* **258**, 8060 (1983).
26. J. Stubbe, W. A. van der Donk, *Chem. Rev.* **98**, 705 (1998).
27. M. Lepoivre, F. Fieschi, J. Coves, L. Thelander, M. Fontecave, *Biochem. Biophys. Res. Commun.* **179**, 442 (1991).
28. O. Guittet, B. Roy, M. Lepoivre, *Cell. Mol. Life Sci.* **55**, 1054 (1999).
29. M. Fontecave, *Cell. Mol. Life Sci.* **54**, 684 (1998).
30. H. M. Hassan, L. W. Schrum, *FEMS Microbiol. Rev.* **14**, 315 (1994).

31. This work was supported by grants from NIH (GM55365 to J.M.B.), the Arnold and Mabel Beckman Foundation (Young Investigator Award to C.K.), and the Camille and Henry Dreyfus Foundation (Teacher Scholar Award to C.K.). The authors thank R. Stevens (University of California, Berkeley) for generously providing *Chlamydia trachomatis serovar D* genomic DNA and J. Stubbe (Massachusetts Institute of Technology) for the kind gift of N_3-ADP.

Supporting Online Material

www.sciencemag.org/cgi/content/full/316/5828/1188/DC1
Materials and Methods
Figs. S1 to S3
References

12 February 2007; accepted 19 April 2007
10.1126/science.1141179

Probing Transcription Factor Dynamics at the Single-Molecule Level in a Living Cell

Johan Elf,[1]* Gene-Wei Li,[2]* X. Sunney Xie[1]†

Transcription factors regulate gene expression through their binding to DNA. In a living *Escherichia coli* cell, we directly observed specific binding of a *lac* repressor, labeled with a fluorescent protein, to a chromosomal *lac* operator. Using single-molecule detection techniques, we measured the kinetics of binding and dissociation of the repressor in response to metabolic signals. Furthermore, we characterized the nonspecific binding to DNA, one-dimensional (1D) diffusion along DNA segments, and 3D translocation among segments through cytoplasm at the single-molecule level. In searching for the operator, a *lac* repressor spends ~90% of time nonspecifically bound to and diffusing along DNA with a residence time of <5 milliseconds. The methods and findings can be generalized to other nucleic acid binding proteins.

In all kingdoms of life, transcription factors (TFs) regulate gene expression by site-specific binding to chromosomal DNA, preventing or promoting the transcription by RNA polymerase. The *lac* operon of *Escherichia coli*, a model system for understanding TF-mediated transcriptional control (*1*), has been the subject of extensive biochemical (*2*–*4*), structural (*5*), and theoretical (*6*, *7*) studies since the seminal work by Jacob and Monod (*8*). However, the in vivo kinetics of the *lac* repressor, and all other TFs, has only been studied indirectly by monitoring the regulated gene products. Traditionally, this was done on a population of cells (*9*), in which unsynchronized gene activity among cells masks the underlying dynamics. Recent experiments on single cells allow investigation of stochastic gene expression (*10*–*15*). However, direct observation of TF-mediated gene regulation (*16*) remains difficult, because it often involves only a few copies of TFs and their chromosomal binding sites. Here we report on a kinetics study of how fast a *lac* repressor binds its chromosomal operators and dissociates in response to a metabolic signal in a living *E. coli* cell.

[1]Department of Chemistry and Chemical Biology, Harvard University, Cambridge, MA 02138, USA. [2]Department of Physics, Harvard University, Cambridge, MA 02138, USA.

* These authors contributed equally to this work.
†To whom correspondence should be addressed. E-mail: xie@chemistry.harvard.edu

Single-molecule detection also makes it possible to investigate how a TF molecule searches for specific binding sites on DNA, a central question in molecular biology. Target location by TFs (and most nucleic acid binding proteins) is believed to be achieved by facilitated diffusion, in which a TF searches for specific binding sites through a combination of one-dimensional (1D) diffusion along a short DNA segment and 3D translocation among DNA segments through cytoplasm (*17*). However, real-time observation in living cells has not been available because of technical difficulties. Here we report on such an investigation, providing quantitative information of the search process.

The *lac* repressor (LacI) is a dimer of dimers. Under repressed conditions one dimer binds the major *lac* operator, O1, and the other dimer binds one of the weaker auxiliary operators, O2 or O3 (*18*) (Fig. 1A). LacI binding to O1 prevents RNA polymerase from transcribing the *lac* operon (*lacZYA*). Upon binding of allolactose, an intermediate metabolite in the lactose pathway, or a nondegradable analog, such as IPTG (isopropyl β-D-1-thiogalactopyranoside), the repressor's affinity for the operator is substantially reduced to a level comparable to that of nonspecific DNA interaction (*19*).

To image the *lac* repressor, we expressed it from the native chromosomal *lacI* locus as a C-terminal fusion with the rapidly maturing (~7 min) yellow fluorescent protein (YFP) Venus (A206K) (*15*, *20*) (Fig. 1A). The short maturation time prevents the *lac* operator sites from being occupied by immature fusion proteins. The C-terminal fusion avoids interference with the N-

terminal DNA binding domain (*21*). Our fusion protein forms a dimer, which like most other C-terminal fusions with LacI (*22*), does not tetramerize (fig. S1). The labeled dimer up-regulates the expression of *lacZ* ~100-fold in response to full induction by IPTG at 37°C (*JE13* in Fig. 1B). This repression factor compares well with that of non-labeled repressors (*4*), indicating that the fusion protein maintains regulatory activity.

The detection of specific binding of LacI to its operators is achieved through localization enhancement (*15*) [see Supporting Online Material (SOM)]. When *E. coli* cells are imaged with a wide-field fluorescence microscope and a charge-coupled device (CCD) camera with a long exposure time (1 s), the fluorescence from TFs that are not specifically bound to DNA is collected from the entire area of the cell because of fast diffusion and is hence overwhelmed by strong cellular autofluorescence. However, a single TF specifically bound to the relatively stationary DNA emits from a highly localized region and can be detected above the autofluorescence background.

A necessary condition for detection through localization enhancement is that the copy number of TF must be low. LacI, like most other TFs in *E. coli*, is naturally expressed at a low level—about 20 monomers per *lacI* gene (*23*). This results from autorepression at the O3 operator, which overlaps part of the *lacI* gene. We further reduced the expression level by replacing

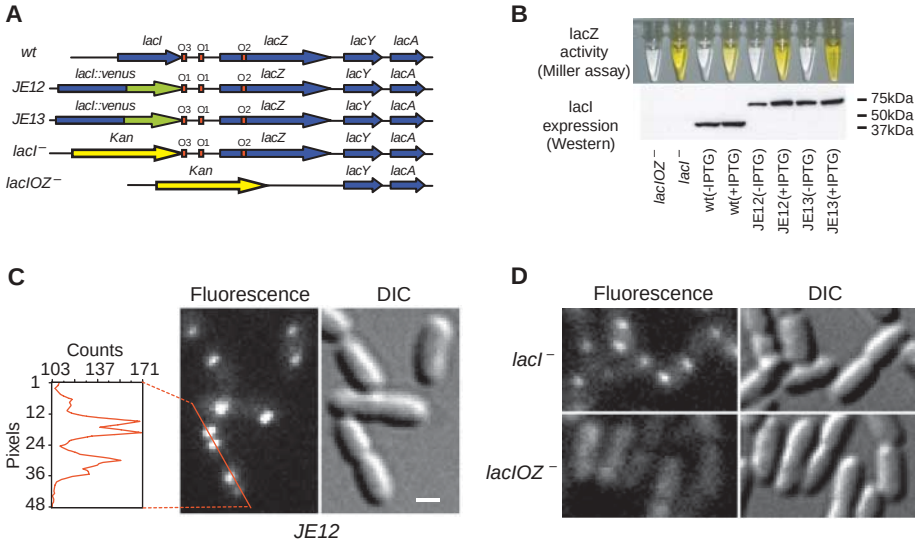

Fig. 1. Specific binding to *lac* operators. (**A**) Strains. The chromosomal *lac* region of the wild-type *E. coli* (BW25933) and various derivatives used in this report. (**B**) Bulk activity assay. The Miller assay (top) shows that the YFP fusion strains (*JE12* and *JE13*) are active and respond to induction by IPTG (1 mM, 3 hours) by derepressing *lacZ* (yellow). The Western blot (bottom) for LacI shows that *JE12* and *JE13* express the full-length fusion protein (67 kD) and that the expression in *JE12*, in the absence of IPTG, is strongly autorepressed as compared to the wild type and *JE13*. (**C**) Fluorescence (1-s exposure) and DIC images of *JE12* grown in M9 glucose with amino acids. The YFP-labeled LacI binds persistently at one or two locations per cell depending on whether the operators have been replicated or not. The graph shows the fluorescence intensity along the red line. Scale bar, 1 μm. (**D**) DIC and fluorescence images (1-s exposure) of LacI-Venus expressed from plasmid in the *lacI*⁻ and *lacIOZ*⁻ strains, respectively. Plasmid expression is used to obtain similar expression levels in the two strains. No specific binding is observed in the absence of the *lac* operators.

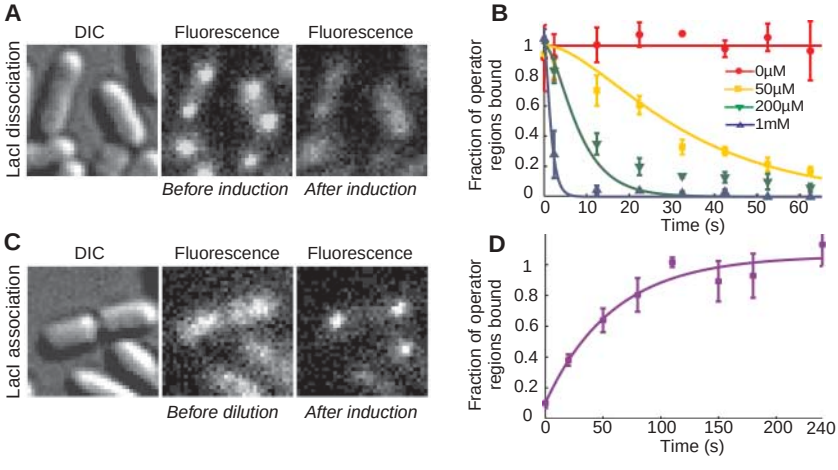

Fig. 2. *lac* repressor kinetics in living cells. (**A**) *JE12* bacteria before and 40 s after addition of IPTG to a final concentration of 1 mM. (**B**) Fraction of the *lac* operator regions that is TF-bound (±SEM, $n \sim 3$) is plotted as a function of time after induction by various concentrations of IPTG. The data are globally fitted with a model in which IPTG binds independently to the two dimers in the operator region (SOM). (**C**) *JE12* bacteria before and 1 min after dilution of IPTG from 100 to 2 μM with the addition of 1 mM ONPF. (**D**) Fraction of the operator regions that is TF-bound (±SEM, $n \sim 3$) as a function of time after rapid dilution of IPTG from 100 to 2 μM by addition of 1 mM ONPF. The data are fitted with an exponentially distributed binding time and yield a time constant of 59 s.

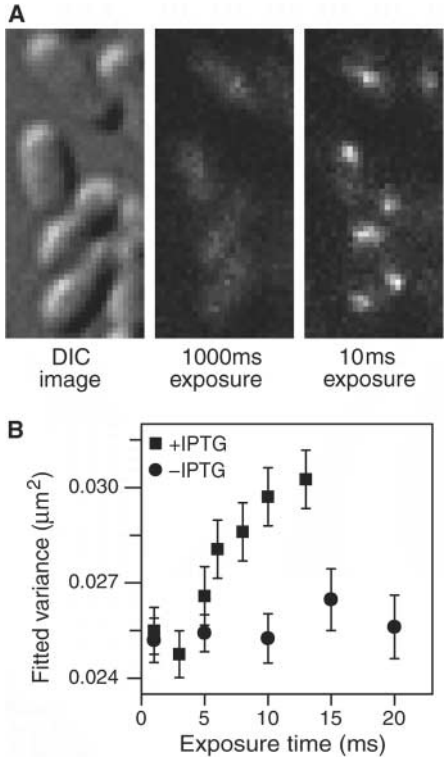

Fig. 3. Imaging nonspecifically bound LacI. (**A**) Two fluorescence images with different exposure times and the corresponding DIC image of IPTG-induced *E. coli* cells. At 1000 ms, individual LacI-Venus appear as diffuse fluorescence background. At 10 ms they are clearly visible as nearly diffraction-limited spots. (**B**) Fluorescence spot size as a function of exposure time. The size is represented as the average variance of a 2D Gaussian function fit to images of fluorescence spots (±SEM, $n \sim 100$). The same total excitation energy is used for different exposure time. The spots are measured before (–IPTG, ●) and after (+IPTG, ■) induction. The size converges to the width of the point spread function (full width at half maximum = 370 nm) below 5ms.

the O3 operator with an O1 operator sequence, thus enhancing autorepression. This reduces the expression level by a factor of ~3 as compared to the wild type (Fig. 1B).

Figure 1C shows a differential interference contrast (DIC) image and the corresponding fluorescence image with a 1-s exposure time. In the image, specifically bound TFs appear as nearly diffraction-limited spots. Most cells have at least one spot per cell. Some have two, owing to replication of the operator region (*24*). We could not distinguish from the spot intensity whether one or two TF dimers were bound to the operator region containing two O1 operators (Fig. 1A and fig. S1). As a control, we showed that the specific LacI binding is dependent on the concentration of inducer (IPTG) (fig. S2). As another control, we proved that LacI binds specifically only to the *lac* operator. We expressed LacI-Venus from plasmid in two different strains, with and without specific chromosomal operators (*lacI*$^-$ and *lacIOZ*$^-$, respectively) (Fig. 1A). The fluorescence images in Fig. 1D with 1-s exposure demonstrate the lack of specific binding in *lacIOZ*$^-$ strain, proving that LacI binds persistently only at the *lac* operators.

We next investigate the response time of TF-mediated induction. Figure 2A shows the same cells before and 40 s after addition of 1 mM IPTG to the growth media. During this time interval, the TFs dissociate from the operators in nearly all cells. As a control, we proved that the disappearance of localized fluorescence is not due to photobleaching (fig. S3). In Fig. 2B the fraction of operator regions with bound TF is plotted as a function of time after induction at different IPTG concentrations. The repressor dissociation kinetics was probed by imaging different groups of cells at different time points after induction (SOM). Because dissociation of the IPTG-bound LacI from the operator is significantly faster than 1 s^{-1} (*2*), we could attribute the kinetics in Fig. 2B to the binding of IPTG to the LacI-operator complex. However, fitting of Fig. 2B (SOM) yields an association rate constant of IPTG to the repressor-operator complex of ~851 M^{-1} s^{-1}. This value is one order of magnitude lower than the in vitro estimate (*2*), which indicates that IPTG's membrane permeability might be rate limiting for LacI binding.

To investigate how fast the TFs find a specific operator site, we rapidly diluted IPTG from 100 to 2 μM by adding growth media with 1 mM ONPF (2-nitrophenyl-β-D-fucoside) (Fig. 2C). ONPF is an anti-inducer that competitively binds to LacI and therefore effectively prevents rebinding of IPTG after its dissociation (*23*). Kinetic analysis (Fig. 2D) yields a time constant of ~59 s for the exponential rise (SOM). Considering that IPTG dissociates from LacI in just a few seconds (*2*) and assuming that ONPF reaches sufficient intracellular concentration rapidly, we would expect the TF's target searching to be rate limiting. Taking into account the possibility of a slower ONPF influx rate, we conclude that the upper bound of the time for the first TF to find one of the two unoccupied O1 operators is 59 s. Because there are about three repressors per cell, it would take at most $\tau \sim 59\ s \times 2 \times 3 = 354$ s for a single *lac* repressor dimer in one cell to find a specific operator.

We next turn our attention to the search process. The conventional view is that the search is facilitated by a combination of 1D diffusion along short DNA segments separated by transfers between segments through cytoplasm. Recent in vitro experiments on DNA-repair enzymes have directly demonstrated the 1D diffusion along nonspecific DNA (*25*). Similarly, we determined the 1D diffusion constant of the dimeric LacI-Venus to be $D_1 = 0.046 \pm 0.01\ \mu m^2\ s^{-1}$ using single-molecule tracking on flow-stretched DNA (SOM). Although the in vitro measurement was done at low salt concentration in order to obtain trajectories with long residence time, the diffusion constant, which is largely independent of ionic strength (*25*), is expected to be similar in a living cell. However, the residence time, which is dependent on salt concentration, is yet to be determined in vivo.

To determine the nonspecific residence time on DNA for IPTG-bound LacI-Venus in a living cell, we obtained fluorescence images at different exposure times. With 1-s exposure, nonspecifically bound LacI cannot be imaged individually, as shown in Fig. 1D. With 10-ms exposure, however, LacI appear as nearly diffraction-limited spots (Fig. 3A). We observed two to four TFs in each cell, consistent with the expected LacI copy number. Figure 3B (and fig. S4) shows that the spot sizes increase for exposure times longer than 5 ms. Because the 1D diffusion along a DNA segment on this time scale is much shorter than the diffraction-limited spot size, we attribute the increase in spot size to 3D translocation between nonspecific binding events. This result indicates that the TF's nonspecific residence time in cells, t_R, was ≤5 ms.

The ability to image nonspecifically bound TFs allowed us to track the movement of individual TFs using stroboscopic laser excitation.

Table 1. Diffusion constants and characteristic times.

Parameter	Value	Method
D_{eff}	$0.4 \pm 0.02\ \mu m^2\ s^{-1}$	In vivo SM tracking
D_3	$3 \pm 0.3\ \mu m^2\ s^{-1}$	In vivo FCS
D_1	$0.046 \pm 0.01\ \mu m^2\ s^{-1}$	In vitro SM tracking
Search time* (τ)	65† to 360 s	Detection by immobilization
Residence time on DNA (t_R)	0.3† to 5 ms	Spot size dependence on exposure time

*Defined as the time for a single TF in one cell to find a target. †Theoretical lower bound considering diffusion-limited association to nonspecific sites (*29*) (SOM).

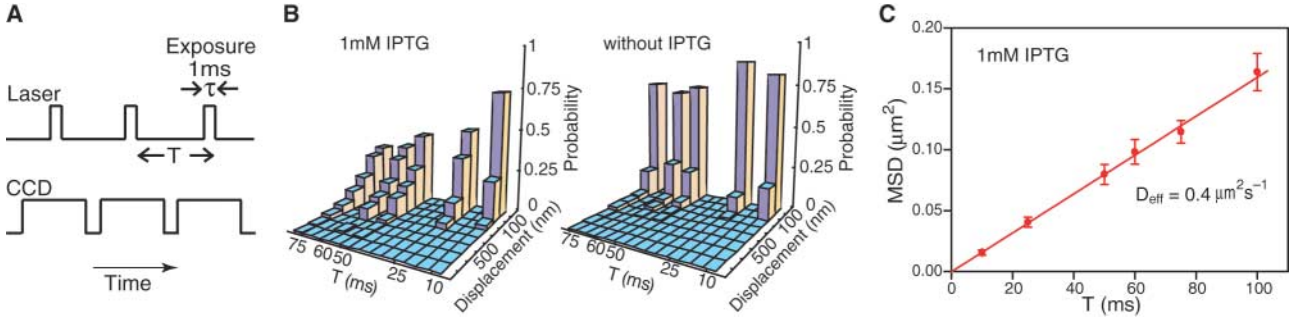

Fig. 4. Single-molecule tracking with stroboscopic illumination. (**A**) Timing diagram for stroboscopic illumination. Each laser pulse (1 ms) is synchronized to a CCD frame time, which lasts time *T*. (**B**) Displacement histograms for different values of *T*. The absolute values of displacement along an arbitrary axis were calculated from 2D Gaussian fittings in two successive image frames. The displacement distribution of nonspecifically bound TFs broadens with time (left), whereas the distribution before induction (right) remains peaked at <100 nm. The contrast between them illustrates the change in TF mobility before and after induction. (**C**) Mean-square displacement for nonspecifically bound TFs at different time intervals. The red line shows a linear fit of the MSDs. Error bars are calculated as described in the SOM. The fitting agrees well with a normal diffusion in the imaging plane, $\langle \Delta x^2 \rangle = 4D_{eff}t$, with $D_{eff} = 0.4\ \mu m^2\ s^{-1}$.

Laser pulses (1 ms) were synchronized to the frame rate of a fast EMCCD (electron multiplying charge-coupled device) camera (Fig. 4A, SOM). Because individual molecules are bleached in three to four frames, we varied the frame rate ($1/T$) to construct net displacement histograms for different time intervals (T = 10 to 75 ms) (Fig. 4B). Without IPTG, both the specific and nonspecific binding events are observed, and the displacement histogram is strongly peaked at <100 nm because most TFs are specifically bound. This shows that the *lac* operator region is confined to within 100 nm during 75 ms. With 1 mM IPTG, however, the displacement distribution broadens with increasing time intervals.

We next determine the apparent diffusion constant. The mean square displacement (MSD) of IPTG-bound LacI measured at various time intervals follows a linear dependence at the time scale >10 ms (Fig. 4C) and does not exhibit anomalous diffusion, as was observed for mRNA in *E. coli* cytoplasm at longer time scales (*26*). The apparent diffusion constant, $D_{eff} = 0.4 \pm 0.02\ \mu m^2\ s^{-1}$, is one order of magnitude higher than the 1D diffusion constant (D_1) of LacI dimers on DNA. Therefore, we attribute apparent diffusion to the contribution from 3D diffusion in between nonspecific bindings. Using fluorescence correlation spectroscopy (FCS) (*27*), we measured the in vivo diffusion constant of LacI-Venus without its DNA binding domain to be $D_3 = 3 \pm 0.3\ \mu m^2\ s^{-1}$ (SOM). This suggests that the Lac I dimer spends ~87% of the time nonspecifically bound and diffusing along DNA (SOM). This fraction is consistent with the previous population-averaged estimate (>90%) on the basis of the LacI tetramer concentration in minicells (*28*).

With the measurements of the diffusion constants and residence time (Table 1), we can give an estimate of the search time using a simple model for facilitated diffusion (*7*). Considering that the repressor spends most of its time bound to DNA, the search time is estimated as the nonspecific residence time (t_R) multiplied by the average number of 1D diffusion events necessary to find the target (*29*). The latter is given by the accessible genome size ($M \approx 4.8 \times 10^6$ bp) divided by the number of base pairs visited per sliding event ($\sqrt{4D_1 t_R} < 85$ bp).

$$\tau \approx t_R \frac{M}{\sqrt{4D_1 t_R}} = M\sqrt{\frac{t_R}{4D_1}} \qquad (1)$$

This results in a search time of $\tau < 270$ s for a single *lac* repressor in one cell to find one target. In the SOM, we further calculate a lower bound of the search time based on diffusion-limited association to nonspecific DNA (Table 1). Hence, the measured and estimated search times are consistent. Despite the uncertainty of these numbers, our measurements provided quantitative information of the target search on DNA in vivo. This result has implications for other DNA binding proteins such as DNA-repair enzymes. Similar single-molecule experiments will advance our quantitative understanding of biochemistry and molecular biology in living cells.

References and Notes

1. B. Müller-Hill, *The Lac Operon* (de Gruyter, Berlin, 1996).
2. M. Dunaway *et al.*, *J. Biol. Chem.* **255**, 10115 (1980).
3. R. B. Winter, P. H. von Hippel, *Biochemistry* **20**, 6948 (1981).
4. S. Oehler, M. Amouyal, P. Kolkhof, B. von Wilcken-Bergmann, B. Muller-Hill, *EMBO J.* **13**, 3348 (1994).
5. M. Lewis *et al.*, *Science* **271**, 1247 (1996).
6. O. G. Berg, C. Blomberg, *Biophys. Chem.* **4**, 367 (1976).
7. O. G. Berg, R. B. Winter, P. H. von Hippel, *Biochemistry* **20**, 6929 (1981).
8. F. Jacob, J. Monod, *J. Mol. Biol.* **3**, 318 (1961).
9. A. Kepes, *Prog. Biophys. Mol. Biol.* **19**, 199 (1969).
10. M. B. Elowitz, A. J. Levine, E. D. Siggia, P. S. Swain, *Science* **297**, 1183 (2002).
11. E. M. Ozbudak, M. Thattai, I. Kurtser, A. D. Grossman, A. van Oudenaarden, *Nat. Genet.* **31**, 69 (2002).
12. E. M. Ozbudak, M. Thattai, H. N. Lim, B. I. Shraiman, A. Van Oudenaarden, *Nature* **427**, 737 (2004).
13. N. Rosenfeld, J. W. Young, U. Alon, P. S. Swain, M. B. Elowitz, *Science* **307**, 1962 (2005).
14. I. Golding, J. Paulsson, S. M. Zawilski, E. C. Cox, *Cell* **123**, 1025 (2005).
15. J. Yu, J. Xiao, X. Ren, K. Lao, X. S. Xie, *Science* **311**, 1600 (2006).
16. J. Yao, K. M. Munson, W. W. Webb, J. T. Lis, *Nature* **442**, 1050 (2006).
17. P. H. von Hippel, O. G. Berg, *J. Biol. Chem.* **264**, 675 (1989).
18. S. Oehler, E. R. Eismann, H. Kramer, B. Muller-Hill, *EMBO J.* **9**, 973 (1990).
19. A. C. Wang, A. Revzin, A. P. Butler, P. H. von Hippel, *Nucleic Acids Res.* **4**, 1579 (1977).
20. T. Nagai *et al.*, *Nat. Biotechnol.* **20**, 87 (2002).
21. M. Lewis, *C. R. Biol.* **328**, 521 (2005).
22. A. Fieck, D. L. Wyborski, J. M. Short, *Nucleic Acids Res.* **20**, 1785 (1992).
23. W. Gilbert, B. Muller-Hill, *Proc. Natl. Acad. Sci. U.S.A.* **56**, 1891 (1966).
24. D. Bates, N. Kleckner, *Cell* **121**, 899 (2005).
25. P. C. Blainey, A. M. van Oijen, A. Banerjee, G. L. Verdine, X. S. Xie, *Proc. Natl. Acad. Sci. U.S.A.* **103**, 5752 (2006).
26. I. Golding, E. C. Cox, *Phys. Rev. Lett.* **96**, 098102 (2006).
27. T. T. Le *et al.*, *Proc. Natl. Acad. Sci. U.S.A.* **102**, 9160 (2005).
28. Y. Kao-Huang *et al.*, *Proc. Natl. Acad. Sci. U.S.A.* **74**, 4228 (1977).
29. R. B. Winter, O. G. Berg, P. H. von Hippel, *Biochemistry* **20**, 6961 (1981).

30. We thank P. Blainey, P. Sims, P. Choi, O. Berg, and M. Lovmar for helpful discussions. We are grateful to P. Blainey, P. Sims, and J. Hearn for protein purification, B. English for help with FCS, and J. Yu for making pVS155 and pVS167. The plasmids pkO3, pKD30, and Venus gene were contributed by G. Church, B. Wanner, and A. Miyawaki, respectively. This work was supported by NIH Director's Pioneer Award Program, the Knut and Alice Wallenberg Foundation (J.E), and NSF Graduate Research Fellowship (G.-W.L.).

Supporting Online Material

www.sciencemag.org/cgi/content/full/316/5828/1191/DC1
Materials and Methods
Figs. S1 to S9
References

1 March 2007; accepted 26 April 2007
10.1126/science.1141967

Abraxas and RAP80 Form a BRCA1 Protein Complex Required for the DNA Damage Response

Bin Wang,[1] Shuhei Matsuoka,[1] Bryan A. Ballif,[2]* Dong Zhang,[1]† Agata Smogorzewska,[1,3] Steven P. Gygi,[2] Stephen J. Elledge[1]‡

The BRCT repeats of the breast and ovarian cancer predisposition protein BRCA1 are essential for tumor suppression. Phosphopeptide affinity proteomic analysis identified a protein, Abraxas, that directly binds the BRCA1 BRCT repeats through a phospho-Ser-X-X-Phe motif. Abraxas binds BRCA1 to the mutual exclusion of BACH1 (BRCA1-associated C-terminal helicase) and CtIP (CtBP-interacting protein), forming a third type of BRCA1 complex. Abraxas recruits the ubiquitin-interacting motif (UIM)–containing protein RAP80 to BRCA1. Both Abraxas and RAP80 were required for DNA damage resistance, G_2-M checkpoint control, and DNA repair. RAP80 was required for optimal accumulation of BRCA1 on damaged DNA (foci) in response to ionizing radiation, and the UIM domains alone were capable of foci formation. The RAP80-Abraxas complex may help recruit BRCA1 to DNA damage sites in part through recognition of ubiquitinated proteins.

The BRCA1 tumor suppressor is associated with hereditary breast and ovarian cancer and functions in maintenance of genomic stability (*1*, *2*). BRCA1 contains an N-terminal RING domain, a Ser-Gln (SQ) cluster domain (*3*), and two BRCT (BRCA1 C-terminal) repeats, which constitute a phosphopeptide recognition domain that binds peptides containing a phospho-SXXF motif (S is Ser, F is Phe, and X varies) (*4*–*6*) and is required for tumor suppression. By dimerizing with BARD1 (BRCA1-associated RING domain protein) through the RING domain, BRCA1 forms an E3 ubiquitin ligase (*7*–*10*).

To identify proteins that bind BRCA1 BRCT domains, we combined peptide affinity purification, stable isotope labeling with amino acids in cell culture, and mass spectrometry (*11*–*13*) to identify and quantify phosphopeptides that directly bind to BRCA1 BRCT domains (fig. S1A). Proteins from cells grown in medium containing heavy isotope and cells grown in normal medium that were treated with 10 Gy ionizing radiation (IR) were prepared, mixed (1:1), and digested with trypsin. Tryptic peptides that bound to a glutathione *S*-transferase (GST)–BRCA1-BRCT fusion protein were identified. Phosphopeptides containing a pSXXF motif were compared with the list of proteins we recently identified as substrates of ATM (mutated in ataxia telangiectasia) and ATR (ATM and RAD3-related) (*14*). In addition to the known BRCA1-binding proteins BACH1 and CtIP, we identified peptides representing a potential ATM or ATR substrate and a novel protein, FLJ13614, that we named Abraxas, and the gene *ABRA1* (fig. S1). A doubly phosphorylated Abraxas peptide, GFGEYS#RS#PTF, containing pSer^{404} and pSer^{406} was enriched eightfold after IR, whereas the singly pSer^{406}-containing peptide bound, but was not enriched after IR (fig. S1). Synthetic peptides containing pSer^{406} bound GST-BRCA1-BRCT, whereas the pSer^{404} and unphosphorylated peptides did not (Fig. 1A and fig. S2A).

Abraxas is conserved in vertebrates (fig. S3). Bioinformatics analysis revealed a protein KIAA0157, we named ABRO1 (Abraxas Brother 1) (fig. S1D), which is 39% identical to ABRA1 in the N-terminal two-thirds of the protein (amino acids 1 to 260), including a coil-coil domain and a region we call the "ABR" domain; however, ABRO1 lacks the pSXXF motif and did not bind to BRCA1.

Abraxas specifically bound to the BRCT repeats of wild-type BRCA1 (Fig. 1B), but not a cancer-causing BRCT mutant, M1775R (fig. S2B). Binding of ABRA1 to BRCA1 requires phosphorylation (Fig. 1C and fig. S2, C and D). Ser^{406} phosphorylation was confirmed in vivo with a phosphospecific antibody but was not increased in cells exposed to IR (Fig. 1D and fig. S2E).

A search for additional BRCA1-BRCT–binding proteins that bound to tandem affinity purification (TAP)–tagged BRCA1-BRCT domains (*15*) identified RAP80, a ubiquitin-interacting motif (UIM)– and zinc finger–containing protein that interacts with retinoid-related testis-associated receptor in vitro (Fig. 1F) (*16*). RAP80 was found to be phosphorylated on three sites, Ser^{140}, Ser^{402}, and Ser^{419}, in response to IR in our ATM and ATR substrate screen (*14*). RAP80 from extracts associates with GST-BRCA1-BRCT in vitro and BRCA1 in vivo in a phosphorylation-dependent manner (fig. S5 and S11). IR treatment induced a mobility shift for Abraxas and RAP80 (Fig. 1, D and G), and both proteins could be detected by antibodies to phospho-SQ sites after IR treatment (Fig. 1, E and 1H). These data combined suggest that Abraxas and RAP80 are ATM or ATR substrates.

[1]Department of Genetics, Center for Genetics and Genomics, Brigham and Women's Hospital, Howard Hughes Medical Institute, Harvard Medical School, Boston, MA 02115, USA. [2]Department of Cell Biology, Harvard Medical School, 240 Longwood Avenue, Boston, MA 02115, USA. [3]Department of Pathology, Massachusetts General Hospital, Boston, MA 02214, USA.

*Present address: Department of Biology, University of Vermont, Burlington, VT 05405, USA.

†Present address: Genomic Instability Group, Oncology Research, Wyeth Research, 401 North Middletown Road, Pearl River, NY 10965, USA.

‡To whom correspondence should be addressed. E-mail: selledge@genetics.med.harvard.edu

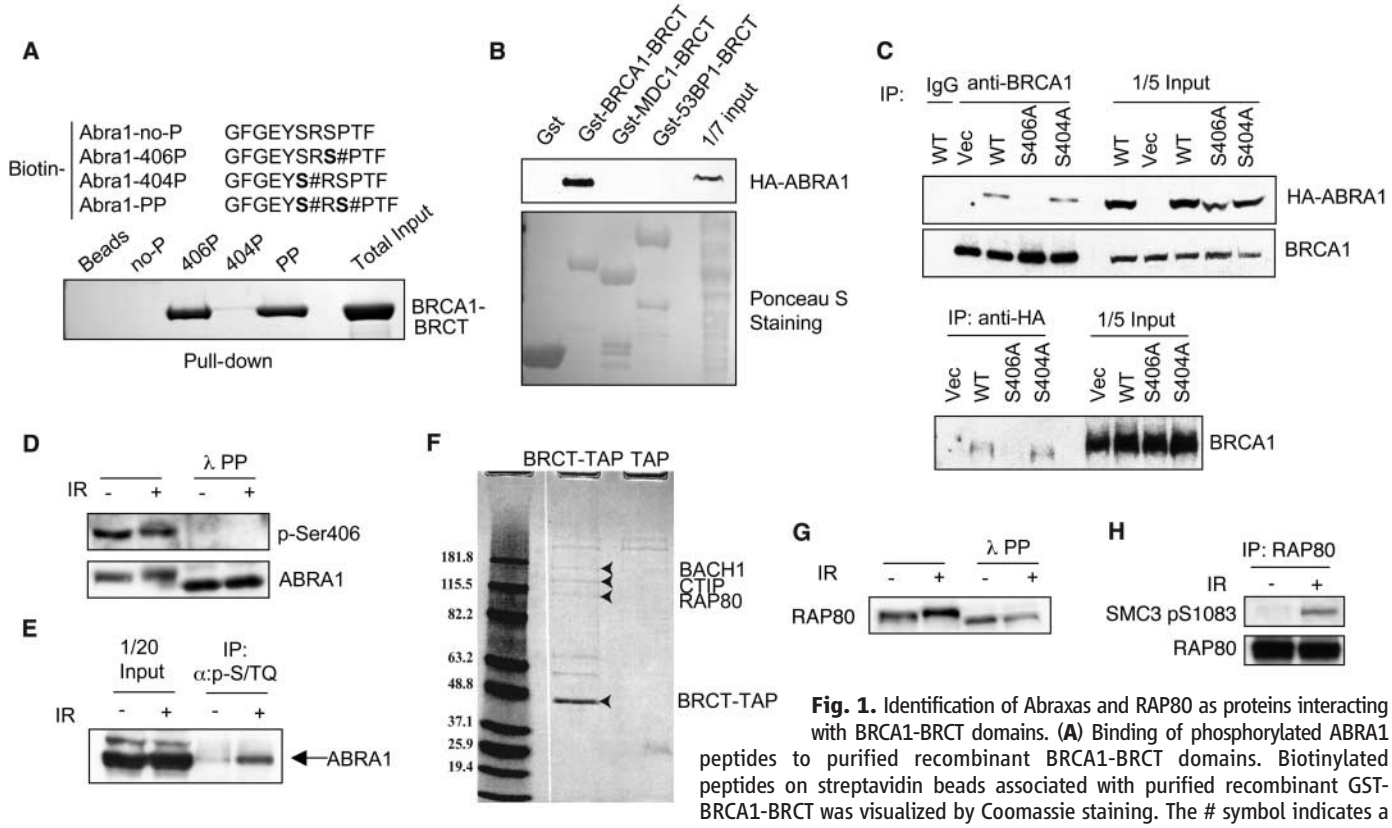

Fig. 1. Identification of Abraxas and RAP80 as proteins interacting with BRCA1-BRCT domains. (**A**) Binding of phosphorylated ABRA1 peptides to purified recombinant BRCA1-BRCT domains. Biotinylated peptides on streptavidin beads associated with purified recombinant GST-BRCA1-BRCT was visualized by Coomassie staining. The # symbol indicates a phosphate resides on the previous residue. (**B**) Specific binding of Abraxas to BRCA1-BRCT domains. Hemagglutinin-tagged ABRA1 (HA-ABRA1) was expressed in 293T cells, and cell lysates were incubated with various purified GST-tagged BRCT domains. (**C**) HA-ABRA1 association with endogenous BRCA1 is dependent on Ser^{406} phosphorylation. HA-ABRA1 wild-type or mutant proteins were expressed in 293T cells. (**D**) Phosphorylation of Ser^{406} of ABRA1 in vivo. Lysates prepared from 293T cells were untreated or treated with IR, untreated or treated with λ-phosphatase. (**E**) Immunoprecipitation of Abraxis with phospho-SQ or TQ antibodies. (**F**) RAP80 was identified in a TAP purification of BRCA1-BRCT domain–associated proteins. Retroviruses expressing either TAP only (TAP) or C-terminal TAP-tagged BRCT domain of BRCA1 (BRCT-TAP) were introduced into HeLa cells, and the infected cells were used for purification. A Coomassie-stained gel is shown. (**G**) Phosphorylation of RAP80 in response to IR. (**H**) Recognition of RAP80 by phospho-antibodies to ATM-ATR substrates. Proteins were immunoprecipitated from 293T cells lysates with antibodies to RAP80 and probed with the indicated antibodies.

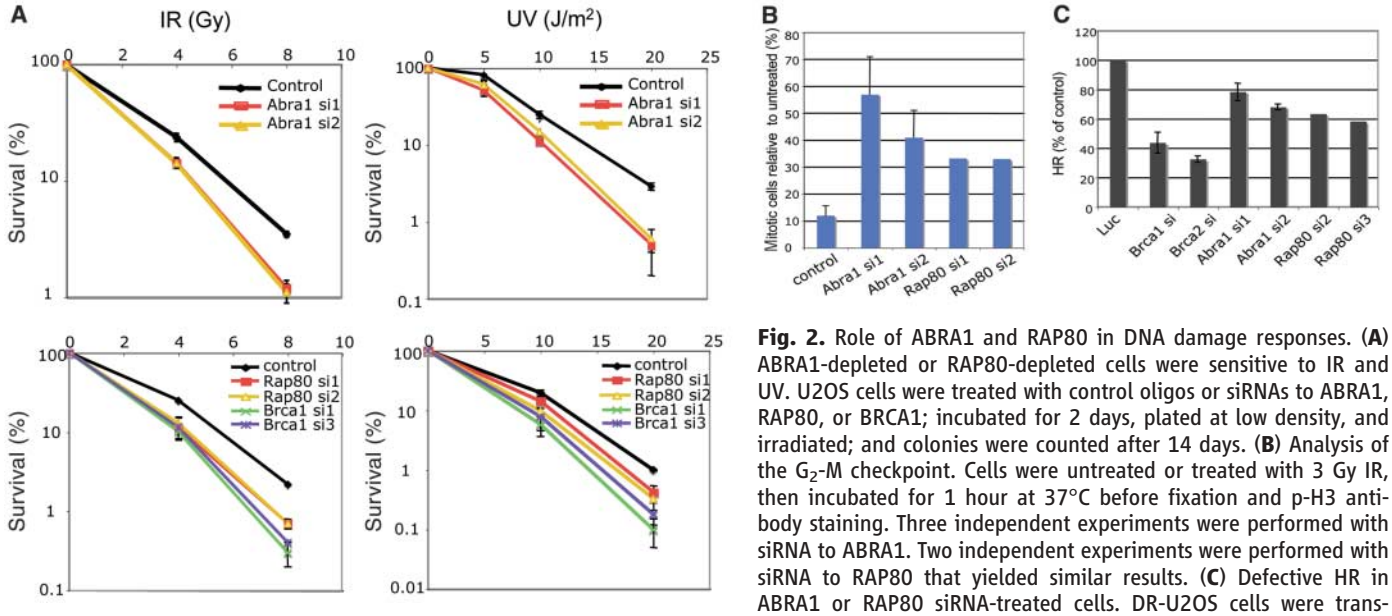

Fig. 2. Role of ABRA1 and RAP80 in DNA damage responses. (**A**) ABRA1-depleted or RAP80-depleted cells were sensitive to IR and UV. U2OS cells were treated with control oligos or siRNAs to ABRA1, RAP80, or BRCA1; incubated for 2 days, plated at low density, and irradiated; and colonies were counted after 14 days. (**B**) Analysis of the G_2-M checkpoint. Cells were untreated or treated with 3 Gy IR, then incubated for 1 hour at 37°C before fixation and p-H3 antibody staining. Three independent experiments were performed with siRNA to ABRA1. Two independent experiments were performed with siRNA to RAP80 that yielded similar results. (**C**) Defective HR in ABRA1 or RAP80 siRNA-treated cells. DR-U2OS cells were transfected with siRNAs to the indicated genes. siRNAs to BRCA1 or BRCA2 were a mixture of three different siRNAs for each gene. Individual siRNA were used for ABRA1 or RAP80. Three independent experiments were performed with siRNAs to luciferase, BRCA1, BRCA2, and ABRA1. The number of green positive cells generated from each sample relative to the number from the luciferase control was indicated as the percentage of HR.

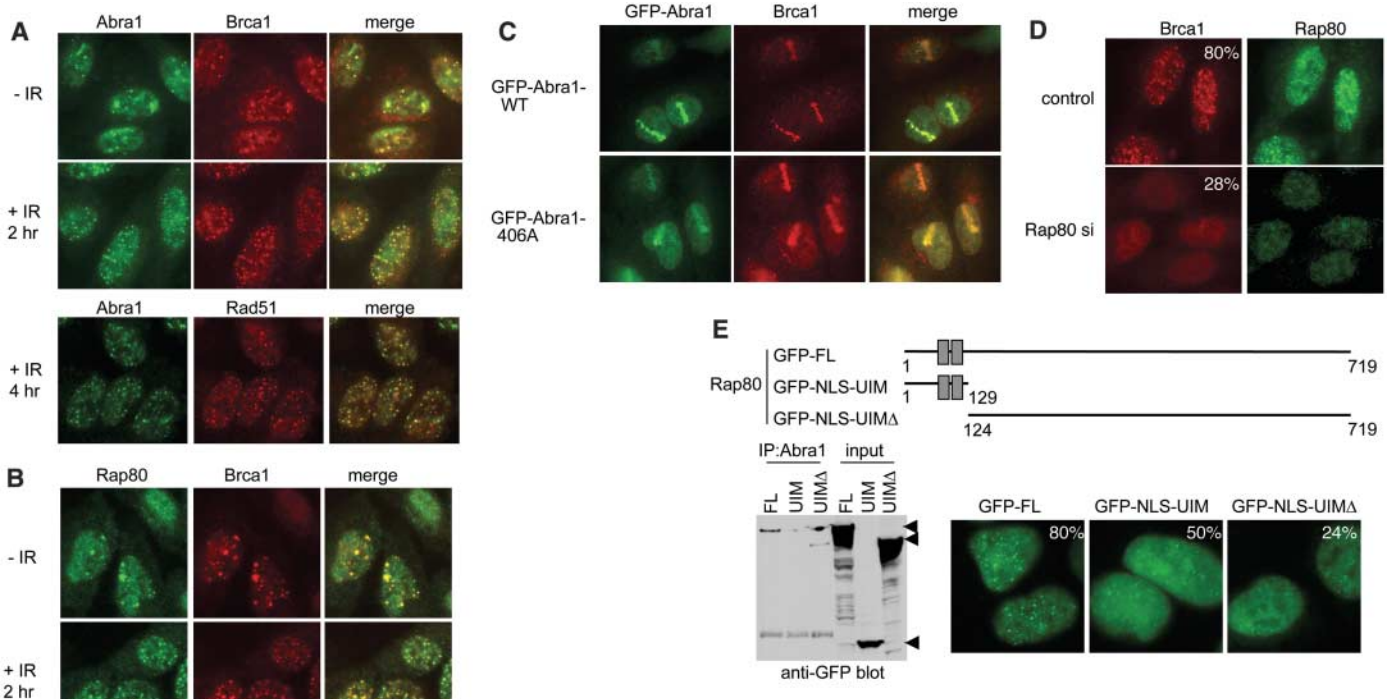

Fig. 3. ABRA1 and RAP80 form DNA damage–induced foci. (**A** and **B**) Colocalization of ABRA1 and RAP80 with BRCA1 and RAD51 at DNA damage–induced foci. U2OS cells were untreated or treated with 10 Gy IR, incubated for 2 hours, fixed and immunostained with antibodies to ABRA1, BRCA1, or RAD51, followed by cognate Alex 488–conjugated (green) or Cy3-conjuated (red) antibodies. (**C**) Localization of ABRA1 to sites of DNA damage is independent of BRCA1 binding. Laser microirradiation of U2OS cells with retrovirally expressed GFP-tagged wild-type or mutant ABRA1 (S406A) was performed. Cells were fixed and stained 15 min after laser treatment. (**D**) Defective BRCA1 foci formation in RAP80-depleted cells. U2OS cells were transfected with control or RAP80 siRNAs for 2 days, then irradiated with 10 Gy IR, incubated for 2 hours, and fixed and immunostained with indicated antibodies. More than 400 cells were analyzed, and cells containing more than 10 BRCA1 foci were deemed positive. (**E**) Dependence of RAP80 IRIF formation on UIM domains. U2OS cells containing retroviruses expressing GFP-WT, GFP-UIM or GFP-UIMΔ were irradiated with 10 Gy IR, incubated for 2 hours, fixed and stained with antibodies against GFP followed with Alexa 488 secondary antibodies. More than 300 cells were counted to determine the percentage of cells forming foci for each cell line. Immunoprecipitation of Abraxas revealed binding to the C-terminal region of RAP80 lacking the UIM domain.

Cells depleted of Abraxas or RAP80 (fig. S8) exhibited hypersensitivity to IR and ultraviolet (UV) light (Fig. 2A), G_2-M checkpoint defects (Fig. 2B and fig. S6), and defects in homologous recombination (HR) repair (Fig. 2C and fig. S6). Each of these defects was less severe than defects in BRCA1-depleted cells (*17*–*20*), which suggests that Abraxas or RAP80 mediates a subset of BRCA1 functions.

Abraxas and RAP80 form foci that colocalize with BRCA1 and RAD51 in S or G_2 phase U2OS cells (*21*) (Fig. 3, A and B). When a UV laser was used to micro-irradiate cells, ABRA1 relocalized to sites of DNA damage within 15 min (Fig. 3C). Unlike BACH1 and CtIP (*22*–*24*), ABRA1 and RAP80 foci formation was BRCA1-independent. The ABRA1 S406A mutant (in which Ala replaces Ser at codon 406), which does not bind BRCA1, efficiently localized to IR-induced (fig. S7A) and UV laser–induced (Fig. 3C) DNA damage. Furthermore, stably expressed green fluorescent protein (GFP)–tagged ABRA1 and RAP80 (fig. S7B) relocalized to UV DNA damage sites efficiently in BRCA1-deficient HCC1937 cells.

Depletion of RAP80 reduced foci formation of BRCA1. Although 80% of control cells formed IR-induced foci (IRIF) for BRCA1, only 28% of RAP80-depleted cells form BRCA1 IRIFs (Fig. 3D). Three nonoverlapping small interfering RNAs (siRNAs) to RAP80 were used in multiple experiments, and similar results were observed.

Deletion analysis determined that the RAP80 UIM domains alone could form IRIFs, although not as efficiently as the full-length protein (only 50% irradiated cells formed IRIF). Point mutations that abolish ubiquitin binding (A88S, S92A, A113S, S117A) prevent foci formation in the fragment containing UIM alone, but not when present in the full-length protein (fig. S10). RAP80 lacking the UIM domains also formed foci, but inefficiently (Fig. 3E), and the percentage of cells with foci did not increase in response to IR. Thus, RAP80 appears to have two different means of forming foci, but only the UIM domain responds to IR.

Abraxas binds BRCA1 mutually exclusively with BACH1 and CtIP as determined by coimmunoprecipitation (Fig. 4A). This is consistent with each of these proteins associating with BRCA1 through the same site on the BRCT motifs. As RAP80 does not contain a pSXXF motif, it might associate with BRCA1 indirectly. A substantial portion of RAP80 could be coimmunoprecipitated with ABRA1 (Fig. 4A). RAP80 lacking the UIM domains was still associated with ABRA1 (Fig. 3E), which indicated that a UIM-independent Abraxas-binding domain was present. The RAP80-ABRA1 interaction is BRCA1-independent, because the S406A ABRA1 mutant maintained RAP80 binding (fig. S9) and because RAP80-ABRA1 association was intact in HCC1937 cells (Fig. 4B). Unlike RAP80-BRCA1, the RAP80-ABRA1 interaction is phosphorylation-independent (fig. S11). Therefore, ABRA1 and RAP80 form a complex that interacts with BRCA1.

CtIP was detected in RAP80 immunoprecipitates (Fig. 4A and fig. S12). To determine the extent Abraxas and CtIP mediate RAP80 binding to BRCA1, we immunoprecipitated RAP80 from cells depleted for ABRA1, BACH1, or CtIP. The RAP80-BRCA1 interaction was decreased when ABRA1, but not BACH1 or CtIP, was depleted (Fig. 4C). Therefore, RAP80 interacts with BRCA1 largely through binding to Abraxas. As Bard1 is also present in ABRA1-RAP80-BRCA1 complexes, ABRA1 and RAP80 might mediate the E3 ligase activity of BRCA1-Bard1 heterodimers.

Our data, together with that from previous studies (*23*, *25*), suggest that BRCA1 BRCT domains form mutually exclusive complexes with ABRA1, BACH1, and CtIP through the pSXXF motif. These proteins may serve as adaptor proteins to recruit the BRCA1-Bard1 E3 ubiquitin ligase to specific target proteins analogous to F-box proteins' role in the SCF (Skp1, cullin, F-box) ubiquitin ligase ubiquitination pathway (*26*, *27*). To distinguish these complexes, we refer to them as the BRCA1 A complex (ABRA1),

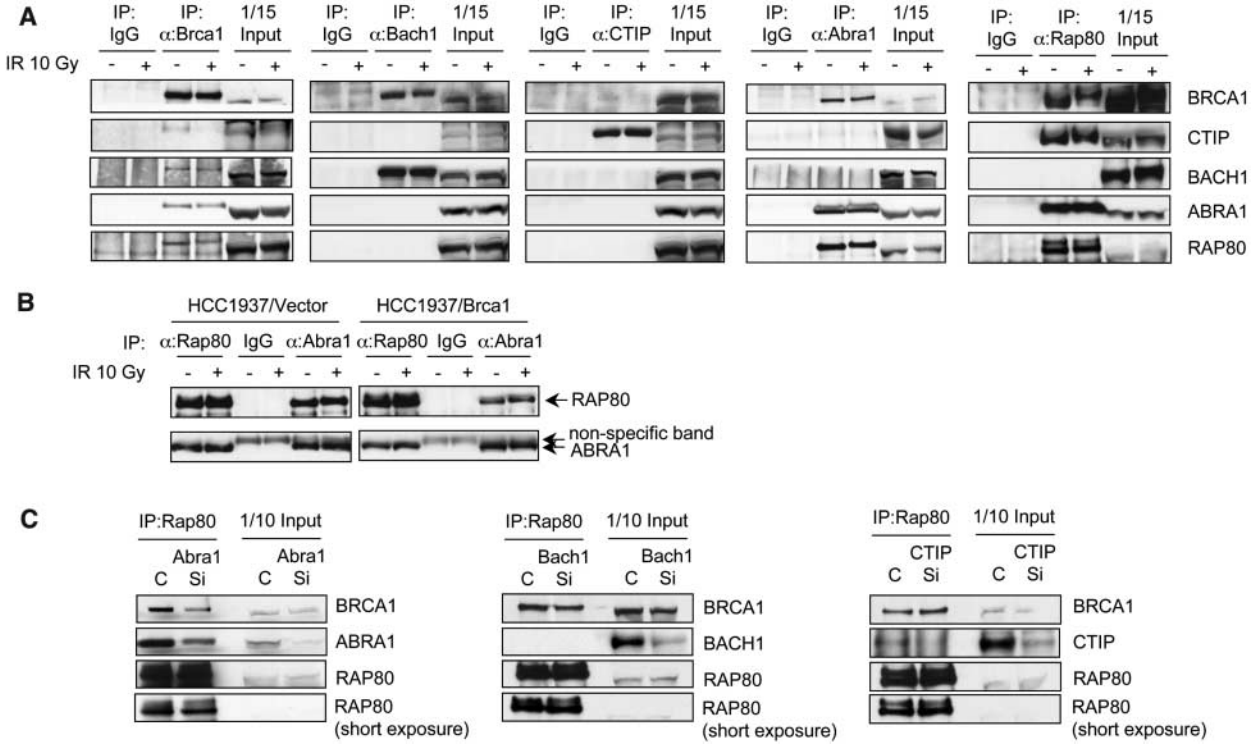

Fig. 4. Association of ABRA1 and RAP80 in a complex with BRCA1. (**A**) BRCA1 forms distinct complexes with ABRA1, BACH1, and CtIP. Proteins were immunoprecipitated with antibodies to BRCA1, BACH1, CtIP, ABRA1, and RAP80 from lysates of 293T cells treated with IR or untreated. (**B**) Intact RAP80-ABRA1 interaction in HCC1937 cells that lack a functional BRCA1. HCC1937 cells were either untreated or treated with IR. Proteins from lysates were immunoprecipitated with antibodies against RAP80 or ABRA1 or with control immunoglobulin IgG. (**C**) Decreased RAP80-BRCA1 interaction in ABRA1-depleted cells. 293T cells were transfected with control (C) or siRNA oligos to ABRA1, BACH1, or CtIP (Si). After 48 hours, proteins were immunoprecipitated with antibodies to RAP80. Immunoblotting was performed with the indicated antibodies.

B complex (BACH1), and C complex (CtIP) (fig. S13).

Abraxas and its paralog, ABRO1, have no known functional motifs, whereas RAP80 contains multiple ubiquitin-interaction motifs. Because RAP80 UIM domains form foci, it is likely that RAP80 localizes to DNA damage sites through its UIM domains by interacting with ubiquitinated proteins at the damaged sites. Furthermore, as RAP80 is required for at least a portion of BRCA1 IRIFs, it may recruit Abraxas-BRCA1 (and possibly CtIP-BRCA1) complexes to DNA damage sites where they may ubiquitinate additional proteins, possibly amplifying ubiquitination in the same way Mdc1 amplifies H2AX phosphorylation by recruiting ATM (*28*).

The BRCA1 A complex is clearly involved in the DNA damage response. However depletion of ABRA1 or RAP80 did not have as strong an effect on the various DNA damage response assays as BRCA1 depletion (fig. S6), which suggests that the BRCA1 A complex controls only part of BRCA1's role in these processes. It is likely that different BRCA1 complexes play redundant roles or promote multiple distinct steps in various DNA damage responses. For instance, all three complexes are required for HR (*22*) (fig. S6C). Furthermore, both the A and C complexes are required for the G_2-M checkpoint (fig. S6B), which suggests they also perform different functions needed for cell cycle arrest. Complexes A and C are also implicated in transcription through their association with RAP80. It is noteworthy that RAP80 was recently found to bind the estrogen receptor (*29*), which suggests that the A or C complex might mediate BRCA1's role in estrogen signaling in breast cancer. The identification of three distinct BRCA1 complexes should allow us to specifically dissect the role of each in the DNA damage response and tumorigenesis.

References and Notes

1. A. R. Venkitaraman, *Cell* **108**, 171 (2002).
2. S. A. Narod, W. D. Foulkes, *Nat. Rev. Cancer* **4**, 665 (2004).
3. D. Cortez, Y. Wang, J. Qin, S. J. Elledge, *Science* **286**, 1162 (1999).
4. I. A. Manke, D. M. Lowery, A. Nguyen, M. B. Yaffe, *Science* **302**, 636 (2003).
5. M. Rodriguez, X. Yu, J. Chen, Z. Songyang, *J. Biol. Chem.* **278**, 52914 (2003).
6. X. Yu, C. C. Chini, M. He, G. Mer, J. Chen, *Science* **302**, 639 (2003).
7. L. C. Wu *et al.*, *Nat. Genet.* **14**, 430 (1996).
8. R. Baer, T. Ludwig, *Curr. Opin. Genet. Dev.* **12**, 86 (2002).
9. R. Hashizume *et al.*, *J. Biol. Chem.* **276**, 14537 (2001).
10. H. Ruffner, C. A. Joazeiro, D. Hemmati, T. Hunter, I. M. Verma, *Proc. Natl. Acad. Sci. U.S.A.* **98**, 5134 (2001).
11. P. A. Everley, J. Krijgsveld, B. R. Zetter, S. P. Gygi, *Mol. Cell. Proteom.* **3**, 729 (2004).
12. S. E. Ong, L. J. Foster, M. Mann, *Methods* **29**, 124 (2003).
13. R. Amanchy, D. E. Kalume, A. Pandey, *Sci. STKE* **2005**, pl2 (2005).
14. S. Matsuoka *et al.*, *Science* **316**, 1160 (2007).
15. D. Zhang, K. Zaugg, T. W. Mak, S. J. Elledge, *Cell* **126**, 529 (2006).
16. Z. Yan, Y. S. Kim, A. M. Jetten, *J. Biol. Chem.* **277**, 32379 (2002).
17. B. Xu, S. T. Kim, D. S. Lim, M. B. Kastan, *Mol. Cell. Biol.* **22**, 1049 (2002).
18. K. Nakanishi *et al.*, *Proc. Natl. Acad. Sci. U.S.A.* **102**, 1110 (2005).
19. M. E. Moynahan, A. J. Pierce, M. Jasin, *Mol. Cell* **7**, 263 (2001).
20. M. E. Moynahan, J. W. Chiu, B. H. Koller, M. Jasin, *Mol. Cell* **4**, 511 (1999).
21. R. Scully *et al.*, *Cell* **90**, 425 (1997).
22. S. B. Cantor *et al.*, *Cell* **105**, 149 (2001).
23. R. A. Greenberg *et al.*, *Genes Dev.* **20**, 34 (2006).
24. X. Yu *et al.*, *Genes Dev.* **20**, 1721 (2006).
25. X. Yu, J. Chen, *Mol. Cell. Biol.* **24**, 9478 (2004).
26. D. Skowyra, K. L. Craig, M. Tyers, S. J. Elledge, J. W. Harper, *Cell* **91**, 209 (1997).
27. C. Bai *et al.*, *Cell* **86**, 263 (1996).
28. Z. Lou *et al.*, *Mol. Cell* **21**, 187 (2006).
29. J. Yan *et al.*, *Nucleic Acids Res.* **35**, 1673 (2007).

30. We are grateful to J. Jin, B. Liu, S. Wu, E. Gillespi, K. Nakanishsi, M. Jasin, and F. Graham for reagents and advice and to D. M. Livingston for exchanging information about RAP80 before submission. B.W. is a recipient of an NCI Howard Temin Award (1KO1, CA116275-01). A.S. is supported by T32CA09216 to the Massachusetts General Hospital (MGH) Pathology Department. This work was supported by grants from the NIH and NIAID 1U19A1067751 to S.J.E and S.P.G. S.J.E. is a Howard Hughes Medical Institute Investigator. The GenBank accession number for *ABRA1* is EF531340.

Supporting Online Material

www.sciencemag.org/cgi/content/full/316/5828/1194/DC1
Materials and Methods
Figs. S1 to S12
References

3 January 2007; accepted 3 April 2007
10.1126/science.1139476

RAP80 Targets BRCA1 to Specific Ubiquitin Structures at DNA Damage Sites

Bijan Sobhian,[1] Genze Shao,[2] Dana R. Lilli,[2] Aedín C. Culhane,[3] Lisa A. Moreau,[4] Bing Xia,[1] David M. Livingston,[1]* Roger A. Greenberg[1]*†

Mutations affecting the BRCT domains of the breast cancer–associated tumor suppressor BRCA1 disrupt the recruitment of this protein to DNA double-strand breaks (DSBs). The molecular structures at DSBs recognized by BRCA1 are presently unknown. We report the interaction of the BRCA1 BRCT domain with RAP80, a ubiquitin-binding protein. RAP80 targets a complex containing the BRCA1-BARD1 (BRCA1-associated ring domain protein 1) E3 ligase and the deubiquitinating enzyme (DUB) BRCC36 to MDC1-γH2AX–dependent lysine[6]- and lysine[63]-linked ubiquitin polymers at DSBs. These events are required for cell cycle checkpoint and repair responses to ionizing radiation, implicating ubiquitin chain recognition and turnover in the BRCA1-mediated repair of DSBs.

DNA repair requires a series of molecular recognition steps that enable DNA damage response proteins to localize at and near DNA lesions. Failure of these responses results in genomic instability and predisposition to malignancy (*1*–*3*). Binding of the mediator of DNA damage checkpoint 1 (MDC1) protein to the phosphorylated tail of histone H2AX (γH2AX) (*4*–*6*) facilitates the formation of BRCA1 nuclear foci at DSBs (*4*, *7*, *8*). BRCT domain mutations also abrogate BRCA1 ionizing radiation (IR)–induced focus (IRIF) formation and localization to laser-induced DNA double-strand breaks (DSBs) (*9*). Thus, this protein-protein interaction domain participates in molecular recognition processes required for homing of BRCA1 to γH2AX- and MDC1-containing DNA repair sites. BRCA1 BRCT mutations disable BRCA1 interactions with two, known ligands, BACH1 (BRCA1-associated C-terminal helicase) (*10*) and CtIP (CtBP-interacting protein) (*11*). However, BACH1 and CtIP deficiency do not substantially alter BRCA1 localization to IRIF or laser-induced DNA DSBs (*9*), suggesting that a heretofore undetected BRCT-interacting protein recruits BRCA1 to DNA damage–induced foci.

To address this hypothesis, we purified BRCA1-BARD1 complexes by double immunoaffinity chromatography of an epitope-tagged BARD1 protein (*9*). Multiple tryptic fragments derived from the tandem ubiquitin interaction motif (UIM) domain–containing protein, RAP80, were identified in this fraction by

[1]Dana-Farber Cancer Institute and Department of Genetics and Department of Medicine, Harvard Medical School, 44 Binney Street, Boston, MA 02115, USA. [2]Department of Cancer Biology and Department of Pathology, Abramson Family Cancer Research Institute, University of Pennsylvania School of Medicine, 421 Curie Boulevard, Philadelphia, PA 19104–6160, USA. [3]Department of Biostatistics and Computational Biology, Dana-Farber Cancer Institute, 44 Binney Street, Boston, MA 02115, USA. [4]Department of Radiation Oncology, Dana-Farber Cancer Institute, 44 Binney Street, Boston, MA 02115, USA.

*To whom correspondence should be addressed. E-mail: david_livingston@dfci.harvard.edu (D.M.L.); rogergr@mail.med.upenn.edu (R.A.G.)

†Present address: Department of Cancer Biology and Department of Pathology, Abramson Family Cancer Research Institute, University of Pennsylvania School of Medicine, 421 Curie Boulevard, Philadelphia, PA 19104–6160, USA.

mass spectrometry (fig. S1A). Endogenous RAP80 coimmunoprecipitated (coIP) with endogenous BRCA1 (Fig. 1A). This interaction depended on the integrity of the BRCT motifs, because two BRCT-domain clinical missense mutations each disrupted RAP80 binding (Fig. 1B). Purification of tagged BARD1 after IR revealed the presence of a DNA damage–induced phosphorylation event between the two RAP80 UIMs at serine 101 (S101) (Fig. 1C). A rabbit polyclonal antibody specific for this phosphopeptide revealed IR-induced RAP80 phosphorylation (Fig. 1C). S101 represents a potential ATM (ataxia telangiectasia mutated) protein kinase phosphorylation site, given its contribution to a serine-glutamine (SQ) motif (*12*). Indeed, it was not phosphorylated in response to 10 gray (Gy) IR in ATM lymphoblasts (Fig. 1D). However, RAP80 IR-induced phosphorylation and DSB localization were independent of RAP80 interaction with BRCA1, as demonstrated in the BRCA1 BRCT–mutated HCC 1937 cell line (Fig. 1, E and F).

A series of green fluorescent protein (GFP)–RAP80 deletion mutants were monitored for IR-induced colocalization with MDC1 (fig. S2A). A six-amino-acid deletion mutant was generated that removed the stretch of conserved glutamates spanning residues 103 to 108 (Δ103-108), creating a hypomorphic UIM2 (103 to 125) domain. This mutant was expressed at equivalent levels to wild-type (WT) RAP80 in stable cell lines, and it coimmunoprecipitated with BRCA1 like WT RAP80 (fig. S2A). However, RAP80Δ103-108 demonstrated greatly reduced colocalization with MDC1 at IRIF formation 1 hour after 6 Gy (85% for WT and 2% for RAP80Δ103-108, $n > 200$) (Fig. 2A). Similar results were obtained for RAP80 UIM1 deletion mutants (fig. S2). These results suggest that RAP80 gains access to DSBs by cooperative UIM binding to ubiquitin or polyubiquitin. In this regard, a glutathione *S*-transferase (GST)–RAP80 fusion protein that included both UIM domains (residues 1 to 233) bound Lys^{63} (K63) isopeptide-conjugated tetra-ubiquitin with higher efficiency than K48-linked ubiquitin tetramers (Fig. 2B). A preference for polymers containing at least four ubiquitin molecules was observed for GST-RAP80 incubated with K63-linked ubiquitin polymers, each containing two to seven ubiquitin molecules (Fig. 2C).

Ubiquitin can form polymers in vivo through any of its seven lysine residues (*13*). K6 isopeptides are the preferred linkage catalyzed by in vitro BRCA1 E3 activity (*14*–*16*). To test whether RAP80 can also interact with K6 linkages, we transfected human embryonic kidney 293T cells with expression vectors for ubiquitin species in which all lysine residues except one were mutated to arginine. This creates the in vivo synthesis of ubiquitin polymers containing defined isopeptide linkages. These chains, however, may also include endogenous ubiquitin and consequently may not be homogenous for a single, defined isopeptide linkage. In 293T cell lysates, GST-RAP80 bound to K6- and K63-linked polyubiquitin to a similar extent as to WT polyubiquitin, but did not recognize K48-linked polyubiquitin (Fig. 2D). These data indicate a preference for K63-, and possibly K6-, but not K48-linked ubiquitin polymers. Moreover, a positive correlation exists between ubiquitin binding and DSB localization, because WT RAP80 bound equally well to K63-linked ubiquitin before and after damage, whereas the UIM2 deletion mutant Δ103-108 demonstrated reduced binding to polyubiquitin (Fig. 2E). The RAP80 ubiquitin binding specificity observed in Fig. 2, B to E, appears to be relevant to the types of ubiquitin structures present at DNA damage sites. HeLa cells were transfected with vectors that produce different hemagglutinin (HA)-tagged ubiquitin chains, and colocalization of each ubiquitin species with BRCA1 at DNA damage sites was examined. BRCA1 colocalized with WT ubiquitin in about 75% of the cells examined and with either K6- or K63-linked ubiquitin in roughly 25% of the cells containing BRCA1 IRIF formation (Fig. 2F). K48-linked ubiquitin did not form foci at DNA damage sites ($n = 500$ transfected cells).

These results suggest that RAP80 is a candidate BRCT-interacting protein required to target BRCA1 to DNA damage sites. After small interfering RNA (siRNA) RAP80 knockdown in HeLa cells, strong BRCA1 foci were observed in just 8% of cells, compared to 82%

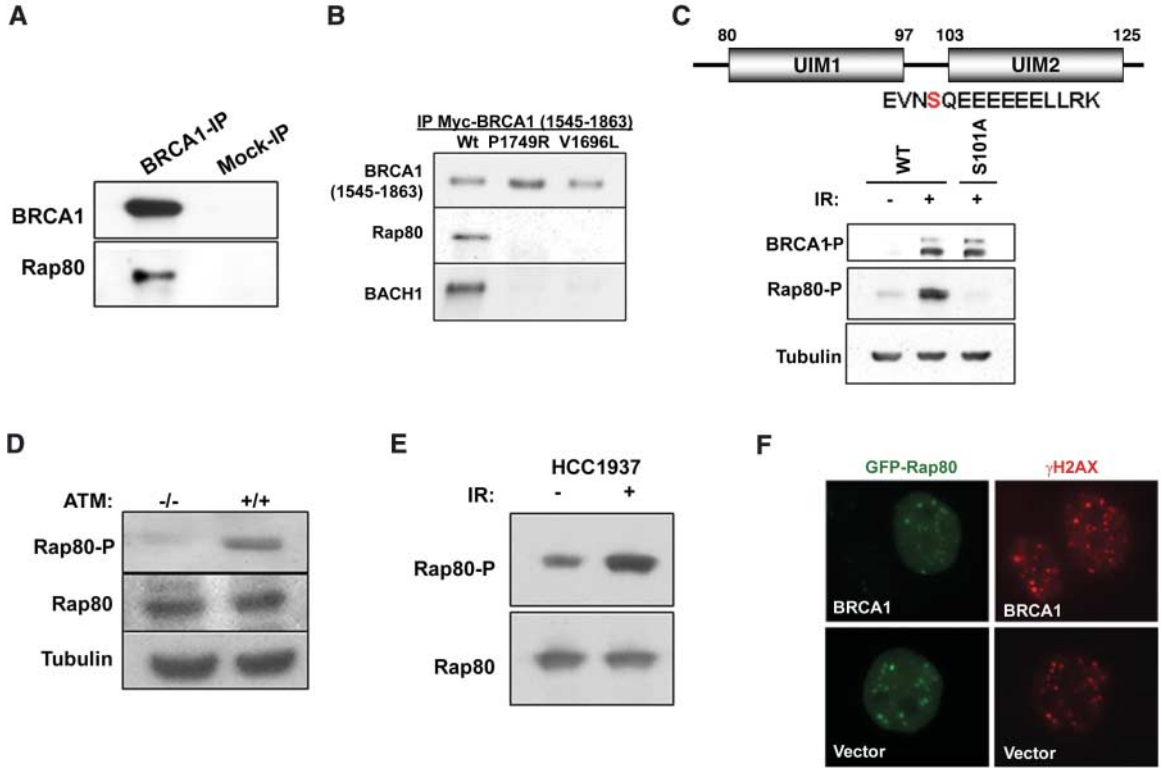

Fig. 1. RAP80 interacts with the BRCA1 BRCT motif and responds to IR independently of BRCA1. (**A**) Co-immunoprecipitation (IP) between endogenous BRCA1 and RAP80. (**B**) Lysates were prepared from 293T cells transfected with WT or clinical mutant myc-BRCA1-BRCT domains. Myc antibody immunoprecipitated material was separated by SDS–polyacrylamide gel electrophoresis, and immunoblotting (IB) was performed. (**C**) HeLa S3 cells stably expressing epitope tagged-WT or S101A mutant RAP80 were IR-treated, and lysates were probed with an antibody specific to phosphorylated (P) RAP80-S-101. E, Glu; L, Leu; N, Asn; R, Arg; and V, Val. (**D**) ATM –/– and +/+ and (**E**) HCC1937 cells were gamma-irradiated, and IB was performed on cell lysates as indicated. (**F**) HCC1937 cells reconstituted with vector or WT BRCA1 were transfected with GFP-RAP80 and gamma-irradiated, and, 1 hour later, IF was performed to assess colocalization with γH2AX.

in control (Ct) cells (n > 200). This indicates that RAP80 is largely required for BRCA1 IRIF formation (Fig. 3A). Moreover, WT RAP80 supported an interaction between the BRCT domain and ubiquitin, whereas the Δ103-108 mutant did not (Fig. 3B), providing in vitro evidence that RAP80 can target BRCA1 to ubiquitinated structures.

BRCA1 IRIF formation depends on the presence of γH2AX and MDC1 (*4*, *7*). RAP80 also demonstrated a strong dependency on MDC1 expression for post-IR foci formation, with >80% of control cells showing eRAP80 foci and only 2% of MDC1-depleted cells exhibiting eRAP80 IRIF (Fig. 3C). Ubiquitin DSB local-

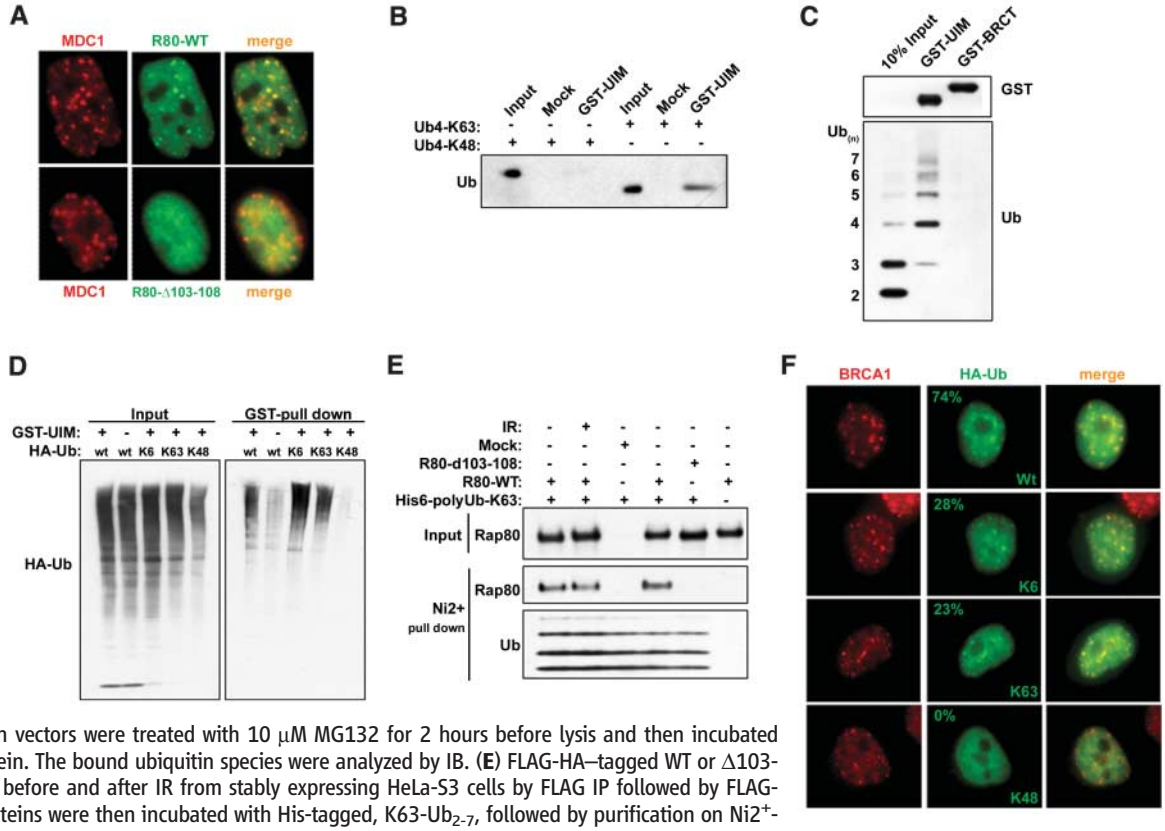

Fig. 2. RAP80 forms IRIF by binding to non-K48–linked ubiquitin. (**A**) HeLa cells stably expressing FLAG-HA–tagged WT or Δ103-108 RAP80 were treated with 6 Gy IR, and IF was performed 1 hour later. (**B**) K63- or K48-linked tetraubiquitin was incubated with the RAP80 GST-UIM domain. GST precipitations were analyzed by IB. (**C**) A mixture of K63-linked ubiquitin polymers containing two to seven molecules of ubiquitin (Ub_{2-7}) was incubated with RAP80 GST-UIM or GST-BRCT. IB was performed as indicated after purification on glutathione-conjugated sepharose beads. (**D**) 293T cells transfected with the indicated HA-tagged ubiquitin expression vectors were treated with 10 μM MG132 for 2 hours before lysis and then incubated with RAP80 GST-UIM protein. The bound ubiquitin species were analyzed by IB. (**E**) FLAG-HA–tagged WT or Δ103-108 RAP80 were purified before and after IR from stably expressing HeLa-S3 cells by FLAG IP followed by FLAG-peptide elution. These proteins were then incubated with His-tagged, K63-Ub_{2-7}, followed by purification on Ni^{2+}-agarose beads. Ubiquitin-associated proteins were detected by IB. (**F**) HeLa cells were transfected with the same ubiquitin-expression vectors as in (D) and analyzed by IF 1 hour after IR. The percentage of transfected cells that display colocalization of epitope-tagged ubiquitin and BRCA1 is indicated (N > 200).

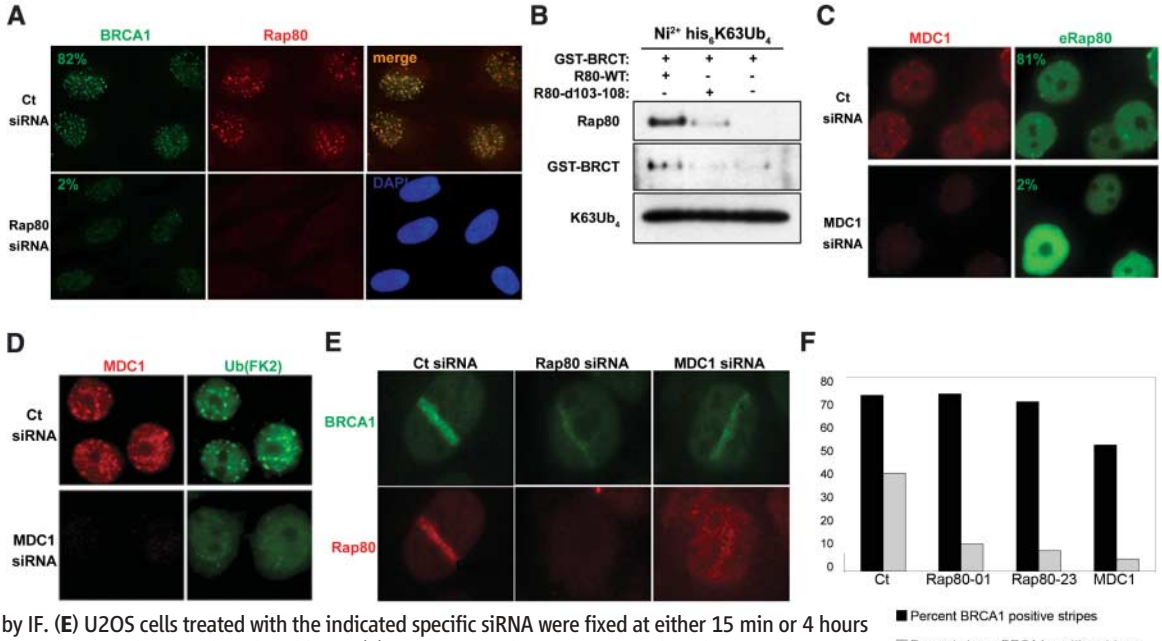

Fig. 3. RAP80 targets BRCA1 to MDC1-dependent polyubiquitin structures at DSBs. (**A**) U2OS cells transfected with control (Ct) or RAP80-specific siRNA were fixed 6 hours after 10 Gy IR and analyzed by IF. (**B**) FLAG IP-purified WT or Δ103-108 RAP80 derived from HeLa S3 cells stably expressing these proteins was incubated with GST-BRCT and K63-linked tetraubiquitin. Ni^{2+}-agarose precipitations were analyzed by IB as indicated. (**C** and **D**) HeLa cells transfected with Ct or MDC1-specific siRNA were fixed 6 hours after 6 Gy IR and analyzed by IF. (**E**) U2OS cells treated with the indicated specific siRNA were fixed at either 15 min or 4 hours after microirradiation by using a 337-nm laser and analyzed by IF. (**F**) Detection of the frequency and qualitative intensity of BRCA1 at γH2AX-positive stripes after treatment of U2OS cells with the indicated siRNA. Experiments were performed in duplicate at 15 min and 4 hours after laser-induced damage, and more than 125 stripes were counted per sample.

ization was also reduced in cells depleted for MDC1 ($n > 200$) (Fig. 3D). As opposed to focus formation, BRCA1 homed to laser-induced DNA DSBs (stripes) at similar frequencies regardless of RAP80 or MDC1 expression (Fig. 3, E and F). However, knockdown of RAP80 or MDC1 (*17*) each reduced the intensity of BRCA1 immunostaining at stripes (Fig. 3, E and F), and RAP80 recruitment to laser stripes was also reduced in cells depleted of MDC1 (Fig. 3E). These results point to an MDC1-dependent pathway that is necessary to recruit RAP80-BRCA1 complexes to polyubiquitin structures at DSBs.

To gain insight into the functional interaction between BRCA1 and RAP80, we purified epitope-tagged RAP80 complex(es). Mass spectrometry revealed the presence of BRCA1 and the BRCA1-BARD1–interacting proteins BRCC45 and BRCC36 (*18*) (Fig. 4A). The abundance of a complex consisting of BRCA1-BARD1, RAP80, and BRCC36 increased in M phase–enriched cells during a nocodazole block compared with S phase–enriched cells that were collected after thymidine treatment (Fig. 4B). This suggests that RAP80 exists in a BRCA1-BARD1–associated complex containing BRCC36 that is different from the BRCA1-BARD1-BACH1 complex that occurs primarily in S phase. Consistent with this model, RAP80 was required for eBRCC36 subcellular localization. Specifically, RAP80 knockdown disrupted BRCC36 IRIF (Fig. 4C) and rendered BRCC36 more readily extractable from nuclear matrix and/or chromatin-rich fractions (Fig. 4D). Conversely, BACH1 IRIF appeared independent of RAP80, and BACH1 knockdown did not affect either RAP80 or BRCA1 stripe localization (fig. S4) (*9*). Moreover, RAP80 and BRCC36 demonstrated similar contributions to BRCA1-dependent DNA damage responses, implying that they contribute to similar DNA damage response functions. In this regard, stable knockdown of RAP80 using either of two different RAP80 short hairpin RNAs (shRNAs) produced dose-dependent IR supersensitivity (Fig. 4E), as previously reported for BRCC36 knockdown (*19*). In addition, depletion of RAP80 by two different siRNAs, like BRCC36 knockdown, resulted in a partial disruption of the G2 phase cell cycle checkpoint after 2 Gy IR compared with controls (Fig. 4F).

BRCA1 ubiquitin ligase activity is activated by DNA damage and is required for its G2 checkpoint function (*16*, *20*). BRCC36 bears homology to the JAMM domain family of deubiquitinating enzymes (DUBs) (*21*), suggesting that, in addition to E3 activity, DUB activity may be involved in the checkpoint and repair functions of this specific BRCA1-BARD1 complex. Wild type and a double active site mutant, $His^{122} \rightarrow Gln^{122}$ (H122Q) and H124Q BRCC36, were purified from HeLa S3 cells and examined for DUB activity on K63-linked tetraubiquitin ($K63\text{-}Ub_4$). DUB activity was detected for WT BRCC36 but not for the mutant (Fig. 4G), establishing that BRCC36 has DUB activity toward K63-linked ubiquitin substrates, the same structures to which RAP80 binds.

These data support a model wherein MDC1-dependent, non–K48-linked ubiquitin chains at DNA damage sites are used as a targeting mechanism by specific BRCA1 complexes (Fig. 4H). Should this be a general phenomenon, RAP80 may represent the first in a new

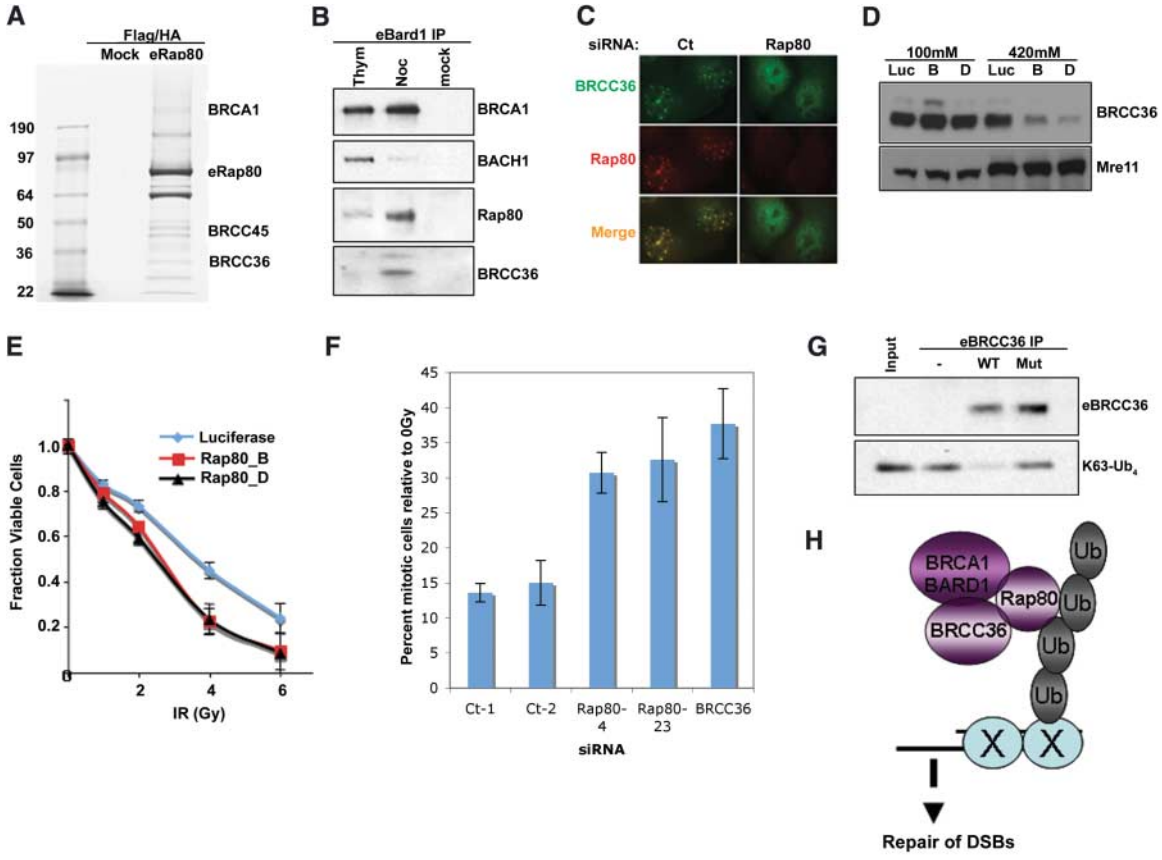

Fig. 4. Interactions of RAP80, BRCC36, and BRCA1. (**A**) Coommassie-stained gel of FLAG and HA double-purified RAP80 complexes from HeLa S3 cells stably expressing eRAP80. (**B**) HeLa S3 cells stably expressing eBARD1 were treated with 2 mM thymidine (Thym) or 0.5 μM nocodazole (Noc). FLAG-purified proteins were analyzed by IB. (**C**) U2OS cells expressing HA-tagged BRCC36 were transfected with shRNA specific to RAP80 or control and, 48 hours later, were monitored for IRIF at 1 hour after 6 Gy. (**D**) HeLa cells expressing stable siRNA vectors specific to luciferase (Luc) or RAP80 (B and D) were sequentially extracted with NETN buffer containing 100 mM NaCl and then NETN buffer containing 420 mM NaCl. Extracts were analyzed by IB. (**E**) HeLa cells expressing stable shRNA vectors specific to luciferase or RAP80 (B and D) were treated with the indicated doses of IR, and the number of viable cells were counted 96 hours later. The fraction of viable cells compared with a culture receiving 0 Gy is expressed graphically. Experiments were done in triplicate. Error bars indicate standard deviation. (**F**) The percentage of phosphohistone H3–positive cells (mitotic population) at 1 hour after 2 Gy IR compared with at 0 Gy (i.e., mock irradiation) was plotted for each siRNA-transfected U2OS population. Experiments were done in triplicate; error bars indicate standard deviation. (**G**) FLAG peptide eluates from FLAG IPs performed on extracts of HeLa S3 cells stably expressing FLAG-HA–tagged WT or a catalytically inactive BRCC36 mutant were incubated with K63-linked tetraubiquitin ($K63\text{-}Ub_4$) for 30 min at 37°C. The reaction mixtures were then analyzed by IB. (**H**) Model for recruitment of a BRCA1-BARD1-BRCC36-RAP80 complex to sites of DNA damage by binding to non-K48–linked ubiquitin structures.

class of DNA repair proteins that uses tandem UIM domains as part of its recruitment to DSBs. In contrast to IRIF formation, incomplete BRCA1 localization at laser-induced DSBs still occurs in the absence of γH2AX (*22*), MDC1 (*17*), or RAP80 (Fig. 3, E and F). These findings may reflect the fact that BRCA1/BARD1 heterodimers are components of multiple distinct complexes (*9*) and that each may access DSBs by different mechanisms. Taken together, these findings strongly suggest an essential role for ubiquitin recognition by a specific BRCA1 complex in the response to DSB formation. In addition, the synthesis and turnover of certain polyubiquitinated structures by BRCA1 E3 and BRCC36 DUB activities, respectively, may contribute to BRCA1-dependent DSB repair.

References

1. C. H. Bassing *et al.*, *Cell* **114**, 359 (2003).
2. A. Celeste *et al.*, *Cell* **114**, 371 (2003).
3. Y. Wang *et al.*, *Nat. Genet.* **37**, 750 (2005).
4. G. S. Stewart, B. Wang, C. R. Bignell, A. M. Taylor, S. J. Elledge, *Nature* **421**, 961 (2003).
5. M. Stucki *et al.*, *Cell* **123**, 1213 (2005).
6. E. P. Rogakou, C. Boon, C. Redon, W. M. Bonner, *J. Cell Biol.* **146**, 905 (1999).
7. A. Celeste *et al.*, *Science* **296**, 922 (2002); published online 4 April 2002 (10.1126/science.1069398).
8. C. H. Bassing *et al.*, *Proc. Natl. Acad. Sci. U.S.A.* **99**, 8173 (2002).
9. R. A. Greenberg *et al.*, *Genes Dev.* **20**, 34 (2006).
10. S. B. Cantor *et al.*, *Cell* **105**, 149 (2001).
11. X. Yu, L. C. Wu, A. M. Bowcock, A. Aronheim, R. Baer, *J. Biol. Chem.* **273**, 25388 (1998).
12. Y. Shiloh, *Nat. Rev. Cancer* **3**, 155 (2003).
13. J. Peng *et al.*, *Nat. Biotechnol.* **21**, 921 (2003).
14. F. Wu-Baer, K. Lagrazon, W. Yuan, R. Baer, *J. Biol. Chem.* **278**, 34743 (2003).
15. J. R. Morris, E. Solomon, *Hum. Mol. Genet.* **13**, 807 (2004).
16. J. Polanowska, J. S. Martin, T. Garcia-Muse, M. I. Petalcorin, S. J. Boulton, *EMBO J.* **25**, 2178 (2006).
17. S. Bekker-Jensen *et al.*, *J. Cell Biol.* **173**, 195 (2006).
18. Y. Dong *et al.*, *Mol. Cell* **12**, 1087 (2003).
19. X. Chen, C. A. Arciero, C. Wang, D. Broccoli, A. K. Godwin, *Cancer Res.* **66**, 5039 (2006).
20. X. Yu, S. Fu, M. Lai, R. Baer, J. Chen, *Genes Dev.* **20**, 1721 (2006).
21. X. I. Ambroggio, D. C. Rees, R. J. Deshaies, *PLoS Biol.* **2**, E2 (2004).
22. A. Celeste *et al.*, *Nat. Cell Biol.* **5**, 675 (2003).

Supporting Online Material

www.sciencemag.org/cgi/content/full/316/5828/1198/DC1
Materials and Methods
Figs. S1 to S4
References and Notes

4 January 2007; accepted 10 April 2007
10.1126/science.1139516

Ubiquitin-Binding Protein RAP80 Mediates BRCA1-Dependent DNA Damage Response

Hongtae Kim,[1] Junjie Chen,[1]* Xiaochun Yu[2]*

Mutations in the breast cancer susceptibility gene 1 (*BRCA1*) are associated with an increased risk of breast and ovarian cancers. BRCA1 participates in the cellular DNA damage response. We report the identification of receptor-associated protein 80 (RAP80) as a BRCA1-interacting protein in humans. RAP80 contains a tandem ubiquitin-interacting motif domain, which is required for its binding with ubiquitin in vitro and its damage-induced foci formation in vivo. Moreover, RAP80 specifically recruits BRCA1 to DNA damage sites and functions with BRCA1 in G_2/M checkpoint control. Together, these results suggest the existence of a ubiquitination-dependent signaling pathway involved in the DNA damage response.

Despite developing various DNA lesions generated during DNA replication or after exposure to environmental agents, cells normally maintain their genomic integrity and prevent neoplastic transformation because of the existence of several cell cycle checkpoints and DNA repair systems (*1*–*3*). Many proteins [including the protein kinase ataxia-telangiectasia mutated (ATM), γ-H2AX, mediator of DNA damage checkpoint protein 1 (MDC1), Nijmegen breakage syndrome 1 (NBS1), BRCA1, and checkpoint kinases 1 and 2 (Chk1 and Chk2)] are involved in the ionizing radiation (IR)–induced DNA damage response pathway (*4*). ATM is recruited to and activated at the sites of DNA breaks. Activated ATM transduces DNA damage signals to downstream proteins, including BRCA1. *BRCA1* encodes a tumor suppressor gene that is mutated in ~50% of hereditary breast and ovarian cancer patients (*5*, *6*). The human BRCA1 protein contains an N-terminal RING finger domain that has intrinsic E3 ubiquitin ligase activity and tandem BRCA1 C-terminal (BRCT) domains at its C terminus, which are phosphoserine- or phosphothreonine-binding motifs (*7*–*9*). Many disease-causing mutations are detected within these two regions of BRCA1.

Although BRCA1 is recruited to the sites of DNA breaks and participates in cell cycle checkpoint control, it remains obscure how the recruitment of BRCA1 is controlled in the cell. We purified BRCA1-BRCT domains from human leukemia K562 cells stably expressing this protein with N-terminal S-tag, Flag epitope, and streptavidin-binding peptide (SFB) triple tags (SFB-BRCA1-BRCT). We detected three specific bands that eluted with the SFB-BRCA1-BRCT domain but not with the SFB-BARD1-BRCT domain (Fig. 1A), where BARD1 signifies the BRCA1-associated RING domain protein 1. Mass spectrometry analysis revealed that these three proteins (respectively) are BRCA1-associated C-terminal helicase (BACH1), C-terminal binding protein–interacting protein (CtIP), and RAP80. BACH1 and CtIP are two known BRCA1 BRCT domain-binding proteins (*9*, *10*). RAP80 was originally identified as a retinoid-related testis-associated protein (*11*). The physiological function of RAP80 is unknown. We first confirmed the association between RAP80 and BRCA1 both in vitro and in vivo (Fig. 1B and fig. S1) (*12*). The interaction between BRCA1 and RAP80 remained the same before or after DNA damage (Fig. 1C).

BRCA1 relocalizes to sites of DNA breaks in cells exposed to IR. Immunostaining showed RAP80 to be evenly distributed in the nucleoplasm in normal cells (Fig. 2A). However, after exposure of cells to IR, RAP80 relocalized to foci that colocalized with γ-H2AX and BRCA1 (Fig. 2, A and B). RAP80 also associated with chromatin only in cells exposed to IR (Fig. 2C). Together, these data indicate that the localization of RAP80, like that of BRCA1, is regulated in response to DNA damage.

RAP80 isolated from irradiated cells migrated more slowly during SDS–polyacrylamide gel electrophoresis (SDS-PAGE) than did RAP80 isolated from unirradiated cells. Moreover, phosphatase treatment reversed the slow mobility of RAP80 prepared from irradiated cells (Fig. 2D), indicating that RAP80 may be phosphorylated in cells exposed to IR. We confirmed this using a phosphospecific antibody raised against a phosphorylation site that we identified (Ser^{101}; fig. S2). The ATM protein kinase is activated in response to DNA damage and phosphorylates many proteins involved in the DNA damage response. Treatment of cells with two different ATM kinase inhibitors, wortmannin and caffeine, abolished the IR-induced mobility shift of RAP80 (fig. S3A). The mobility shift of RAP80 was only observed in cells expressing wild-type (WT) ATM but not in ATM-deficient cells (Fig. 2E). These data suggest that ATM is required for damage-induced phosphorylation of RAP80.

The accumulation of RAP80 to the sites of DNA breaks depended on MDC1 and H2AX (Fig. 2, F and G) but not on NBS1, p53 binding

[1]Department of Therapeutic Radiology, Yale University School of Medicine, Post Office Box 208040, New Haven, CT 06520, USA. [2]Division of Molecular Medicine and Genetics, Department of Internal Medicine, University of Michigan Medical School, 109 Zina Pitcher Place, 1520 Biomedical Science Research Building, Ann Arbor, MI 48109, USA.

*To whom correspondence should be addressed. E-mail: Junjie.chen@yale.edu (J.C.); xiayu@med.umich.edu (X.Y.)

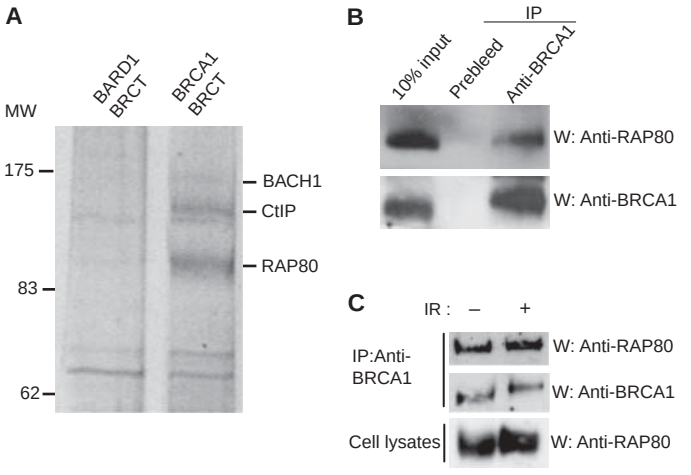

Fig. 1. Identification of RAP80 as a BRCA1-binding protein. (**A**) Silver staining of affinity-purified BRCA1-BRCT complexes. The cell extracts prepared from K562 cells stably expressing SFB-BRCA1-BRCT or SFB-BARD1-BRCT were subjected to two rounds of affinity purification. Final elutes were analyzed by SDS-PAGE and visualized by silver staining. The specific bands were excised from the silver-stained gel, and the peptides were identified by matrix-assisted laser desorption/ionization–time-of-flight mass spectrometry. Lines indicate protein bands corresponding to BACH1, CtIP, and RAP80. (**B**) The interaction between endogenous BRCA1 and RAP80. We performed immunoprecipitation (IP) reactions using preimmune serum or antibody to BRCA1. The immunoprecipitates were subjected to immunoblotting analyses with antibodies to BRCA1 or RAP80. (**C**) The interaction between BRCA1 and RAP80 before and after exposure of cells to IR. Lysates prepared from mock-treated or irradiated 293T cells were immunoprecipitated with antibody to BRCA1. The immunoprecipitates were separated by SDS-PAGE and immunoblotted with the indicated antibodies (top two lanes). The amount of endogenous RAP80 in cells before and after radiation was shown in the bottom lane.

protein 1 (53BP1), or BRCA1 (fig. S3, B to D). When we reduced endogenous RAP80 expression using RAP80 small interfering RNAs (siRNAs), we still detected damage-induced foci formation of MDC1, γ-H2AX, and 53BP1. However, no BRCA1 foci were present in these RAP80-depleted cells (Fig. 2H), suggesting that RAP80 acts upstream of BRCA1 and is required for the accumulation of BRCA1 to sites of DNA breaks.

We also determined which regions of RAP80 are important for its focus localization. Full-length and several internal deletion mutants of RAP80 localized to nuclear foci in cells with DNA damage, whereas RAP80D1 and RAP80D2 did not (Fig. 3A and fig. S4A). Because RAP80D1 and RAP80D2 are the only two internal deletion mutants that lack the two putative ubiquitin-interacting motifs (UIMs) (*13*), these results imply that the region containing UIMs may be required for RAP80 localization to DNA damage foci. The putative UIMs in RAP80 largely match with the UIM consensus sequence (fig. S4B). To determine whether the tandem RAP80 UIMs indeed bind to ubiquitin, we used a ubiquitin–

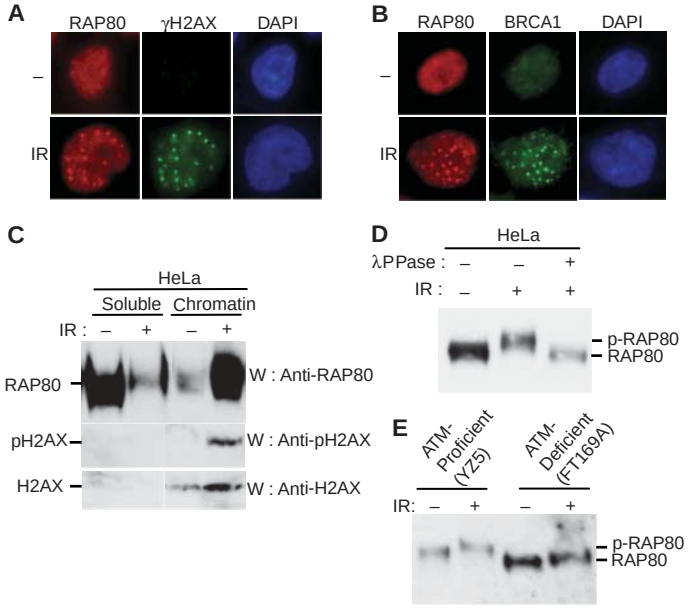

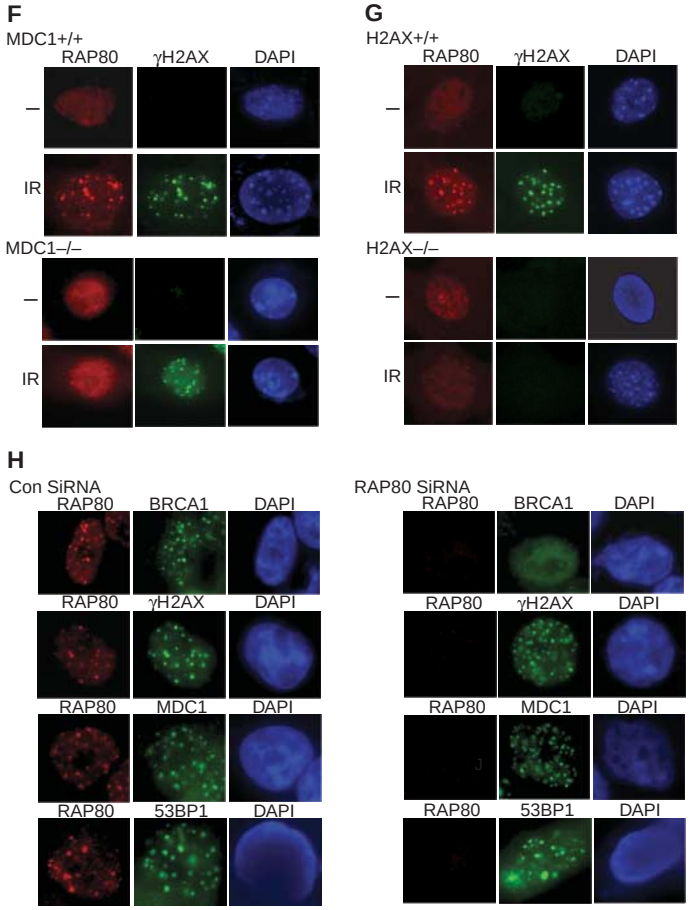

Fig. 2. Localization and phosphorylation of RAP80 in cells exposed to IR. DNA damage–induced RAP80 foci formation and its colocalization with γ-H2AX (**A**) and BRCA1 (**B**) are shown. DAPI, 4′,6′-diamidino-2-phenylindole. Mock-treated or irradiated 293T cells were fixed and stained with monoclonal antibodies to γ-H2AX or BRCA1 and polyclonal antibody to RAP80. (**C**) Association of RAP80 with chromatin after DNA damage. The soluble and chromatin fractions were prepared from mock-treated or irradiated 293T cells and subjected to Western blot analysis with antibodies to RAP80 (top lanes), phosphorylated H2AX (p-H2AX) (middle lanes), and H2AX (bottom lanes). (**D**) Phosphorylation of RAP80 after DNA damage. Lysates prepared from control or irradiated HeLa cells were immunoprecipitated with antibody to RAP80 and then incubated with or without λ phosphatase for 1 hour at 30°C. λPPase, λ protein phosphatase. The samples were subjected to immunoblotting with antibody to RAP80. (**E**) Requirement of ATM for IR-induced phosphorylation of RAP80. ATM-deficient FT169A cells and cells reconstituted with WT ATM (YZ5) were exposed to IR. Immunoprecipitation and immunoblotting were performed as described in (D). (**F** and **G**) Dependence of DNA damage–induced RAP80 foci formation. MDC1$^{+/+}$ and MDC1$^{-/-}$ mouse embryo fibroblasts (MEFs) (F) and H2AX$^{+/+}$ and H2AX$^{-/-}$ MEFs (G) were exposed to IR. The immunostaining experiments were performed as described in (A). (**H**) Requirement of RAP80 for damage-induced BRCA1 foci formation. Control (con) or RAP80 siRNA-transfected 293T cells were exposed to IR. Immunostaining was conducted with monoclonal antibodies to BRCA1, MDC1, 53BP1, or γ-H2AX and polyclonal antibody to RAP80.

glutathione *S*-transferase fusion protein (Ubi-GST). Ubi-GST specifically bound to the WT RAP80 but not to RAP80 lacking the two putative UIMs (RAP80D1; Fig. 3B). We also tested the binding of WT or mutant RAP80 UIMs [mutation of Ala^{88}→Gly^{88} (A88G) (*14*) and S92A in the first UIM and A113G and S117A in the second UIM] with Ubi-GST. The Ubi-GST specifically interacted with RAP80 UIM but not with the UIMs containing point mutations (Fig. 3B). We further checked whether point mutants within RAP80 UIMs would disrupt RAP80 foci formation in vivo. WT RAP80 and the RAP80P4 mutant (mutation of the linker region between two UIMs) formed detectable damage-induced nuclear foci, whereas the RAP80P1, RAP80P2, and RAP80P3 point mutants did not (Fig. 3C and fig. S4A). RAP80P1, RAP80P2, and RAP80P3 contain mutations within the first UIM (A88G and S92A), the second UIM (A113G and S117A), or both UIMs (A88G, S92A, A113G, and S117A), respectively. Therefore, the ubiquitin-binding activity of RAP80 correlates with its ability to localize to damage-induced foci in vivo. Like RAP80, the *Homo sapiens* DnaJ1A (HSJ1A) protein localizes to nuclei and also contains two UIMs. However, full-length HSJ1A or a construct containing the HSJ1A UIM region did not form nuclear foci in cells with DNA damage (fig. S4C). Thus, the ability to form nuclear foci is specific for the RAP80 UIM region. Notably, RAP80 UIMs bind specifically to Lys^{63}-linked but not to Lys^{48}-linked polyubiquitin chains in vitro (fig. S5).

Cells carrying BRCA1 mutants display increased sensitivity to IR and defective G_2/M checkpoint control (*15*). We examined whether the loss of the RAP80 would result in similar defects in the DNA damage response. Both RAP80 siRNAs that we synthesized efficiently decreased RAP80 expression in cells (Fig. 4A). Using a previously established G_2/M checkpoint assay (*16*), we showed defective G_2/M checkpoint control in RAP80-depleted cells (Fig. 4B). Similar G_2/M checkpoint defects were also observed in BRCA1- or CtIP-depleted cells (fig. S6). The protein kinase Chk1 is required for the G_2/M checkpoint control (*17*, *18*) and acts downstream of BRCA1 in response to IR (*19*, *20*). If RAP80 functions upstream of BRCA1, we would expect a defective Chk1 activation in RAP80-depleted cells. This is indeed the case (Fig. 4C). RAP80-depleted cells were also more sensitive to radiation than control cells (Fig. 4D). These data together indicate that RAP80 acts upstream of BRCA1 and specifically regulates BRCA1 functions after DNA damage.

Exactly how RAP80 is recruited to DNA damage sites is still unknown. Because RAP80 UIMs bind directly to ubiquitin in vitro, we reason that one or several ubiquitinated proteins might bind RAP80 and recruit RAP80 to the DNA damage sites. There are several proteins known to be ubiquitinated and localized to the sites of DNA damage (*21*–*23*). One of them is Fanconi anemia complementation group D2 (FANCD2). However, RAP80 foci still form normally after irradiation in FANCD2-deficient cells (fig. S7), suggesting that there may be other as-yet-unidentified ubiquitinated proteins that act

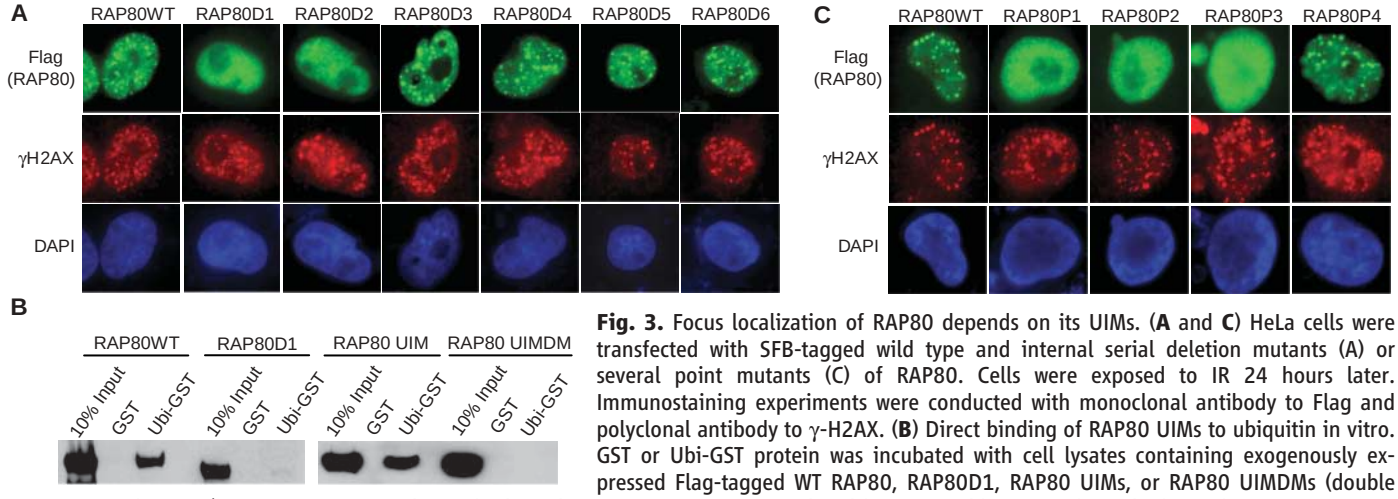

Fig. 3. Focus localization of RAP80 depends on its UIMs. (**A** and **C**) HeLa cells were transfected with SFB-tagged wild type and internal serial deletion mutants (A) or several point mutants (C) of RAP80. Cells were exposed to IR 24 hours later. Immunostaining experiments were conducted with monoclonal antibody to Flag and polyclonal antibody to γ-H2AX. (**B**) Direct binding of RAP80 UIMs to ubiquitin in vitro. GST or Ubi-GST protein was incubated with cell lysates containing exogenously expressed Flag-tagged WT RAP80, RAP80D1, RAP80 UIMs, or RAP80 UIMDMs (double mutations in the UIMs). After extensive washing, the bound RAP80 proteins were analyzed by immunoblotting with antibody to Flag.

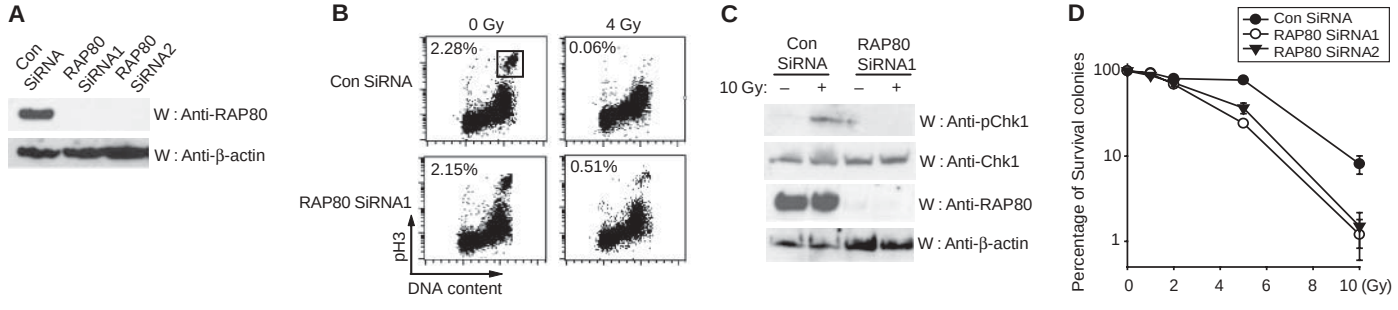

Fig. 4. Requirement of RAP80 for the IR-induced G_2/M checkpoint. (**A**) Western blot analysis for RAP80 expression level. RAP80 protein levels were analyzed by immunoblotting with antibodies to RAP80 with the use of control or RAP80 siRNA-transfected cell lysates. (**B**) G_2/M checkpoint in RAP80-depleted cells. HeLa cells transfected with control or RAP80 siRNAs were exposed to 0 or 4 grays (Gy) of IR. Cells were incubated for 1 hour before fixation and subjected to staining with antibody to phosphorylated histone H3 (pH3) and propidium iodide. The percentages of mitotic cells were determined by fluorescence-activated cell sorting analysis. The boxed area in the top left panel indicates mitotic cells. (**C**) Requirement of RAP80 for Chk1 phosphorylation after DNA damage. Control or RAP80 siRNA-transfected HeLa cells were exposed to IR. Cells were harvested 2 hours later, and lysates were immunoblotted with indicated antibodies. (**D**) Radiation sensitivity of cells lacking RAP80. HeLa cells were transfected with control or RAP80 siRNAs. Cells were counted and irradiated with various doses of IR. Percentages of surviving colonies were determined 11 days later. These experiments were performed in triplicate, and the results represent the average of two or three independent experiments. Error bars indicate SD for different doses of irradiation.

early in DNA damage response and regulate RAP80 localization.

Many cell cycle checkpoint proteins, including ATM, Chk2, BRCA1, and p53, play critical roles in the maintenance of genomic stability. Their mutation often results in increased tumor incidence, highlighting the importance of the integrity of DNA damage pathways in tumor suppression. As a BRCA1-associated protein involved in DNA damage checkpoint control, RAP80 may also function as a tumor suppressor and be dysregulated or mutated in human patients. Future genetic studies will allow us to test this possibility.

References and Notes

1. B. B. Zhou, S. J. Elledge, *Nature* **408**, 433 (2000).
2. J. Rouse, S. P. Jackson, *Science* **297**, 547 (2002).
3. W. C. Hahn, R. A. Weinberg, *N. Engl. J. Med.* **347**, 1593 (2002).
4. T. T. Su, *Annu. Rev. Genet.* **40**, 187 (2006).
5. F. J. Couch *et al.*, *N. Engl. J. Med.* **336**, 1409 (1997).
6. D. Ford *et al.*, *Am. J. Hum. Genet.* **62**, 676 (1998).
7. R. Hashizume *et al.*, *J. Biol. Chem.* **276**, 14537 (2001).
8. A. Chen, F. E. Kleiman, J. L. Manley, T. Ouchi, Z. Q. Pan, *J. Biol. Chem.* **277**, 22085 (2002).
9. X. Yu, J. Chen, *Mol. Cell. Biol.* **24**, 9478 (2004).
10. S. B. Cantor *et al.*, *Cell* **105**, 149 (2001).
11. Z. Yan, Y. S. Kim, A. M. Jetten, *J. Biol. Chem.* **277**, 32379 (2002).
12. Materials and methods are available as supporting material on *Science* Online.
13. S. Hirano *et al.*, *Nat. Struct. Mol. Biol.* **13**, 272 (2006).
14. Single-letter abbreviations for the amino acid residues are as follows: A, Ala; C, Cys; D, Asp; E, Glu; F, Phe; G, Gly; H, His; I, Ile; K, Lys; L, Leu; M, Met; N, Asn; P, Pro; Q, Gln; R, Arg; S, Ser; T, Thr; V, Val; W, Trp; and Y, Tyr.
15. C. X. Deng, S. G. Brodie, *Bioessays* **22**, 728 (2000).
16. B. Xu, S. Kim, M. B. Kastan, *Mol. Cell. Biol.* **21**, 3445 (2001).
17. Q. Liu *et al.*, *Genes Dev.* **14**, 1448 (2000).
18. H. Takai *et al.*, *Genes Dev.* **14**, 1439 (2000).
19. R. I. Yarden, S. Pardo-Reoyo, M. Sgagias, K. H. Cowan, L. C. Brody, *Nat. Genet.* **30**, 285 (2002).
20. P. B. Deming *et al.*, *Proc. Natl. Acad. Sci. U.S.A.* **98**, 12044 (2001).
21. X. Yu, S. Fu, M. Lai, R. Baer, J. Chen, *Genes Dev.* **20**, 1721 (2006).
22. X. Wang, P. R. Andreassen, A. D. D'Andrea, *Mol. Cell. Biol.* **24**, 5850 (2004).
23. R. Montes de Oca *et al.*, *Blood* **105**, 1003 (2005).

24. We thank J. Wood for proofreading the manuscript; J. Hohfeld and B. Horazdovsky for providing constructs encoding HSJ1A and Ubi-GST, respectively; and A. D'Andrea for providing FANCD2-deficient and FANCD2-reconstituted cells. This work was supported by grants from NIH (grant number RO1CA089239 to J.C.), the Ovarian Cancer Research Fund (X.Y.), the University of Michigan Cancer Center Developmental Fund (X.Y.), the U.S. Department of Defense (DOD) Era of Hope Scholars Award (J.C.), and the DOD Breast Cancer Research Program Idea Award (X.Y.).

Supporting Online Material

www.sciencemag.org/cgi/content/full/316/5828/1202/DC1
Materials and Methods
Figs. S1 to S9
References

5 January 2007; accepted 10 April 2007
10.1126/science.1139621

How Synaptotagmin Promotes Membrane Fusion

Sascha Martens,[1] Michael M. Kozlov,[2] Harvey T. McMahon[1]*

Synaptic vesicles loaded with neurotransmitters are exocytosed in a soluble *N*-ethylmaleimide–sensitive factor attachment protein receptor (SNARE)–dependent manner after presynaptic depolarization induces calcium ion (Ca^{2+}) influx. The Ca^{2+} sensor required for fast fusion is synaptotagmin-1. The activation energy of bilayer-bilayer fusion is very high (≈40 k_BT). We found that, in response to Ca^{2+} binding, synaptotagmin-1 could promote SNARE-mediated fusion by lowering this activation barrier by inducing high positive curvature in target membranes on C2-domain membrane insertion. Thus, synaptotagmin-1 triggers the fusion of docked vesicles by local Ca^{2+}-dependent buckling of the plasma membrane together with the zippering of SNAREs. This mechanism may be widely used in membrane fusion.

At the synapse, neurotransmitter release is mediated by the Ca^{2+}-induced fusion of transmitter-loaded synaptic vesicles with the presynaptic plasma membrane. The plasma membrane–localized target (t)-SNAREs ([soluble *N*-ethylmaleimide–sensitive factor attachment protein 25 (SNAP-25) and syntaxin-1)] and the vesicle (v)–localized v-SNARE (synaptobrevin) and synaptotagmin-1 (syt1) are involved in the Ca^{2+}-triggered fusion of synaptic vesicles with the plasma membrane (*1*). The three SNAREs are believed to bring the two membranes destined for fusion into close apposition. Syt1 has been shown to be the Ca^{2+} sensor responsible for Ca^{2+}-triggered fusion (*2*), but the molecular mechanism by which syt1 accomplishes this is not fully understood. Syt1 is a vesicle-localized transmembrane protein with two cytoplasmic C2 domains, C2A and C2B (Fig. 1A). The C2A and the C2B domains each bind Ca^{2+}, which enables them to interact with membranes (*3*, *4*). This activity is implicated in the triggering of membrane fusion (*5*, *6*). In addition, Ca^{2+}-dependent and -independent interactions between syt1 with SNAREs have been shown (*7*).

The fusion of two membranes is now widely believed to occur through a hemifusion intermediate (*8*). For hemifusion to occur, high energy barriers must be overcome, which are thought to be related to the curvature deformations generated within the membranes during stalk formation and subsequent stages of membrane merging (*8*, *9*). Syt1 has been shown to trigger Ca^{2+}-induced fusion and bind to membranes in a Ca^{2+}-dependent manner, and thus we investigated whether it could promote membrane fusion and, consequently, exocytosis, by affecting local membrane curvature.

Ca^{2+} binding by syt1 is mediated by a series of conserved aspartate residues that line pockets on one end of each of the C2A and C2B domains (*3*, *10*) (Fig. 1A). We used a syt1 construct lacking the transmembrane domain but having the double C2 domain module (C2AB) (*11*). Ca^{2+} binding allows the C2A and C2B domains to interact with negatively charged phospholipids such as phosphatidylserine (PtdSer) and phosphatidylinositol-4,5-bisphosphate [PtdIns(4,5)P_2] (*12*, *13*) (fig. S1). This interaction results in the insertion of four loops (two from each of the C2 domains) into the lipid bilayer (*14*, *15*). M173, F234, V304, and I367 (*16*) located on the tips of the membrane-binding loops (Fig. 1A) penetrate to a third of the lipid monolayer depth (*15*). This kind of hydrophobic-loop insertion should generate a tendency for the monolayer to bend to relieve the tension created by the insertion. If syt1 contributes to spontaneous membrane curvature (*8*), the closer the membrane curvature is to that preferentially produced by syt1, the stronger the syt1 affinity for membrane binding should be. Conversely, addition of syt1 to initially flat membranes should induce a positive curvature.

We incubated liposomes of different sizes, and, consequently, of different curvatures, with syt1 C2AB domains in the presence and absence of 1 mM Ca^{2+}. The binding of syt1 to membranes was monitored by a cosedimentation assay (Fig. 1B). Syt1 showed a clear preference for binding smaller liposomes (Fig. 1, Bii and C). This effect was observed only in the presence of Ca^{2+}, whereas the Ca^{2+}-independent interaction of syt1 with liposomes was size independent (Fig. 1Bi). This positive-curvature preference was largely lost when we increased the strength of interaction of syt1 with the membrane by elevating the PtdSer content in the liposomes from 15 to 25% (Fig. 1D). Likewise, the binding to Folch liposomes, which are rich in PtdSer, was largely curvature independent. The syt1 C2AB domain

[1]Medical Research Council–Laboratory of Molecular Biology, Hills Road, CB2 0QH Cambridge, UK. [2]Department of Physiology and Pharmacology, Sackler Faculty of Medicine, Tel Aviv University, 69978 Tel Aviv, Israel.

*To whom correspondence should be addressed. E-mail: hmm@mrc-lmb.cam.ac.uk

thus lost its ability to sense membrane curvature when the strength of interaction with the membrane was increased. To determine if the insertion of the hydrophobic loops accounted for syt1's preferential binding to small liposomes, we mutated M173, F234, V304, and I367 to alanines (4A mutant). The 4A mutant bound to 0.8-μm liposomes with an affinity similar to that of wild-type syt1 but showed no increased binding to small liposomes (Fig. 1, Biii and C). A mutant with all four residues mutated to tryptophans (4W mutant) showed an increased curvature preference (Fig. 1, Biv and C), but like the wild-type C2AB domain, lost its curvature preference when the PtdSer content in the liposomes was increased to 25%. Another mutant, K326E, with a point mutation in the polybasic region of the C2B domain that is remote from the Ca^{2+}-dependent membrane interaction site (Fig. 1A), was defective in Ca^{2+}-independent binding to liposomes but showed unaltered Ca^{2+}-mediated membrane interactions (fig. S1). Furthermore, as expected, K326E bound more effectively to small liposomes (Fig. 1, Bv and C).

To determine if syt1 could induce positive membrane curvature, we incubated Folch liposomes with syt1 in the presence and absence of Ca^{2+}. We observed extensive tubulation of Folch liposomes by syt1 only in the presence of Ca^{2+} (Fig. 2, A and B). The average diameter of tubules was 17.5 ± 3 nm from outer bilayer to outer bilayer, showing that the interaction of syt1 with membranes results in the induction of high positive curvature. For comparison, the N-BAR module (Bin/amphiphysin/Rvs domain with an N-terminal amphipathic helix) of amphiphysin makes lipid tubules of 46 nm (*17*). Using the syt1 C2A and C2B crystal structures (*3*, *10*) and the depth of insertions determined by electron paramagnetic resonance spectroscopy (*15*), we estimated that ~30% of the tubular surface needs to be covered to stabilize this curvature.

The tubulation of liposomes required the C2A and C2B domains to be linked to each other; the separated C2A and C2B domains did not tubulate Folch liposomes in the presence of Ca^{2+} (Fig. 2C). The 4A mutant failed to induce tubulation of Folch liposomes; in contrast, the 4W mutant caused tubulation and fragmentation of the liposomes, indicating further destabilization of the membrane (Fig. 2, D and E, and fig. S2). This destabilization is likely to have resulted from the greater volume occupied by the bulkier residues within the monolayer. The K326E mutant showed tubulation to an extent similar to that shown by the wild-type C2AB fragment (Fig. 2F). A C2AB fragment with mutations in the Ca^{2+}-binding site of the C2A domain (D230N, D232N) tubulated Folch liposomes (Fig. 2G), whereas a C2AB fragment with mutations in the Ca^{2+}-binding site of the C2B domain (D363N, D365N) did not induce membrane curvature (Fig. 2H). These results correlate with the ability of the former and inability of the latter mutant to promote synaptic vesicle exocytosis in vivo (*18*, *19*). We next investigated whether the tubulation of liposomes required the specific presence of the C2A and the C2B domains by fusing two C2A domains (C2AA) and two C2B domains (C2BB) and incubating them with liposomes in the presence of Ca^{2+}. Both fragments tubulated liposomes (Fig. 2, I and J), suggesting that the requirement for the induction of positive membrane curvature is the presence of two tethered C2 domains and their penetration of the lipid monolayer.

Next, we examined whether the Ca^{2+}-dependent induction of membrane curvature by syt1 is required for the promotion of SNARE-mediated membrane fusion in an in vitro assay (*11*, *20*, *21*). SNAREs alone were inefficient in promoting fusion of liposomes (Fig. 3A). Full-length syt1 had no effect in this assay but, as expected (*21*), we observed accelerated fusion by the addition of syt1 C2AB domain only in the presence of Ca^{2+} (Fig. 3A). This effect depended absolutely on the presence of SNAP-25 and syntaxin-1 in the target liposomes (Fig. 3A). The C2A and C2B domains had to be linked in order to promote membrane fusion (fig. S3) (*21*). The 4A mutant was unable to promote membrane fusion, whereas the 4W mutant showed increased promotion of membrane fusion compared with the wild-type C2AB fragment (Fig. 3B). Indeed, the expression in hippocampal neurons of a mutant syt1 carrying tryptophans in the membrane-binding loops results in an increased probability of synaptic vesicle release (*6*). The inability of the 4A mutant to promote membrane fusion was not due to its lower affinity for membranes, because increasing the concentration of the 4A mutant in the membrane fusion assay did not lead to increased fusion but rather led to a slight inhibition, perhaps due to masking of phospholipids (fig. S3). The K326E mutant, which could induce membrane curvature (Fig. 2), promoted membrane fusion to an extent similar to that shown by the wild-type protein, suggesting that the polybasic stretch was not required for the promotion of fusion in vitro (Fig. 3B). These results correlate well with the ability of wild-type syt1 and the syt1 mutants to induce tubulation of liposomes (Fig. 2).

Next, we tested the syt1 C2AA and C2BB domains for their ability to promote SNARE-dependent membrane fusion (Fig. 3C). Both proteins were indeed able to tubulate liposomes (Fig. 2). In our fusion assay, however, the C2AA domain was unable to promote fusion, whereas the C2BB domain was even more active than the syt1 C2AB domain, indicating that the induction

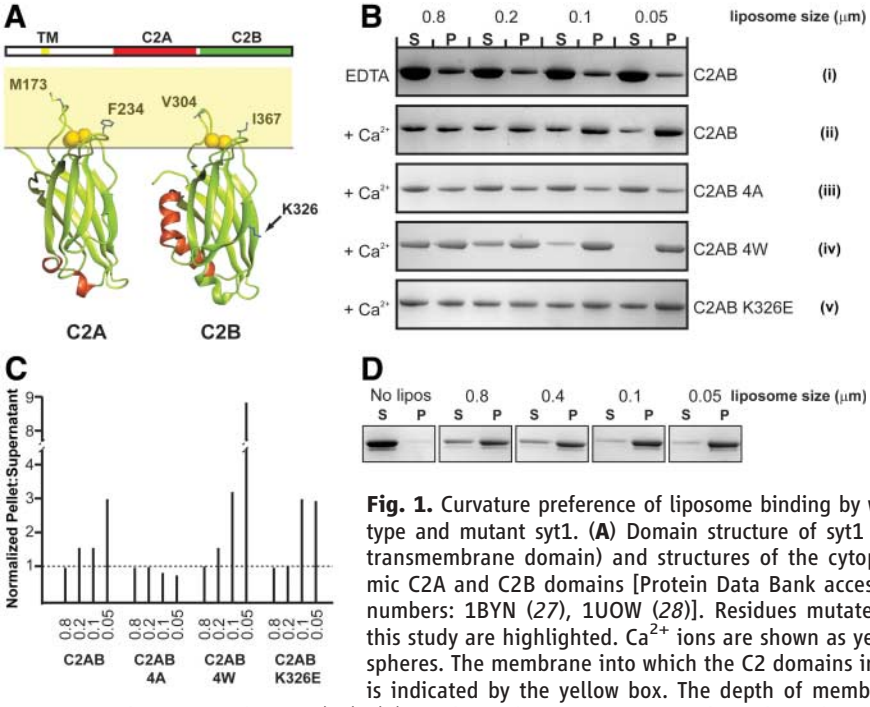

Fig. 1. Curvature preference of liposome binding by wild-type and mutant syt1. (**A**) Domain structure of syt1 (TM: transmembrane domain) and structures of the cytoplasmic C2A and C2B domains [Protein Data Bank accession numbers: 1BYN (*27*), 1UOW (*28*)]. Residues mutated in this study are highlighted. Ca^{2+} ions are shown as yellow spheres. The membrane into which the C2 domains insert is indicated by the yellow box. The depth of membrane insertion is shown according to (*15*). (**B**) Lipid cosedimentation assay. The indicated proteins were incubated with liposomes of different sizes (0.8 to 0.05 μm) in the absence (1 mM EDTA) or presence of 1 mM Ca^{2+}. P, pellet formed by centrifuging; S, supernatant. Representative gels from one of three independent experiments are shown. (**C**) Quantification of lipid cosedimentation experiments presented in (B). The P/S ratio for the 0.8-μm liposomes was set to 1. The numbers indicate the size of the liposomes (in micrometers). (**D**) The curvature preference of syt1 for smaller liposomes is largely lost when the PtdSer content is increased to 25%, as determined by liposome cosedimentation. The numbers indicate the size of the liposomes used for cosedimentation.

of membrane curvature alone is not sufficient to promote fusion. We attribute the lack of fusion-promoting activity by the C2AA domain to its inability to correctly interact with the SNARE complex, whereas the C2BB domain might be better positioned in respect to the SNARE complex. The C2B domain interacts more strongly with the SNARE complex (*22*).

We further tested the syt4 C2AB domain in our fusion assay. Syt4 lacks Ca^{2+}-dependent phospholipid-binding activity and did not tubulate Folch liposomes (fig. S1), but it displays SNARE binding to an extent similar to that shown by the syt1 C2AB domain (*23*). The syt4 C2AB domain failed to promote fusion (Fig. 3C), indicating that membrane binding and deformation by synaptotagmins are essential for the promotion of membrane fusion.

We further tested three synaptotagmin-related proteins—syt3, syt9, and synaptotagmin-like protein 2 (slp2)—for the induction of membrane curvature (Fig. 3). Syt3 and syt9 showed substantial Ca^{2+}-independent binding to liposomes, which increased upon the addition of Ca^{2+}, whereas the binding of slp2 to Folch liposomes was not affected by Ca^{2+} (Fig. 3D). Syt3 and syt9 both tubulated Folch liposomes in a Ca^{2+}-dependent manner, whereas slp2 tubulation did not require Ca^{2+} (Fig. 3E). The induction of positive curvature in the target membrane thus appears to be a property shared by many double C2 domain–containing proteins.

We propose the following model for the action of syt1 during Ca^{2+}-dependent synaptic vesicle release (fig. S4). Because of its Ca^{2+}-independent interaction with the tSNAREs and/or PtdIns(4,5)P_2 in the plasma membrane (*13*, *24*), syt1 in the synaptic vesicle is closely associated with the trans-SNARE complexes, which have been suggested to be ordered ringwise around the future fusion site (*20*). Upon Ca^{2+} influx and subsequent Ca^{2+} binding by syt1, the C2A and C2B domains penetrate the plasma membrane, resulting in the local induction of positive membrane curvature under the SNARE complex ring. This causes buckling toward the synaptic vesicle of the plasma membrane within the SNARE ring, reducing the distance between the two membranes. Furthermore, the buckled membrane is under curvature stress, which reduces the energy barrier the membrane has to overcome at the intermediate stage of fusion and, hence, accelerates the fusion reaction. An estimate of the energy released on going from buckle to stalk formation is 20 k_BT. This reduces the overall energy of stalk formation from ~40 k_BT (*9*) to about 20 k_BT (*11*). The remaining energy can be overcome by the membrane spontaneously (*9*, *25*). According to our model, syt1 has to bind the SNARE complex in order to target the membrane buckle under the vesicle. Indeed, the failure of syt1 to promote yeast SNARE-mediated membrane fusion correlates with its inability to bind the yeast SNAREs (*26*).

We have shown that, for syt1, the multiple C2 domain (MC2D) module promotes membrane fusion by the Ca^{2+}-dependent induction of membrane curvature, explaining how syt1 couples Ca^{2+} entry into a synapse to vesicle fusion. MC2D-containing proteins are found throughout the eukaryotic kingdom and constitute a large protein superfamily that includes molecules such as synaptotagmin-like proteins, ferlins, rabphilin, Rim, and DOC2. The promotion of membrane fusion by local induction of membrane curvature stress by MC2D-containing proteins may thus be a widespread phenomenon.

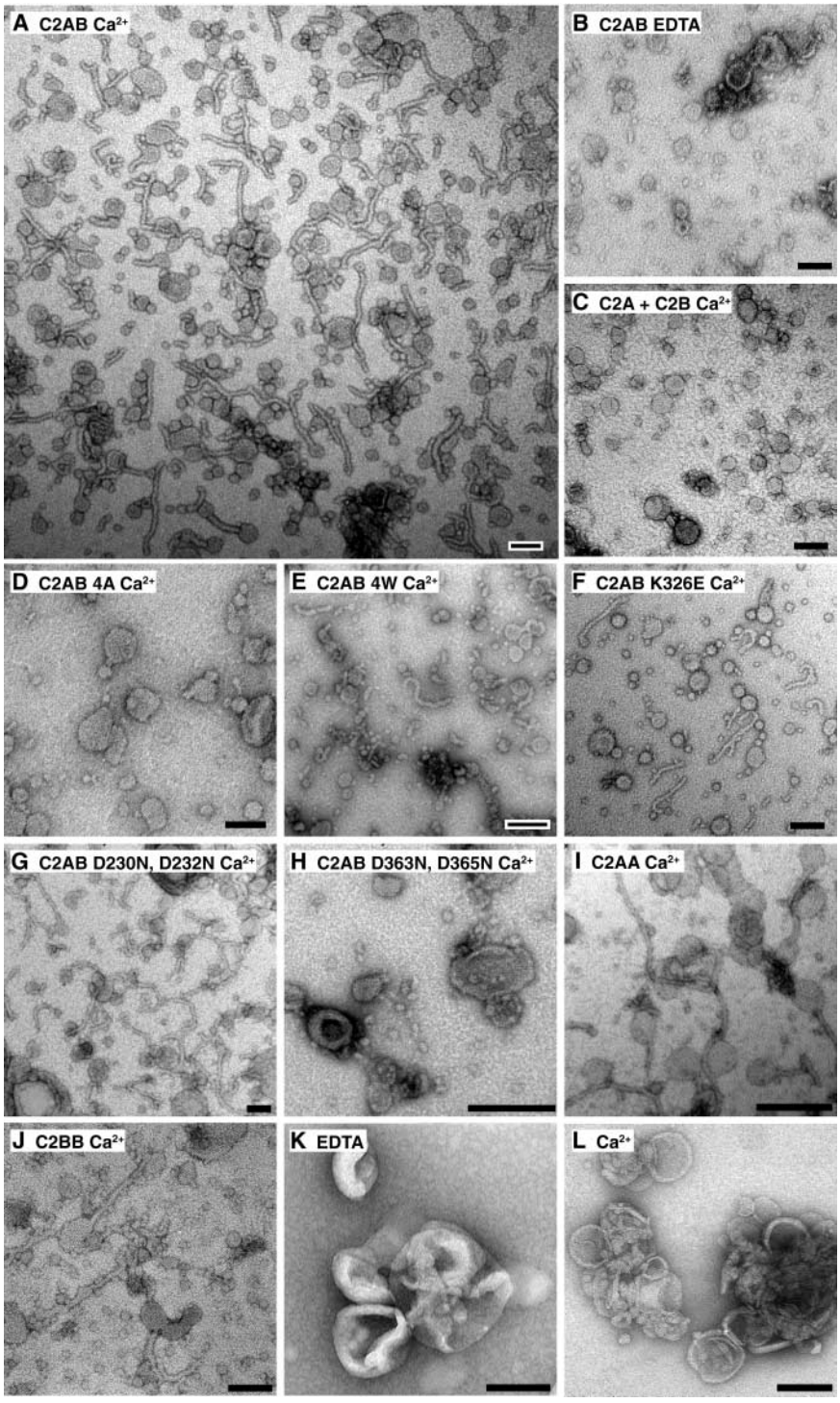

Fig. 2. Ca^{2+}-dependent induction of positive membrane curvature seen as tubulation by wild-type and mutant syt1. (**A** to **L**) Electron micrographs of Folch liposomes incubated with the indicated proteins at a concentration of 10 μM (*11*). Scale bar: 100 nm.

References and Notes

1. T. C. Sudhof, *Annu. Rev. Neurosci.* **27**, 509 (2004).
2. M. Geppert *et al.*, *Cell* **79**, 717 (1994).

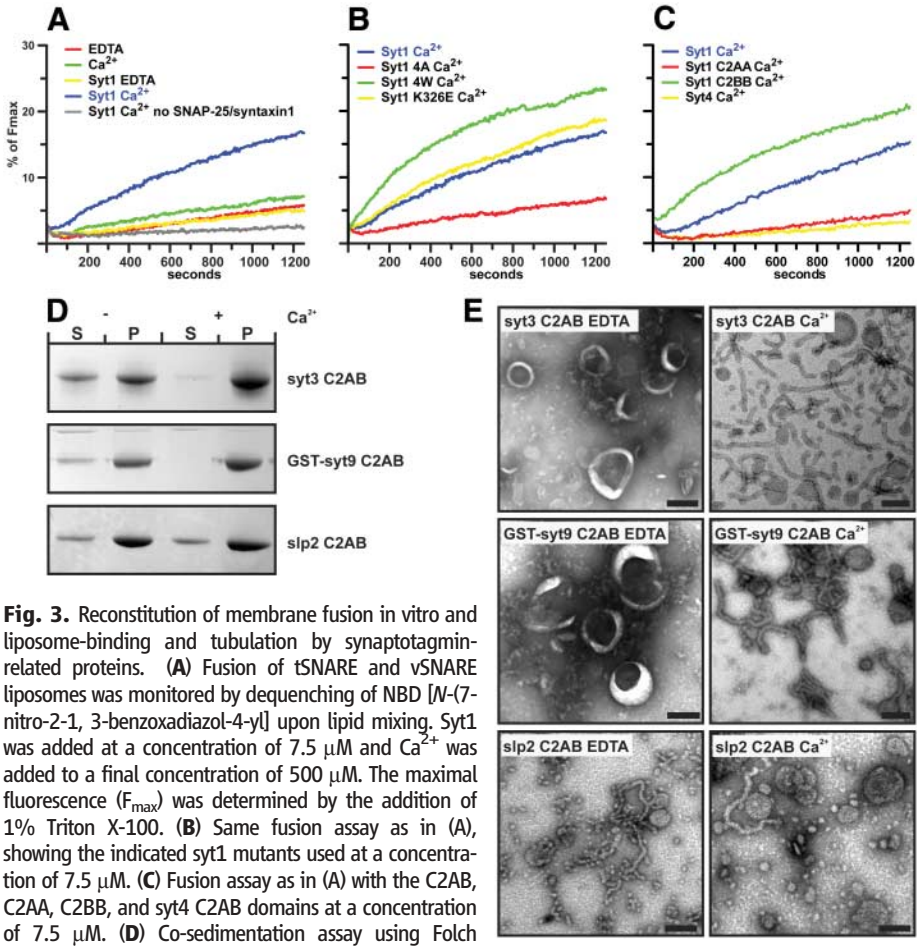

Fig. 3. Reconstitution of membrane fusion in vitro and liposome-binding and tubulation by synaptotagmin-related proteins. (**A**) Fusion of tSNARE and vSNARE liposomes was monitored by dequenching of NBD [*N*-(7-nitro-2-1, 3-benzoxadiazol-4-yl] upon lipid mixing. Syt1 was added at a concentration of 7.5 μM and Ca^{2+} was added to a final concentration of 500 μM. The maximal fluorescence (F_{max}) was determined by the addition of 1% Triton X-100. (**B**) Same fusion assay as in (A), showing the indicated syt1 mutants used at a concentration of 7.5 μM. (**C**) Fusion assay as in (A) with the C2AB, C2AA, C2BB, and syt4 C2AB domains at a concentration of 7.5 μM. (**D**) Co-sedimentation assay using Folch liposomes and the indicated proteins. (**E**) Electron micrographs of Folch liposomes incubated with the indicated proteins. Ca^{2+} was added to a final concentration of 1 mM in (D) and (E). Scale bar: 100 nm.

3. I. Fernandez *et al.*, *Neuron* **32**, 1057 (2001).
4. B. A. Davletov, T. C. Sudhof, *J. Biol. Chem.* **268**, 26386 (1993).
5. R. Fernandez-Chacon *et al.*, *Nature* **410**, 41 (2001).
6. J. S. Rhee *et al.*, *Proc. Natl. Acad. Sci. U.S.A.* **102**, 18664 (2005).
7. J. Tang *et al.*, *Cell* **126**, 1175 (2006).
8. L. V. Chernomordik, M. M. Kozlov, *Annu. Rev. Biochem.* **72**, 175 (2003).
9. Y. Kozlovsky, M. M. Kozlov, *Biophys. J.* **82**, 882 (2002).
10. R. B. Sutton, B. A. Davletov, A. M. Berghuis, T. C. Sudhof, S. R. Sprang, *Cell* **80**, 929 (1995).
11. Materials and methods and calculations are available as supporting material on *Science* Online.
12. M. S. Perin, V. A. Fried, G. A. Mignery, R. Jahn, T. C. Sudhof, *Nature* **345**, 260 (1990).
13. J. Bai, W. C. Tucker, E. R. Chapman, *Nat. Struct. Mol. Biol.* **11**, 36 (2004).
14. E. Hui, J. Bai, E. R. Chapman, *Biophys. J.* **91**, 1767 (2006).
15. D. Z. Herrick, S. Sterbling, K. A. Rasch, A. Hinderliter, D. S. Cafiso, *Biochemistry* **45**, 9668 (2006).
16. Single-letter abbreviations for the amino acid residues used are as follows: A, Ala; D, Asp; F, Phe; K, Lys; L, Leu; M, Met; V, Val; and W, Trp.
17. B. J. Peter *et al.*, *Science* **303**, 495 (2004).
18. I. M. Robinson, R. Ranjan, T. L. Schwarz, *Nature* **418**, 336 (2002).
19. J. M. Mackler, J. A. Drummond, C. A. Loewen, I. M. Robinson, N. E. Reist, *Nature* **418**, 340 (2002).
20. T. Weber *et al.*, *Cell* **92**, 759 (1998).
21. W. C. Tucker, T. Weber, E. R. Chapman, *Science* **304**, 435 (2004).
22. H. Dai, N. Shen, D. Arac, J. Rizo, *J. Mol. Biol.* **367**, 848 (2007).
23. C. Rickman, M. Craxton, S. Osborne, B. Davletov, *Biochem. J.* **378**, 681 (2004).
24. C. Rickman *et al.*, *Mol. Biol. Cell* **17**, 283 (2006).
25. P. I. Kuzmin, J. Zimmerberg, Y. A. Chizmadzhev, F. S. Cohen, *Proc. Natl. Acad. Sci. U.S.A.* **98**, 7235 (2001).
26. A. Bhalla, M. C. Chicka, W. C. Tucker, E. R. Chapman, *Nat. Struct. Mol. Biol.* **13**, 323 (2006).
27. X. Shao, I. Fernandez, T. C. Sudhof, J. Rizo, *Biochemistry* **37**, 16106 (1998).
28. Y. Cheng *et al.*, *Protein Sci.* **13**, 2665 (2004).
29. We thank B. Davletov for the provision of synaptotagmin 3, 4, and 9 plasmids and members of the lab for extensive discussions. This work was supported by the Medical Research Council (UK). We also gratefully acknowledge a long-term fellowship from the European Molecular Biology Organization (ALTF 21-2006) to S.M. and the Israel Science Foundation, United States–Israel Binational Science Foundation, and the Marie Curie Network "Flippases" funding for M.M.K.

Supporting Online Material

www.sciencemag.org/cgi/content/full/316/5828/1205/DC1
Materials and Methods
SOM Text
Figs. S1 to S6
References

12 January 2007; accepted 17 April 2007
Published online 3 May 2007;
10.1126/science.1142614
Include this information when citing this paper.

Myosin V Walks by Lever Action and Brownian Motion

Katsuyuki Shiroguchi and Kazuhiko Kinosita Jr.*

Myosin V is a molecular motor that moves cargo along actin filaments. Its two heads, each attached to a long and relatively stiff neck, move alternately forward in a "hand-over-hand" fashion. To observe under a microscope how the necks move, we attached a micrometer-sized rod to one of the necks. The leading neck swings unidirectionally forward, whereas the trailing neck, once lifted, undergoes extensive Brownian rotation in all directions before landing on a site ahead of the leading head. The neck-neck joint is essentially free, and the neck motion supports a mechanism where the active swing of the leading neck biases the random motion of the lifted head to let it eventually land on a forward site.

Linear molecular motors such as myosin, kinesin, or dynein are often Y-shaped, with two identical arms of Y each ending in a globular motor domain that binds to a track in an adenosine triphosphate (ATP)–dependent manner. Traditionally the motor domain has been called a "head" and the rest of the arm a "neck" (Fig. 1A). How the heads and necks cooperate to propel the motor is best understood in those motors that take many discrete steps without falling off a filamentous track (*1*–*7*): The two heads move forward alternately in a "hand-over-hand" fashion, as in human walking (*8*–*11*). However, the mechanism for bringing the lagging head onto a forward landing site is not yet firmly established. Here we focus on myosin V (*12*, *13*) that walks on an actin filament with ~35-nm steps (*14*, *15*). The necks of this motor are stiff relative to those of other motors such as kinesin, and they are called "lever arms" because they would serve as a lever. In electron micrographs (*16*), myosin V's long necks form a V-shape when both heads are attached to actin. Every step would thus result in leaning of a neck alternately forward and backward, as indeed was shown when a fluorophore

Department of Physics, Faculty of Science and Engineering, Waseda University, Okubo 3-4-1, Shinjuku-ku, Tokyo 169-8555, Japan.

*To whom correspondence should be addressed. E-mail: kazuhiko@waseda.jp

was attached to a neck (*17*, *18*). Our aim here was to resolve the neck motion during the transition between the two static orientations, and to infer the force behind the motion. Translational motion of a neck during the transients was recently reported (*19*). To examine rotational motion, we attached a micrometer-sized, fluorescently labeled microtubule to one of the necks of myosin V.

We replaced calmodulin light chains that wrap around the necks (Fig. 1A) with an engineered fusion protein in which calmodulin was connected to a motor domain of a mutated kinesin (*20*) that irreversibly binds to a microtubule (Fig. 1B). Then we added fluorescently labeled microtubules, hoping that in some myosin molecules only one of the two necks would bind a microtubule at multiple points. An actin filament was suspended in solution by holding two polystyrene beads attached to the filament ends with dual optical tweezers (*21*). By moving the microscope stage, we manipulated a floating microtubule, typically 2 to 3 μm long and binding at most eight myosin V molecules per μm, onto the actin filament. On rare occasions, the microtubule bound to actin, presumably through myosin V, and swung to and fro several times, primarily in the image plane (Fig. 1; see also fig. S1 and movies S1 and S2). We think the swings reflect the myosin neck motion because (i) the two relatively stationary angles (blue and red horizontal bars in Fig. 1D and fig. S1) were separated by ~100° (±20° SD for 17 swings), consistent with the angles between the V-shaped necks in the electron micrographs (*16*); (ii) dwell times on the stationary angles averaged 3 to 4 s, as expected for ATP-initiated swings at 0.2 to 0.3 μM ATP with a rate of ATP binding (*22*) of 0.9×10^6 M^{-1} s^{-1}; and (iii) the swings accompanied microtubule translocation. Swings in one direction (from blue to red bars) were always unidirectional, indicative of a power stroke. The other direction often involved extensive fluctuations, as in Fig. 1D at 15 to 17 s, suggesting Brownian search of a lifted neck for a next binding site. The micrometer-sized microtubule probe thus allowed us to visualize neck motion and confirm the expected behavior, but we were unable to obtain sufficient data to study details of the stepping dynamics.

We thus tried a reverse scheme (Fig. 2A): Instead of fixing an actin filament in space, we fixed a microtubule carrying myosin V (0.3 to 1 molecule μm^{-1}) on a glass surface and waited for a short (~1 μm) actin filament to land on it and move. For myosin V on the top surface of a microtubule 25 nm in diameter, movement of the actin filament in a horizontal plane would not be hindered by the glass surface. Note that the bound neck of myosin V is not necessarily parallel to the thick microtubule consisting of 13 tubulin protofilaments (Fig. 2A). In this reverse configuration, the actin filament would swing between two stationary angles where both heads of myosin V bind the filament. In between, the filament would be carried by one neck and would report the orientation of the actin-binding surface of the head. The actin filament would be translocated, with respect to the neck immobilized on the microtubule, by ~70 nm in the swing 3 → 5 in Fig. 2A; no translocation would accompany the swing 1 → 3. If a free joint(s) existed between two necks, the actin filament would undergo rotational Brownian fluctuation during swings accompanying the ~70-nm translocation, whereas the opposite swings would be unidirectional.

We observed the expected motions, and we analyzed 11 actin filaments that met the criteria of four or more swings between two stationary angles and translocation per swing of >25 nm (Figs. 2 and 3, fig. S5, and movies S3 and S4). A prominent feature was the asymmetry of swings (Fig. 2C and fig. S5), clearly noticeable because of the fast motions of short actin relative to longer microtubules above. Actin swings in one direction (39 swings, shown as anticlockwise and positive-going angular transitions in all figures) were accompanied by little translocation (–9 ± 23 nm, Fig. 3A), ended within ~50 ms (fig. S2), and were always unidirectional (Fig. 3B). Opposite, clockwise swings (38 swings) were accompanied by a large translocation averaging 73 ± 28 nm (Fig. 3A) except for three irregularities possibly due to backstepping (green arrow in Fig. 2C). Most of the clockwise swings involved fluctuations in either direction (Fig. 3C), continuing for

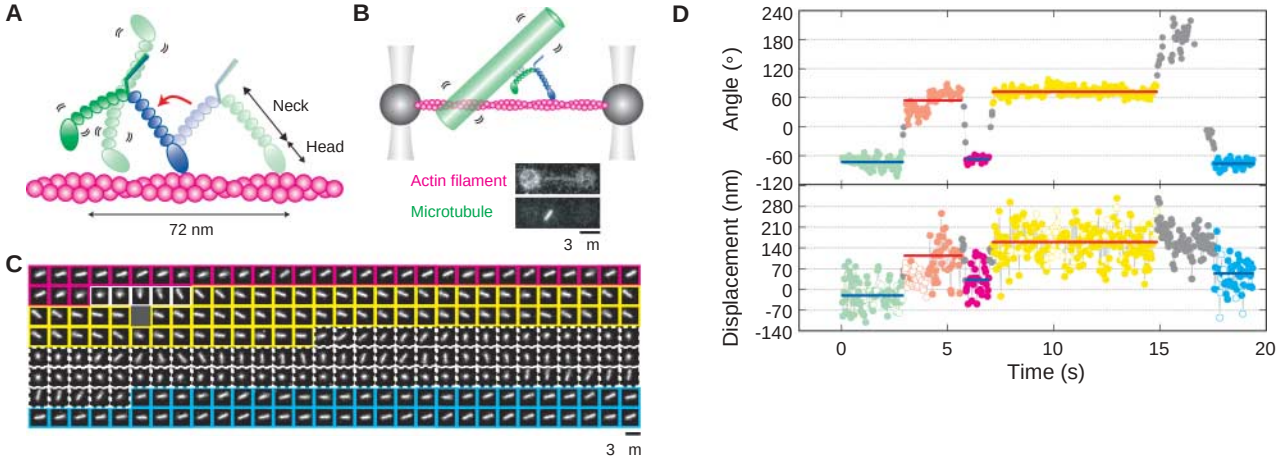

Fig. 1. Observation of neck motion in myosin V. (**A**) Postulated walking scheme for myosin V. Myosin V has two long necks (blue and green) reinforced with six calmodulin light chains (small ellipsoids) and catalytic heads (large ellipsoids) that hydrolyze ATP. Walking (toward left) on an actin filament (magenta) begins with binding of ATP to the trailing head to dissociate it from actin. The leading neck (blue) then leans forward (lever action: red arrow), powered by ATP hydrolysis (presumably phosphate release) in the leading head. The lifted neck (green) fluctuates around the neck-neck junction until the head binds to a site ~35 nm ahead of the blue head. (**B**) Observation of neck motion through a microtubule (light green cylinder) attached to a neck by linking calmodulins to a mutated kinesin (small gray circles) that irreversibly binds to a microtubule. Necks of myosin and thicknesses of the actin filament and microtubule are approximately to scale. The actin filament was bound to beads coated with α-actinin (dark gray) and held by dual-beam optical tweezers. The images of actin (and beads) stained with Alexa 488 and of a microtubule stained with tetramethylrhodamine were captured simultaneously. (**C**) Sequential images at 33-ms intervals of a microtubule, carrying fewer than four myosin V molecules per μm, apparently walking toward the left at 0.2 μM ATP. Magenta, yellow, and blue frames show two relatively stable angles; white solid frames, a unidirectional swing; white dotted frames, fluctuations; dark gray image, omission of 166 frames. Part of movie S1. (**D**) Upper panel: Swing angle anticlockwise from 0 o'clock; stationary angles are colored as in (C), and bars show the average. Swings are shown in gray. Omissions indicate orientations nearly vertical to the image plane. Lower panel: Movement of the centroid of the microtubule image calculated within a horizontal band of height 600 nm along the actin filament. Bars indicate averages over solid dots where the microtubule remained within 15° from the average stationary angle (open dots, orientations beyond 15°). Only comparisons among blue bars, or among red bars, are meaningful, because the centroids depended on the microtubule orientation to some extent.

0.6 s on average. The fluctuation period was distributed roughly exponentially, accounting for the apparent absence of fluctuations in some swings (fig. S3). Net translocation per swing pair was 62 ± 21 nm (Fig. 3D), somewhat smaller than the 70 nm obtained in experiments where beaded myosin V was allowed to spiral around actin (*15*). Here, actin displacement estimated from the centroid of the whole actin image is intrinsically imprecise, and the actin filament may have rotated around its axis to allow shorter steps. Dwells on the two stationary angles both averaged 7 to 8 s (fig. S4), consistent with the expected (*22*) ATP-waiting dwell of 5.6 s at 0.2 μM ATP. In the stationary phases, we sometimes noticed small angular steps (e.g., at ~52 s and several other places in Fig. 2C) that might indicate the existence of two V-shaped postures in the two-head bound state, such as bending of a neck(s) or shift of a head onto a neighboring actin monomer. Such substeps were not always observed and the direction was variable (fig. S5); thus, steric hindrance (e.g., between actin and microtubule surfaces) can also account for this phenomenon.

In the fluctuation phase, the mean square angle increased linearly with time (Fig. 3E). The slope gives a rotational diffusion constant of 11 $rad^2\ s^{-1}$. This value is close to 17 $rad^2\ s^{-1}$ calculated for a rod of diameter 10 nm and length 0.6 μm (average actin length between the myosin attachment and farther end) rotating around one end in water. The fluctuation angle eventually spreads over >600° (Fig. 3C). Thus, the fluctuation represents basically unhindered rotational diffusion in water, although actin occasionally gets stuck for a while. The free diffusion is consistent with the presence of a free joint at the neck-neck junction, as indicated earlier for myosin II (*23*) and myosin V (*16*). Two-headed motors with necks in basic twofold symmetry cannot walk without flexible joints (*24*, *25*). Our study further indicates that the joint is almost completely free, in that thermal agitation suffices to let an unattached neck assume all orientations in space (see below for three-dimensional fluctuations). Dunn and Spudich (*19*) attached a 40-nm gold particle to a neck of walking myosin V and showed that the particle undergoes rapid translational diffusion between two stationary phases where, presumably, both heads are bound to actin. Our results are consistent with their finding and further indicate that the diffusion is primarily of rotational nature.

Anticlockwise swings, in contrast, were always unidirectional, without a significant sign of reversal (at the video resolution of 33 ms), indicating that they are driven by active force. These swings without translocation are made by reorientation of the head on the neck immobilized on a microtubule (Fig. 2A). Our observation clearly shows that this reorientation, if viewed on actin, results in leaning of the neck forward (lever action), toward the direction in which myosin V would move, because actin is translocated by ~70 nm rearward at the completion of the next, fluctuating clockwise swing. The final phase of the anticlockwise swing may be assisted by binding of the free head, leading to the next

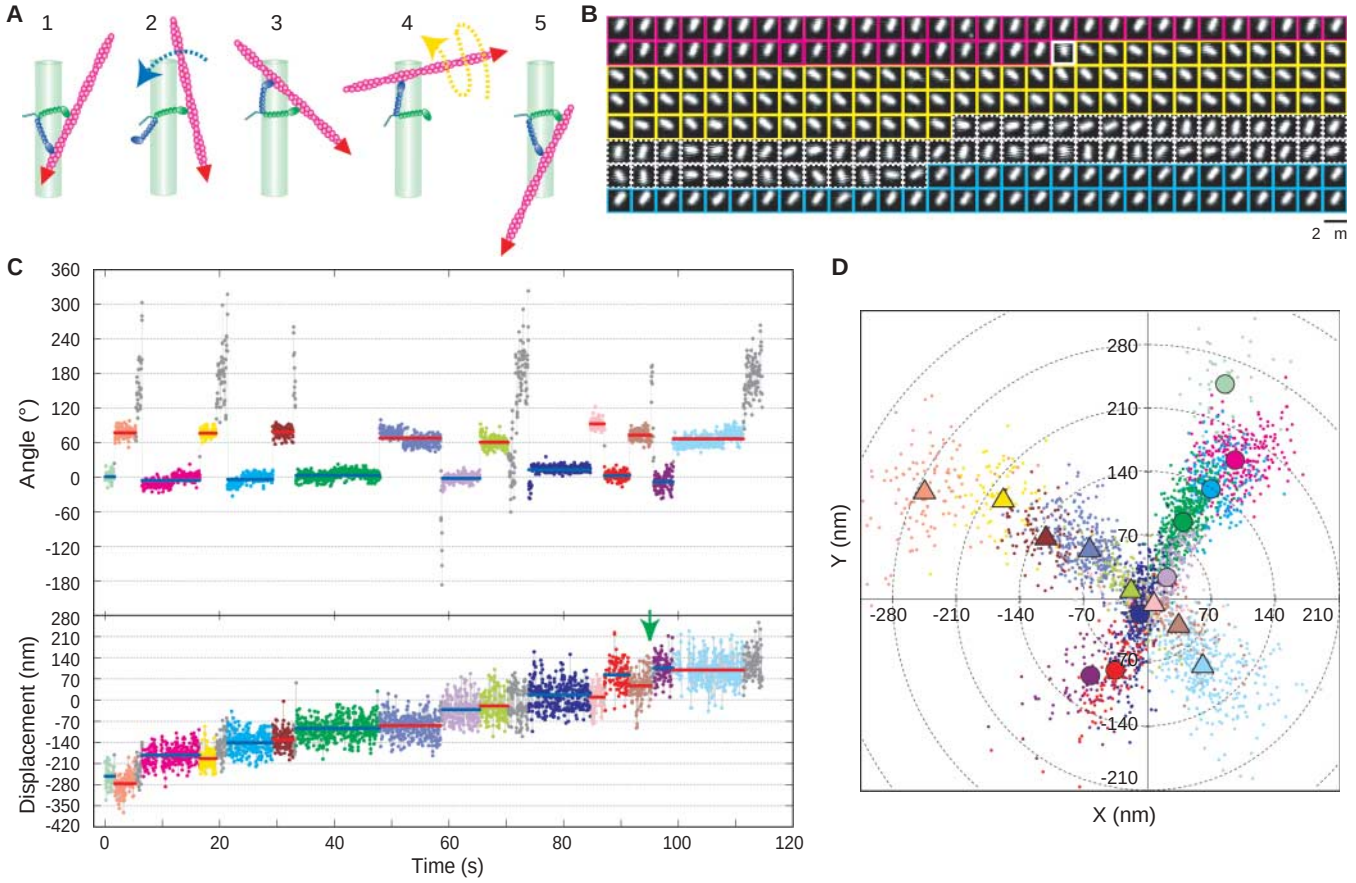

Fig. 2. Actin motion in the actin moving assay on a surface. (**A**) Expected movement of an actin filament (magenta) driven by myosin V with one neck (green) attached to a microtubule (light green cylinder) lying on a glass surface. One swing (blue arrow), mainly by lever action, is quick and unidirectional, whereas the other swing (yellow arrow) goes through Brownian fluctuation before final attachment. At the completion of the return swing, the actin filament proceeds by ~70 nm. Red arrowheads indicate the pointed end toward which the actin filament moves. The thick microtubule and myosin neck (approximately to scale) are not necessarily parallel, and the configuration here applies to (B) to (D) below. (**B**) Sequential images at 33-ms intervals of a moving actin filament at 0.2 μM ATP. Colors are as in (C). Part of movie S3. (**C**) Time courses of angular [anticlockwise from 1 in (A), unrestricted in the fluctuation phase] and positional changes. Displacements were estimated from (D). Blue and red bars, average of the stationary angles; green arrow, possible backstepping. (**D**) Frame-by-frame plot of the centroid of the actin filament image while it was in two stationary angles. Circles and triangles denote averaged positions; colors are as in (C).

stationary angle. Veigel *et al*. (*26*) showed that a one-neck construct of myosin V forces actin to move for ~25 nm by hydrolyzing one ATP molecule and that the movement can oppose a backward force of a few piconewtons. They proposed that the movement represents ATP-powered lever action of the neck and that, during 36-nm step walking of two-headed myosin V, the difference between the step size of 36 nm and the lever action of ~25 nm would be covered by diffusion of the lifted head. Similar results have been reported by Moore *et al*. (*27*). Our observations confirm the rotational nature of the lever action and its expected direction, as well as the presence of a diffusive phase. Nucleotide-dependent conformational changes corresponding to a lever action have been seen in crystal structures (*28*), although so far only in the absence of actin.

The swing angle, the difference between the two stationary angles, averaged 92° ± 21° (Fig. 3F), whereas single-fluorophore assays (*17*, *18*) have reported 70° to 75°. Presumably, the swing angle equals the angle between necks when myosin V stands on actin with both heads attached. In electron micrographs (*16*), the leading neck was often curved forward as in the telemark stance. Our swing angle is close to the average angle between whole necks. Fluorophores probably bound to a lower part of a neck.

To find the 11 actin filaments that satisfied the criteria for analysis, we observed >1000 filaments that apparently bound to a microtubule, but most did not move. The low success rate was anticipated, because binding of only one of the two necks to a microtubule through multiple points, in an orientation that does not hinder actin binding and subsequent lever action, must be a rare circumstance; furthermore, bound actin must be precisely parallel to the glass surface to swing freely. Also, because myosin density on a microtubule could not be too low, actin swing often ceased when the actin filament became parallel to the microtubule, presumably by binding to a second myosin.

One could argue that the asymmetric behavior described above may have resulted from surface obstructions. We therefore performed the

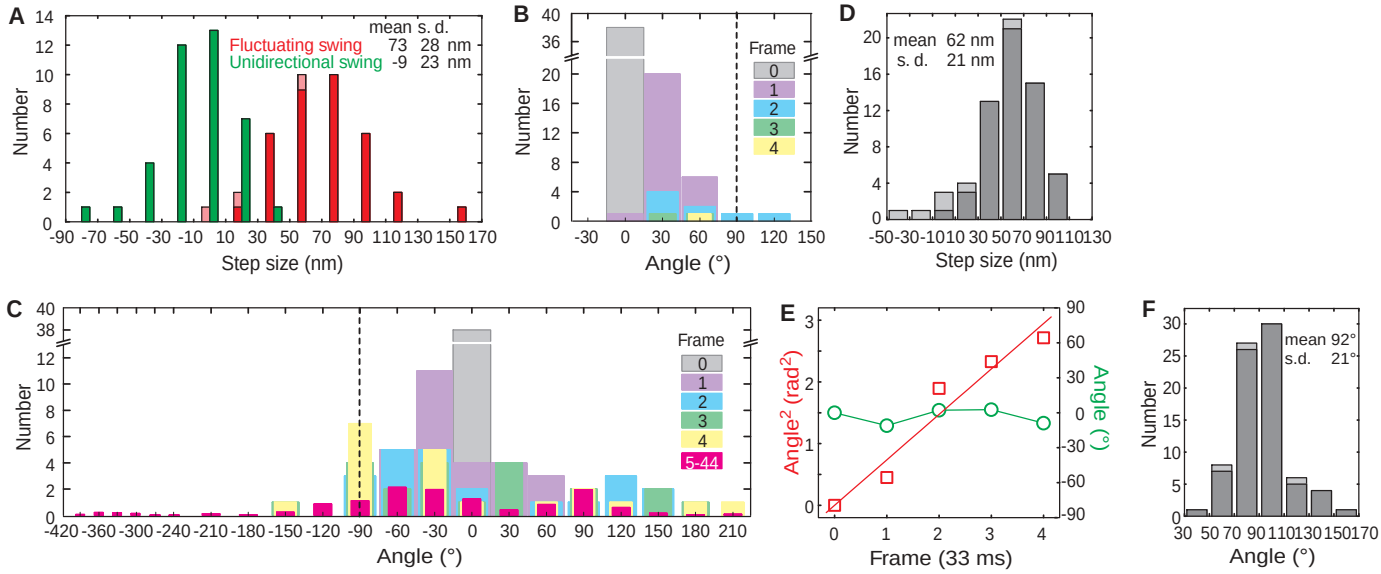

Fig. 3. Analyses of the swings in the actin moving assay on a surface. (**A**) Translocation during an anticlockwise (green) or clockwise (red) swing: displacement from blue to red bars and from red to blue, respectively, in Fig. 2C and fig. S5. Apparent backsteps (light colors) are excluded from the mean. (**B** and **C**) Angle histograms at indicated frames (33 ms per frame) during anticlockwise unidirectional (B) and clockwise fluctuating (C) swings of 11 actin filaments in Fig. 2C and fig. S5. Time and angle immediately before a swing are taken as frame 0 and 0°. Swings terminate, on average, at the dashed line showing the next stationary angle. Magenta in (C), average over frames 5 to 44. (**D**) Steps per swing pair: blue to blue and red to red in Fig. 2C and fig. S5. Apparent backsteps (light gray) are excluded from mean. (**E**) Average angular evolution in the clockwise, fluctuating swings. Slope of the red line, twice the rotational diffusion constant, is 22 rad^2 s^{-1}. (**F**) Amplitudes of all 77 swings. Light gray, apparent backstep.

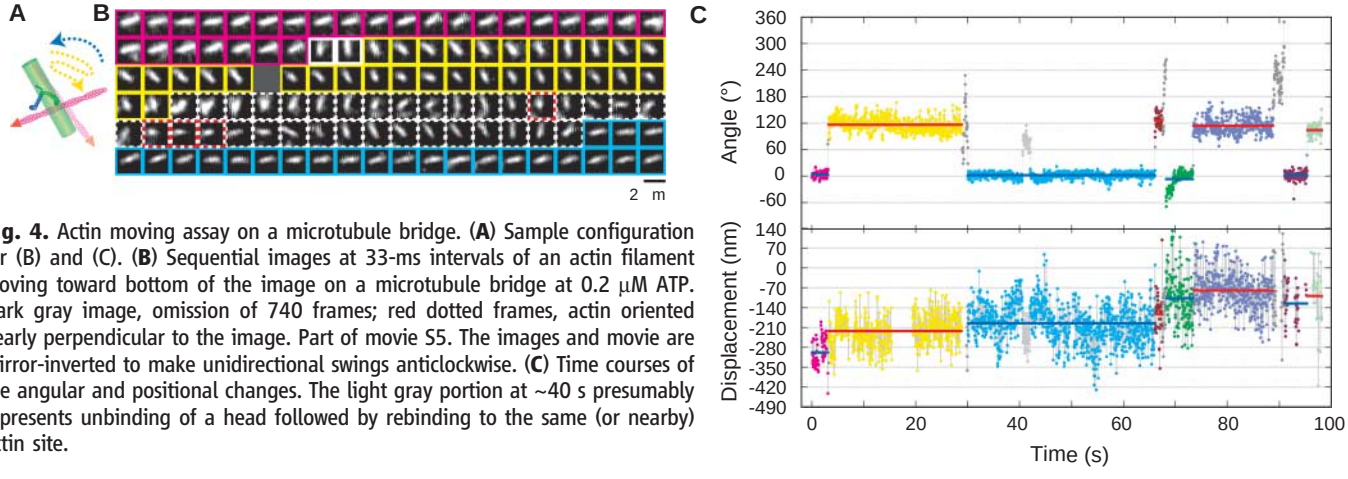

Fig. 4. Actin moving assay on a microtubule bridge. (**A**) Sample configuration for (B) and (C). (**B**) Sequential images at 33-ms intervals of an actin filament moving toward bottom of the image on a microtubule bridge at 0.2 μM ATP. Dark gray image, omission of 740 frames; red dotted frames, actin oriented nearly perpendicular to the image. Part of movie S5. The images and movie are mirror-inverted to make unidirectional swings anticlockwise. (**C**) Time courses of the angular and positional changes. The light gray portion at ~40 s presumably represents unbinding of a head followed by rebinding to the same (or nearby) actin site.

actin moving assay on a microtubule bridge (*21*), a modification of the actin-bridge assay (*15*), by suspending a microtubule between two large beads immobilized on a glass surface to let the actin filament freely rotate in any direction. We found three swinging actin filaments that stayed primarily in the image plane and that were simultaneously translocated. All showed asymmetric swings (Fig. 4, fig. S6, and movies S5 and S6). When these filaments fluctuated, we saw moments when the filament became perpendicular to the image plane, appearing as a bright dot (red dotted frames in Fig. 4B; also Fig. 1C). Apparently the free neck could assume all orientations in space.

By attaching a micrometer-sized rod to a neck of the nanometer-sized molecular motor, we have been able to infer the neck motion continuously in real time. Viscous friction on the rod must slow down the motion, but essential features are likely preserved, as shown for the rotation of F_1-ATPase (*29*). The two necks of myosin V are connected via a free joint. Thus, the sole mechanism that can move a lifted head is Brownian rotation of the neck, but this is purely random, carrying the head in either direction with an equal probability. Ensuring forward landing thus requires a biasing mechanism(s). ATP-powered lever action of the landed neck, originally proposed for myosin II (*30*), moves forward the pivot of the Brownian rotation, producing the required bias, as has been suggested in electron microscopy and single-molecule studies (*16*, *19*, *26*, *27*). The rotational diffusion observed here implies that the lifted head stays off the actin surface for most of the time, as opposed to diffusional sliding of the myosin head along the actin surface (*31*). The rotational diffusion plus lever action, however, may not be sufficient. We have proposed that, to ensure forward landing of a lifted head in the presence of backward load, the track-binding surface of the head must be properly oriented such that forward swing of the neck makes the surface parallel with the track surface (*24*, *25*, *32*). One way to prove this orientational biasing experimentally is to attach a micrometer-sized rod. A rod that directly reports molecular orientations will be useful in studies where a conformational change in a protein machine, necessarily accompanying reorientation, is to be visualized during function.

References and Notes

1. K. Svoboda, C. F. Schmidt, B. J. Schnapp, S. M. Block, *Nature* **365**, 721 (1993).
2. R. D. Vale, *J. Cell Biol.* **163**, 445 (2003).
3. J. R. Sellers, C. Veigel, *Curr. Opin. Cell Biol.* **18**, 68 (2006).
4. R. S. Rock *et al.*, *Proc. Natl. Acad. Sci. U.S.A.* **98**, 13655 (2001).
5. S. Nishikawa *et al.*, *Biochem. Biophys. Res. Commun.* **290**, 311 (2002).
6. R. Mallik, B. C. Carter, S. A. Lex, S. J. King, S. P. Gross, *Nature* **427**, 649 (2004).
7. S. Toba, T. M. Watanabe, L. Yamaguchi-Okimoto, Y. Y. Toyoshima, H. Higuchi, *Proc. Natl. Acad. Sci. U.S.A.* **103**, 5741 (2006).
8. A. Yildiz *et al.*, *Science* **300**, 2061 (2003); published online 5 June 2003 (10.1126/science.1084398).
9. A. Yildiz *et al.*, *J. Biol. Chem.* **279**, 37223 (2004).
10. A. Yildiz, M. Tomishige, R. D. Vale, P. R. Selvin, *Science* **303**, 676 (2004); published online 18 December 2003 (10.1126/science.1093753).
11. S. L. Reck-Peterson *et al.*, *Cell* **126**, 335 (2006).
12. E. M. Espreafico *et al.*, *J. Cell Biol.* **119**, 1541 (1992).
13. R. E. Cheney *et al.*, *Cell* **75**, 13 (1993).
14. A. D. Mehta *et al.*, *Nature* **400**, 590 (1999).
15. M. Y. Ali *et al.*, *Nat. Struct. Biol.* **9**, 464 (2002).
16. M. L. Walker *et al.*, *Nature* **405**, 804 (2000).
17. J. N. Forkey, M. E. Quinlan, M. A. Shaw, J. E. Corrie, Y. E. Goldman, *Nature* **422**, 399 (2003).
18. E. Toprak *et al.*, *Proc. Natl. Acad. Sci. U.S.A.* **103**, 6495 (2006).
19. A. R. Dunn, J. A. Spudich, *Nat. Struct. Mol. Biol.* **14**, 246 (2007).
20. I. M. Crevel *et al.*, *EMBO J.* **23**, 23 (2004).
21. See supporting material on *Science* Online.
22. E. M. De La Cruz, A. L. Wells, S. S. Rosenfeld, E. M. Ostap H. L. Sweeney, *Proc. Natl. Acad. Sci. U.S.A.* **96**, 13726 (1999).
23. K. Kinosita Jr., S. Ishiwata, H. Yoshimura, H. Asai, A. Ikegami, *Biochemistry* **23**, 5963 (1984).
24. K. Kinosita Jr., K. Shiroguchi, M. Y. Ali, K. Adachi, H. Itoh, *Adv. Exp. Med. Biol.* **592**, 369 (2007).
25. K. Kinosita Jr., M. Y. Ali, K. Adachi, K. Shiroguchi, H. Itoh, *Adv. Exp. Med. Biol.* **565**, 205 (2005).
26. C. Veigel, F. Wang, M. L. Bartoo, J. R. Sellers, J. E. Molloy, *Nat. Cell Biol.* **4**, 59 (2002).
27. J. R. Moore, E. B. Krementsova, K. M. Trybus, D. M. Warshaw, *J. Cell Biol.* **155**, 625 (2001).
28. P.-D. Coureux, H. L. Sweeney, A. Houdusse, *EMBO J.* **23**, 4527 (2004).
29. R. Yasuda, H. Noji, M. Yoshida, K. Kinosita Jr., H. Itoh, *Nature* **410**, 898 (2001).
30. H. E. Huxley, *Science* **164**, 1356 (1969).
31. T. Okada *et al.*, *Biochem. Biophys. Res. Commun.* **354**, 379 (2007).
32. M. Y. Ali *et al.*, *Biophys. J.* **86**, 3804 (2004).

33. We thank M. Shio for designing a stable microscope stage, Y. Oguchi for help in myosin V purification, K. Adachi for an image analysis program, M. Fukatsu and K. Sakamaki for encouragement and lab management, and members of the Kinosita lab for discussions. Supported by Grants-in-Aid for Specially Promoted Research and the 21COE Program from the Ministry of Education, Sports, Culture, Science and Technology, Japan. K.S. was a Research Fellow of the Japan Society for the Promotion of Science.

Supporting Online Material

www.sciencemag.org/cgi/content/full/316/5828/1208/DC1
Materials and Methods
Figs. S1 to S6
Movies S1 to S6
References

26 January 2007; accepted 10 April 2007
10.1126/science.1140468

Hardwiring the Brain: Endocannabinoids Shape Neuronal Connectivity

Paul Berghuis,[1]* Ann M. Rajnicek,[2]* Yury M. Morozov,[3]* Ruth A. Ross,[2] Jan Mulder,[4] Gabriella M. Urbán,[5] Krisztina Monory,[6] Giovanni Marsicano,[6]† Michela Matteoli,[7] Alison Canty,[4] Andrew J. Irving,[8] István Katona,[5] Yuchio Yanagawa,[9] Pasko Rakic,[3] Beat Lutz,[6] Ken Mackie,[10]‡ Tibor Harkany[1]§

The roles of endocannabinoid signaling during central nervous system development are unknown. We report that CB_1 cannabinoid receptors (CB_1Rs) are enriched in the axonal growth cones of γ-aminobutyric acid–containing (GABAergic) interneurons in the rodent cortex during late gestation. Endocannabinoids trigger CB_1R internalization and elimination from filopodia and induce chemorepulsion and collapse of axonal growth cones of these GABAergic interneurons by activating RhoA. Similarly, endocannabinoids diminish the galvanotropism of *Xenopus laevis* spinal neurons. These findings, together with the impaired target selection of cortical GABAergic interneurons lacking CB_1Rs, identify endocannabinoids as axon guidance cues and demonstrate that endocannabinoid signaling regulates synaptogenesis and target selection in vivo.

In the cerebral cortex, information processing requires the precise temporal and spatial coordination of synaptic communication among excitatory pyramidal cells, inhibitory γ-aminobutyric acid–containing (GABAergic) interneurons, and subcortical afferents (*1*). Cortical neurons are born in progenitor zones that are distant from their final positions, and their layer-specific patterning is achieved through extensive migration in the developing cerebrum (*1*, *2*). En route to their destination, cortical neurons establish their synaptic connectivity patterns (*3*), thus providing the blueprint for their functional diversification.

In the adult central nervous system (CNS), presynaptic $G_{i/o}$ protein–coupled CB_1 cannabinoid receptors (CB_1Rs) (*4*) are the targets of marijuana (*Cannabis* spp.)–derived psychoactive phytocannabinoids and of the endocannabinoids anandamide (AEA) and 2-arachidonoylglycerol (2-AG). Endocannabinoids released from postsynaptic neurons serve as retrograde messengers that suppress neurotransmitter release at mature cortical synapses (*4*). During brain development, CB_1Rs are first expressed in early neural progenitors (*5*), with receptor levels increasing throughout neuronal specification and synaptogenesis (*6*). Although functionally active CB_1Rs are localized to developing axonal projections (*6*, *7*), it remains unknown whether endocannabinoids function as diffusible axon guidance factors before the growth cone differentiates into a presynaptic nerve terminal.

We defined the precise cellular distribution of CB_1Rs on neuronal precursors during cortical cell migration, axonal navigation, and synaptogenesis

by high-resolution laser-scanning microscopy of genetically tagged neurons, in situ hybridization, and electron microscopy (*3*, *8*). From embryonic day 13.5 (E13.5) until birth, CB_1Rs were present on pyramidal cells (Fig. 1, A to C) with their axons coursing in the intermediate zone of the developing cerebral cortex (*9*) (Fig. 1, D and E) and establishing the fornix pathway in the hippocampus (figs. S1 and S2). These projections primarily contained CB_1Rs associated with the surface of distal axon segments, with CB_1Rs being largely absent from their growth cones (Fig. 1F). In contrast, CB_1Rs were expressed in GABAergic interneurons during late gestation as they were undergoing intracortical tangential or radial migration (Fig. 1G). Here, CB_1Rs were preferentially found on axons and axonal growth cones (Fig. 1, H to J) coincident with establishing target-specific synaptic connectivity patterns (*3*, *10*).

CB_1R expression is spatially and temporally coordinated with endocannabinoid synthesis during brain development: *sn*-1-diacylglycerol lipases α and β (DAGLα/β), which synthesize 2-AG, predominated in elongating long-range telencephalic axons at around E14.5 (fig. S2) (*11*). By E18.5, however, DAGLα/β expression was localized to postsynaptic dendrites of glutamatergic pyramidal cells (Fig. 1, K to N), so that focal 2-AG release could control axonal growth cone steering and the formation of CB_1R^+ terminals (Fig. 1O). Postsynaptic DAGLα expression exceeded that of DAGLβ in the perinatal neocortex, in agreement with previous observations establishing DAGLα as the major postnatal DAGL isoform (*11*). Unexpectedly, the expression of *N*-acyl-phosphatidyl-ethanolamine-selective phospholipase D (NAPE-PLD), an enzyme participating in AEA synthesis (*4*), was delayed until E18.5, at which age NAPE-PLD was strongly associated with cortical pyramidal cells (Fig. 1, P and Q). GABAergic interneurons did not possess these endocannabinoid synthetic enzymes until their engagement in radial intracortical migration, coincident with the onset of postsynaptic target selection (Fig. 1R) (*3*).

To identify the functions of endocannabinoid signaling in axonal growth and guidance, we established GABAergic interneuron cultures with high CB_1R expression (*12*). Early growth cones of quiescent axons contained CB_1Rs localized to their leading filopodial tips (Fig. 2A). Morphological growth cone differentiation was associated with a gradual enrichment in CB_1Rs that were invariably present in motile filopodial tips at the leading edge of the growth cones (Fig. 2, B and C, and movie S1), which are critical for sensing guidance cues (*13*). Application of AEA for 15 to 30 min induced CB_1R translocation from filopodial tips to the central growth cone domain of GABAergic interneurons (Fig. 2, D and D′) and triggered receptor internalization and retrograde transport in hippo-

[1]Division of Molecular Neurobiology, Department of Medical Biochemistry and Biophysics, Karolinska Institutet, S-17177 Stockholm, Sweden. [2]School of Medical Sciences, Institute of Medical Sciences, University of Aberdeen, Aberdeen Scotland AB25 2ZD, UK. [3]Department of Neurobiology, Kavli Institute for Neuroscience, Yale University School of Medicine, New Haven, CT 06510, USA. [4]Department of Neuroscience, Karolinska Institutet, S-17177 Stockholm, Sweden. [5]Laboratory of Cerebral Cortex Research, Institute of Experimental Medicine, Hungarian Academy of Sciences, H-1083 Budapest, Hungary. [6]Department of Physiological Chemistry, Johannes Gutenberg University Mainz, D-55099 Mainz, Germany. [7]Department of Medical Pharmacology and Consiglio Nazionale della Richerche Institute of Neuroscience, University of Milan, I-20129 Milan, Italy. [8]Neurosciences Institute, Division of Pathology and Neuroscience, Ninewells Hospital and Medical School, University of Dundee, Dundee, Scotland DD1 9SY, UK. [9]Department of Genetic and Behavioral Neuroscience, Gunma University Graduate School of Medicine and Solution Oriented Research for Science and Technology, Japan Science and Technology Corporation, Maebashi 371-8511, Japan. [10]Departments of Anesthesiology Physiology, and Biophysics, University of Washington, Seattle, WA 98195-6540, USA.

*These authors contributed equally to this work.
†Present address: U 862 Centre de Recherche François Magendie, INSERM, Equipe AVENIR 8 Université Bordeaux 2, 146 rue Léo Saignat, F-33077 Bordeaux, France.
‡Present address: Department of Psychological and Brain Sciences, Indiana University, Bloomington, IN 47405, USA.
§To whom correspondence should be addressed. E-mail: Tibor.Harkany@ki.se

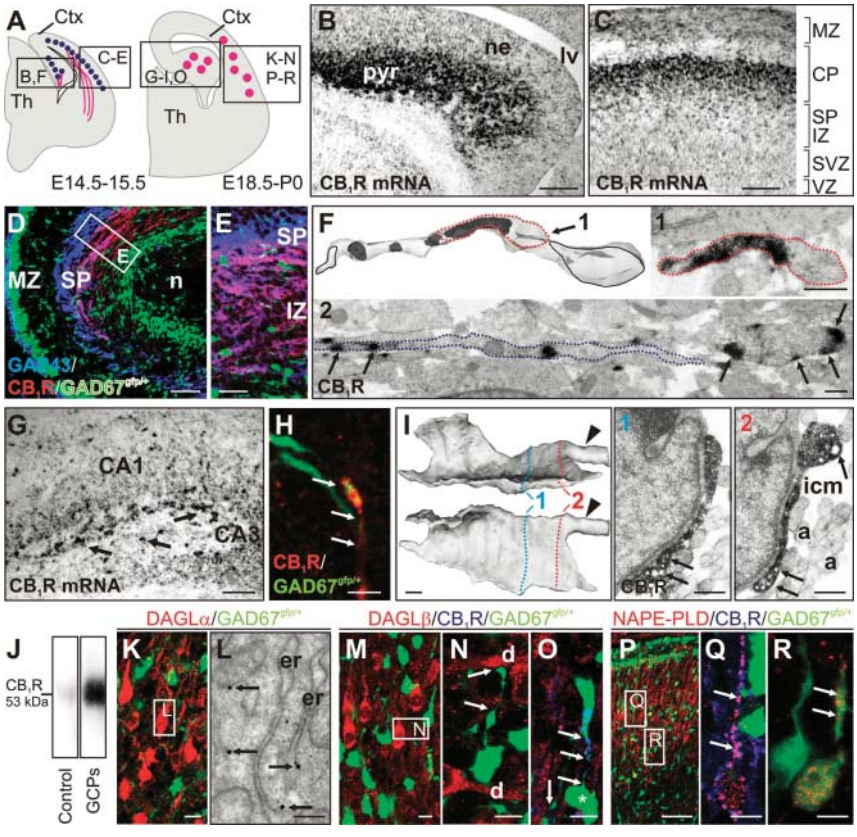

Fig. 1. The temporal and spatial coincidence of CB_1R localization with endocannabinoid availability during corticogenesis. (**A**) Schemes of the telencephalon at the embryonic days indicated. Colored symbols refer to particular structures in adjoining photomicrographs. At E14.5 to 16.5 (fig. S2B), CB_1R mRNA is preferentially expressed in pyramidal cells of the hippocampus (**B**) and cerebral cortex (**C**), with CB_1R immunoreactivity localized to developing long-range axons, coexpressing growth-associated protein 43 (GAP43), in the intermediate zone (*9*) (**D** and **E**). (**F**) CB_1R^+ processes, axons emitted by pyramidal neurons, in the fimbria. A three-dimensional reconstruction of a process is depicted in a semitransparent manner. A dotted line encircles the individual profile (1) shown to the right. (2) Adjacent CB_1R^+ processes (dotted line) with 3,3′-diaminobenzidine (DAB)–Ni reaction end products (black) precipitating on the inner plasmalemmal surface (arrows) after the use of an antibody recognizing the C terminus of CB_1R. (**G**) Hippocampal interneurons (arrows) express CB_1R mRNA at E18.5. (**H**) At birth, CB_1Rs are spatially associated with GABAergic axons (arrows) navigating locally in the hippocampus. (**I**) Reciprocally perpendicular projections of a single CB_1R^+ growth cone from the hilus of newborn rat hippocampus. Numbers indicate the positions of planar images. Arrowheads indicate the truncated axon. DAB precipitation fills the cytoplasm, which also contains numerous vesicles (arrows). (**J**) CB_1Rs concentrate in growth cone particles (GCPs) relative to total cortical lysates, as shown by Western analysis. (**K**) DAGLα predominates in the neocortex at birth and (**L**) is expressed by pyramidal cells. Arrows point to gold particles indicating the precise subcellular localization of DAGLα. (**M**) Similarly, DAGLβ is expressed by pyramidal cells in the neonatal cortex. (**N**) A putative GABAergic presynaptic bouton on a $DAGL\beta^+$ dendrite is marked by arrows. (**O**) A CB_1R^+ GABAergic axon (arrows) is targeted toward a $DAGL\beta^-$ interneuron (*) in the hippocampus at E18.5. (**P** and **Q**) NAPE-PLD is first expressed at E18.5 and is preferentially targeted to dendritic spines (arrows) in neocortical pyramids. (**R**) Some vertically migrating GABAergic interneurons possess NAPE-PLD expression. Arrows denote NAPE-PLD in the leading process. Abbreviations are defined in SOM text. Scale bars, 6 μm in (H), (K), (M) to (O), (Q), and (R); 50 μm in (E); 100 μm in (B) to (D), (G), and (P); and 500 nm in (F), (I), and (L).

campal neurons and PC12 pheochromocytoma cells recombinantly expressing CB_1Rs (fig. S3). Agonist-induced activation and trafficking of CB_1Rs translated into downstream signaling in cultured interneurons, because AEA (100 nM), like brain-derived neurotrophic factor (BDNF) (*14*), induced significant phosphorylation of Erk1 and Erk2 (Erk1/2) (*15*) in the central growth cone domain within 10 min (Fig. 2, E and E′). Studies in the growth cone particulate fraction isolated from embryonic rat cortices corroborated our in vitro findings by showing significant Erk2 phosphorylation that peaked 5 to 10 min after AEA (2 μM) application (Fig. 2F).

Direct involvement of chemotropic (endo) cannabinoid signaling in growth cone guidance was tested by assaying the growth cone turning responses of GABAergic interneurons induced by the synthetic CB_1R agonist WIN55,212-2 (*16*–*18*). A microgradient of BDNF, an established chemoattractive factor for GABAergic interneurons (*12*), induced attractive turning (*16*), whereas WIN55,212-2 at a concentration of 20 μM in the micropipette and ~200 nM at the growth cone (*16*) elicited growth cone repulsion (Fig. 3, A and B, and table S1). In $n = 13$ out of 20 motile growth cones (65%), WIN55,212-2 induced growth cone collapse and neurite retraction within the 60 min of recording (Fig. 3, A and B, and table S1). The lack of directional growth cone turning or neurite retraction in a control [dimethyl sulfoxide (DMSO)] gradient excluded recording artefacts produced by positive ejection pressure or the vehicle solution itself. Coapplication of the CB_1R antagonist AM251 (1 μM simultaneously in the pipette and bath solution) converted WIN55,212-2-induced chemorepulsion to attractive growth cone turning without significantly affecting the rate of neurite extension (Fig. 3B and table S1). Together with the lack of detectable CB_2 cannabinoid receptor expression in cultured GABAergic interneurons (*12*), these findings indicate that WIN55,212-2-induced chemorepulsion is mediated by CB_1Rs.

Next, we analyzed whether AEA and WIN55,212-2 modify directional growth cone steering of *Xenopus laevis* spinal neurons, which also express CB_1Rs (Fig. 3C). Growth cones steadily turned toward the cathode of a direct current (DC) electric field (EF) of 150 mV/mm (Fig. 3, D and E), a gradient that mimics the ~400 mV/mm DC-EF present naturally in the developing *Xenopus* neural tube (*19*) [supporting online material (SOM) text and fig. S4]. Bath application of either AEA or WIN55,212-2, but not its inactive stereoisomer WIN55,212-3, diminished both the mean angle turned toward the cathode and the frequency of cathodal turning in a dose-dependent fashion (Fig. 3, E and F, and table S1). Reminiscent of the ability of WIN55,212-2 to induce chemorepulsion (Fig. 3A), AEA or WIN55,212-2, but not WIN55,212-3, increased the frequency of EF-induced cathodal repulsion (anodal attraction) relative to vehicle controls (Fig. 3F).

Dynamic polarization of the growth cone cytoskeleton underlies chemotropism and galvanotropism: Extending microfilaments predominate on the side of the growth cone nearest to a chemoattractant source, whereas localized collapse of the actin cytoskeleton occurs near a repellent stimulus (*18*, *19*). Cytoskeletal integrity in axonal growth cones is controlled by members of the Rho family of small guanosine triphosphatases (GTPases) (*19*, *20*), which act as molecular switches that transduce extracellular stimuli to the actin cytoskeleton (*18*). Accordingly, WIN55,212-2 (2 μM) treatment selectively increased the GTP-bound active state of RhoA but not cumulative RhoA, -B, and -C activity (*20*) in primary cortical cultures after 5 min of stimulation (Fig. 4A). The involvement of CB_1Rs in this process was confirmed by the lack of RhoA activation in the presence of AM251 (2 μM; Fig. 4B). AEA (2 μM) induced RhoA activation in a manner similar to that of WIN55,212-2 (Fig. 4B). Spatially restricted activation of RhoA in the collapsing growth cone is associated with filopodial retraction and growth cone repulsion in response to chemical and electrical extracellular cues (*18*, *19*) through activation of the serine-threonine kinase Rho kinase (ROCK) and subsequent phosphorylation of myosin light chains (*19*, *21*) (fig. S5). Pretreating interneuron cultures with the ROCK-selective inhibitor Y-27632 (50 μM) (*18*) abolished WIN55,212-2-induced neurite retraction and converted CB_1R-mediated neurite repulsion into chemoattraction without significantly affecting the rate of neurite extension (Fig. 3, A and B, and table S1). The agonist-induced coupling of CB_1Rs to RhoA is

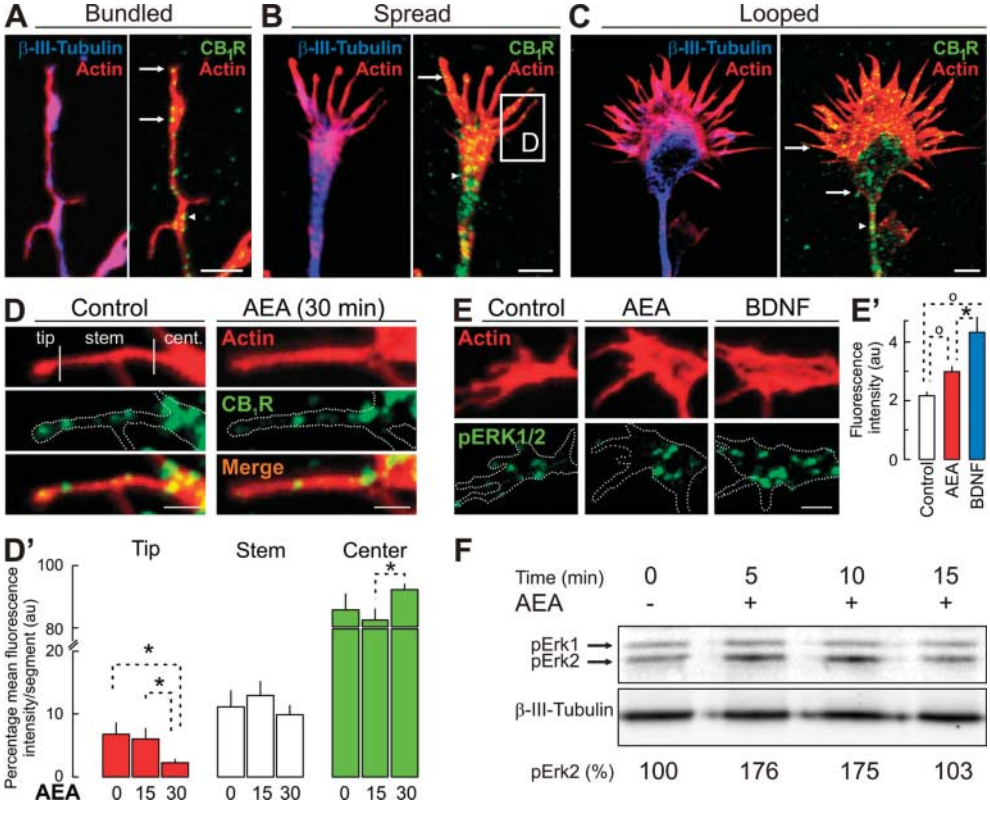

Fig. 2. Agonist stimulation induces CB_1R removal from filopodia and Erk1/2 phosphorylation in the central growth cone domain. (**A** to **C**) CB_1Rs are present in axonal growth cones of GABAergic interneurons in vitro. CB_1Rs are transported from the initial neurite segment through the neurite stem (arrowheads) to the growth cone, where they concentrate in filopodial tips (arrows) (movie S1). The structural classification of growth cones was based on whether microtubules in the central domain were bundled, spread, or looped (*29*). (**D** and **D′**) AEA (100 nM) induces CB_1R removal from filopodia. $^*P < 0.05$, $n = 13$ to 15 filopodia per group from two independent experiments. Numbers indicate the periods of AEA exposure, in minutes. (**E**) CB_1R activation induces Erk1/2 phosphorylation (pERK) in the central growth cone domain. (**E′**) Quantitative analysis of Erk1/2 phosphorylation 10 min after stimulation. $^oP < 0.01$, $^*P < 0.05$ ($n = 10$ growth cones per group). BDNF (100 ng/ml) was used as a positive control (*14*). (**F**) AEA induces Erk1/2 phosphorylation in growth cones isolated from embryonic rat cortices. β-III tubulin served as a loading control. Error bars represent SEM. Scale bars, 3 μm in (A) to (C), 2.5 μm in (E), and 1 μm in (D).

consistent with the concept that Rho family GTPases control growth cone integrity by stimulating contraction of the actin cytoskeleton on the side facing the repellent gradient, thus leading to growth cone collapse (*19*, *22*). The conversion of growth cone steering decisions upon ROCK inhibition suggests that CB_1Rs also activate the Cdc42 or Rac pathways, primary transducers of BDNF-induced chemoattraction (*18*, *20*), whose spatial and temporal antagonism with RhoA may be sufficient to switch (endo)cannabinoid-induced chemorepulsion to attractive turning (*18*).

We addressed the in vivo significance of the above findings in adult mice (4.5 to 6 months of age) lacking endocannabinoid-mediated retrograde signaling at cortical inhibitory synapses (*23*) because of conditional CB_1R deletion in GABAergic neurons by Cre-mediated recombination redirected by intergenic regulatory sequences of the genes *Dlx5* and *Dlx6* ($CB_1R^{f/f;Dlx5/6\text{-}Cre}$ mice) (*24*). We identified perisomatic GABAergic terminals that would otherwise have expressed CB_1Rs in the neocortex and hippocampus of $CB_1R^{f/f;Dlx5/6\text{-}Cre}$ mice by their coexpression of the vesicular GABA (VGAT) and vesicular glutamate 3 (VGLUT3) transporters (*25*, *26*) (Fig. 4C and fig. S6). Analysis of the distribution of $VGAT^+/VGLUT3^+$ boutons in layer 2/3 of the neocortex revealed a significant increase in the probability of pyramidal cells receiving $VGAT^+/VGLUT3^+$ inputs (Fig. 4, D to E′), indicating impaired postsynaptic target selection of cortical interneurons lacking CB_1R-mediated endocannabinoid signals. These changes occurred in the absence of altered interneuron migration or neurochemical specification (fig. S7).

Our findings outline an essential developmental role for endocannabinoid signaling in growth cone steering decisions, identifying endocannabinoids as a class of signaling molecules that regulate axon guidance. This function is evident in diverse CB_1R-expressing neuron populations as demonstrated in vitro by growth cone turning assays on CB_1R-expressing GABAergic interneurons in rodents and *Xenopus* spinal cord neurons. Our evidence that CB_1R-mediated endocannabinoid signals underpin growth cone steering by chemical and electrical extracellular directional cues, both of which are present in the embryonic CNS, suggests that endocannabinoid signals play an unexpectedly fundamental role in axonal pathfinding and neuritogenesis. The coincidence of intrinsic endocannabinoid synthesis in elongating long-range and GABAergic axons

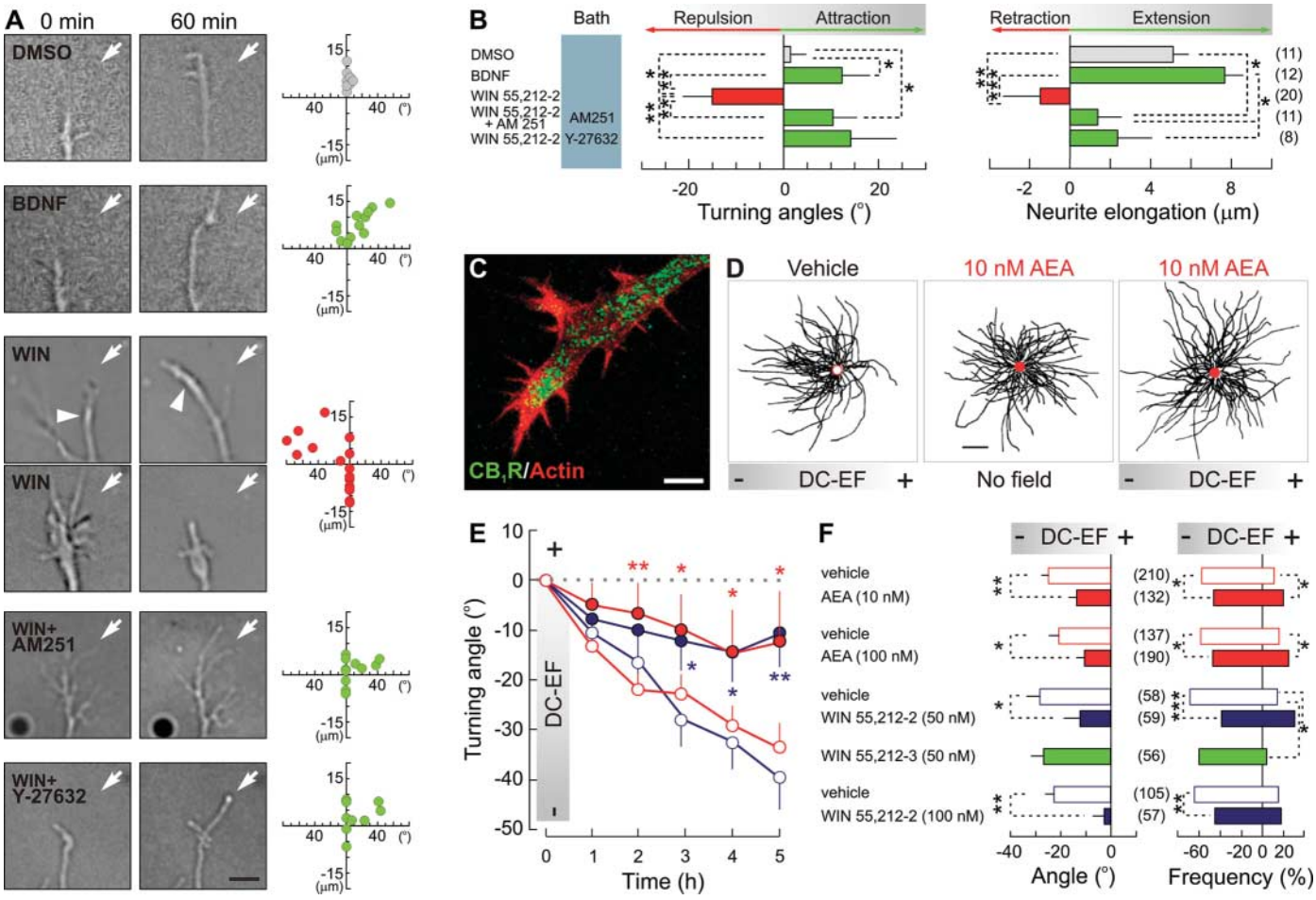

Fig. 3. CB_1R activation induces ROCK-dependent growth cone repulsion. (**A**) Neurites of cultured rodent GABAergic interneurons before and after 60 min of drug application. The microgradient direction is indicated by arrows. Arrowheads identify the neurites studied. Scatter plots show individual growth cone turning responses. Negative values represent neurite retraction. (**B**) Histograms of averaged growth cone turning responses in control and after drug treatments. Bath concentrations of the CB_1R antagonist AM251 and the ROCK-selective inhibitor Y-27632 were 1 μM and 50 μM, respectively (*18*). (**C**) Growth cones of *X. laevis* spinal neurons contain CB_1Rs. (**D**) Composite drawings of individual neurons at 3 hours were made by superimposing cell bodies at the colored dot, and the path of each neurite was traced. AEA inhibits growth cone turning toward the cathode in the DC-EF. (**E**) Time course of EF-induced growth cone turning. WIN55,212-2 (50 nM, solid blue circles) and AEA (100 nM, solid red circles) significantly inhibit cathodal growth cone steering over 5 hours in a continuous DC-EF, whereas growth cones in corresponding vehicle control cultures (open blue and red circles) turn increasingly toward the cathode. (**F**) The angle and frequency of cathodal growth cone turning (>10°) are each inhibited by both WIN55,212-2 and AEA but not by WIN55,212-3 after 3 hours. Negative angles indicate steering toward the cathode. Data represent means ± SEM. Sample sizes are indicated in parentheses. The statistical analysis is referred to in table S1. Scale bars, 4 μm in (A), 10 μm in (C), and 100 μm in (D).

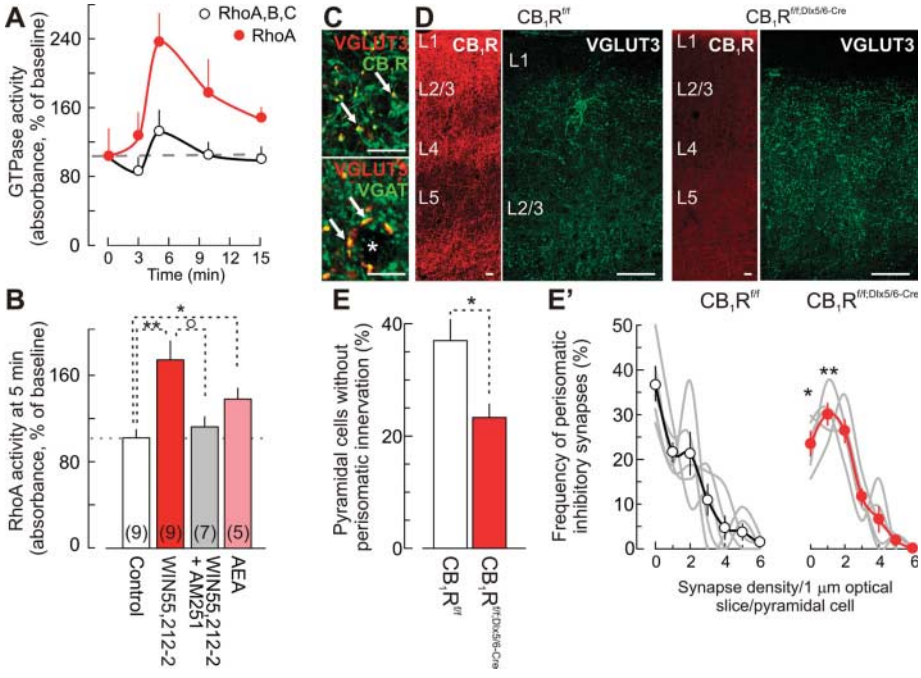

Fig. 4. The physiological importance of CB_1R-mediated growth cone repulsion. (**A**) Time course of WIN55,212-2 (2 μM)–induced Rho GTPase activation (n = 3 cortical cultures per data point from a representative experiment; mean ± SEM). (**B**) Both AEA and WIN55,212-2 activate RhoA through CB_1Rs, because this response is inhibited by pretreatment with AM251, a CB_1R antagonist. Sample sizes are given in parentheses (four independent experiments; mean ± SEM). $^{**}P = 0.008$, $^{*}P = 0.023$, $^{\circ}P = 0.014$. (**C**) In layer (L) 2/3 of the mouse somatosensory cortex, VGLUT3 labels inhibitory terminals of GABAergic basket cells (*25*) coexpressing CB_1Rs and VGAT (arrows). Asterisk denotes the pyramidal cell soma. (**D**) In $CB_1R^{f/f;Dlx5/6\text{-}Cre}$ mice (*23*), the lack of CB_1Rs in GABAergic interneurons is accompanied by the redistribution of VGLUT3-containing inhibitory afferents in L2/3. (**E** and **E'**) Cre recombinase–mediated CB_1R knockout leads to impaired postsynaptic target selection in $CB_1R^{f/f;Dlx5/6\text{-}Cre}$ mice, as indicated by the altered distribution and density of $VGLUT3^+/VGAT^+$-labeled perisomatic terminals on L2/3 pyramidal cells. Data are means ± SEM, $^{**}P = 0.024$, $^{*}P = 0.030$ (n = 5 mice per genotype, ≥32 cells per animal). Scale bars, 16 μm in (C) and 35 μm in (D).

demonstrates that autocrine endocannabinoid signaling (*11*) contributes to the initial growth of axons, whereas target-derived endocannabinoid signals control axonal navigation and positioning. Our conclusion is also supported by neuroanatomical findings showing endocannabinoid synthetic enzymes in cortical neurons coincident with the enrichment of CB_1Rs in neuronal growth cones during the critical period of postsynaptic target selection. Genetic evidence in $CB_1R^{f/f;Dlx5/6\text{-}Cre}$ mice (*24*) reveals that interneuron-specific deletion of CB_1R-mediated endocannabinoid signaling is sufficient to relieve the restriction of axonal elongation and branching (*12*), synaptogenesis (*27*), and target innervation mediated by endocannabinoid signals in neurochemically identified cortical interneurons. The present study also expands our understanding of how prenatal exposure to the CB_1R agonist Δ^9-tetrahydrocannabinol (THC), the major psychoactive constituent in cannabis, could affect CNS development and induce cognitive and behavioral deficits enduring into adolescence of THC-exposed offspring (*28*). Thus, our data, together with THC-induced impairment of synapse formation (*27*), imply that maternal marijuana consumption may affect neurodevelopment through sustained CB_1R activation and disrupt the proper positioning, postsynaptic target selectivity, and functional differentiation of developing axons.

References and Notes

1. P. Rakic, *Cereb. Cortex* **16** (suppl. 1), i3 (2006).
2. C. P. Wonders, S. A. Anderson, *Nat. Rev. Neurosci.* **7**, 687 (2006).
3. Y. M. Morozov, A. E. Ayoub, P. Rakic, *J. Neurosci.* **26**, 5017 (2006).
4. T. F. Freund, I. Katona, D. Piomelli, *Physiol. Rev.* **83**, 1017 (2003).
5. T. Aguado *et al.*, *FASEB J.* **19**, 1704 (2005).
6. X. Wang, D. Dow-Edwards, E. Keller, Y. L. Hurd, *Neuroscience* **118**, 681 (2003).
7. S. Mato, E. Del Olmo, A. Pazos, *Eur. J. Neurosci.* **17**, 1747 (2003).
8. Materials and methods are available as supporting material on *Science* Online.
9. A. R. Bicknese, A. M. Sheppard, D. D. O'Leary, A. L. Pearlman, *J. Neurosci.* **14**, 3500 (1994).
10. Y. M. Morozov, T. F. Freund, *Eur. J. Neurosci.* **18**, 1213 (2003).
11. T. Bisogno *et al.*, *J. Cell Biol.* **163**, 463 (2003).
12. P. Berghuis *et al.*, *Proc. Natl. Acad. Sci. U.S.A.* **102**, 19115 (2005).
13. T. P. O'Connor, J. S. Duerr, D. Bentley, *J. Neurosci.* **10**, 3935 (1990).
14. A. Patapoutian, L. F. Reichardt, *Curr. Opin. Neurobiol.* **11**, 272 (2001).
15. P. Derkinderen *et al.*, *J. Neurosci.* **23**, 2371 (2003).
16. G. X. Wang, M. M. Poo, *Nature* **434**, 898 (2005).
17. Y. Xiang *et al.*, *Nat. Neurosci.* **5**, 843 (2002).
18. X. B. Yuan *et al.*, *Nat. Cell Biol.* **5**, 38 (2003).
19. A. M. Rajnicek, L. E. Foubister, C. D. McCaig, *J. Cell Sci.* **119**, 1723 (2006).
20. A. B. Jaffe, A. Hall, *Annu. Rev. Cell Dev. Biol.* **21**, 247 (2005).
21. M. Amano *et al.*, *J. Biol. Chem.* **271**, 20246 (1996).
22. R. Kozma, S. Sarner, S. Ahmed, L. Lim, *Mol. Cell. Biol.* **17**, 1201 (1997).
23. M. R. Domenici *et al.*, *J. Neurosci.* **26**, 5794 (2006).
24. K. Monory *et al.*, *Neuron* **51**, 455 (2006).
25. T. Harkany *et al.*, *J. Neurosci.* **24**, 4978 (2004).
26. H. Hioki *et al.*, *Cereb. Cortex* **14**, 1266 (2004).
27. D. Kim, S. A. Thayer, *J. Neurosci.* **21**, RC146 (2001).
28. M. S. Spano, M. Ellgren, X. Wang, Y. L. Hurd, *Biol. Psychiatry* **61**, 554 (2007).
29. H. Morii, Y. Shiraishi-Yamaguchi, N. Mori, *J. Neurobiol.* **66**, 1101 (2006).

30. We thank M. Guzmán, Y. L. Hurd, G. Kunos, and M.-M. Poo for their critical comments; J. L. Rubenstein and M. Ekker for providing Dlx5/6-Cre mice; C. Ledent for $CB_1R^{-/-}$ colony founders; H. Hioki for antibody to VGLUT3; O. K. Penz for assistance with immunohistochemistry; K. M. Sousa for help with in situ hybridization; J. Bruce, H. Díack, and P. Wilson for assistance with galvanotropic turning assays; and A. Hubbard for high-resolution video microscopy. This work was supported by the Swedish Medical Research Council (T.H.); Stiftelsen Ragnhild och Einar Lundströms Minne (J.M. and T.H.); the Deutsche Forschungsgemeinschaft (B.L.); the Alzheimer's Association (K. Mackie and T.H.); the Ministry of Education, Culture, Sports, Science, and Technology of Japan (Y.Y.); the Ministry of Health, Labor, and Welfare of Japan (Y.Y.); Országos Tudományos Kutatási Alapprogramok (F046407, I.K.); Egészségügyi Tudományos Tanács (561/2006, I.K.); EUSynapse (M.M.); and NIH grants DA11322, DA015916, and DA00286 (K. Mackie). P.B. and I.K. are recipients of Hjärnfonden (Sweden) and János Bolyai (Hungary) scholarships, respectively. G.M.U. and I.K. were supported by the Howard Hughes Medical Institute and European Union contract LSHM-CT-2004-005166.

Supporting Online Material

www.sciencemag.org/cgi/content/full/316/5828/1212/DC1
Materials and Methods
SOM Text
Figs. S1 to S7
Table S1
References
Movie S1

10 November 2006; accepted 19 April 2007
10.1126/science.1137406

NALDI Chips

New nanotechnology-enabled matrix-free target plates are available for use primarily with Bruker's FLEX-series of matrix-assisted laser desorption ionization (MALDI) time-of-flight (TOF) mass spectrometers. These Nanosys plates are known as Capture and Analyze NALDI chips. NALDI chips provide significant sensitivity, throughput, and ease-of-use benefits for the analysis of small molecules such as drug compounds, small peptides, natural products, pesticides, and many other low-mass molecules that previously were difficult to analyze. These molecules typically have to be analyzed through liquid chromatography-mass spectrometry, which is time-consuming, is less robust, and requires more operator training. Potential applications of NALDI chips combined with TOF mass spectrometers include chemistry and molecular biology research, molecular diagnostics and molecular imaging research, pharmaceuticals, biotechnology, and other research and analysis.

Nanosys/Bruker Daltonics For information 978-667-9580 www.bdal.com

Literature

The "Gold Standard" Tools for Hematopoietic Stem Cell Research is a product guide with a variety of reagents and services. Examples of products include MethoCult, a methylcellulose-based medium for hematopoietic colony assays. Specific formulations are available for human, mouse, and rat hematopoietic cells. RoboSep is a fully automated cell separator based on the column-free EasySep system. It can label and separate up to four different samples at one time. It allows for positive or negative selection of virtually any cell type from any species and sample type, including whole blood.

StemCell Technologies For information 800-667-0322 www.stemcell.com

Coated Roller Bottles

The NUNC InVitro PDL Coated PETG Roller Bottles come coated with poly-d-lysine (PDL) through a proprietary process. PDL is a synthetic mimic of the extracellular matrix that has been shown to enhance cell attachment, growth, and differentiation in serum-free and serum-containing media of select cell lines such as HEK-293 cells. The bottles are constructed of shatter-resistant, optically clear polyethylene terephthalate glycol (PETC). The bottles have a shelf-life of two years at temperatures from 4 to 25 °C.

Thermo Fischer Scientific For information 800-446-2543 www.nuncbrand.com

Microplate Handler

The R-Series BenchCel Microplate Handling System features enhanced positional accuracy, increased payload, reduced installation time, and simple user adjustment. A new quick-swap robot module allows for fast exchange of one of the most critical and complex mechanical assemblies in a plate handler. The R-Series features a unique high-speed plate shuttle that accesses the integrated microplate stacks and peripheral instruments. Even the smallest system in the series can support three peripheral instruments, allowing customers to create highly configurable workstations that combine a broad range of functionality, including barcode labeling, microplate sealing, plate reading, and centrifugation. Users can choose from two-stack, four-stack, and six-stack configurations and from four sizes of removable racks. A delidding function removes and replaces microplate lids.

Velocity11 For information +44 1763 269115 www.velocity11.com

Spectroscopy and Chemical Information Software

Version 3.0 of KnowItAll Enterprise Server and KnowItAll AnyWare 1.0, a new browser-based client, have been released. KnowItAll Enterprise Server version 3.0 allows a database to be built on a server and viewed worldwide at all sites of an organization via the KnowItAll Informatics System Windows client or the KnowItAll AnyWare browser client. The same server technology that was first introduced in 2003 to deliver Bio-Rad's Sadtler infrared and nuclear magnetic resonance reference spectral database to users via the Internet can now be used behind an organization's firewall to store and search proprietary structural, spectral, chromatographic, and other textual data from chemical, biological, or process environments. KnowItAll AnyWare is a platform-independent, browser-based, and device-independent client that permits the searching and browsing of data stored on a KnowItAll Enterprise Server. KnowItAll AnyWare extends the reach of the KnowItAll platform client throughout organizations so any user, using any hardware platform, any operating system, or any web browser, can access spectral, structural, or chromatographic data anywhere in the world.

Bio-Rad Laboratories For information 267-322-6948 www.bio-rad.com

Premade Western Blots

Human cell line premade western blots are prepared with various cellular lysates from epithelial, endothelial, skin cells, muscle cells, and cancer cell lines. The epithelial cell blot includes mammary, renal cortical, renal proximal tubule, bronchial, and prostate epithelial cells. The endothelial cell blot includes pulmonary artery, coronary artery, iliac artery, aortic artery, lung microvascular, umbilical vein, umbilical artery, and dermal microvascular endothelial cells. The skin cell blot includes epidermal keratinocytes adult, epidermal keratinocytes neo, dermal fibroblasts adult and fibroblasts neo, microvascular endothelial adult, and microvascular endothelials neo cells.

G-Biosciences/Genotech For information 314-991-6034 www.GBiosciences.com

Infrared Spectrometer

The Spectrum 400 is an advanced tool combining optimized near-infrared (NIR) and mid-infrared (MIR) spectroscopy in a single, research-grade instrument. The Spectrum 400 features the ability to automatically switch between NIR and MIR measurement modes and dual sampling positions, enabling the user to rapidly change between applications. It includes an extensive software suite to guide and trouble-shoot method development and validation. It can be used in conjunction with the Spotlight 400 Fourier transform-infrared imaging system.

Perkin-Elmer For information 781-663-6900 www.perkinelmer.com/spectrum400

Newly offered instrumentation, apparatus, and laboratory materials of interest to researchers in all disciplines in academic, industrial, and government organizations are featured in this space. Emphasis is given to purpose, chief characteristics, and availability of products and materials. Endorsement by *Science* or AAAS of any products or materials mentioned is not implied. Additional information may be obtained from the manufacturer or supplier.

Published by AAAS